University of Bath

PHD

Development of new bis(thiosemicarbazonates) and investigations into their potential as molecular imaging and therapeutic agents

Arrowsmith, Rory

Award date:
2013

Awarding institution:
University of Bath

Link to publication

Alternative formats
If you require this document in an alternative format, please contact:
openaccess@bath.ac.uk

Copyright of this thesis rests with the author. Access is subject to the above licence, if given. If no licence is specified above, original content in this thesis is licensed under the terms of the Creative Commons Attribution-NonCommercial 4.0 International (CC BY-NC-ND 4.0) Licence (https://creativecommons.org/licenses/by-nc-nd/4.0/). Any third-party copyright material present remains the property of its respective owner(s) and is licensed under its existing terms.

Take down policy
If you consider content within Bath's Research Portal to be in breach of UK law, please contact: openaccess@bath.ac.uk with the details. Your claim will be investigated and, where appropriate, the item will be removed from public view as soon as possible.

Download date: 05. May. 2023

Development of new bis(thiosemicarbazonates) and investigations into their potential as molecular imaging and therapeutic agents

Rory Louis Arrowsmith

A thesis submitted for the degree of Doctor of Philosophy University of Bath

Department of Chemistry

February 2013

Copyright

Attention is drawn to the fact that copyright of this thesis rests with the author. A copy of this thesis has been supplied on condition that anyone who consults it is understood to recognise that copyright rests with the author and they must not copy it or use it except as permitted by law or with the consent of the author.

This thesis may be made available for consultation within the University Library and may be photocopied or lent to other libraries for purposes of consultation.

University of Bath, February **2013**

List of publications resulting from this PhD

1. P. A. Waghorn,* M. W. Jones, M. B. M. Theobald, **R. L. Arrowsmith**, S. I. Pascu, S. W. Botchway, S. Faulkner and J. R. Dilworth*. Shining light on the stability of metal thiosemicarbazonate complexes in living cells by FLIM. (Edge Article) *Chemical Science,* **2013**, Advance Article

2. **R. L. Arrowsmith**, S. I. Pascu* and H. Smugowski. New developments in the biomedical chemistry of transition metal complexes: from small molecules to nanotheranostics design. *RSC Specialist Periodical Reports,* **2012**, 38, *1-35*.

3. Z. Y. Hu, G. D. Pantos, N. Kuganathan, **R. L. Arrowsmith**, R. M. J. Jacobs, G. Kociok-Köhn, J. O'Byrne, K. Jurkschat, P. Burgos, R. M. Tyrrell, S. W. Botchway, J. K. M. Sanders and S. I. Pascu*. Interactions between Amino acid-Tagged Naphthalenediimide and Single Walled Carbon Nanotubes: Synthesis, Spectroscopic Investigations, DFT calculations and Cellular Translocation of NDI-SWNT Composite. *Advanced Functional Materials* **2012**, *22(3), 503-518*

4. **R. L. Arrowsmith**, P. A. Waghorn,* M. W. Jones, A. Bauman, S. K. Brayshaw, Z. Y. Hu, G. Kociok-Köhn, T. L. Mindt, R. M. Tyrrell, S. W. Botchway, J. R. Dilworth, and S. I. Pascu*. Fluorescent Gallium and Indium *Bis*(thiosemicarbazonates) and their Radiolabelled Analogues: Synthesis and Cellular Confocal Fluorescence Imaging. *Dalton Trans.* **2011**, *40*, 6238-6252.

5. S. I. Pascu*, **R. L. Arrowsmith**, S. R. Bayly, S. Brayshaw and Z. Y. Hu. Towards nanomedicines: design protocols to assemble, visualize and test carbon nanotube probes for multi-modality biomedical imaging. *Philos. Trans. R. Soc. A-Math. Phys. Eng. Sci.* **2010**, *368*, 3683-3712.

6. S. I. Pascu,* P. A. Waghorn, B. W. C. Kennedy, **R. L. Arrowsmith**, S. R. Bayly, J. R. Dilworth, M. Christlieb, R. M. Tyrrell, J. Zhong, R. M. Kowalczyk, D. Collison, P. K. Aley, G. C. Churchill and F. I. Aigbirhio. Fluorescent Copper(II) Bis(thiosemicarbazonates): Synthesis, Structures, Electron Paramagnetic Resonance, Radiolabeling, In Vitro Cytotoxicity and Confocal Fluorescence Microscopy Studies. *Chem.- Asian. J.* **2010**, *5*, 506.

List of talks presented during this PhD

1. **R. L. Arrowsmith**, B. M. Zeglis, N. Viola-Villegas, V. Divilov, M. W. Jones, P. A. Waghorn, F. L. Phillips, T. L. Mindt, I. M. Eggleston, S. W. Botchway, J. R. Dilworth, F. I. Aigbirhio, , J. S. Lewis, S. I. Pascu*. *19th International Symposium on Radiopharmaceutical Sciences, VuMC, Amsterdam, the Netherlands,* **28th August – 2nd September 2011**.

2. **R. L. Arrowsmith**, J. L. Zhong, G. Kociok-Köhn, P. A. Waghorn, J. R. Dilworth, Rex M. Tyrrell, S. I. Pascu*. New intrinsically fluorescent Zn(II), Cu(II), Ga(III) and In(III) bis(thiosemicarbazonato) complexes for multimodal imaging of cancer. *Royal Society of Chemistry – Photochemistry Group, Young and Early Career Researchers', Meeting 2010, Department of Chemistry, Durham University,* **13th January 2010**.

3. **R. L. Arrowsmith**, J. L. Zhong, B. W. C. Kennedy, R. M. Tyrrell, J. R. Dilworth, S. I. Pascu*. Bio-Imaging and Cytotoxicity of Bis(thiosemicarbazonato) complexes. *Metals in Medicine, Trin, Switzerland,* **5th February 2009**.

Contents

Abstract

Chapter 1 – Introduction, describes medical imaging modalities focussing on molecular imaging agents for SPECT and PET, where examples of dual modal imaging with either technique or theranostics (simultaneous diagnosis and therapy) are highlighted. Significant examples of imaging probes using technetium and rhenium are included with an emphasis on emerging zinc, copper, gallium and indium complexes. Development of metal complexes conjugated to agents enabling targeting of receptors is described as well as hypoxia and its diagnosis and therapy.

Chapter 2-5 describe the synthesis and characterisation of bis(thiosemicarbazonato) ligands (Chapter 2) and zinc & copper (Chapter 3), gallium (Chapter 4) and indium (Chapter 5) complexes. An interesting isomerism is explored using Density Functional Theory (DFT). The complexes are investigated for their suitability as molecular imaging probes, firstly by testing their spectroscopic properties using UV-visible and fluorescence spectroscopies. This is followed by assessing their stability, utilising the aforementioned techniques with biologically relevant media in solution and in biological cells *in vitro*, using fluorescence lifetime imaging microscopy (FLIM). Laser scanning confocal microscopy is used to investigate cell uptake demonstrating localisation within organelles. Furthermore, gallium and indium complexes are evaluated for their potential as hypoxia imaging agents, *in vitro* in addition to the investigation of indium complex nuclear and chromosomal uptake. Lastly, copper and gallium complexes are studied in nude mice with PC-3 xenografts under normoxic conditions (by the Jason Lewis Group, MSKCC, NYC).

Chapter 6. Compounds introduced in chapters 2-5 are studied and compared for their *in vitro* cytotoxicity using MTT and LDH assays. MTT assay is used to determine a quantitative value of toxicity, to enable a direct comparison of all compounds tested and in cancerous and non-cancerous cell lines. LDH assay on the other hand, provides insight into the mechanism of molecular action upon the cell membrane, which may explain differences obtained using MTT assay in this study and trypan blue experiments, which relies upon membrane integrity.

Chapter 7 explores methods of attaching a targeting agent, a bombesin analogue, to the bis(thiosemicarbazonato) complexes. Novel complexes are characterised and subsequently investigated in cells for cytotoxicity and by confocal microscopy and FLIM.

Chapter 8 describes a summary of this thesis.

Chapter 9 contains the entire experimental data for the work of this thesis.

Acknowledgements

I would first like to thank my supervisor Dr Sofia I. Pascu for her support, guidance and inspiration throughout this project. I am very appreciative to Prof Paul Raithby and all of his group, especially Dr Simon K. Brayshaw who helped me get started in the lab and with computational chemistry and Dr Chris Woodall for photochemistry experiments. I would like to thank Gabriele Kociok-Köhn for X-ray crystallographic studies. Thanks are also due to Brett Kennedy for my initial training, Haobo Ge for assistance in acquiring some of the MTT data and Johan Stojanović for help with acquiring stability assay data. I would like to acknowledge project students Jennifer Williams, Fatima Merzoug, Francesca Phillips and Rosie Chhatwal and all other members of the SIP group. I am very grateful for the training in pharmacology by Dr Julia L. Zhong and for access to cell culture facilities, Prof Rex M. Tyrrell. I very much appreciate the help and guidance of Dr Ian M. Eggleston with peptide synthesis, coupling and purification. I am very appreciative of the microscopy help and training provided by Dr Adrian Rogers and Mrs Ursula Potter, Microscopy and Analysis Suite, University of Bath.

I would like to thank Dr Franklin I. Aigbirhio, Dr. Patrick Riss, Dr Laurent Brichard, University of Cambridge, and Dr Phillip A. Waghorn and Prof Jon R. Dilworth, University of Oxford, Dr Laurence Carroll, Mr Frazer J. Twyman, Hammersmith Hospital, Imperial College London for help with radiolabelling experiments. Thanks are due to Dr Israt S. Alam for conducting *in vitro* hypoxia experiments. I would like to thank Sofia, Dr Brian Zeglis and Jason Lewis, Memorial Sloan-Kettering Cancer Center, New York for carrying out *in vivo* experiments. Thanks are due to Prof Thomas Mindt and his group, University Hospital Basel and his group for ^{68}Ga radiolabelling. I would like to acknowledge Dr Stan Botchway, Dr Michael Jones (University of Oxford), Mr Haobo Ge (University of Bath), Mr Rahul Yadav, Dr Pierre Burgos, Mr Alistair Mackenzie, Mr Alexander Henman, Dr Yusuf Mohammed and Ms Ana Estandarte for their assistance in running samples at the Rutherford Appleton Laboratory.

Last, but certainly not least, I would like to thank my wife, Merle, who has been a great person to discuss my science with and supported me through thick and thin.

Abbreviations

2D two-dimensional
3D three-dimensional
A absorbance
Å Angstrom
Ac acetyl
Ar aromatic
ATSM/A diacetyl-2-(4-*N*-methyl-3-thiosemicarbazone)
ATP Adenosine Triphosphate
BAM biologically active molecule
BIAN bis(imino)acenaphthene
bipy 2,2'-biyridine
Bodipy boron-dipyrromethane
Bq Becquerel
C Curie
°C degrees Celsius
cm centimetre
CT Computed Tomography
cyclam 1,4,6,11-tetraazacyclotetradecane
D Emission Integral
δ chemical shift
DABCO 1,4-diazabicyclo[2.2.2]octane
DCC *N,N'*-dicyclohexylcarbodiimide
DCM dichloromethane
DDQ 2,3-dichloro-5,6-dicyano-1,4-benzoquinone
deg degree
DIPEA *N,N'*-diisopropylethylamine
DMEM Dulbecco's Modified Eagles Medium
DMF *N,N'*-dimethylformamide
DMSO dimethyl sulfoxide
DNA deoxyribonucleic acid
DOTA 1,4,7,10-tetraazacyclododecane-1,4,7,10-tetraacetic acid
DPA dipicolylamine
DTPA diethylene triamine pentaacetic acid
EC electron capture
eV electron volt
EDC 1-ethyl-3-(3'-dimethylaminopropyl) carbodiimide
EDTA ethylenediaminetetraacetic acid
EGFR epidermal growth factor receptor
EPR electron paramagnetic resonance
eq equivalents
ESI electrospray ionization
Et ethyl
f femto
fab antibody binding fragment
Φ quantum yield
fab antibody fragment
FDG 2-fluoro-2-deoxy-D-glucose
FLIM fluorescence lifetime imaging microscopy
FMISO fluoromisonidazole
FRET Fluorescence Resonance Energy Transfer

FWHM full width at half maximum

g gram

h hour

η refractive index

HBED *N*,*N*′-bis(2-ydroxybenzyl)ethylene-diamine-*N*,*N*′-diacetic acid

HBSS Hank's Buffered Salt Solution

HER2 Human Epidermal Growth Factor Receptor 2

HIF hypoxia-inducible factor

HOBt hydroxybenzotriazole

HPLC high performance liquid chromatography

Hz hertz

GLP-1 Glucagon-like peptide receptor-1

I_R Flux Intensity

IR infra-red

K Kelvin

k kilo / equilibrium constant

L litre

LC Liquid Chromatography

LLP2A *N*-[[4-[[[2-ethylphenyl)amino]carbonyl]amino]phenyl]acetyl]-N^{ε}-6-[(*2E*)-1-oxo-3-(3-pyridinyl-2-propenyl)]-*L*-lysyl-*L*-2-aminohexanedioyl-(1-amino-1-cyclohexane)carboxamide

λ wavelength

λ_{ex} excitation wavelength

λ_{max} maximum wavelength of absorption

M molar / mega

m milli / meter

μ micro

MAG mercaptoacetylglycylglycylglycine

MDP methyl diphosphonate

Me methyl

MEM minimum essential medium

min minute

mol mole

MRI magnetic resonance imaging

MS mass spectrometry

m/z mass-to-charge ratio

n nano

NAD nicotinamide adenine dinucleotide

NADH nicotinamide adenine dinucleotide phosphate

NHS *N*-hydroxysuccinimide

NIR near-infrared

NMR nuclear magnetic resonance

NOTA 1,4,7-triazacyclononane-1,4,7-carboxylic acid

OFI Optical Fluorescence Imaging

ORTEP Oak Ridge Thermal Ellipsoid Program

P partition coefficient

p pico

PBS phosphate buffered solution

PDT photodynamic therapy

PEG polyethylene glycol

PET positron emission tomography

Ph phenyl

pH $-\log_{10}[H^+]$

ppm parts per million

PTSM pyruvaldehyde-*bis*(methyl-*N*-thiosemicarbazone)
RGD L-Arginyl-Glycyl-L-Aspartic acid
RPMI Royal Park Memorial Institute
rt room temperature
R_t retention time
s second
SPECT single photon emission computed tomography
$t_{1/2}$ half life
τ fluorescence lifetime
τ_1 major component of fluorescence lifetime
τ_2 minor component of fluorescence lifetime
τ_m weighted average of fluorescence lifetime components
TCSPC Time-Correlated Single Photon Counting
t-Boc *tert*-butyloxycarbonyl
TETA 1,4,8,11-tetraazacyclododecane-1,4,8,11-tetraacetic acid
TFA trifluoroacetic acid
THF tetrahydrofuran
US ultrasound
UV ultraviolet
vis visible

Numbering of compounds

Mono(thiosemicarbazonato) ligands

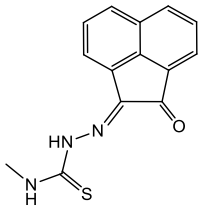

Compound **ia**

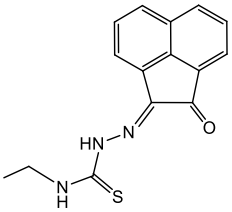

Compound **ib**

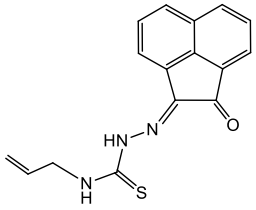

Compound **ic**

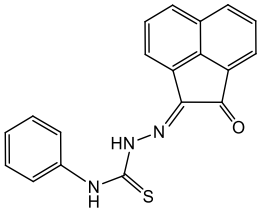

Compound **id**

Bis(thiosemicarbazonato) ligands

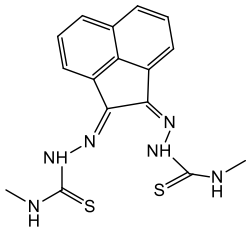

Compound **iia**

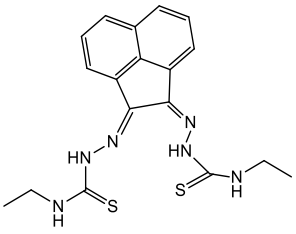

Compound **iib**

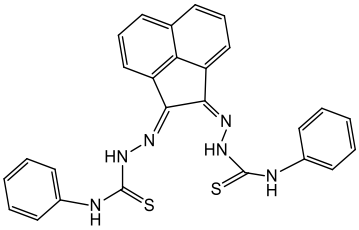

Compound **iic**

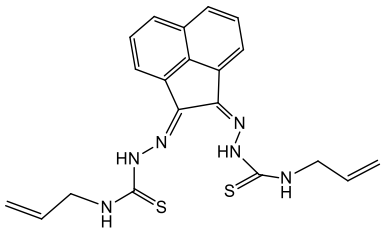

Compound **iid**

Zinc bis(thiosemicarbazonato) complexes

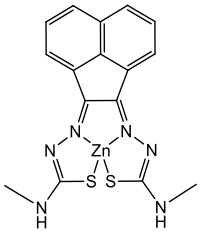

Compound **1a**

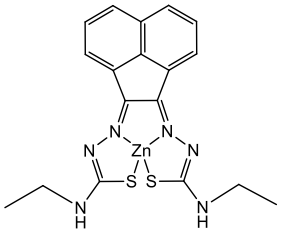

Compound **1b**

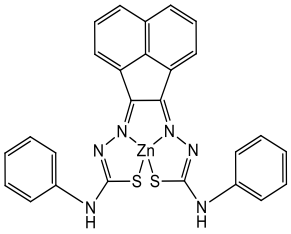

Compound **1c**

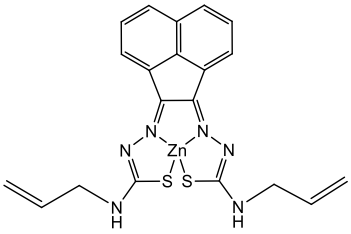

Compound **1d**

Copper bis(thiosemicarbazonato) complexes

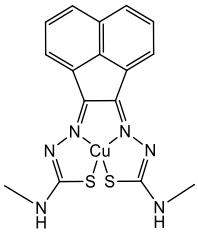

Compound **2a**

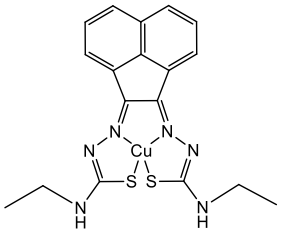

Compound **2b**

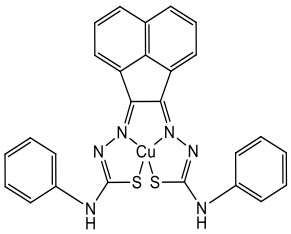

Compound **2c**

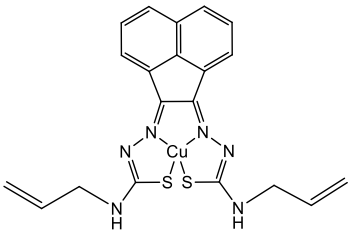

Compound **2d**

Gallium Chloride bis(thiosemicarbazonato) complexes

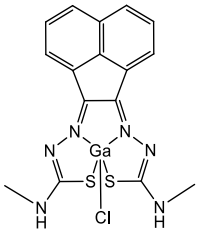

Compound **3a**

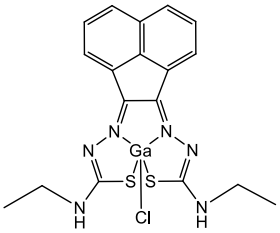

Compound **3b**

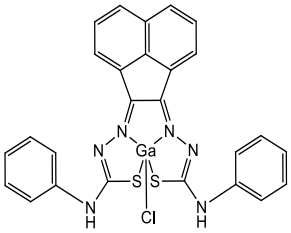

Compound **3c**

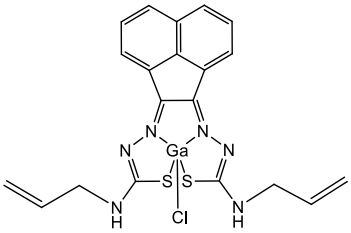

Compound **3d**

Indium Chloride bis(thiosemicarbazonato) complexes

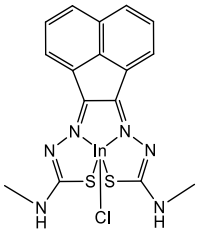

Compound **4a**

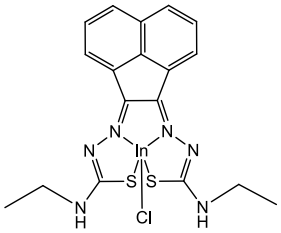

Compound **4b**

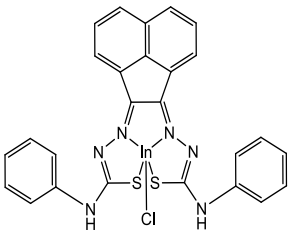

Compound **4c**

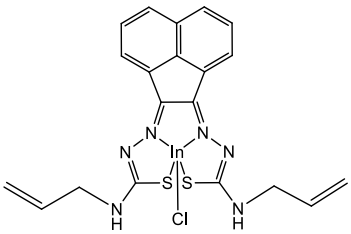

Compound **4d**

Asymmetric zinc bis(thiosemicarbazonato) complexes

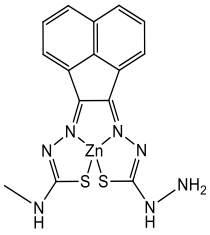

Compound **1aN**

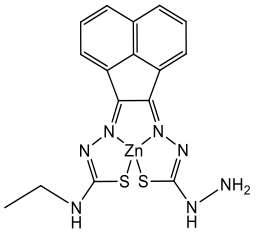

Compound **1bN**

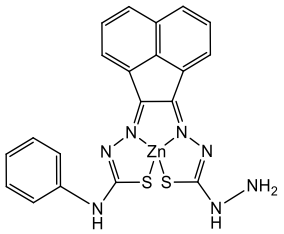

Compound **1cN**

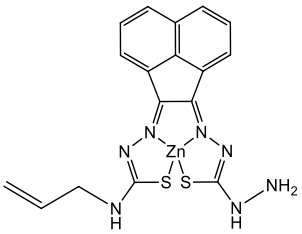

Compound **1dN**

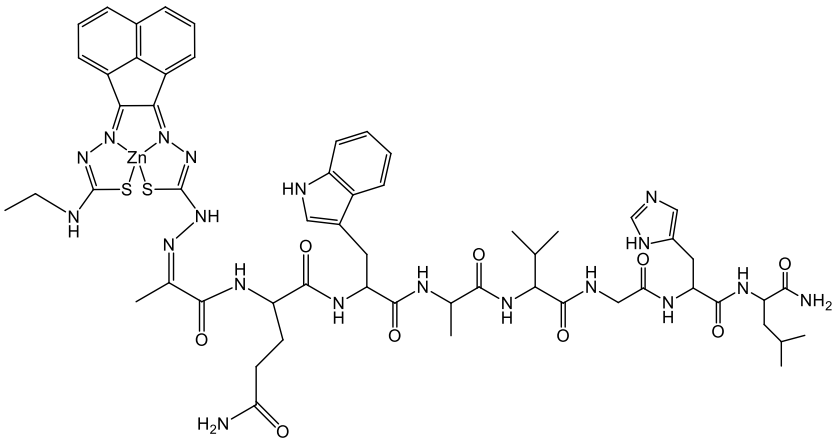

Compound **1bB**

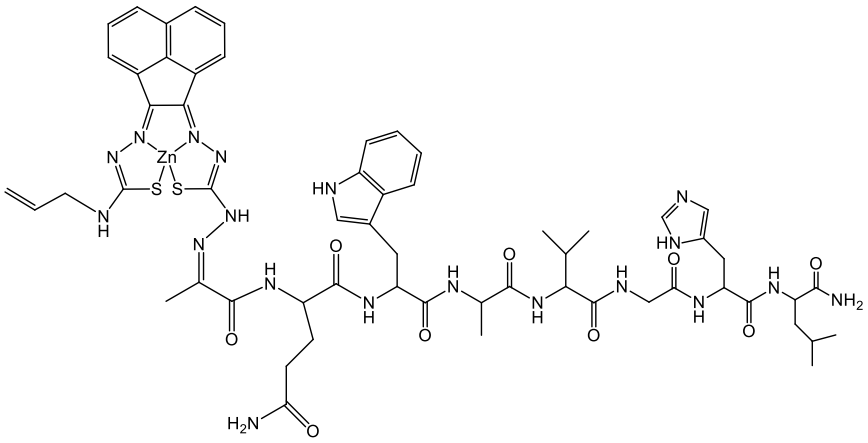

Compound **1dB**

Asymmetric gallium bis(thiosemicarbazonato) complex

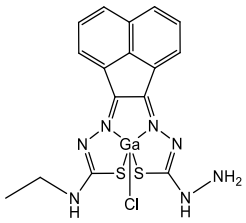

Compound **3bN**

Chapter 1. Introduction

1.1. Perspective

Cancer accounts for more than a third of deaths in the England and Wales,[1] (44.3 % males and 32.2 % females). Furthermore, current lifetime risk of developing a malignant tumour has recently been calculated as high as 40%, and rising, therefore the necessity for earlier cancer detection, identification and effective therapy of later cancer stages is becoming increasingly important.[2] Hypoxic tissue develops under low in oxygen concentrations and has been correlated to cancer, strokes and heart disease.[3, 4] As a tumour grows the intercapillary distance increases until it becomes greater than the diffusion range of oxygen (ca. 200 μm) *(Figure 1.1)*. Furthermore, limited perfusion and as a result erratic blood supply has also been shown to increase hypoxia.

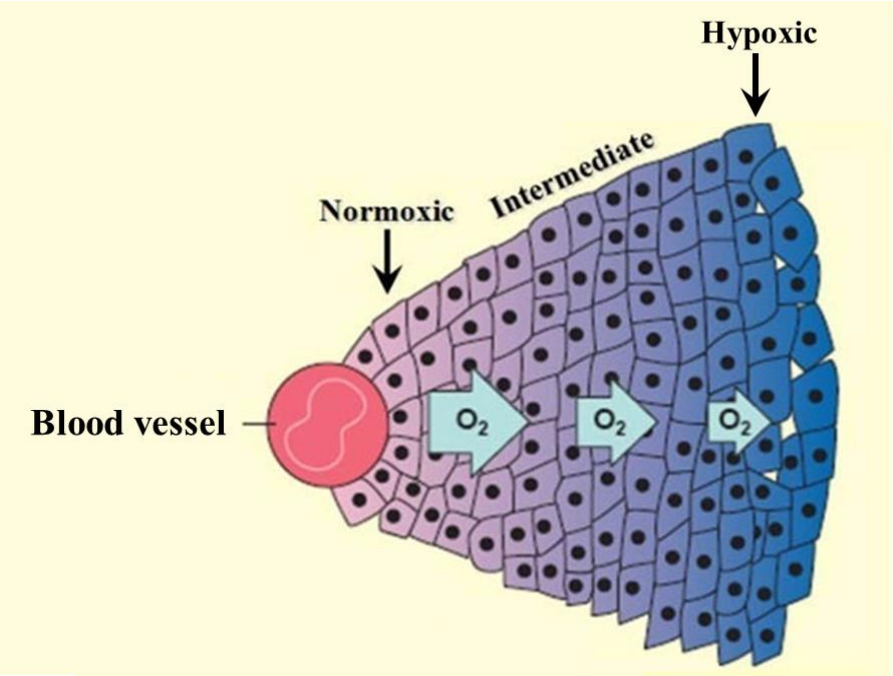

Figure 1.1. Illustration of relative oxygen levels in a tumour, whereby a greater distance from the blood vessel signifies a lower threshold of oxygen.[5]

A crucial protein in the development of this process is hypoxia inducible factor-1 (HIF-1), the mechanism of action of which is beautifully simple: under normal oxygen conditions (normoxia) the protein, HIF-1α, is hydroxylated at numerous proline residues resulting in ubiquitination and proteasomal degradation; under insufficient oxygen conditions, however, HIF-1α translocates to the nucleus and combines with protein HIF-1β to form the heterodimer, HIF-1 *(Figure 1.2)*. This transcription factor is subsequently responsible for the upregulation of up to 100 proteins, in turn altering the cellular glucose metabolism, metastasis, cell proliferation, angiogenesis, iron metabolism and drug resistance, all of which increase the chances of cancer cell survival and decrease prognosis.[6]

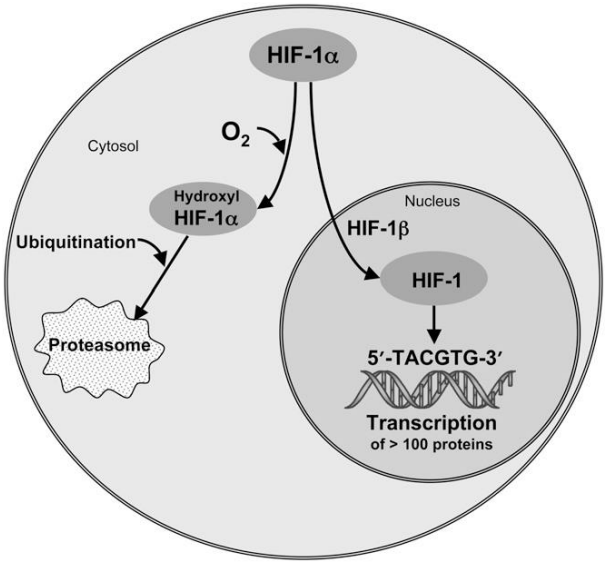

Figure 1.2. A diagram summarising the mechanism of hypoxia inducible factor-1 release, from Ref [6].

Early diagnosis of hypoxia would allow a change in treatment plan and therefore improve patient survival chances. Prognosis is often poor at this stage of cancer since traditional therapies do not reach hypoxic tissue due to isolation from capillaries. Additionally, most therapies target rapidly dividing cells, whereas under hypoxic conditions cells grow slowly due to reduced oxygen and nutrient supply. Finally, as mentioned above, hypoxia promotes genetic instability, thus increasing the likelihood of drug resistance and metastases.[7,8] As a result there is growing interest in molecular imaging as a non-invasive, highly sensitive method capable of both revealing solid tumours and enhancing our understanding of the molecular basis of the disease –

essential for diagnosis, assessing tumour progression and patient prognosis.[9,10] The aims of this project were to develop molecular imaging probes with therapeutic potential to be studied both *in vivo*, by positron emission tomography (PET) or single photon emission computed tomography (SPECT) and also *in vitro*, by fluorescence imaging and cytotoxicity assays.

Table 1.1. Summary of the characteristics of medical imaging modalities. OFI = Optical Fluorescence Imaging, A = Anatomical, P = Physiological, M = molecular, nwc = not well characterised. Adapted from references [9] and [10].

Technique	Resolution	Depth	Information	Sensitivity/M
CT	50 µm	No limit	A, P	nwc
MRI	10 – 100 µm	No limit	A, P, M	10^{-3}-10^{-5}
Ultrasound	50 µm	Frequency Dependant	A, P	nwc
SPECT	1 – 2 mm	No limit	P, M	10^{-10}-10^{-11}
PET	1 – 2 mm	No limit	P, M	10^{-11}-10^{-12}
OFI	2 – 3 mm	<1 cm	P, M	10^{-9} -10^{-12}

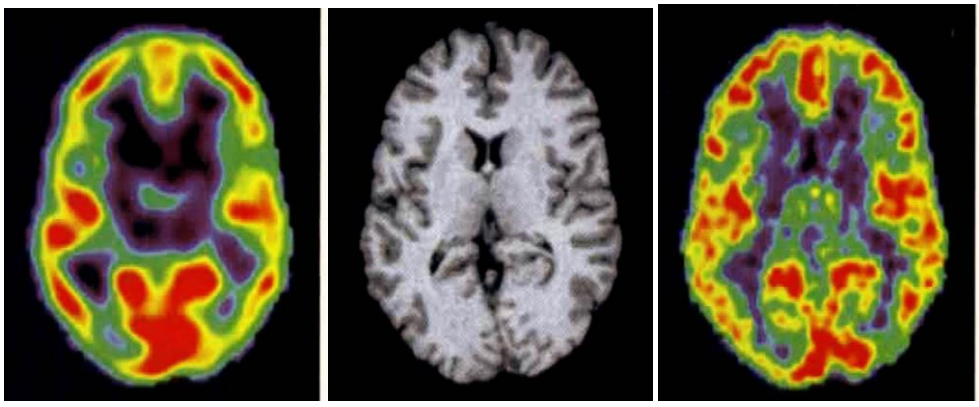

Figure 1.3. Normal human brain imaged by SPECT ^{123}I-liomazenil (left), MRI (middle) and ^{11}C-flumazenil (right), which correspond to the same slice.[11]

Medical imaging techniques can provide anatomical, physiological and even molecular information *(Table 1.1, Figure 1.3)*. Traditional imaging modalities such as X-ray and computerised tomography (CT) irradiate tissue with harmful radiation and provide anatomical information. Anatomical imaging tools have benefited from progress in spatial and temporal resolution, but they do not readily recognise

physiological abnormalities. The capacity of these methods to differentiate cancer is therefore reserved for the later stages of disease progression. Consequently there is a current trend towards developing more sensitive molecular imaging techniques utilising radionuclides for PET or SPECT, which enter diseased tissue selectively. Furthermore, healthy tissues remain unharmed due to the low concentrations required (ca. 10^{11} M). These modalities give both functional and metabolistic information, which not only accelerate understanding of the molecular basis of disease, but also enable accurate detection and diagnosis. Metallic radionuclides ultimately undergo uptake within cells and, while the distribution of their complexes can be determined *in vivo* at the 1-2 mm range of resolution, little is known of their fate once they reach the intercellular environment. This hampers the rational design of new diagnostics and therapeutics and ultimately the accurate diagnosis of cancer. However, there is growing interest in molecular imaging as a non-invasive, highly sensitive tool capable of both early diagnosis and enhancing the understanding of the molecular basis of the disease. [9,10]

Intense research is currently underway for the development of new PET and SPECT agents for imaging a wide range of disease states, and of new drugs for targeted radiotherapy. Radiopharmaceuticals chosen for the purpose of diagnosis are usually positron emitters (PET) or gamma emitters (SPECT), whereas therapeutic radiopharmaceuticals usually rely upon β^- emission and the Auger effect causing cell death. The choice of radioisotope is also made according to an optimum half-life, which at the same time minimises radiation doses whilst giving sufficient time for synthesis and accumulation.

In 2007, this was defined by the Society of Nuclear Medicine defined Molecular Imaging as a new interdisciplinary research field, which is at the interface between clinical and preclinical research. The rapid development of this key area is highlighted by the increasing demand for new imaging probes for specific biological targets.[12] By the end of 2010 more than 3.2 million positron emission tomography (PET) studies had been carried out worldwide and this number continues to rise. It is widely recognised that optimal disease management can only be achieved by

monitoring patient status before, during and after therapy. PET agents offer high resolution, high sensitivity, non-invasive imaging with provision of invaluable diagnosis of biological function at agent concentrations below the pharmacological threshold, at which dosage no significant drug effect is observed.

Since no medical imaging technique is ideal for acquiring all the necessary information, the combination of modalities such as SPECT/CT, PET/X-ray, PET/MRI or, most frequently PET/CT, allows for better image quality, shorter scanning time and reduced costs. Such multimodal imaging results in more efficient use of radiopharmaceuticals (i.e. drugs containing a radionuclide) and more facile recognition of abnormalities. A combination with optical imaging enables both greater understanding of the probe both in cells and in organisms as well as enabling the identification of tumours. The advantages of combining the high sensitivity of PET or SPECT, which are not limited by tissue penetration with optical imaging presents a very useful marriage of modalities with potential to improve both scientific knowledge and patient diagnosis and therapy.

1.2. Single Photon Emission Computed Tomography

The first tomographic device for medical imaging, Single Photon Emmision Computed Tomography, SPECT, was reported by Kuhl and Edwards in 1963.[13] The technique utilises gamma emission, which occurs when a highly energetic nucleus relaxes to a ground state. This type of emission can be detected using a gamma camera, yielding a 3D image of radionuclide uptake.[14] Commonly used radioisotopes for SPECT include ^{123}I, ^{131}I, ^{67}Ga and ^{111}In *(Table 1.2)*. The most frequently used however is ^{99m}Tc, which will be discussed further in section 1.4.

Table 1.2. Relevant radionuclides for SPECT imaging

Radionuclide	Half-life ($t_{1/2}$) / hours	Mode of Decay (% branching ratio)	Availability	Application
^{99m}Tc	6.0	it (99.9)	Gen: ^{99}Mo/^{99m}Tc	SPECT
^{111}In	67.392	ec (100)	Cyclotron	SPECT/e^- therapy
^{67}Ga	78.281	ec (100)	Cyclotron	SPECT
^{123}I	13.2	ec (100)	Cyclotron	SPECT
^{131}I	193	[a]	Reactor	SPECT/ β^- therapy

[a] Iodine-131 has a process of six β^- and fourteen γ-ray emissions

1.3. Positron Emission Tomography

Compared to SPECT, PET imaging has a crucial advantage in terms of sensitivity and resolution *(Table 1.1)*. PET was first reported by Michel Ter-Pogossian in 1972 and is based on the monitoring of positron-electron annihilation. PET therefore relies on the presence of a positron emitting radionuclide where a proton is converted into a neutron. A single annihilation causes emission of two gamma rays ca. 180^o apart, each with a 511 keV energy *(Figure 1.4)*. Detectors are placed around the patient so that simultaneous gamma ray detection can be traced to the point of annihilation by following the line of response (LOR). These are subsequently reconstructed to produce a 3D image of the respective environment and characterise any abnormalities.

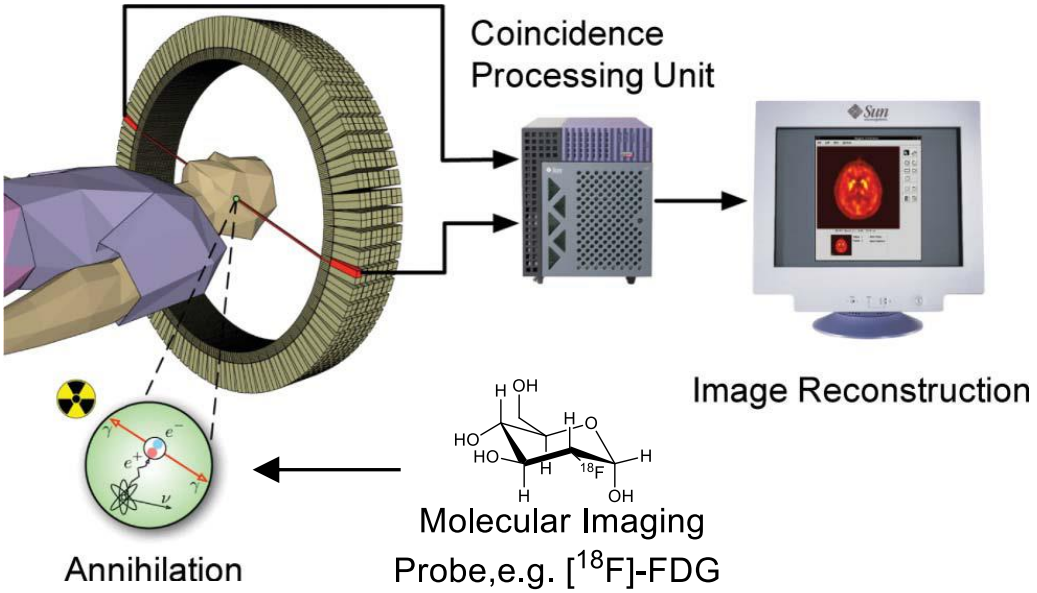

Figure 1.4. A representation of PET imaging, adapted with permission from reference [15].

Use of PET was initially limited by the requirement of an on-site cyclotron, the short half-lives of available positron emitting radionuclides, and highly expensive equipment. Predominantly a research tool in the beginning, it has now become an essential diagnostic technique, with more than 2,000 PET centres worldwide.[16]

Table 1.3. Commonly used radionuclides for PET imaging

Radionuclide	Half-life ($t_{1/2}$)	Mode of Decay (% branching ratio)	Availability	Application
^{18}F	1.83 h	β^+ (97) ec (3)	Cyclotron	PET
^{11}C	0.34 h	β^+ (100)	Cyclotron	PET
^{64}Cu	12.701 h	ec + β^+ (61.5) β^+ (17.6) β^- (38.5)	Cyclotron	PET
^{62}Cu	0.16 h	ec + β^+ (100) β^+ (98)	Gen: $^{62}Zn/^{62}Cu$	PET
^{68}Ga	1.13 h	ec + β^+ (100) β^+ (89.14)	Gen: $^{68}Ge/^{68}Ga$	PET
^{89}Zr	78.41 h	ec + β^+ (100) β^+ (22.74)	Cyclotron	PET
^{86}Y	14.74 h	ec + β^+ (100) β^+ (31.9)	Cyclotron	PET

The choice of radionuclide is dependent on availability, half-life and pharmacokinetics. The isotope ^{18}F ($t_{1/2}$ 109.8 min) is most widely used for imaging applications, especially incorporated into 2-[^{18}F]-fluoro-2-deoxy-D-glucose (^{18}F-FDG) where there are no limitations owing to the availability of a cyclotron typically needed for radionuclide generation. ^{18}F-FDG, the "gold standard" for PET imaging tumours / ischaemic myocardium in clinical practice, lacks selectivity for cancer and is not universally applicable for imaging all tumours: for example it does not image hypoxic tumors *per se*.

1.4. Radionuclides for therapy

Diagnosis using radiometals, such as ^{64}Cu, ^{67}Ga, ^{68}Ga, ^{99m}Tc, can be followed up by treatments with radiotherapeutic agents *(Table 1.4)* such as ^{177}Lu, ^{90}Y, and ^{111}In provided that the chemical properties of the complex are not significantly changed. Therapeutic radionuclides are emitters of either α-particles, β^--particles or low energy Auger electrons.

Table 1.4. Radionuclides for therapy

Radionuclide	Half-life ($t_{1/2}$)	Mode of Decay (% branching ratio)	Availability	Application
^{131}I	8.02 d	β^- (100)	Nuclear reactor	β-therapy
^{90}Y	64.00 h	β^- (100)	Gen: $^{90}Sr/^{90}Y$	β-therapy
^{177}Lu	6.647 d	β^- (100)	Nuclear reactor	β-therapy
^{188}Re	17.00 h	β^- (100)	Gen: $^{188}W/^{188}Re$	β-therapy
^{153}Sm	46.50 h	β^- (100)	Nuclear reactor	β-therapy
^{213}Bi	0.759 h	α (2.20)	Gen: $^{225}Ac/^{213}Bi$	α-therapy
		β^- (97.8)		β-therapy
^{225}Ac	240 h	α (100)	Gen:$^{229}Th/^{225}Ra/^{225}Ac$	α-therapy
^{223}Ra	11.4 d	α (100)	Gen: $^{227}Ac/^{227}Th/^{223}Ra$	α-therapy
^{67}Cu	2.6 d	β^-(100)	Cyclotron/reactor	β-therapy

Furthermore, a diagnostic agent combined with a therapeutic agent form a

'theranostic pair'. Intrinsically cytotoxic agents can also be radiolabelled while the use of nanoparticles filled with a biologically active molecule (BAM)-targeted drug may provide a different approach to single theranostic compounds.

1.5. Radiopharmaceuticals and multimodality probe design considerations

Radiopharmaceuticals are designed to answer a specific medical need and are based on the knowledge of molecular biology. The first generation of radiopharmaceuticals involved radioactive isotopes aimed at mimicking normal biological processes, such as 2-[^{18}F]-fluoro-2-deoxy-D-glucose and [$^{99m}TcO_4$]$^{2-}$, which take advantage of upregulated glucose uptake by cancer cells and mimic iodine uptake by the thyroid, respectively.[17] The current trend is moving towards 'second generation' of radiopharmaceuticals, which use a BAM, such as a peptide or antibody for specific targeting.

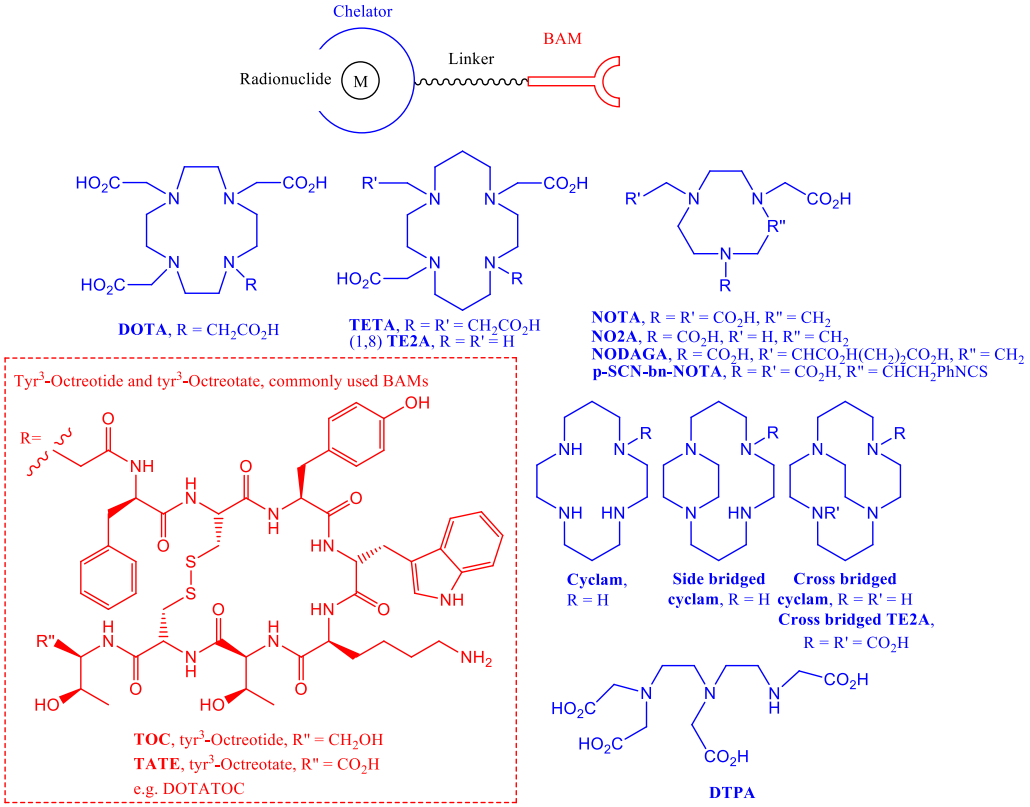

Figure 1.5. Chelator structures and targeting groups frequently used with radiopharmaceuticals

Much of the work makes use of the labelling of standard chelating agents such as 1,4,7,10-tetraazacyclododecane-N,N′,N″,N‴,-tetraacetic acid (DOTA), 1,4,8,11-tetraazacyclododecane-1,4,8,11-tetraacetic acid (TETA), 1,4,7-triazacyclononane-1,4,7-triacetic acid (NOTA), cylam or cyclam variants conjugated to a BAM *via* a linker *(Figure 1.5)*. Reviewed below are recent developments in luminescent zinc, copper, gallium, indium metal complexes for *in vitro* and/or *in vivo* imaging, multimodal imaging, theranostics (combined 'all-in-one' diagnostics and therapeutics) as well as selected examples from relevant coordination chemistry.

1.6. Technetium and rhenium based imaging probes

^{99m}Tc is metastable, which means that it does not transmute into another nucleus upon emission and was first isolated in 1959 and initially used in 1961 for thyroid diagnosis. As previously mentioned, technetium-99m is the most regularly used SPECT imaging probe, which is owed largely to its ideal half life of ca. 6 hours and its ready availability *via* a ^{99}Mo generator.

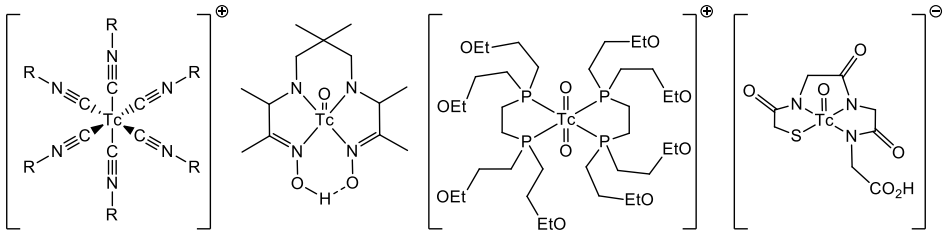

Figure 1.6. Structures of selected ^{99m}Tc complexes in commercial use

There are numerous ^{99m}Tc molecular probes in clinical use covering a wide range of imaging applications of the: brain (Ceretec™), heart (Cardiolite™ and Myoview™), kidney ([^{99m}TcO(MAG$_3$]$^+$) and bone (^{99m}Tc-MDP). Technetium complexes are additionally under development as hypoxia targeting agents, with early attempts *via* conjugation of chelate derivatives to a nitroimidazole, such as BMS-181321 *(Figure 1.7)*. [17, 18] Nitroimidazoles are promising as hypoxia selective probes, such as pimonidazole hydrochloride (Hypoxyprobe™), which is used in

immunohistochemistry or ^{18}F-fluoromisonidazole (^{18}F-FMISO), which will be discussed later. High liver uptake, due to the lipophilicity of the compound however, caused it to be unsuitable. Rey *et al.* however, recently developed a metronidazole based technetium complex with a good tumour to muscle ratio and low liver uptake *(Figure 1.7)*.[19]

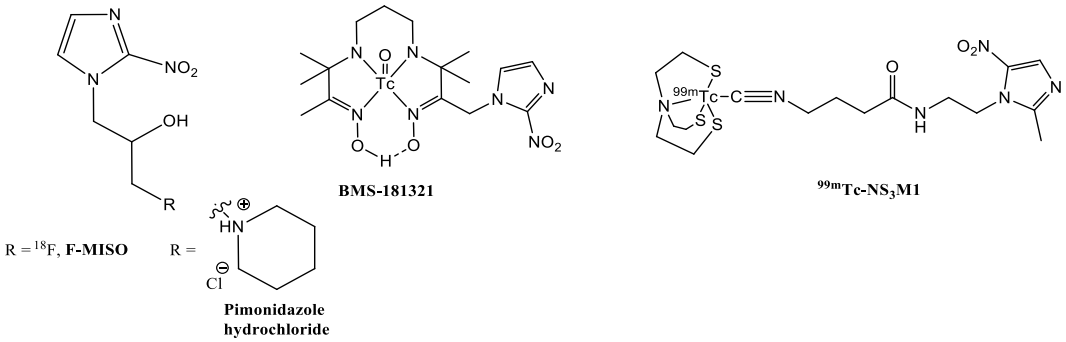

Figure 1.7. Structures of compounds developed for hypoxia selectivity

Despite the popularity of this radiometal, it does have its drawbacks. Firstly that ^{99m}Tc hinders the binding of organ specific pharmaceuticals, due to its non-physiological nature and secondly, there is no stable isotope of technetium.

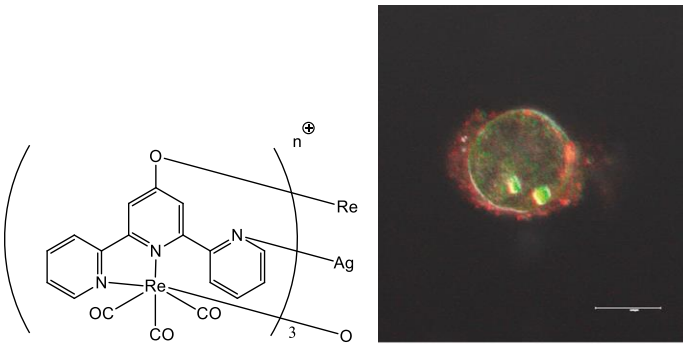

Figure 1.8. Rhenium(I) complex (left), which enters the nucleoli of cells (right)

Isostructural rhenium complexes however, are often used as analogues for *in vitro* luminescence studies, as well as being exciting *in vitro* imaging agents in their own right and with broad applications.[20] Rhenium(I) polypyridine complexes are of particular relevance as sensors, due to good quantum yields, especially since the high environmental sensitivity of rhenium(I) polypyridine complexes was reported.[21,22] Rhenium(I) complexes have long luminescent lifetimes and significant

Stokes shifts, making them highly suitable as *in vitro* probes. Coogan *et al.* have developed numerous tricarbonyl polypyridyl rhenium(I) complexes for imaging cells, [23, 24, 25] notably reporting in 2011 a Re(I) complex that can act as a carrier of ions such as silver and copper. The unfilled form of the complex does not enter cells; however, when filled with Ag^+ cations it can enter the nucleoli *(Figure 1.8).*[26] Interestingly, dinuclear tricarbonyl rhenium(I) complexes appended to peptide nucleic acid showed rapid cell uptake, low cytotoxicity and have the ability to discriminate between the nucleus and cytoplasm *via* different excitation/emission properties *(Figure 1.9).*[27] Tricarbonyl rhenium complexes have also been developed by Lo *et al.* for *in vitro* metal ion sensing and displayed increased luminescence emission and a longer lifetime upon Zn(II) or Cd(II) binding.[28] Furthermore, Alberto *et al.* developed tricarbonyl Re(I) and Tc(I) complexes in 2012 for *in vitro* and *in vivo* imaging of Altzheimer's disease. The ligand contained a phenylbenzothiazole, known to have high affinity for amyloid plaques of the disease.[29]

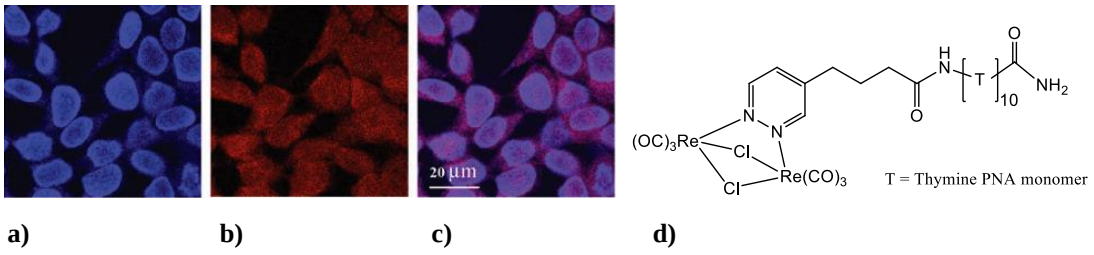

Figure 1.9. A bimetallic Re(I) complex (d) in the nucleus (a) and in the cytoplasm (b), where (c) is an overlay of (a) and (b). [27]

Numerous rhenium(I) complexes suitable for bioconjugation and fluorescence imaging are currently under development.[30] Notably, a cytotoxic folic acid-PEG derivatised Re(I) complex was investigated in A2780/AD cells, which are a multidrug resistant ovarian cancer cell line.[31] Rhenium(I) complexes with an appended α–D-glucose were developed with the purpose of monitoring glucose uptake, which is increased in cancer and showed mitochondrial uptake as well as cytotoxicity that did not depend on cell type.[32] Polypyridinerhenium(I) bis-biotin complexes were observed in HeLa cells by laser scanning confocal microscopy. [33,34] Subsequently, rhenium complexes with polylactide conjugates displayed cell uptake in A2780 cells.[35]

As mentioned above, isostructural Re/^{99m}Tc complexes can be developed for *in vitro* and *in vivo* investigations respectively. For example, Pelecanou *et al.* designed rhenium and technetium complexes incorporating the [M(CO)$_3$(NNO)] unit covalently attached to anticancer agent 2-(4'-aminophenyl)benzothiazole for theranostic SPECT applications.[36] Recently they developed new rhenium and technetium complexes of the same family for optical and SPECT imaging respectively, which demonstrate greater uptake in cell lines of cancerous origin with respect to non-cancerous lines.[37]

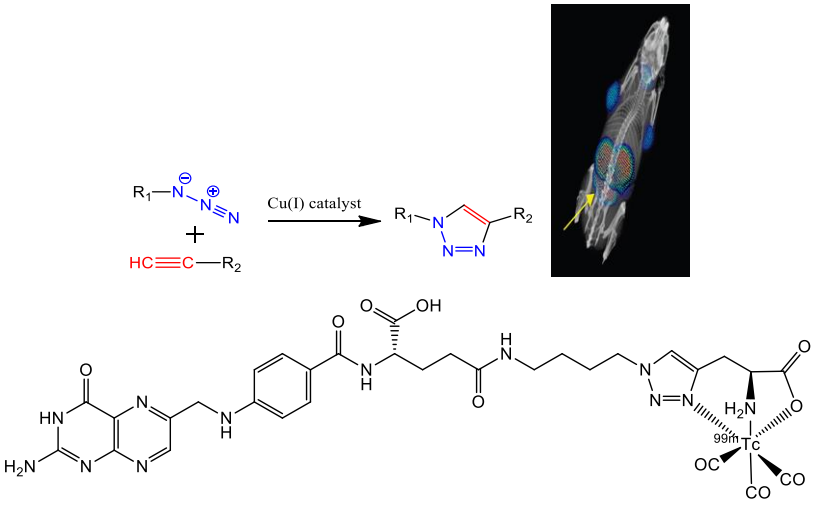

Figure 1.10. Reaction scheme of "click chemistry" (above, left), folic acid derivatised technetium complex by SPECT (below).

The first instance of substituting a well established chelator with a 1,2,3-triazole analogue for complexation of Re/^{99m}Tc without modifying the biological effects of the compound was reported by Mindt *et al.* in 2008.[38] The isostructural Re/^{99m}Tc folic acid analogues were synthesised using a Cu(I) catalysed cycloaddition method, known as a "click reaction" that allowed chelation and bioconjugation in one step, which the authors named "click-to-chelate" *(Figure 1.10)*. Moreover, Mindt *et al.* designed several new imaging probes for PET, SPECT, Near Infra-red (NIR) or MRI from a single folic acid based precursor, using ^{67}Ga, ^{111}In and ^{99m}Tc agents for SPECT, fluorophore Cy 5.5 for optical imaging and ^{18}F for PET.[39] The ^{111}In-DTPA folate complex has recently been reported as with the capacity to quantify macrophage activation *(Figure 1.10)*.[40] The authors demonstrated that the later

stages of osteoarthritis can be correlated to reduced macrophage activation, allowing monitoring of the disease activity, for which there are no clinical measures at present. Furthermore the same group has used click reactions to design tridentate di-1,2,3-triazole chelator imaging tracers as well as multifunctional ^{99m}Tc complexes, as a platform for a broad number of potential purposes including multimodal imaging probe development.[41, 42] This efficient and facile synthesis combined with uptake in folic acid receptor expressing KB (human epidermoid carcinoma) cells and tumour targetting in mice confirms the promise of this procedure.

Rhenium and technetium complexes have also been designed to enter the nucleus and bind to DNA, a significant example of which was published by Santos *et al.* who synthesised tricarbonyl pyrazolyl-diamine rhenium(I) complexes that show potential for the development of future targeted radiopharmaceuticals.[43] Furthermore, tricarbonyl rhenium and technetium complexes with acridine derivatives showed nuclear uptake *via* fluorescence and activity based studies respectively.[44] Policar *et al.* designed a tricarbonyl rhenium(I) complex in 2012 to selectively enter Golgi apparatus, with its uptake in breast cancer cells followed by fluorescence microscopy and IR mapping. Already a dual-modal imaging agent, the analagous technetium complex would present potential for a tri-modal imaging.[45] Another example of a dual-modal imaging probe under developmentwas reported by Faulkner *et al.* combining a Gd^{3+} for MRI and a Re fluorophore for luminescence investigations.[46] Furthermore, the first dinuclear rhenium/technetium complex was designed for dual-modal fluorescence/SPECT imaging with potential for therapy *via* ^{188}Re.[47]

1.7. Copper-based imaging probes

Radionuclides of copper include ^{60}Cu, ^{61}Cu, ^{62}Cu and ^{64}Cu, all of which are positron emitters, as well as ^{67}Cu, which is a β^- emitter. Copper-64, with a half-life of 12.7 h, decays 41% by electron capture, 40% by β^- radiation and 19% by β^+ radiation,[48] making this radioisotope highly appropriate for simultaneous diagnosis and therapy. A challenge to dual-modal imaging with copper(II) complexes is the

paramagnetic quenching caused by the d^9 electronic configuration of the metal centre. Despite this, a number of fluorescent copper(II) complexes have been reported in the literature, most of which are conjugated to fluorophores such as fluorescein, rhodamine or BODIPY as well as BAMs for selectivity *(Figure 1.11)*.

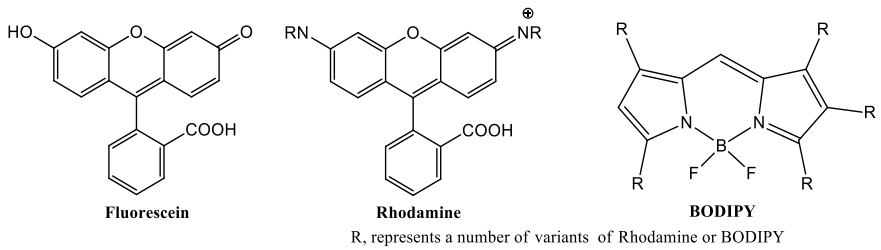

Figure 1.11. Commonly used fluorophores

With possible coordination numbers between four and six and a wide range of geometries the $3d^9$, 2+ oxidation state represents the most significant proportion of copper complexes developed as radiopharmaceuticals. Thus, there are a large number of potential chelators for this metal, which include EDTA, DTPA, NOTA, NO2A, DOTA and cyclam derivatives, all of which represent a large proportion of copper(II) research.[49] Research is ongoing to improve chelators for use as bifunctional agents, as well as to achieve better yields and very high stability with a recent example by Archibald and co-workers using cross-bridged cyclam derivatives.[50]

Some examples of copper(II) complexes used in conjunction with bifunctional chelators are described below. Colorectal cancers often express receptors for the E. coli enterotoxin, STh; analogues of these show promise for imaging and therapy. A STh analogue was conjugated to DOTA, TETA and NOTA at the *N*-terminus and labelled with ^{64}Cu of which the NOTA complex gave the best tumour uptake with respect to organs, when investigated by biodistribution and PET studies.[51] Similarly 4-((8-amino-3,6,10,13,16,19-hexaazabicyclo [6.6.6] icosane-1-ylamino) methyl) benzoic acid (AmBaSar), a cage like bifunctional chelator conjugated to cyclic RGD, was synthesised in high yield and showed increased stability and tumour specificity when compared to ^{64}Cu-DOTA-RGD.[52] A bombesin analogue conjugated to NO2A radiolabelled with ^{64}Cu also allowed visualisation of PC-3 xenografts.[53] Moreover, Maecke *et al.* developed and evaluated 4 new ^{64}Cu and ^{68}Ga complexes, chelated with

NODAGA and cross-bridged-TE2A conjugated to somatostatin antagonist p-Cl-Phecyclo(D-Cys-Tyr-D-4-amino-Phe(carbamoyl)-Lys-Thr-Cys)D-Tyr-NH_2.[54]

Furthermore, dual-modal MRI/PET nanoparticles have been reported by Lee *et al.* involving polyaspartic acid iron oxide nanoparticles conjugated to argenine–glycine–aspartic acid (RGD) peptide for integrin targeting and DOTA chelation of ^{64}Cu for PET.[55] MRI and PET both indicated selective uptake and offer the potential for higher accuracy and earlier detection of cancer. A monoclonal antibody for endoglin – an indicator of poor prognosis in cancer – was conjugated to a near infrared dye and ^{64}Cu *via* NOTA, by Cai *et al.* in 2012.[56] This dual-modal imaging agent was capable of rapidly and selectively entering endoglin expressing cells and could be useful for assessment of cancer disease progression. Furthermore a multi-modal imaging agent was developed for MRI, NIRF, and SPECT or PET imaging using liposomes as a drug-delivery mechanism.[57] ^{64}Cu-DOTA and Gd-DOTA could be conjugated to liposome surface, whilst technetium, rhenium or a drug such as doxorubicin, could be loaded within. The NIRF dye (IRDye-DSPE) was postinserted into the liposomes enabling luminescence imaging. Therefore, this kind of system presents the potential advantages of the aforementioned imaging techniques combined with therapy especially if combined with a BAM.

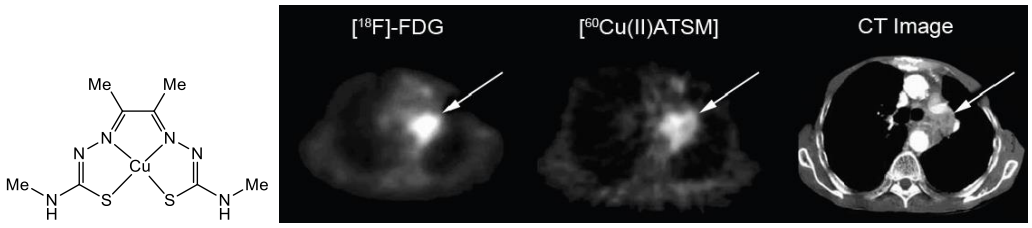

Figure 1.12. a) Copper bis(thiosemicarbazonato) complex, Cu[ATSM] (left). The following images are pretherapy scans of ^{18}F-FDG-PET (middle left), ^{60}Cu[ATSM]-PET (middle right) and CT scan. The arrow indicates lung cancer. The outside of the tumour shows greater ^{60}Cu[ATSM] uptake, in contrast to the uniform uptake of ^{18}F-FDG.[58]

A significant complex for molecular imaging, aliphatic copper(II)-diacetyl-bis(N(4)-methylthiosemicarbazone) (Cu[ATSM]) has been shown to be selective for hypoxic tissue and has progressed to phase II clinical trials for cervical cancer diagnosis *(Figure 1.12).* ^{18}F-FMISO, also in clinical trials, shows promise as a hypoxia selective agent,

but presents drawbacks such as slow body clearance and low contrast images. Cu[ATSM] has shown more rapid uptake in hypoxic cells and greater hypoxic-to-normoxic ratio than ^{18}F-FMISO.[6] The mechanism of Cu[ATSM] selectivity for hypoxic cancer cells was originally postulated to be due based on the irreversible reduction of Cu(II) to Cu(I) occurring in oxygen-poor environments. [59] Dearling *et al.* however, proposed that reduction occurs in both normoxic and hypoxic conditions, but and that the compound may undergo re-oxidation in normoxic cells only. As a result, the Cu(II) complex can cross the cell membrane, but is trapped within the cell and accumulates in the form of an anionic Cu(I) complex *(Figure 1.13).*

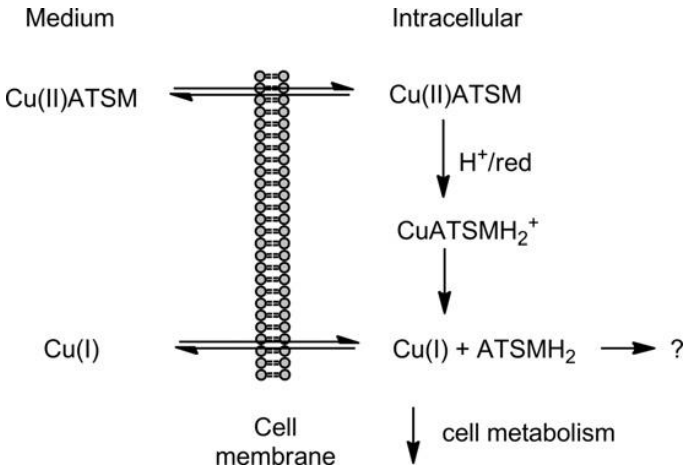

Figure 1.13. Mechanism of Cu[ATSM] hypoxia selectivity as proposed by Dearling *et al.*[60]

The therapeutic potential of Cu[ATSM] was recently demonstrated by Fujibayashi *et al.*, who reported its ability to inhibit tumour growth and malignancy.[61] The mechanism of cell uptake of bis(thiosemicarbazones) can be investigated thanks to the weak intrinsic fluorescence of thiosemicarbazones, which can be enhanced by binding to a diamagnetic metal such as Zn[ATSM] or by addition of a fluorophore. The first *in vitro* fluorescence study of zinc bis(thiosemicarbazone) complexes in human cancer cells was carried out in 2005 by Dilworth *et al.* using the Zn[ATSM] analogue in a number of cell lines.[62] As Cu[ATSM] is not fluorescent zinc analogues have been used as models for Cu[ATSM] *in vitro*. Since zinc(II) and copper(II) are of comparable atomic radii and electronegativity, however there are some limitations of this model. Zinc(II) does not possess significant redox potential as does copper(II) and therefore can only represent the uptake of the complex under

normoxic conditions. Recently a series of new fluorescent zinc bis(thiosemicarbazonato) complexes were reported showing *in vitro* uptake in cells.[63] Copper and zinc bis(thiosemicarbazonato) complexes bearing an appended fluorescent pyrene tag and reactive styrene with potential for dual modal imaging have also been synthesised by Holland *et al.*[64,65] Moreover, the better stability attributed to copper(II) complexes, indicated by the Irving-Williams series,[66] allows clean synthesis of a copper(II) complex *via* a zinc(II) complex transmetallation as well as by synthesis *via* a ligand precursor.

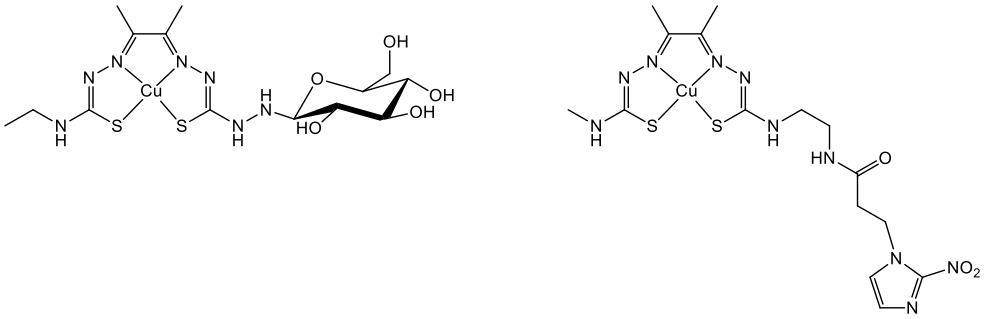

Figure 1.14. Bis(thiosemicarbazonato) complexes conjugated to glucose (left) or to a nitroimidazole (right)

There are, however, limitations of Cu[ATSM], including serum instability and high liver uptake, due to its lipophilicity. It would therefore be attractive to develop similar hypoxic imaging probes, which are biologically stable, with intrinsic fluorescence and reduced lipophilicity. As a consequence, current research aims to improve upon Cu[ATSM], with recent attempts *via* bioconjugation. Glucose, for example, was appended to copper bis(thiosemicarbazonato) complexes by Christlieb *et al.*, the resultant complex retained hypoxia selectivity yet without the drawback of significant uptake in the heart and brain as displayed by ^{18}F-FDG *(Figure 1.14)*.[67] Subsequently, bombesin conjugates were developed displaying binding to PC-3 cells, which appear suitable for PET applications. Furthermore, Bayly *et al.* recently coupled a nitroimidazole to a copper bis(thiosemicarbazonato) complex *(Figure 1.14)*.[68] The conjugates displayed superior hypoxia selectivity and reduced non-target uptake when compared to propyl derivatives used as controls and CuATSM/A derivatives respectively.

It is possible to chelate a wide range of metals due to the "soft donor" characteristics of the tridentate S,N,N these include zinc and copper (as already

mentioned above), iron, nickel, rhenium, technetium, gallium, indium, platinum and palladium. Therefore, chelation of PET or SPECT radiometals such as gallium or indium with a counterion, for example chlorine could be another means of reducing the lipophilicity and therefore the uptake in the liver.

Table 1.5. Represents a broad range of bis(thiosemicarbazonato) complexes

Ligand	R_1	R_2	R_3	R_4
GTS	H	H	H	H
PTS	Me	H	H	H
PTSM	Me	H	Me	Me
PTSE	Me	H	Et	Et
PTSP	Me	H	Ph	Ph
ATS	Me	Me	H	H
ATSM	Me	Me	Me	Me
CTS	Et	Me	H	H
CTSM	Et	Me	Me	Me
DTS	Et	Et	H	H
DTSM	Et	Et	Me	Me
KTS	$CH_3(EtO)CH$	H	H	H
KTSM	$CH_3(EtO)CH$	H	Me	Me

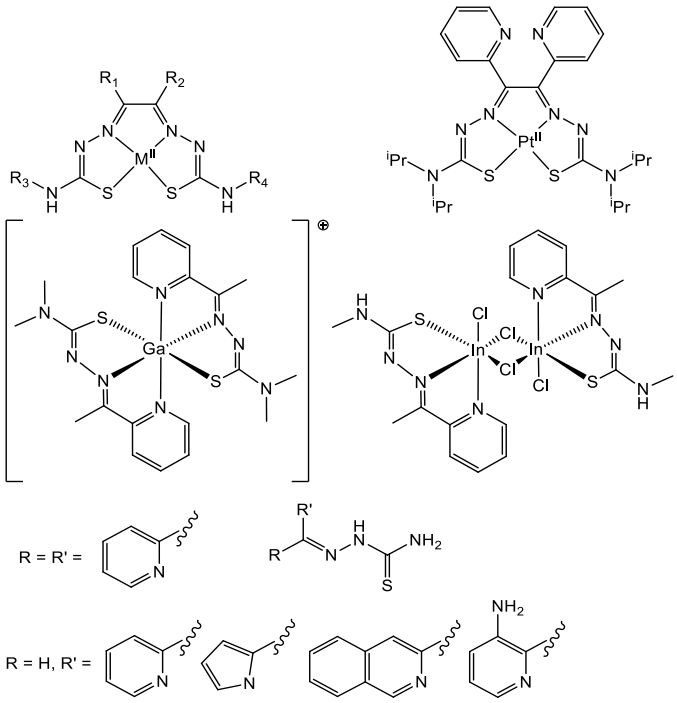

Figure 1.15. Structures of thiosemicarbazones found in Refs [69-72]

Furthermore, there is a broad scope of biological and medical activity of this family of compounds, which includes complexes and their ligand precursors. Uncomplexed ligands are active against leukaemia, TB, malaria, viruses (including HIV), bacterial cells and superoxide dismutase-like radical scavenger properties with enhanced activity displayed when bound to a transition metal.[73],[74] α-*N*-heterocyclic thiosemicarbazones *(Figure 1.15)*, have been shown to possess anti-tumour action *via* inhibition of the ribonucleotide diphosphate reductase (RR) enzyme, which is involved DNA synthesis. Since pyridine-2-carboxaldehyde thiosemicarbazone anti-tumour properties were observed in 1956, a number of other heterocyclic ring systems have been synthesised showing anticancer activity and include isoquinoline-1-carboxaldehyde thiosemicarbazone, 3-aminopyridine-2-carboxaldehyde thiosemicarbazone (Triapine) and di-2pyrirylketone 4,4-dimethylthiosemicarbazone, which is the most potent *(Figure*

1.15).[75] Furthermore, Platinum(II) and palladium(II) thiosemicarbazone complexes, have shown activity against cancer cells resistant to *cis*-platin, one of the most commonly used anti-tumour drugs.[76] French and Freelander assayed fifty bis(thiosemicarbazonato) ligand precursors and were the first to observe their anti-tumour properties, with determined KTS and KTSM *(Figure 1.15, Table 1.5)* as the most active. Moreover, it was discovered that their antitumour properties are due to their ability to chelate copper(II) ions, which lead to the investigation of chelation of other biological metal ion chelation including zinc(II), nickel(II) and iron (II/III).[28] The potential scope therefore, of thiosemicarbazonates is significant in the development of diagnostics and therapeutics, with reports of gallium(III) and indium(III) thiosemicarbazonates *(Figure 1.15).*[69, 70]

1.8. Zinc

Zinc(II) is a d^{10} metal ion with coordination geometries ranging for example from tetrahedral, square pyramidal or trigonal bipyramidal thus giving rise to versatile probes for the development of luminescence imaging using transition metal complexes: some recent developments will be highlighted hereby.[77] A series of zinc salen complexes (*Figure 1.16)* were designed by Xu *et al.* and investigated by single and two-photon microscopy in cells displaying colocalisation in the lysosome, endosome and ER as well as excellent photostability and low cytotoxicity *(Figure 1.16).*[78]

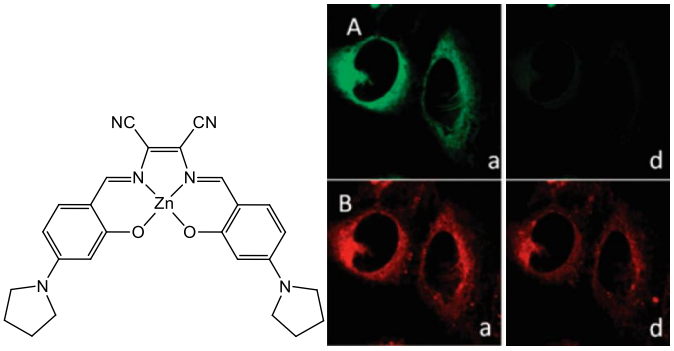

Figure 1.16. Zinc salen complexes and colocalisation in endoplasmic reticulum *via* single-photon confocal microscopy before and after irradiation for 315 s.[78]

A fluorescent DAQZ@2Zn^{2+} complex, was reported as a sensor in live cells for oxalic acid, an inhibitor of lactate dehydrogenase (LDH), presence of which resulted in quenching *(Figure 1.17)*.[79] Cancer cells more frequently undergo anaerobic respiration than non-cancer cells, particularly under hypoxia. Therefore oxalic acid could provide one method of treating cancer as well as indicating the necessity for this type of treatment. Additionally, a binuclear BODIPY-based fluorescent zinc complex was developed and investigated in cells by Hamachi *et al.*[80] Histological studies demonstrated that the complex could distinguish neurofibrillary tangles of hyperphosphorylated tau proteins and amyloid plaques in the hippocampus of a patient who had Alzheimer's disease.

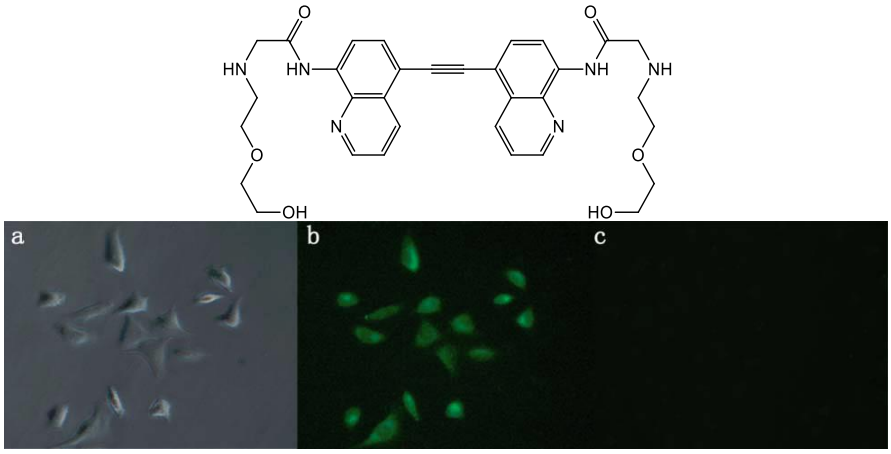

Figure 1.17. *In vitro* fluorescence microscopy of a Zn^{2+} complex of DAQZ ligand **7** in HeLa cells (DIC sown in image a), before (b) and after incubation with oxalic acid (c).[79]

Keppler *et al.* studied triapine, which is under investigation as an anticancer agent, by fluorescence microscopy. The corresponding zinc complex [Zn(Triapine)Cl_2].HCl was also synthesised and imaged in colon carcinoma cells to show uptake in nucleoli.[81] The unusual attribute of intrinsic fluorescence of this particular anticancer drug may help to facilitate personalised medicine *via* monitoring the uptake within patient biopsy samples and subsequent morphological changes.

In 2005, trimetallic zinc meso-to-meso ethyne-bridged tris[(porphinato)zinc(II)] complexes were designed as NIR fluorophores with potential for *in vivo* imaging

showing uptake by fluorescence in murine melanoma cells.[82] Furthermore, NIR *in vivo* fluorescence imaging of cell death was enabled by the use of a bimetallic zinc(II)-dipicolylamine (Zn-DPA) complex, conjugated to a ligand with affinity for phosphatidylserine, which is present on dying and dead cell surfaces *(Figure 1.18)*.[83]

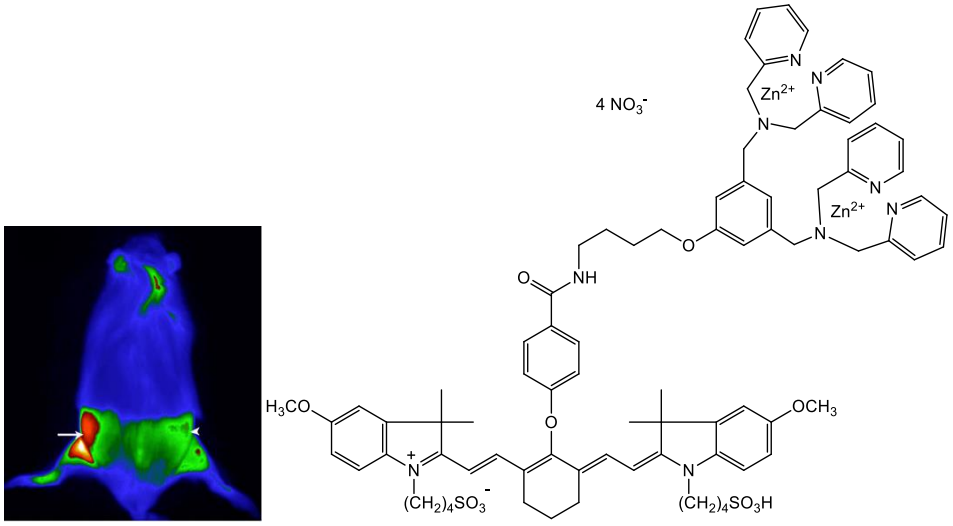

Figure 1.18. Near-IR fluorescence image of tumour cell death after radiation therapy (a) as a result of treatment with imaging probe **14**, (b). Image reproduced with permission from Ref. [83].

When compared to Annexin-Vivo 750 (a commercially available NIR fluorescence sensor for apoptosis) the complex possessed higher target to non-target ratio on account of lower bladder uptake, giving complementary information as two probes and good clearance indicating potential for radiolabelling studies due to a resultant reduced radiation exposure.[84] Further, this probe shows promise for the assessment of patient response to therapy as well as evaluation of novel anticancer treatments. The probe potentially has broader applications and was shown to be capable of detecting tissue infected by *S. aureus*.[85] The same group developed a series of Zn-DPA complexes of which the hydrophilic variants are non-toxic to mammalian cells yet toxic to *S. aureus*, including antibiotic resistant strains. Moreover, the uptake of a fluorescent analogue was imaged in *E. coli* and *S. aureus*.[86] In 2012 Hnatowich *et al.* combined ^{111}In-DOTA-biotin with a fluorophore-conjugated Zn-DPA analogue *via* a noncovalent linker and investigated the potential of Zn-DPA for assessing infection *in vivo* for the first time. There was notably greater uptake in infected areas

when compared to induced inflammation indicating that the probe could help with diagnosis of bacterial disease.[87]

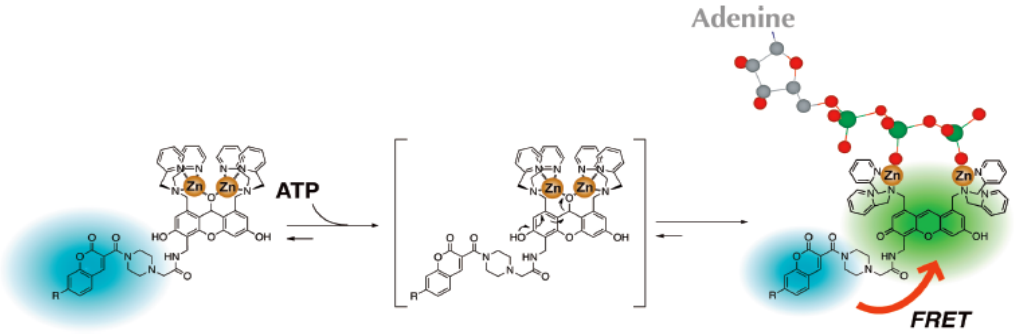

Figure 1.19. FRET mechanism of Zn-DPA complexes for sensing of nucleosides (reproduced with permission from Ref. [88])

Hamachi *et al.* developed another series of Zn-DPA complexes containing four zinc nuclei and demonstrated that their D4 tag/Zn-DPATyr pair can successfully label proteins.[89] Moreover, new Zn-DPA complexes were developed by Hamachi *et al.* for the recognition of nucleoside polyphosphates (including ATP), whereby fluorescence is activated by the presence of the desired compound *via* fluorescence resonance energy transfer (FRET) yielding a ratiometric response *(Figure 1.19)*.[88] A zinc(II) dipicolylamine complex with ATP sensitivity and conjugated to nanoparticles with a silica core was imaged in fixed non-cancerous rat epithelial (NRK) cells with potential use in metabolic studies.[90] Furthermore, targeted cancer imaging of oral epithelial cancer was reported by Menon *et al. via* the conjugation of a mannose ligand to chitosan-zinc sulphide nanocrystals.[91]

1.9. Gallium

Gallium is predominantly found in the 3+ oxidation state and has a coordination number range of 3-6. A hard acidic cation, Ga(III) strongly binds to multiple anionic donor sites including oxygen and thiolates. Gallium is known to bind to chelators EDTA, DTPA, DOTA and has promising thermodynamic stability with NOTA (including under acidic conditions), DFO and HBED, and show favourable characteristics for bifunctional chelators *(Figure 1.20)*.

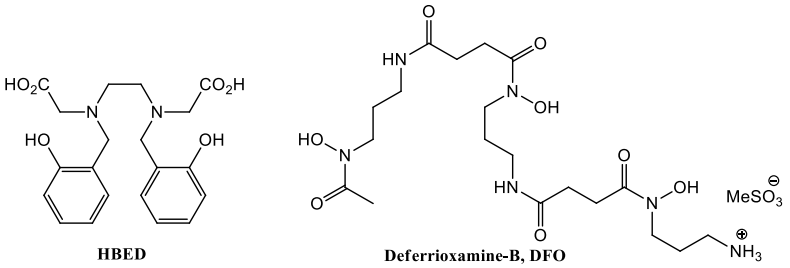

Figure 1.20. Useful ligands for chelating Ga(III).

There are three gallium isotopes of interest for molecular imaging: ^{66}Ga (9.5 hour half-life) and ^{68}Ga (68 minute half-life), which are positron emitters and ^{67}Ga (3.26 days half-life), a gamma emitter.[92] The PET radioisotope ^{68}Ga, has a major advantage in that it does not require a nearby cyclotron and is relatively simple to obtain *via* a commercially available ^{68}Ge (half-life of 270.8 days) generator. Furthermore, ^{67}Ga is used as a prognostic of non-Hodgkin's and Hodgkin's lymphoma as well as to detect bone infection in scintigraphy. [93-97]

There have been a number of bioconjugated gallium complexes with an outlook towards theranostics, some examples of which will be presented here. A DOTA-Gly-Glu-Cyc lactam bridged cyclised α-melanocyte stimulating hormone peptide was radiolabelled with ^{67}Ga to allow the visualisation of primary and metastatic melanoma. There is potential for further development of this probe as a theranostic agent since the versatility of DOTA could allow chelation of a radiotherapeutic metal in the place of gallium.[98] Furthermore, a DOTA-PEG4-BN(7-14) bombesin analogue labelled with $^{67/68}$Ga and ^{177}Lu showed good tumour uptake in PC-3 xenografted nude mice, where $^{67/68}$Ga acted as a diagnostic radionuclide and ^{177}Lu as a therapeutic.[99] ^{68}Ga DOTATOC was utilised as a diagnostic and indicated the necessity for ^{177}Lu-DOTATATE treatment, where FDG PET had not shown any increased uptake.[100]

Additionally, a quadruple-modality imaging probe, which can be detected by fluorescence, bioluminescence resonance energy transfer (BRET), PET and MRI, was reported by Kim *et al.* (*Figure 1.21*).[101] The probe consisted of a cobalt–ferrite nanoparticle (for MRI), incorporating rhodamine (for fluorescence) and

conjugated to luciferase (for bioluminescence) and a *p*-SCN-bn-NOTA chelating group that was tagged with ^{68}Ga (a generator-produced PET radionuclide). Each imaging modality displayed dose dependence *in vivo*. Further functionalisation with targeting groups could enhance the potential for effective delivery to tumours.

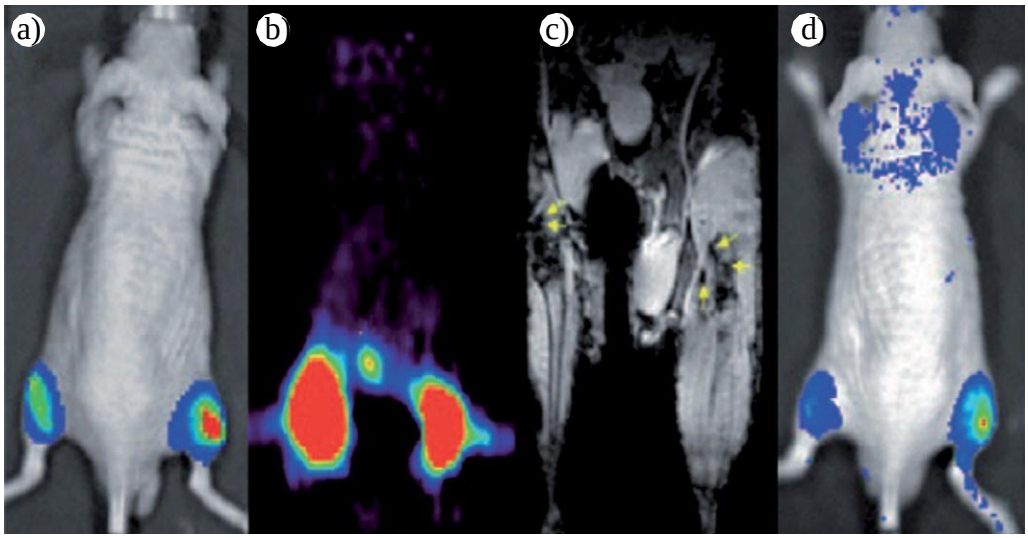

Figure 1.21. Quadruple modal imaging: (a) bioluminescence, (b) micro-PET, (c) MRI and (d) fluorescence imaging, adapted from Kim *et al.* 2009. [101]

1.10. Indium

Indium predominantly exists in the 3+ oxidation state when complexed and can be from 3 to 8 coordinate. Despite the possibility of the higher coordination numbers indium, like gallium, forms its most stable complexes with hexadentate chelators. In contrast to gallium, indium has a higher affinity for softer donors and therefore EDTA, DTPA and DOTA bind more securely to indium. There are a number of indium radiometals, such as ^{110}In, ^{110m}In and ^{114m}In, however the most commonly reported indium radioisotope is ^{111}In. Indium-111 is a commercially produced radionuclide for SPECT imaging, with a half-life of 2.8 days and photon energies of 171 and 245 keV. Notable applications to date include tumour-targeted imaging. There have been a number of reported peptide/antibody targeted small molecules involving indium-111, therefore some selected examples will be reviewed here, in

particular those pertaining to multimodal imaging or theranostics.

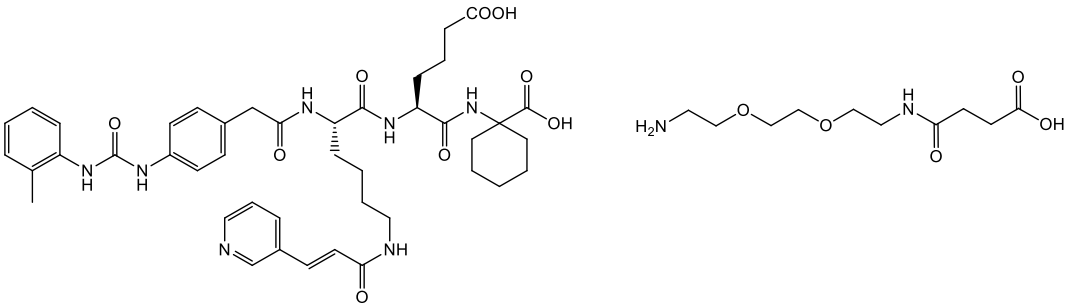

Figure 1.22. LLP2A *N*-[[4-[[[2-ethylphenyl)amino]carbonyl]amino]phenyl]acetyl]-N^{ε}-6-[(*2E*)-1-oxo-3-(3-pyridinyl-2-propenyl)]-*L*-lysyl-*L*-2-aminohexanedioyl-(1-amino-1-cyclohexane)carboxamide (left) and linker (right).

LLP2A coupled to DOTA and PEG was labelled with ^{111}In and showed good tumour uptake.[102] The drawback of renal retention however, would require further modification. Nevertheless the ^{111}In-(LLP2A-DOTA)$_4$-PEG$_{10,000}$ displayed potential for simultaneous imaging and therapy. Glucagon-like peptide receptor-1 (GLP-1) imaging with In-[Lys^{40}(Ahx-diethylenetriaminepentaacetic acid [DTPA])NH$_2$]-exendin-4 and ^{68}Ga DOTATATE enabled the assessment of receptor status as well as the imaging of benign insulinomas, which contrary to malignant insulinomas often lack somatostatin receptor subtype 2 (sst2) and express GLP-1 receptors.[103] DOTATE radiotherapy could be applied to patients with sst2 suppressing tumours.

Ibritumomab, a monoclonal antibody, was complexed for ^{90}Y-ibritumomab therapeutic purposes was combined with ^{111}In-ibritumomab for pre-therapy scans. The ^{111}In scans proved capable of predicting disease progression and could be a useful tool to tailor therapy towards more aggressive therapeutic strategies.[104]Additionally, Yoshimoto *et al.* radiolabelled DOTA-c(RGDfK) with ^{111}In and ^{90}Y, reporting high tumour uptake due to specificity for $\alpha_v\beta_3$ integrin, which is present in cancerous melanoma cells, and therefore promise as a theranostic pair.[105] Indium complexes are also currently being developed for multimodal imaging. In 2006 Li *et al.* designed a dual-labelled probe for tumour imaging, ^{111}In-DTPA-Lys(IRDye800)-cyclic(KRGDf), which binds to integrin $\alpha_v\beta_3$.[106] Figure 1.23 shows the uptake of the imaging probe within $\alpha_v\beta_3$-positive tumours, with no uptake

observed within $\alpha_v\beta_3$-negative tumours, demonstrating the selectivity of this agent.

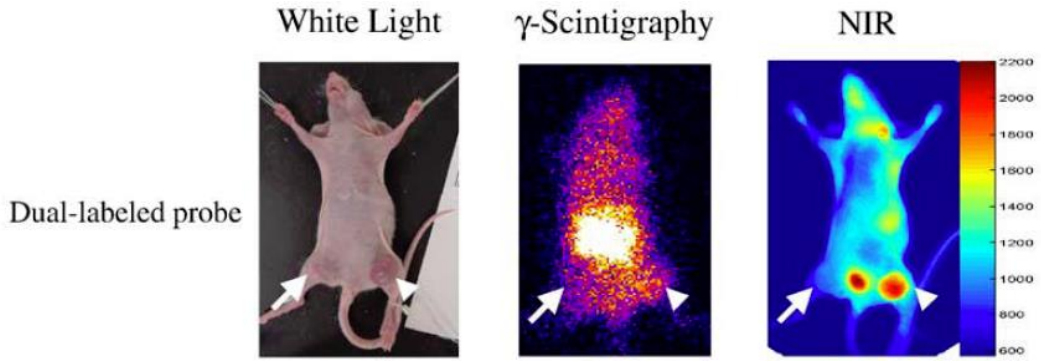

Figure 1.23. ^{111}In-DTPA-Bz-SA-Lys(IRDye800)-c(KRGDf) in nude mice visualised by (from left to right) white light, γ-scintigraphy and NIR. Arrows represent the tumours [106]

DOTA-neurotensin (DOTA-NT) analogues labelled with ^{68}Ga or ^{111}In for PET were designed by Gruaz-Guyon *et al*. for the purpose of targeted radiotherapy in combination with ^{90}Y or ^{177}Lu.[107] The ^{68}Ga and ^{111}In DOTA-NT complexes showed higher tumour and renal uptake than the DOTA-LB119, with very low background in other tissue with exception of the kidneys. Despite the poor affinity of the indium DOTA-NT complex for colorectal carcinoma cell line HT29, the respective Yttrium complex possessed could bind significantly better, indicating potential for tumour targeting as a radiotherapeutic. Tumours were visualised using NIR optical imaging, with good resolution and sensitivity, which was complemented by γ-scintigraphy for tissue penetration. Another cyclic peptide c(CGRRAGGSC) was applied for combined near infrared fluorescence and SPECT imaging of tumours, allowing unambiguous visualisation of the tumour by both modalities.[108] Moreover, in 2012, Häfeli *et al*. designed a trimodal imaging agent for SPECT, MRI and fluorescence imaging.[109] This consisted of hyperbranched glycerols conjugated to ^{111}In-DOTA, Gd-DOTA and the fluorescent dye Alexa Fluor. The imaging probe was excreted slowly, allowing the image contrast to be significantly enhanced with time.

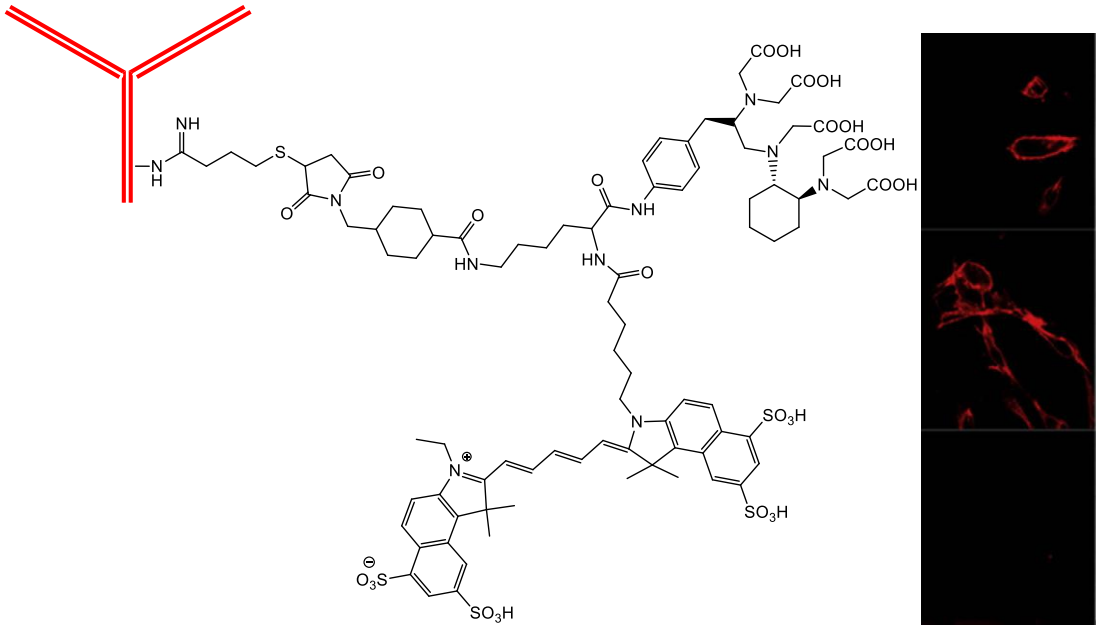

Figure 1.24. Trastuzumab-Cy5.5-CHX-A" (left), investigated using confocal microscopy in cells expressing HER2 (top and middle) and cells seldom expressing HER2 (bottom).

Monoclonal antibodies trastuzamab (binds to HER2 (Human Epidermal Growth Factor Receptor 2 expressing cells)) or cetuximab (selective for EGFR Epidermal Growth Factor Receptor expressing cells) were conjugated to chelators (CHX-A") for the incorporation of radioisotopes (in this case, ^{111}In) *(Figure 1.24)*. The uptake of the respective ligands was followed in LS174T, EGFR expressing A431 and two strains of HER2 expressing cells (NIH3T3-HER2^{+}).[110] Furthermore, antibodies for the targeting of tumours *via* epidermal growth factor receptors has been utilised by Kobayashi *et al.* allowing discrimination between three types of tumour to be (EGFR-1, EGFR-2 and a tumour that did not overexpress HER2).[111] Using cetuximab or trastuzumab conjugated to a linker and to a fluorophore (Rhodamine Green, Cy5.5 or Cy7) it was possible to utilise the wavelength of *in vivo* emission as an indication of response to the antibody. For comparative purposes ^{111}In-labelled antibodies were used in this study – with the fluorescent probes possessing the advantages of avoidance of ionising radiation and the potential to discriminate between up to three tumour types. Additionally Kobayashi *et al.* developed a probe, which can be labelled with ^{111}In and a fluorophore, for antibody-based targeting (panitumumab and separately trastuzumab) to enable dual modal optical and SPECT imaging.[112] The fluorescent probes were activated upon internalisation by the cell,

thus providing a clear visualisation of tumours, which was well complemented by the "always on" of nuclear imaging.

Small molecules containing copper-64 and indium-111 have been targeted using peptides/antibodies, allowing for the possibility of both PET and SPECT. Recently an ^{111}In labelled antibody binding fragment (fab) for c-kit (a proto-oncogene significant for many malignancies) was tested for *in vitro* binding and by cellular internalisation assays, whilst ^{64}Cu c-kit fab was evaluated *in vivo* by PET, allowing clear tumour visualisation. This makes it a promising tool for enabling an informed decision to be made before beginning c-kit targeted therapy.[113] ^{64}Cu and ^{111}In DOTA-HSA-Z(HER2:342) were also studied by PET and SPECT respectively, both displaying high tumour and liver uptake. This ligand is likely to be suitable for labelling with radionuclides such as ^{90}Y and ^{177}Lu, which could open the door to usage as a theranostic pair.[114] Moreover, a diabody (a bivalent single-chain antibody dimer fragment) was attached to a DOTA-PEG, labelled with ^{125}I, ^{111}In and ^{64}Cu and investigated by biodistribution and ^{64}Cu PET in athymic mice, indicating tumour uptake and low kidney uptake.[115] Furthermore, visualisation of the tumour was possible after 22 h, which suggests potential as a theranostic pair in combination with ^{125}I.

1.11. Summary

Medical imaging provides essential diagnosis for a multitude of diseases including cancer, whilst nuclear imaging can offer highly sensitive molecular and physiological information, enabling rapid detection of early stages of disease. The combination of imaging modalities (optical/PET and or SPECT/ MRI) can allow for more accurate diagnoses thanks to the specific advantages in terms or resolution and sensitivity of each technique, with optical imaging enabling a crucial insight into cellular behaviour of a probe under development. One of the crucial research areas is that of hypoxia detection, which is a symptom present in numerous diseases and is highly significant in the development of cancer. There is currently no clinically

approved hypoxia imaging probe, therefore the necessity for further development remains. Although there has been a recent increase in the development of agents capable of both detection and therapy. Thus, the progression of current research moves towards a future of personalised medicine and as a result promises an improved patient response to therapy.

1.11.1. Aims of thesis

1. Synthesise copper, gallium and indium acenaphthenequinone bis(thiosemicarbazones) with intrinsic fluorescence, which can be rapidly and cleanly radiolabelled and have selectivity for cancer cells and hypoxic tissue.
2. Investigate the stability, cell uptake and cytotoxicity of bis(thiosemicarbazonato) complexes to allow *in vivo* studies to commence. Usage of computational studies to study electronic configuration and thermodynamic stability of these complexes in gas phase and solution models.
3. Explore acenaphthenequinone bis(thiosemicarbazone) complexes for selective dual modal imaging and/or enabling of targeted nanomedicines with potential for therapy.

Chapter 2. Synthesis, characterisation and spectroscopic investigation of mono(substituted) and bis(substituted) thiosemicarbazonato ligand precursors

2.1 Overview

The objective of this project was to synthesise new complexes based upon the design of Cu[ATSM], but with improved kinetic stability, reduced liver and other non-target organ uptake and increased intrinsic fluorescence. The design was modified by introducing a bis(imino)acenaphthene (BIAN) backbone, which is likely to provide superior kinetic stability and fluorescence. The BIAN ligand itself possesses redox activity, which conceivably could affect the hypoxia selectivity.[116, 117] Moreover three ligands containing an acenaphthyl moiety were recently shown to display greater uptake *in vitro* under hypoxia than normoxia by fluorescence microscopy.[118] The compounds were designed to work on the same principle as many fluorescent hypoxia probes based on 2-nitroimidazole, whereby bioreduction of the nitro group under hypoxia results in increased fluorescence. This BIAN compound did not contain a nitroimidazole, however, and instead was based upon 6-aminoquinoxaline and acenaphtho[1,2-b]quinoxaline substituted with a nitro group, for bioreduction. Redox properties of the BIAN backbone therefore, did not impede the hypoxia selectivity.

The aim of this chapter was to synthesise and characterise proligands that could firstly act as potential precursors to analogous metal complexes. Secondly, the comparison between ligand precursors and their metal complexes is essential for assessing the stability of the latter in biologically relevant conditions as well as *in vitro*. The next objective was to investigate these compounds by UV-visible and fluorescence spectroscopy, followed by the determination of their fluorescence lifetime in solution and *in vitro*, to allow comparisons with their corresponding metal complexes described in later chapters.

2.2 Ligand precursor synthesis and characterisation

Mono(substituted) ligand precursors were synthesised by refluxing one equivalent of thiosemicarbazide (incorporating R substituents as peripheral functionalities such as methyl, ethyl, phenyl or allyl), with one equivalent of acenaphthenequinone, in presence of acid as a catalyst. These mono(thiosemicarbazone) proligands present an opportunity to synthesise asymmetric bis(substituted) compounds and will be discussed in Chapter 7. To synthesise the bis(thiosemicarbazone) ligand precursors, three or more equivalents of thiosemicarbazide were added to the diketone starting material using the same procedure, in ethanol with ten drops of concentrated hydrochloric acid *(Figure 2.1)*. In both cases the suspension was filtered after three hours and the solid product washed with methanol.

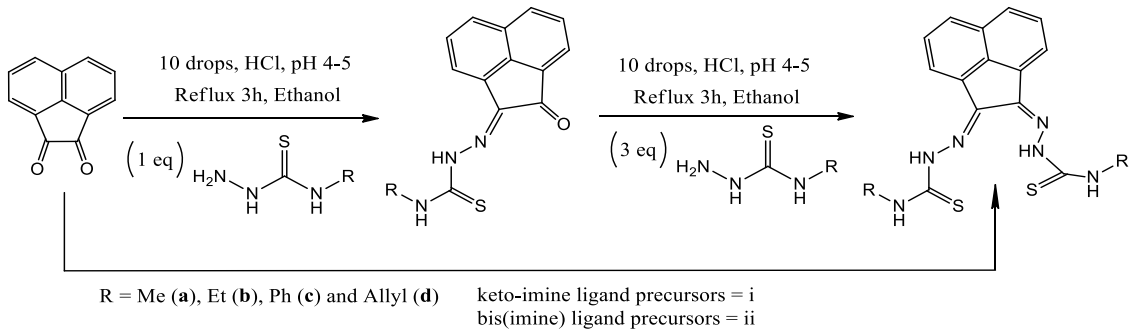

Figure 2.1. Reaction scheme of ligand synthesis method.

Isolated ligand precursors were yellow solids, with the exception of phenyl-substituted compound **ic** which was pale orange. The yields of the mono(substituted) ligand precursors **ia** – **id** were good (72 - 85 %). Mass spectrometry and NMR spectroscopy were used for their characterisation, whereby the mono(substituted) ligand precursor m/z resonances were found in agreement with calculated $[M + H]^+$ as 292.05, 306.07, 332.09, and 318.11 (**ia**, **ib**, **ic** and **id** respectively). All bis(substituted) ligand precursors were isolated in moderate to good yields of (64 - 85 %). ESI-MS were confirmed in negative ionisation mode as 355.08, 383.12, 479.12 and 407.11, for the bis(substituted) ligand precursors **iia**, **iib**, **iic** and **iid**, respectively.

^{1}H-NMR spectroscopy indicated the high purity of the ligand precursors and that the bis(substituted) compounds showed an asymmetric conformation. Figure 2.2 shows ^{1}H-NMR spectra of proligands **ib** and **iib** in d_6-DMSO. The asymmetric structure of the

bis(substituted) proligands is characteristic of an (*E*,*Z*) isomerism at the imine functionality and has been structurally confirmed using X-ray crystallography *(vide infra)*. Moreover, when H_2ATSM was optimised by DFT (Density Functional Theory), the conformer possessing the (*E*,*Z*) isomerism was found to be the most energetically favourable.[119]

Distinctive nitrogen-bonded protons (referred to as N*H*) for both mono(substituted) and bis(substituted) ligand precursors appear between 8.8 and 12.9 ppm. The (*E*,*Z*) N*H* resonances can be assigned accurately for the bis(substituted) ligand precursor, due to the characteristic resonances corresponding to the mono(substituted) proligand, which has been determined crystallographically to represent the Z geometry.

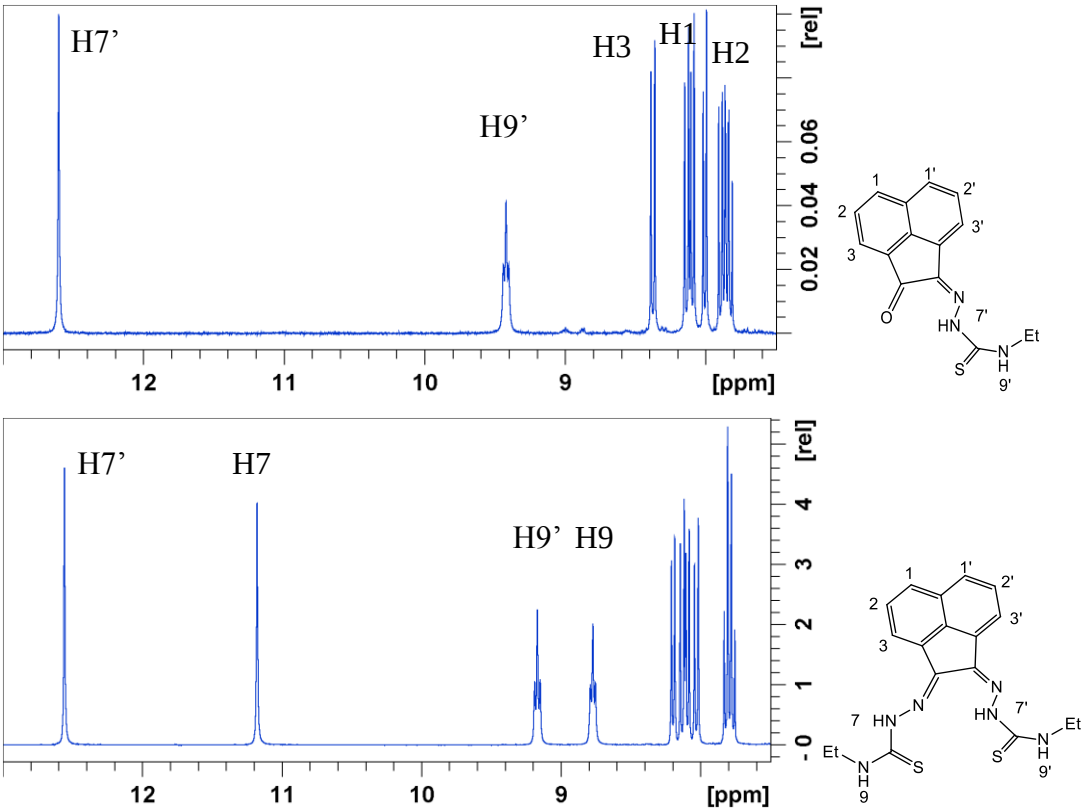

Figure 2.2. ^{1}H NMR (300 MHz, d_6-DMSO) spectroscopy of the aromatic and amino N*H* shifts of the mono-ethyl substituted and bis-ethyl substituted ligand precursors in the 7.5 to 13 pm region.

In the case of compounds **iia**, **iib** and **iid** bis(substituted) proligand resonances analogous to the mono(substituted) ligand precursor for between 12.5 and 12.7 ppm are representative of the Z hydrazone proton, with shifts between 9.1 and 9.4 ppm corresponding to external Z proton. This indicates that shifts of the E nitrogen-bound hydrogen atoms are upfield of their Z counterparts, with resonances between 11.2 and

11.3 ppm (hydrazonal) and 8.8 and 9.1 ppm (external). Structural data and DFT calculations *(vide infra)* suggest that the Z hydrazone proton is involved in hydrogen bonding to the ketone or the imine of the respective mono(substituted) and bis(substituted) ligand precursors. This would likely result in deshielding and the observed downfield shift of Z hydrazone proton. When comparing the methyl and ethyl-substituted proligands (**ia** to **ib** or **iia** to **iib**) the N*H* chemical shifts were almost identical, as expected from the similar nature of these alkyl substituents. In comparison the **id** and **iid** allyl-substituted ligand precursor external N*H* shifts were slightly downfield, for example 9.32 ppm and 9.02 ppm for **iid** and 9.19 ppm and 8.80 ppm for **iib**. This signifies the reduced shielding due to the electron-withdrawing functionality. In comparison with other functionalities there was a significant downfield shift observed for the two NH resonances of **ic** (12.79 ppm and 10.93 ppm) and the four N*H* resonances of **iic** (12.95 ppm, 11.54 ppm, 10.74 ppm and 10.68 ppm). This can also be attributable to the electron-withdrawing nature of the phenyl substituent.

2.3 Structural investigations by X-ray crystallography and DFT modelling

Yellow crystals of bis(thiosemicarbazonato) ligand precursor of **iid** and of a sulphur-sulphur dimerised form of **iib** (**iib**$_{S\text{-}S}$) suitable for X-ray crystallographic analysis were grown from DMSO solutions. The proligands was an (*E*,*Z*) isomer, whereby the literature reflects a scope of geometries for such compounds. For similar compounds such as bis(alklimino)acenaphthene (alkyl-BIAN) ligand precursors the (*E*,*E*) geometry would be expected, however Cowley *et al.* reported (*E*,*Z*) alkyl-BIAN proligand isomers. Authors suggested that the observed geometry was due to the substituents steric effects, imino-nitrogen lone pair repulsion and crystal packing.[120] It would be reasonable to consider that the isomerism displayed by compound **iid** and the **iib** dimer are of similar origins. Structures were reported by Besenyei *et al.* also reported that aryl(BIAN) derivatives may be observed as either (*E*,*E*) (major isomer) or (*E*,*Z*) isomers depending on the solvent.[121] Furthermore, Dilworth *et al.* reported a benzil bis(phenylthiosemicarbazone) ligand precursor and a benzil bis(methylthiosemicarbazone) proligand, which display an (*E*,*E*) and a (*Z*,*Z*) geometry respectively.[122]

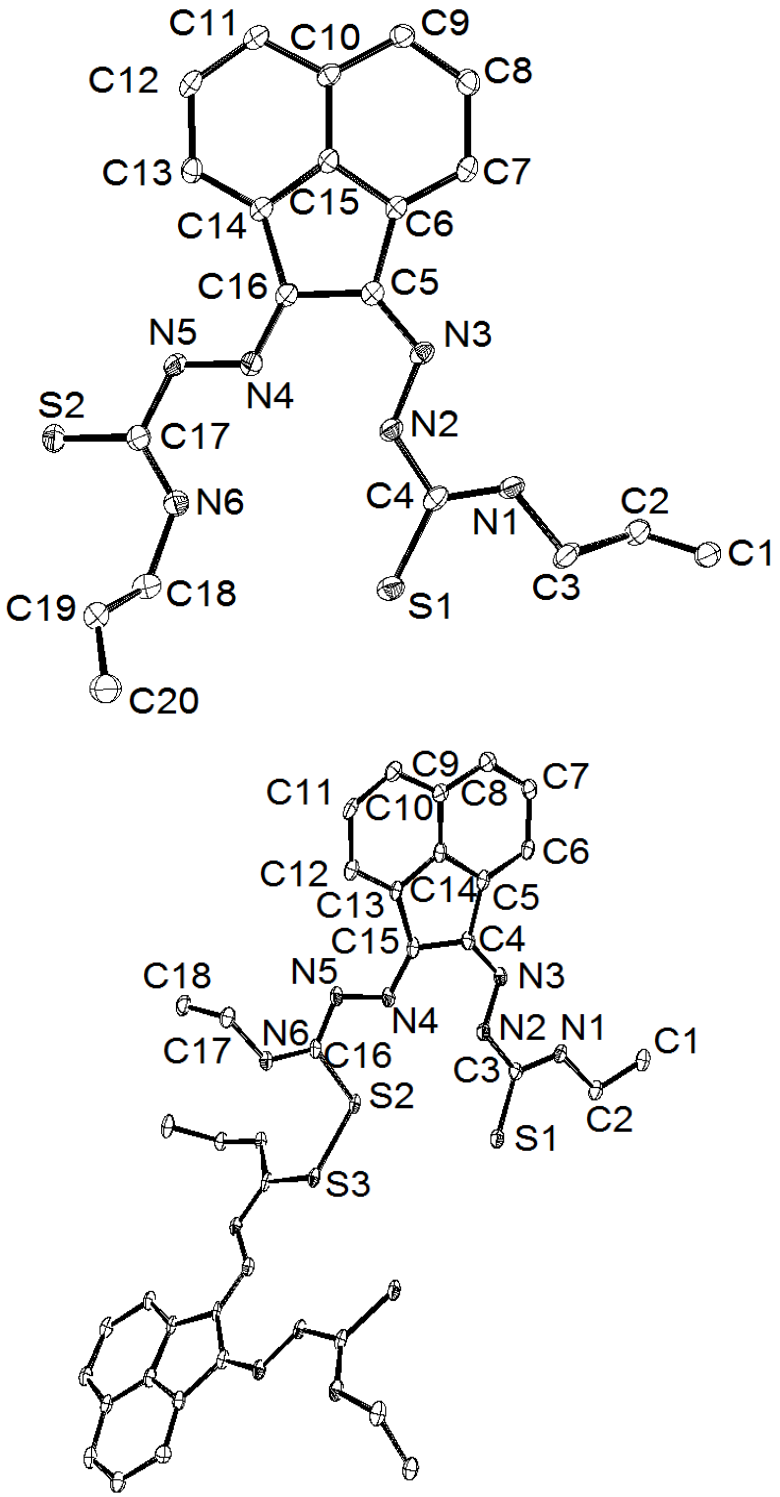

Figure 2.3. ORTEP representations of allyl-functionalised bis(thiosemicarbazonato) ligand precursor **iid** (above) and dimer of ethyl-substituted bis(thiosemicarbazonato) ligand precursor **iib** (below). Ellipsoids drawn at 30 %, hydrogen atoms omitted for clarity.

The results of X-ray diffraction experiments are presented in Figure 2.3, with selected bond lengths presented in Table 2.1. This allows comparisons to be made with the

mono(substituted) thiosemicarbazonato ligand **ib**. Almost all corresponding bonds of **ib**, **iib** and **iid** are similar therefore little discussion structural is possible, but allows for later comparisons with analogous metal complexes. The only exception is the carbon-sulphur bond of **iib** involved in the sulphur bridge, which is a single bond and therefore significantly longer than the corresponding bonds of **iid** or **ib**. This may have been formed by tautomerisation, followed by deprotonation as illustrated in Figure 2.4. Both crystal structures display an (*E*,*Z*) geometry, which is consistent with their NMR spectra.

Table 2.1. Selected bond lengths of the ligand precursor crystal structures and optimised structures of **iic** and **iic'** by B3LYP 6-31++ (d,p) IEFPCM, DMSO, in Angströms.

Compound/ Molecular Parameters	**ib**[123]	Sulphur-bridged **iib**$_{S\text{-}S}$ dimer	**iic** optimised DFT structure	**iic'** optimised DFT structure	**iid**
N-N	1.352(2)	1.391(7)	1.356	1.359	1.367(4)
		1.392(6)	1.356	1.348	1.361(4)
C=N or	1.294(2)	1.280(7)	1.293	1.297	1.297(4)
C=O for ib	1.224(2)	1.311(8)	1.293	1.303	1.306(4)
C=S	1.6780(19)	1.683(6)	1.691	1.692	1.678(4)
*C-S		1.807(6)*	1.691	1.692	1.674(4)

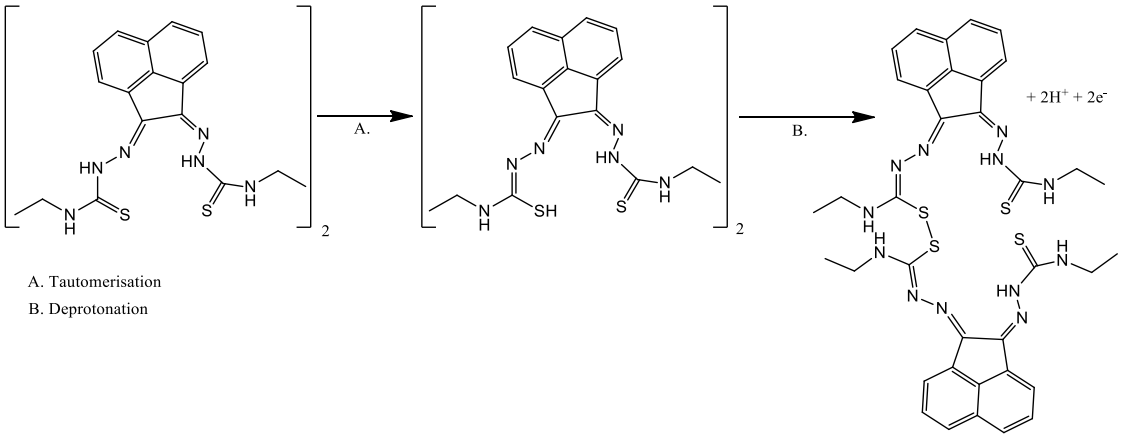

Figure 2.4. Proposed dimerisation of proligand **iib**.

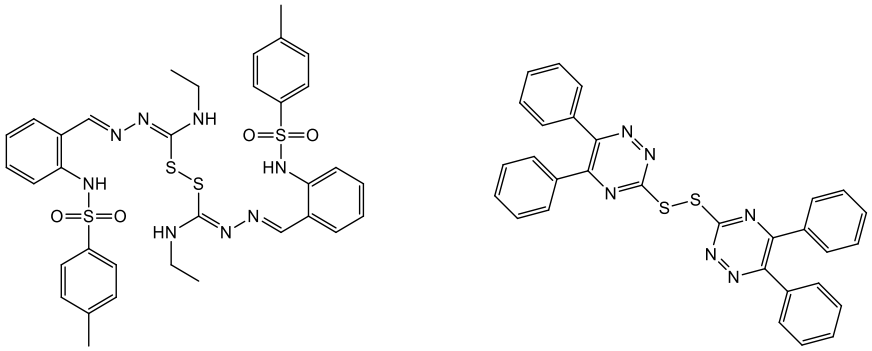

Figure 2.5. Structures of relevant sulphur-bridged thiosemicarbazones by Bermejo *et al.* (left) and López-Torres *et al.* (right).[124, 125]

It is notable that a dimerised structure of the ethyl-functionalised bis(substituted) ligand precursor has been formed *via* sulphur-sulphur bridging under aprotic conditions. The capacity for DMSO to form disulphide bonds of peptides is well-known. All previously reported thiosemicarbazone disulphide-bridged ligand precursors were formed by oxidation *via* a metal-based catalyst. It has been well documented that Cu(II) and Fe(III) oxidise organo-thiols to produce sulphur-sulphur bonds.[124] Cu(II) and Mn(II) catalysed thiosemicarbazone sulphur-bridged proligand were reported by López-Torres *et al.* and Bermejo *et al.* respectively *(Figure 2.5).*[125] The S-S bond lengths of these published ligand precursors were 2.0335(11) Å and 2.039(1) Å correspondingly, which is somewhat shorter than the disulphide bond of the **iib** dimer, 2.051(2) Å. This suggests that the **iib** dimer bond may be labile and the dimerisation reversible. Literature show that the resultant disulphide may be formed intentionally *via* metal-based catalysis or by aerial oxidation in DMSO, which in this case is the latter.[126]

2.3.1 Density functional theory calculations

To provide insight into the geometry of the bis(imino) ligand-precursor (*E*,*Z*) and (*E*,*E*) isomers were optimised by DFT in the gas phase and in solution. Phenyl-functionalised compound optimisations were used as representatives of the bis(imino) ligand-precursors and were based on available crystal structures.

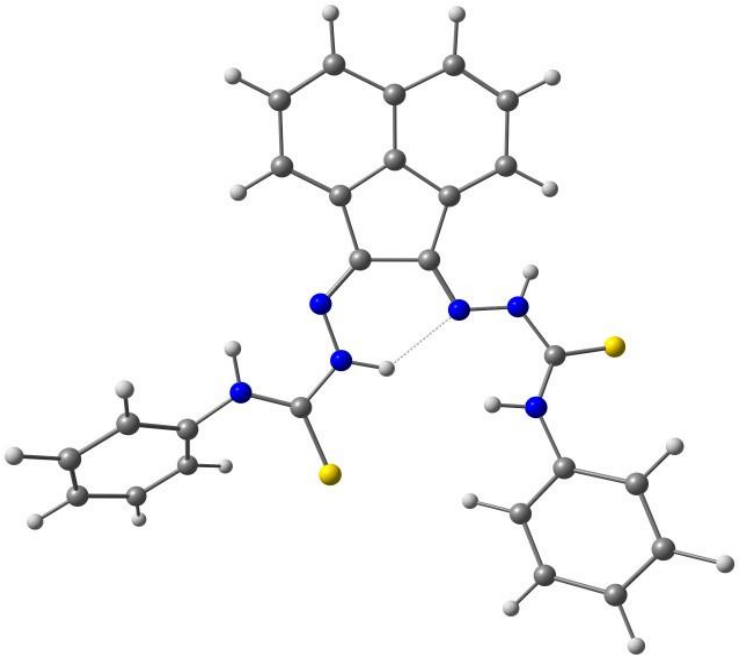

Figure 2.6. Optimised in solution of asymmetric **iic'** by B3LYP 6-31++ (d,p) IEFPCM, DMSO. Where grey = carbon, white = hydrogen, blue = nitrogen.

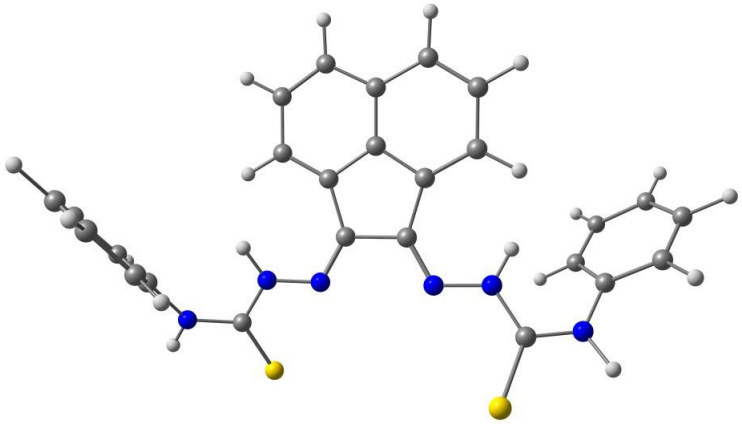

Figure 2.7. Optimised in solution structures of symmetric **iic** by B3LYP 6-31++ (d,p) IEFPCM, DMSO. Where grey = carbon, white = hydrogen, blue = nitrogen.

Following the method used by Holland *et al.*,[119] the ligand precursors were initially optimised in the gas phase using B3LYP 6-31G(d,p), followed by B3LYP 6-31++ (d,p) IEFPCM, DMSO to obtain an optimised structure in solution *(Figures 2.7 and 2.8).* Bond lengths of the optimised structures were comparable to crystallographic data acquired for compounds **iib** and **iic** *(Table 2.1).* In the gas phase the calculated energy difference is 4.17 kJ mol^{-1}, indicating that the asymmetric structure **iic'** is more stable than the symmetric structure **iic**. Likewise, when solvent effects were considered in DMSO, the asymmetric structure was more energetically favourable when compared to the symmetric by 2.04 kJ mol^{-1}, confirming what was observed by NMR spectroscopy and X-ray crystallography. The (*E*,*Z*) structure **iic'** is likely stabilised by internal hydrogen-bonding, whilst the (*E*,*E*) structure **iic** may be more favourable for complexation as it offers more space for a metal. For example, the alkyl-BIAN ligand precursor reported by Cowley *et al.* as the (*E*,*Z*) isomer was metallated to form a zinc complex, which possessed the (*E*,*E*) geometry.[120] Likewise, the 1,2-cyclohexanedione bis(4-methylthiosemicarbazone) ligand precursor reported in the above study possessed an (*E*,*Z*) isomeric structure, with its analogous copper complex possessing the (*E*,*E*) structure.

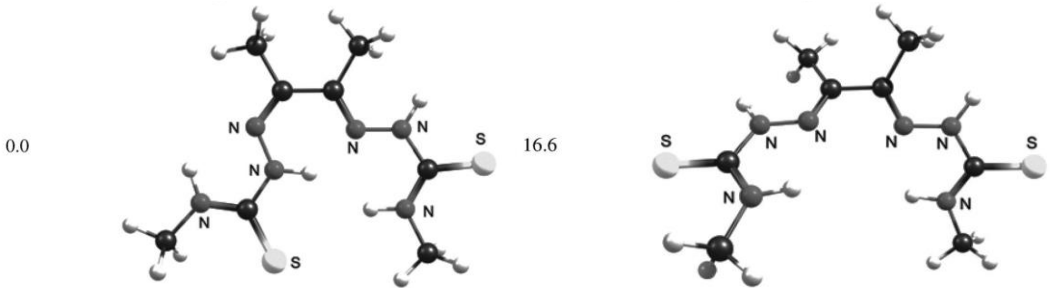

Figure 2.8. DFT calculations on H_2ATSM by Holland *et al.*,[119] which show (*E*,*Z*) isomer, 0.0 kJ mol^{-1} (left) to be more energetically favourable than the (*E*,*E*) isomer, 16.6 kJ mol^{-1} (right). (Numbers to the left represent the relative energy of the calculated structure in kJ mol^{-1}.)

Furthermore, the study by Holland *et al.* demonstrated that the most stable conformer of H_2 ATSM is the (*E*,*Z*) geometry.[119] The energy difference between the two conformers of H_2 ATSM examined was 16.6 kJ mol^{-1}. The low energy difference between the (*E*,*Z*) and the (*E*,*E*) structures is an encouraging result indicating that metal chelation may be possible.

2.4 Fluorescence Spectroscopy

Light emitted from a fluorophore is detectable *via* fluorescence spectroscopy and microscopy. These spectroscopic and imaging techniques allow the monitoring of a fluorescent compound in solution and in biological cells. The naphthyl backbone of ligand precursors above provides electron-rich π-bonds and facilitates fluorescence emission.[118] This bypasses the necessity of conjugating a commercially available fluorophore, such as fluorescein or BODIPY which are expensive and may significantly affect the biological properties of the compound under investigation. Appropriate biological assays and microscopy conditions can be chosen once the fluorescent properties of the ligand precursors are understood. Therefore fluorescence scans between 200-800 nm were obtained in 100 μM DMSO solutions, allowing maxima of excitation ($\lambda_{ex\text{-}max}$) and emission ($\lambda_{em\text{-}max}$), useful information for fluorescence microscopy. Furthermore ranges of absorption and emission were assessed using 2D contours, which are significant to the choice of cytotoxicity assays and fluorescence imaging settings. Since relevant cytotoxicity assays use absorbance readings at 570 nm, it is preferable that there should be minimal or no excitation at this wavelength. This was confirmed for each ligand precursor making them suitable for later *in vitro* studies. In general the fluorescence of the bis(substituted) ligand precursors was very weak, with the overall range of absorption for these compounds approximately between 260 nm and 550 nm and an emission range of 450 nm and 680 nm *(Table 2.2, Figures 2.9 and 2.10).*

Table 2.2. Fluorescence spectroscopy of bis(thiosemicarbazonato) ligand precursors.

Compound	$\lambda_{ex\text{-}max}$ / nm	Excitation range / nm	$\lambda_{em\text{-}max}$ / nm	Emission range / nm
id	490	240-615	554	454-735
iia	470	260-610	618	432-800
iib	490	380-530	550.5	496-663
iic	490	270-560	545.5	476.5-715
iid	480	260-560	547	499.5-695

The wavelengths resulting in maximum excitation ($\lambda_{ex\text{-}max}$) were found between 470 to 490 nm, indicating that compounds would be appropriate for excitation *via* a standard 488 nm confocal microscopy laser. With $\lambda_{em\text{-}max}$ lying between 545 and 555 nm the

emission can be expected in a standard green channel of a confocal microscope. The notable exception of methyl substituted ligand **iia** with the λ_{max} of emission at 618 nm and a significantly broader emission range of 432 nm to 800 nm is likely to be observable in both green and red channels of a standard confocal microscope. The mono(substituted) ligand precursor was only weakly fluorescent compared to the corresponding bis(substituted) compound. As a representative example the allyl-substituted mono(substituted) ligand precursor showed broader excitation and emission (240 nm to 615 nm and 454 nm to 735 nm respectively). While $\lambda_{ex\text{-}max}$ and $\lambda_{em\text{-}max}$ were 490 nm and 554 nm respectively for **id**, were comparable to the maxima of **iid** *(Table 2.2)*.

Considering that the fluorescence of their analogous complexes is likely to be significantly greater, due to metal to ligand charge transfer (MLCT) and ligand to metal charge transfer (LMCT) this is a positive result. Encouraged by these preliminary results a study of the ligand precursors was conducted *in vitro*, in order to allow comparisons with their corresponding metal complexes in later chapters.

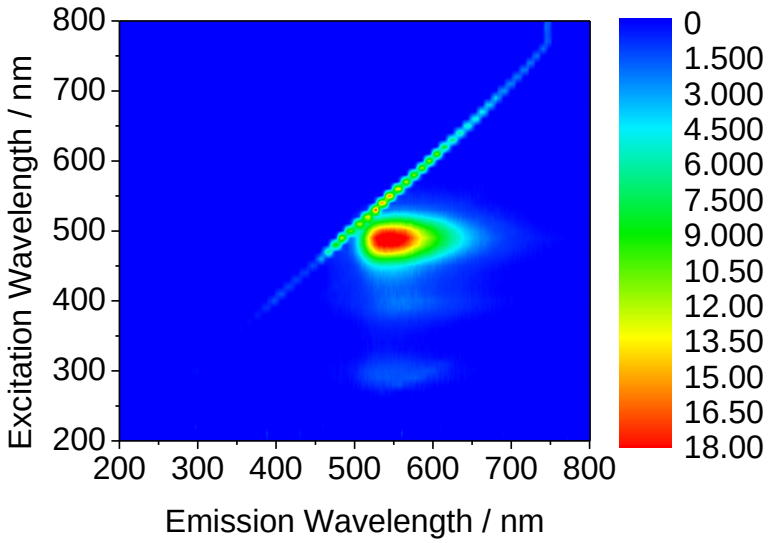

Figure 2.9. Excitation/emission map of compound **iic.**

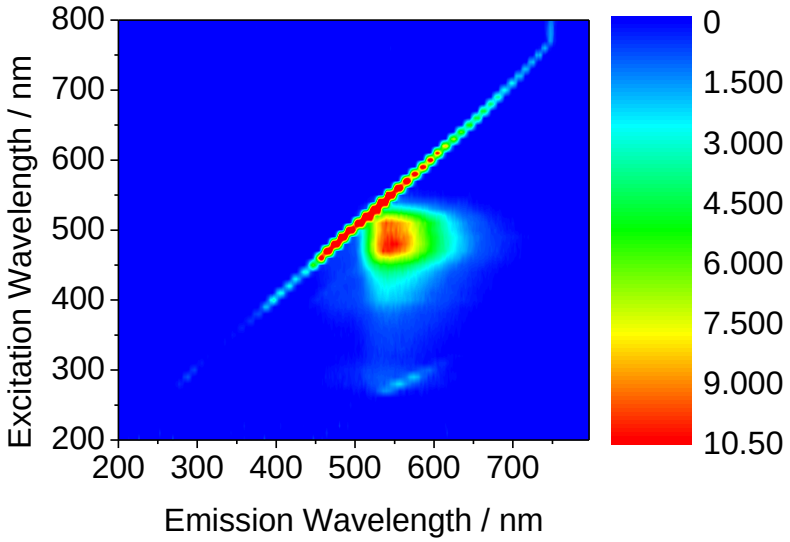

Figure 2.10. Excitation/emission map of compound **iid**

2.5 Laser scanning confocal microscopy

Experiments were carried out to ascertain if the weak fluorescence of the ligand precursors was sufficient to be observed *in vitro*. Cells were cultured using standard protocols, analogous to earlier investigations on fluorescent thiosemicarbazones in the group. [127, 128]

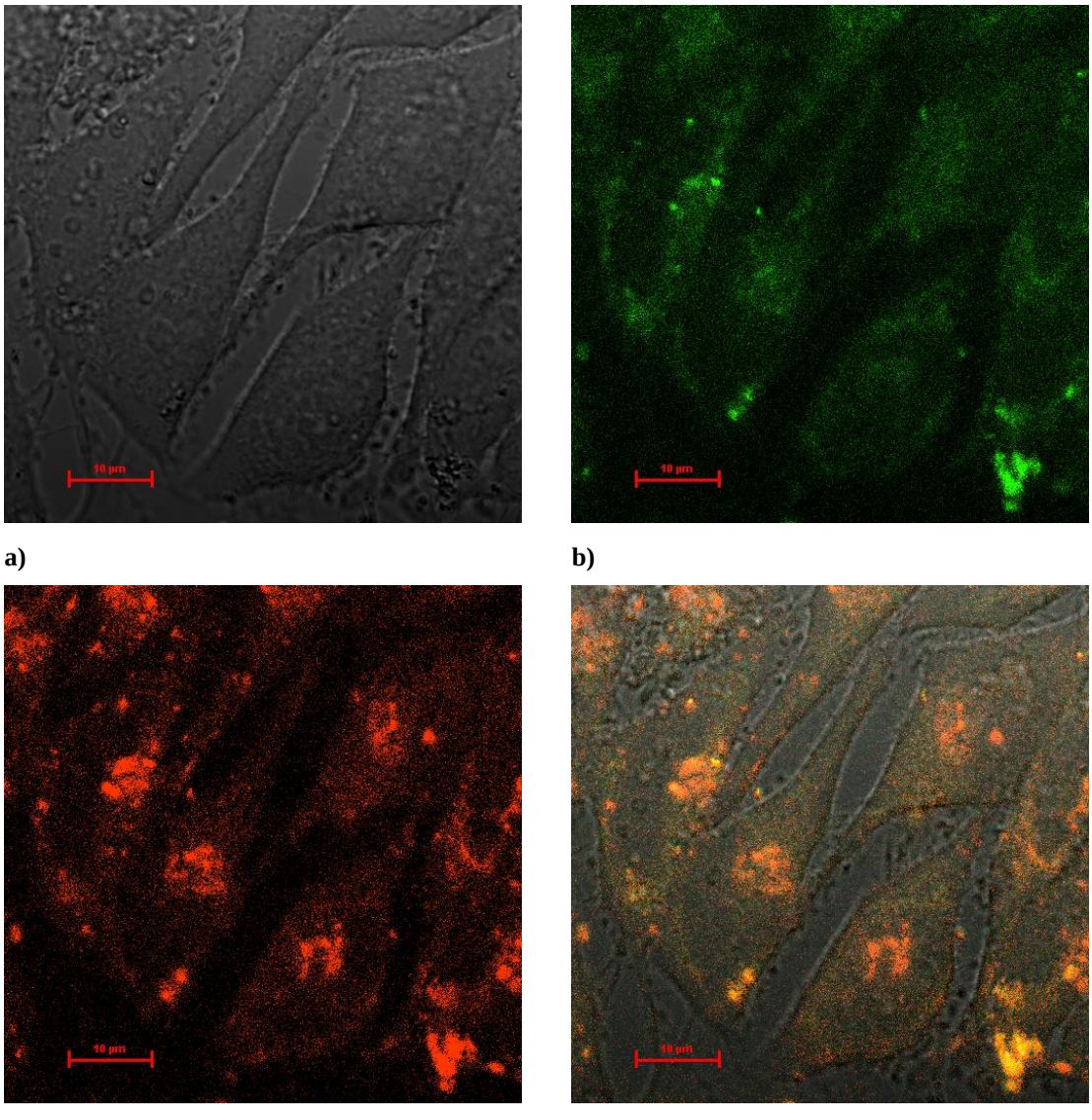

a) **b)**

c) **d)**

Figure 2.11. Single-photon confocal microscopy images of **ia** in HeLa cells, incubated with lysotracker 100 µM, 1% DMSO, 20 minutes, at 37°C. a) Differential Interference Contrast (DIC) image. b) Micrograph of cells after excitation at 488 nm, green channel, showing localisation of the compound **ia**. c) Micrograph of cells after excitation at 543 nm, red channel, showing localisation of the lysotracker. d) Overlay of a), b) and c). Scalebar: 10 µm.

Cell viability prior to experiments and over their course was monitored by optical microscopy, and validated at the start of the experiments by standard trypan blue tests. The compounds were imaged in HeLa (cervical carcinoma), PC-3 (prostate carcinoma), MCF-7 (breast cancer) and FEK-4 (non-cancerous fibroblast) cell lines using standard confocal fluorescence microscopy with one photon excitation at 488 nm.

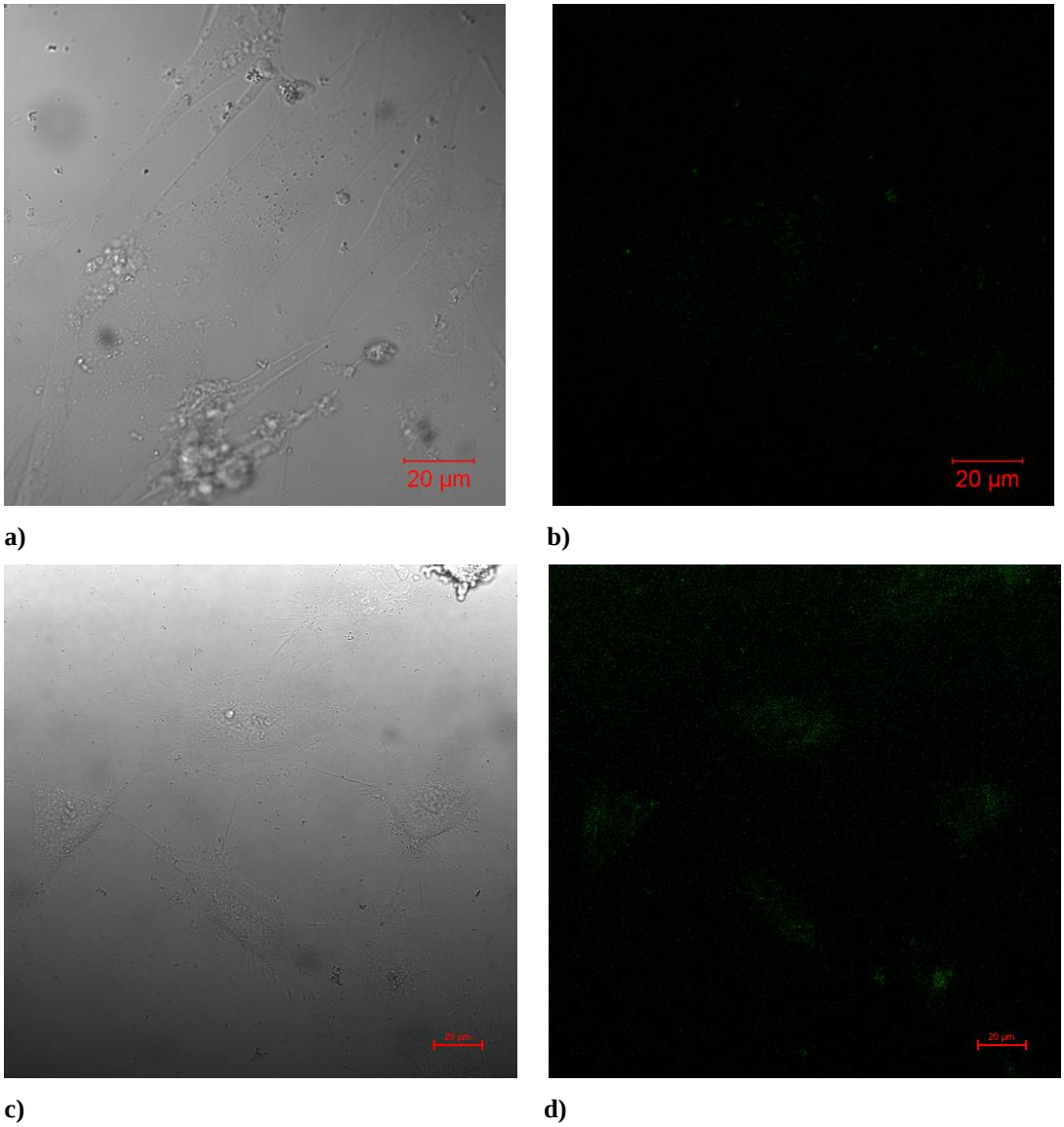

Figure 2.12. (a – b) Single-photon confocal microscopy of compound **iid** in FEK-4 at 50 µM, 0.5 %, DMSO incubated for 20 minutes, washed then **iid** was incubated at 100 µM, 1% DMSO and incubated for 20 minutes, (c – d) **iid** at 100 µM, 1% DMSO, after 20 minutes in HeLa. (a, c) DIC image. (b, c) Florescence images at 488 nm excitation. Scalebar 20 µm.

The imaging studies were performed using concentrations of 100 µM in a DMSO: RPMI (Royal Park Memorial Institute) cell medium 1:99 solvent mix, whereby the final DMSO concentration on the imaging plate was lower than 1%. The fluorescence of the compounds was very weak, therefore such high concentrations of the ligand precursors were necessary to assess uptake within cells. Compound **ia**, the methyl substituted mono(substituted) thiosemicarbazone ligand was incubated in HeLa cells and was found to possess a good colocalisation with lysotracker *(Figure 2.11)*, suggesting that this compound is likely to enter the lysosome.

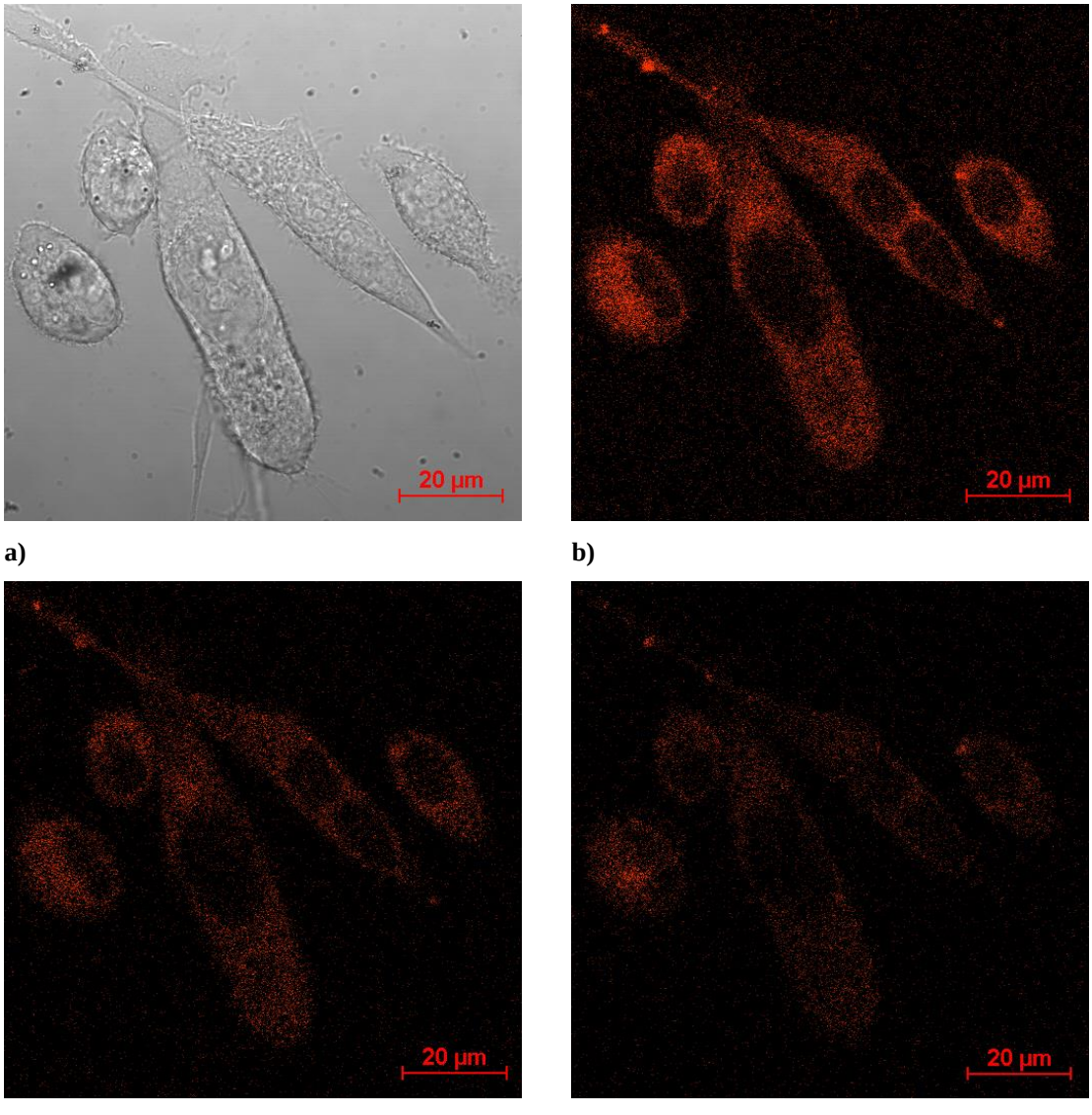

a) **b)**

c) **d)**

Figure 2.13. Single-photon confocal microscopy of **iic** at 100 µM in PC-3, 1% DMSO, incubated for 20 minutes. a) Micrograph of DIC. b) Red channel, excitation 405 nm. c) Red channel, excitation 488 nm. d) Red channel, excitation 543 nm.

Further investigations with colocalisation dyes demonstrated that the ligand precursor did not localise in the mitochondria or nucleus *(Appendix Figures G.2-3)*. Experiments showed that bis(substituted) ligand precursor **iid** possessed weak uptake in HeLa cells, which was barely detectable when incubated in FEK-4 cells, under the same conditions *(Figure 2.12)*. The latter result suggests that there could be a preference for the compound to enter cancerous cell lines over non-cancerous cells *(Figure 2.12 and Appendix Figures G.4-8)*. Optimal imaging conditions were found to be at 405 nm rather than at 488 nm excitation and this emission was observed maximally in the green channel for methyl, ethyl and allyl substituents *(Appendix G)*. A blue shift in absorbance can be expected in a more polar solvent such as water. A higher level of solvation of a lone pair lowers the n-orbital energy, resulting in a larger energy $n \rightarrow \pi^*$ transition and thus absorption at a lower wavelength. Absorption of the phenyl bis(substituted) ligand precursor was most favourable when using the 405 nm laser, however, the emission was maximised in the red channel *(Figure 2.13)*. A comparison between the fluorescence observed in the 2D spectra in DMSO solution and within cells shows a blue shift in the $\lambda_{ex\text{-}max}$ from ca. 480 nm to ca. 405 nm, with a redshift in emission. This redshift can be understood as a solvent effect, whereby a more polar solvent reduces the energy difference between the excited and ground states. The process, known as solvent relaxation occurs when solvent molecules stabilise and decrease the excited state energy level, therefore resulting in a higher wavelength emission.

Rather than being a hindrance, the weak fluorescence of the ligand precursors within cells is a significant advantage in being able to assess the stability of their respective metal complexes *in vitro* as will be demonstrated in subsequent chapters. Moreover, stability in cells was subsequently investigated using fluorescence lifetime imaging microscopy (FLIM), as a quantitative means of stability assessment. In addition to a qualitative evaluation using standard fluorescence microscopy this may provide another powerful means of evaluating complex stability *in vitro*.

2.6 Two-photon excitation and fluorescence lifetime imaging microscopy

Two-photon absorption occurs when the combined energy of two simultaneous photons results in molecular excitation. The first photon to interact generates what is known as a virtual state, which has no classical analogue and only exists transiently (generally for femtoseconds) in which time a photon can travel ca. 1 μm. Arrival of the second photon must occur before the virtual state decays (dephases), which will occur if the laser intensity is high and focussed. The probability of single photon absorption is proportional to the intensity of light and is in contrast to two-photon absorption, which is dependent on both spatial and temporal coincidence *(Equations 2.1 and 2.2)*.[129] Therefore, where NA_x is the number of photons absorbed per second, I is the intensity, σ_x is the cross-section and x is 1 or 2 photon absorption.

Single-photon absorption: $NA_1 = \sigma_1 I$ (Equation 2.1)

Two-photon absorption: $NA_2 = \sigma_2 I^2$ (Equation 2.2)

An advantage of two-photon excitation therefore, is that imaging occurs only from the focal plane. This is contrasting with single-photon excitation microscopy, in which the image is often distorted as it may occur outside the focal plane.[129] Furthermore, despite the requirement of high-powered lasers, two-photon microscopy has been found to cause less damage to biological cells than single-photon microscopy, as well as to decrease photo-bleaching and augment imaging depth.[130]

Two-photon absorption has been used in the development and application of two-photon fluorescence confocal microscopy since 1990 and provides significantly greater control from a clinical perspective, with ongoing research seeking to enable an in-depth understanding of biological processes. In turn this allows for selection of individual cells and as a consequence, the capacity to improve treatments of sensitive tissues such as the retina.[131,132]

Recent advancements have resulted in the design of two-photon fluorescence lifetime imaging (FLIM), which combined with highly sensitive single-photon counting lifetime measurements poses an attractive method for investigating small molecule fluorescence. Fluorescence lifetime is often considered as a means of distinguishing between different

fluorophores, which possess sufficiently different lifetimes and can also be achieved using spectrally resolved microscopy.

FLIM is frequently used to separate different portions of the same fluorophore, for purposes such as quenching of luminescence by intracellular ions (e.g. Ca^{2+} or Cl^-) or by oxygen. Furthermore, this technique can be used to monitor binding of and even distance from a fluorophore, with a conformational change is likely to result in a different rate of internal non-radiative decay and, therefore, a modification of the fluorescence lifetime.[133, 134] pH effects can also be studied, since protonated and non-protonated forms of a molecule may possess different lifetimes. In addition investigations of aggregation, viscosity, proximity to metal surfaces and nanoparticles (due to their long luminescent lifetimes) are carried out.[133] There has, however, been little use of FLIM for the purpose of assessing the stability of sodium[135] and magnesium[136] complexes *in vitro*, but thus far no reports of use of the stability evaluations technique with transition metal complexes.

Consequently, if the fluorescence lifetime of the complex is significantly different to that of the ligand precursor, FLIM could be utilised to assess the complex stability *in vitro*. Two-photon excitation experiments were performed at the Rutherford Appleton Laboratory following the methodology described in Botchway *et al.* 2008[137] and in our recent publication (Pascu *et al.* 2011[138]) with assistance of Dr S Botchway, Dr P Burgos, Mr A. Mckenzie and Mr A. Henman.

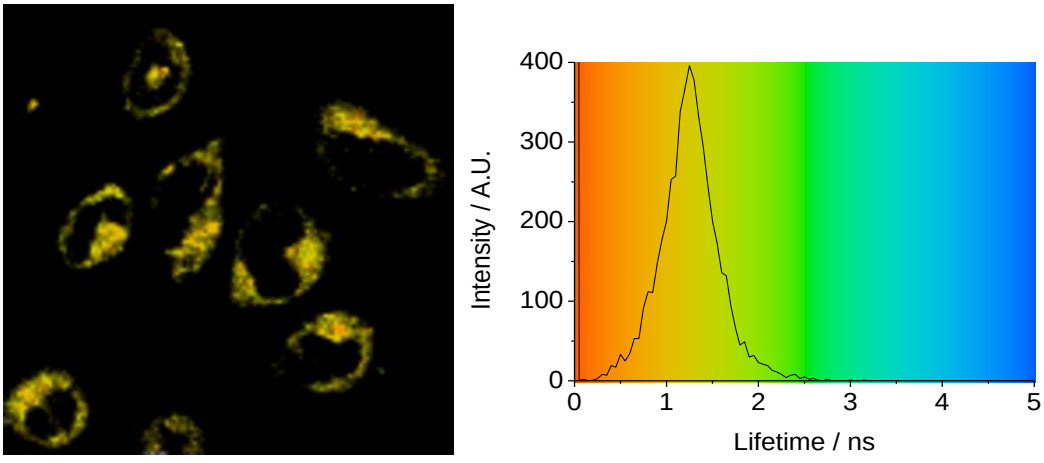

a) **b)**

Figure 2.14. Control experiment at 810 nm, in HeLa cells where **a)** is the colour image corresponding to the two-photon fluorescence lifetime map of the τ_m (the weighted average fluorescence lifetime), **b)** is the distribution curve of the τ_m where the colour represents the lifetime of a).

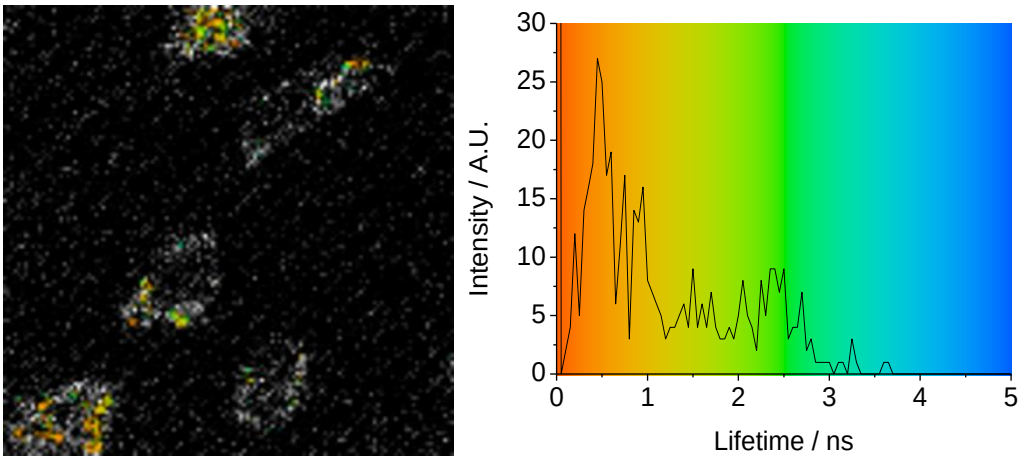

a) **b)**

Figure 2.15. Control experiment at 910 nm, two-photon fluorescence lifetime map (τ_m) in HeLa cells showing weak autofluorescence where **a)** is the colour image corresponding to the two-photon fluorescence lifetime map of the τ_m, **b)** is the distribution curve of the τ_m where the colour represents the lifetime of a).

In order to be able to quantify compound fluorescence the background autofluorescence of cells had first to be assessed. The 810 nm control possessed the fluorescence lifetimes of 0.812 ns (τ_1 79 % 0.214 ns FWHM) and 3.140 ns (τ_2 21 %, 0.647 ns FWHM). Figure 2.11b and 2.12b represent the mean lifetime of both components in HeLa cells when modelled to two components. Autofluorescence when excited at 910 nm, however, was negligible therefore all compounds displaying significant fluorescence at 910 nm were tested at the latter wavelength *(Figure 2.14).* It is in agreement with literature that autofluorescence is less at 900 nm than 800 nm.[139] The background fluorescence can be attributable to biological fluorophores; at 910 nm these include flavin adenine dinucleotide (FAD) and lipoamide dehydrogenase (LipDH), which also absorb at 810 nm.[140] Biological molecules such as reduced nicotinamide adenine dinucleotide (NADH) and nicotinamide adenine dinucleotide phosphate (NADPH) absorb 810 nm light, but not 910 nm, therefore contributing to the difference in autofluorescence intensity observed at the respective wavelengths.[140]

The full width at half maximum (FWHM), calculated from the lifetime distribution curve within the focal area was used to assess the error. The percentage of components τ_1 (major) and τ_2 (minor) in cells was from the respective amplitudes a_1 and a_2

calculated using SPCImage software, which models the data for each individual pixel to Equation 2.3, where *F* is fluorescence, a_0 is background and t is time:

$$F(t) = a_0 + a_1 e^{-t/\tau_1} + a_2 e^{-t/\tau_2} \quad \text{(Equation 4.3)}$$

2.6.1 Ligand precursor fluorescence lifetime investigation

For each bis(substituted) ligand precursor tested by Time-Correlated Single Photon Counting (TCSPC) two fluorescence lifetime components could be determined in DMSO at 10 mM, with the τ_1 accounting for at least 94 % in each case. The τ_1 values were very similar for compounds **iia**, **iib** and **iic** when excited at 810 nm (0.226 ns with χ^2 of 1.88, 0.183 ns with a χ^2 of 1.63 and 0.158 ns with a χ^2 of 1.71 respectively). The excitation wavelength did not appear to have a significant effect on the fluorescence lifetime. For example when **iic** was excited at 910 the major component was 0.156 ns. Similarly the τ_1 of **iid** was comparably shorter (0.020 ns at 810 nm and 0.021 ns at 910 nm), indicating no observable difference between the lifetimes when exciting at the respective wavelengths in DMSO solution.

The minor component (τ_2) of the fluorescence lifetime of the ligand precursors in DMSO at 10 mM did not follow the same pattern. While compounds **iia** and **iic** had a τ_2 of ca. 2.5 ns as the minor component for **iib** was 3.969 ns. By contrast the minor component for **iid** was one order of magnitude longer, with τ_2 values of 0.274 ns and 0.468 ns for excitation with 810 nm and 910 nm respectively. These numbers, however, are to be taken with caution as the errors are much larger than for τ_1 due to the weakness of this second component (< 5%). Excitation at 810 nm produced considerably higher quality data than at 910 nm for the ligand precursors in cells *(Figures 2.16-2.17)*, which is why *in vitro* studies were also conducted at 810 nm excitation wavelength.

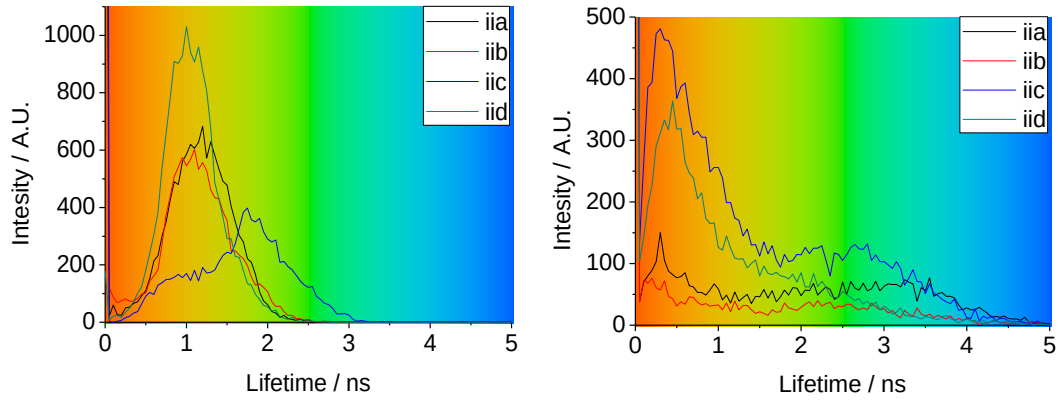

Figure 2.16. Two-photon mean fluorescence lifetime distribution curve (τ_m) in HeLa cells of **iia**, **iib**, **iic** and **iid** at 100 μM at **a)** 810 nm and **b)** 910 nm.

The fluorescence lifetime of the compounds were obtained from the FLIM distribution curve in cancer cells (HeLa, MCF-7 and PC-3 cells). Standard conditions used were 1% DMSO 100 μM, with an incubation time of 20 minutes. The majority of cellular studies could be modelled to two fluorescence lifetime components, one of which was short (ca. 0.2 ns) with the other being long (ca. 2.5 ns). The solution data were within the FWHM, which represents the error for *in vitro* data and thus confirms their comparability.

There were some exceptions however, such as the long components of **iib** in PC-3 cells (0.434 ns, 0.209 ns FWHM) and of **iid** in HeLa and PC-3 cells at 910 nm (0.436 ns, 0.653 ns FWHM and 0.418 ns, 0.455 ns FWHM, respectively). Other notable exceptions were the major components observed for **iia** and **iib** when excited at 810 nm, with lifetimes of 0.903 ns and 0.868 ns, correspondingly. These are within the FWHM of the control, which suggests that most of the fluorescence observed at this wavelength for these two compounds is as a result of cellular autofluorescence. This could indicate the weakness of the fluorescence of the proligand or simply that the conformation of the compound within the cell and in turn the fluorescence lifetime has been significantly altered as opposed to in DMSO.

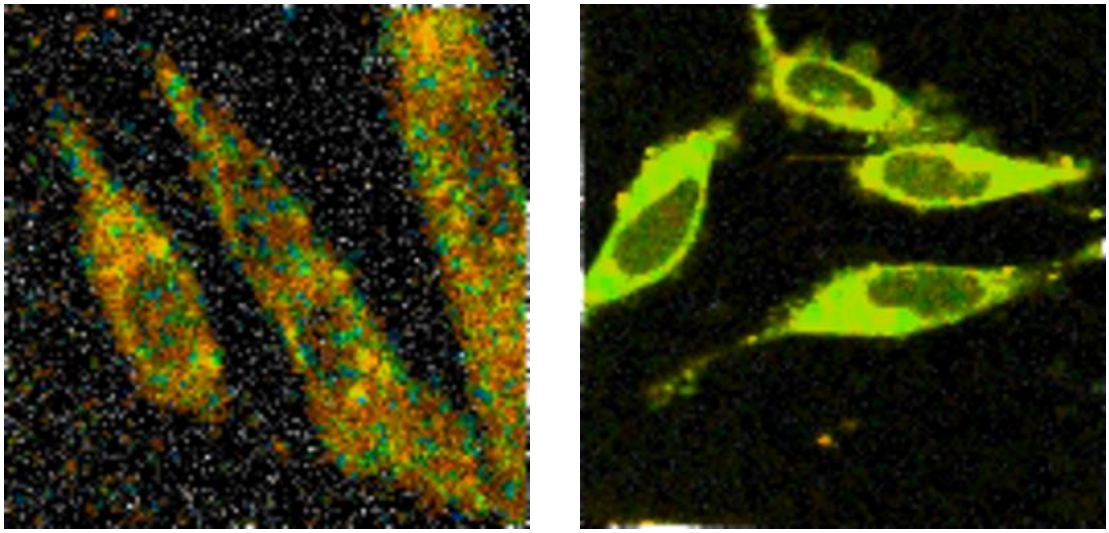

a) **b)**

Figure 2.17. Two-photon fluorescence lifetime map (τ_m) of **iic a)** in PC-3 cells with excitation at 910 nm and **b)** in HeLa cells with excitation at 810 nm.

The minor components nevertheless, could be correlated to the ligand precursor, confirming the weak fluorescence of the compound in cells. The fluorescent lifetime measurements of the mono(substituted) ligands were similar to their bis(substituted) analogues, possessing in general a short, major component of the order of 0.4 ns and a long, minor component in the region of 3 ns. Unlike the bis-thiosemicarbazonato ligands, this was consistently observed in cells when excited at 910 nm. Different molecular orientations would result in a change in fluorescent lifetime, which could suggest that the mono(substituted) proligand geometry was less variable than its bis(substituted) counterpart.[133] Interestingly, although consistency of data was observed in cells, the respective short, major component is slightly shorter (ca. 0.2 ns), which suggests that the complexity of the cellular environment does have impact on the lifetime. There appeared to be a more limited effect on the mono(substituted) than the bis(substituted) ligand precursor, which displayed greater variation of lifetime within cells. Notably, the fluorescence of the mono(substituted) ligand precursors was very weak and comparable to the bis(substituted) ligands.

2.7 Summary to Chapter 2

Mono(thiosemicarbazonato) and bis(thiosemicarbazonato) ligand precursors were successfully synthesised and characterised by ESI-MS and NMR spectroscopy. Furthermore their fluorescence properties were analysed, showing weak, but detectable emission in solution and in cancerous and non-cancerous cells at 100 μM concentration. Fluorescence of respective complexes of these proligands would be expected to be higher due to MLCT and LMCT, therefore strong fluorescence at this concentration or lower would provide a qualitative indication of complex stability. Furthermore, the fluorescence lifetime components of these compounds were determined in solution and in cells with characteristic data that proved distinguishable from cellular autofluorescence. This means that if a complex decomposes in the cell by deconvoluting the various fluorescence lifetime components, provided that these are sufficiently dissimilar to allow discrimination between them.

Chapter 3. Synthesis, characterisation, spectroscopic, *in vitro* and *in vivo* analysis of zinc and copper bis(thiosemicarbazonato) complexes

3.1 Overview

In this Chapter, the transmetallation reactions to generate new copper complexes are described. Zinc bis(thiosemicarbazonato) complexes precursors provide a clean means of synthesising other metal complexes (such as copper) *via* transmetallation. The fluorescent analogue of the known tracer Cu[ATSM] is its zinc analogue Zn[ATSM]. Therefore a means of comparison can be provided by synthesising zinc bis(thiosemicarbazonato) complexes containing a acenaphthenequinone based backbone, which were first synthesised in the group. [123, 127, 128] Subsequently the aims were to synthesise zinc and copper bis(thiosemicarbazonato) complexes, acquire and discuss new structural data and distinguish, for the first time, their stability in biological cells.

3.2 Zinc complex synthesis

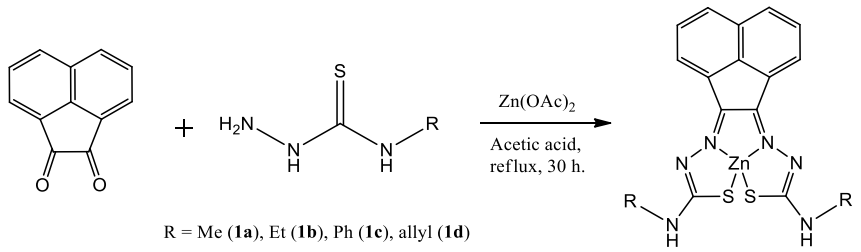

Figure 3.1. Synthesis of acenaphthenequinone zinc bis(thiosemicarbazones)

Earlier studies in the group, showed that acenaphthenequinone zinc bis(thiosemicarbazone) complexes can be made in a one-pot synthesis by reflux in acetic acid, followed by filtration and washing of the product with diethyl ether. Terminal functionalities in this study included methyl, ethyl, phenyl and allyl groups *(Figure 3.1)*. [123, 127, 128] The complexes were obtained as orange or red solids in moderate to good yields of (49% to 68%). The compounds (**1a**, **1b**, novel complex **1c** and **1d**) were characterised by ^{1}H and ^{13}C NMR spectroscopy and ES-MS, giving peaks at m/z 419.01, 447.04, 543.04 and 471.03 respectively, which represent $[M + H]^{+}$.

3.3. Copper complex synthesis

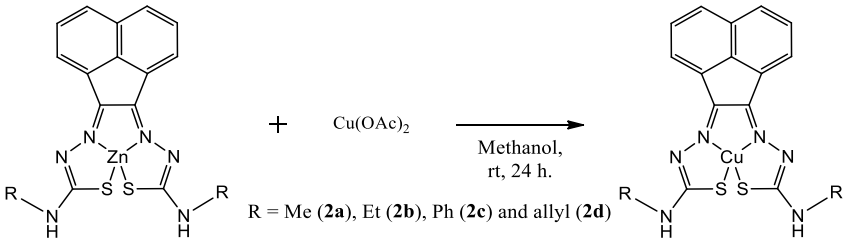

Figure 3.2. Synthesis of acenaphthenequinone copper bis(thiosemicarbazones) *via* transmetallation

The zinc compounds (**1a-d**) act as precursors to the analogous copper complexes in transmetallation reactions. One equivalent of the respective zinc complex and two equivalents of copper acetate were stirred in methanol at room temperature for 24 hours and the product isolated as a brown solid by filtration, after washing with water and methanol the yields were good (53 % to 77 %) for **2a**, **2b**, **2c** and **2d** *(Figure 2)*.[123, 127]

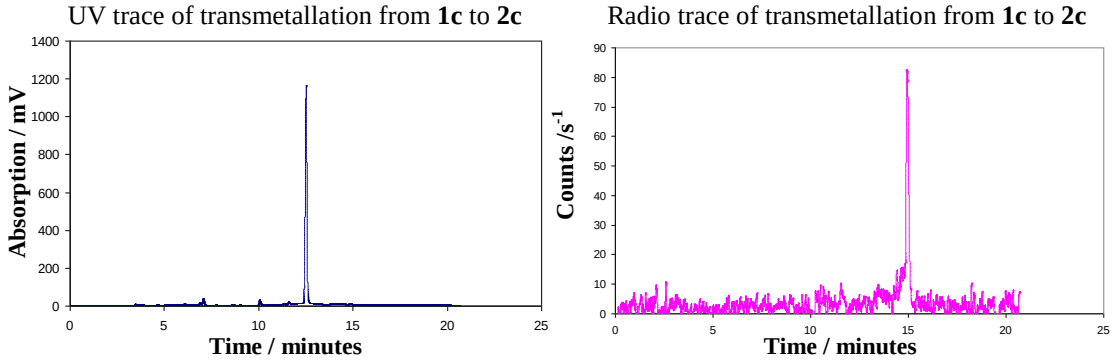

a) **b)**

Figure 3.3. HPLC of transmetallation from **1c** to **2c** showing **a)** the UV trace (blue) and **b)** the radio trace (pink).

LC-MS was used to characterise these compounds since NMR spectroscopy was not informative due to the paramagnetic nature of copper, giving m/z values of 418.01, 446.04, 542.32 and 470.03, which represent $[M + H]^+$. Complexes **2a** and **2b** were first reported in Reference 123 for which the writer of this thesis is a co-author. Furthermore, EPR spectroscopy of novel complex **2c** gave comparable spectra to **2a**, **2b** and **2d** and confirms the presence of a paramagnetic species *(Appendix I)*. Moreover it was possible to cleanly and rapidly radiolabel complex **1c** with ^{64}Cu using $^{64}Cu(OAc)_2$ at Oxford Siemens Molecular Imaging Laboratory under the supervision of Dr Phillip A. Waghorn and Prof Jon Dilworth.

The partition coefficient log *P*, which is an indicator of lipophilicity, were calculated with **2a**, **2b** and **2c** possessing values of 1.209 ± 0.076, 1.188 ± 0.043 and 1.436 ± 0.062 respectively. The ^{64}Cu compound was added to a mixture of equal volumes of water and octanol, followed by vortexing and centrifugation for 5 minutes. The activity of each phase was measured and the log *P* was calculated as log(octanol [radioactivity] ÷ water [radioactivity]), a value above 1 meaning that the compound is lipophilic.[141] The value for Cu[ATSM] under the same conditions was found to be 1.48, which indicates that uptake of these copper complexes, in particular for **2c** is likely to occur in the liver *in vivo*, as does Cu[ATSM].[142]

Cyclic voltammetry of complexes **2a** and **2b** was carried out by Dr Phillip A. Waghorn. The compounds were found to possess reduction potentials of -0.517 V and -0.536 V, respectively.[123] Since these are close to the reduction potential of Cu[ATSM] (-0.581 V) under comparable conditions it appears that the additional acenaphthene ligand backbone has not significantly affected the reduction potentials. Surprisingly, despite displaying a log *P* and reduction potential equivalent to that of Cu[ATSM] a preliminary hypoxia study by Dr Waghorn showed that complex **2b** did not possess hypoxia selectivity within one hour. It can be speculated that longer incubation times may be required to observe selectivity.

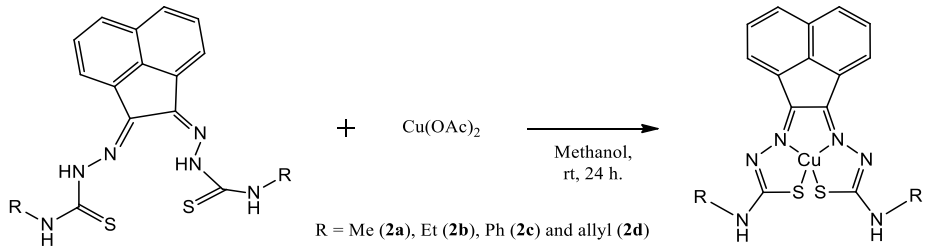

Figure 3.4. Synthesis of acenaphthenequinone copper bis(thiosemicarbazones) *via* the free ligand

Another method of synthesising the copper complexes was attempted *via* the free ligand by stirring in methanol for 24 h with 3 equivalents of copper acetate *(Figure 3.4).* Despite demonstrating some success, this synthesis method did not prove reliable as significant batch-to-batch variations in the product were found, frequently producing a black powder, which did not possess the desired spectroscopic properties, as opposed to a brown solid expected for compounds in this family. This could be explained by the

dimerisation observed by X-ray crystallography *(Chapter 2.3)*, which could cause formation of a copper-based polymeric compound which proved to be intractable. Therefore the transmetallation method was chosen in preference to the free ligand process.

3.4 X-ray crystallography

Crystals suitable for X-ray diffraction were obtained from DMSO or THF:pentane solvent mixtures. The crystals were grown slowly by solvent diffusion techniques at room temperature. Data will be compared to the previous crystallographic results reported in references 123, 127 to 128 and work carried out during this project. The bond lengths and angles below of the newly acquired phenyl-substituted crystal structures are discussed below. The structures here will be discussed in terms of how their structure is affected by functionality, whereby the effect of the metal centre will be discussed in Chapter 5.

It is notable that all of the copper complex crystal structures were determined to be an (*E*,*E*) the symmetrically bound isomer. Whereas zinc complexes **1a**, **1b** and **1d** were found to possess the asymmetric structure. In previous studies in the group, the Zn(II) complexes only yielded suitable crystals for X-ray determinations when they were co-crystallised with DABCO and possessed (*E*,*Z*) isomerism. Here, it was possible to obtain X-ray crystallographic data for the phenyl-substituted zinc complex without co-crystallisation. This structure contained a DMSO adduct has been isolated showing that ligand may also be bound as the an (*E*,*E*) isomer in these Zn(II) complexes *(Figures 3.5-3.6)*.

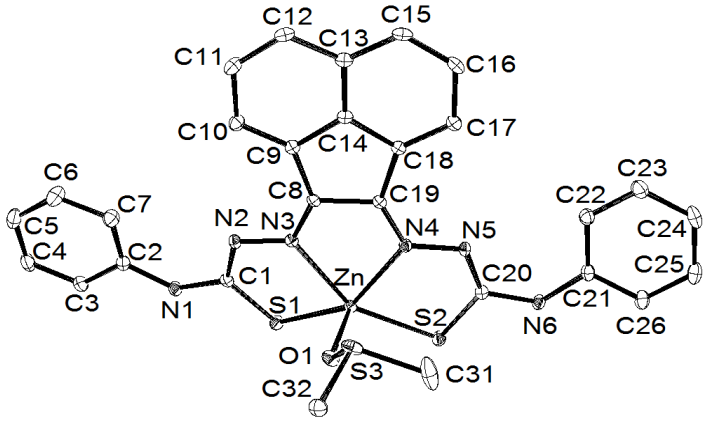

Figure 3.5. ORTEP representation of **1c**, ellipsoids drawn at 30% probability, hydrogens omitted for clarity.

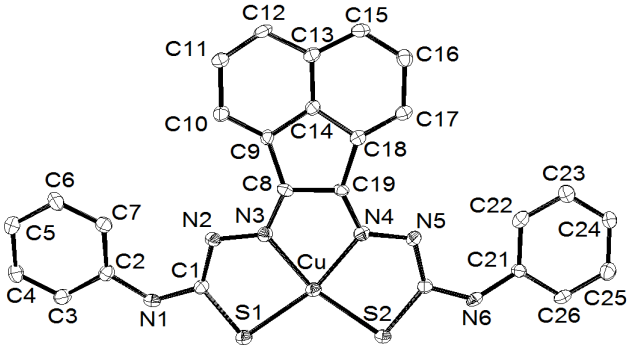

Figure 3.6. ORTEP representation of **2c**, ellipsoids drawn at 30% probability, hydrogens omitted for clarity.

For the zinc and the copper complexes there was little variation in the M-N bond lengths, however when considering the longest of the two Zn-N bonds it is possible to note that phenyl-substituted and the ethyl-substituted zinc complex bond was longer than those of the methyl and allyl-substituted bond. Furthermore, the functionality of the copper complex did not appear to greatly affect the bond lengths, whereby the N-N bonds were similar as were the C=N bonds, with little differences observed in Cu-S bonds where **2b** and **2d** possessed comparable data, which were longer than for the similar Cu-S bond lengths of **2a** and **2c**. A greater degree of variation was observed when comparing zinc complexes of different functionality *(Tables 3.1-3.2)*. The length of the Zn-S bond pattern was the reverse when compared to those of Zn-N, with **1d** the longest, followed by **1a** and with **1c** possessing the shortest *(Table 3.1)*. Meanwhile there was little variation in C=N bond lengths according to functionality and N-N bond lengths with respect to the substituent group.

Notably the C-C bonds in both the zinc and copper complexes (here for **1c** and **2c** this bond is C8-C19, *(Figures 3.5-3.6)* were shortest for the methyl-functionalised compounds. The length of this bond was similar for the other substituents in the case of the copper complexes, with the methyl substituted zinc complex possessing a shorter C-C bond than **1b** and **1d**. It had previously been noted that the asymmetric (*E*,*Z*) zinc structures possessed longer C-C bonds than their analogous (*E*,*E*) copper and nickel structures. Here there was no significant difference between the C-C bond of the zinc compound of various functionalities. Indeed a closer look at one (*E*,*E*) isomer (the phenyl-substituted zinc complex **1c**) suggested that the dissimilarity observed was caused by the nature of the metal centres employed rather than that of the isomer. This hypothesis will be further explored in subsequent chapters.

The bond angles around the zinc atom showed small variations with different substituents. For example, the N-M-N angle of complex **1b**, 75.5(3)° is smaller than the respective angles of the other zinc complexes, of which complex **1d** possessed the largest N-M-N angle of 88.55(15)°. Conversely the corresponding angles of **1a** and **1c** are comparable, 85.87(17)° and 86.6(1)°. The inverse was observed for the S-M-S angle, whereby the largest angle was 118.49(13)°, of complex **1b** and the smallest angle of 110.69(5)° was possessed by compound **1d**. Interestingly complex **1b** possessed greater symmetry in comparison to the other zinc complexes in that the angles around the zinc atom within the same molecule were similar (for example the S-M-N angles, 79.7(3)° and 79.6(2)°, S-M-A angles, 100.30(19)° and 100.4(2)° and N-M-A angles, 98.4(3)° and 98.0(3)°.) Allyl-substituted complex **1d** possessed similar S-M-A angles (103.43(9)° and 103.16(10)°) and N-M-A angles (107.36(13)° and 107.40(15)°), yet different S-M-N angles (83.88(10)° and 60.55(12)°). Meanwhile with comparably less symmetry, complex **1a** had equivalent N-M-A angles (105.16(14)° and 105.13(14)°), with disimilar S-M-N (83.47(12)° and 64.89(13)°) and S-M-A angles (102.94(10)° and 99.15(10)°). Complex **1c**, which was an (*E*,*E*) isomer was interestingly found to possess the least symmetry whereby its respective S-M-N (83.25(8)° and 80.27(4)°), S-M-A (104.31(4)° and 102.01(4)°) and N-M-A (101.11(5)° and 93.77(5)°) angles within the same compound were different.

Table 3.1. Selected bond lengths (Å) and bond angles (°) for compounds **1a-1d,** determined by X-ray diffraction, where A is the adduct atom.

Compound/ Molecular Parameters	**1a. DABCO** (*E*,*Z*) isomer[123]	**1b. DABCO** (*E*,*Z*) isomer[128]	**1c. DMSO** (*E*,*E*) isomer	**1d. DABCO** (*E*,*Z*) isomer[127]
M-N	2.111(4)	2.132(9)	2.1092(14)	2.082(4)
	2.022(4)	2.132(8)	2.1603(14)	2.010(4)
M-S	2.2992(14)	2.378(3)	2.3330(5)	2.829(2)
	2.6845(19)	2.368(3)	2.3691(5)	2.3063(11)
C-C	1.495(7)	1.508(13)	1.499(3)	1.508(7)
N-N	1.316(6)	1.338(11)	1.364(2)	1.365(5)
	1.363(5)	1.384(10)	1.364(2)	1.375(5)
C=N	1.315(6)	1.277(12)	1.294(2)	1.303(5)
	1.284(7)	1.328(13)	1.292(2)	1.314(7)
S-M-S	113.91(5)	118.49(13)	114.68(3)	110.69(5)
S-M-N	83.47(12)	79.7(3)	83.25(8)	83.88(10)
	64.89(13)	79.6(2)	80.27(4)	60.55(12)
N-M-N	85.87(17)	75.5(3)	86.6(1)	88.55(15)
S-M-A	102.94(10)	100.30(19)	104.31(4)	103.43(9)
	99.15(10)	100.4(2)	102.01(4)	103.16(10)
N-M-A	105.16(14)	98.4(3)	101.11(5)	107.36(13)
	105.13(14)	98.0(3)	93.77(5)	107.40(15)

The copper complexes, in comparison showed much greater symmetry with respect to the bond angles around the metal centre, for example the equivalent angles of S-M-N of **2c**, which were 83.72(15)° and 83.64(16)° respectively. Little functionality-dependent variation was observed for example with similar angles for complexes **2b** and **2c** for S-M-S (111.12(4)° and 110.99(7)° respectively) and N-M-N (82.45(14)° and 81.6(2)° correspondingly). Interestingly, the S-M-S and N-M-N angles of the bis(acenaphthenequinone) copper complexes were significantly larger in comparison with Cu[ATSM], 105.25(5)° and 76.09(6)° respectively.

Table 3.2. Selected bond lengths (Å) and bond angles (°) for compounds **2a**-**2d,** determined by X-ray diffraction

Compound/ Molecular Parameters	Cu[ATSM][143]	**2a** (*E*,*E*) isomer[123]	**2b** (*E*,*E*) isomer[123]	**2c** (*E*,*E*) isomer	**2d** (*E*,*E*) isomer[127]
M-N	1.9590(14)	1.983(4)	1.987(3)	1.967(5)	1.9855(17)
	1.9616(13)	1.977(4)	1.980(3)	1.976(5)	1.9779(17)
M-S	2.2462(4)	2.2539(14)	2.2575(11)	2.2508(17)	2.2620(6)
	2.2367(4)	2.2562(13)	2.2693(11)	2.2598(18)	2.2699(6)
C-C	1.478(2)	1.470(6)	1.493(5)	1.481(8)	1.476(3)
N-N	1.3673(18)	1.364(5)	1.359(5)	1.382(6)	1.358(2)
	1.3697(15)	1.358(5)	1.360(5)	1.384(6)	1.360(2)
C=N	1.299(2)	1.309(6)	1.289(5)	1.286(7)	1.291(3)
	1.2961(2)	1.321(6)	1.294(5)	1.293(7)	1.297(2)
S-M-S	109.234(17)	110.11(5)	111.12(4)	110.99(7)	111.52(2)
S-M-N	85.20(4)	83.69(12)	82.92(10)	83.72(15)	83.01(5)
	85.08(4)	83.45(12)	83.51(10)	83.64(16)	83.30(5)
N-M-N	80.62(5)	82.95(16)	82.45(14)	81.6(2)	82.28(7)

3.5 Density functional theory calculations

The crystal structure of the above complexes were first optimised by B3LYP 6-31G(d,p) and then by B3LYP 6-31++ (d,p) IEFPCM, DMSO, following the method of Holland *et al.*[119] Whereby an unrestricted spin was used for the optimisation of the copper(II) complex due to its paramagnetic nature *(Figure 3.7).*

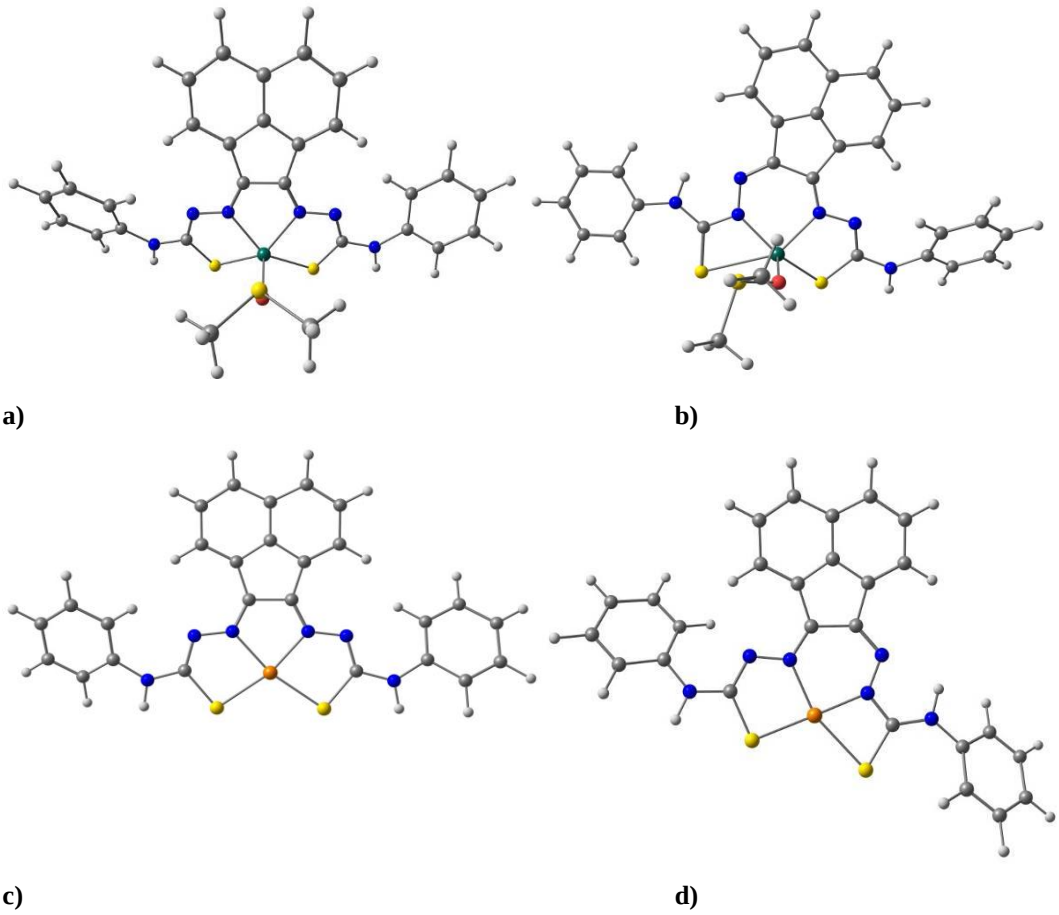

Figure 3.7. Optimised in solution structures by B3LYP 6-31++ (d,p) IEFPCM, DMSO, where a) is symmetric **1c** and b) is asymmetric **1c'**, c) is symmetric **2c** and d) is asymmetric **2c'**. Where grey = carbon, white = hydrogen, blue = nitrogen, red = oxygen, green = zinc, orange = copper.

In the gas phase the asymmetric isomers of the zinc and the copper complexes were more energetically favourable with energy differences in energy of 6.18 kJ mol^{-1} for **1c** and 4.68 kJ mol^{-1} respectively for **2c**. In solution however, the (*E*,*E*) symmetric form was more stable for each complex with a difference of -0.96 kJ mol^{-1} and -4.37 kJ mol^{-1}, for **1c** and **2c** correspondingly. This is in agreement with similar structures as discussed

in Chapter 2.3 that a ligand structure possessing (*E*,*Z*) geometry would re-orientate to the (*E*,*E*) conformation to allow more space for metal chelation.

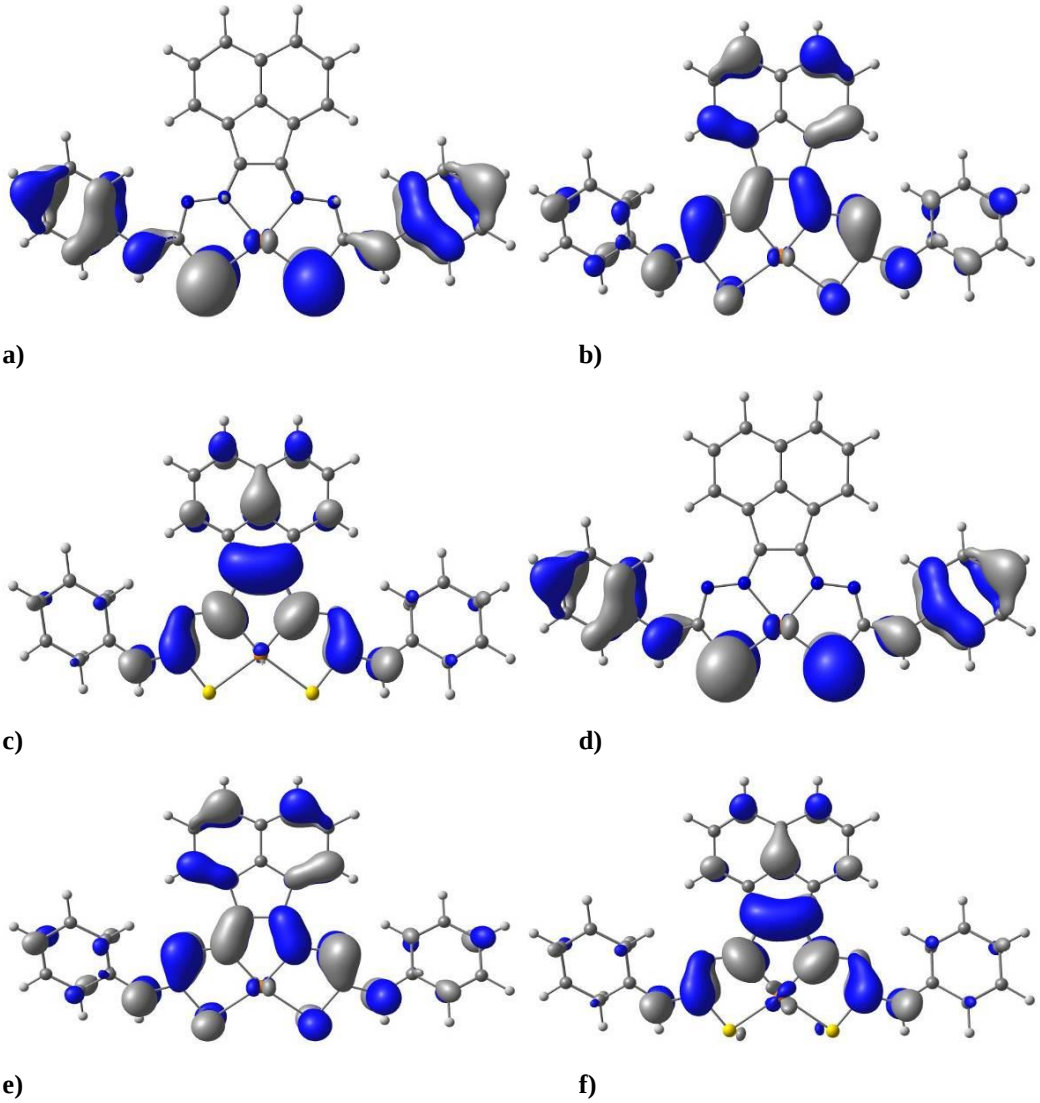

Figure 3.8. Calculated electronic distribution for the molecular orbitals of complex **2c** involved in the 13th excitation state, in which the most significant absorption occurs, where a) is 137α (HOMO -2), b) is 139α (HOMO), c) is 140α (LUMO), d) is 137β (HOMO-1), e) 138β (HOMO) and f) is 140β (LUMO +1)

It is notable that the copper complex symmetric structure was more energetically favourable when compared to its corresponding asymmetric structure, in agreement with the observation that all the crystal structures of the copper acenaphthenequinone bis(thiosemicarbazonato) complexes determined by in the group have been determined as the symmetric isomer. The difference in the energy between the symmetric and the asymmetric isomers is relatively low and since the asymmetric has slightly lower energy in the gas phase it can be speculated that the asymmetric form may exist in

solution in small proportions. Subsequently, TD-DFT was calculated for the first 24 excited states using uB3LYP 6-31++ (d,p) methodology, of which excited state 13 had the most significant oscillator strength, f *(Figure 3.8, Appendix I)*. Since the molecular orbitals involved the ligand (including the phenyl substituent) and the metal it is very likely that both contribute to the fluorescent properties. This could explain the observed similarity between the fluorescent lifetimes of complexes in this family of compounds as well as the small metal dependency.

3.6 Fluorescence spectroscopy

Fluorescence spectra were recorded in DMSO for initial scans between 200-800 nm, in order to obtain information about intrinsic fluorescence and $\lambda_{em\text{-}max}$ using solutions of 100 μM. The ranges of absorption and emission were selected to be of relevance with regards to future cytotoxicity assays and fluorescence imaging, were assessed using the 2D contours as a guideline *(Figures 3.9-3.10)*. Relevant cytotoxicity assays use absorbance readings at 570 nm, therefore there should be minimal or no excitation at this wavelength, which was true for zinc and copper complexes analysed in this manner, with very low absorbance for each.

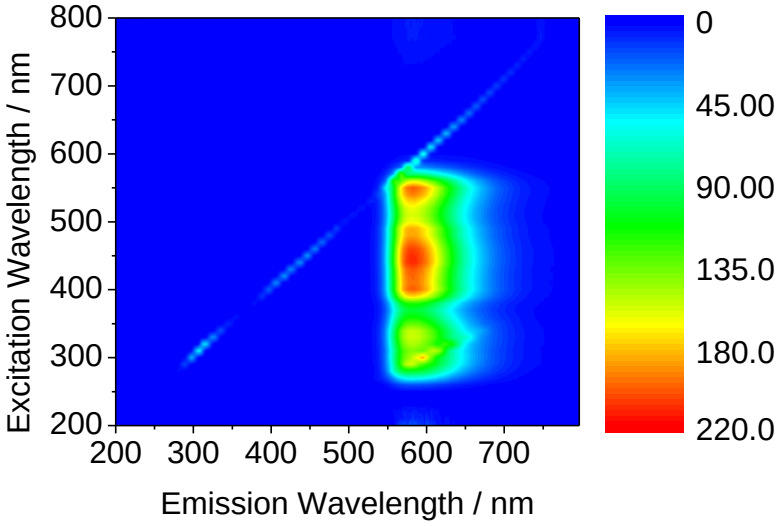

Figure 3.9. Excitation/emission map of compound **1c**.

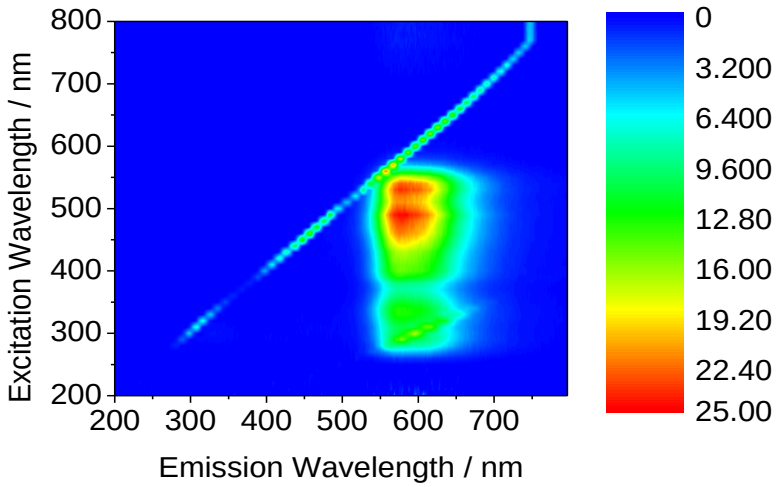

Figure 3.10. Excitation/emission map of compound **2c**.

Initial spectroscopic data for **1a**, **1b** and **1d** and **2a**, **2b** and **2d** have been already studied by Pascu *et al.* [123, 127, 128] The spectroscopy of compounds **1c** and **2c** is described below. The absorption range was similar when comparing the zinc and copper complexes, however the λ_{max} of absorption was significantly red shifted in the case of the copper complex, whilst the emission maxima was slightly lower for **2c**, indicating a reduction in the Stokes shift. Interestingly, the range of emission was larger for **2c** with respect to **1c**. As was expected, **2c** possessed significantly reduced fluorescence when compared to **1c**, which can be explained by paramagnetic quenching.

Table 3.3. Fluorescence measurements of complexes **1c** and **2c**.

Compound	$\lambda_{em\text{-}max}$ / nm	Excitation range / nm	$\lambda_{ex\text{-}max}$ / nm	Emission range / nm
1c	440	250-590	581.5	535-723.5
2c	490	250-590	576.5	514.5-737

3.7 Kinetic stability testing

In vitro assays to determine the stability of complexes for use as medical imaging probes is very desirable. Demetallation could result in non-target tissue uptake and poor image contrast *in vivo*. Stability is therefore essential for the intended function of these complexes and a series of assays with excess of numerous chemicals found in biological systems have been carried out up to 24 hours. These include Glutathione (GSH), L-cysteine, L-histidine, L-methionine, citric acid, ethylenediaminetetraacetic acid (EDTA), biomimetic eagle's modified essential media (EMEM) (both with and without foetal calf serum) and biologically relevant pH buffers. Indeed, stability of these complexes in a range of pHs is significant due to the tendency of cancer cells to be slightly more acidic than non-cancerous cells. UV-visible spectroscopy was utilised therefore to assess the kinetic stability of complexes and fluorescence to provide further insight whilst in the presence of biological media.

Table 3.4. Summary of estimated complex remaining from UV-visible data at 1:1 DMSO:assay agent at 15 minutes and 24 h where Citric Acid, EDTA, L-Cys, L-His, L-Met and GSH were in MilliQ water.

Assay	**1d**, 100 μM	
	15 min[a]	24 h[a]
DMSO	89.1	88.3
H_2O	72.2	63.1
PBS	80.3	65.3
5% FCS, MEM	92.1	92.4
SFM, MEM	67.9	47.3
Citric Acid	83.2	79.0
EDTA	69.5	55.9
L-Cys	82.4	81.9
L-His	69.2	68.4
L-Met	61.1	32.7
GSH	91.0	59.1

Tests were carried out at room temperature at 100 μM in a 1:1 DMSO: assay solution to ensure sufficient solubility and at a concentration providing detectable fluorescence. Stability of the allyl-derivatised copper complexes in solution was previously observed in solution but only some very preliminary studies were undertaken prior to this

work.[123, 127] This investigation utilised both UV-visible absorption (at 10 μM and at 100 μM) and fluorescence emission at 100 μM, with 1:1 DMSO:challanger to limit precipitation.

This allowed a % stability to be estimated *via* UV-Visible spectroscopy at 15 minutes and 24 hours as calculated by (100 % - percentage converted to free ligand) *(Table 3.4)*. The first assays carried out in DMSO, water, PBS, 5% FCS EMEM and SFM EMEM enabled complex stability to be understood in media likely to be encountered in a cell biology experiment.

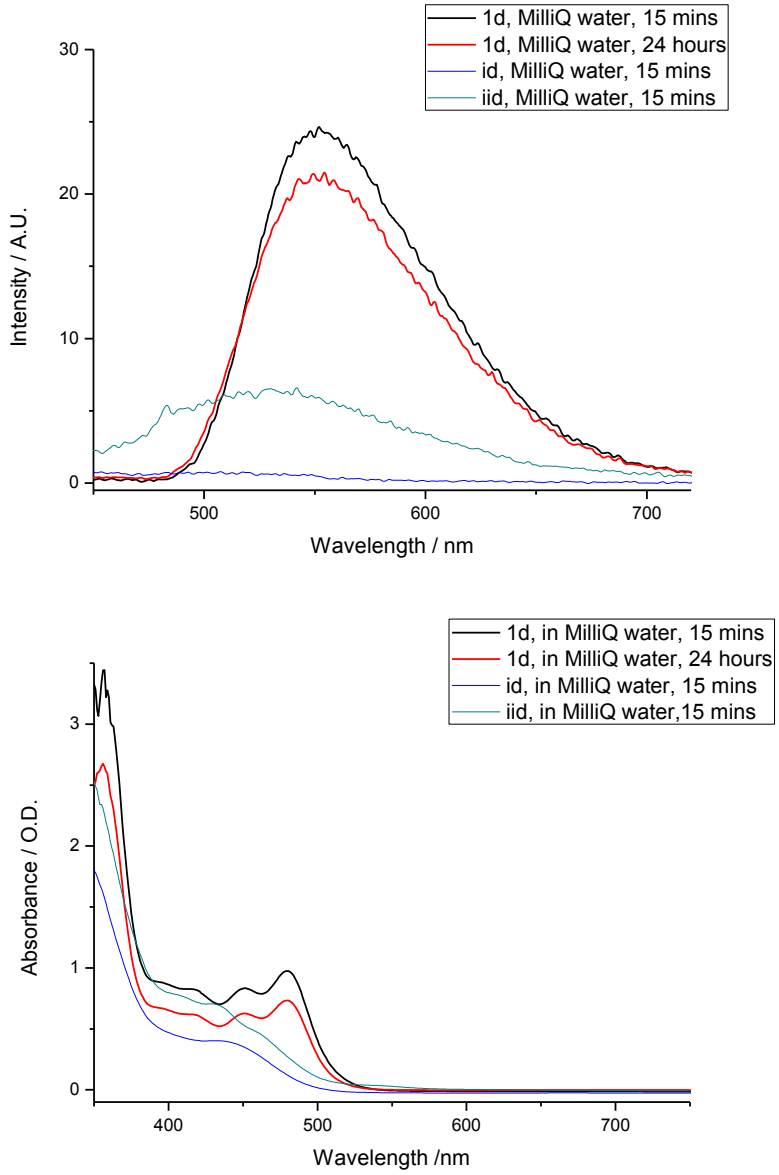

Figure 3.11. Water assays (50% DMSO, 50% water) for compound **1d** at 100 μM, by fluorescence spectroscopy (above) UV/Vis (below) monitored at time intervals up to 24h at room temperature.

The zinc complex **1d**, demonstrated very good stability in each solvent with 88.3 %, 63.1 %, 65.3 % 92.4 % and 47.3 % estimated complex remaining after 24h in DMSO, water, PBS, 5% FCS EMEM and SFM EMEM respectively *(Appendix Figures D.1-3).* Whilst displaying encouraging results in DMSO, water and 5% FCS complex (88.2 %, 39.6 % and 79.1 % after 24 h respectively) *(Figures 3.11 and Appendix Figures D.1-3).* The stability of the complexes was tested against Eagle's Minimum Essential Medium Serum Free Medium (SFM), which complexes are often incubated in for cell imaging.

As may be expected a decrease in fluorescence was observed with time, when complex **1d** was assayed with DMSO, and SFM. Conversely, when assayed with FCS and PBS the complex showed an increase in fluorescence emission at ca. 450 nm and 460 nm *(Appendix Figures D.1-9).* This could suggest an interaction with the media perhaps *via* binding to a component of the solvent for example a protein within serum or phosphate respectively. Binding of an anion such as a phosphate, however would result in a small shift in absorbance, which was not observed in either case.[144] Nevertheless, the fluorescence observed with each solvent (above) was significantly greater than that of the proligands, this combined with the presence of the characteristic UV-vis band of the zinc complex is highly indicative of complex stability.

3.7.1 Investigation testing stability using biologically relevant agents

Biologically relevant agents were chosen to provide a better insight into the stability of these complexes *(Figure 3.12)*.[145] For example, L-methionine and L-cysteine can act as S-donor models and L-Histidine as a N-donor model. Furthermore glutathione, a tripeptide containing glycine, cysteine and glutamate can function as both an S- and N-model. Moreover, cysteine and GSH *via* the thiol have potential to reduce the metal, which would likely result in decomplexation. Citric acid can act as a weak organic acid in addition to as a chelating agent, with possibility to form salts such as gallium or indium citrate. In addition EDTA, also a chelator was tested for its ability to demetallate zinc, gallium and indium complexes.

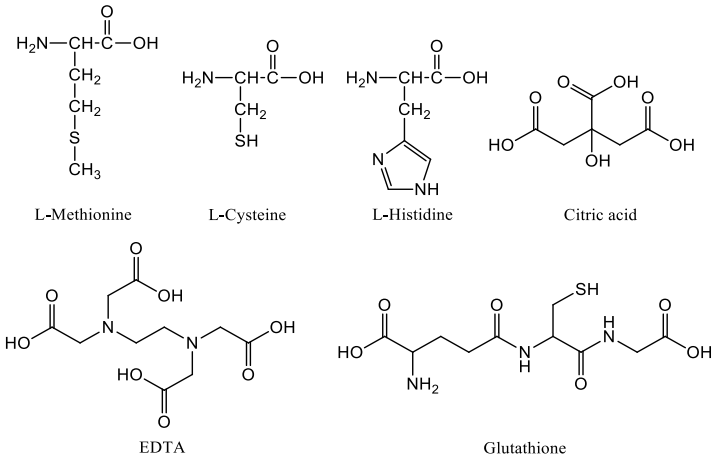

Figure 3.12. Structures of biologically relevant assay agents used hereby.

Complexes were tested in the presence of 2 equivalents of citric acid, L-methionine, Glutathione (GSH), L-cysteine, L-histidine, and EDTA. Zinc complex **1d** displayed an increase in fluorescence and no significant shift in λ_{max} in each scenario under each of these conditions at 100 μM, which is indicative of stability, since the proligands possess much weaker fluorescence.

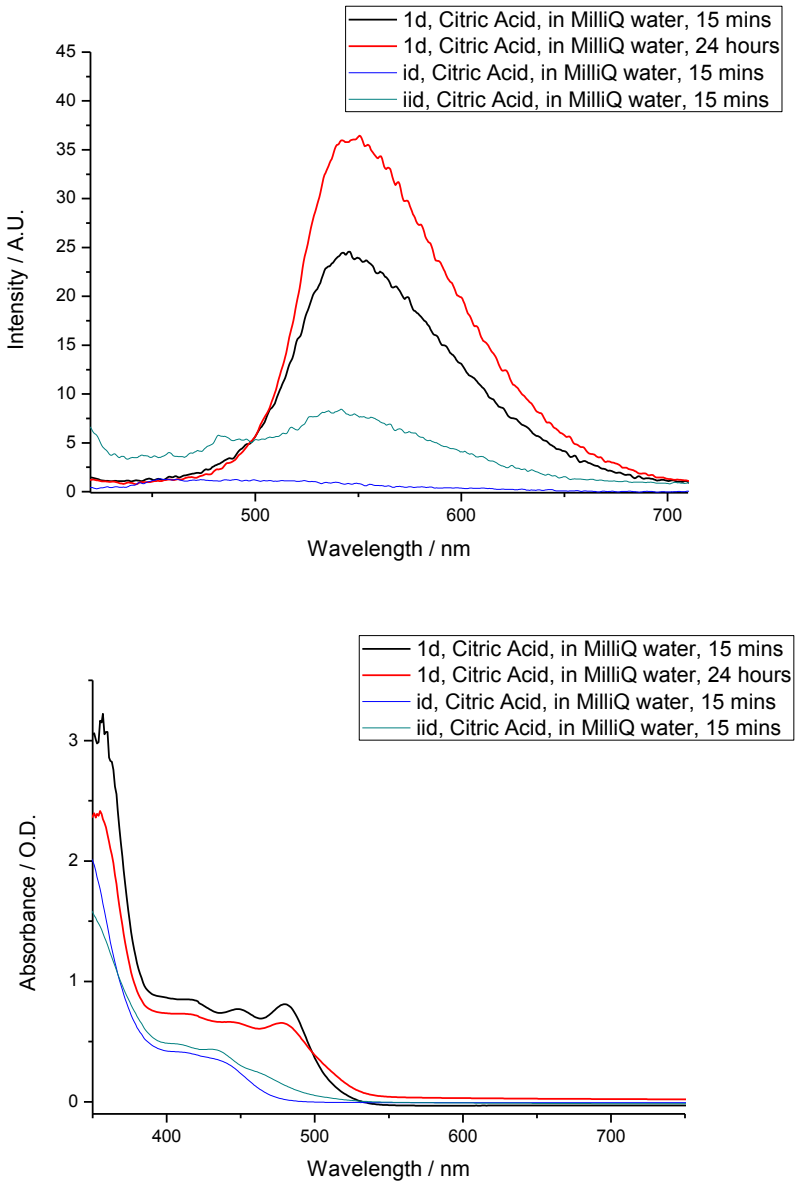

Figure 3.13. Citric acid assays (50% DMSO, 50% water, 2 eq of citric acid) for compound **1d** at 100 µM, by fluorescence spectroscopy (above) UV/Vis (below) monitored at time intervals up to 24h at room temperature.

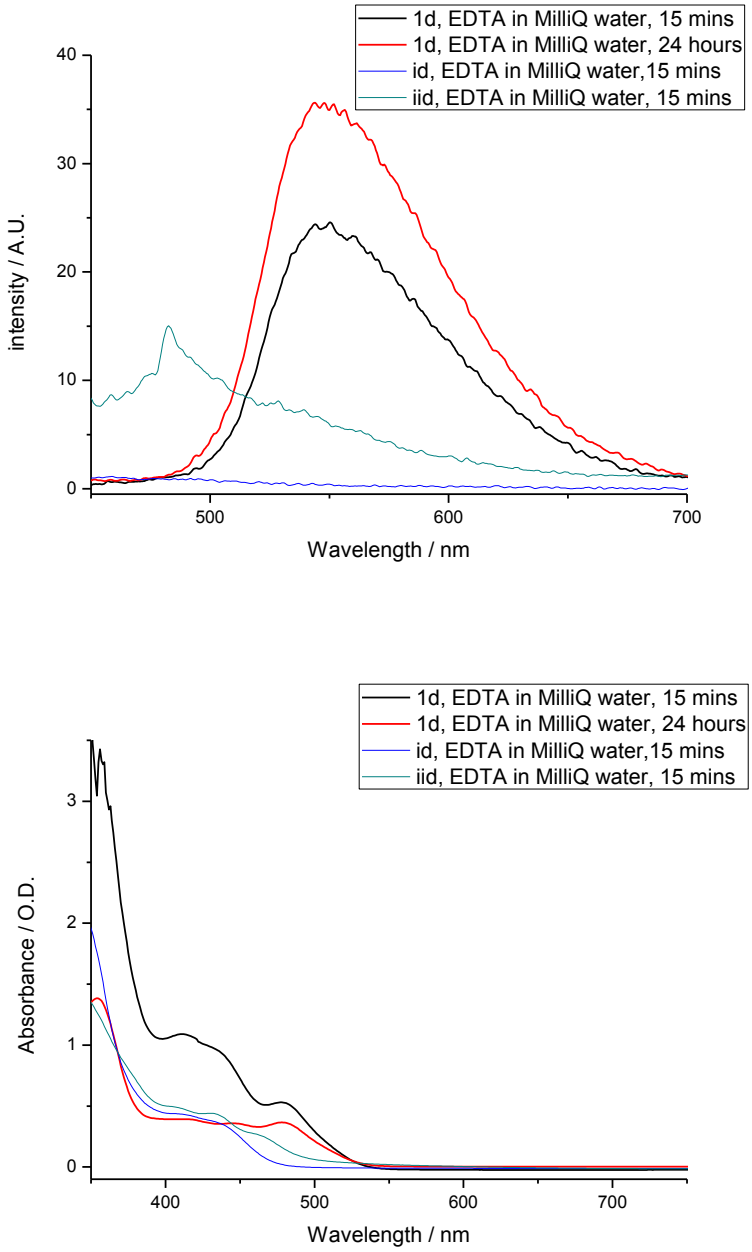

Figure 3.14. EDTA assays (50% DMSO, 50% water, 2 eq of EDTA) for compound **1d** at 100 µM, by fluorescence spectroscopy (above) UV/Vis (below) monitored at time intervals up to 24h at room temperature.

The characteristic spectrum of Compound **1d** was observed when assayed with each agent with the exception of EDTA, therefore allowing speculation that zinc leaves the bis(thiosemicarbazonato) ligand in preference for chelation by EDTA *(Figure 3.14)*. Conversely **1d** in EDTA solution possessed notable absorbance at 478 nm at 24 h where the free ligand does not, signifying that some zinc complex remains in the solution. The

zinc complex can therefore be considered most likely stable under these conditions tested.

3.7.2 pH stability estimation

The stability of complexes at biologically relevant pH is an important factor in this study. Cancer cells are slightly more acidic than non-cancerous cells, therefore it is important that the molecular probes are stable at lower pH.[146] All fluorescence scans were carried out with an excitation wavelength of 400 nm and at a concentration of 100 μM, with a 1:1 DMSO:buffer solution.[146] The stability of complexes at biologically relevant pH is an important factor in this study.

Following the above preliminary study allyl-substituted compounds were selected as a representative of the other functionality to assess the stability of newly synthesised gallium and indium complexes using UV-visible and fluorescence spectroscopy both at 15 minutes and 24 hours, with 1:1 DMSO:buffer solution. The pH of the samples was measured and found to have no significant difference to the blank, however with a notable variance from that of the original pH solution in each case *(Appendix Table D.1.)*.

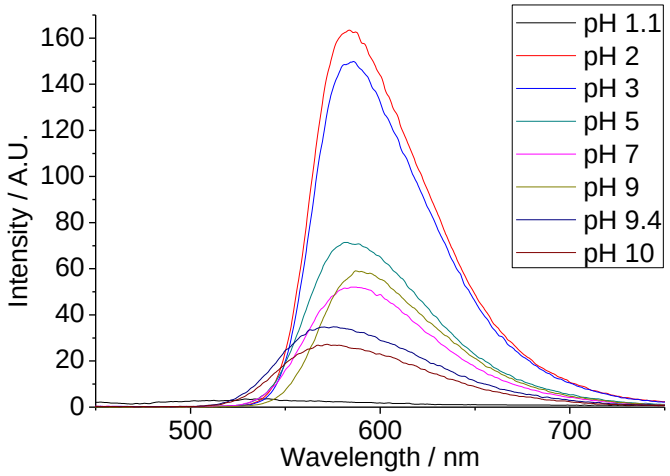

Figure 3.15. Fluorescence spectroscopy buffer assay **1c** pH study where: pH 2 > pH 3 > pH 5 > pH 9 ≥ pH 7 > pH 9.4 ≥ pH 10 ≥ pH 1.1

Complex **1d** displayed the best stability in neutral solutions, with dissociation more likely under acidic conditions, which is consistent with data acquired in the MChem thesis of Brett Kennedy[6] using citric acid based buffers *(Figure 3.15)*. The copper

complex, however showed the most intense fluorescence using weakly acid buffers of pH 5 and pH 3 *(Figure 3.16)*.

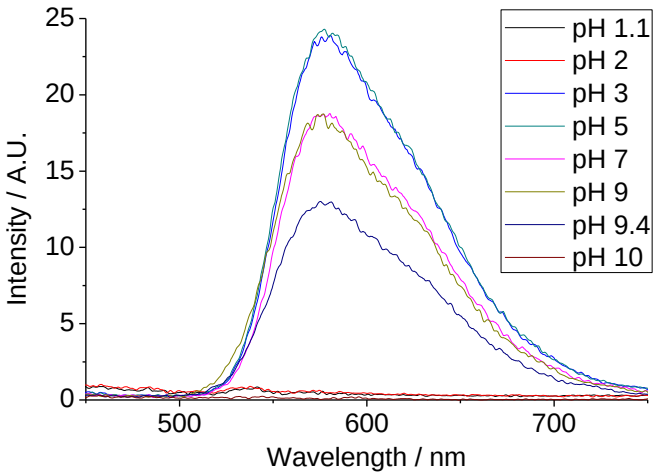

Figure 3.16. Fluorescence spectroscopy buffer assay **2c** pH study where: pH 5 > pH 3 > pH 7 ≥ pH 9 > pH 9.4 > pH 1.1 ≥ pH 2 > pH 10.

In a pH 1.1 and pH 2.0 buffer the UV-visible and fluorescence spectra of complex **1d** closely resembled that of **iid**, indicating that most of the complex had decomposed to form the proligand *(Figure 3.17, Appendix Figures D.50 and D.51)*. After 24 hours however, the complex appeared to have decomposed entirely since the absorption spectra resemble neither **iid** nor **id**. Within the pH 3 buffer the absorbance and emission of **1d** decreased with a blueshift ca. 5 nm in the fluorescence spectrum after 24 h, suggesting some conversion to the bis-substituted ligand, yet with a significant proportion of the complex remaining.

When assayed with a Sodium phosphate Monobasic / Sodium phosphate Dibasic based pH 7 buffer, the UV-visible spectrum of **1d** at both 15 minutes and 24 hours was similar to that of **iid** implying that most of the complex has formed the ligand precursor *(Figure 3.17)*. Conversely **1d** displayed significantly higher fluorescence than **iid**, suggesting that some complex was still remaining. Furthermore it is unlikely that the complex has poor stability at this pH due to the data acquired for SFM (pH 7.0 – 7.4) and PBS (pH 7.4). It therefore is more probable that the apparent decomposition of **1d** was due to interaction with the buffer components rather than due to the pH.

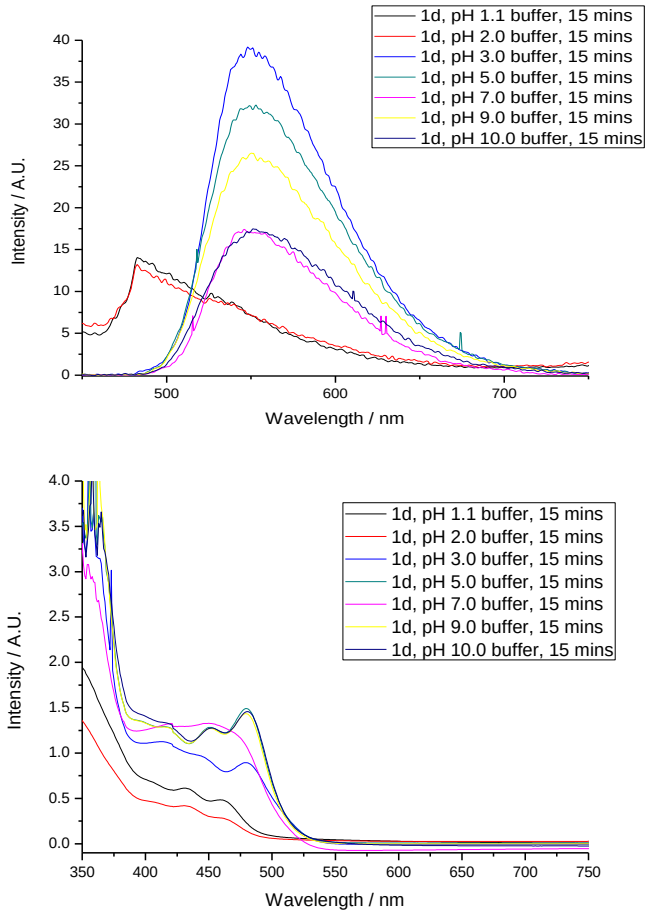

Figure 3.17. Buffer assays (50% DMSO, 50% water, pH 1.1 buffer, blank measured pH 1.6) for compound **1d** at 100 μM by fluorescence spectroscopy (above) and UV/Vis (below) monitored at 15 minutes at room temperature.

Meanwhile, in buffers of pH 5, pH 9 and pH 10 complex **1d** showed an increase in fluorescence intensity after 24 h incubation, with a decrease in absorbance, but no shift in either absorption or emission spectra indicating good stability of this complex in these buffers. It can therefore be considered from this study that zinc complex **1d** is stable within the range of pH 4.4 and pH 12.7 (the measured pH of buffer:DMSO 1:1 for buffers of pH 3.0 and pH 10.0). This indicates that the complex is stable over a very broad range of pHs in a biological capacity, with complex presence as long as after 24 h and can be considered representative of the other zinc complexes.

3.7.3 Two-photon fluorescence lifetime investigations

The two-photon investigations were first introduced in Chapter 2 and all studies were performed at the Rutherford Appleton Laboratory under the supervision of Dr S. Botchway. Zinc complexes **1b-d** were tested in both DMSO and in cells. In solution, **1b** was found to possess a fluorescence lifetime with 2 components, at 810 nm the lifetime of the major component was 0.261 ns and representative of 98.2% of the lifetime, with the minor component 0.597 ns at 10 mM (χ^2 = 1.52). This was highly comparable to the single exponential decay with the excitation wavelength of 910 nm, 0.275 ns, with a χ^2 of 1.25. Furthermore, at 910 nm the phenyl- and allyl-substituted complexes possessed similar major component lifetimes of 0.30 ns and 0.28 ns respectively in solution.

If the complex were to demetallate within cells there could potentially be four components, two corresponding to the free ligand and two representing the complex. The long component (ca. 2.5 ns) of the bis(substituted) proligands which was often observed in HeLa and PC-3 cells is significantly different to the short major component and long minor component of the zinc complexes and would therefore allow facile resolution. Moreover, the amount of data necessary to enable resolution of the short components (in solution ca. 0.2 ns and 0.28 ns for ligand and complex respectively) to be sufficiently spaced would require acquisition times of many minutes. It would be possible however, to evaluate dissociation modelling the analysis to up to two decays only, compiling the longer and shorter components, with the longer providing insight into the presence of free ligand.

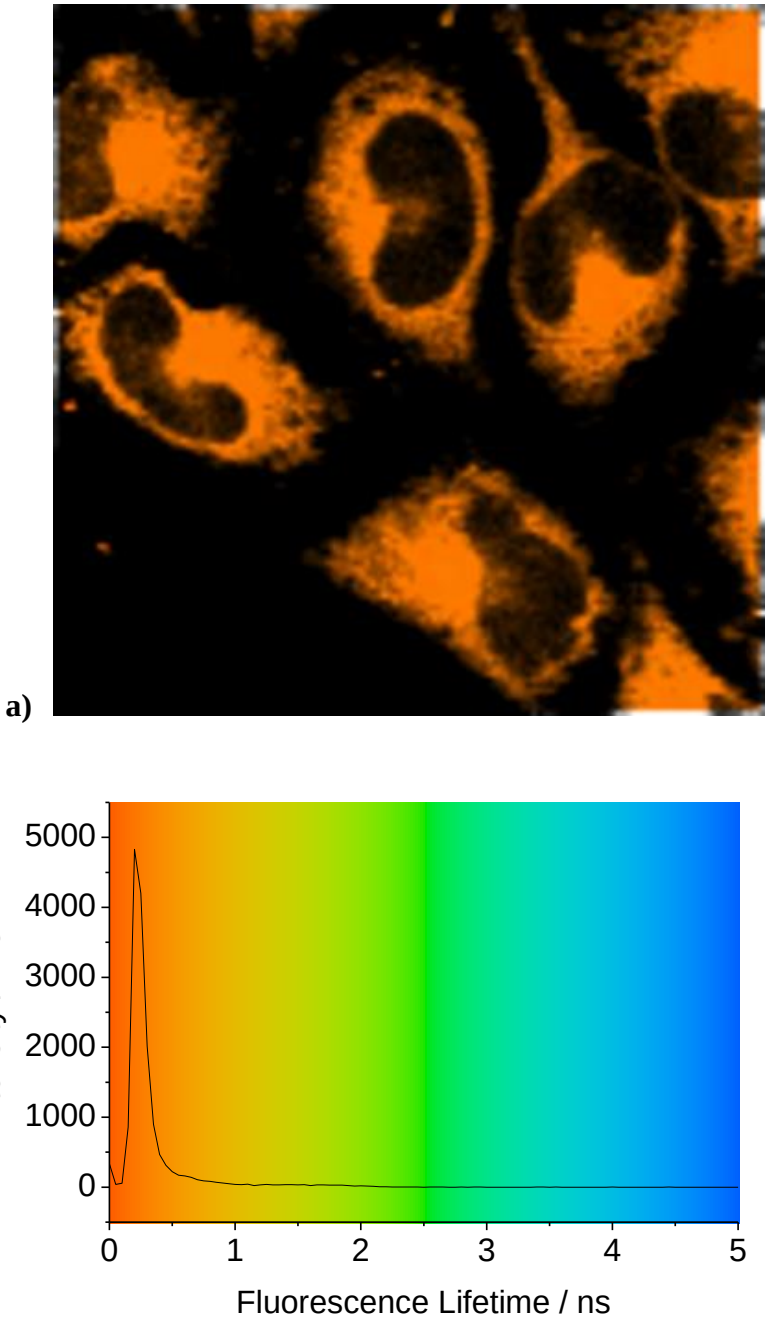

Figure 3.18. a) Two-photon fluorescence lifetime map (τ_m) of compound **1b** incubated in HeLa cells b) is the distribution curve of the τ_m where the colour represents the lifetime of a).

When **1b** was incubated in cancer cells *(Figure 3.18a)* the lifetime observed at 910 nm was 0.217 ns, 0.098 ns FWHM (major component) and 0.505 ns, 0.821 ns (minor component), which was very close to and within the FWHM of what was observed in solution. When excited at 810 nm, the lifetimes were 0.152 ns, 0.093 ns FWHM and 0.433 ns, 0.625 ns FWHM major and minor components respectively. This indicates that in cells the lifetime was not significantly different (within the FWHM) when

excited by the two respective wavelengths. Moreover the lifetimes observed in cells at 910 nm and 810 nm closely matched data acquired for compound **1b** at 10 mM, 810 nm excitation, importantly so in the case of the minor component of ca. 0.5 ns. Furthermore, the lifetimes in solution of **1c** and **1d**, for example 0.302 ns and 0.283 ns for the corresponding compound, were similar to those observed in cells 0.284 ns (0.087 ns FWHM) and 0.266 ns (0.146 ns FWHM) respectively.

In cells the major components of these zinc complexes were all short (in the region of 0.15 to 0.28) and their respective long components were either less than 1.5 ns or not present, this is highly indicative that no significant portion of the zinc complexes have dissociated to free ligand for which the long component would be far in excess of this value (1.5 ns). These data, therefore are in strong support of the stability of this family of zinc complexes, especially due to the high correlation between the lifetime in solution and in cells, including the second component, which not comparable with the very long component observed for the free ligand.

Copper complexes tested in solution and in cells (50 μM, 0.5 % DMSO, 3 h incubation) showed very similar τ_1 values confirming their stability under these conditions *(Figure 3.19)*. The major component observed both in DMSO solution and in cells was in the region of 0.3 ns for **2c** and **2d** was a minor component that was not observable within the cell, of ca. 1 – 1.9 ns, perhaps suggesting a preference for the major conformation within the cell. As was discussed regarding the zinc complex data, the presence of a long component of ca. 2.5 ns within the cell would be indicative of dissociation.

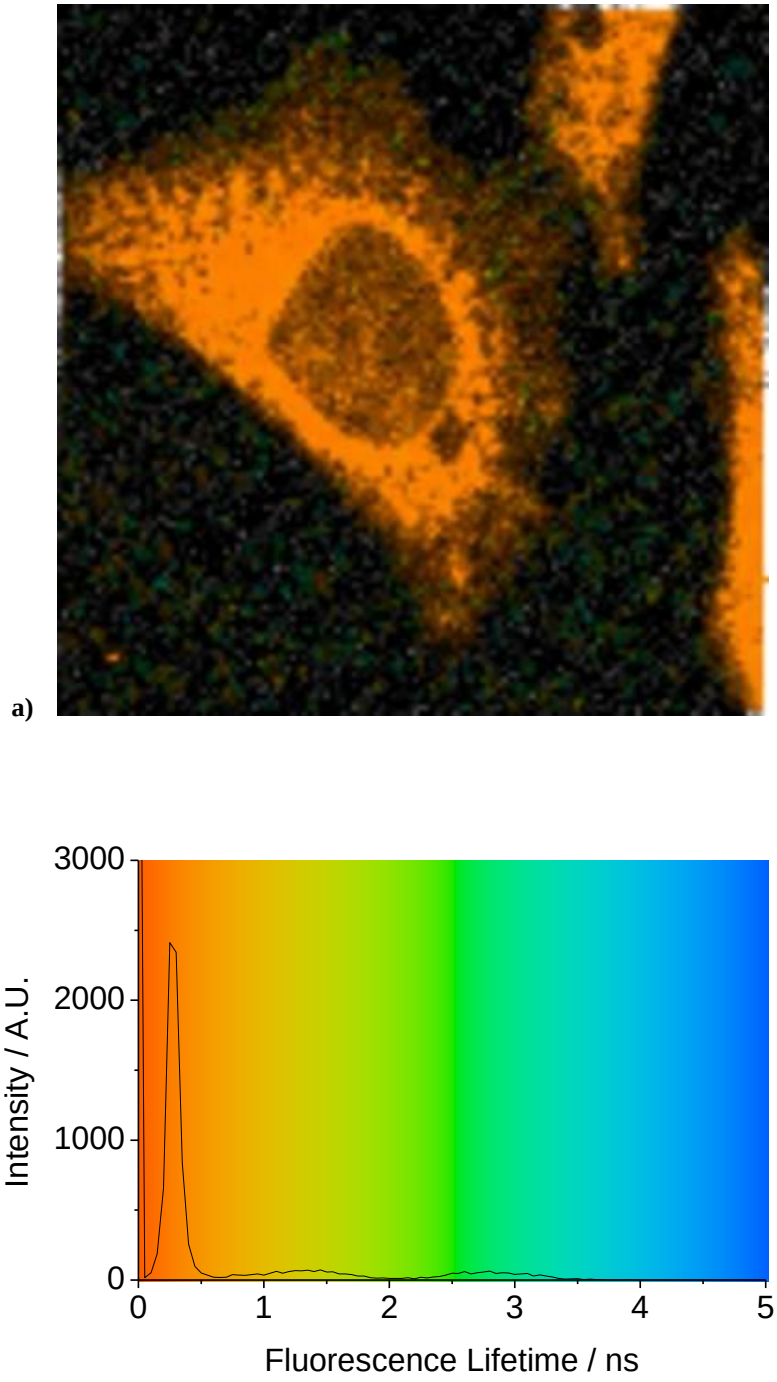

Figure 3.19. a) Two-photon fluorescence lifetime map (τ_m) of **2c** in HeLa cells with excitation at 910 nm **b)** is the distribution curve of the τ_m where the colour represents the lifetime of a).

Therefore, since there was no presence of a long component in any significant proportion when complex **2c** was incubated in cells it can be considered that little demetallation has occurred. Furthermore, due to the high correlation between solution and cell data these investigations signify that the copper complexes are stable within cells and the timeframe of these experiments.

3.8 Laser scanning confocal microscopy

Cells were cultured using standard protocols, analogous with earlier investigations of fluorescent thiosemicarbazones. Cell viability prior to experiments and over the course of experiments was monitored by optical microscopy, and validated at the start of the experiments by standard trypan blue tests and MTT assays.[127, 128] Complexes were imaged in HeLa (cervical carcinoma), PC-3 (prostate carcinoma), MCF-7 (breast cancer) and FEK-4 (non-cancerous fibroblast) cell lines, cultured as described in the Experimental section by confocal fluorescence microscopy using one photon excitation at 488 nm with the emission long-pass filtered at 515 nm.

The imaging studies were performed using concentrations of 50 μM compound in a DMSO: RPMI 0.5:99.5 cell medium solvent mix, (RPMI = Royal Park Memorial Institute), whereby the final DMSO concentration on the imaging plate was lower than 1%. It was found that complexes **1b-1d** yielded near-identical results to each other under analogous conditions yet displayed significantly different uptake to Zn[ATSM], which had notable uptake in the nucleoli.[62] The consistently higher fluorescence intensity of the zinc complexes **1b-1d** allowed the procedure to be optimised for better comparisons with the respective free ligand and indication of stability. It was found that concentrations of 50 μM and incubation times of 20 minutes could be used, which had previously been predominantly 100 μM, with longer incubations. An interesting effect was observed when incubating HeLa cells with complex **1c**, a significant phototoxicity could be observed with cell health visibly diminishing after 15 minutes and was not observed in absence of compound *(Figure 3.20)*.

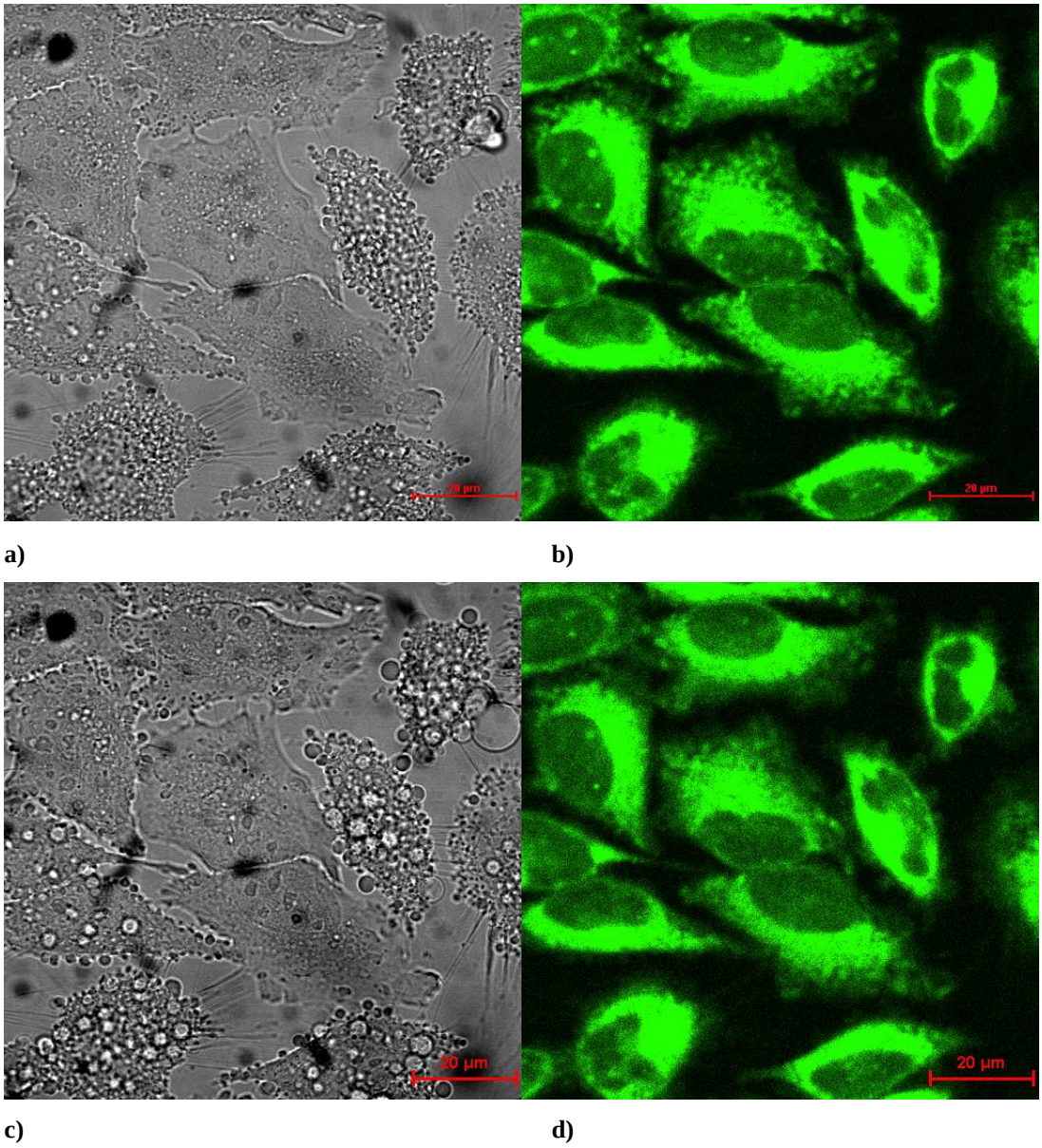

a) **b)**

c) **d)**

Figure 3.20. Single-photon laser scanning confocal microscopy of **1c**, 50 µM, 0.5% in HeLa cells before irradiation **(a – b)** and after 15 minutes of irradiation **(c – d)**. Where **(a)** and **(c)** are the DIC channel land **(b)** and **(d)** are the fluorescence micrograph of with excitation at 488 nm.

Copper complexes were initially incubated for longer periods of time of 2 hours to ensure uptake. To investigate the mechanism of uptake copper complex **2b**, the compound was incubated in HeLa cells at both at 4 ^{o}C and 37 ^{o}C, whereby if uptake was only observed at 37 ^{o}C it would be highly suggestive that the complex enters the cell by an active means *(Figure 3.21).*[147] The experiment showed that uptake occurred under both conditions and it can therefore be considered as entering by passive diffusion. The fluorescence was slightly less intense at 4 ^{o}C, which could be explained by a lower rate of diffusion.

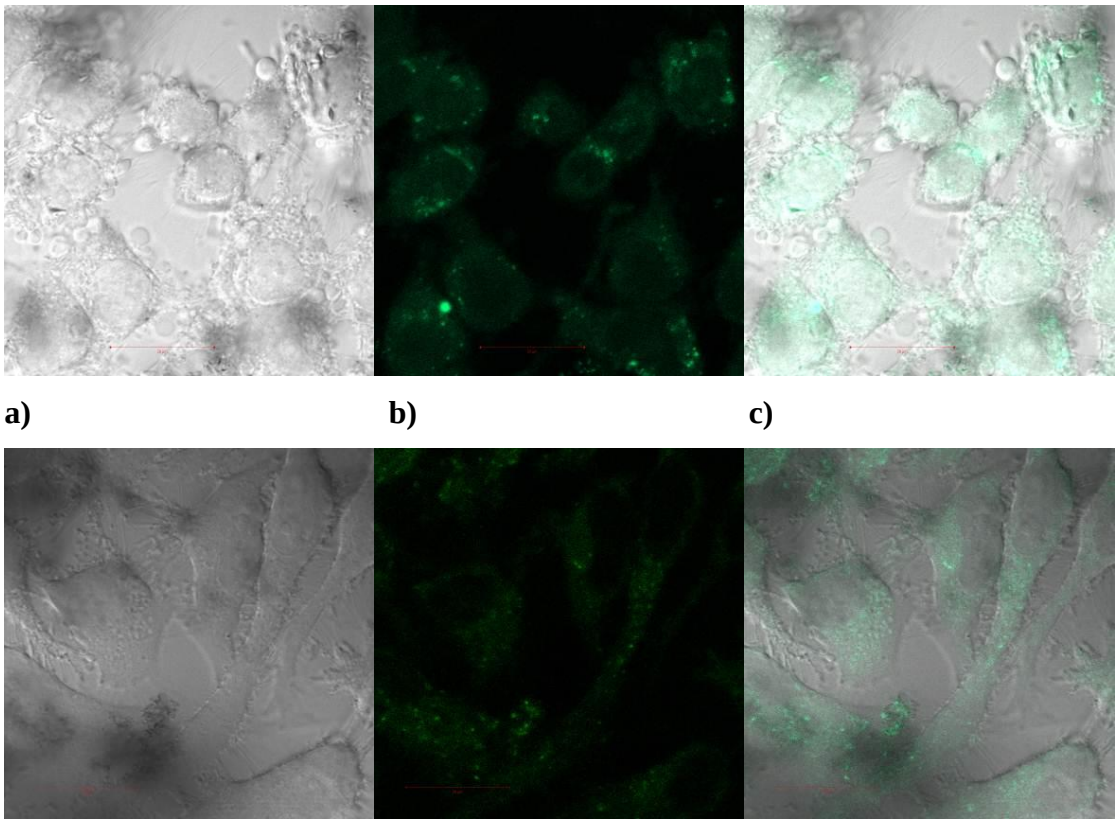

a) **b)** **c)**

d) **f)** **g)**

Figure 3.21. Confocal microscopy of HeLa cells incubated with **2b** at 100 μM for 3h. **(a - c)** represents an incubation at 37 ˚C and **(d – g)** at 4 ˚C, where **(a, d)** is an overlay of **(b, e)** the DIC image and of **(c, f)** the micrograph with excitation at 488 nm.

3.9 *In vivo* imaging

Normoxic PC-3 xenografts were grown on the right shoulder of nude mice in Memorial Sloan-Kettering Cancer Center (MSKCC), New York by Dr Brian Zeglis. M = ^{64}Cu, R = Et and Ph were labelled from their respective precursor in ethanol achieving high radiochemical yield by a 5 minute microwave-assisted reaction, followed by semi-preparative HPLC purification. MicroPET and biodistribution data collection were carried out for ^{64}Cu these complexes at MSKCC by Zeglis and Pascu. Welsh *et al.* investigated the biodistribution of ^{64}Cu [ATSM] in 1998. After 40 minutes, Welsh and co-workers found significant radioactivity in non-target organs of the lungs, liver, spleen, kidney and intestines, with uptake in the hypoxic tumour (4.17 %ID/g ± 1.03 SD). The preliminary normoxic experiments of this study using radiolabelled complexes

2b and **2c** were 0.34 %ID/g ± 0.04 SD and 0.44 %ID/g ± 0.18 SD respectively *(Figures 3.22 and 3.23)*. It is desirable that retention within normoxic tumours is low, since it would allow a hypoxic tumour to be distinguished more readily.

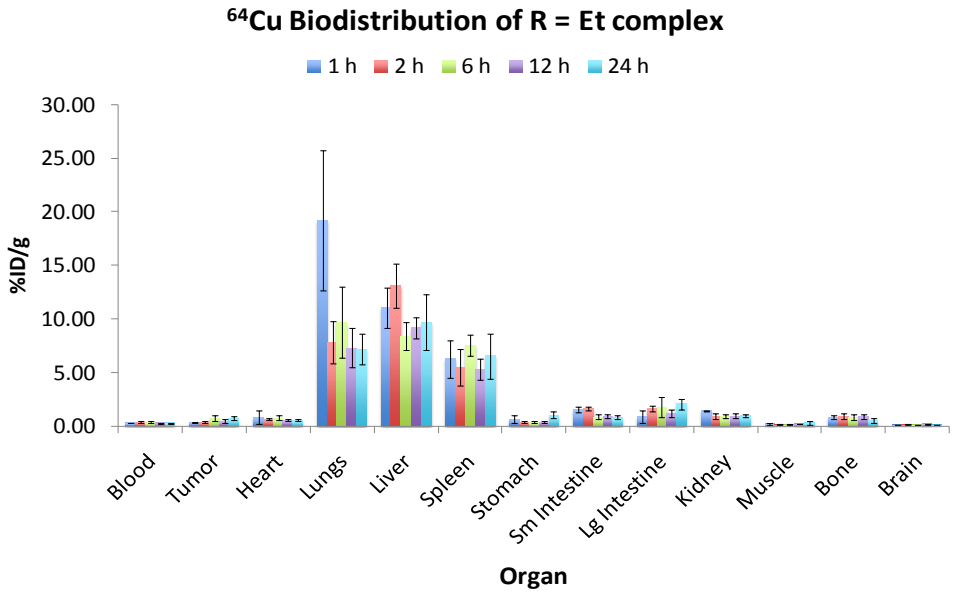

Figure 3.22. Biodistribution study in nude mice, of **2b**.

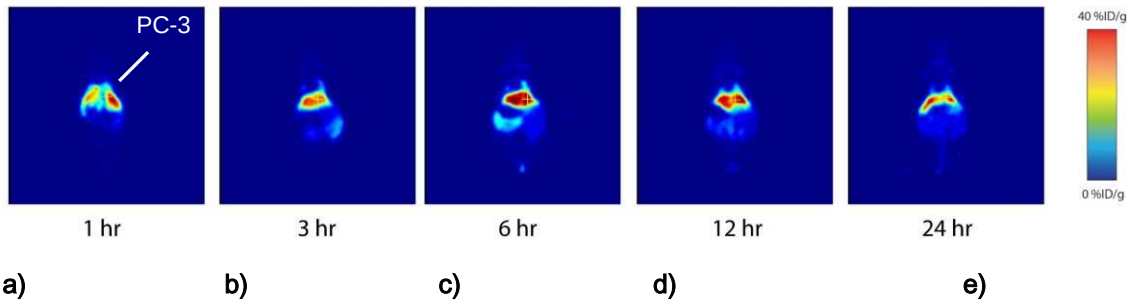

Figure 3.23. MicroPET images of in nude mice, **2b**, where **(a)**, **(b)**, **(c)** **(d)** and **(e)** are at timepoints 1h, 3h, 6h, 12 h and 24 h respectively.

Furthermore, non-target organ uptake of compounds **2b** and **2c** was lower when compared to ^{64}Cu[ATSM] in the liver, kidneys, brain, heart, intestines, bone and in the blood. Retention levels in the lung were comparable (19.17 %ID/g ± 6.55 SD, 23.33 %ID/g ± 7.73 SD, respectively) and biodistribution of compound **2b** was similar to that of Cu[ATSM] in the spleen. Spleen uptake levels of phenyl-substituted copper-64 labelled complex were the only non-target organ with significantly higher uptake than ^{64}Cu[ATSM], with biodistribution levels of 14.48 %ID/g ± 2.80. Moreover, good renal

clearance was observed, therefore the reduced uptake within vital organs combined with limited retention in the normoxic tumour represents promising results for probes designed for hypoxia selectivity

3.10 Summary to Chapter 3

Zinc and copper bis(thiosemicarbazonato) complexes were synthesised and characterised in this study. New crystallographic and computational data were acquired for the phenyl-substituted complexes, with X-ray diffraction results compared to those of different functionality, showing interesting differences in structure. Furthermore, DFT calculations allowed insight into the isomeric exchange observed in solution by NMR spectroscopy for **1c**, as well as for paramagnetic **2c**, each indicating that in solution the symmetric isomer was more stable. The kinetic stability of these complexes was demonstrated in solution and importantly in cells. Moreover complexes **2b** and **2c** were radiolabelled with ^{64}Cu and assessed *in vivo* displaying limited tumour uptake in nude mice under normoxic conditions, indicating that a thorough study of hypoxic selectivity of these complexes could prove useful. If significantly better uptake is observable in hypoxic cells, the copper complexes possess potential as PET molecular imaging probes for the purpose of diagnosing hypoxia.

Chapter 4. Synthesis, characterisation, spectroscopic, *in vitro* and *in vivo* analysis of gallium bis(thiosemicarbazonato) complexes

Despite the majority of copper bis(thiosemicarbazonato) complex studies focussing on their hypoxia selectivity these complexes are receiving growing interest as bifunctional chelators (discussed in greater detail in Chapters 1 and 2). However, there remains high liver uptake of the copper complex *in vivo*, with attempts to lower uptake by introducing hydrophilic groups on the exocyclic structure having some, yet limited success.[67] Therefore, another method of reducing liver accumulation is by way of using gallium(III) and indium(III) (*vide infra*, Chapter 5) complexes. Gallium complexes hold potential for the development of new molecular imaging probes largely due to the readily available ^{68}Ga positron emitting radioisotope that is generated from ^{68}Ge and therefore does not require a nearby cyclotron. Therefore the aim of this chapter was to synthesise new intrinsically fluorescent gallium complexes that could act as agents capable of detecting cancer, whilst understanding their physical and chemical properties in solution, *in vitro* and *in vivo*.

4.1. Gallium complex synthesis

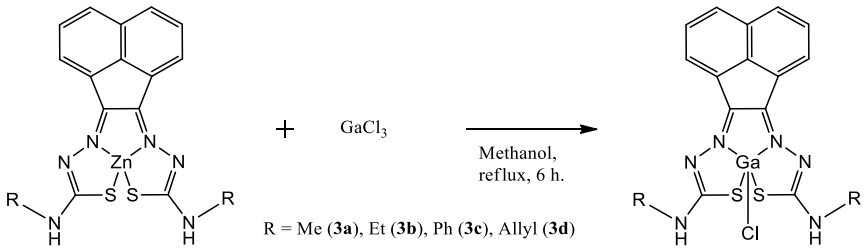

Figure 4.1. Synthesis of acenaphthenequinone gallium bis(thiosemicarbazones)

Transmetallation served as a reliable, rapid and clean means of synthesising the gallium complex by the following method. The acenaphthenequinone gallium(III) chloride bis(thiosemicarbazone) complexes was successfully synthesised by reflux in methanol in excess of $GaCl_3$ for 20 minutes, with 5 equivalents of $GaCl_3$ sufficient when refluxed for 6 hours *(Figure 4.1)*. Methyl, ethyl, phenyl and allyl analogues were prepared using this method and isolated by filtration after reaching room temperature as

orange-red powders in moderate yield (36% to 67%). Characterisation proceeded by NMR spectroscopy, ES-MS and X-ray crystallography. Crystals suitable for X-ray crystallography for each of these compounds were grown by vapour diffusion method of THF:Hexane and the molecular structure proved the connectivity of ligand to the [Ga Cl] in each case. Mass spectrometry (ESI) gave peaks for $[M-H]^-$ or $[M+H]^+$ at m/z = 458.96, 484.99 and 580.99, 502.94 and 508.99 for **3a**, **3b**, **3c**, **3d** respectively, all values being within 0.1% error of those calculated.

4.1.1 NMR spectroscopy

Studies in the group had indicated that the **1d** complex displays a dynamic equilibrium between a symmetric and an asymmetric isomer in solution.[127, 128] This is strongly shifted towards an asymmetric conformation when wet DMSO was bound, or in the presence of DABCO or bipy. ^{1}H NMR spectroscopy of **3a-d** showed similar splitting of proton resonances between an asymmetric and a symmetric form. Proportions of the different isomers were calculated by comparing the integrations of the *H-3* or *H-1* resonances for both isomers, which appear as two distinct (1H) doublets for the asymmetric version and a single (2H) doublet for the symmetric isomer *(Figure 4.2)* and *(Table 4.1)*.

Table 4.1. Proportions of symmetric and asymmetric isomers in the gallium complexes.

	3a	**3b**	**3c**	**3d**
Proportion of isomers at 25^{o}C in d_6-DMSO	Symmetric ca. 58% Asymmetric ca. 42%	Symmetric ca. 49% Asymmetric ca. 51%	Symmetric ca. 73% Asymmetric ca. 27%	Symmetric ca. 38% Asymmetric ca. 62%

Figure 4.2 shows the splitting of ^{1}H resonances in the aromatic region for the **3a** complex, which is representative of the **3b** and **3d** spectrum for this part of the spectrum.

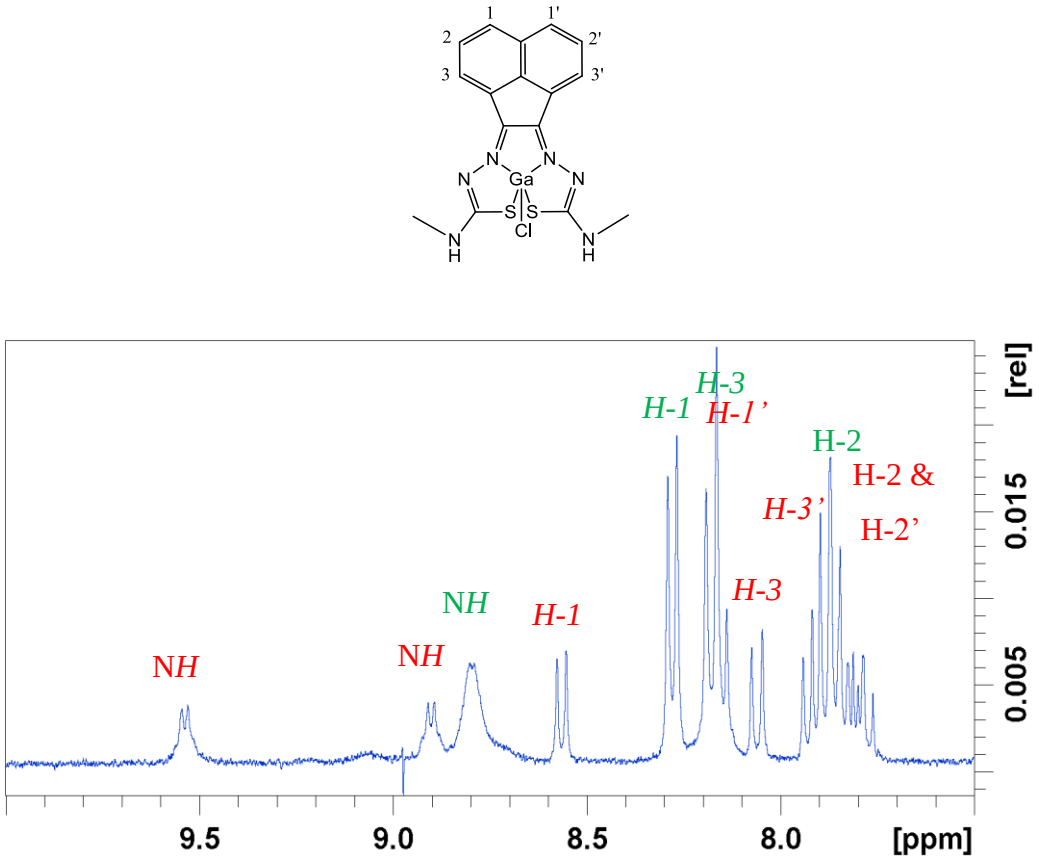

Figure 4.2. The proton numbering of complex **3a** (above), ^{1}H NMR spectroscopy of complex **3a**, where green indicates the (*E*,*E*) isomer and red indicates the (*E*,*Z*) isomer (below).

The methyl signals around 3.10-3.16 ppm, displayed interesting feature. The groups are represented as doublets due to the proximity of exocyclic NHs, therefore, if there were a mixture of symmetric and asymmetric only three doublets would be expected rather than the four that appear in this spectrum. Furthermore, using the approximate ratio of the number of expected protons of 1.9:2.5 a total integration of 13.5 would be expected for these methyl groups. Yet, an integral of 14.5 is observed, therefore it is possible that there are in fact 3 species: 2 symmetric and 1 asymmetric, where the abnormal symmetric isomer is of low proportion (ca. 5%), with another possibility being the formation of $[Ga\text{-}DMSO]^{+}$ Cl^{-} *(Figures 4.3 and 4.4)*. The isomerism was investigated further by VT-NMR spectroscopy to identify possible isomers and their equilibrium constants and will be discussed later *(Section 4.3.3)*.

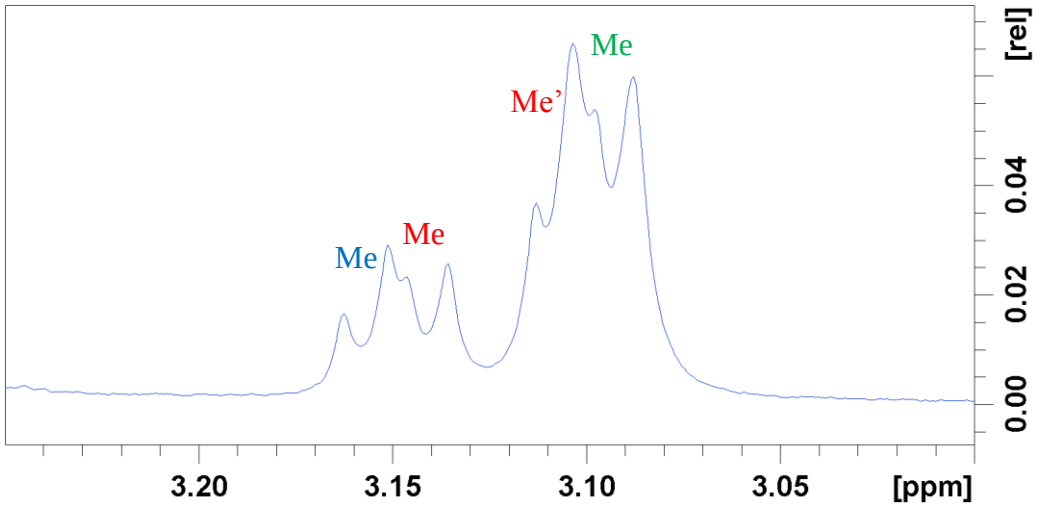

Figure 4.3. ^{1}H NMR spectroscopy of **3a** complex δ 3-3.3 ppm. In red, the asymmetric shifts, in green the symmetric resonances and in blue the third possible isomer.

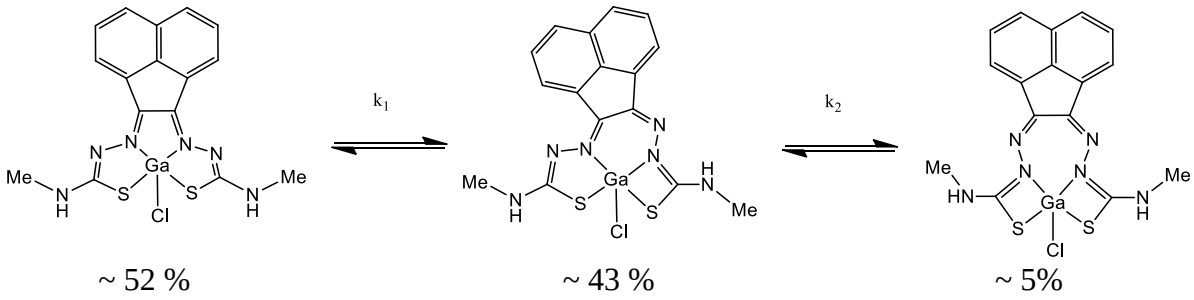

Figure 4.4. Proposed isomeric exchange for the gallium methyl complex

3b presented proportions of the symmetric and asymmetric isomer that were calculated as 49% and 51% respectively. The calculated integral for the CH_3(Et) groups would be ca. 12.2H and for the CH_2(Et) groups ca. 8.1H, which is close to the actual integrals of 12.1H and 8.4H respectively. The resonances overlap significantly and are likely due to the expected 3 overlapping triplets for the CH_3 and 3 doublets of doublets.

For **3c**, the proportions of asymmetric isomer appeared low, as demonstrated by the features observed in the ^{1}H NMR spectroscopy *(Figure 4.5)*. It was however difficult to estimate the actual proportion, which is about 25% of asymmetric isomer. This was due to overlapping and poor resolution of the asymmetric signals, only those corresponding to the symmetric isomer were fully assigned.

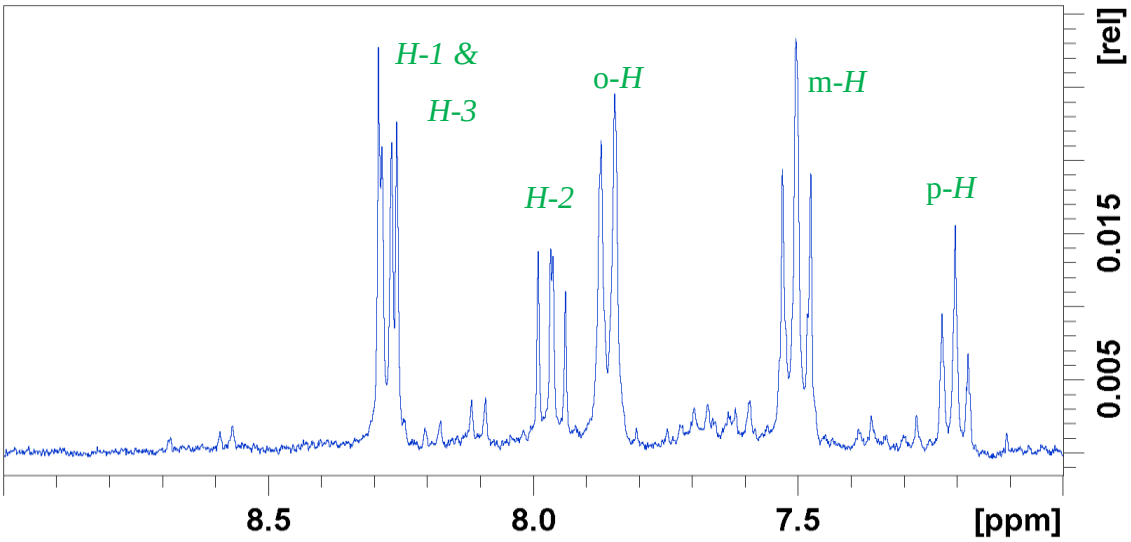

Figure 4.5. ^{1}H NMR (300 MHz, d_6-DMSO) spectroscopy of complex **3c**.

Moreover, complex **3d** displayed both the asymetric and symetric isomers with a ratio of 2:1 asymmetric:symmetric.Interestingly, the integral of the CH_2 group is 6H, which is what would be expected as calibrated below, appears as two overlapping triplets and so does not indicate the presence of a third species *(Figure 4.6)*.

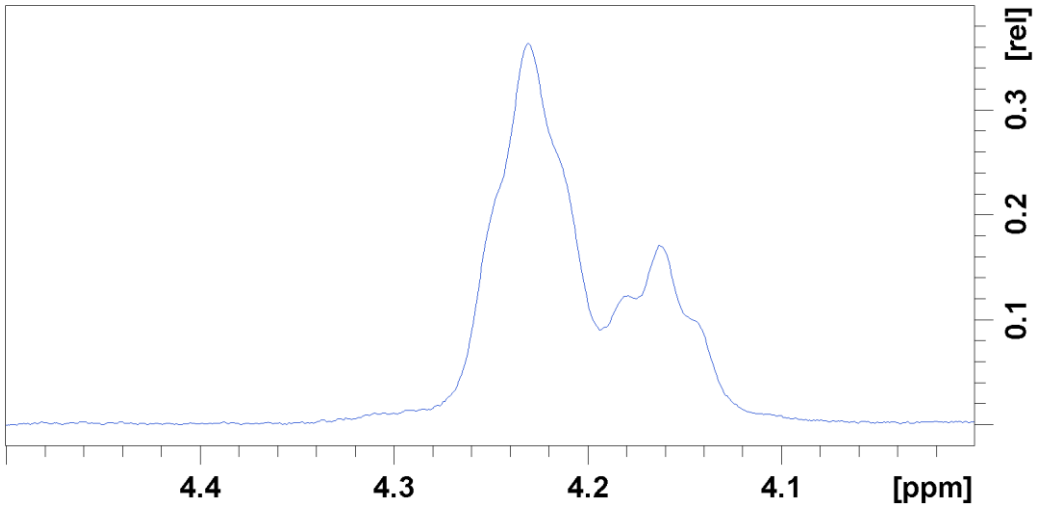

Figure 4.6. ^{1}H NMR (300 MHz, d_6-DMSO) spectroscopy of complex **3c**.(expansion: δ 4.0-4.5 ppm).

In summary, the gallium complexes were characterised by ^{1}H-NMR and ^{13}C-NMR spectroscopy confirming their high purity and indicating an interesting isomeric exchange.

4.2 Radiolabelling

Zinc precursors and free ligand were radiolabelled under the supervison of Prof Eric Aboagye by Frazer Twyman at Hammersmith Hospital, London *(Figure 4.7 and Appendix Figures B.6-8)*. A ^{68}Ga generator was used to elute 10 mL of 0.1 M HCl, ca. 6 mCi of ^{68}Ga, which was trapped on a 30 mg/1 mL Strata X-C cartridge and eluted with 700 µL of 0.02 M HCl (98% acetone). This was subsequently dried for 15 minutes under a nitrogen stream at 110°C. Next the of bis(thiosemicarbazonato) compound was added in dry DMSO (2 mg/mL) and 2 mL of injectable ethanol. This was heated at 90 ^{o}C for 30 minutes and injected into a radio-HPLC. Conversion to the respective gallium complex occurred rapidly (within 30 minutes), however with remaining $^{68}GaCl_3$ indicating that radiolabelling had not gone to completion.

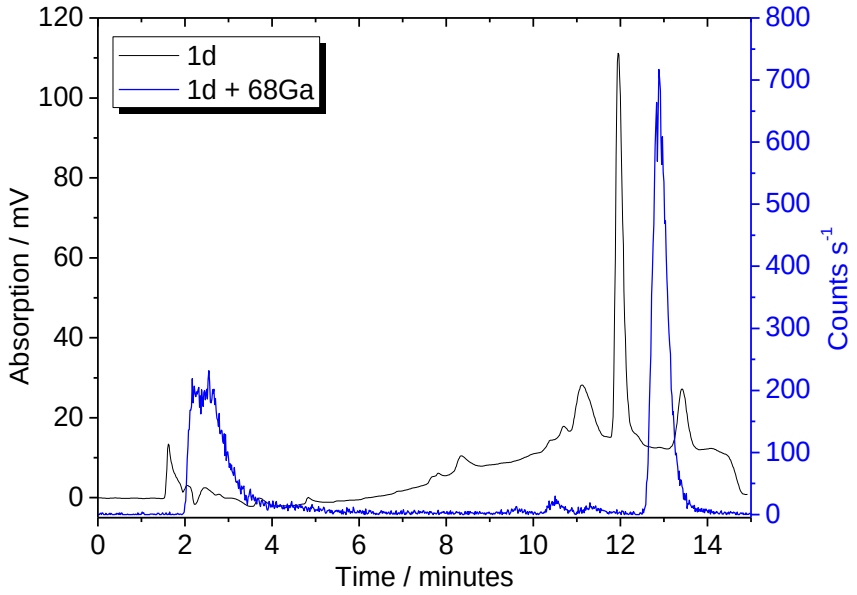

Figure 4.7. Overlay of UV-HPLC trace (black) of aromatic zinc bis(thiosemicarbazonato) precursor **1d** (R = allyl) with the radio-HPLC trace (blue) of aromatic ^{68}GaCl bis(thiosemicarbazonato) complex.

Radiolabelling with the zinc complex *via* transmetallation was successful showing highly comparable data when considering the UV-HPLC spectrum of the 'cold' gallium compound and the Radio-HPLC of the 'hot' Ga-68 complex. The process was made more efficient using microwave-assisted reactivity with the Lewis group in the Memorial Sloan-Kettering Cancer Center, New York, for the radiolabelling of **3b** with the achievement of >95% radiochemical yield in ethanol.

4.3 Structural studies

4.3.1 Crystallographic analyses

Crystal structures of **3a-d** have been obtained and were grown in THF:hexane or THF:pentane either by standard liquid diffusion or gas diffusion methods, with the crystals of **3d** grown by Dr. Phillip A. Waghorn *(Figures 4.8-10).* In agreement with the NMR spectroscopy **3c** was solved as a symmetric structure, whereas **3b** and **3d** were asymmetric, interestingly **3a** displayed the symmetric and asymmetric form within the same asymmetric unit. It is noticeable that all symmetric compounds possess a plane of symmetry across the backbone and symmetric binding to the metal, yet the terminal functionalities (Me, Ph and Allyl) are not symmetric. All complexes display a distorted square pyramidal structure around the metal centre with the Cl in the axial position with the base formed by the two nitrogen and two sulphur atoms.

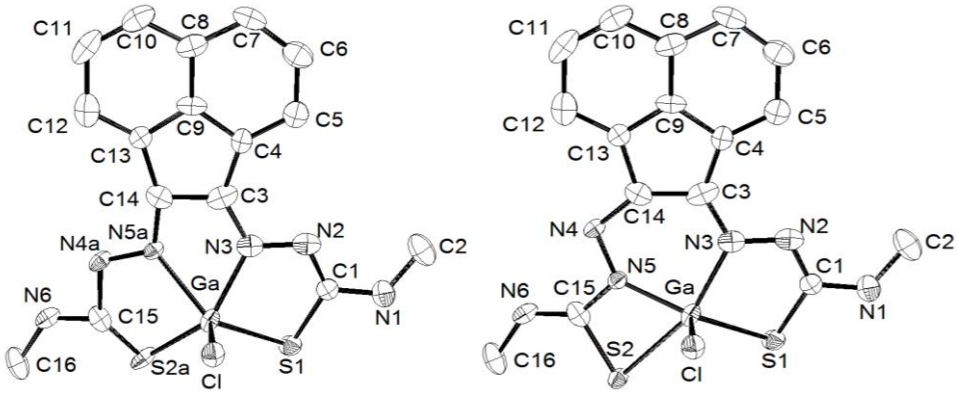

Figure 4.8. Ellipsoids drawn at 30% probability. Hydrogens omitted for clarity. For **3a** two molecules (left) **3a** and (right) **3a'** were present in the asymmetric unit, only one is represented here.

It was notable in Reference 127 that the C-C bond (C3-C14 of **3a**, C1-C2 of **3b**, C8-C19 of **3c** and C2-C3 of **3d**) of asymmetric zinc compounds are longer than for symmetric nickel complexes. However, there was no significant difference in bond length when varying the substituent group indicating that the previously observed pattern is most likely metal-dependant rather than isomer-based. Furthermore, the fortuitous occurrence of **3a** demonstrating both the symmetric and the asymmetric isomer in the same asymmetric unit allow for more facile comparisons between the isomers to be made.

Table 4.2. Selected bond lengths (Å) and bond angles (°) for compounds **3a**-**3d**, determined by X-ray diffraction.

Compound/ Molecular Parameters	[GaCl(ATSM)][138]	**3a** (*E*,*E*) isomer[138]	**3a'** (*E*,*Z*) isomer[138]	**3b'** (*E*,*Z*) isomer	**3c** (*E*,*E*) isomer	**3d'** (*E*,*Z*) isomer[138]
M-Cl	2.415(5)	2.2121(19)	2.2121(19)	2.230(3)	2.2096(14)	2.237(6)
M-N	2.0538(15)	2.004(6)	2.004(6)	2.028(11)	2.069(4)	2.033(15)
	2.0638(15)	1.924(11)	2.13(3)	1.947(11)	2.075(4)	1.926(16)
M-S	2.3009(5)	2.302(2)	2.302(2)	2.282(3)	2.3130(16)	2.262(6)
	2.3065(5)	2.17(2)	2.537(9)	2.474(4)	2.3171(15)	2.528(6)
C-C	1.483(2)	1.468(12)	1.468(12)	1.469(18)	1.488(6)	1.480(2)
N-N	1.363(2)	1.332(9)	1.332(9)	1.278(14)	1.372(5)	1.360(2)
	1.367(2)	1.32(5)	1.39(3)	1.340(15)	1.371(5)	1.380(2)
C=N	1.300(2)	1.356(9)	1.356(9)	1.394(16)	1.383(7)	1.30(2)
	1.292(2)	1.30(3)	1.37(2)	1.307(16)	1.369(7)	1.30(2)
S-M-S	105.25(5)	107.1(3)	103.96(19)	106.38(13)	105.11(5)	104.8(2)
S-M-N	82.47(4)	83.5(2)	83.5(2)	84.4(3)	81.42(12)	84.9(5)
	82.19(5)	84.0(8)	67.2(5)	68.0(3)	81.43(11)	68.1(1)
N-M-N	76.09(6)	94.1(7)	67.2(4)	88.4(5)	77.33(15)	68.0(5)
S-M-Cl	105.13(2)	108.34(8)	108.34(8)	106.7(1)	108.56(6)	109.06(5)
	108.891(19)	111.0(5)	101.1(2)	102.6(1)	108.38(6)	102.14(6)
N-M-Cl	99.31(5)	99.3(2)	99.3(2)	98.8(3)	99.7(1)	101.72(14)
	101.45(4)	102.2(7)	106.5(4)	107.1(4)	98.4(1)	106.84(14)

The M-S(1) and M-S(2) bond lengths are different for all asymmetric complexes whereas, for symmetric **3c** both M-S bonds are similar. Furthermore, where the bond angles for S-M-N are dissimilar for asymmetric complexes they are similar for all symmetric complexes. It is also noticeable that both Ga-(N) bonds are shorter for the asymmetric **3a** than for both other symmetric gallium compound. Interestingly, the N-M-Cl bond angle of the (*E*,*Z*) isomer of complex **3a**, 106.5(4)°, is larger than that of the (*E*,*E*) isomer, 102.2(7)°. Moreover the same angle of the **3a** (*E*,*Z*) isomer is equivalent to that of the (*E*,*Z*) isomers of **3b** and **3d**, indicating that the increase in this angle is largely an isomeric effect. For compounds **3a**, **3b** and **3d**, the molecular structures

identified an asymmetric binding mode of the ligand compared to the structures obtained for the aliphatic compound.

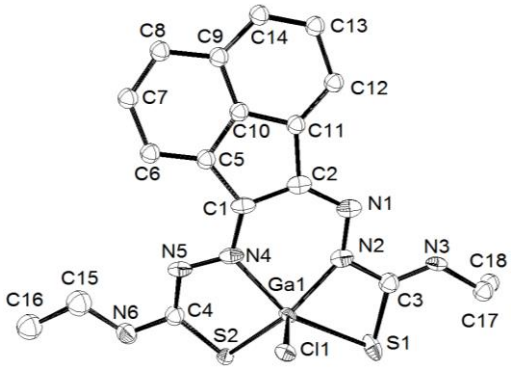

Figure 4.9. ORTEP representation of **3b**, ellipsoids drawn at 30% probability. Hydrogen atoms were omitted for clarity.

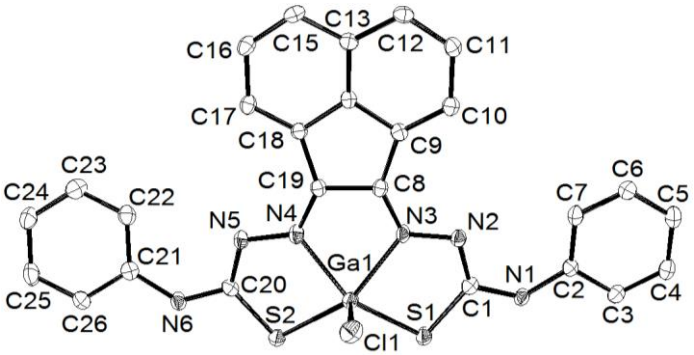

Figure 4.10. ORTEP representation of **3c**, ellipsoids drawn at 30% probability. Hydrogens were omitted for clarity. For **3c** two molecules were present in the asymmetric unit, only one is represented here.

For **3a**, X-ray structure determination further showed that both symmetric and asymmetric binding modes were possible for this class of Ga(III) compounds supporting NMR spectroscopy analyses. All bond lengths and angles of **3a - 3d** are within the range expected for this class of compounds, and close to those determined for their reported Zn(II) precursors.[127, 128] It is likely that that the rigid backbone and tight control of the ligand bite angles by the presence of the aromatic naphthyl substituents in complexes **3a** – **3d** may account for the significantly higher kinetic stability of aromatic gallium complexes with respect to aliphatic analogues. This trend is consistent with what was found for the aromatic Cu(II) analogues.[123, 127]

4.3.2 DFT optimisations

To provide insight into isomeric exchange of the gallium complexes with the phenyl functionality the were optimised from their crystal structures, following the method used by Holland *et al*.[119] Initially the compounds were optimised in the gas phase using B3LYP 6-31G(d,p), followed by B3LYP 6-31++ (d,p) IEFPCM, DMSO to obtain an optimised structure in solution *(Figure 4.11)*. In the gas phase the calculated energy difference is 4.99 kJ mol^{-1}, indicating that the asymmetric structure **3c'** is more stable than the symmetric structure **3c**. Likewise, when solvent effects were considered in DMSO, the symmetric structure was more energetically favourable when compared to the asymmetric (the energy difference is -4.34 kJ mol^{-1}), which is in agreement with ^{1}H-NMR spectroscopy data.

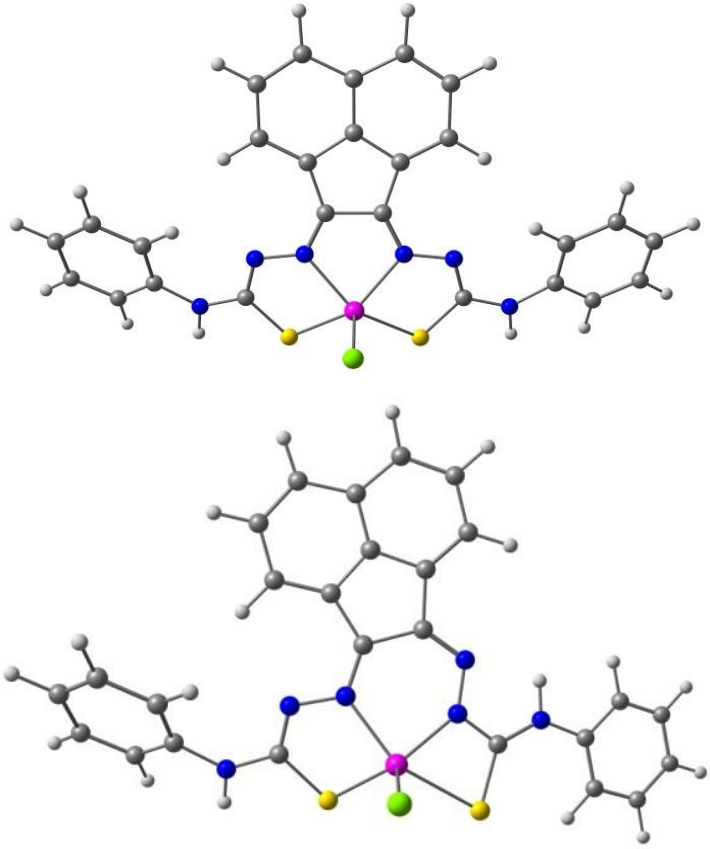

Figure 4.11. Optimised in solution structures by B3LYP 6-31++ (d,p) IEFPCM, DMSO, where (above) is symmetric **3c** and (below) is asymmetric **3c'.** Where grey = carbon, white = hydrogen, blue = nitrogen, red = oxygen, green = chlorine, deep pink = gallium.

4.3.3 Variable temperature NMR spectroscopy

To investigate the isomerism further **3a** was studied in d_8-THF, by Variable Temperature -NMR spectroscopy (400 MHz) *(Figures 4.12-13)*. Change in enthalpy, entropy and Gibbs free energy were calculated from the VT-NMR spectroscopy data using Van't Hoff analysis and the equation:

$$ln(K) = \frac{\Delta H}{RT} + \frac{\Delta S}{R}$$

Complex **3a** displayed some observable fluxional behaviour in solution. Considering Figure 4.12, k is ratio of symmetric / asymmetric isomer at each temperature, i.e. the equilibrium from asymmetric to symmetric isomer. ΔH was calculated to be -3626.65 J/mol, whilst ΔS equals -12.0412 J/K/mol, with ΔG at 298 K calculated as -38.3824 J/mol, indicating that there is a small preference towards the symmetric isomer.

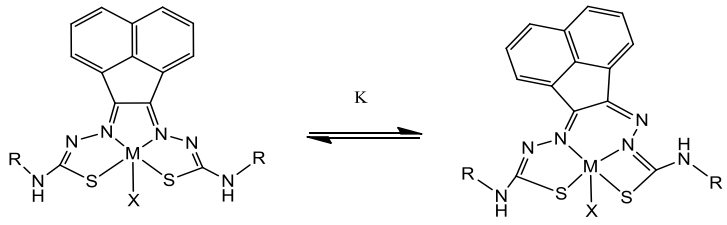

Figure 4.12. Proposed isomeric exchange for the aromatic bis(thiosemicarbazone) complexes studies hereby where M = Zn, Cu, Ga or In, R = Me, Et, Ph or allyl, X = DMSO, THF, DABCO, bipy, and K is the exchange constant.

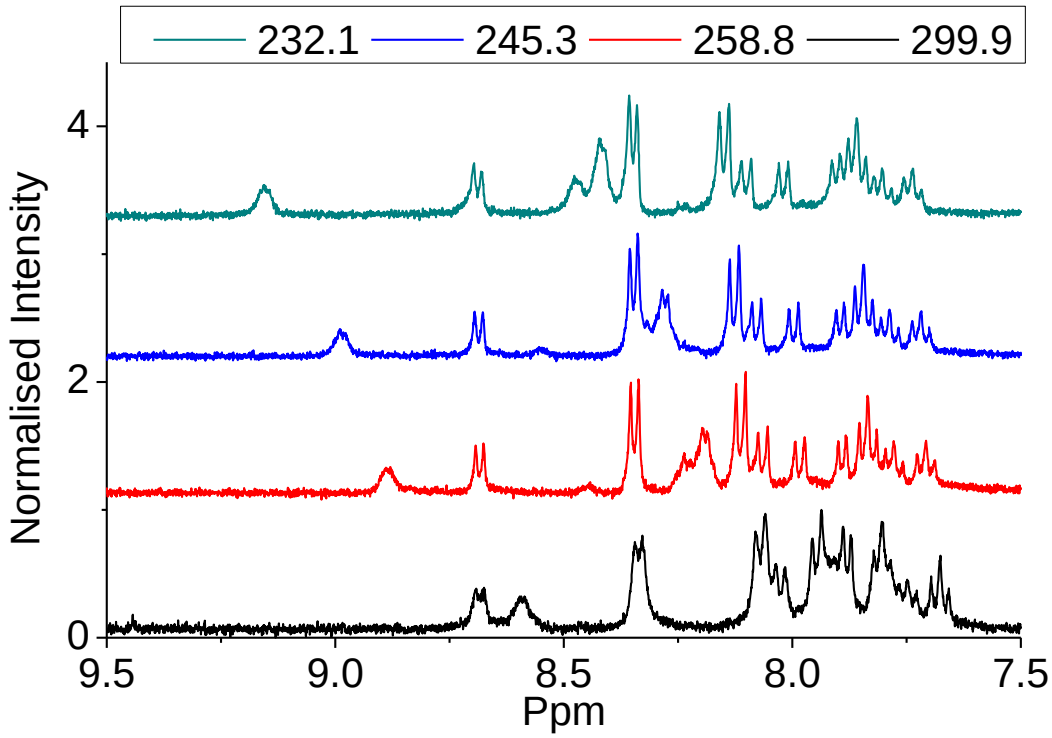

Figure 4.13. ^{1}H NMR spectroscopy showing resonances corresponding to **3a** at 232.1 K, 245.3 K, 258.8 K and 299.9 K in d_8-THF.

4.4 Spectroscopy

Fluorescence spectroscopy was performed on DMSO solutions, using initial scans for excitation wavelengths between 200-800 nm. This provided information about the intrinsic fluorescence of the complexes and the corresponding $\lambda_{em\text{-}max}$ using solutions of 100 μM. Ranges of absorption and emission, which are important with regards to cytotoxicity assays and fluorescence imaging, were also assessed using the 2D contours as a guideline. Relevant cytotoxicity assays use absorbance readings at 570 nm, therefore there should be minimal or no excitation at this wavelength, which was true for all complexes except **3c** *(Figure 4.14b).*

Compounds generally emitted between 520 and 675 nm, whereas excitation mainly occurred between 250 and 570 nm *(Table 4.3, Figure 4.14 and Appendix Figure C.2*. All compounds displayed intrinsic fluorescence. $\lambda_{em\text{-}max}$ was found to vary for gallium complexes depending on the functionalities: 510 nm, 400 nm, 450 nm and 520 nm for

3a, **3b**, **3c** and **3d** complexes respectively. Quantum yields were calculated using the standard solution of $[Ru(bipy)_3](PF_6)$ in water as a reference and utilising the equation:

$$\Phi_S = \Phi_R \cdot \left(\frac{D_S}{D_R}\right) \cdot \left(\frac{A_R}{A_S}\right) \cdot \left(\frac{I_R}{I_S}\right) \cdot \left(\frac{\eta_S}{\eta_R}\right)^2$$

Where Φ = quantum yield, D = integrated area under emission band, S = sample, A = absorbance of solution at excitation wavelength, R = reference, η = refractive index of solvent, I = maximum intensity of excitation band $[Ru(bipy)_3][PF_6]_2$ in water was used as a reference, with a quantum yield of 0.042. Importantly, the quantum yields indicate sufficient fluorescence imaging in biological cells, with similar values for each gallium compound.

Table 4.3. Fluorescence quantum yield measurements of complexes **3a**-**3d**.

Compound	$\lambda_{ex\text{-}max}$ / nm	Excitation range / nm	$\lambda_{em\text{-}max}$ / nm	Emission range / nm	Quantum Yield
3a	410	250-560	551	495-685	0.11
3b	500	250-570	556	500-685	0.19
3c	450	250-610	599	550-740	0.08
3d	520	250-550	554	490-690	0.12

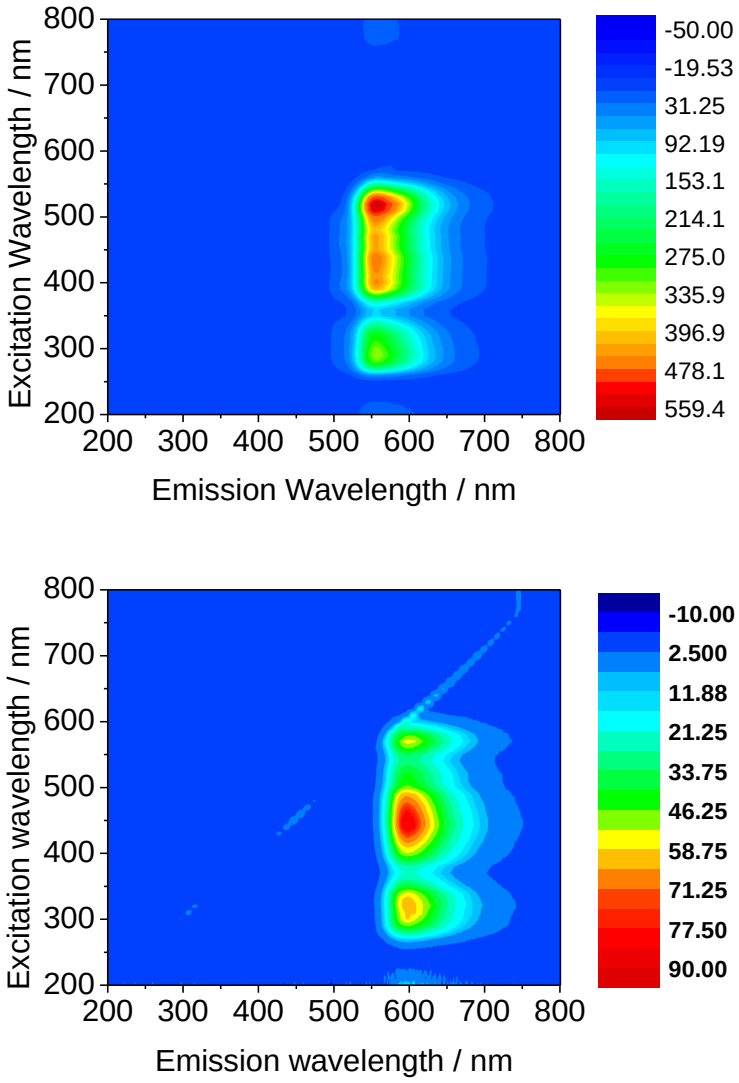

Figure 4.14. Excitation/emission map at 100 μM in DMSO of compound **3b** (above) compound **3c** (below)

4.5 Kinetic stability testing in an aqueous environment

Gallium complexes **3a** and **3c** *(Figures 4.15-4.16)* had an unexpected intensity increase with time up to 8h. The compounds remained fluorescent at 24h, but at a lower intensity than at 8h. Preliminary assays with media in the absence of serum displayed a gradual decrease in fluorescence with time, which is consistent with the zinc complexes **1d** in serum and serum free media. The difference between these two assay types is protein content, indicating that the gallium compounds likely interact with the protein. Interestingly, compound **3c** showed that the fluorescence band maxima shifts from ca. 590 nm at t = 0 h to ca. 530 nm at t = 2 h, indicating that the complex may bind to a component of the serum *(Figure 4.16)*.

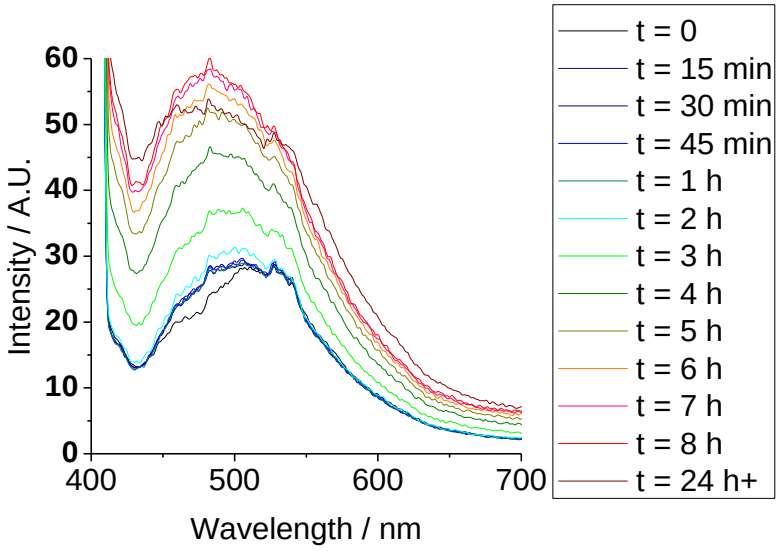

Figure 4.15. FCS stability assay by fluorescence spectroscopy for compound **3a** in FCS: DMSO, 1: 1 ratio

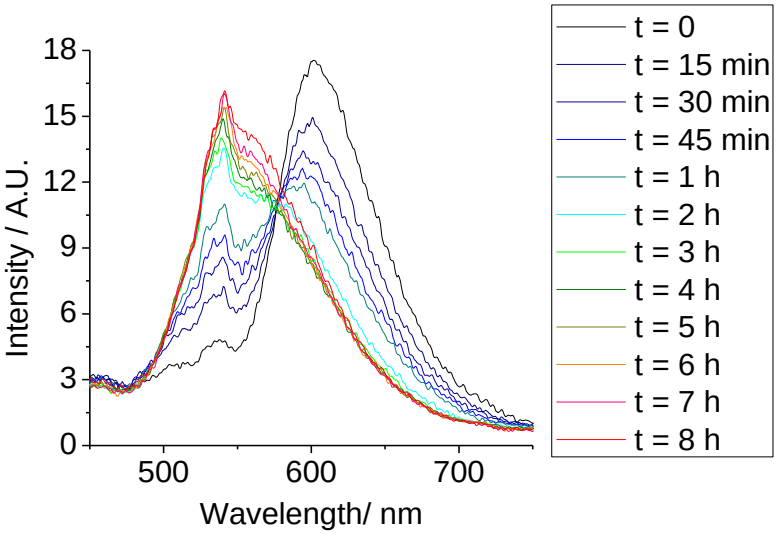

Figure 4.16. Fluorescence spectroscopy - FCS stability assay **3c** FCS: DMSO 1: 1

Due to the significantly greater fluorescence of the gallium complexes in comparison to its respective proligand, fluorescence intensity observed is indicative of complex stability. However, since the free ligand does possess some fluorescence, it is important to consider the UV-Visible spectra of complexes to confirm stability under these conditions. In conjunction with a study allowing comparisons with [GaCl(ATSM)], which was found to form the corresponding ligand precursor within 5 minutes in 99% FCS, 1% DMSO, the gallium complex **3d** was tested under analogous conditions *(Figure 4.17)*.

Whilst changes in the UV/Vis spectra for the gallium complex **3d** were observed over an incubation of 24 h in serum *(Figure 4.17)*, it is apparent that the product of the assay has not completely converted to free ligand **iid**. UV/Vis spectroscopy studies on **3d** suggested that little decomposition occurs up to 3 h although some deteriation of the gallium species is evident after 18 h with LCMS analysis at this time suggesting the presence of both the parent chloride complex and some of the analogue in which the chloride ion is replaced by hydroxide.

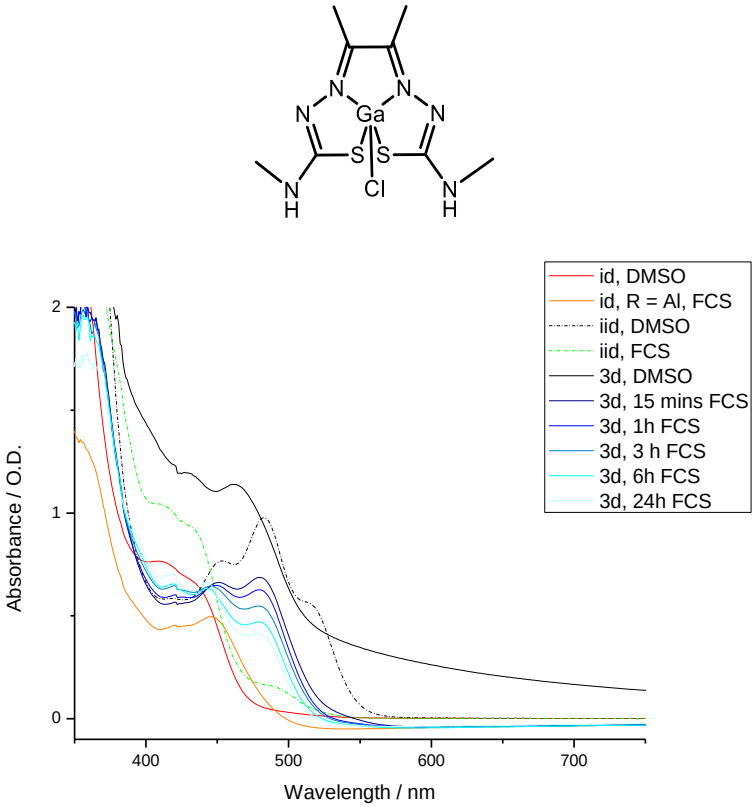

Figure 4.17. Serum assay (99% FCS, 1% DMSO) by UV/Vis for compounds **3d** at 100 µM, monitored at time intervals up to 24h at room temperature and filtered using a 0.45 µm PTFE microfilter, Compound [Ga-Cl(ATSM)] (shown above) was found not to be stable under comparable conditions.[138]

This investigation utilised both UV-visible absorption (at 10 µM and at 100 µM) and fluorescence emission at 100 µM, with 1:1 DMSO:[assay agent] to limit precipitation. This allowed a % stability to be estimated *via* UV-Visible spectroscopy at 15 minutes and 24 hours as calculated by (100 % - percentage converted to free ligand) *(Table 4.4)*. The first assays carried out in DMSO, water, PBS, 5% FCS EMEM and SFM EMEM enabled complex stability to be understood in media likely to be encountered in a cell biology experiment. UV-visible spectroscopy data for each of the above assays are described first, followed by the analysis of their corresponding fluorescence studies, which were carried out in parallel.

By UV-vis complex **3d** displayed encouraging results in DMSO, water and 5% FCS (88.2 %, 39.6 % and 79.1 % after 24 h respectively) *(Figures 4.17 and 4.20)* complex **3d** was not stable during a 24 h incubation in PBS *(Figure 4.18)* or in SFM *(Figure 4.19)* and showed contrastingly high stability in SFM after 15 minutes (64.3 %) and limited

remaining complex in PBS (10.9% after 15 minutes.) Moreover, **3d** demonstrated 75.3 % estimated stability in DMSO:water 1:1 after 15 minutes, but with a significant decrease in absorbance representing 39.6 % remaining complex after 24 h.

Table 4.4. Summary of estimated complex remaining from UV-visible data at 1:1 DMSO:biologically relevant agent at 15 minutes and 24 h where Citric Acid, EDTA, L-Cys, L-His, L-Met and GSH were in MilliQ water.

Assay	Compound **3d**, 100 µM	
	15 min[a]	24 h[a]
DMSO	92.1	88.2
H_2O	75.3	39.6
PBS	10.9	NS
5% FCS, MEM	75.4	79.1
SFM, MEM	64.3	NS
Citric Acid	80.0	NS
EDTA	87.1	51.6
L-Cys	80.0	51.1
L-His	44.6	28.1
L-Met	58.1	45.1
GSH	52.8	7.7

For the fluorescence spectra, there was no significant change in intensity of complex **3d** in DMSO over a period of 24 h, which had showed a small decrease in fluorescence for the zinc complex **1d** *(Appendix Figures D.11-15 and Chapter 3)*. Subsequently complexes were tested and compared to the ligand precursor **iid** in a 1:1 MilliQ water:DMSO solution over a period of 24 h *(Figure 4.17)*. Under these conditions the gallium complex displayed a significant decrease in fluorescence after 1 day of incubation and a blue shift in fluorescence maxima of 13 nm after 24 h from 559.5 nm at 15 mins, indicative of some conversion to free ligand (a λ_{max} of 542 nm at 15 mins) *(Figure 4.8)*. The fluorescence intensity observed was sufficient to indicate the presence of some remaining gallium complex after 1 day, in agreement with UV-visible data.

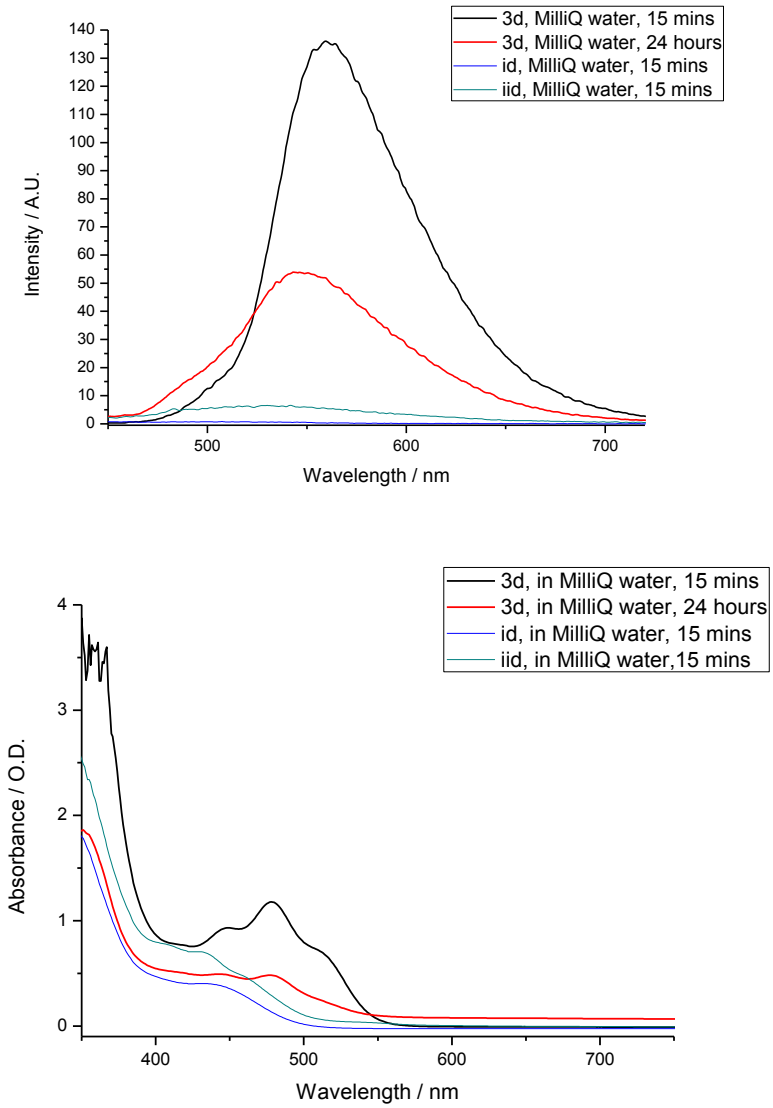

Figure 4.18. Water assay (50% DMSO, 50% water) for compound **3d** at 100 µM, by fluorescence spectroscopy (above) UV/Vis (below) monitored at time intervals up to 24h at room temperature.

Fluorescence data in PBS were significantly weaker than in water, in combination with a blue shift in absorbance is indicative of decomposition into bis-substituted free ligand *(Figures 4.17-4.18).* Most of the gallium complex appears to have become ligand within 15 minutes as confirmed by the estimated 10.9 % remaining complex calculated using UV-visible measurements and possessed very similar λ_{max} of 537.5 nm for **3d** at 24 h and 538 nm for compound **iid** at 15 mins.

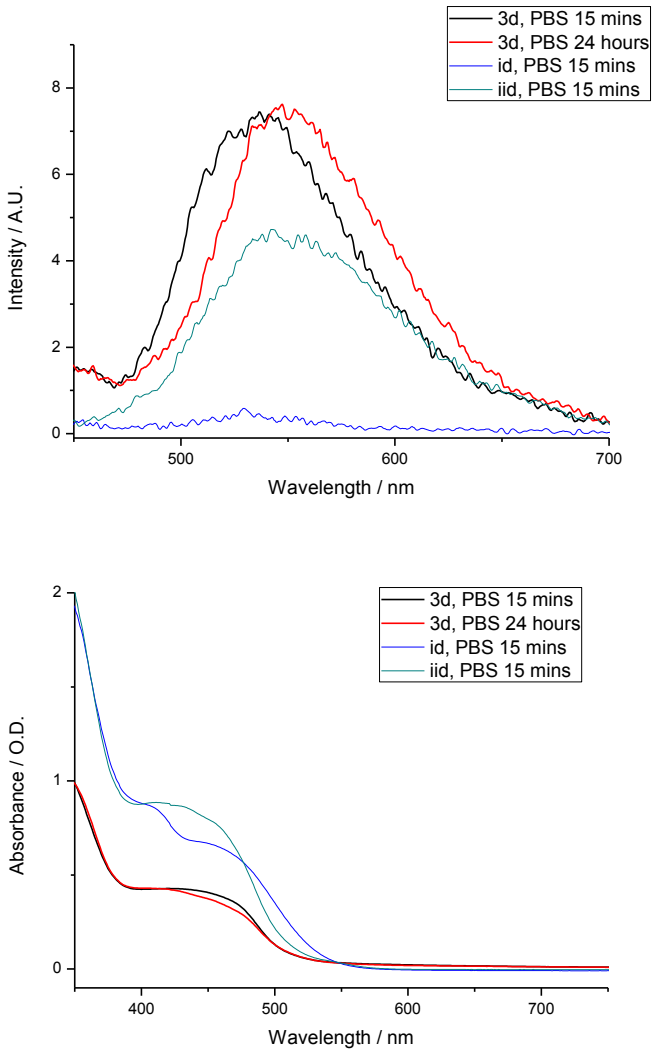

Figure 4.19. PBS assay (50% DMSO, 50% PBS) for compound **3d** at 100 µM, by fluorescence spectroscopy (above) UV/Vis (below) monitored at time intervals up to 24h at room temperature.

The stability of the complexes was tested against Eagle's Minimum Essential Medium Serum Free Medium (SFM), which complexes are often incubated in for cell imaging. The fluorescence of each complex decreases over the time period studied at the λ_{max}, however complexes **1d** and **3d** interestingly show an increase in fluorescence at ca. 450 nm and 460 nm *(Figures 4.20-4.21)*. This could suggest that a new species is being formed or interaction with the media perhaps *via* binding to a component of the solvent for example amino acids or glucose. The λ_{max} of **iid** under these conditions is 531 nm indicating that the new band does not correspond to free ligand, however the λ_{max} of **id** of 469 nm implies that the new band may be similar to the mono-substituted free ligand.

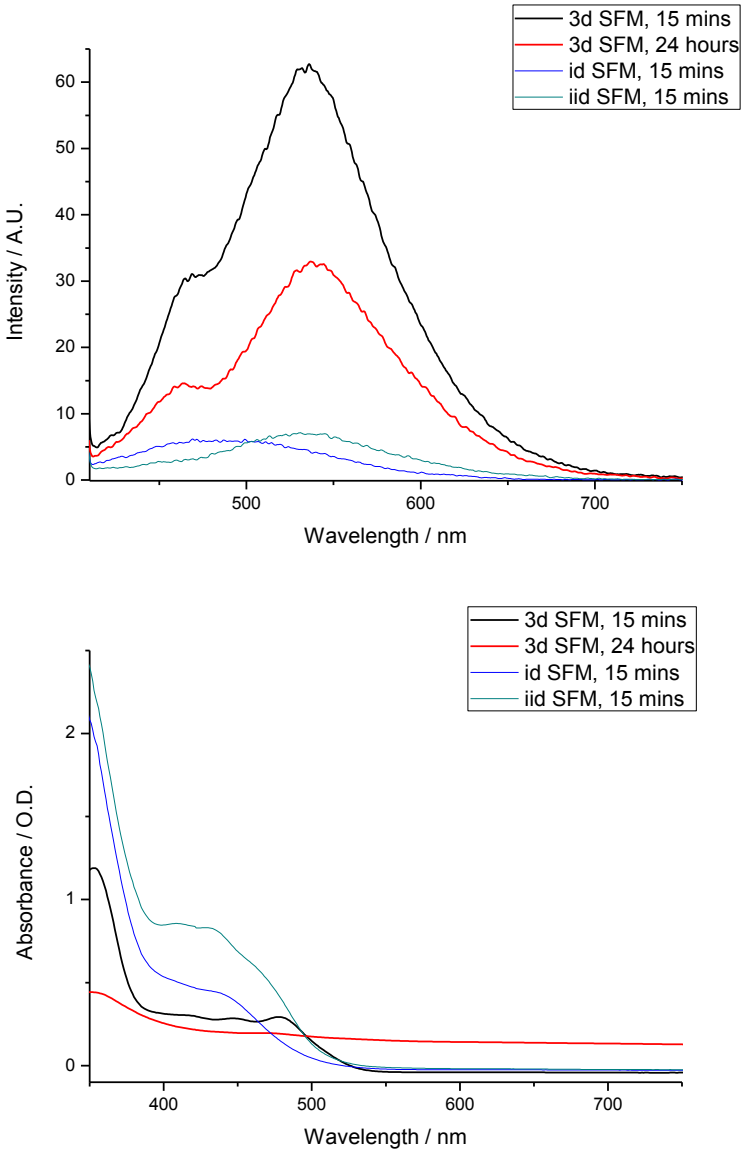

Figure 4.20. EMEM SFM assay (50% DMSO, 50% SFM) for compound **3d** at 100 µM, by fluorescence spectroscopy (above) UV/Vis (below) monitored at time intervals up to 24h at room temperature.

With λ_{max} of **3d** 536 and 537 nm at 15 minutes and 24 h respectively it is likely that a significant proportion of complex has rapidly become free ligand. An augmentation of absorbance and fluorescence was also observed in the case of complex **3d** after incubation of 24 h and retaining a band in the UV-visible spectrum at ca. 500 nm not observed in either free ligand **id** or **iid** (*Figure 4.20).*

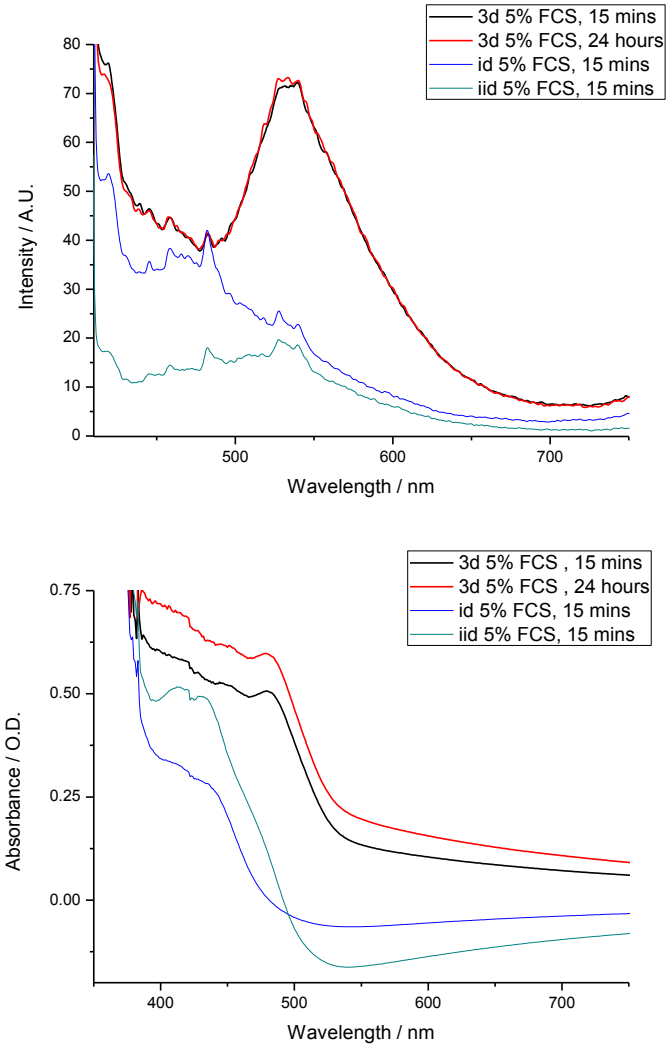

Figure 4.21. FCS assay (50% DMSO, 45% EMEM, 5% FCS) for compound **3d** at 100 µM, by fluorescence spectroscopy (left) UV/Vis (right) monitored at time intervals up to 24h at room temperature.

This is not surprising since FCS is known to increase background absorbance; interestingly, there was no fluorescence increase at ca. 450 nm or 460 nm as was observed in the absence of serum. This shows that presence of FCS is significant with regards to interaction of media and likely causes formation of the zinc and gallium complexes in an orientation or binding mode unlike that produced in EMEM alone.

4.5.1 Stability assays to estimate kinetic stability against common biologically-relevant agents

Biologically relevant agents were chosen to provide a better insight into the stability of these complexes,[145] as were introduced in *(Chapter 3)*. Complexes were tested in presence of 2 equivalents of citric acid, L-methionine, Glutathione (GSH), L-cysteine, L-histidine, and EDTA. Complex **3d**, however displayed less promising stability. In citric acid **3d** demonstrated significantly reduced fluorescence and absorbance in milliQ water whereby the complex appears stable at 15 minutes, at 24 h both fluorescence and UV-visible spectra were not characteristic of the allyl functionalised gallium complex *(Appendix Figure D.11)*. When incubated in PBS and citric acid rapid conversion to free ligand was observable due to similarity of the **3d** spectrum to distinctive absorption spectrum of **iid** under the same conditions *(Figure 4.22)*.

Conversely it is apparent that the **3d** UV-vis spectrum is not identical to **iid** at 15 minutes, with significantly greater fluorescence at this timepoint showing that some gallium complex is remaining in PBS with citric acid. It is likely that **3d** has almost completely converted to **iid** after 24 h of incubation attributable to the comparable spectra. In aqueous solutions of L-methionine, L-cysteine, L-histidine, or EDTA, **3d** displayed similar properties, each with the characteristic **3d** absorbance spectrum at 15 minutes followed by a significant decrease in absorbance at ca. 480 nm, but not the formation of data corresponding to that of the **iid** free ligand *(Figures 4.23-4.24 and Appendix Figure D.12-15)*.

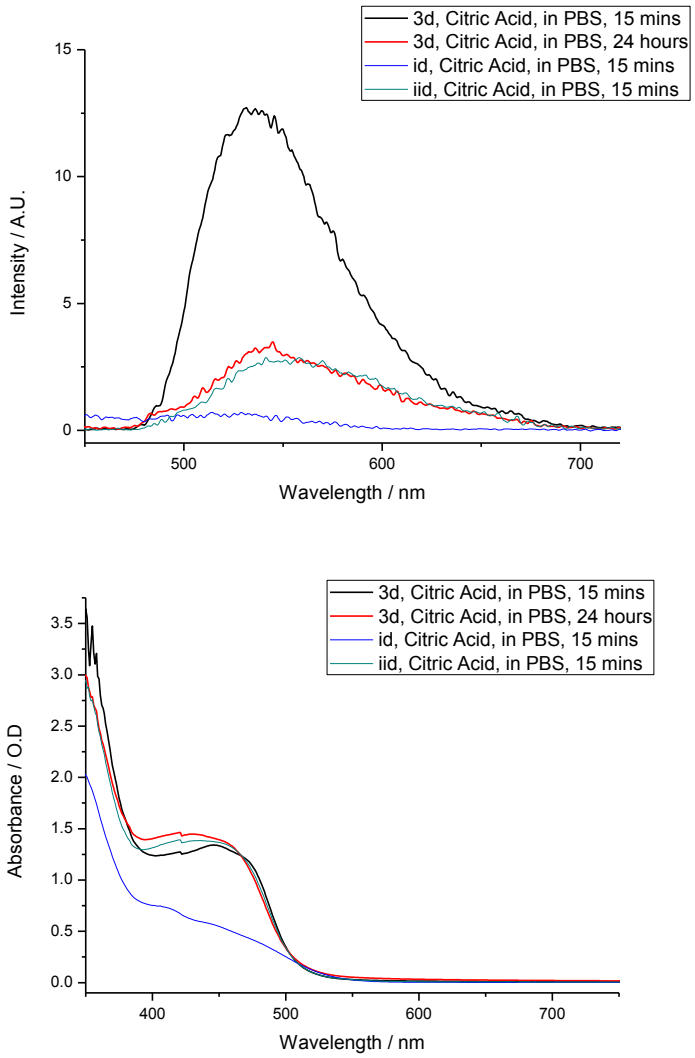

Figure 4.22. Citric acid assays (50% DMSO, 50% PBS, 2 eq of citric acid) for compound **3d** at 100 µM, by fluorescence spectroscopy (above) UV/Vis (below) monitored at time intervals up to 24h at room temperature.

This combined with the greater fluorescence of **3d** after 24 h incubation as compared with **iid** at 15 minutes is indicative that not all of the complex has formed free ligand. The 24 h spectrum of **3d** in GSH is very similar to that of **iid** at 15 minutes, displaying a very similar absorbance spectrum, indicating that most of **3d** has been converted to compound **iid** under these conditions *(Figure 4.24)*.

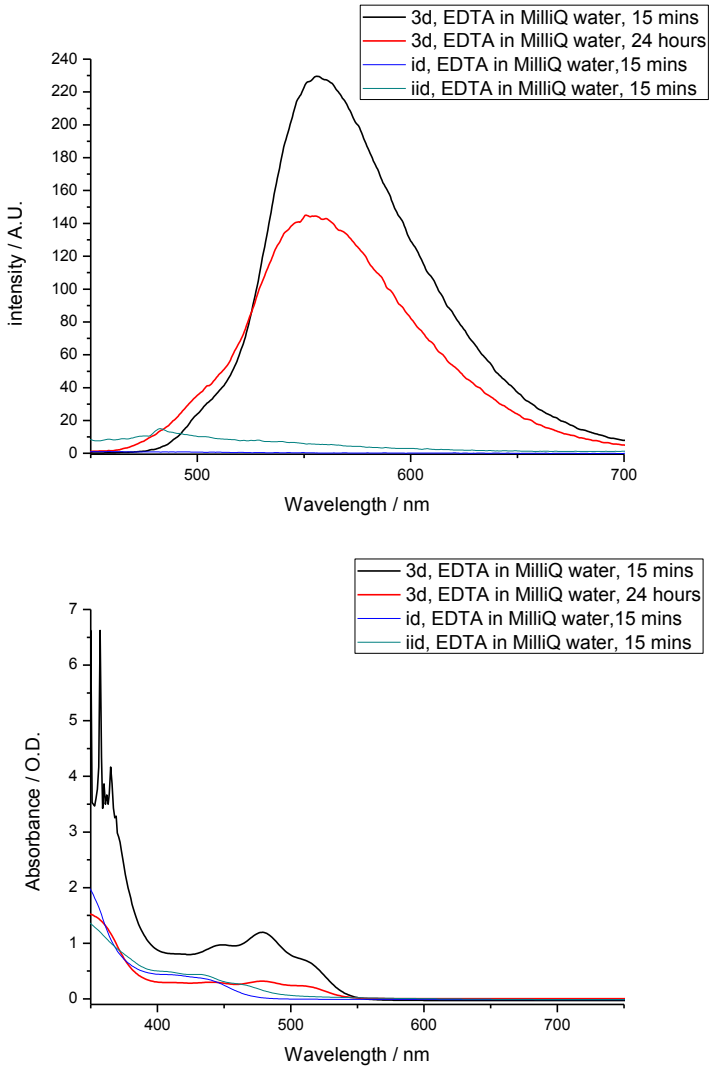

Figure 4.23. EDTA assays (50% DMSO, 50% water, 2 eq of EDTA) for compound **3d** at 100 µM, by fluorescence spectroscopy (above) UV/Vis (below) monitored at time intervals up to 24h at room temperature.

It can be observed that there is a much higher fluorescence intensity for **3d** at 24h than for **iid** at 15 minutes, indicating that although most complex may have converted to free ligand, it is likely that not all of the complex has. In contrast to the data acquired for L-cysteine, L-methionine and L-histidine, in which **3d** appeared much more stable, it can be speculated that this combination of three peptides, containing both N- and S- groups presents a much more potent biomolecule for the purpose of demetallating the complex.

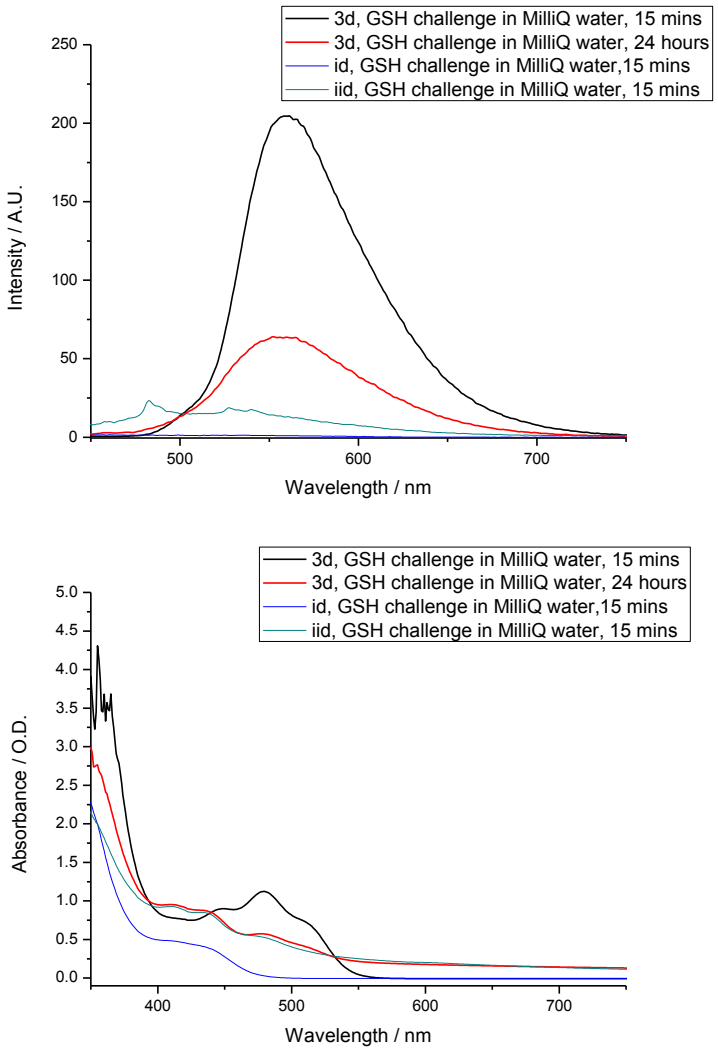

Figure 4.24. Glutathione assays (50% DMSO, 50% water, 2 eq of Glutathione) for compound **3d** at 100 μM, by fluorescence spectroscopy (above) UV/Vis (below) monitored at time intervals up to 24h at room temperature.

4.5.2 pH study

The stability of complexes at biologically relevant pH is an important factor in this study. Cancer cells are slightly more acid than non-cancerous cells it is important that the molecular probes are stable at lower pH.[146] All fluorescent scans were carried out with an excitation wavelength of 400 nm and at a concentration of 100 μM, with a 1:1 DMSO:buffer solution. An initial preliminary study was carried out using fluorescence spectroscopy for the gallium complexes.

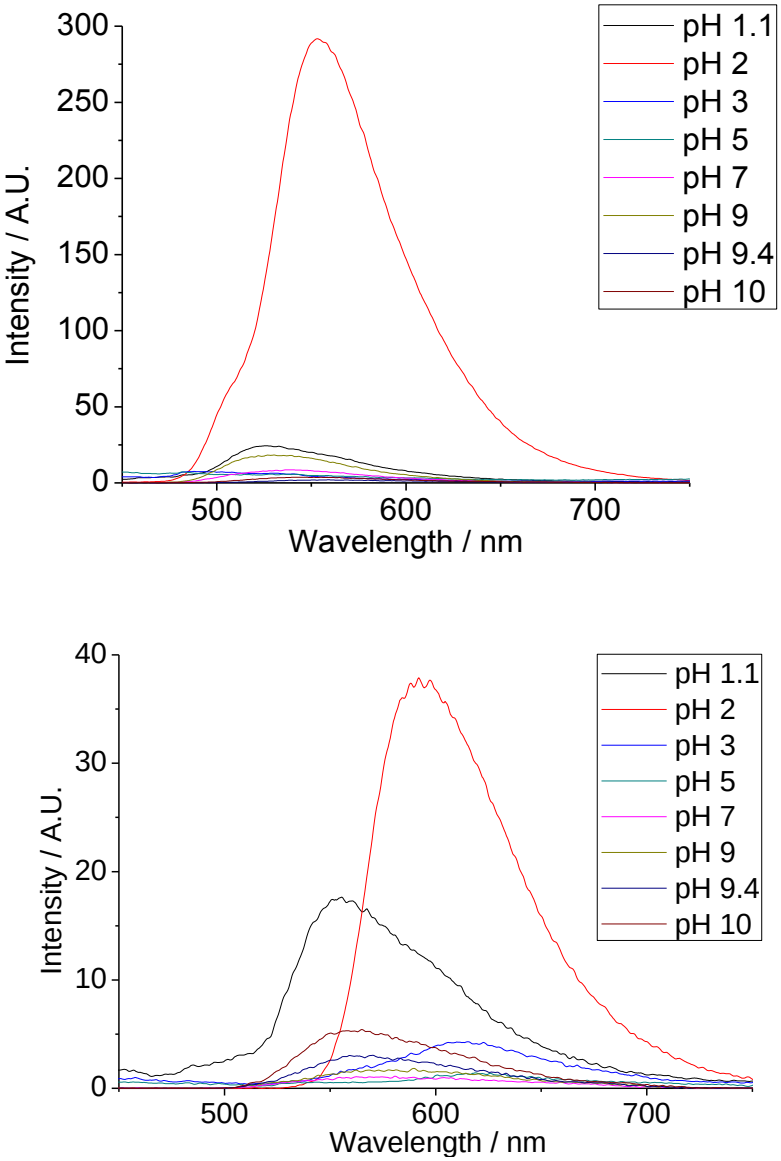

Figure 4.25. Fluorescence spectroscopy buffer assay **3b** pH study (above). Where pH 2 >> pH 1.1 > pH 9 > pH 7 > pH 3 ≥ pH 5> pH 10 > pH 9.4 and **3c** pH study (below) Where pH 2 >> pH1.1 > pH 10 > pH 3 > pH 9.4 > pH 9 > pH 5 ≥ pH 7

The gallium compounds all displayed maximum fluorescence at pH 2, with particularly intense fluorescence for **3a** and **3b** at this pH. It is interesting to notice that **3a** and **3b** are very fluorescent at pH 2, but very little fluorescent at pH 3. This could be explained by the nature of the species involved in the buffer. Buffer pH 2 contained HCl and KCl, whereas the pH 3, pH 5 and pH 7 buffers contained citric acid. Holland *et al.* have recently shown that citric acid can be used to remove zinc from zinc bis(thiosemicarbazonato) complexes, [148] which may have happened in the preliminary study, since dissociation of the metal centre would cause a decrease in fluorescence.

Table 4.5. Summary of UV-visible data at 50: 50 DMSO: pH buffer at 15 minutes and 24 h, where NS = not stable.

	3d, 100 µM		
Buffer	Measured pH	% stability at 15 mins	% stability at 24 h
pH 1.1	1.6	68.6	NS
pH 2	2.5	85.5	53.9
pH 3	4.4	86.9	NS
pH 5	6.9	73.7	51.7
pH 7	9.4	5.0	NS
pH 9	9.35	6.2	NS
pH 10	12.7	6.8	NS

Therefore an intial study where citric acid was used was carried out (prior to the assays described above) followed by another investigation that did not include citric acid as part of the buffer systems, a means to monitor if the nature of the buffer had a significant effect. These gallium complexes are therefore very pH sensitive, for example, **3c** is fluorescent at pH 1 and pH 2, indicating that it can readily be protonated, but shows little fluorescence under more alkaline conditions *(Figure 4.25)*.

Following the above preliminary study, the allyl-substituted compounds were selected as a representative of the other functionalities to assess the stability of newly synthesised gallium and indium complexes using UV-visible and fluorescence spectroscopy both at 15 minutes and 24 hours, with 1:1 DMSO:buffer solution with the assistance of Johan Stojanović, technician student from ESCOM, France. The pH of the samples was measured and found to have no significant difference to the blank, however with a notable variance from that of the original pH solution in each case *(Table 4.5)*.

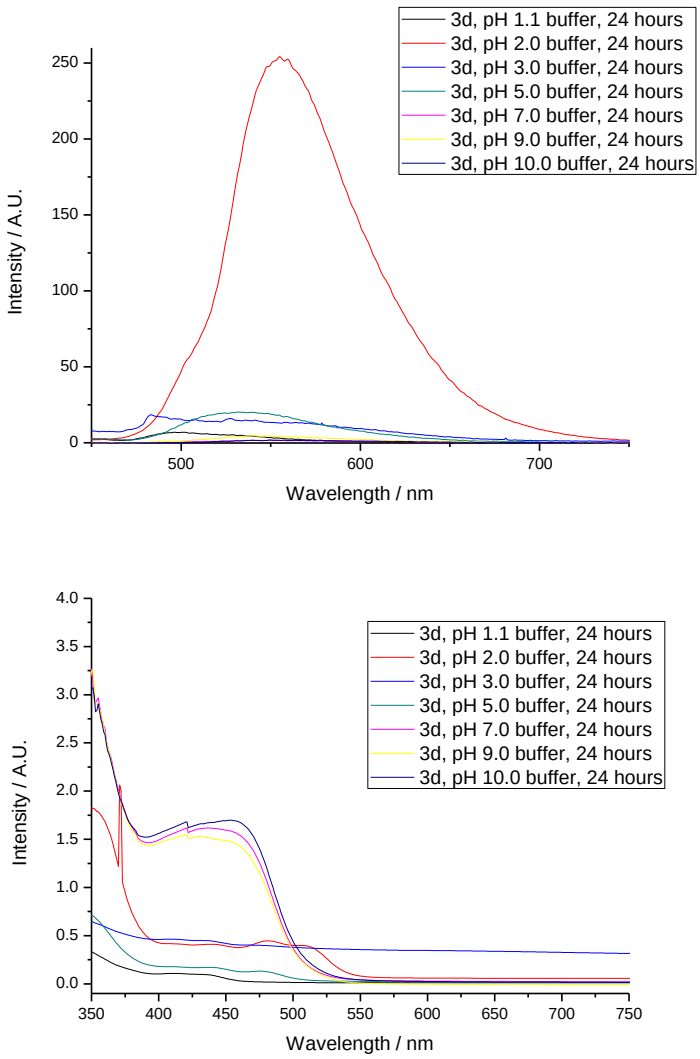

Figure 4.26. All buffer assays (50% DMSO, 50% water) for compound **3d** at 100 µM by fluorescence spectroscopy (above) and UV/Vis (below) monitored at 24 hours at room temperature.

Furthermore all gallium complexes *(Figure 4.26 and Appendix Figures D.16, D.20-27)* appeared most stable at either pH 2 or pH 3 after 15 minutes or less, which is also in agreement with data acquired where citric acid was a component of the buffer solutions. By UV-visible spectrometry compound **3d** seems to decompose completely after 24 hours when incubated in a pH 1.1 buffer, yet appears to remain intact at 15 minutes, as its spectrum has formed the shape characteristic of **iid** in this time, fluorescence however appears to be fully quenched at 15 minutes (*proligand **iid** buffer study Appendix Figures D.50 and D.51).* It is likely that stability of the gallium complex is poor at this pH. In pH buffers 2.0, 3.0 and 5.0 there is complex presence indicated by both absorption and emission spectra at 15 minutes, however a clear decrease in

fluorescence intensity and absorbance including a blue shift for pH 3.0 and pH 5.0 buffers are indicative of instability of this compound at longer incubations.

As was observed with **1d**, **3d** spectra closely resembled those of compound **iid** when incubated with a pH 7.0 buffer, however due to the high stability observed in the 5% FCS assay the apparent lack of stability could be explained by interaction with the components of the buffer rather than the pH itself. When considering the measured pH of the pH 7.0 buffer blanks 1:1 DMSO:buffer is 9.4 (a Sodium phosphate Monobasic / Sodium phosphate Dibasic based buffer), as was the measured pH when incubating with the pH 9.0 buffer was pH 9.35 (a glycine / sodium hydroxide based buffer) and that spectra were comparable the most likely outcome is in fact that the complex has poor stability under alkaline conditions, which are seldom observed in a biological environment.

Whilst spectroscopic (fluorescence and UV-vis) data acquired with the pH 7.0 and pH 9.0 buffers were similar, in both cases it was observable that conversion to **iid** was not complete, indicating a small proportion of complex remaining. UV-visible and Fluorescence spectra of **3d** when incubated with a pH 10.0 buffer (measured pH with blank pH 12.7) displayed spectra more closely resembling the free ligand **iid**, indicating that the stability was poorer under more alkaline conditions. The range of good stability of this complex when considering the measured pH with the blank is pH 2.5 to pH 6.9, however under no conditions tested using the pH buffers was complete conversion to **iid** after 15 minutes, indicating that short-term experiments in biological environments are valid with this compound, especially with the stability observed after 24 h in 99% FCS for this complex, with a blank pH of 7.35. In summary the spectra acquired support the legitimacy carrying out cell uptake experiments, where incubations would be less than 20 minutes, whereby the complex would most likely intact under these biomimetic conditions.

4.3 Two-photon fluorescence lifetime study

The two-photon investigations were first introduced in Chapter 2 and all studies were performed at the Rutherford Appleton Laboratory under the supervision of Dr S Botchway. Gallium complexes possessed two components in solution with τ_1 comparable to the τ_1 of the ligand precursor under the same conditions, yet slightly longer for each complex. The τ_2, on the other hand was significantly lower at ca. 1 – 1.5 ns *(Appendix Figure E.3., Table E.5).* This combined with the stability study in solution using UV-vis and fluorescence signifies that this similarity is most likely due to the ligand-dependant nature of the fluorescence *(Chapter 3)* according to TD-DFT calculations carried out for the copper complex **2c**, rather than decomposition to free ligand in solution. The presence, therefore of a long component by FLIM *in vitro* of more than 2 ns may thus be the best indication of complex becoming proligand using this technique.

In cells when exciting at 910 nm results were similar to those observed within solution for all major components, and most minor components under standard conditions. Gallium complexes were incubated at 50 μM, 0.5% DMSO, for 20 minutes, unless stated otherwise in the text. The τ_2 (minor component) are highly comparable to the lifetimes observed for the free ligand **3a** HeLa (0.588 ns, 0.406 ns FWHM), **3b** PC-3 (0.475 ns, 0.094 ns, FWHM) and **3c** MCF-7 (0.567ns, 0.228 ns FWHM), for example the major component of **iic** at 910 nm was 0.531 ns, 0.508 ns FWHM. Equally, this could signify some conversion to free ligand 4%, 8% and 20% respectively) or that the gallium complex forms similar interactions for the cell as its ligand counterpart.

Further investigations, using excitation of 810 nm showed that τ_2 was higher than expected for the complex in HeLa cells **3b** and **3c** (2.026 ns 0.865 ns FWHM and 2.523 ns, 1.562 ns FWHM respectively), therefore making some ligand formation the more probable of the two above mentioned outcomes. These minor components respectively accounted for 11% and 16 %, thus indicating that most of the complexes are stable within cells under standard conditions. In each case (at 810 nm or 910 nm) the fluorescence intensity was significantly greater than observed for the proligand, indicating complex stability, with FLIM providing quantitative means of evaluating

stability and demetallation. The combined use therefore of UV-Visible spectroscopy, fluorescence spectroscopy and FLIM offer a powerful method of investigating small molecule stability in both solution and in cells and confirm the stability of these complexes.

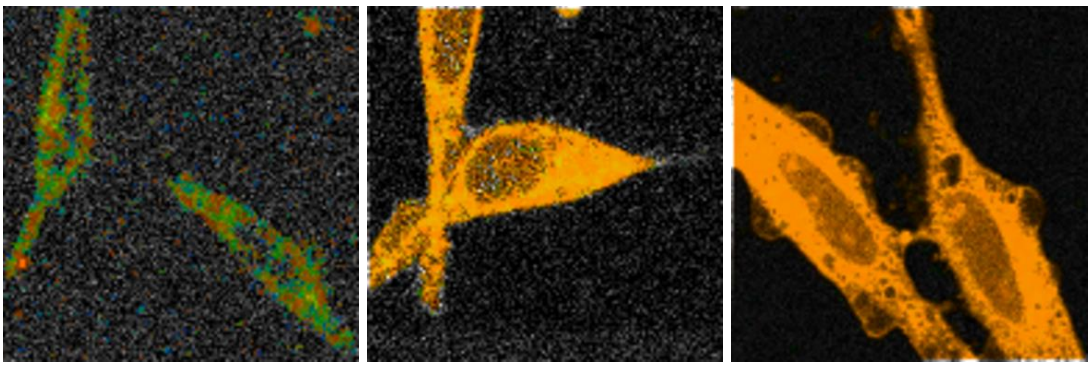

a) **b)** **c)**

Figure 4.27. Two- photon FLIM (τ_m) at 910 nm in HeLa cells after 20 minutes of incubation of **a) iib** at 100 μM, 1% DMSO, **b) 3b** at 50 μM, 0.5% DMSO **c) 4b** at 50 μM, 0.5% DMSO

4.6 Laser scanning confocal microscopy

Cells were cultured using standard protocols, analogous with earlier investigations on fluorescent thiosemicarbazones. Cell viability prior to experiments and over the course of experiments was monitored by optical microscopy, and validated at the start of the experiments by standard trypan blue tests and MTT assays.[127, 128] Complexes **3a**-**3d** were imaged in HeLa (cervical carcinoma), PC-3 (prostate carcinoma), MCF-7 (breast cancer) and FEK-4 (non-cancerous fibroblast) cell lines, cultured as described in the Experimental section by confocal fluorescence microscopy using one photon excitation at 488 nm with the emission long pass filtered at 515 nm.

The imaging studies were performed using concentrations of 50 μM compound in a DMSO: RPMI 0.5:99.5 cell medium solvent mix, whereby the final DMSO concentration on the imaging plate was lower than 1%. The solutions were left to incubate with the adherent cancer cell lines for 20 or 60 min, with preliminary investigations incubating up to 3 hours and at concentrations of 100 μM, at 4 °C or 37 °C. The cells were carefully washed with Phosphate Buffered Saline (PBS) pre-warmed to 37°C, which was replaced by FCS-free medium to remove the non-

internalised fluorescent dispersion prior to fluorescence imaging. As before, the imaging work was carried out in the presence of minimum amount of serum to avoid potential background fluorescence and for suitability for investigation *via* colocalisation dyes.[123, 127, 128]

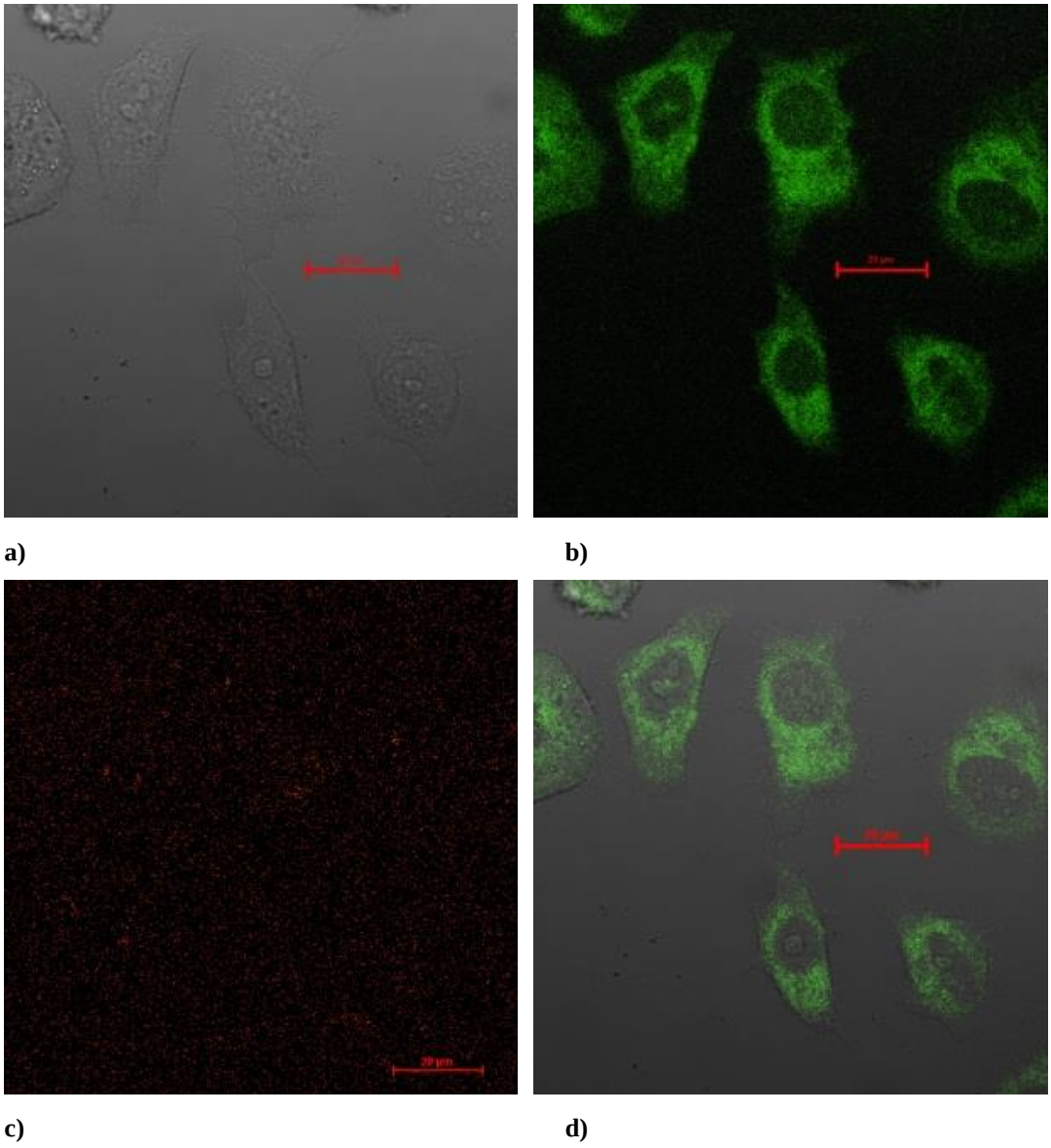

a) **b)**

c) **d)**

Figure 4.28. Single-photon confocal microscopy images of **3a** PC-3 cells, 50 μM, 0.5% DMSO, 20 minutes, at 37°C (a) DIC image, (b) excitation at 488 nm, emission >505 nm, (c) excitation at 405 nm, emission 420-480 nm (d) is an overlay of (a), (b) and (c). Scalebar: 20 μm.

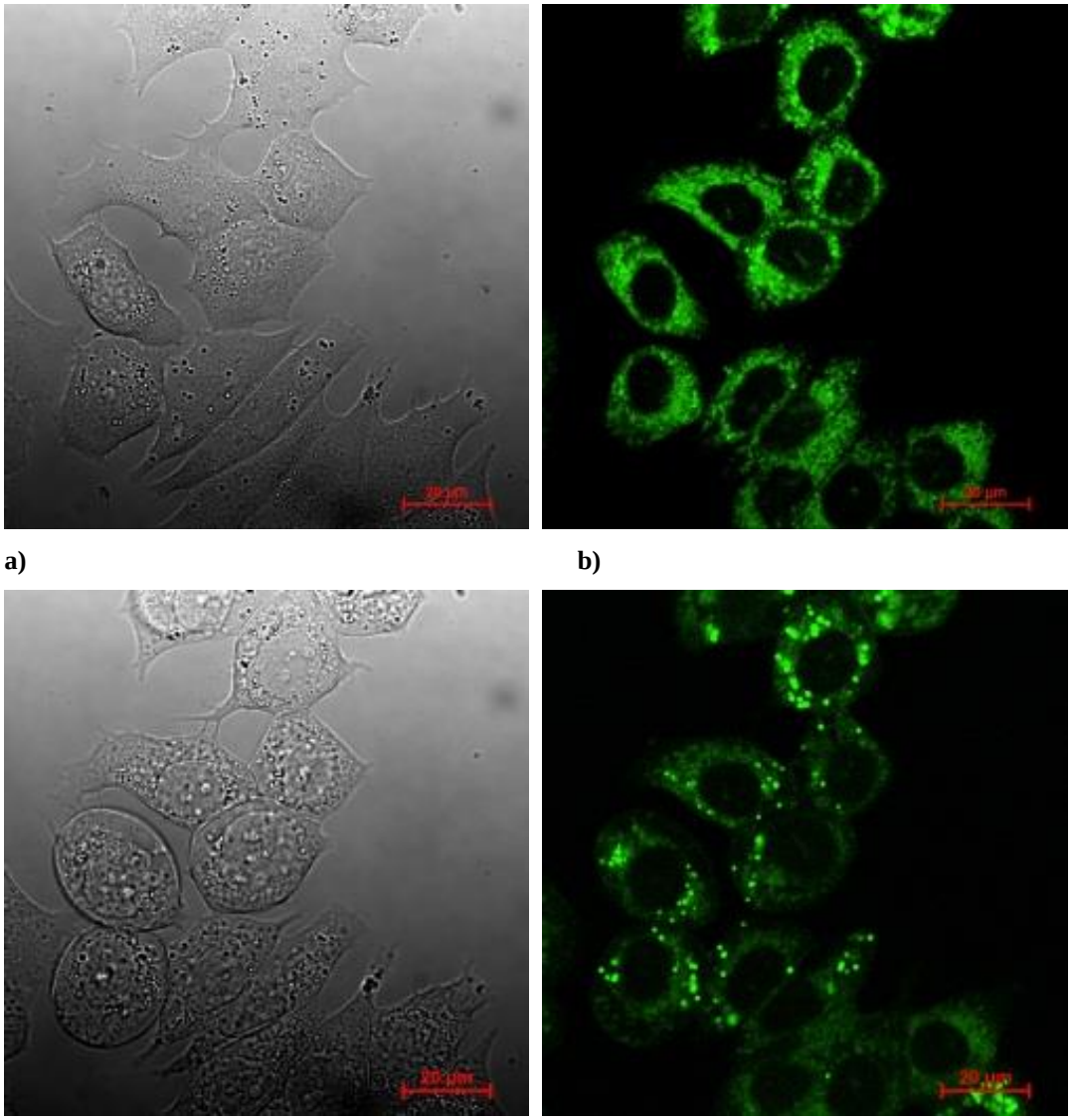

a) **b)**

c) **d)**

Figure 4.29. Complex **3b**, 50 μM, 0.5% DMSO, 20 minutes, at 37°C irradiation experiment at 488 nm in MCF-7 cells: (a – e) before irradiation and (f – j) after irradiation for ca. 10 minutes, where DIC image (a, f), micrograph of cells after excitation at 405 nm (b, g), micrograph of cells after excitation at 488 nm (c, h, compound, green channel), micrograph of cells after excitation at 543 nm (d, i, compound, red channel). Image (e) is an overlay of (a), (b) and (c) images, whereas (j) is an overlay of images (f – i). Scalebar: 20 μm.

The necessity to use concentrations as high as 50 μM in these studies was a result of the rather weak fluorescence emissions (by comparison with organic, commercial dyes). Control experiments prior to incubation of cells with the compounds of interest were obtained by fluorescence imaging *(Appendix G)* to ensure that the cell morphology remains unaltered prior to the imaging experiments. No significant changes in cell morphology were observed by optical microscopy after 20 min incubation with respect

to control. After 60 min incubation at 37 ˚C with compounds **3a**–**3d** the cell morphology gave evidence of stress thus suggesting that these metal complexes are toxic at the 1 h timepoint. The following figures below depict representative confocal fluorescence microscopy images in HeLa and PC-3 cells for these complexes.

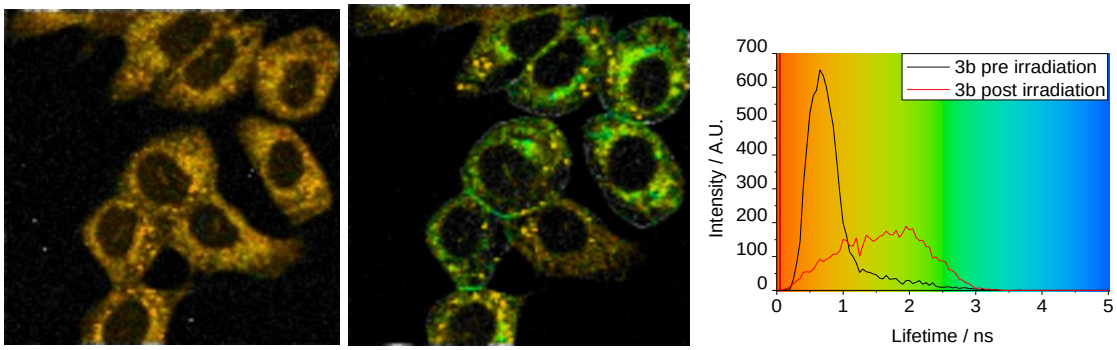

a) **b)** **c)**

Figure 4.30. 2- photon FLIM (t_m) of **3b** in MCF-7 **a)** before irradiation, **b)** after irradiation for 9 minutes at 488 nm, **c)** fluorescence lifetime distribution curve (t_m) at 910 nm before and after irradiation.

Co-localisation dyes and cells are shown and were recorded a minimum incubation of 20 minutes and a maximum of up to 3 hours. The observation of fluorescence in these images suggests that substantial amounts of these complexes remain intact inside the cell. Within the first 20 minutes there is widespread distribution of the gallium complexes within the cell cytoplasm *(Figure 4.28)*.

Co-localisation with commercially available dyes (e.g. Mitotracker Red and Green, Hoechst, Lysotracker Red and Green) were used to identify regional uptake within the cell, investigating whether the gallium complexes enter the mitochondria, lysosomes, the nucleus and lipid-rich regions of the cell, which may in turn shed light upon the nature of compound activity.

Additionally, complex **3b** displayed interesting photoinduced changes in intracellular localisation within cells and was studied in MCF-7 and PC-3 cells, showing comparable data in each cell line *(Figure 4.29 and Appendix Figure G.12)*. After irradiation with 488 nm light the green fluorescence was less evenly distributed within the cell with a more punctuated appearance. It was noticeable that the cell morphology was dramatically altered resulting in rounder and larger cells indicating occurrence of blebbing, which occurs during the process of apoptosis (programmed cell death). This

signifies that the photoactivity of the complex results in greater cytotoxicity implying a potential for photodynamic therapy using these compounds. The effect of light on the complex was further investigated in solution by NMR spectroscopy, using LEDs producing light broadly around 500 nm with the assistance of Mr Christopher Woodall.

Interestingly, after irradiation for 9 minutes a significant change in fluorescent lifetime was observed when incubating **3b** in MCF-7 cells *(Figure 4.30),* resulting in a fluorescence lifetime of 2.001 ns, 1.118 ns FWHM. It can be speculated that the metabolism of this particular cell line has caused formation of free ligand, since no change in fluorescence lifetime was observed in PC-3 under the same conditions.

4.6.1 ^{1}H NMR spectroscopy investigation

The study was carried out using a 400 MHz NMR spectroscopy and 5 mg of **3b** in 0.5 mg/mL of d_6-DMSO at room temperature. An initial control was carried out keeping the solution in the dark at room temperature for 6 hours measuring a NMR spectrum before and after the required time to investigate if the spectrum changed without irradiation. The spectra were identical, indicating that there is no significant change observable by NMR spectroscopy when the solution is stored in the dark *(Figure 4.31)*.

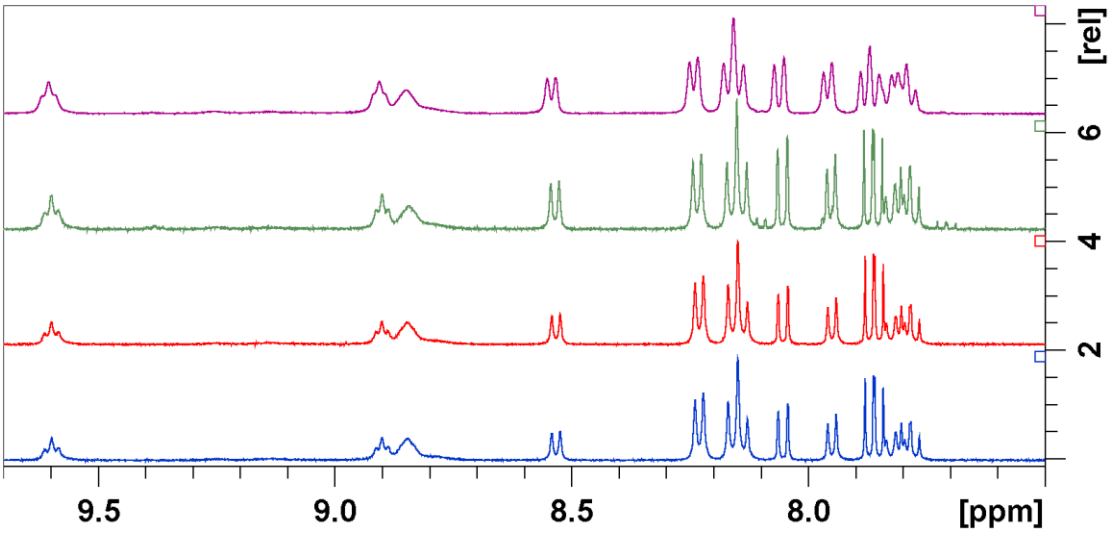

Figure 4.31. 1H NMR spectroscopy (400 MHz at 10 mg/mL in d_6-DMSO) of **3b** where blue line shows the spectrum of a freshly made solution, red is after 6 hours in solution protected from light, green is the same solution irradiated with LEDs producing light of ca. 500 nm for 14 hours and lilac/top is the same solution stored in the dark at room temperature for 10 hours.

Moreover, the solution was irradiated using LEDs that produce light broadly around 500 nm for 5 minutes. This resulted in the appearance of new resonances at 9.38 ppm, 8.10 ppm and 7.71 ppm. The solution was then irradiated a further 14 hours, a spectrum taken and subsequently protected from light followed by spectra taken after an additional 45 minutes and another 10 hours *(Table 4.6)*. The ratio of the first asymmetric N(H) proton at 9.60 ppm (which will be referred to as **'resonance 1'**) to the new resonance at 9.38 ppm (**'resonance 2'**) was measured for each of these spectra integrating between 9.662 - 9.501 ppm and 9.418 and 9.350 respectively allowing direct comparisons to be made. The ratio was also calculated for the spectrum before

irradiation to give an indication of a 'background' in which there was no visible triplet resonance, which accounted for 2.21%. It is apparent that a new species is formed upon irradiation, which is produced rapidly after just 5 minutes with **resonance 2** representing 10.6 % of a **resonance 1**. Further irradiation did not increase this ratio (with the slight decrease to 9.79 % after a further 14 hours of irradiating indicating that the new species) signifying that the species very quickly reaches its maximum proportion whilst using these LEDs.

Table 4.6. 'Resonance 2' integral percentage of 'Resonance 1' integral. 'Resonance 1' was integrated between 9.662 - 9.501 ppm and 'Resonance 2' 9.418 - 9.350 ppm.

Irradiation details of **3b** in d_6-DMSO	9.38 ppm resonance % integral of 9.60 resonance
Before irradiation	2.21
< 5 min after irradiation for 5 minutes	10.6
< 5 min after irradiation for 14 h	9.79
45 min after irradiation	9.7
10 h after irradiation	5.95

This implies that more highly powered light producing instruments, such as lasers may be able to produce a more significant fraction of this species and should be investigated using high-powered lasers. Despite the fast production of the new species, conversion back to produce the original spectrum was not as rapid since after 45 minutes in the dark the proportion was 9.7 %.

After a further 10 hours protected from light the percentage was reduced to 5.95 % indicating that the process is slowly reversible. One possibility is that the new species is the alternative symmetric isomer as discussed above for complex **3a** *(Section 4.1.1)*. This is plausible since two of the new resonances are triplets, one in the region expected for nitrogen bound protons and the other in the aromatic region. If this is correct each of the new resonances represent two protons of the alternate symmetric isomer as compared to the one proton of the asymmetric isomer and so meaning that there is ca. 5% of the isomer in solution.

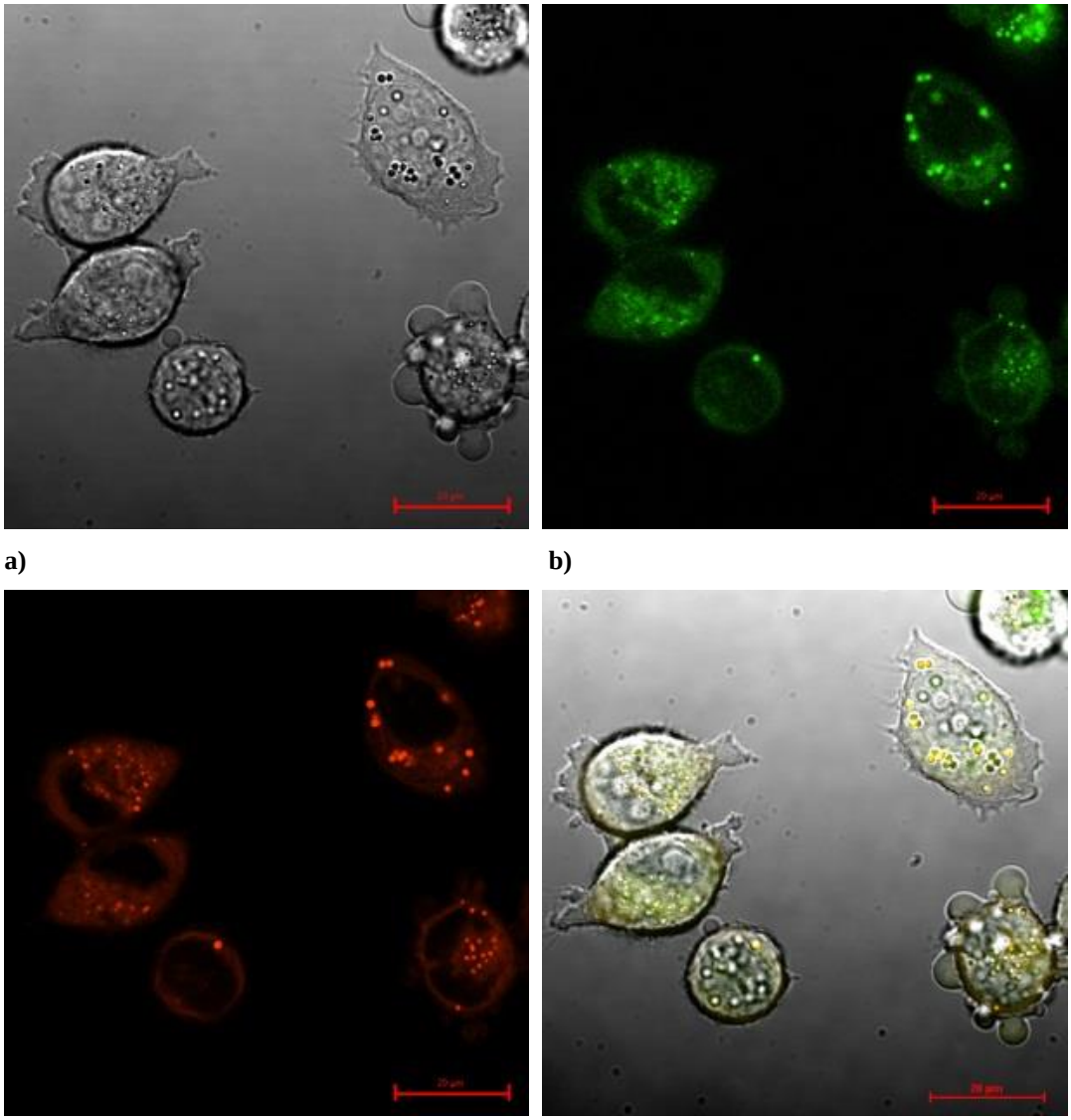

a) **b)**

c) **d)**

Figure 4.32. Complex **3b**, 50 μM, 0.5% DMSO, 20 minutes at 37°C and Nile Red in MCF-7 cells after ca. 5 minutes of irradiation: DIC image (a), micrograph of cells after excitation at 488 nm (b, compound, green channel), micrograph of cells after excitation at 543 nm (c, Nile Red, red channel). Image (d) is an overlay of (a), (b) and (c) images suggesting localisation with lipid rich regions of the cell. Scalebar: 20 μm

Currently, it can be hypothesised that high power lasers would be required to achieve the difference observed within cells. Another possibility however, is that the new species can enter different organelle(s) more rapidly than its other respective isomers, which upon entry begin to convert back to its more usual forms, which are thus effectively trapped within the cell. Likewise as the alternate symmetric isomer outside the organelle is produced it is removed from the cytoplasm, forcing the uptake of the complex to appear as a punctuated shape. To explore the nature of organelle in question

MCF-7 cells were incubated with Nile Red dye, which is a marker for lipid-rich regions of the cell, which showed very strong correlation as to that of the uptake of **3b** after irradiation (*Figure 4.32).*

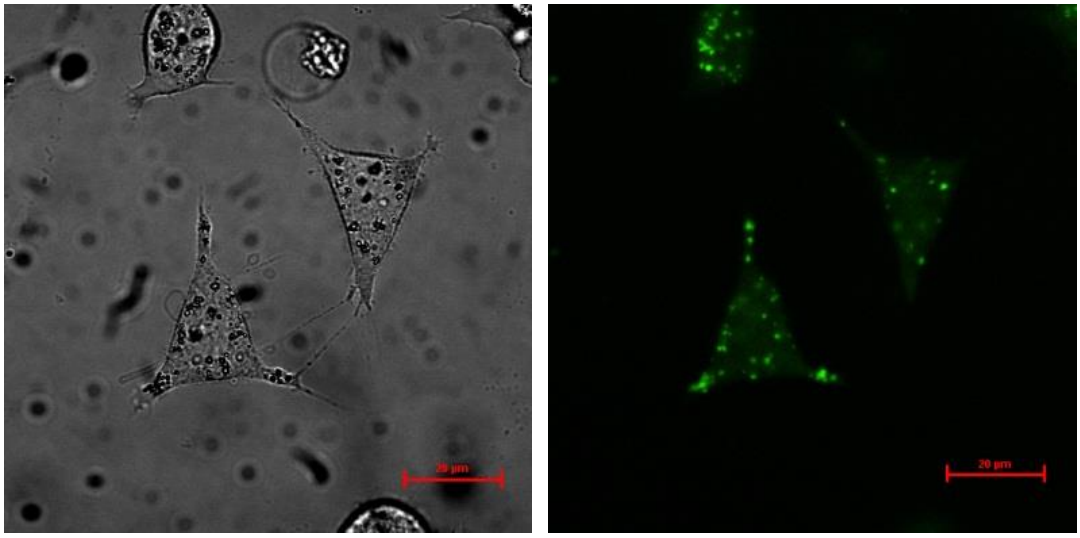

a) **b)**

Figure 4.33. Single-photon Confocal fluorescence imaging: Complex **3d**, 50 μM, 0.5% DMSO, at 37°C in HeLa cells incubated for 1 hour: (a – b) the cells were irradiated with 488 nm light for less than 5 minutes, where DIC image is represented by (a) and micrograph of cells after excitation at 488 nm by (b, compound, green channel). Scalebar: 20 μm.

Interestingly, complex **3d** when incubated for 60 minutes, punctuation was also observed during the process of finding a representative area to image, indicating that the effect is also rapid with the allyl functionality *(Figure 4.33)*. A further study was carried out incubating HeLa cells with **3d** for 3 hours at 100 μM, 1% DMSO to determine if this effect occurs without irradiation when incubation is longer and more compound is present. This effect was not observable in absence of irradiation indicating that this process does not occur with time alone. Additionally, the study was carried out at 37°C and 4°C, to investigate if the uptake occurred by passive diffusion alone, since mechanisms such as endocytosis do not occur at low temperatures *(Figure 4.34)*. **3d** entered cells both at 4 ºC and 37 ºC, implying that cell uptake occurs by passive diffusion alone in fixed cells with the nucleus stained with DAPI. Nuclear uptake was observed at 37 ºC, but not at 4 ºC, signifying that the process did not occur by passive diffusion.

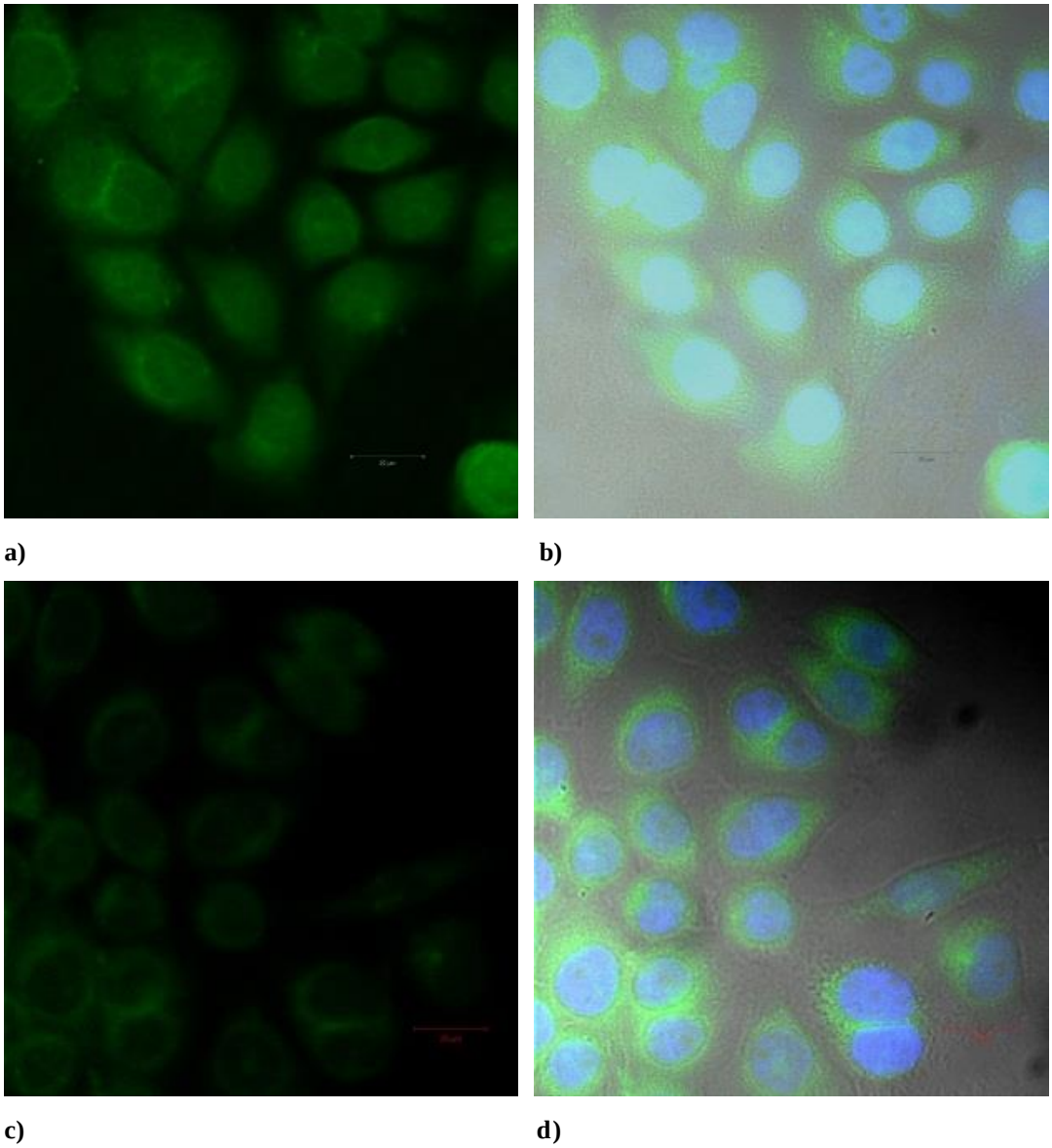

a) **b)**

c) **d)**

Figure 4.34. Single-photon confocal microscopy images of complex **3d** and DAPI in HeLa (fixed cells), incubated for 3h, 100 µM, 1% DMSO where (a) – (b) at 37 ^{o}C and (c) – (d) at 4 ^{o}C; (a) and (c) represent the micrograph with excitation at 488 nm, emission >505 nm, (b) and (f) represent an overlay of the micrograph of excitation at 405 nm, emission 420-480 nm (a) and (c) respectively and the DIC image.

The study was further carried out with **3b** with more standard incubation times of 20 minutes and 50 µM 0.5% DMSO, to determine if the same effect is observed for shorter incubations and lower concentrations, which indicated no nuclear uptake at 4ºC and very little complex within the nucleus at 37°C signifying that entry to the nucleus is only significantly achieved at longer time-points as above. Interestingly it appears that the fluorescence of **3b** was red-shifted at 4ºC as well as being taken up by HeLa cells *(Figure 4.35)*.

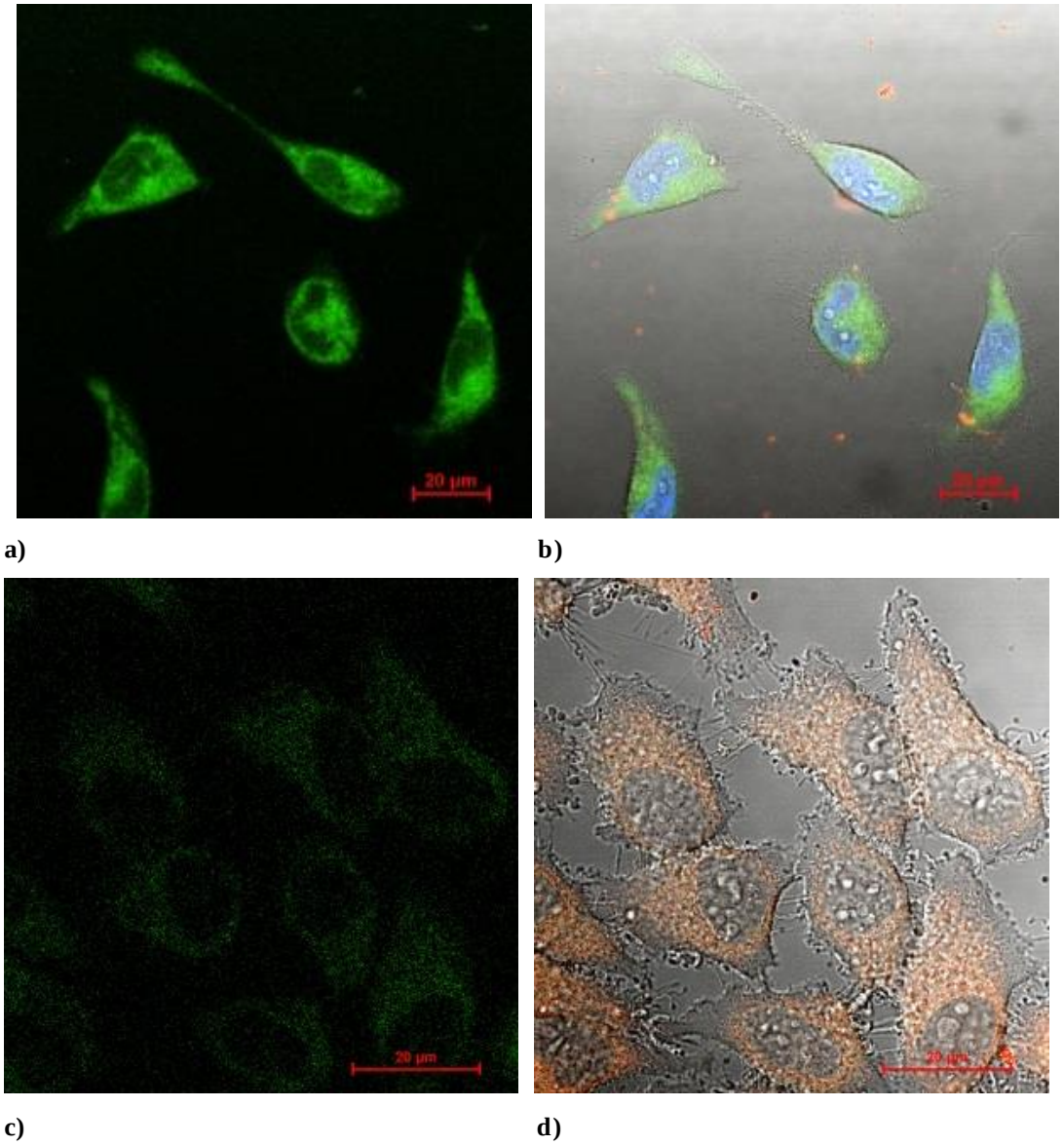

Figure 4.35. Single-photon confocal microscopy images of (a-d) Complex **3b**, 50 µM, 0.5% DMSO, 20 minutes and Hoechst (nuclear stain) in HeLa cells at 37°C: DIC image (a), micrograph of cells after excitation at 488 nm (b, compound, green channel), micrograph of cells after excitation at 543 nm (c, compound, red channel). Image (d) is an overlay of (a), (b), (c) and the micrograph from excitation at 405 nm. (e-h) **3b**, 50 µM, 0.5% DMSO, 20 minutes in HeLa cells incubated at 4 ^{o}C, (e) DIC image, (f) excitation at 488 nm, emission >505 nm, (g) after excitation at 543 nm and (h) is an overlay of (e), (f) and (g). Scalebar: 20 µm.

Complex **3d** was additionally incubated in FEK-4 cells, a non-cancer cell line, which displayed similar properties as to in the cancer cell lines tested with the majority of uptake in the cytoplasm and little in the nucleus. Likewise, longer incubation times of 3 hours and 100 µM concentrations resulted in nuclear uptake in FEK-4 cells *(Figure 4.36)*.

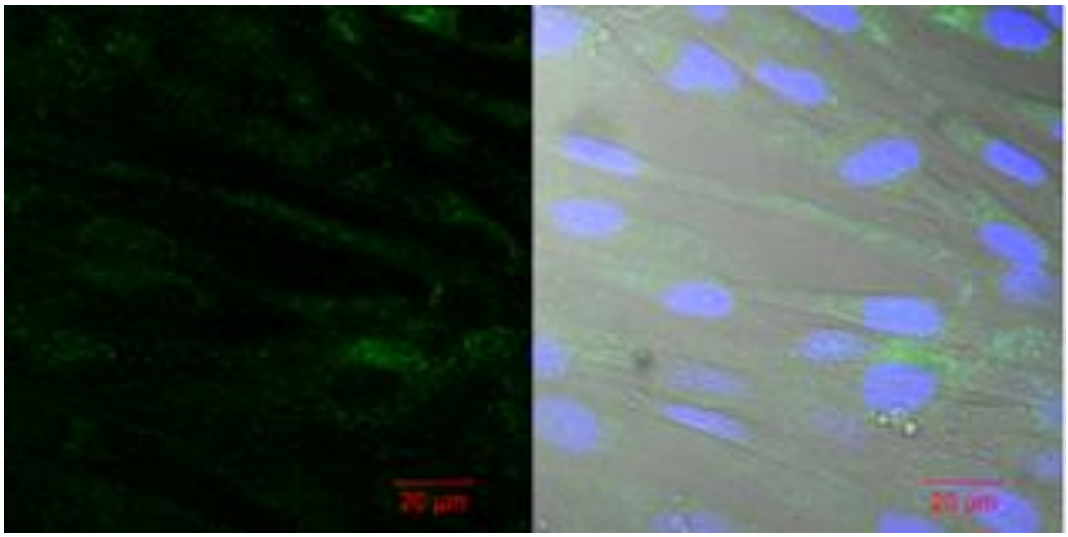

a) **b)**

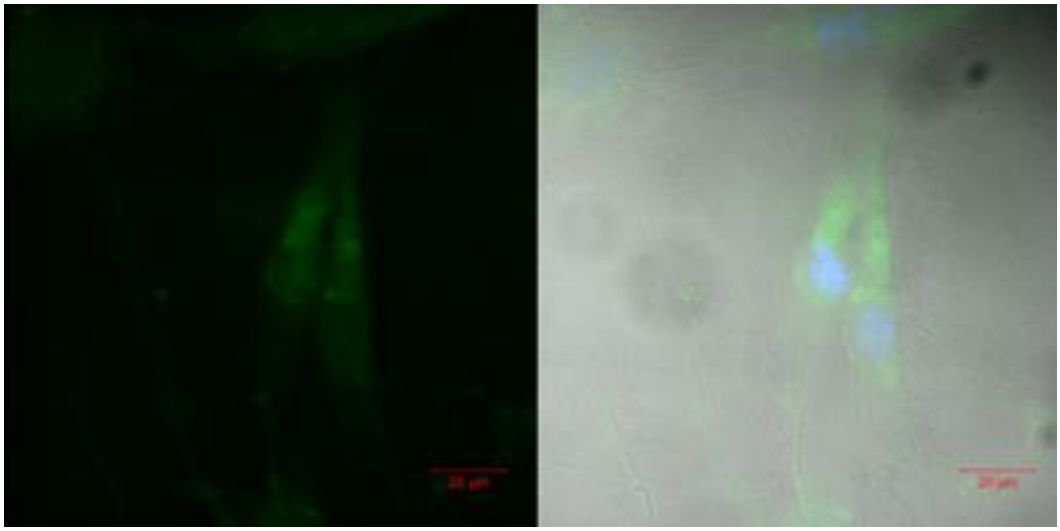

c) **d)**

Figure 4.36. (a-b) Complex **3d** in FEK-4 cells, 50 μM, 0.5% DMSO, 20 minutes: (a) is micrograph of cells after excitation at 488 nm (compound, green channel). Image (b) is an overlay of (a), the DIC image and micrograph of cells after excitation at 405 nm. Figure (c-d) Complex **3d** irradiation experiment at 488 nm in FEK-4 cells, 100 μM, 1 % DMSO, ca. 3 hours images, fixed cells stained with DAPI, scalebar: 20 μm, (c) is micrograph of cells after excitation at 488 nm, (d) is an overlay of (c), the DIC image and micrograph of cells after excitation at 405 nm.

Moreover, strong red emission with weak green emission was also observed for **3c** when incubated at 37°C. This is in agreement with the fluorescence data in solution described above. Thus, imaging is suggesting that this complex unsuitable for investigation *via* green and red colocalisation dyes, however staining with Hoechst

demonstrated that this complex does not enter the nucleus within 20 minutes at 50 µM *(Figure 4.37)*.

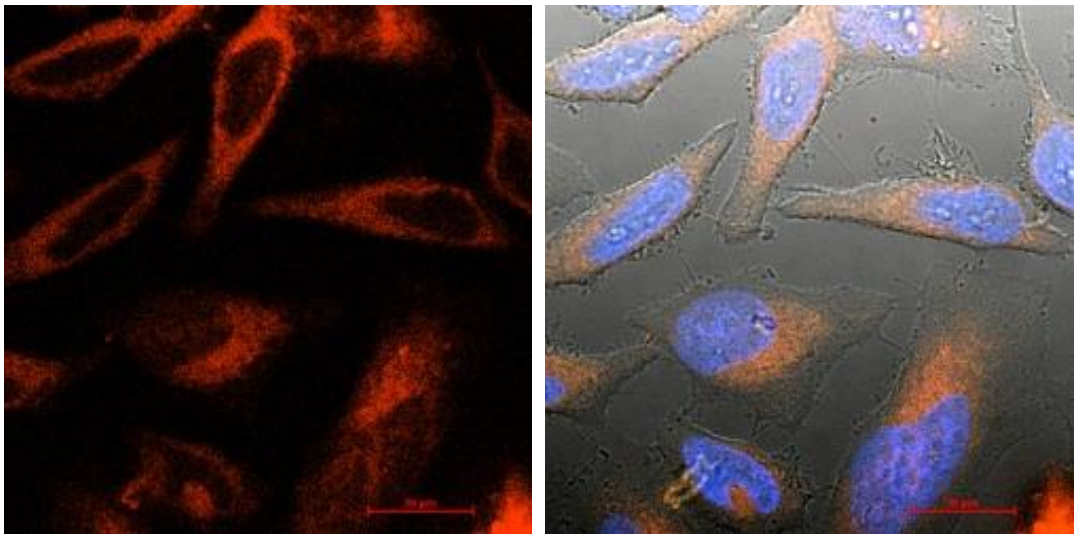

a) **b)**

Figure 4.37. Complex **3c**, 50 µM, 0.5% DMSO, 20 minutes at 37°C in HeLa cells incubated with Hoechst dye, where DIC image (a), micrograph of cells after excitation at 405 nm (b), micrograph of cells after excitation at 488 nm (c, compound, green channel), micrograph of cells after excitation at 543 nm (d, i, compound, red channel). Image (e) is an overlay of (a), (b) and (c) images. Scalebar: 20 µm.

Initial tests on the co-localisation of **3a** and **3d** with the mitochondrial stains Mitotracker Red and lysosome stain Lysotracker Red(Invitrogen) were carried out and results show mitochondrial *(Figure 4.39 and Appendix Figures G.16)* and lysosomal colocalisation in line with earlier observations for their Zn(II) precursors[127, 128] Data were highly comparable for **3a** and **3d** in both HeLa and PC-3 cells. *(Figure 4.39 and Appendix Figures G.17-18)*

In summary, this family of gallium complexes enter both cancer and non-cancer cells. Localisation appears to occur in many organelles and indicates that, if cytotoxic these compounds may have many modes of action. Long incubations saw the complex **3d** enter the nucleus indicating a possibility DNA damage during prolonged exposure, whereas rapid uptake was observable in the lysosome and the mitochondria, meaning that these complexes may possess potential to disrupt these organelles. Data suggest that the complex can enter cells by passive diffusion, yet enters the nucleus *via* other means. Moreover, the photoactivity of **3b** presents a prospect of photodynamic therapy, with

the evolution of a new species in a reversible process as well as localisation in lipid-rich regions of the cell.

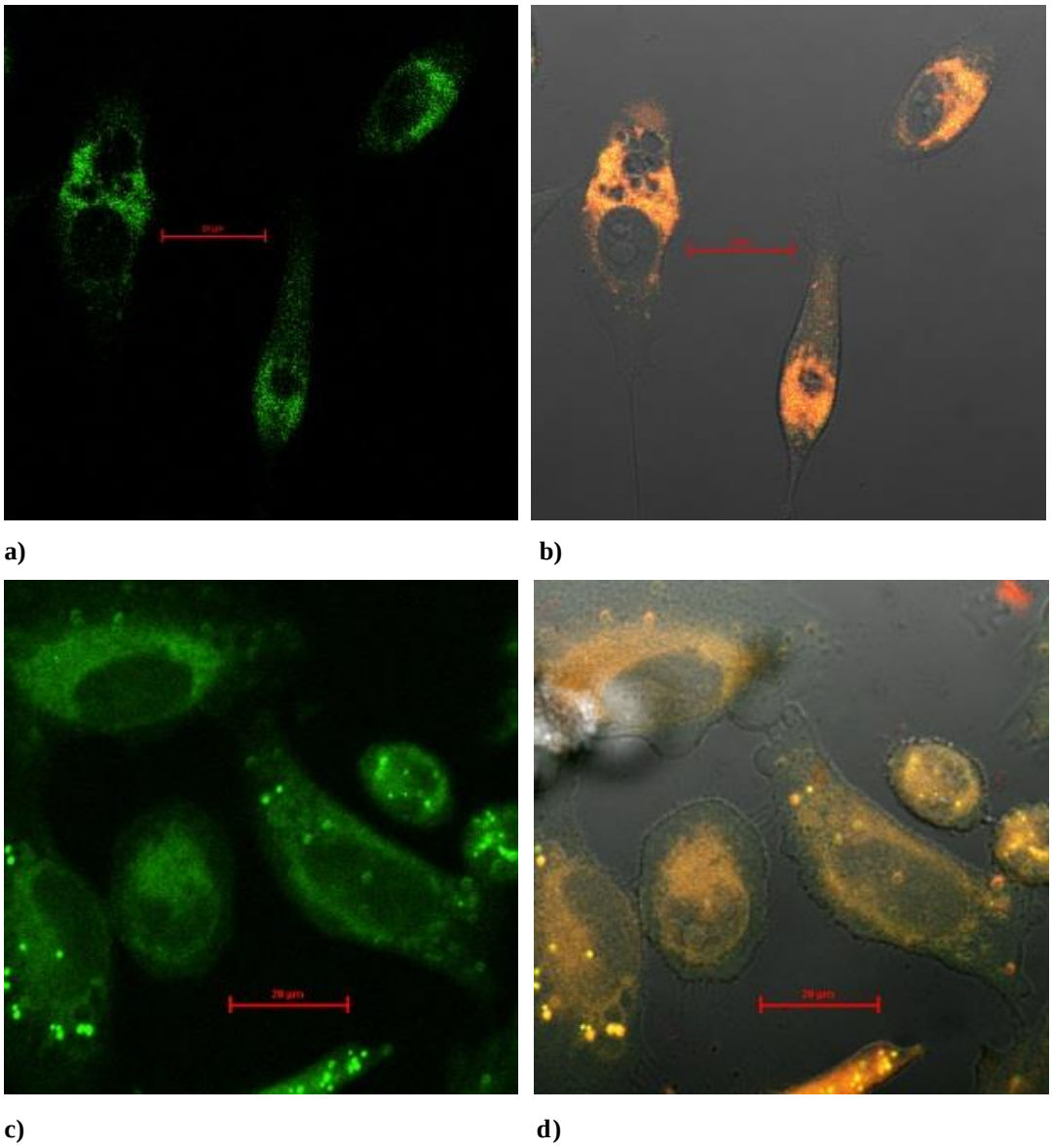

a) **b)**

c) **d)**

Figure 4.38. (a – b) Complex **3a**, 50 μM, 0.5% DMSO, 20 minutes at 37°C and Mitotracker in PC-3 cells: (a) micrograph of cells after excitation at 488 nm, (b) is an overlay of (a), DIC image and micrograph of cells after excitation at 543 nm. Images (c-d). Complex **3d**, 50 μM, 0.5% DMSO, 20 minutes at 37°C and Lysotracker in HeLa cells, (c) micrograph of cells after excitation at 488 nm, (d) is an overlay of (c), DIC image and micrograph of cells after excitation at 543 nm. Scalebar: 20 μm

4.7 Preliminary *In vivo* imaging

Normoxic PC-3 xenografts were grown on the right shoulder of nude mice in Memorial Sloan-Kettering Cancer Center, New York by Dr Sofia I. Pascu and Dr Brian Zeglis. MicroPET was carried out for ^{68}Ga complex **3b**, good renal clearance was observed, indicating suitability of these probes *(Figure 4.39)*. Furthermore, no tumour uptake under these normoxic conditions was observed for all cases, with some limited uptake in the lungs, liver and spleen and clear bladder localisation/excretion. This represents a promising result for probes designed for hypoxia selectivity, signifying that it would be beneficial for an *in vitro* hypoxia study to be carried out data processing is in process reveal the exact biodistribution.

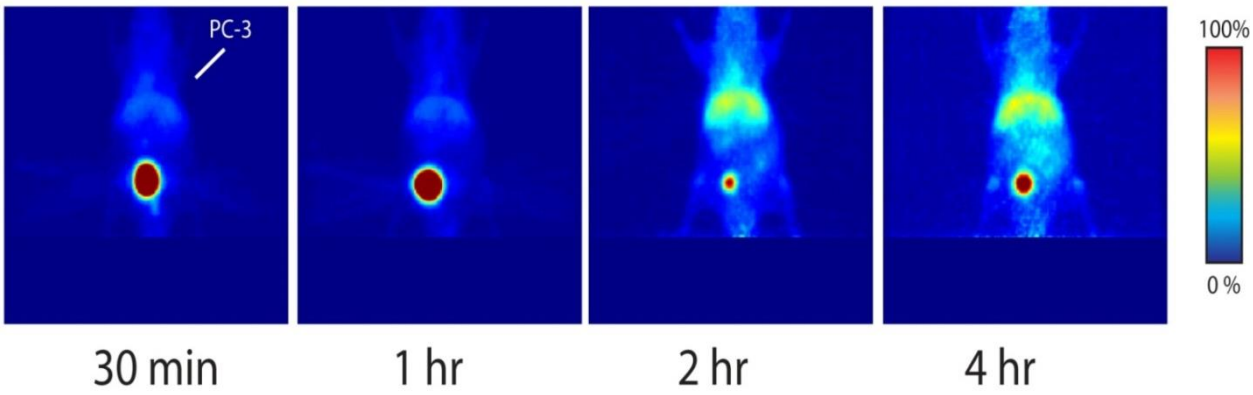

a) **b)** **c)** **d)**

Figure 4.39. MicroPET images of in nude mice, M = 68-Ga, R = Et, where a, b, c and d are at timepoints 30 mins, 1h, 2h and 4h respectively.

4.8 Hypoxia selectivity testing

An investigation to assess the hypoxia selectivity of these complexes was carried out by the collaborating group of Professor Eric Aboagye (Dr Israt S. Alam) in EMT6 (murine breast carcinoma) and PC-3 cells, grown under standard conditions described in Experimental Section.

Compound **3d** was incubated in cells at 50 µM, 4% DMSO, with normoxic conditions of 20.7% O_2 and 5% CO_2 at 37 °C, with hypoxic samples pre-incubated for 20 minutes

at 1% O_2, 5% CO_2 at 37 °C before complex addition. Following addition of the compound cells were incubated for a further 20 minutes and subsequently washed three times with PBS before being returned to serum free media and imaged immediately.

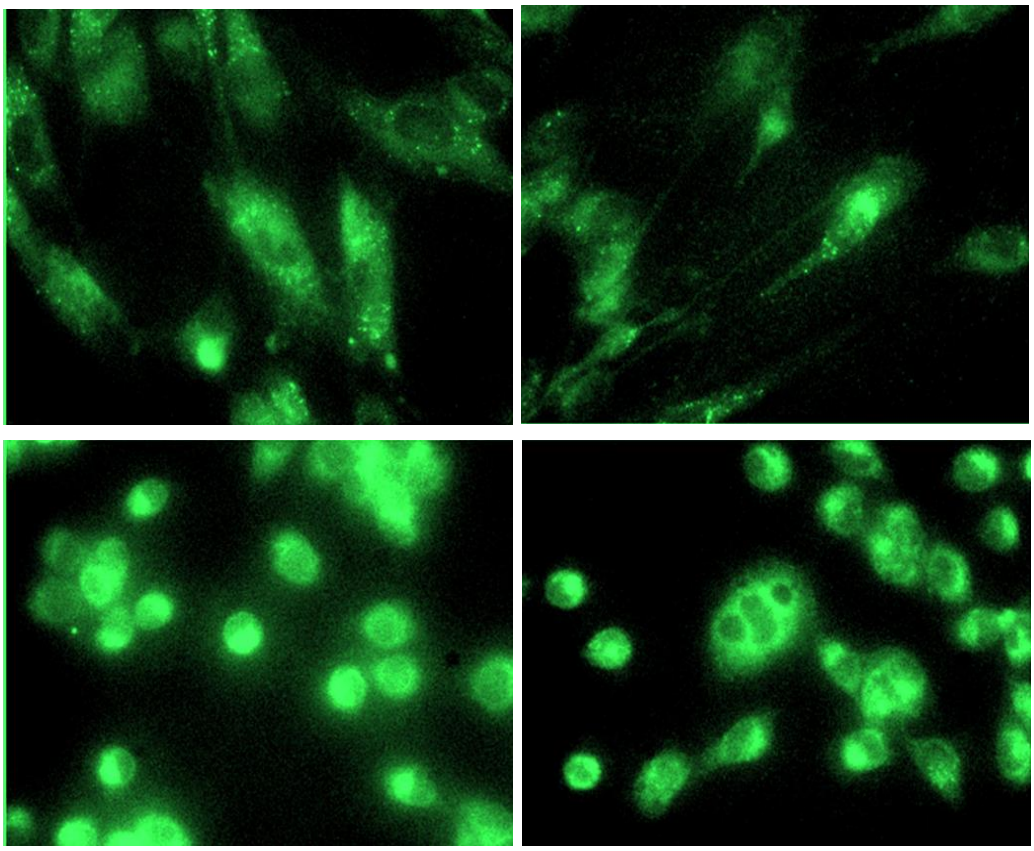

Figure 4.40. Confocal micrographs of **3d** in FEK-4 (top) and EMT6 (bottom) cells under normoxic (left) and hypoxic (right) conditions.

Using confocal imaging the compound preference for hypoxia was not easily deducible *(Figure 4.40)*, however, flow cytometry and radioactive cell uptake studies, provided quantitative means to assess the selectivity (conditions used are within the experimental section).

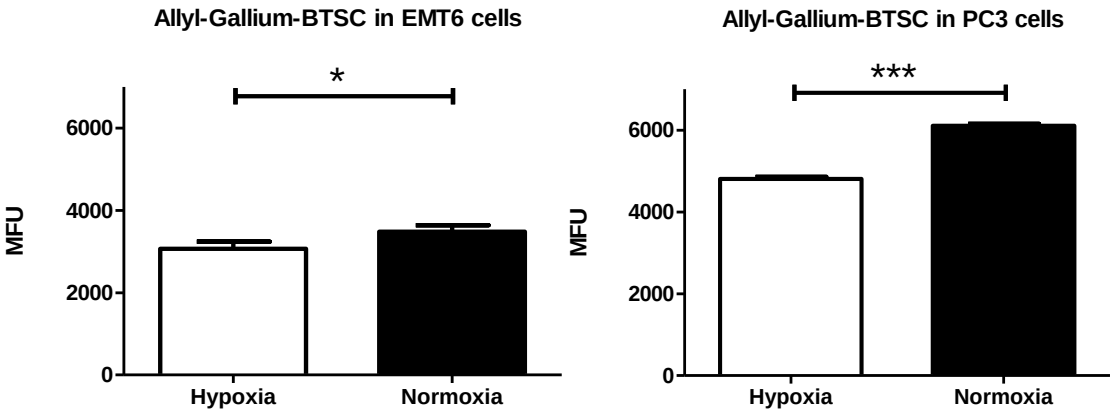

Figure 4.41. Flow cytometry studies under normoxia and hypoxia of **3d (a)** in EMT6 and **(b)** in PC-3 cells.

Median fluorescence intensities (MFU) obtained using flow cytometry under hypoxic conditions were lower than those of the normoxic cells (12% lower for EMT6 (*P<0.05) and 21 % lower in PC-3 cells (***P<0.001)) *(Figure 4.41)*. Although this decrease in fluorescence may be understood as lower uptake, it is more likely that incubation under hypoxic conditions causes reduction of the complex, which would result in demetallation and therefore loss of fluorescence. It consequently is difficult using this technique alone to determine if the lower fluorescence is due to less uptake, conversion to ligand and lower uptake or conversion to ligand and increased uptake.

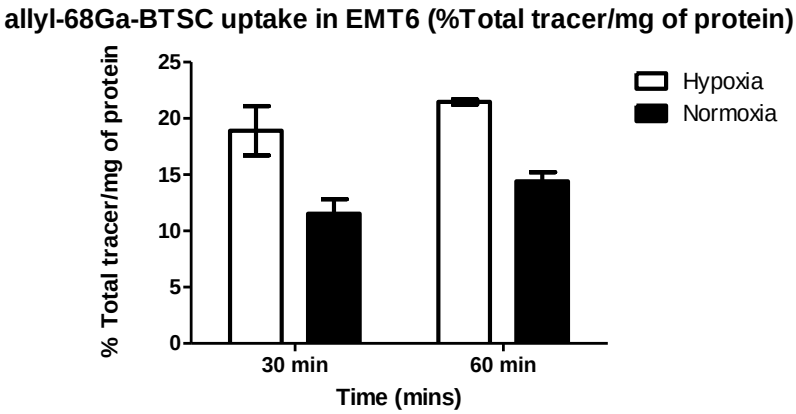

Figure 4.42. Radioactive cell uptake studies under normoxia and hypoxia of **3d** in EMT6 cells.

To investigate this issue a preliminary radioactive cell uptake experiment was carried out, showing that ^{68}Ga uptake was greater in hypoxic cells than normoxic cells (64% and 49% higher at 30 and 60 minutes respectively) *(Figure 4.42)*. This therefore indicates that the most likely cause of the reduction in fluorescence is due to the

combination of increase in uptake as well as conversion to free ligand, signifying that the gallium complexes possesses selectivity for cells under hypoxic conditions.

4.9 Summary to Chapter 4

New intrinsically fluorescent gallium complexes were synthesised and characterised using ES-MS, NMR spectroscopy and X-ray crystallography. The complexes displayed a symmetric and an asymmetric isomer in solution, which were further explored using VT-NMR spectroscopy and DFT for complexes **3a** and **3c** respectively each indicating a small preference towards formation of the symmetric isomer. Laser scanning confocal microscopy studies showed that the gallium complexes enter cancer and non-cancerous cells and rapidly localise in the lysosome and mitochondria, whilst nuclear uptake occurs more gradually. Entry to cells occurred at 4°C, indicating the process occurs by passive diffusion, however penetration into the nucleus was only achieved at 37°C meaning that that this did not occur by passive diffusion alone.

Complex **3b** demonstrated photoactivity and appears to form a new species upon irradiation with light around 500 nm, causing a change in localisation in the cell and initiation of cell death *via* apoptosis. *In vivo* experiments demonstrated suitability for **3b** in that there was good renal clearance and seldom any uptake in the tumour under normoxic conditions – an essential feature of a hypoxia imaging agent. Furthermore, an investigation to discover the hypoxia selectivity of these complexes has been carried out indicating a preference for hypoxic cells of ca. 20%. Further experiments should be carried out to ascertain if complex uptake occurs under hypoxic conditions *in vivo*, which would confirm the suitability of these complexes as hypoxia imaging agents.

Chapter 5. Synthesis, characterisation, spectroscopic, *in vitro* and *in vivo* analysis of indium(III) bis(thiosemicarbazonato) complexes

Indium complexes were designed and synthesised since they present an alternative method of reducing liver uptake of bis(thiosemicarbazonato) complexes, with the radioactive isotope In-111 an attractive agent for SPECT, by way of its gamma decay and for radiotherapeutics due to its auger electron emission. Aromatic indium bis(thiosemicarbazonato) complexes are likely to be sufficiently intrinsically fluorescent, due to metal to ligand charge transfer, to enable their progress to be monitored *in vitro* and potentially for dual-modal imaging. The main objective of this chapter was therefore to develop new indium(III) bis(thiosemicarbazonato) complexes that would be highly stable in biological media, rapidly and cleanly radiolabelled and capable of entering cancer cells.

5.1 Indium complex synthesis

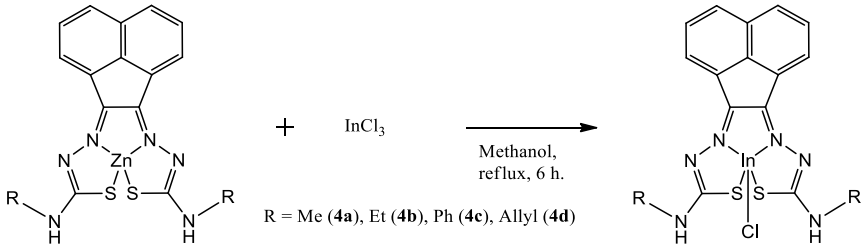

Figure 5.1. Synthesis of acenaphthenequinone indium bis(thiosemicarbazones)

As was found with the gallium complexes transmetallation provided a clean means of obtaining the indium complexes. Indium(III) compounds **4a**, **4b**, **4c** and **4d** were successfully synthesised in methanol under reflux for 6 hours, *via* the zinc precursor and vast excess of $InCl_3$ *(Figure 5.1)*.[138] Following filtration and washing with diethyl ether the product was isolated as the solid as a red coloured powder for **4a**, **4b**, and **4d,** with **4c** isolated from the filtrate, which was rotary evaporated and subsequently washed with diethyl ether. NMR spectroscopy and ES-MS were used for characterisation, with crystals suitable for X-ray crystallography obtained by liquid diffusion method in

THF:Hexane. Mass spectrometry (ESI) gave peaks for $[M-H]^-$ at m/z =502.94, 530.97, 556.98 and 626.97 **4a**, **4b**, **4c** and **4d** respectively, all values being within 0.1% error of those calculated.

Unlike the gallium complexes discussed in the previous chapter the indium complexes did not display the same kind of isomeric mixture, with only the symmetric isomer present in a significant proportion *(Figure 5.2)*.

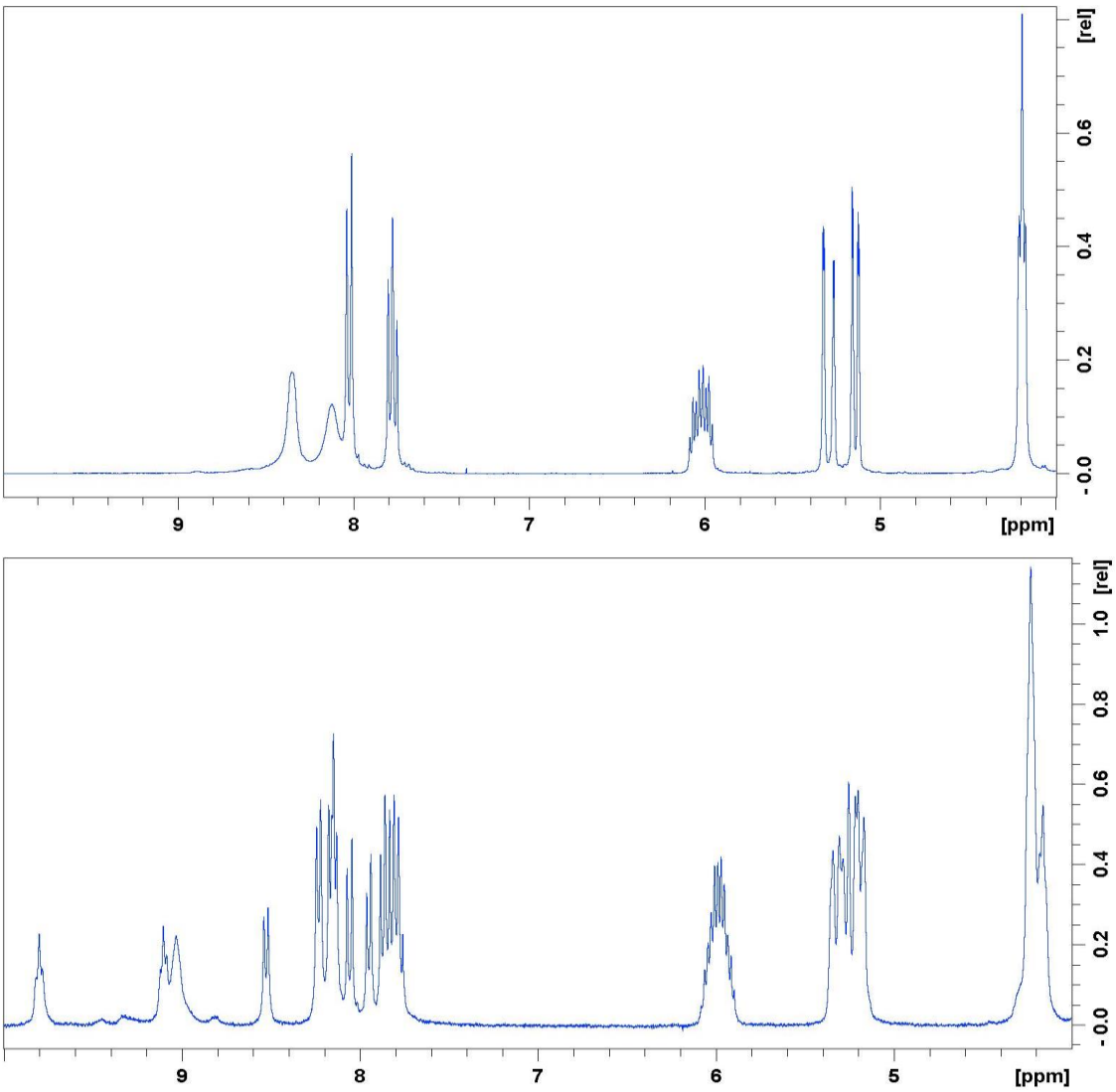

Figure 5.2. ^{1}H NMR spectra of **3d** (above) and **4d** (below) in d_6-DMSO, 4.0 ppm to 10.0 ppm.

5.2 Density functional theory calculations

The isomerism was investigated further for the indium complexes with the phenyl substituent in an analogous study to the previous chapter by Density Functional Theory, following the method used by Holland *et al.*[119]. An initial optimisation was carried out where the basis set was 6-31G(d,p) for S, Cl, C, N, H and SDD for In in the gas phase, with a final optimisation of with a basis set of B3LYP 6-31++ (d,p) IEFPCM, DMSO for S, Cl, C, N, H and SDD for In in solution *(Figure 5.3)*.

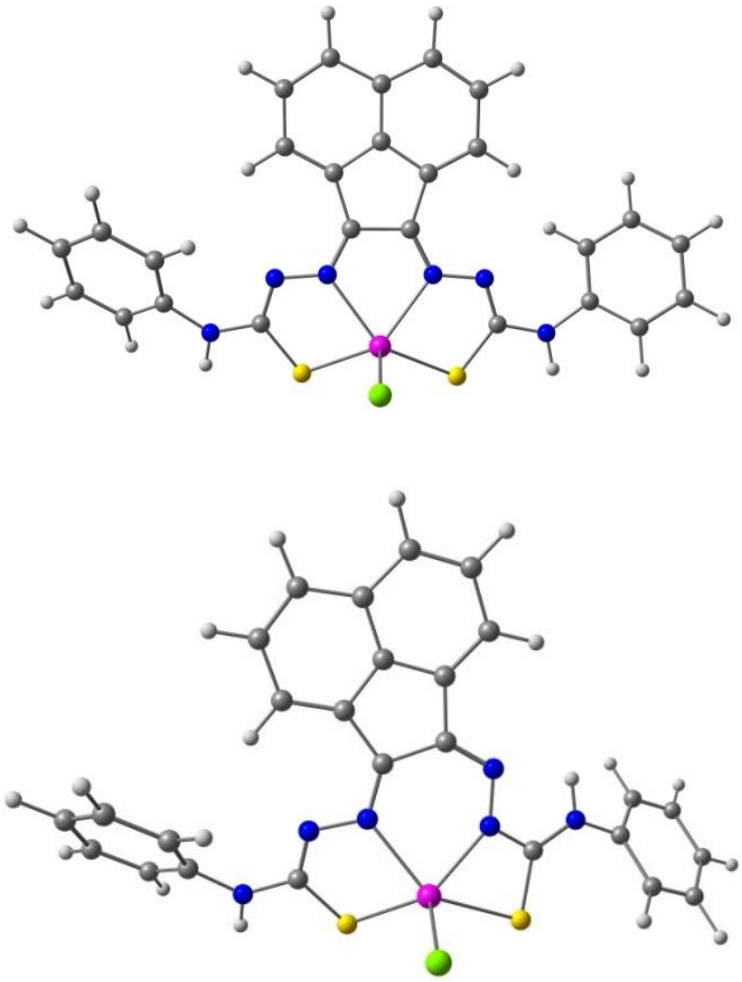

Figure 5.3. Second level optimisations where (above) is symmetric **4c** and (below) is asymmetric **4c'.** Where grey = carbon, white = hydrogen, blue = nitrogen, red = oxygen, green = chlorine, deep pink = indium.

In the gas phase the calculated energy difference is -3.53 kJ mol^{-1}, indicating that the asymmetric structure **4c** is more stable than the symmetric structure **4c'**. Likewise,

when solvent effects were considered in DMSO, the symmetric structure was more energetically favourable when compared to the asymmetric, with an energy difference of -7.69 kJ mol^{-1}. This was the largest for any of the complexes in strong agreement with NMR spectroscopy and crystallographic data, both of which show a strong preference for the symmetric isomer.

5.3 Radiochemistry experiments

A major goal of this Chapter was to establish whether the indium complexes could be readily radiolabelled, as this would render them useful as new SPECT molecular imaging probes. These experiments were carried out at the Oxford Siemens Laboratory, University of Oxford under the supervision of Dr Phillip A. Waghorn and Prof Jon Dilworth.

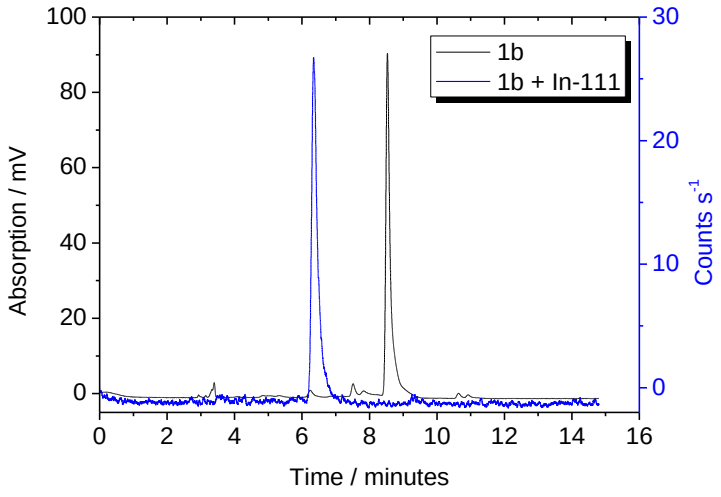

Figure 5.4. Overlay of UV-HPLC trace (black) of aromatic zinc bis(thiosemicarbazonato) precursor with the radio-HPLC trace (blue) of aromatic ^{111}InCl bis(thiosemicarbazonato) complex with compound **1b**.

In a typical experiment, a 1 mg/mL stock solution of the complex was prepared in DMSO, from which 10 µL was added to 100 µL of ethanol and was further diluted with 100 µL of water. Subsequently 10 µL of $InCl_3$ (ca. 10 MBq) was added to the solution and was heated at 60°C. After 15 minutes, an aliquot of 30 µL was removed from the solution and analysed using HPLC with a C18 column and a mobile phase of 0.1 % (*v/v*) TFA in acetonitrile/water. Figure 5.4 shows an overlay of the UV-HPLC trace of the zinc

precursor and the indium-111 complex for **1b**. Data show that could be made rapidly and cleanly for these complexes by transmetallation despite the UV traces indicating that **1c** contained a mixture of symmetric and asymmetric isomers as shown by the two slightly differing retention times *(Figure 5.5)*.

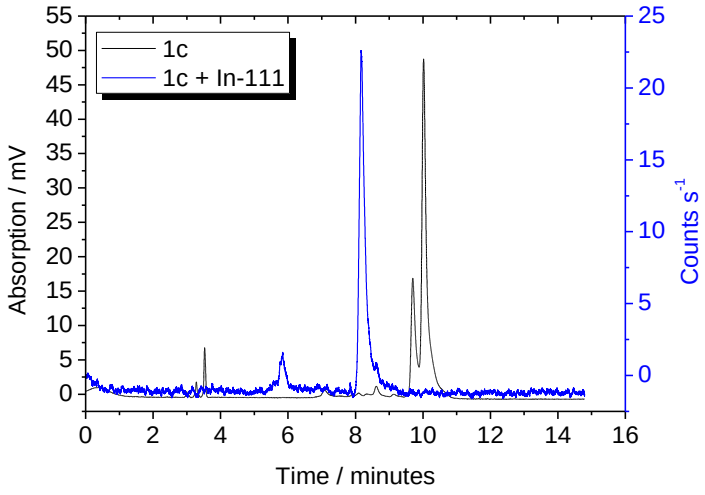

Figure 5.5. Overlay of UV-HPLC trace (black) of aromatic zinc bis(thiosemicarbazonato) precursor with the radio-HPLC trace (blue) of aromatic ^{111}InCl bis(thiosemicarbazonato) complex with compound **1c**.

Due to the importance of lipophillicity and liver uptake the partition coefficient (log *P*) was calculated for these complexes with values of 1.19 ± 0.09, 1.07 ± 0.03, 0.94 ± 0.13 and 1.20 ± 0.11 for compounds **4a**, **4b**, **4c** and **4d** respectively. The log *P* values were comparable to yet slightly lower than their analogous copper complexes, importantly they are significantly less lipophilic than Cu[ATSM], with a log *P* of ca. 1.48, indicating a likely reduction of accumulation in the liver with respect to this well-known copper analogue.[149]

5.2 Single crystal X-ray crystallography

Crystals were grown in THF:Hexane by a standard liquid or gas phase diffusion method for complexes **4a**, **4b**, **4c** and **4d**. X-ray structure determinations showed that, in agreement with NMR spectroscopy and DFT calculations, there is a strong preference for the symmetric isomer formation, and this was observed in the crystal structures of

all compounds studied here. As was observed with symmetric gallium compounds, each indium complex possessed a plane of symmetry across the backbone and symmetric binding to the metal, yet the terminal functionalities (Et, Ph and Allyl) are asymmetric *(Figures 5.6 and 5.7).*

Table 5.1: Selected bond lengths (Å) and bond angles (°) for compounds **4a-d,** determined by X-ray diffraction

Compound/ Molecular Parameters	**4a** (*E*,*E*) isomer	**4b** (*E*,*E*) Isomer	**4c** (*E*,*E*) isomer	**4d** (*E*,*E*) isomer
M-Cl	2.434(4)	2.4180(16)	2.3960(15)	2.4157(8)
M-N	2.260(13)	2.244(4)	2.281(4)	2.257(2)
	2.305(14)	2.250(4)	2.278(4)	2.270(2)
M-S	2.474(5)	2.4602(14)	2.4638(14)	2.4784(7)
	2.472(5)	2.4658(14)	2.4998(14)	2.4693(8)
C-C	1.492(2)	1.487(7)	1.478(7)	1.492(4)
N-N	1.349(18)	1.360(6)	1.349(6)	1.364(3)
	1.381(19)	1.343(6)	1.359(6)	1.354(3)
C=N	1.320(19)	1.294(6)	1.297(7)	1.292(4)
	1.306(19)	1.299(6)	1.292(7)	1.299(4)
S-M-S	123.19(15)	117.93(5)	120.54(5)	120.15(3)
S-M-N	76.8(4)	77.39(11)	75.46(11)	76.72(6)
	74.2(4)	77.47(11)	76.44(11)	77.03(6)
N-M-N	72.2(4)	73.17(15)	71.55(15)	72.56(8)
S-M-Cl	109.5(2)	106.42(5)	106.72(5)	105.63(3)
	108.2(2)	107.14(5)	106.41(5)	104.52(3)
N-M-Cl	91.0(4)	98.8(1)	102.2(1)	102.16(7)
	94.1(1)	98.7(1)	100.1(1)	99.26(7)

A distorted square pyramidal around the metal centre was also notable and was likewise comparable to the gallium complexes with the Cl in the axial position with the base formed by the two nitrogens and two sulphurs. The bond distance of M-Cl is similar for **4a** and **4b** (2.434(4) Å and 2.4180(16) Å correspondingly) and **4b** and **4d** (2.4180(16) Å and 2.4157(8) Å respectively) *(Table 5.1)*, but is smaller for **4c** (2.3960(15) Å). Likewise the N-M-N angle was shorter for **4c** (71.55(15)°) than for **4b**

(73.17(15)°) and **4d** (72.56(8)°) (whereby the N-M-N of **4a** (72.2(4)°) was similar to each of the respective indium complexes.) Moreover, the S-M-S angle of **4b** (117.93(5)°) was shorter than those of **4c** (120.54(5)°) and **4d** (120.15(3)°), which were similar, whilst **4a** (123.19(15)°) was notably larger than those of the other indium complexes of this family. Notably, the N-M-Cl angle appeared to increase the larger the functionality (91.0(4)° for methyl-substituted indium complex **4a** and 102.2(1)° for phenyl-functionalised indium complex **4c**) with the opposite observed for the S-M-Cl angle (e.g. 109.5(2)° in **4a** and 106.72(5)° in **4c**). The other bond lengths and angles of these indium compounds were comparable indicating that despite the functionality at the exocyclic nitrogen atoms having some effect on the rest of the structure, this effect is limited.

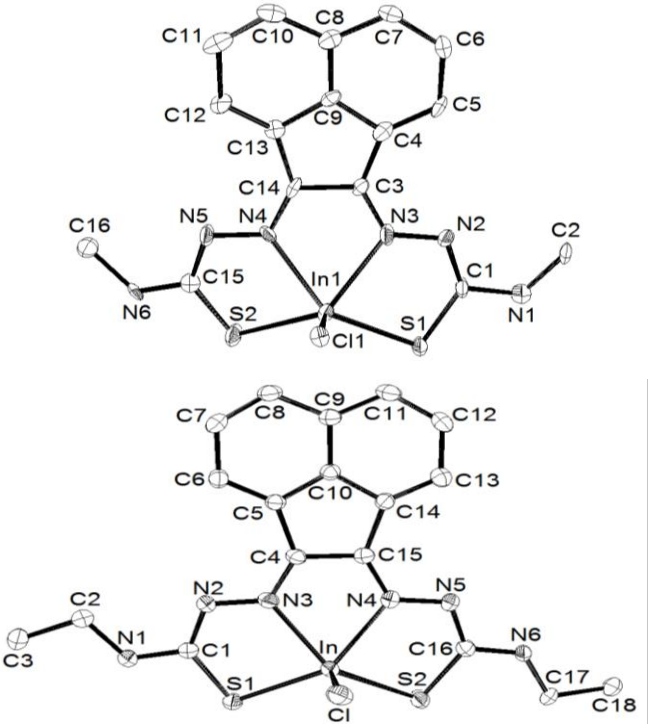

Figure 5.6. Molecular structures of compounds **4a** (above) and **4b** (below), ellipsoids drawn at 30% probability, hydrogens omitted for clarity.

Since the phenyl-substituted complex crystal structures were acquired during this study, each possessing the symmetric conformation their comparison can shed light upon the effect of the metal centre on the structure and will be considered below *(Table 5.2)*. For all metal bonds, M-X (where X is Cl or DMSO), M-N, M-S, the bond lengths

were longest for the indium complex, followed by the zinc and the gallium, with the copper complex possessing the shortest metal bonds. Interstingly, the C-C bond is similar for each metal complex, therefore it can be speculated that the difference in this bond length reported previously in the group between (*E*,*Z*) isomer of the zinc complex **1d** and the (*E*,*E*) isomer of the copper complex may be due to crystal packing forces rather than an isomeric or metal-dependant effect.[127]

Table 5.2. Selected bond lengths (Å) and bond angles (°) for compounds **1c-4c,** determined by X-ray diffraction, where A is adduct atom.

Compound/ Molecular Parameters	**1c** (*E*,*E*) isomer	**2c** (*E*,*E*) Isomer	**3c** (*E*,*E*) isomer	**4c** (*E*,*E*) isomer
M-Cl/M-O	*2.0642(12)		2.2096(14)	2.3960(15)
M-N	2.1092(14)	1.967(5)	2.069(4)	2.281(4)
	2.1603(14)	1.976(5)	2.075(4)	2.278(4)
M-S	2.3330(5)	2.2508(17)	2.3130(16)	2.4638(14)
	2.3691(5)	2.2598(18)	2.3171(15)	2.4998(14)
C-C	1.499(3)	1.481(8)	1.488(6)	1.478(7)
N-N	1.364(2)	1.382(6)	1.372(5)	1.349(6)
	1.364(2)	1.384(6)	1.371(5)	1.359(6)
C=N	1.294(2)	1.286(7)	1.383(7)	1.297(7)
	1.292(2)	1.293(7)	1.369(7)	1.292(7)
S-M-S	115.636(19)	110.99(7)	105.11(5)	120.54(5)
S-M-N	80.27(4)	83.64(16)	81.42(12)	75.46(11)
	78.96(4)	83.72(15)	81.43(11)	76.44(11)
N-M-N	76.65(5)	81.6(2)	77.33(15)	71.55(15)
S-M-A	104.31(4)	n/a	108.56(6)	106.72(5)
	102.01(4)	n/a	108.38(6)	106.41(5)
N-M-A	101.11(5)	n/a	99.7(1)	102.2(1)
	93.77(5)	n/a	98.4(1)	100.1(1)

For **1c this is representative of a DMSO adduct*

Interestingly, the C=N of the gallium complex is significantly longer than that of the other molecules, for which this bond is similar in length. Moreover, the S-M-A angle

was largest for gallium compound **3c** (108.56(6))° and smallest for zinc complex **1c** (104.31(4)°), with the N-M-A largest for indium complex **4c** (102.2(1)°). The angles S-M-N and N-M-N are largest with the copper metal centre (83.64(16)° and 81.6(2)° respectively), followed by with a gallium atom (81.42(12)° and 77.33(15)° correspondingly), whereby for the indium complex these angles are the smallest (75.46(11)° and 71.55(15)° respectively). The opposite trend is true (with the gallium the smallest angle rather than the copper) for S-M-S angle indicating that whilst the sulphur atoms are closer in comparison to each other, the nitrogen atoms are further away from each other around the metal centre for the indium complexes, when compared to the copper and gallium complexes.

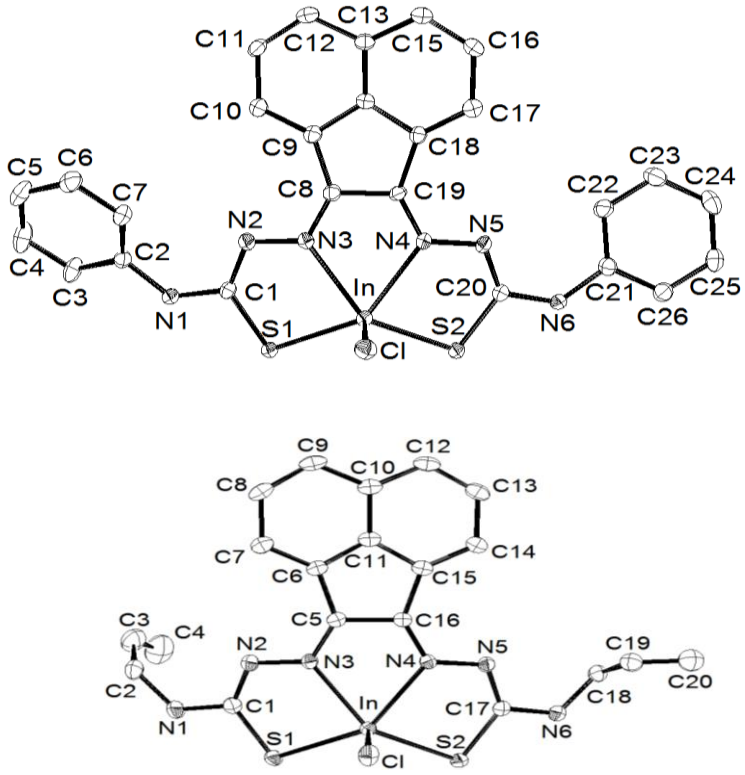

Figure 5.7. Crystal structures of **4c** (above) and **4d** (below), ellipsoids drawn at 30% probability, hydrogens omitted for clarity.

5.4 Spectroscopy

Fluorescence spectra were obtained in DMSO for initial scans between 200-800 nm, in order to obtain information about intrinsic fluorescence and $\lambda_{em\text{-}max}$ using solutions of

100 μM. Ranges of absorption and emission, which are important with regards to cytotoxicity assays and fluorescence imaging, were also assessed using the 2D contours as a guideline *(Figure 5.8)*. Relevant cytotoxicity assays use absorbance readings at 570 nm, therefore there should be minimal or no excitation at this wavelength, which was true for all of the indium complexes, with very low absorbance for each.

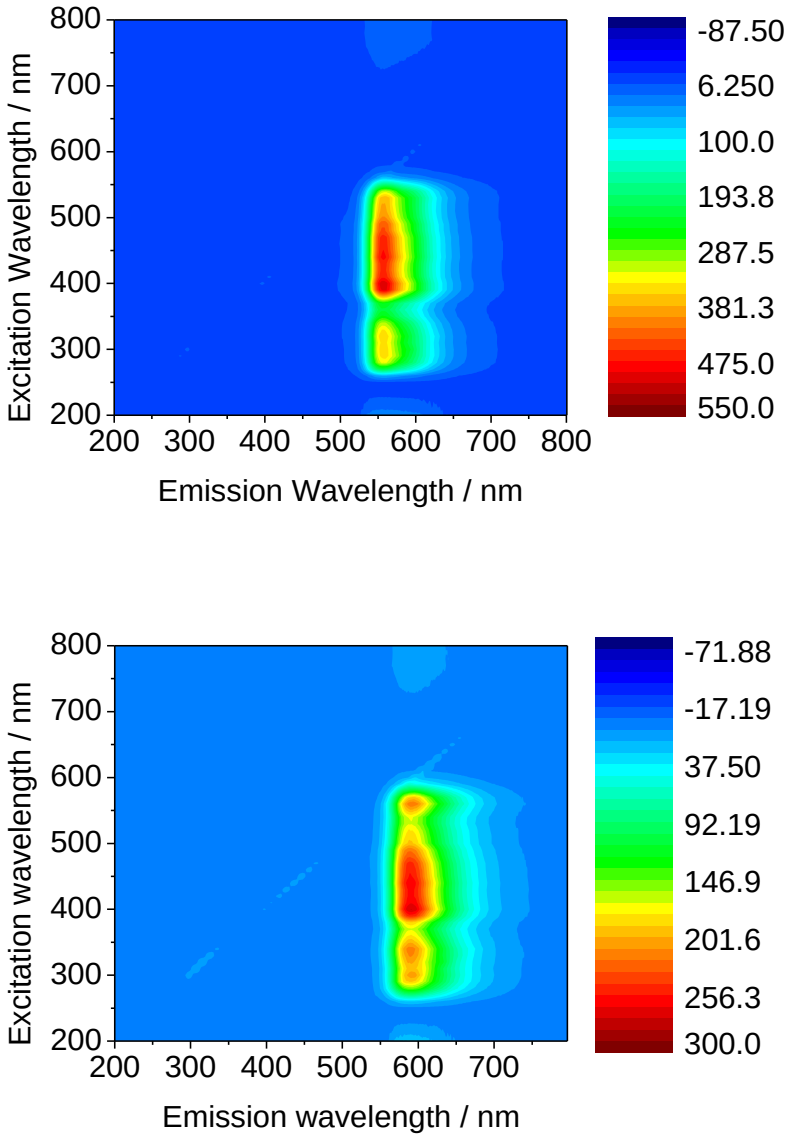

Figure 5.8. Excitation/emission map at 100 μM in DMSO of compound **4b** (above) and **4c** (below)

Complexes **4a**, **4b** and **4d** displayed very similar absorption (ca. 250 – 570 nm) and emissions (ca. 515 – 685 nm), each with λ_{max} of emission ca. 560 nm *(Table 5.3)*. Each compound had a λ_{max} of 400 nm, with **4c** possessing a much broader range of excitation

and emission than the other functionalities, as well as a higher λ_{max} of emission of 590 nm.

Table 5.3. Fluorescence quantum yield measurements of complexes **4a**-**4d**,

Compound	$\lambda_{ex\text{-}max}$ / nm	Excitation range / nm	$\lambda_{em\text{-}max}$ / nm	Emission range / nm	Quantum Yield
4a	400	250-570	556	520-680	0.31
4b	400	250-570	556	515-685	0.19
4c	400	250-610	590	540-740	0.15
4d	400	250-580	559	515-685	0.13

$$\Phi_S = \Phi_R \cdot \left(\frac{D_S}{D_R}\right) \cdot \left(\frac{A_R}{A_S}\right) \cdot \left(\frac{I_R}{I_S}\right) \cdot \left(\frac{\eta_S}{\eta_R}\right)^2$$

Quantum yields were calculated using the standard solution of $[Ru(bipy)_3](PF_6)$ in water as a reference and utilising the equation above. Where Φ = quantum yield, D = integrated area under emission band, S = sample, A = absorbance of solution at excitation wavelength, R = reference, η = refractive index of solvent, I = maximum intensity of excitation band $[Ru(bipy)_3][PF_6]_2$ in water was used as a reference, with a quantum yield of 0.042. The quantum yields of the indium compounds higher than their respective gallium complexes and were sufficient to proceed to fluorescence imaging in biological cells.

5.5 Kinetic stability tests

In vitro assays were carried out to determine the stability of complexes for use as medical imaging probes. Demetallation could result in non-target tissue uptake and poor image contrast *in vivo*. Stability is therefore essential for the intended function of these complexes and a series of assays with excess of a numerous biologically relevant chemicals have been carried out up to 24 hours. These include Glutathione (GSH), L-cysteine, L-histidine, L-methionine, citric acid, ethylenediaminetetraacetic acid (EDTA), biomimetic eagle's modified essential media (EMEM) (both with and without foetal calf serum) and biologically relevant pH buffers. Indeed, stability of these complexes in a range of pHs is significant due to the tendency of cancer cells to be slightly more acidic than non-cancerous cells.

UV-visible spectroscopy was utilised therefore to assess the kinetic stability of complexes and fluorescence to provide further insight whilst in the presence of biological media. Tests were carried out at room temperature at 100 μM in a 1:1 DMSO: assay agent solution to ensure sufficient solubility and at a concentration providing detectable fluorescence, with the assistance of Johan Stojanoviç, technician student from ESCOM, France.

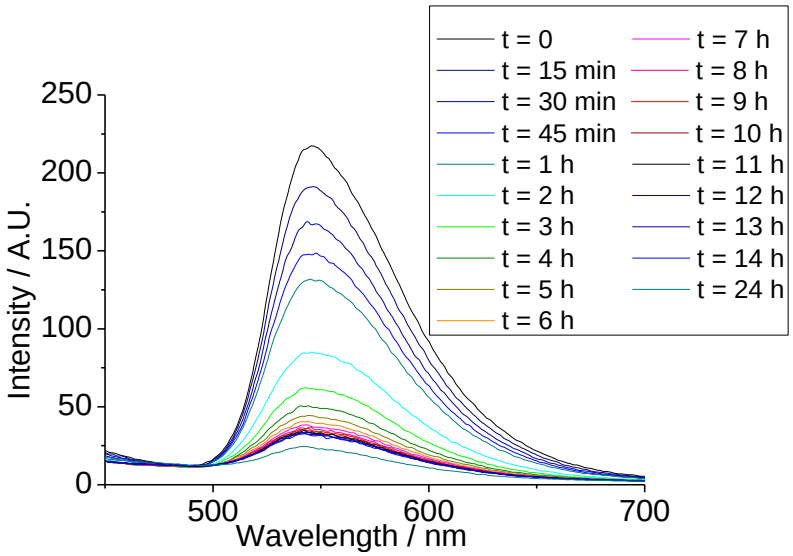

Figure 5.9. Fluorescence spectroscopy of compound **4a**: FCS stability assay (100 μM FCS: DMSO, 1: 1).

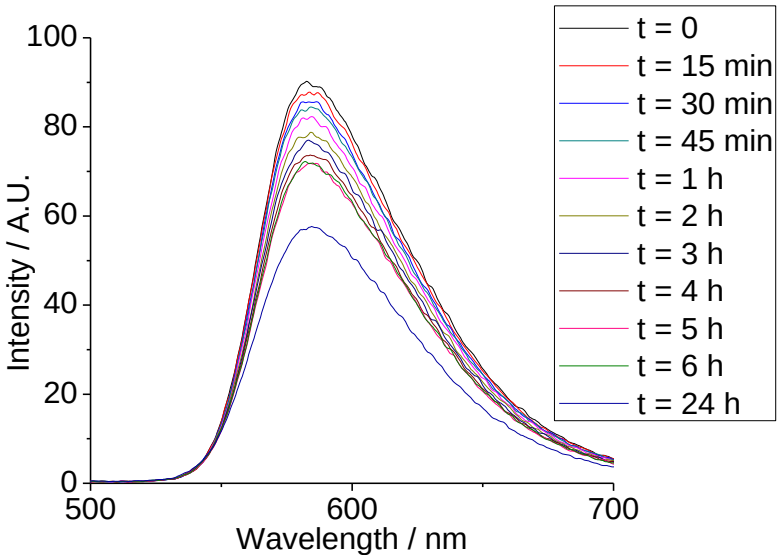

Figure 5.10. Fluorescence spectroscopy of compound **4c:** FCS stability assay (100 µM FCS: DMSO, 1: 1).

Preliminary fluorescence studies focussing on EMEM containing 10% Foetal Calf Serum (FCS) demonstrated a general decreased intensity with time for all indium compounds, with the most significant reduction within the first hour, followed by equilibration after ca. 6h *(Figures 5.9-5.10, Appendix Figures D.31-34, D.46).* There was only a very limited a shift in the fluorescence maxima implying that no new species evolved. Spectra are almost identical for **4a**, **4b** and **4d**, whereas **4c** had a much lower initial fluorescence, but also a much lower rate of decline, indeed **4c** displayed notable fluorescence even after 24 h. Due to the significantly greater fluorescence of the indium complexes in comparison with the free ligand, fluorescence intensity observed is indicative of complex stability (as was also observed with the gallium complexes). However, since the free ligand does possess some fluorescence, it is important to consider the UV-Visible spectra of complexes to confirm stability under these conditions.

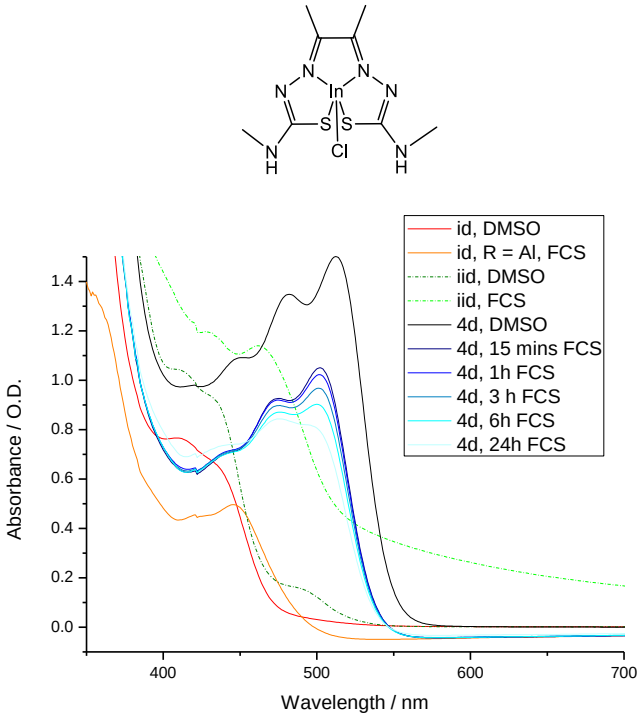

Figure 5.11. Serum assays (99% FCS, 1% DMSO) by UV/Vis (below) for compound **4d**, at 100 µM, monitored at time intervals up to 24h at room temperature and filtered using a 0.45 µm PTFE microfilter. (above) The structure of [GaCl(ATSM)] is also shown. This compound which was found not to be stable under comparable conditions.

In conjunction with a study comparing [In-Cl(ATSM)], which was found to form the corresponding to free ligand within 5 minutes in 99% FCS, 1% DMSO, with indium complex **4d** tested under analogous conditions *(Figure 5.11)*. Whilst changes in the UV/Vis spectra for the indium complex **4d** were observed over an incubation of 24 h in serum, it is apparent that the product of the challenge has not completely converted to free ligand **iid**.

Table 5.4. Summary of estimated complex remaining from UV-visible data at 1:1 DMSO:biologically relevant agent at 15 minutes and 24 h where Citric Acid, EDTA, L-Cys, L-His, L-Met and GSH were in MilliQ water.

Assay	**4d**, 100 μM	
	15 min[a]	24 h[a]
DMSO	86.6	86.6
H_2O	94.8	94.4
PBS	66.8	61.5
5% FCS, MEM	77.9	69.4
SFM, MEM	81.4	76.9
Citric Acid	85.2	87.8
EDTA	94.2	90.4
L-Cys	94.3	94.0
L-His	80.8	79.6
L-Met	77.6	77.5
GSH	62.1	50.5

Following initial stability tests in pH buffers, in EMEM and in FCS a more in-depth study focussing on the indium allyl derivative as a representative example of this class of compounds. Indium complex **4d**, however exhibited good stability in each media with no significant change in absorbance between 15 minutes and 24 hours room temperature incubation in DMSO and high percentage remaining complex after 24 h incubation in each of the above solvents (94.4 %, 61.5 %, 69.4 %, 76.9 % respectively).

This investigation utilised both UV-visible absorption (at 10 μM and at 100 μM) and fluorescence emission at 100 μM, with 1:1 DMSO:challanger to limit precipitation. This allowed a % stability to be estimated *via* UV-Visible spectroscopy at 15 minutes and 24 hours as calculated by (100 % - percentage converted to free ligand) *(Table 5.4).* The first assays carried out in DMSO, water, PBS, 5% FCS EMEM and SFM EMEM enabled complex stability to be understood in media likely to be encountered in a cell biology experiment.

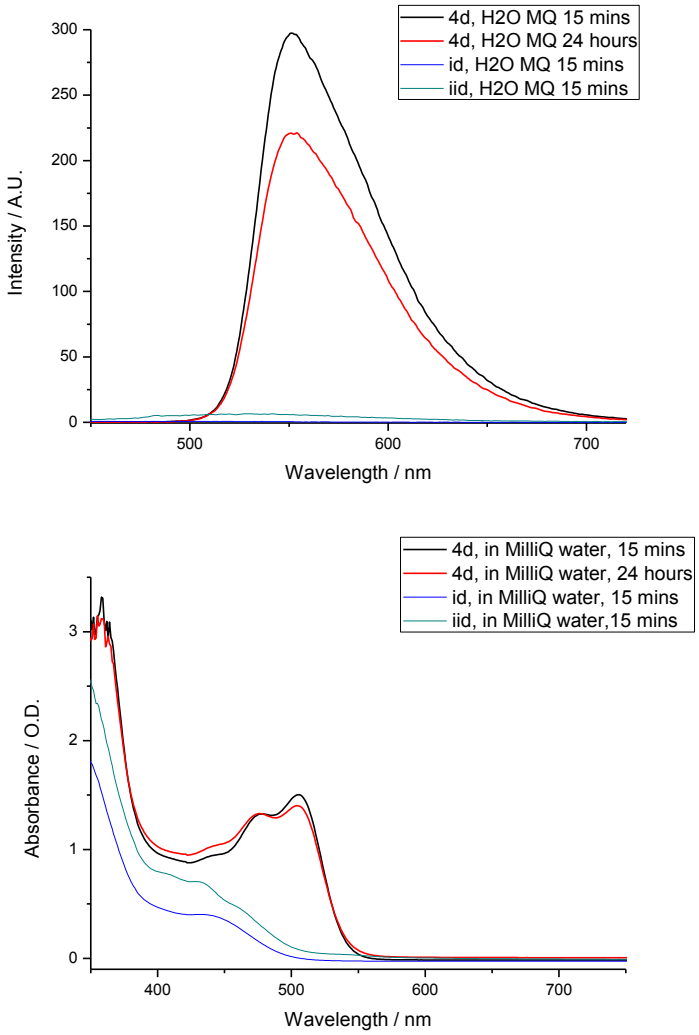

Figure 5.12. Fluorescence (above) and UV/Vis (below) spectroscopy in aqueous media monitored at time intervals up to 24h at room temperature, (50% DMSO, 50% water, for compound **4d** at 100 μM)

Indium complex **4d**, contrary to the gallium complex **3d** exhibited good stability in each media with no significant change in absorbance between 15 minutes and 24 hours in DMSO and high percentage remaining complex after 24 h incubation in each of the aforementioned solvents (86.6, 94.4 %, 61.5 %, 69.4 %, 76.9 % respectivly) *(Figures 5.12-15, Appendix Figures D.31, D.46)*. The fluorescence study was carried out in parallel largely confirming the UV-visible spectroscopy data. There was no significant change in fluorescence intensity of the indium complex in DMSO over a period of 24 h.

As was observed for the gallium complex, the fluorescence intensity for the indium complex in PBS were significantly lower than in water, combined with a shift in

absorbance is indicative of some decomposition into bis-substituted free ligand *(Figure 5.13)*. The absorbance of the indium complex remained yet reduced at 500 nm after 24 h, in contrast characteristic bands of the gallium complex *(Chapter 4.5)* were no longer present and displayed the form of the bis-substituted free ligand as investigated using UV-visible spectroscopy.

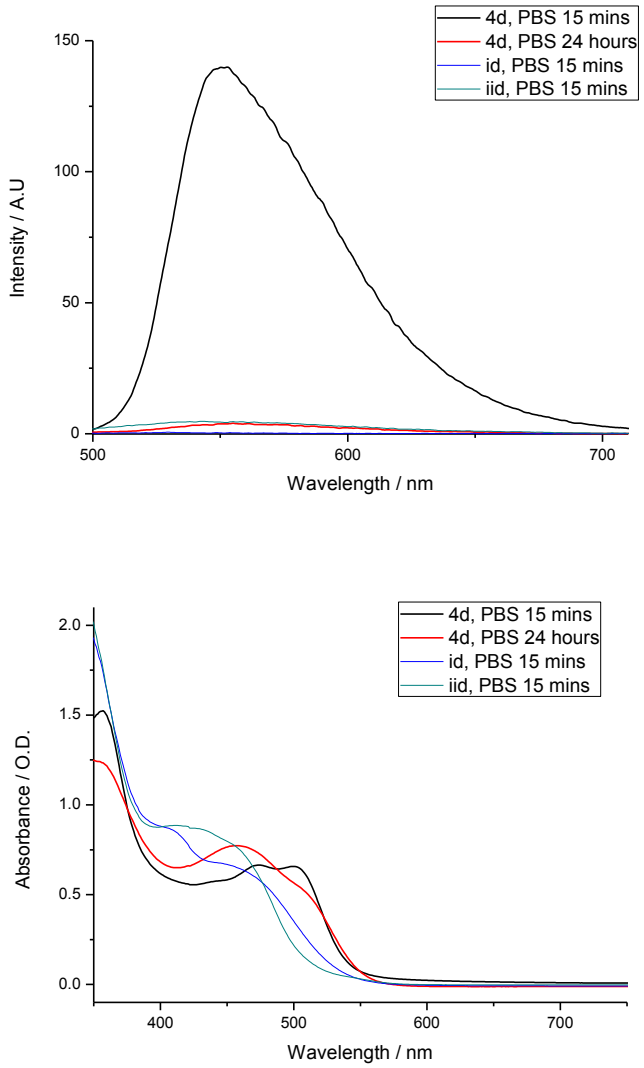

Figure 5.13. PBS assays (50% DMSO, 50% PBS) for compound **4d** at 100 µM, by fluorescence spectroscopy (above) UV/Vis (below) monitored at time intervals up to 24h at room temperature.

This suggests that in the case of the indium complex a significant proportion of the complex has remains intact over the observation period. This was in contrast to the finding for the gallium complex, which appeared to have converted into the ligand within 15 minutes incubation under the conditions above. This may be assigned to the

higher affinity of the indium complex for soft donor ligands, such as a bis(thiosemicarbazone).

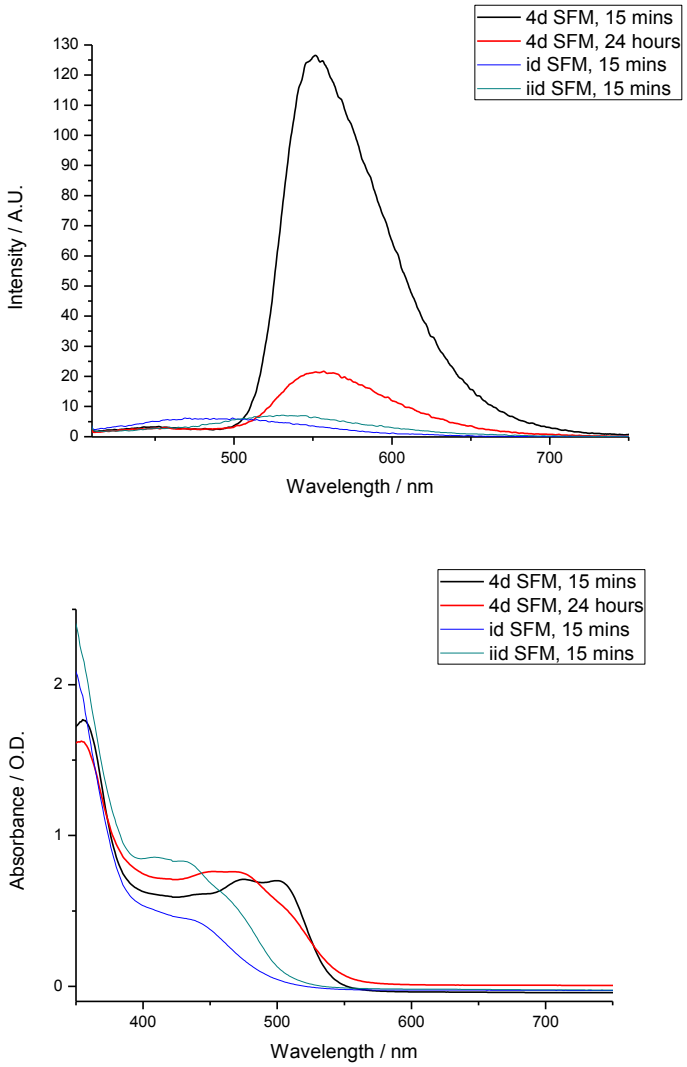

Figure 5.14. EMEM SFM assays (50% DMSO, 50% SFM) for compound **4d** at 100 µM, by Fluorescence(above) UV/Vis (below) spectroscopies monitored at time intervals up to 24h at room temperature.

Interestingly, the zinc complex **1d** displayed little change in fluorescence and maintained its characteristic absorption spectrum *(Chapter 3.7)*, signifying better stability than that of the gallium and indium complex in PBS. The stability of the complex **4d** was tested against Eagle's Minimum Essential Medium Serum Free Medium (SFM), which complexes are often incubated in for cell imaging.

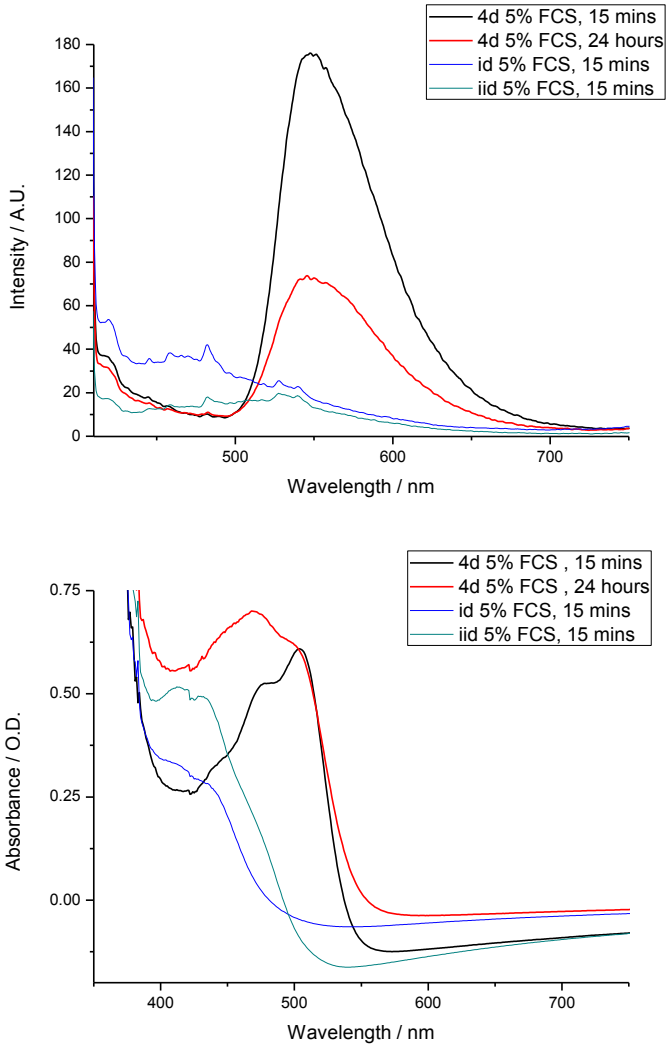

Figure 5.15. FCS assay (50% DMSO, 45% EMEM, 5% FCS) for compound **4d** at 100 µM, by fluorescence spectroscopy (above) UV/Vis (below) monitored at time intervals up to 24h at room temperature.

The fluorescence emission of each of the complex decreases over the time period studied at the λ_{max}. Compound **4d** showed a very significant decrease in fluorescence over 24 h (to 17 % of the original), coupled with a small red shift from 551.5 nm to 556.5 nm. Since the free ligand formation would be accompanied by a blue shift (approaching λ_{max} 531 nm) presumably the shift and intensity decrease are due to quenching, which may be caused by the interaction with the media, protonation or excimer formation, rather than significant decomposition to free ligand.

Moreover, these data suggest that it is likely that the complex remains intact under the conditions investigated hereby. When incubated in FCS EMEM, indium complex **4d** displayed a significant reduction in fluorescence and an increase in absorbance at 468 nm, this could either indicate conversion to Compound **iid** (λ_{max} 412 nm) or interaction with protein molecules present in serum and quenching. It is apparent, however, that **4d** did not fully convert into the corresponding free ligand **iid**, confirming stability of this complex up to 24 hours *(Figure 5.15).*

The complex **4d** was therefore found to be intact for all five of the above media (DMSO, water, PBS, SFM and 5% FCS EMEM). It was thus appropriate to explore specific interactions with several specific biologically relevant agents in common use.

5.5.1 Assays with biologically relevant agents

Biologically relevant agents were chosen to provide a better insight into the stability of these complexes, as were introduced in *(Chapter 3)*.[145] Complexes were tested in presence of 2 equivalents of citric acid, L-methionine, Glutathione (GSH), L-cysteine, L-histidine, and EDTA. Indium complex **4d** displayed very similar properties in citric acid, and sulphur containing L-Met and L-Cys in water in that there was little observable change in the spectral properties between 15 minutes and 24 h *(Figure 5.16 and Appendix Figure D.34)*. The characteristic absorbance spectrum for Compound **4d** was observable indicating very good stability of this complex up to 24 h in these solutions.

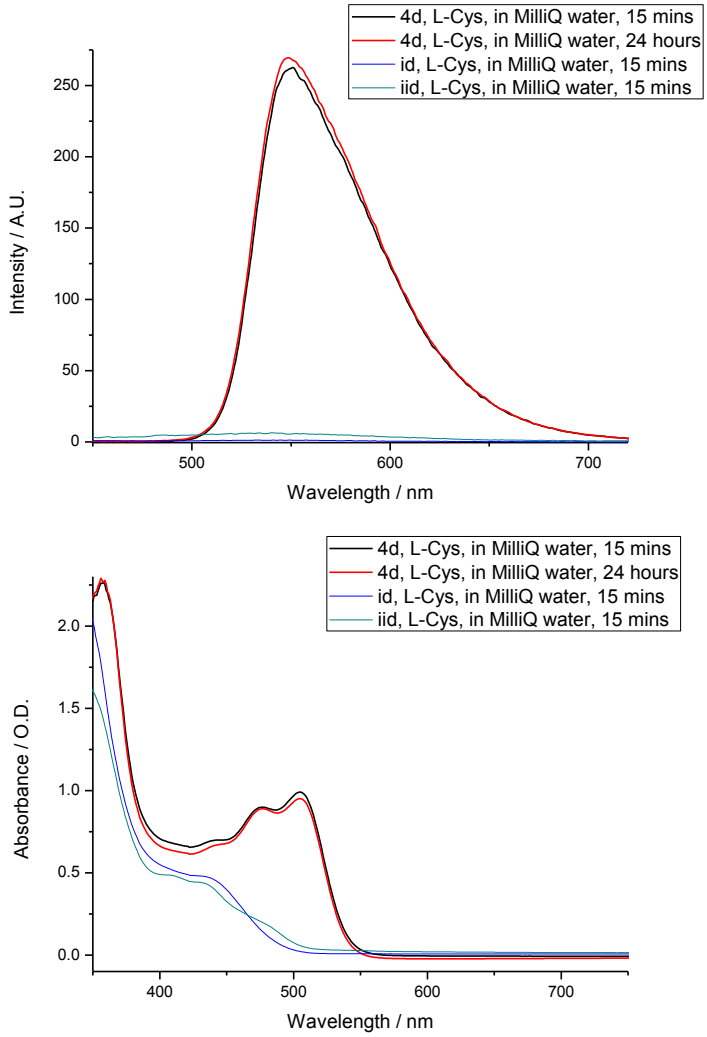

Figure 5.16. L-cysteine spectroscopic stability assays (50% DMSO, 50% water, 2 eq of L-cysteine) for compound **4d** at 100 µM, by fluorescence spectroscopy (above) UV/Vis (below) spectra monitored at time intervals up to 24h at room temperature.

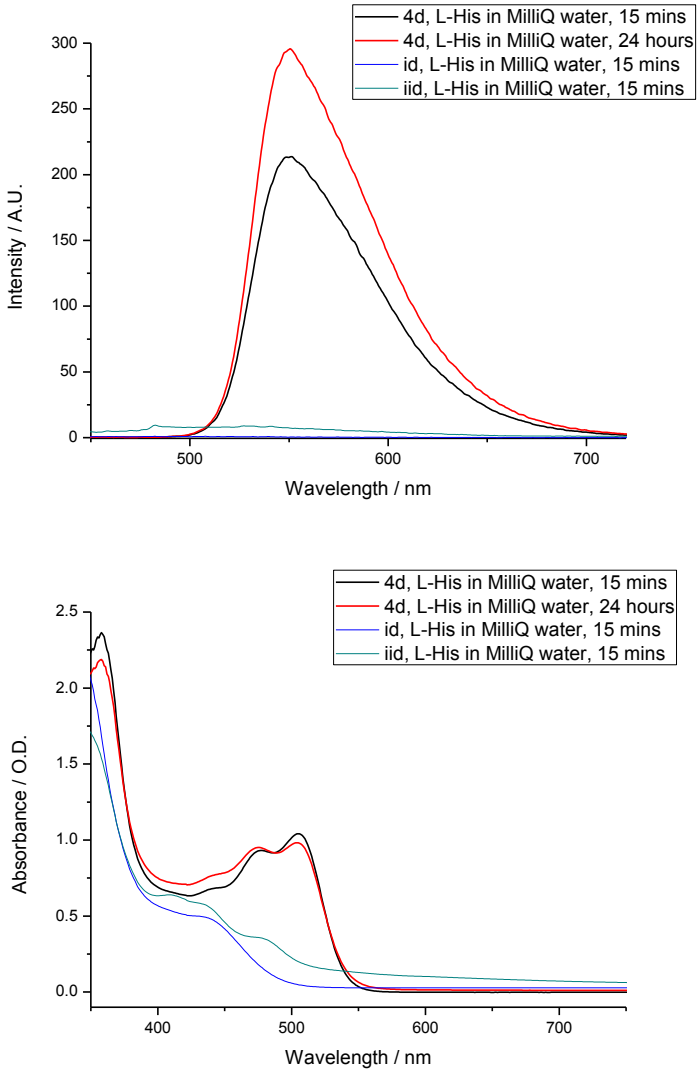

Figure 5.17. L-histidine challenge by spectroscopic assays (50% DMSO, 50% water, 2 eq of L- histidine) for compound **4d** at 100 µM, by fluorescence spectroscopy (above) UV/Vis (below) monitored at time intervals up to 24h at room temperature.

The fluorescence spectroscopy assay involving the addition of N-donating L-His to solutions of Compound **4d** resulted in a significant increase in fluorescence emission (505 nm). UV-Visible Spectroscopy showed that the mixture possessed spectral characteristics typical of **4d**. The absorbance band decreased slightly, but remained notable *(Figure 5.17)*. This therefore suggests that whilst some of the indium complex may have been converted to free ligand it appears that most of it remains chelated.

When GSH was added to compound **4d** a notable increase in fluorescence emission and a slight increase in absorbance band (in the UV-Vis spectrum at both 10 µM and 100 µM concentrations) with the distinctive **4d** spectrum were observable up to 24 h. This assay also suggests the compound stability under these conditions (*Figure 5.18).*

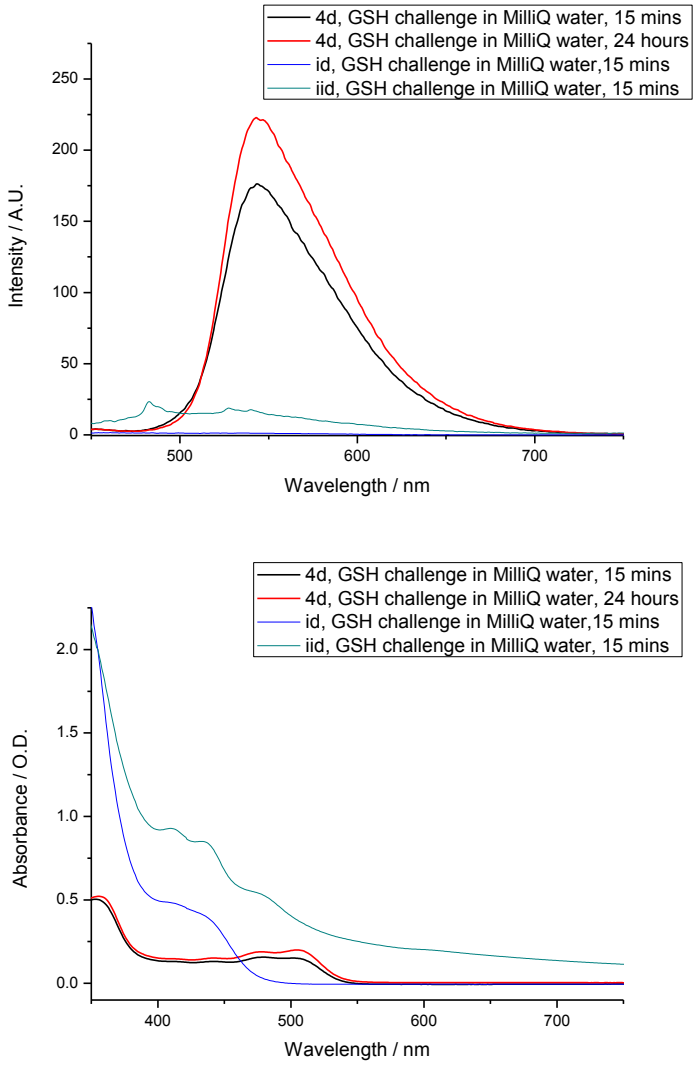

Figure 5.18. Glutathione challenge by spectroscopic assays (50% DMSO, 50% water, 2 eq of Glutathione) for compound **4d** at 100 µM, by fluorescence spectroscopy (above) UV/Vis (below) monitored at time intervals up to 24h at room temperature.

When compound **4d** was assayed with 2 equivalents of EDTA, in aqueous media, fluorescence spectroscopies showed a notable decrease in fluorescence emission (12% of original) and blue shift of 64 nm. A decrease in absorbance band was observed in UV-Vis spectroscopy and the characteristic shape of **4d** spectra was found. This

demonstrates some stability of this complex up to 24 h, indicative of the high stability of this complex in the presence of a strong chelator *(Figure 5.20)*.

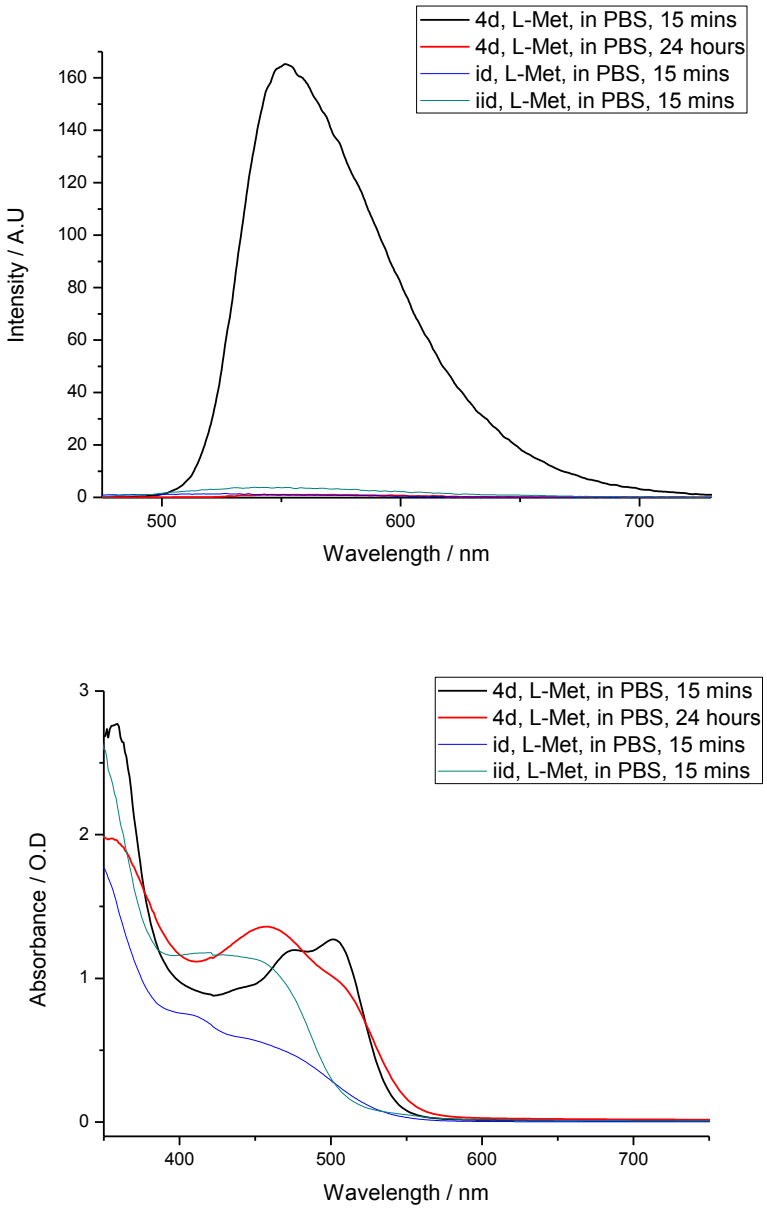

Figure 5.19. L-methionine spectroscopic assays (50% DMSO, 50% PBS, 2 eq of L-methionine) for compound **4d** at 100 µM, by fluorescence spectroscopy (above) UV/Vis (below) spectra were monitored at time intervals up to 24h at room temperature.

Additionally, the kinetic stability of compound **4d** was evaluated in aqueous solutions of PBS (phosphate buffered saline, which contains NaCl, KCl, Na_2O_4HP and KO_4H_2P). Unlike similar assays with L-Met or citric acid carried out without PBS (which all showed disappearance of most of the fluorescence emission intensity) an increased

absorbance at 460 nm and the decrease of the band at ca. 505 nm was observed agents tested, suggesting that complex had demetallated and therefore that PBS reduces the stability of these complexes *(Figure 5.19, Appendix Figure D.32-34)*.

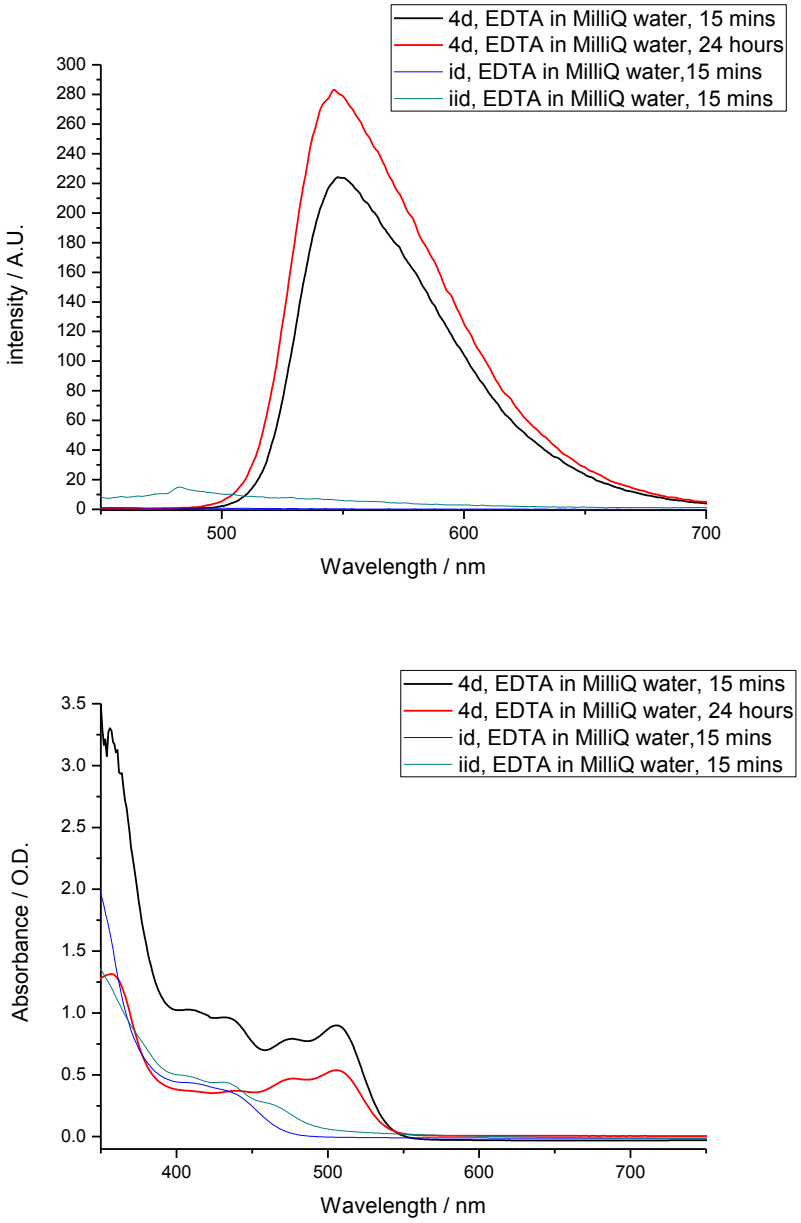

Figure 5.20. EDTA assays (50% DMSO, 50% water, 2 eq of EDTA) for compound **4d** at 100 µM, by fluorescence spectroscopy (above) UV/Vis (below) monitored at time intervals up to 24h at room temperature.

Overall these tests provide strong evidence that **4d** is stable in the presence of biologically relevant agents in water, whereby challenger assays did not reveal a specific stability based vulnerability.

5.5.2 pH buffer stability tests

The stability of complexes at biologically relevant pH is an important factor in this study. Cancer cells are slightly more acid than non-cancerous cells it is important that the molecular probes are stable at lower pH.[146] All fluorescent scans were carried out with an excitation wavelength of 400 nm and at a concentration of 100 μM, with a 1:1 DMSO:buffer solution. An initial preliminary study was carried out using fluorescence spectroscopy for gallium and indium complexes. There is a clear trend in the behaviour of the indium complexes in these buffers. All displayed fluorescence between pH 2 and pH 9, indicating that compounds have good stability at normal physiological pH and reflecting their potential for protonation and deprotonation *(Figure 5.21)*. Under more alkaline conditions the emission bands are slightly blueshifted, which indicates that a different species may be present, perhaps OH^- has interchanged with the Cl^-.

Table 5.5. Summary of UV-visible data at 50: 50 DMSO: pH buffer at 15 minutes and 24 h, where NS = not stable.

	4d, 100 μM		
Buffer	Measured pH	% stability at 15 mins	% stability at 24 h
pH 1.1	1.6	76.1	NS
pH 2	2.5	99.0	NS
pH 3	4.4	95.1	95.0
pH 5	6.9	93.3	93.0
pH 7	9.4	86.4	37.3
pH 9	9.35	83.9	81.4
pH 10	12.7	87.9	87.7

Following the above preliminary study allyl substituted compounds were selected as representative of the other functionality to assess the stability of newly synthesised gallium and indium complexes using UV-visible and fluorescence spectroscopy both at 15 minutes and 24 hours, with 1:1 DMSO:buffer solution. The pH of the samples was

measured and found to have no significant difference to the blank, however with a notable variance from that of the original pH solution in each case *(Table 5.5)*.

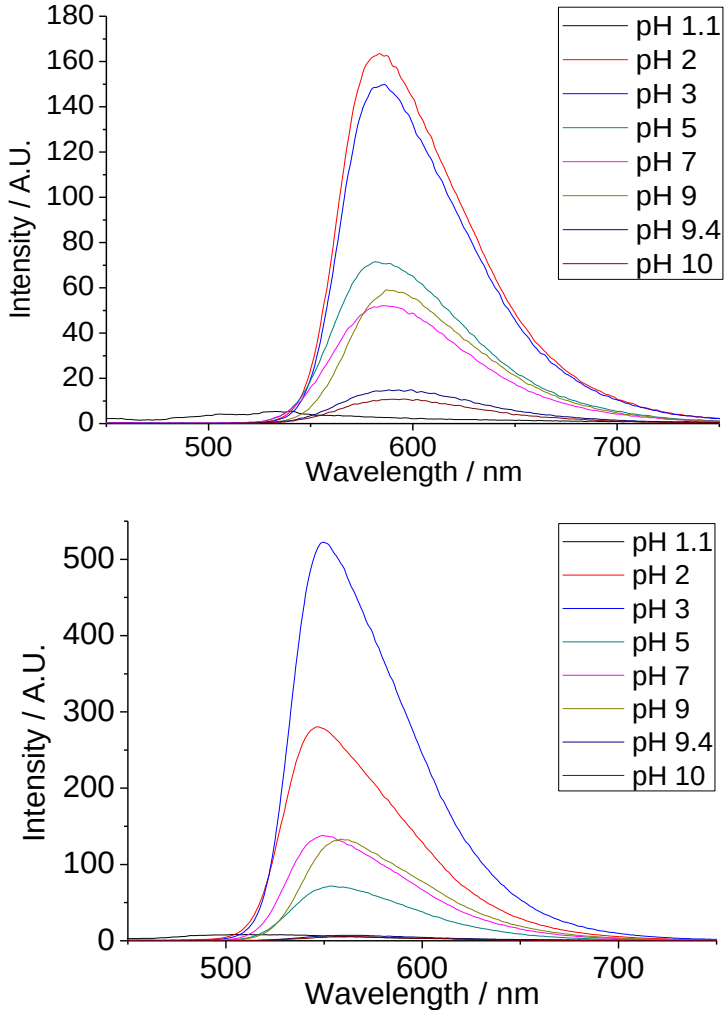

Figure 5.21. Fluorescence spectroscopy buffer assay **4a** pH study (above). Where pH 3 > pH 2 > pH 7 > pH 9 > pH 5 > pH 1.1 ≥ pH 9.4 ≥ pH 10, **4b** pH study (below). Where pH 2 > pH 3 >> pH 5 > pH 9 > pH 7 > pH 9.4 ≥ pH 10 ≥ pH 1.1.

Furthermore complex **4d** *(Figures 5.22-5.23 and Appendix Figure D.39-45)* appeared most stable at either pH 2 or pH 3 after 15 minutes or less, which is also in agreement with data acquired where citric acid was a component of the buffer solutions. When incubated in pH 1.1 buffer the absorption spectrum of **4d** maintained some of its original characteristic shape, suggesting some yet poor stability especially when comparing its fluorescence spectrum, which was almost identical to that of **iid (***proligand iid buffer study Appendix Figures D.50 and D.51*). As was observed with

both **1d** and **3d** after 24 h fluorescence and absorption of **4d** diminished signifying complete decomposition and instability of these complexes under the harsh conditions of a pH 1.1 buffer. Interestingly, despite complex **4d** displaying very high stability by both fluorescence and UV-visible after 15 minutes, after 24 h absorbance has decreased and no longer possessed the characteristic **4d** complex absorption spectrum in pH 2 buffer. It is most likely, however that some complex does remain since the fluorescence intensity is significantly greater than that of free ligand **iid** and the UV-visible spectrum of **4d** after the 24 h incubation does not resemble that of the free ligand.

Incubations in pH 3.0 and pH 5.0 buffers demonstrated very strong stability, with almost identical spectra by both UV-visible and fluorescence spectroscopy after 15 mintes and 24 hours, each displaying the typical **4d** complex absorption spectrum. When challenged with a pH 7.0 and pH 9.0 buffer highly comparable results were found in that good fluorescence and characteristic UV-visible spectra were observable after 15 minutes. This was followed by a blue shift in absorbance and a considerable decrease in fluorescence indicating that a large proportion of the complex has likely formed the free ligand Compound **iid**, yet with a significant proportion of the indium complex **4d** remaining intact under the conditions tested.

Similar to observations made with regards to the zinc and gallium complexes, stability appeared poorer when incubated with a pH 10.0 buffer than with a pH 9.0 or pH 7.0 buffer, here with the blue shift observable after 15 minutes when compared to the characteristic shape of the absorption spectrum of **4d** and a similar reduction in fluorescence after 24 h that was observed with the previously discussed pH 7.0 and pH 9.0 buffers. Interstingly, the UV-visible spectrum after 15 minutes was identical to that after 24 hours signifying that the loss of fluorescence intensity could be due to quenching as a result of solvent interaction rather than demetallation.

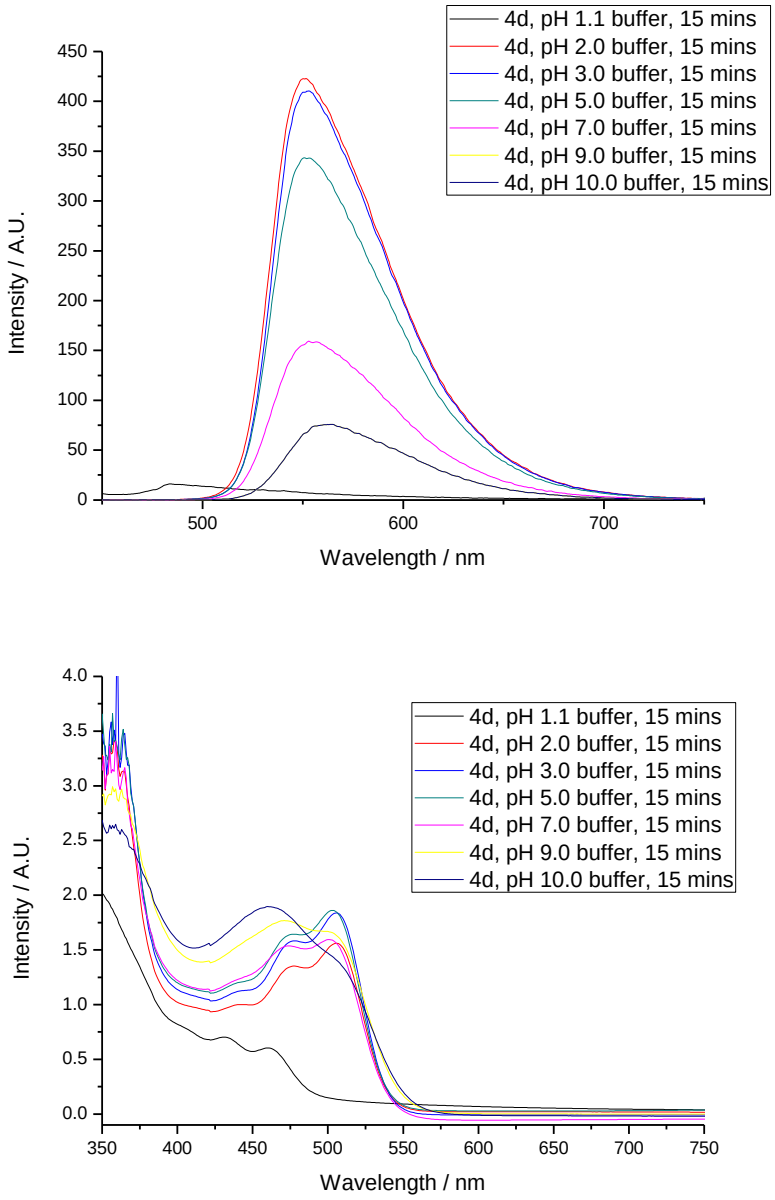

Figure 5.22. Buffer stability assays (50% DMSO, 50% water) for compound **4d** at 100 µM by fluorescence spectroscopy (above) and UV/Vis (below) monitored at 15 minutes at room temperature.

Therefore the stability of this indium complex **4d**, representative of the other indium complexes of this family, can be considered to be very broad with significant stability for all buffers in exception of pH 1.1 after 15 minutes, thus displaying fluorescence within a range of pH 2.5 and pH 12.7 for short-term incubations. Longer-term incubations demonstrated fluorescence between pH 2.5 and pH 6.9, with stability observable by UV-visible spectroscopy within the ranges of pH 4.4 and pH 12.7. This

is well within the requirements of biological experiments in strong support of *in vitro* experiments carried out on the indium complexes.

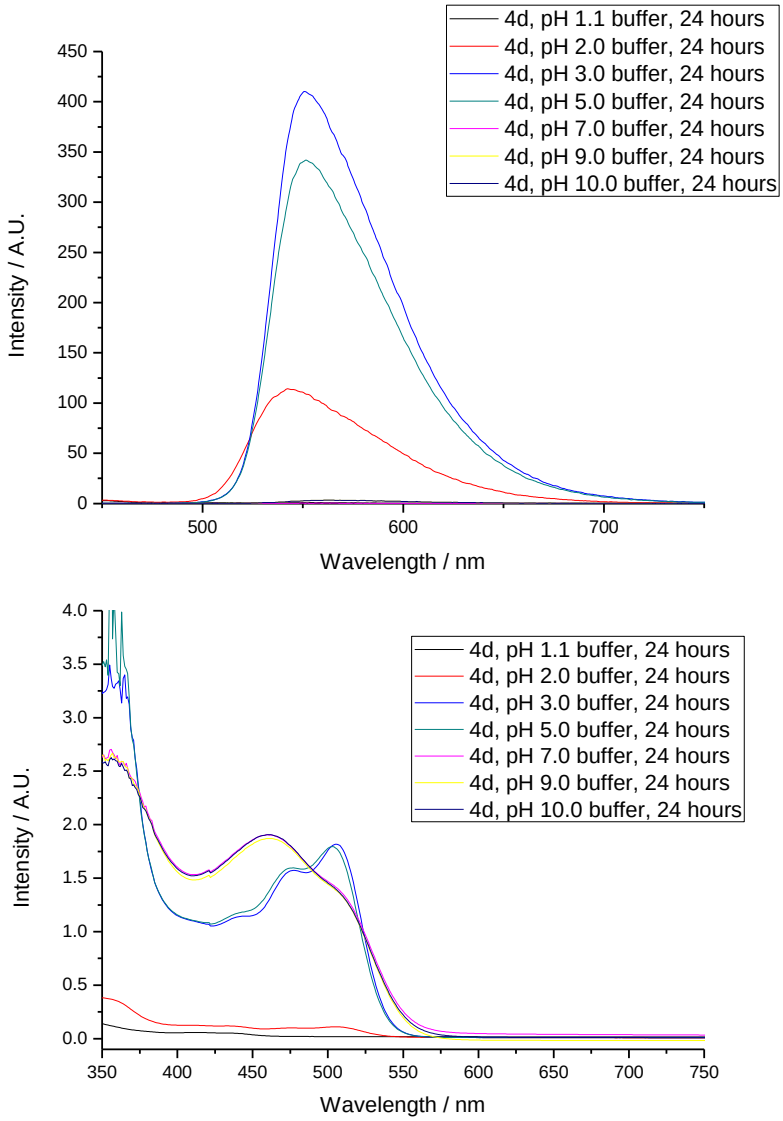

Figure 5.23. Buffer stability assays (50% DMSO, 50% water) for compound **4d** at 100 µM by fluorescence spectroscopy (left) and UV/Vis (right) monitored at 24 hours at room temperature.

In summary, all complexes tested possess good stability in biological media within 15 minutes incubation, with the indium complexes appearing kinetically stable after 24 h when assayed with 5% FCS, SFM, Citric Acid, EDTA, L-Cys, L-His, L-Met, GSH and pH 3.0 to pH 10.0 buffers. It was notable that the gallium complex was considerably less kinetically stable than the indium complex under the conditions tested, which could be accountable to the greater affinity of indium for soft donor ligands such as

bis(thiosemicarbazonates) resulting in lower lability in aqueous media.[150] These assays are a good indicator of strong biological stibility, indicating that experiments could proceed to testing *in vitro*.

5.6 Two-photon fluorescence lifetime study

The two-photon investigation was introduced in Chapter 2 and was performed at the Rutherford Appleton Laboratory under the supervision of Dr S Botchway. Indium complexes were incubated at 50 μM, 0.5% DMSO, for 20 minutes, unless stated otherwise in the text. The fluorescence lifetime components τ_1, of the indium complexes in solution were ca. 0.45 ns for **4a**, ca. 0.4 ns for **4b**, ca. 0.2 ns for **4c** and ca. 3.5 ns for **4d** *(Table 5.6)*. TCSPC using either 810 nm or 910 nm gave highly similar results under the same conditions.

Table 5.6. Two-photon Time Correlated Single Photon Counting data of solutions in DMSO of indium bis(thiosemicarbazonato)complexes.

	4a	**4b**	**4c**	**4d**
λ_{ex} = 810 nm	χ^2 = 1.06	χ^2 = 1.19	χ^2 = 1.24	χ^2 = 1.11
	0.454 ns 100%	0.454 ns 100%	0.174 ns 54.4%	0.458 ns 100%
			0.391 ns 45.6%	
λ_{ex} = 910 nm	χ^2 = 1.42	χ^2 = 1.32	χ^2 = 1.42	χ^2 = 1.43
	0.466 ns 100 %	0.453 ns 100%	0.182 ns 58.9%	0.442 ns 100%
			0.375 ns 41.1%	

Table 5.7. Two-photon fluorescence lifetime imaging data in HeLa cells of indium bis(thiosemicarbazonato) complexes, λ_{ex} = 810 nm.

Compound	**4b**	**4c**
χ^2	1.33	1.26
τ_1 %	92	83
τ_1 / ns	0.262	0.278
FWHM / ns	0.066	0.412
τ_2 %	8	17
τ_2 / ns	1.314	2.265
FWHM / ns	0.915	2.065

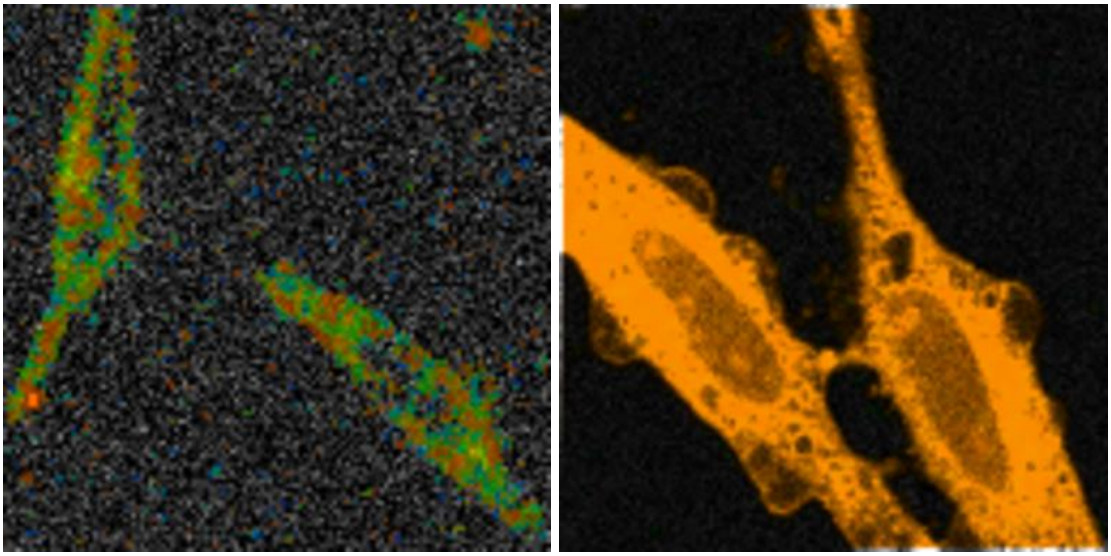

Figure 5.24. Two-photon fluorescence lifetime map (τ_m) at 910 nm in HeLa cells after 20 minutes of incubation of **iib** (left) at 100 μM, 1% DMSO, **4b** at 50 μM, 0.5% DMSO (right)

There were small differences between the τ_1 values of the indium complexes in cancer cells and in solution, but this can largely be attributable to the interaction with cellular components or biological media. As was the case with the gallium complexes when excited with 810 nm or 910 nm *in vitro*, the minor component was longer than expected according to the solution data *(Appendix Table F.8)*. A long component of ca. 2 ns for **4b** and **4c** was observable as a minor component using λ_{ex} = 810 nm indicating that a small proportion of the complex may convert to free ligand within the cell during the time course of this experiment. This could mean in both cases the presence of autofluorescence or of ligand precursor, however for the purposes of these experiments is not significant since the longer minor component was proportionally quite small (between 8 and 17 %) and therefore most of the complex is stable under these conditions *(Table 5.7)*. Additionally, the indium compounds were considerably more fluorescent than their corresponding proligand at 910 nm, therefore the better intensity obtained at lower concentrations for the complexes is also indicative of stability *(Figure 5.24)*.

Fluorescence lifetime imaging was therefore used to provide evidence that the newly synthesised bis(thiosemicarbazonato) complexes have good stability in cells. The

combined use of UV-Visible spectroscopy, fluorescence spectroscopy and FLIM offer a powerful method of investigating small molecule stability in both solution and in cells.

5.7 Laser scanning confocal microscopy

Cells were cultured using standard protocols, analogous to earlier investigations on fluorescent thiosemicarbazones, as described in Chapter 4.5. Imaging conditions for complexes **4a**-**4d** were standardised in an identical manner to the gallium complexes, with standard incubations of 0.5 % DMSO, 50 μM for 20 minutes. Cells were washed three times with PBS, which was replaced with serum free medium. As was observed with complexes **3a**-**3d**, compounds **4a**-**4d** caused significant changes in cell morphology after 60 minutes and therefore 20 minute incubation times were used, which showed little cytotoxicity.

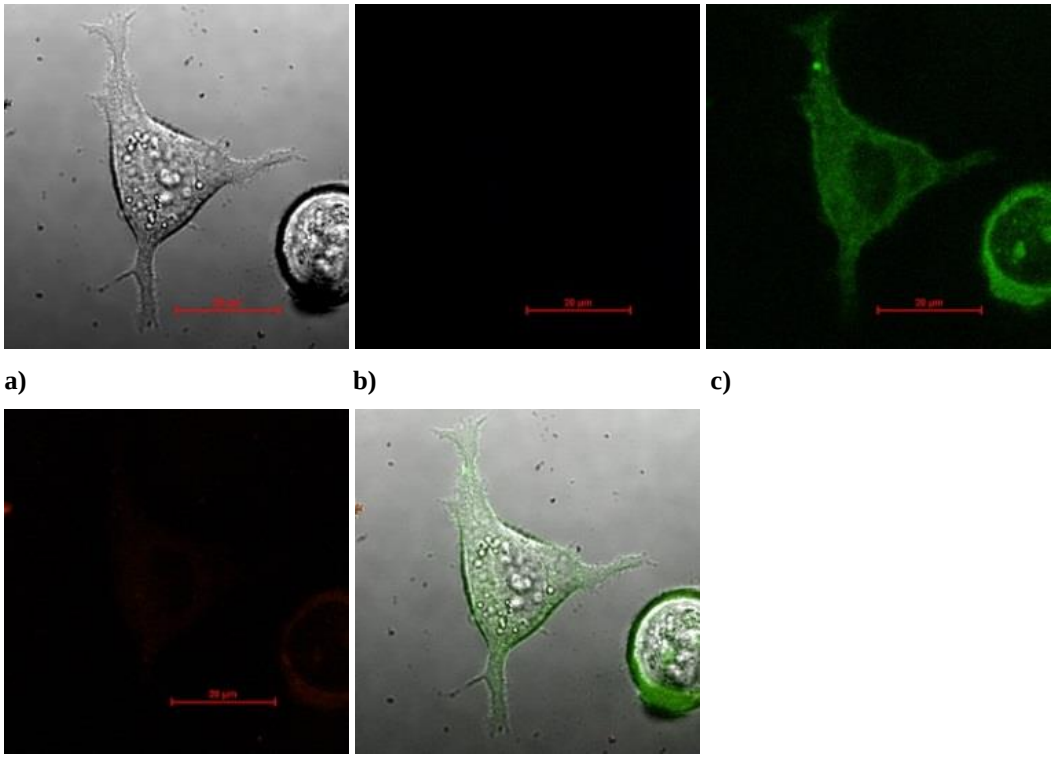

a) **b)** **c)**

d) **e)**

Figure 5.25. Single-photon confocal microscopy images of **4c** in MCF-7 cells, 20 minute incubation, 50 μM 0.5% DMSO at 37°C (a) DIC image, (b) excitation at 405 nm, emission 420-480 nm (c) excitation at 488 nm, emission >505 nm, (d) micrograph of cells after excitation at 543 nm and (e) is an overlay of (a), (b), (c) and (d) Scalebar: 20 μm

Initial experiments were carried out with the complex incubated alone, whereby each compound displayed significant fluorescence within cells when excited at 488 nm, with a long pass filer of 515 nm *(Figure 5.26)*. With the exception of **4b**, each complex showed sufficiently weak fluorescence when excited at 543 nm, using a long pass filter at 606 nm enabling experiments with red colocalisation dyes to proceed *(Figure 5.27)*.

There was seldom any fluorescence in the blue channel when exciting at 405 nm at 37°C for all of the indium complexes an example of which is included *(Figures 5.26, 5.27 and Appendix G)*.

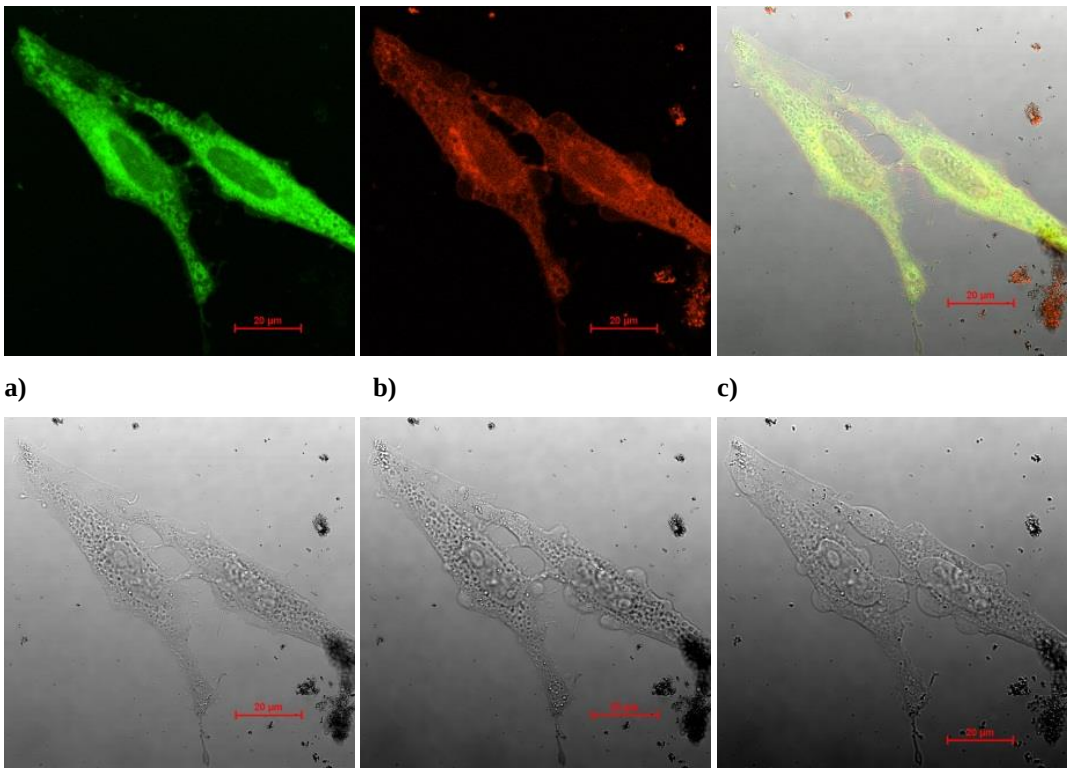

Figure 5.26. Single-photon confocal microscopy images of **4b** at 50 µM 0.5% DMSO in HeLa cells, 20 minute incubation, at 37°C (b) excitation at 488 nm (c) micrograph of cells after excitation at 543 nm and (d) is an overlay of fluorescence micrographs excitation at 405 nm and (a -b) and (e), (e), (f) and (g) are the DIC image from excitation at 405, 488 and 543 nm, respectively. Scalebar: 20 µm.

At 4°C red-shifted fluorescence emission was observed an effect that was also displayed for the analogous gallium complex *(Appendix Figure G.20)*. Interestingly, rapid phototoxicity was observed when irradiating with light (405 nm, 488 nm or 543 nm)

when HeLa cells were incubated with **4b** *(Figure 5.27)*, which occurred in the time taken to acquire the image. Such an intense photoactivity was not observed for any other complex of this class, with the ethyl-substituted complex therefore possessing interesting photosensitive properties.

Furthermore, Figures 5.27 e-g shows blebbing occurring within the cell, however no changes in localisation were observed as with complex **3b** *(Section 4.5)*. Uptake was observed at both 37°C and 4°C, which indicates that entry to cells can occur by passive diffusion alone. Interestingly, emission in the green channel was much weaker at 4°C *(Appendix Figure G.25)*, with increased fluorescence in the blue channel (λ_{ex} = 405) and in the red channel (λ_{ex} = 543). However, complex **4c** was irradiated for ca. 10 minutes with 488 nm and did not result in a significant change in cell morphology or size indicating that this compound was not phototoxic under the conditions tested, confirming the significance of functionality to this study *(Appendix Figures G.26-27)*.

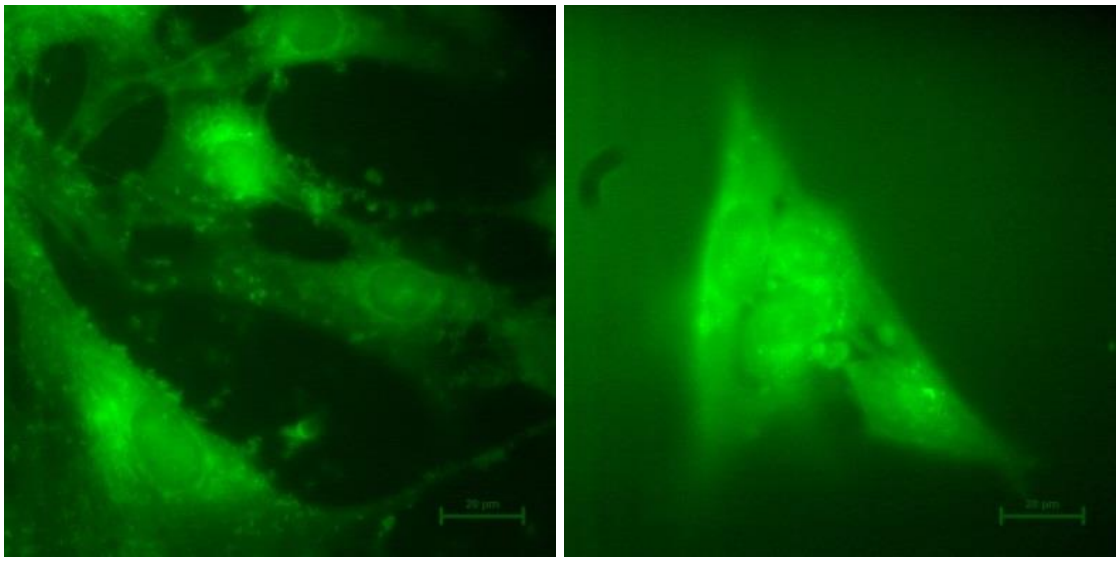

Figure 5.27. Single-photon Epi-fluorescence microscopy images of **4d** in FEK-4 cells, excitation with light 400-500 nm, emission >505 nm 3 hour incubation, 100 μM, 1% DMSO at 37 °C (left) and at 4°C (right). Scalebar: 20 μm.

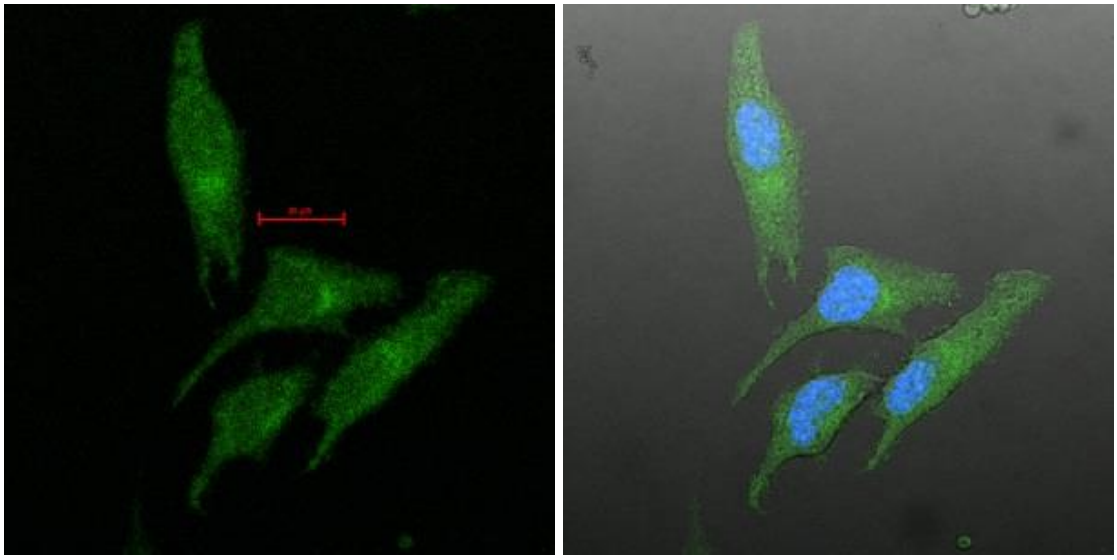

Figure 5.28. Single-photon confocal microscopy images with Hoechst stain of **4a** at 50 µM 0.5% DMSO at 37°C, and in HeLa cells after 20 minutes. (a) Micrographs of cells after excitation at 488 nm. b) Overlays of respectively, of the corresponding DIC image and the micrograph after excitation at 405 nm. Scalebar: 20 µm

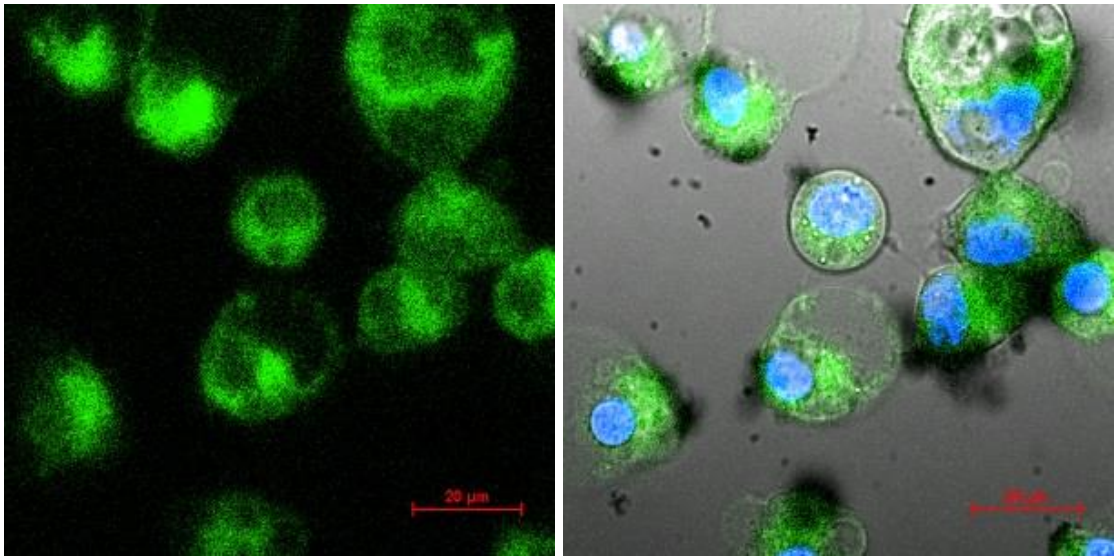

a) **b)**

Figure 5.29. Single-photon confocal microscopy images with Hoechst stain and **4c at** 50 µM 0.5% DMSO at 37°C, 6 hour incubation in PC-3 cells (c-d). (a) Micrograph of cells after excitation at 488 nm. b) Overlay of (a), of the corresponding DIC image and the micrograph after excitation at 405 nm, emission 420-480 nm (a), (b) and (c). Scalebar: 20 µm

Incubations of **4b** and **4d** in FEK-4 cells over 3 hours (with concentrations as high as 100 µM) followed by Epi-Fluorescence microscopy showed that compounds entered cells at both 4°C and 37°C. Fluorescence imaging seems to suggest that the compound

enters the nucleus under both conditions *(Figures 5.28)*. Additionally cellular morphology was not visibly affected on the timescale of this experiment, with highly comparable data acquired for **4b** and **4d**. This contrasts with the results observed at the incubation of these compounds (50 μM) in HeLa and PC-3 cells, which showed morphological changes even after 60 minutes at either 4°C and 37°C.

This suggests that these compounds may be more cytotoxic towards cancer cell lines than non-cancer cells and are explored in Chapter 6. To obtain further confirmation of the nuclear uptake, cells were co-stained with Hoechst (nuclear stains from Invitrogen) as well as the compounds. Cells were incubated with 50 μM of the compound using 0.5% DMSO for 20 minutes, 60 minutes and up to 6 hours. Complexes **4a**, **4b** and **4d** entered the nucleus of cancer cells within 60 minutes, with low levels of uptake after 20 minutes *(Figure 5.29 and Appendix Figures G.35-45)*. Compound **4c**, however did not co-localise with Hoechst after 6 hours confirming that the compound does not enter the nucleus *(Figure 5.30 and Appendix Figure G.45)*. Intact cellular morphologies were observed after 20 minute incubations suggesting that uptake does not compromise the nuclear membrane as a result of complex toxicity.

5.7.1 Fluorescence images of the nucleus and chromosomes

Due to the observed nuclear uptake a preliminary investigation was carried out at the Rutherford Appleton Laboratory with Dr Yusuf Mohammed and Ms Ana Estandarte to assess whether the complexes bind to chromosomes. Non-cancerous lung cell line CCD37-LU was cultured in DMEM containing 10% foetal bovine serum (FBS) and 1% L-Glutamine at 37°C in a 5% CO2 incubator. Chromosomes were isolated *via* a Colcemid (Gibco BRL) treatment before cells were trypsinised and subsequently resuspended in pre-warmed KCl hypotonic solution (0.075M) at 37°C for 12 minutes. This was followed by fixing in a 3:1 methanol/acetic acid solution, which was added onto a glass microscope slide, to which 100 μL of Compound **4d** (100 μM) was aliquoted and was washed with DMSO after 15 minutes.

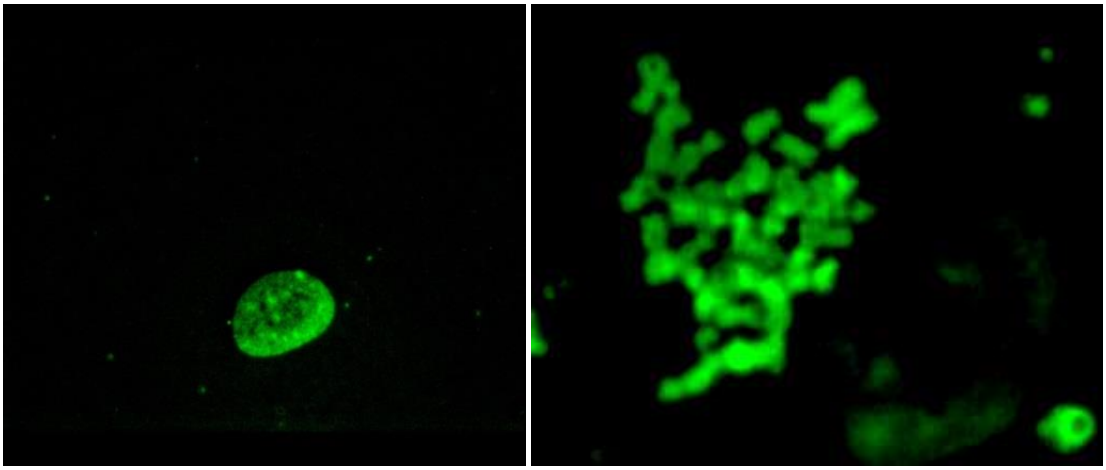

a) **b)**

Figure 5.30. Epi-fluorescence images of **4d** in (a) Isolated Cellular nucleus b) Isolated chromosomes

Finally images were acquired using a Zeiss Axio Imager 2 microscope, which showed uptake of the complex in both the nucleus and in chromosomes. The entry to the nucleus was expected and is in agreement with the Hoechst study above and with apparent uniform binding to chromosomes *(Figure 5.30)*. Further work could be carried out to assess if band patterns observed with this complex **4d** is different for cancer and non-cancer cells, which if so could present diagnostic potential as a chromosomal fluorescent stain.[151]

As discussed above, **4c** did not enter the nucleus and therefore behaves differently when compared to other indium compounds. It was subsequently was found to localise within the endoplasmic reticulum, which is involved in protein and lipid synthesis *(Figure 5.31a)*. It can be hypothesised that the aromatic functionality enables different binding modes within the cell when compared to the other substituent groups. Moreover compounds **4a**, **4c** and **4d** appeared to localise in the lysosome and the mitochondria *(Figure 5.31 b-d)*.

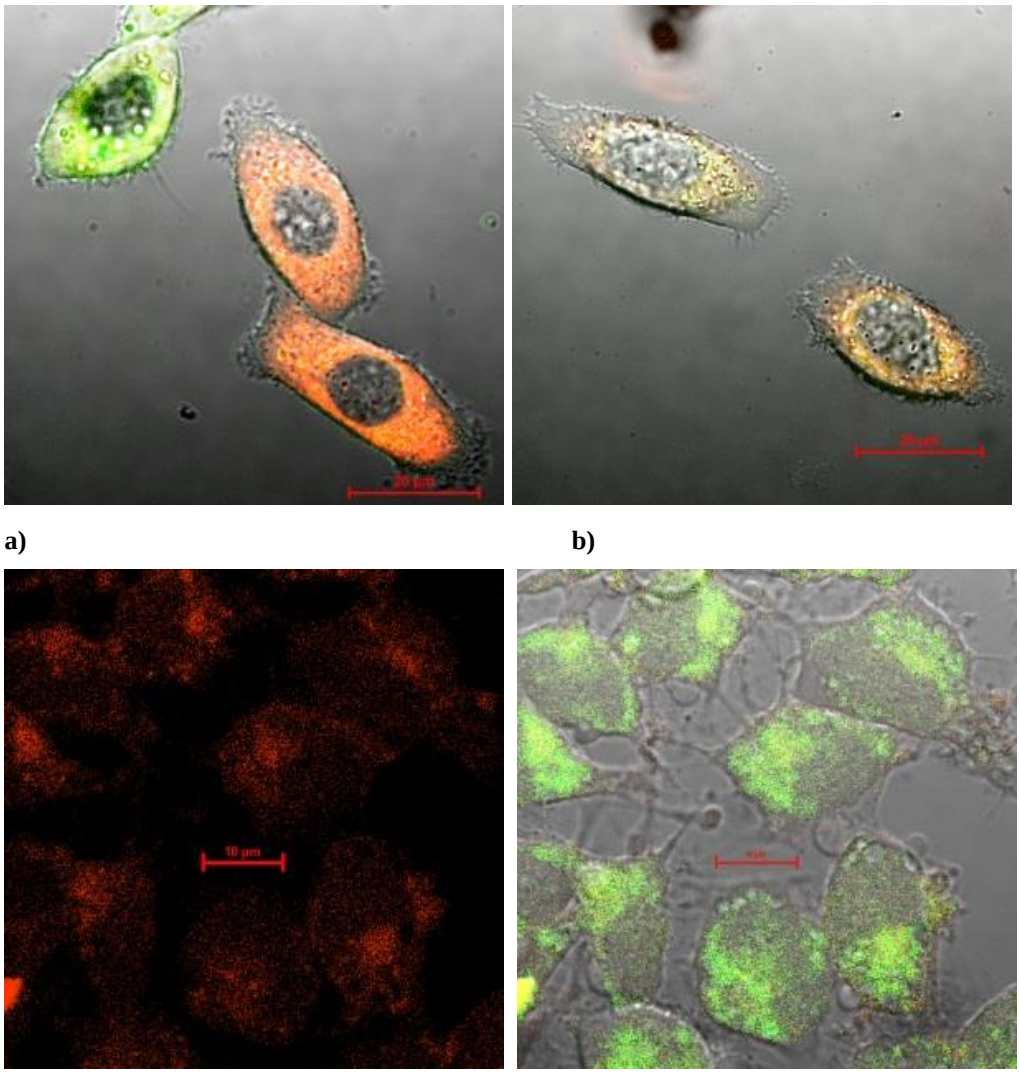

a) **b)**

c) **d)**

Figure 5.31. Single-photon confocal microscopy images 20 minute incubation, 50 µM 0.5% DMSO at 37°C of a) **4c** and ER tracker in PC-3 cells, b) **4c** and Mitotracker in PC-3 cells, c) and d) **4a** and Lysotracker Red in HeLa cells. Where a), b) and d) are overlays of images of DIC, a micrograph of excitation at 488 nm, emission >505 nm and a micrograph of cells after excitation at 543 nm, (c) is a micrograph of cells after excitation at 543 nm.

In summary uptake of indium complexes was similar to that of the gallium complexes in that localisation was observed in the mitochondria and the lysosome, long-term experiments more than 20 minutes caused cytotoxicity and photoactivity was observed for the ethyl-substituted complex. Interestingly localisation did not change when irradiated with light. Another notable difference was that indium complexes entered the nucleus much more readily than other compounds of this type, with a further study

showing that complex **4d** uniformly binds to the chromosomes of a non-cancer cell line, CCD37-LU. Tests in cancer cells can evaluate if a difference can be observed, which could assess the potential of the compound as a clinical diagnostic.

5.8 In vitro hypoxia selectivity testing

An analogous study to the one carried out using the gallium complexes in EMT6 (murine breast carcinoma) and PC-3 cells, was carried out under the supervision of Prof Eric Aboagye (by Dr Israt S. Alam) at Hammersmith Hospital, Imperial College London. Compounds **4c** and **4d** were incubated in cells at 50 μM, 4% DMSO, with normoxic conditions of 20.7% O_2 and 5% CO_2 at 37°C, with hypoxic samples pre-incubated for 20 minutes at 1% O_2, 5% CO^{o}_2 at 37°C before complex addition. Following addition of the compound, cells were incubated for a further 20 minutes and subsequently washed three times with PBS before being returned to serum free media and imaged immediately.

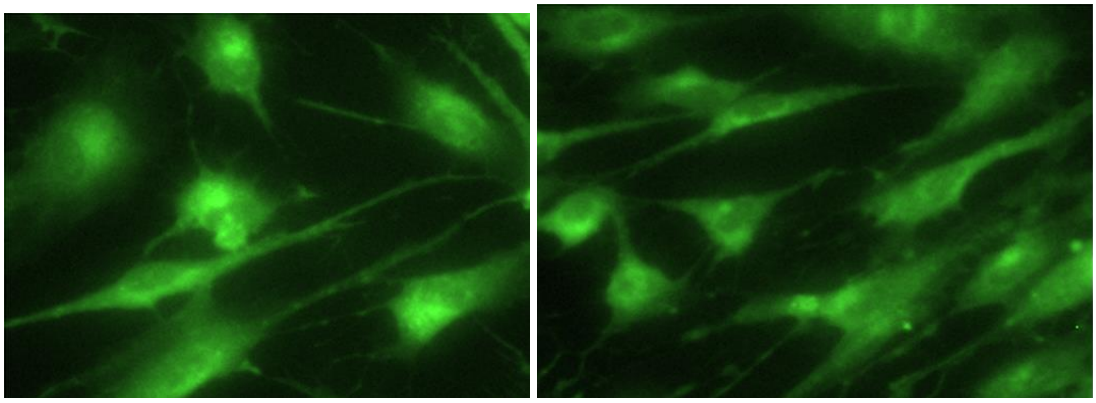

Figure 5.32. Confocal micrographs of **4d** in FEK-4 cells under normoxic (left) and hypoxic (right) conditions.

An initial confocal study was carried out within which significant differences in fluorescence were biologically relevant to determine *(Figure 5.32)*. Therefore a flow cytometry study was carried out, which as was observed in the gallium complex, fluorescence was lower under hypoxic conditions than normoxic conditions. For the allyl-substituted indium complex, the fluorescence was lower by 25.4% (*P<0.01) in EMT6 cells and by 19.1% (*P<0.05) in PC-3 cells. Meanwhile the fluorescence

emission under hypoxic conditions for complex **4c** seems lower by 22% (*P<0.05) in EMT6 cells and by 8% (*P<0.05) in PC-3 cells *(Figure 5.33)*.

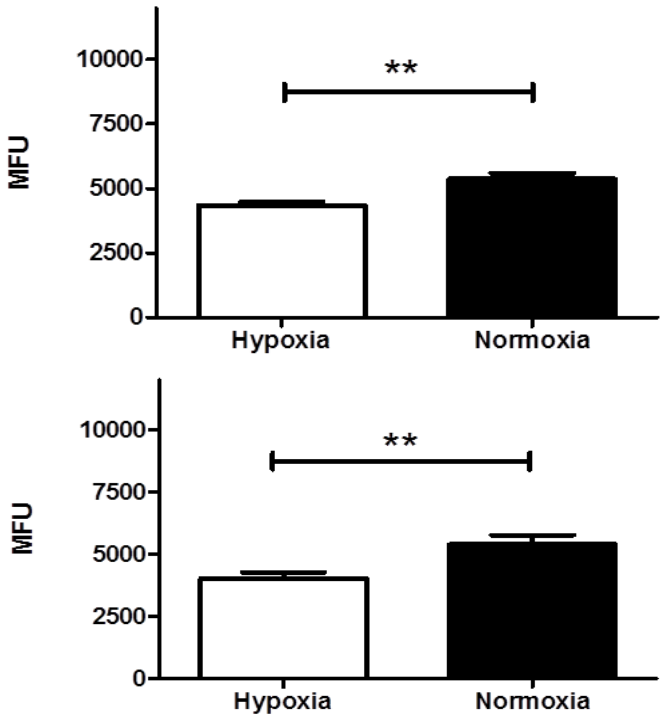

Figure 5.33. Flow cytometry studies under normoxia and hypoxia of **4d** in EMT6 (above) and in PC-3 cells (below).

The level of hypoxia selectivity is therefore similar for **4c** and **4d**, with the selectivity of **4d** slightly greater than that of **4c**. It is likely as was observed with the gallium complex that under hypoxia and the resultant reduction of the metal centre the complex demetallated causing a loss of fluorescence. A future study using radiochemical techniques could further confirm the hypoxic selectivity of these complexes.

5.9 Summary to Chapter 5

New indium bis(thiosemicarbazonato) complexes have been synthesised and characterised by NMR spectroscopy, ES-MS and X-ray crystallography. Data show a strong preference towards the symmetric isomer, with only this isomer assignable by NMR X-ray crystallography and DFT calculations are in agreement with this, with the optimised symmetric complex more stable than the asymmetric complex in the gas phase and in solution (a finding not observed for the respective zinc, copper or gallium complex). Furthermore complexes were cleanly and rapidly radiolabelled in addition to possessing sufficient fluorescence to continue the study with an *in vitro* cell uptake study. Complexes were found to possess excellent stability *via* tests in solution biomimetic media, biologically relevant agents and possessed stability over a broad pH range (pH 4.4 to pH 12.7 by UV-visible spectroscopy and pH 2.5 to pH 12.7 by fluorescence spectroscopy). Furthermore, two-photon fluorescence lifetime imaging microscopy confirmed the stability of these complexes in cancer cells. Additionally, indium compounds of this type localised in the mitochondria and lysosome, with the phenyl-substituted complex entering the endoplasmic reticulum.

Moreover, the indium complex with an ethyl functionality displayed phototoxicity, as did the corresponding gallium complex, yet without a change in localisation within the cell. Interestingly the indium complexes (with the exception of the phenyl-substituted complex) localised within the nucleus and were found to bind to chromosomes in a preliminary study. Furthermore hypoxia selectivity was observed for complexes **4c** and **4d** in EMT6 and PC-3 cells by way of a reduction of fluorescence monitored by flow cytometry. In summary, these complexes show potential in diagnostics either as hypoxic or chromosome-binding contrast agents, with the possibility of therapy *via* photoactivity.

Chapter 6. Cellular investigations of new bis(thiosemicarbazonato) complexes by cytotoxicity assays

In this chapter pharmacological assays were performed in order to understand the cellular toxicity of the newly synthesised compounds. Standard MTT and LDH assays were adapted and used hereby. Cell viability and cytotoxicity assays cause a colorimetric response, which allow a chosen biological characteristic or process to be monitored. An increase in absorbance can either be the result of living cells retaining normal functions and/or morphology (cell viability assay) or alternatively the result of cellular disruption (cytotoxicity assay).

Various assays monitor different functions and do not always give the same result. Therefore it is beneficial to carry out more than one. On one hand, the Lactate Dehydrogenase (LDH) assay is informative on cell membrane lysis over short periods of time, but instead indicates overall toxicity for longer periods of time, such as 24 h. Methyl Tetrazolium (MTT) assay on the contrary is indicative of the number of live cells and therefore the overall toxicity of a particular drug. Mitochondria of live cells convert MTT into formazan, which absorbs broadly around 500 nm; increased toxicity therefore results in low absorbance, with all MTT assays carried out at 570 nm. The mitochondria of any non-viable cell will not be functional; therefore this assay is not informative *per se* on action on the mitochondria.

6.1 Time series assays by MTT

A preliminary study was carried out in FEK-4, a non-cancer fibroblast cell line at 10 μM at 1 hour, 3 hours, 6 hours and 24 hours to assess the effect of the complexes and Cu[ATSM] on cells with time by MTT assay. The allyl substituted complexes were chosen as representatives of the other functionalities to allow the effect of the metal on cytotoxicity to be considered, whilst the indium complexes were selected for the purpose of assessing the influence of the substituent *(Figure 6.1)*.

The analogous allyl compounds and Cu[ATSM] enabled an initial comparison between metal centre, the addition of the acenaphthenequinone backbone and allyl functionality to be investigated for the first time. Zinc and copper, metals of biological significance represented the acenaphthenequinone complexes of highest and lowest cytotoxicity respectively. The gallium and indium compounds displayed very similar, gradual toxicity, which indicates that the mechanism of action may be due to their polarity, since both bear a chloride counter-ion.

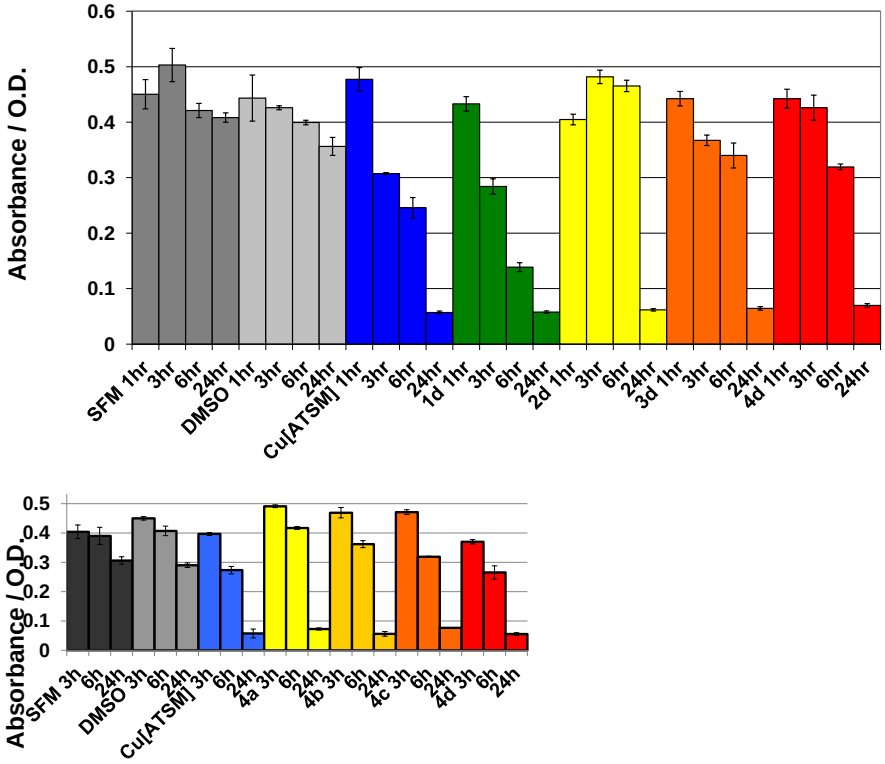

Figure 6.1. MTT assays at 10 μM in FEK-4 in SFM EMEM of allyl complexes (above), indium complexes (below).

In contrast **1d** and Cu[ATSM] demonstrated more rapid activity upon cells each with ca. 60% viability after 3 hr, with **2d**, **3d** and **4d** ca. 80% viability after incubation at this timepoint. The comparison between Cu[ATSM] and **2d** implies that the addition of the acenaphthenequinone backbone significantly decreased toxicity, which is a desired

attribute for a potential diagnostic. This could perhaps be due to the greater stability and subsequently lower reactivity of **2d** with respect to Cu[ATSM].

The absorbances of **4a**, **4b** and **4c** were comparable, indicating that the effect of the functionality may be less significant than that of the metal centre. **4d** is an exception, with somewhat higher cytotoxicity displayed here and may be due to the greater reactivity of this substituent compared to the relatively unreactive methyl, ethyl or phenyl groups.

6.2 MI_{50} determinations by MTT

To explore this further and to obtain quantitative measures of the cytotoxicity of this family of compounds the MI_{50}, the concentration at which metabolism is reduced to 50%, were calculated using MTT assay for a 48 h incubation with the compound, 1% DMSO. The value corresponding to 50% cells was corrected for background absorbance, which corresponded to the point at which all cells of a sample were dead.

Previous studies in the group using trypan blue and an incubation time of 48 hours found that zinc complex **1d** and copper complex **2d** possessed LD_{50} values of ca. 15 µM and 25 µM respectively in MCF-7 cells,[127] with zinc complexes **1a**, **1b** and **1c** cytotoxicity estimations of 15 µM.[128] Similarly, **2b** had LD_{50} values of ca. 12.5 µM in IGROV (ovarian cancer) cells and ca. 50 µM in MCF-7 (breast cancer) cells.[123] This hence indicates that the zinc complexes may be marginally more cytotoxic than the copper compounds. (Since quantitative data from trypan blue is achieved by the counting of cells, of which the dye stains the membrane of intact cells, metabolism is not measured and therefore was referred to as LD_{50}, here defined as the concentration to kill 50% of cells.) *Cis*-Platin (**CP**), in comparison was estimated to possess LD_{50} values of ca. 4.0 µM in IGROV cells and ca. 12.0 µM for MCF-7, meaning that whilst the zinc and copper complexes appeared to possess comparable cytotoxicity to **CP**, however were slightly less toxic.

6.2.1 Cell viability assays in HeLa cells

MTT assay was chosen as an alternative to the more time consuming and less sensitive trypan blue. Control experiments were used to determine a MI_{50} of **CP** and was calculated to be 27 µM ± 5 µM under comparable conditions and in agreement with the literature[152], whilst Cu[ATSM] was found to be 0.55 µM ± 0.03 µM in HeLa cells, a cervical cancer cell line. By crystal violet method Cu[ATSM] had previously been estimated to have a value of ca. 18.6 µM in HeLa indicating a stark difference in nature of the cytotoxicity tests, whereby crystal violet stains DNA as opposed to MTT assay which is dependent on metabolism of mitochondria.[153] Considering Table 6.1, which includes the MI_{50} data gathered on all compounds tested in HeLa, each with at least 3 repeat experiments allowed this family of molecules to be compared in terms of their cytotoxicity.

Table 6.1. MI_{50} data of compounds in HeLa cells, where N/A = no significant cytotoxicity and nd = not done. †Compound **iib** did not reach 100% cell death, therefore this number represents the minimum MI_{50} value.*

	a	**b**	**c**	**d**
i	0.105 µM ± 0.006 µM	6.5 µM ± 0.7 µM	6.4 µM ± 1.8 µM	0.18 µM ± 0.04 µM
ii	N/A	28 µM ± 13 µM†	5.2 µM ± 0.8 µM	N/A
1	nd	3.0 µM ± 0.2 µM	3.0 µM ± 0.6 µM	nd
2	nd	17 µM ± 4 µM	19 µM ± 1µM	nd
3	0.49 µM ± 0.03 µM	1.6 µM ± 0.2 µM	3.6 µM ± 0.8 µM	0.91 µM ± 0.03
4	0.37 µM ± 0.10 µM	1.0 µM ± 0.2 µM	0.38 µM ± 0.07 µM	0.44 µM ± 0.16 µM

* Some MI_{50} values in HeLa were obtained with assistance of Haobo Ge

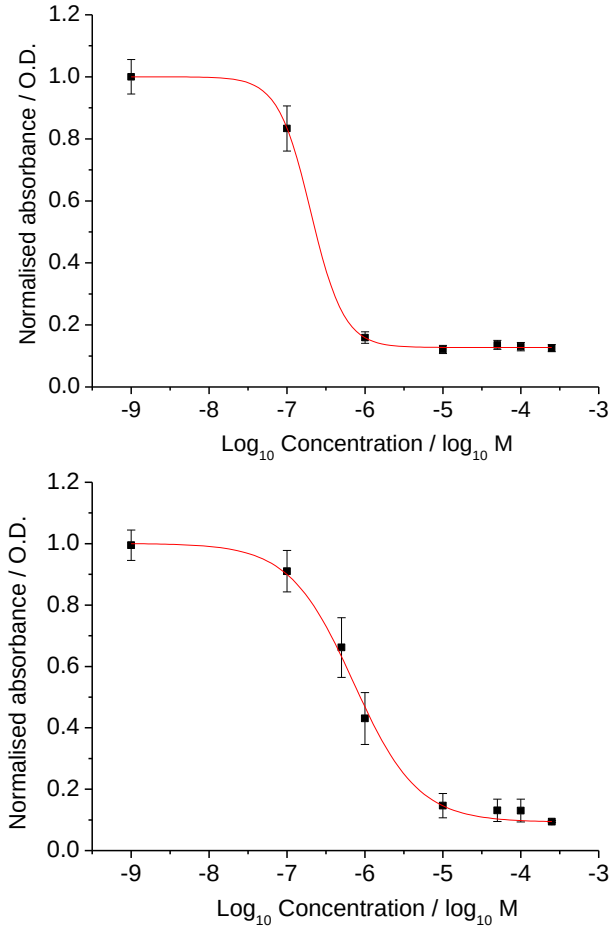

Figure 6.2. Scatter graph representing MI_{50} in HeLa cells a) of **id** b) of **4b**

General patterns were observable that the indium complexes possessed greater cytotoxicity than the gallium complexes, which in turn were more active than the zinc complexes (*Appendix Figures H.1-H.9*). Of the complexes copper was the least cytotoxic, with comparable potency to **CP**. Proligands **iib** demonstrated low levels of cytotoxicity, with compound **iia** and **iid** showing little cytotoxicity in preliminary experiments, indicating that chelation improves the activity of bis(thiosemicarbazones). Much greater cytotoxicity, however, was expressed by **iic** at 5.2 µM ± 0.8 µM, yet this was less toxic than its corresponding complexes, with the exception of the comparatively lower activity of the copper compound **2c**. Mono-substituted free ligands displayed the most variable properties with **ia** the most potent compound tested and **ib** with similar cytotoxicity to **2b** in HeLa cells. Interestingly compounds **1b** and **1c** possess significantly lower MI_{50} values by MTT assay when compared to trypan blue studies. Trypan blue experiments are dependent on cell membrane integrity therefore if

it were that this family of complexes cause little membrane damage including after longer incubation times it could explain why the estimations differ, this is explored in section 6.3.

6.2.2 Non-cancerous cells assays by MTT – investigations in FEK-4 cells

To prepare cancer diagnosing or treating agents, action against non-cancer cells is important to explore. In FEK-4 cells these data were greatly contrasted by **ia** causing limited cell death compared with in HeLa, with a MI_{50} of 9 µM ± 3 µM, with **id** also possessing a MI_{50} of much higher than in HeLa cells (*Appendix Figures H.10-12*). The MI_{50} of the gallium and indium complexes tested were comparable, yet possessing notably lower toxicity against the non-cancer cell line. This data therefore provides strong evidence that these compounds possess selectivity towards cancer over non-cancer. Exhaustive studies in numerous cell lines (both cancer and non-cancer) could confirm if this effect is general for cancer.

Table 6.2. MI_{50} data of compounds in FEK-4 cells

	a	**d**
i	9 µM ± 3µM	5 µM ± 2 µM
3	1.25 µM ± 0.07 µM	3 µM ± 2 µM
4	0.95 µM ± 0.06 µM	0.82 µM ± 0.08 µM

6.3 *In vitro* investigation to provide insight into the complex mode of action

Bis(thiosemicarbazonato) complexes had previously been tested for cytotoxicity by Pascu *et al.*,[127, 128] and Ackerman *et al.*[153]. Compounds generally showed low to medium toxicity, theorised to be mediated *via* initial the mitochondria followed by entry into the nucleus.[128] To allow pharmacological comparison of the new compounds presented in Chapters 2-4 with known complexes such as Cu[ATSM], Zn[ATSM] as well as **1d**, **3d** and **2b** a study of cytotoxicity and cell uptake was carried out using lactate dehydrogenase (LDH) assays in HeLa (cervical cancer cells), MCF-7 (breast cancer cells) and FEK-4 (fibroblast, non-cancerous cells).

LDH assay indicates potential cell membrane action as a mechanism of toxicity when cells are incubated with the drug for short periods of time (up to ca. 6 h). LDH catalyses the conversion of lactate into pyruvate, which reacts with tetrazolium salt INT to produce formazan. High absorbance therefore indicates high LDH activity and a high amount of cell lysis. For longer periods of time (e.g. 24 hours) this assay is representative of overall toxicity rather than action by membrane lysis. All LDH assays were carried out at 570 nm.

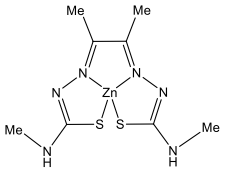

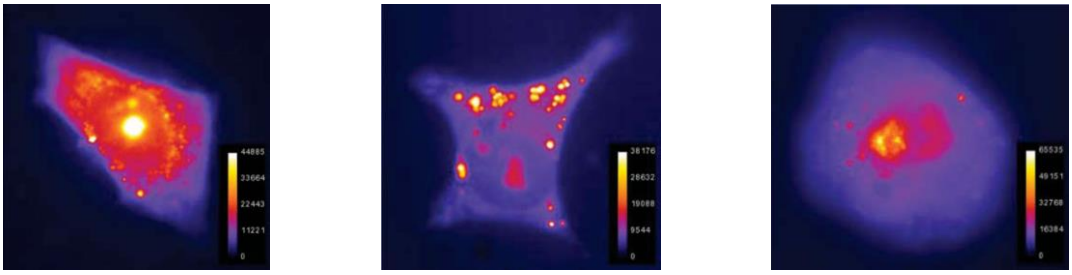

a) **b)** **c)**

Figure 6.3. Published fluorescence images of Zn[ATSM] in MCF-7 (a), IGROV (b) and PC-3 (c) (breast, ovarian and prostate cancer cell lines respectively).[62]

As illustrated in Figure 6.3 (Dilworth *et al.* 2005)[62] one compound can behave differently according to the cell line it is in. It was therefore important to investigate the effect of each compound in this study on a number of various cell types. Cu[ATSM] is currently under clinical trials as a PET hypoxia molecular imaging probe for cancer and has so far been tested mainly in cancer lines. Because of its therapeutic potential, however, it may be more important to test its cytotoxicity on non-cancerous cells. In this study FEK-4 cells, which are non-cancerous were used for comparative purposes of anti-cancer selectivity. HeLa (cervical cancer) and MCF-7 (breast cancer) were the cancerous cell lines chosen to investigate this compound class. Each dataset is a repeat of at least 3 experiments.

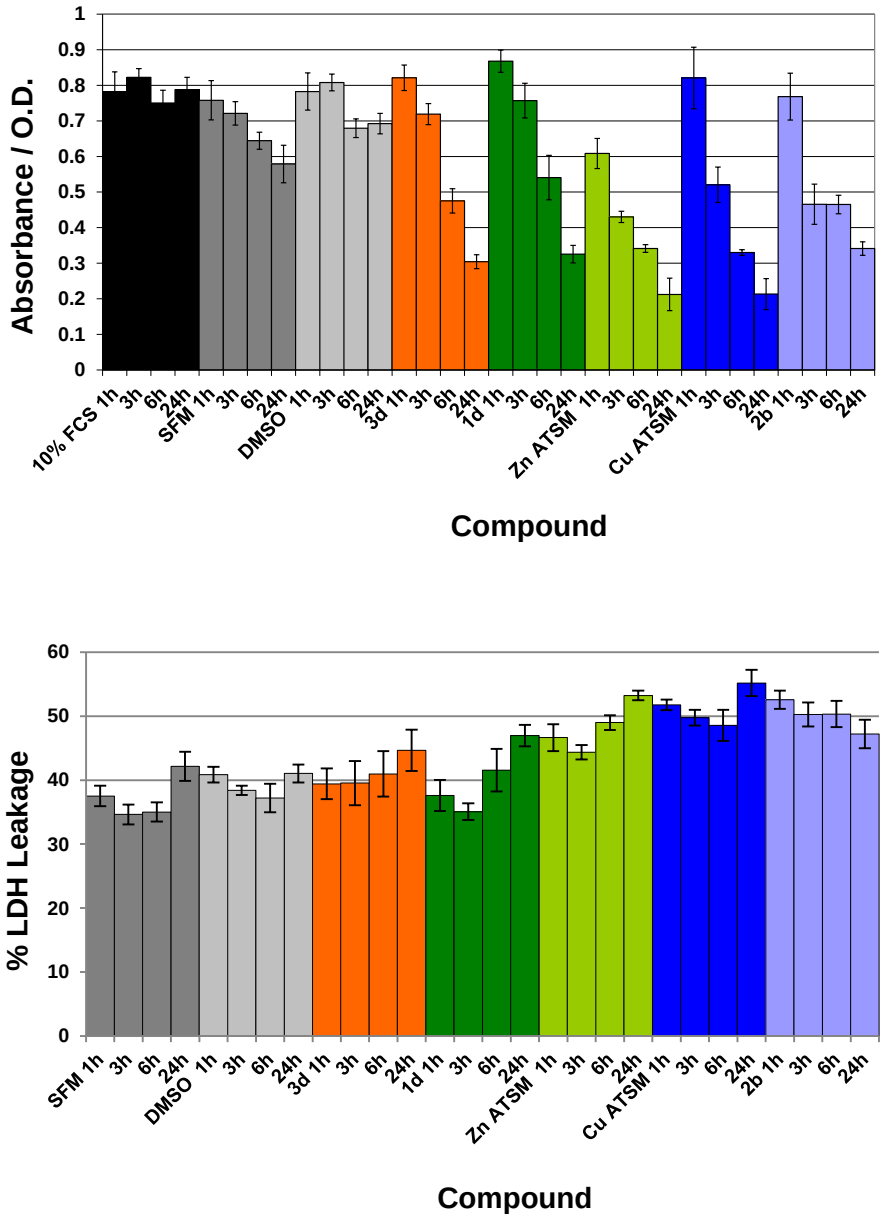

Figure 6.4. MTT assay (above) and LDH assay (below) of HeLa cells, where black is medium control, containing Foetal Calf Serum (FCS), dark grey is the serum free medium (SFM) control, light grey is the DMSO control (99:1, SFM:DMSO), orange is **3d**, dark green is **1d**, light green is Zn[ATSM], dark blue is **2b**. Compounds were incubated in 99:1, SFM:DMSO at 10 μM concentration.

Both assays were in agreement that the (M = Zn and Cu) [ATSM] compounds showed greater overall toxicity and that the remaining compounds were of relatively equal toxicity in this cell line. Zn[ATSM] was the only compound with fast-acting cytotoxicity *(Figure 6.4)*. **2b** showed most of its toxicity within the first 3 hours, which implies that the complex has rapid action on HeLa cells.

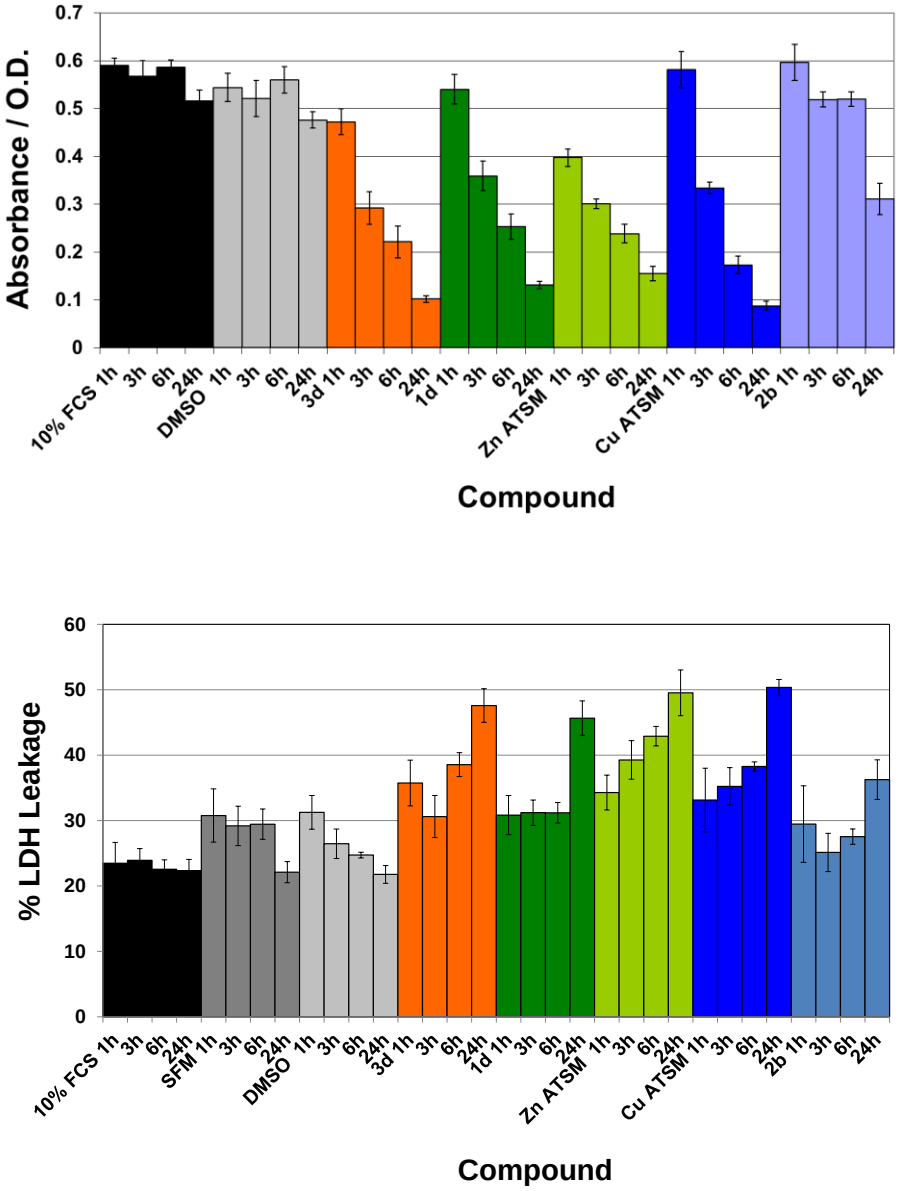

Figure 6.5. MTT assay (above) and (below) LDH assay of MCF-7 cells, where black is medium control, containing FCS, dark grey is the SFM control, light grey is the DMSO control (99:1, SFM:DMSO), orange is **3d**, dark green is **1d**, light green is Zn[ATSM], dark blue is **2b**. Compounds were incubated in 99:1, SFM:DMSO at 10 μM concentration.

LDH leakage was higher than for controls in the first 3 hours for the (M = Zn and Cu) [ATSM] complexes and **2b**, indicating that they cause cell membrane lysis and possibly explaining why there was such a strong correlation between the MI_{50} and the LD_{50} values obtained for **2b**. The **1d** and **3d**, however, did not appear to act on the cell membrane, with similar LDH leakage when compared to the SFM control after 24 hours.

This could clarify the discrepancy of lower cytotoxicity observed for the zinc complexes when tested using trypan blue, which relies on cell membrane damage to assess cytotoxicity.

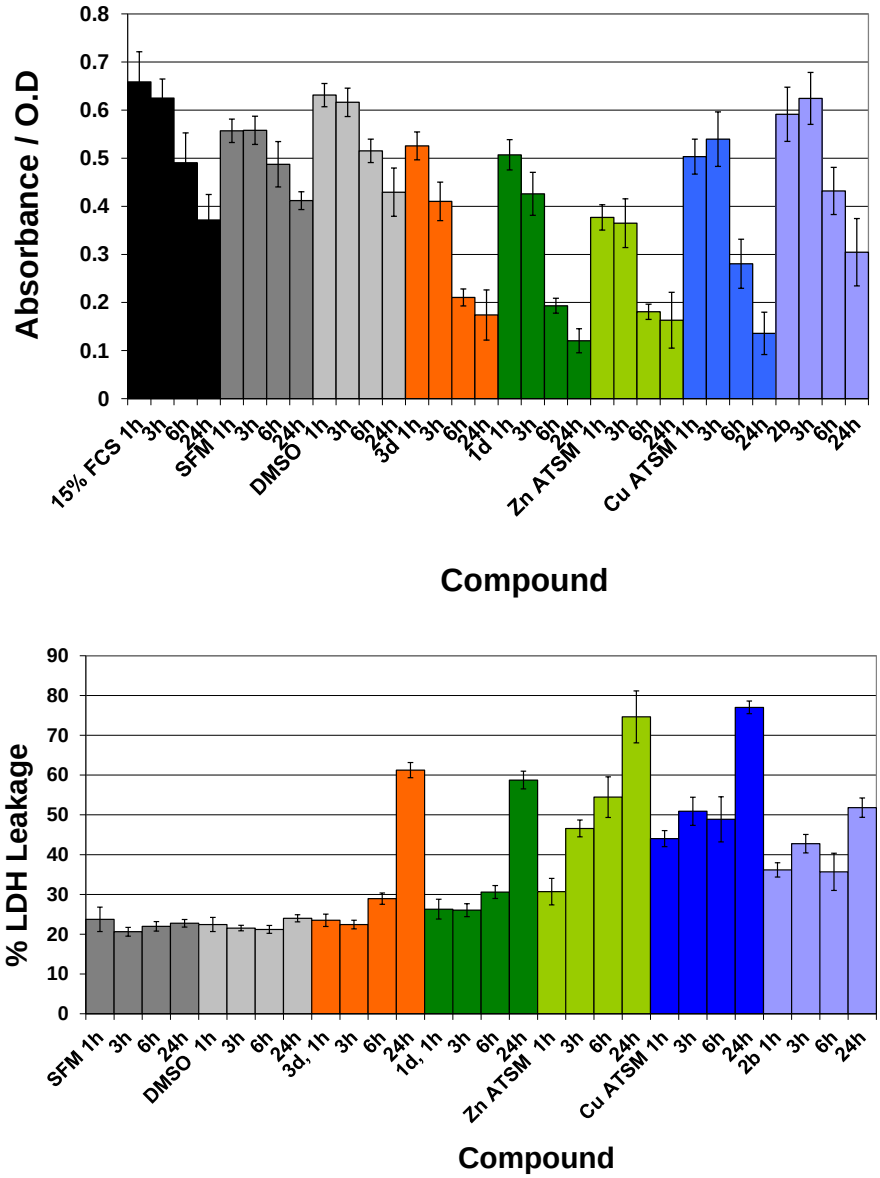

Figure 6.6. MTT assay (above) and LDH assay (below) of FEK-4 cells, where black is medium control, containing FCS, dark grey is the SFM control, light grey is the DMSO control (99:1, SFM:DMSO), orange is **3d**, dark green is **1d**, light green is Zn[ATSM], dark blue is **2b**. Compounds were incubated in 99:1, SFM:DMSO at 10 μM concentration.

All (M = Zn and Cu) [ATSM] and **1d** and **3d** displayed a significant toxicity from 3 hours onwards, where **3d** and Zn[ATSM] showed faster acting toxicity, with maximum

effect during the first hour for Zn[ATSM] *(Figure 6.5)*. **2b**, in comparison showed little toxicity until 24 hours. The LDH assays indicated that some membrane activity was displayed by (M = Zn and Cu) [ATSM] compounds and **3d**.

With exception of Zn[ATSM] all compounds displayed little toxicity until 3 hours. From 6 hours onwards, however, all compounds, excluding **2b** showed high toxicity. The LDH assays indicate significant cell membrane lysis by the (M = Zn and Cu) [ATSM] complexes and **2b** and slight lysis by both **1d** and **3d** compounds. After discussing these compounds in the respective cell lines it was next possible to consider them per compound.

6.3.1 Discussion of trends emerging from *in vitro* cytotoxicity investigations

*6.3.1.1 Compounds: **1d** and **3d***

1d and **3d** displayed rapid moderate toxicity, showing significant difference from the controls at 3 h for FeK4 (non-cancer) and MCF-7 and at 6 h for HeLa and a gradual decrease in cell viability for all cell lines *(MTT assays, Figures 6.4-6.6a)*. **1d** showed significantly greater LDH leakage after 24h in MCF-7 and FEK-4 cells, rendering membrane activity very unlikely for this compound.

For **3d** the LDH assays showed a considerable leakage in MCF-7 and slight leakage in FEK-4 at 6 h, but there was no significant difference between the leakage of controls in HeLa cells. It is therefore possible that for **3d** cell membrane lysis is a mechanism of action in MCF-7, whereas it is more likely to be another mechanism, perhaps DNA damage for HeLa cells. This is a possibility due to the gradual nuclear uptake of **1d** (previously carried out by the group) and **3d** observed in this study by fluorescence microscopy *(Chapter 4.5)*. Furthermore, a long-term LDH assay showed less LDH leakage for **1d** and **3d** than controls, which could be indicative of DNA repair by Poly-ADP ribose polymerase (PARP) *(Figure 6.7)*.[154]

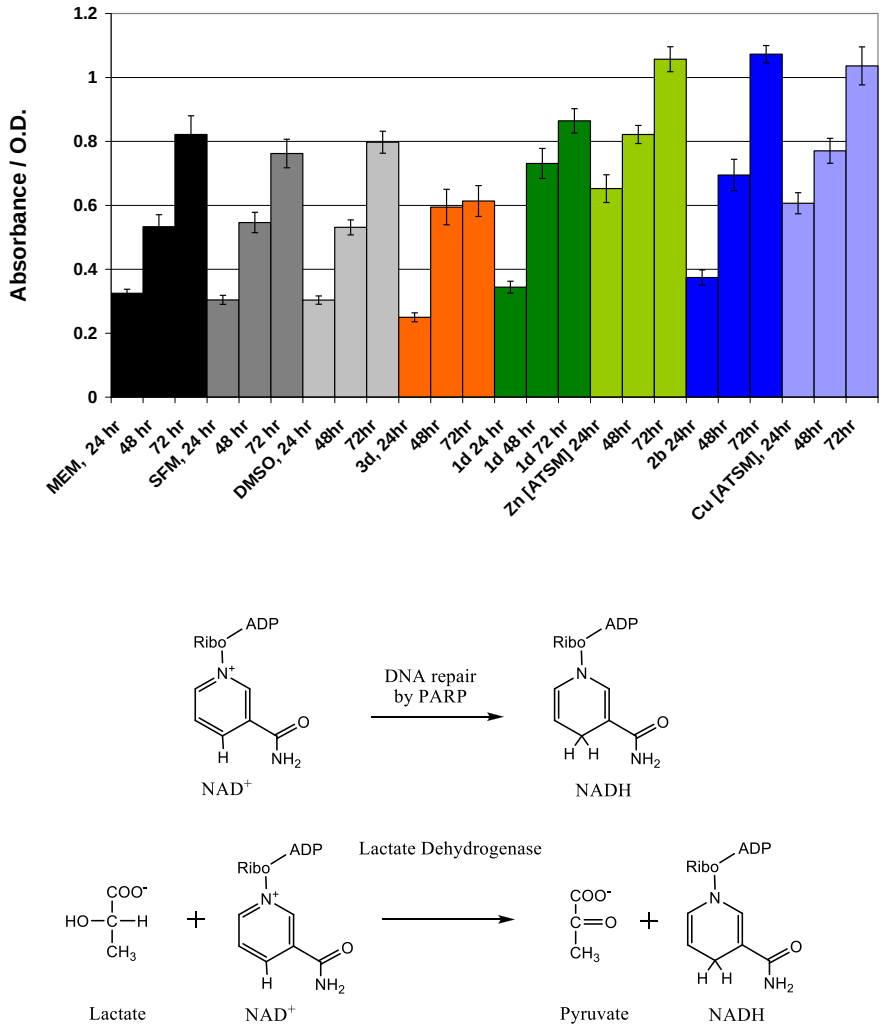

Figure 6.7. long-term LDH assay in HeLa cells (above), where black is medium control, containing FCS, dark grey is the SFM control, light grey is the DMSO control (99:1, SFM:DMSO), orange is **3d**, dark green is **1d**, light green is Zn[ATSM], dark blue is 2b. Compounds were incubated in 99:1, SFM:DMSO at 10 μM concentration. A comparison between the pathways of PARP and LDH, indicating that DNA repair in cancer cells could be the cause of reduced absorbance in an LDH assay (below).

6.3.1.2 Known compound: Zn[ATSM]

Zn[ATSM] displayed rapid toxicity on all cell types, resulting in significantly less cell viability after only 1h incubation and was therefore the most toxic of the compounds tested. Microscopy by Dilworth *et al. (Figure 6.3)* showed nuclear uptake by MCF-7, PC-3 and IGROV (however most of the localisation for IGROV was in the lysosome), indicating that DNA damage is one possible mechanism of toxicity. Leakage was

observed after 3h in all cell lines tested pointing to cell membrane damage as a likely cytotoxicity mechanism *(Figures 6.4-6.6b)*, which is supported by the work of Dilworth *et al*. in that fluorescence was observed in the plasma membrane of MCF-7 cells *(Figure 6.3)*.[62]

6.3.1.3 Known Compound: Cu[ATSM]

The known compound Cu[ATSM] displayed medium toxicity to the cancer cell lines tested and there was significantly less toxicity to non-cancerous FEK-4 cells. This is a promising result since ^{64}Cu[ATSM] is currently in clinical trials as an *in vitro* PET molecular imaging probe, indicating that cytotoxicity is negligible at concentrations required for nuclear imaging. The data show that this compound is likely to cause cell membrane damage in FEK-4 and HeLa cells, and may also in MCF-7 cells, since LDH leakage was observed up to 6h incubation with the complex. Zn[ATSM] is used as a model for the cell uptake of Cu[ATSM], which is not fluorescent due to quenching by the Cu(II) ($3d^9$). Therefore in consideration that Zn[ATSM] enters the nucleus it is reasonable to expect Cu[ATSM] to do likewise indicating DNA damage as another possible mechanism.

*6.3.1.4 Compound: **2b***

Cell viability observed in MCF-7 and FEK-4 when incubated with **2b** showed little variation with controls, making it the least toxic of the compounds tested in this study. The compound, however, showed medium toxicity towards cervical cancer cells, indicating that investigations with further cell lines are necessary to fully understand the cytotoxicity of **2b**. The LDH study indicated significant cell leakage from 1h in HeLa and FEK-4 cells, which decreased with time for HeLa cells. This could indicate that the mechanism of cytotoxicity is by a non-linear mechanism of cell membrane lysis. The microscopy study indicated localisation in the cell membrane, which is suggestive of membrane lysis *(Chapter 2.4)*.

6.4 Summary to Chapter 6

The cytotoxicity of this family of compounds have been investigated in three cell lines allowing comparisons to be made between metal centre, functionality, relative speed of and mode of action on cancerous and non-cancerous cells. It was possible to make general conclusions such as: (a) the metal complexes were more toxic than their bis-substituted free ligands, (b) copper complexes were the least cytotoxic of the metal compounds tested, (c) for all compounds tested so far more activity was observed against cancerous cells than non-cancerous cells indicating a possibility of selectivity.

Further experiments however, in numerous cell lines are needed to fully elucidate if this is a universal prospect for future cancer treatment and diagnosis. The phototoxic effect of these compounds discovered in previous Chapters could be explored as it was not investigated using cell viability or cytotoxicity assays. Whilst there was some exposure to light as the compounds were added to cells, all samples were incubated in absence of light.

The comprehensive localisation of these compounds in a number of organelles observed in previous Chapters indicate that numerous modes of action are plausible, many of which could be investigated further in another study. However the activity on the cell membrane observed in this project suggest that this is a plausible mode of action for the copper complexes, Cu[ATSM] and **2b**, with the lack of membrane activity by the zinc complexes indicative of the different results obtained here by MTT assay and by trypan blue assays.

Chapter 7. Investigations towards the syntheses of a peptide-targeted bis(thiosemicarbazonato) complex, spectroscopic and *in vitro* imaging

7.1 Introduction to Chapter 7

Receptors of many peptides are overexpressed in a large number of cancers and therefore form a means of targeting cancer. Furthermore peptides have an advantage in that they enable fast uptake into tissue of interest and more efficient body clearance when compared to antibodies.[155] Imaging of tumours using peptides was first achieved in 1989 as Krenning *et al.* detected radiolabelled somatostatin using a gamma counter.[156] Each peptide facilitates the targeting of its own unique selection of receptors and tumours, for example somatostatin analogues provide a means of targeting neuroendocrine tumours.

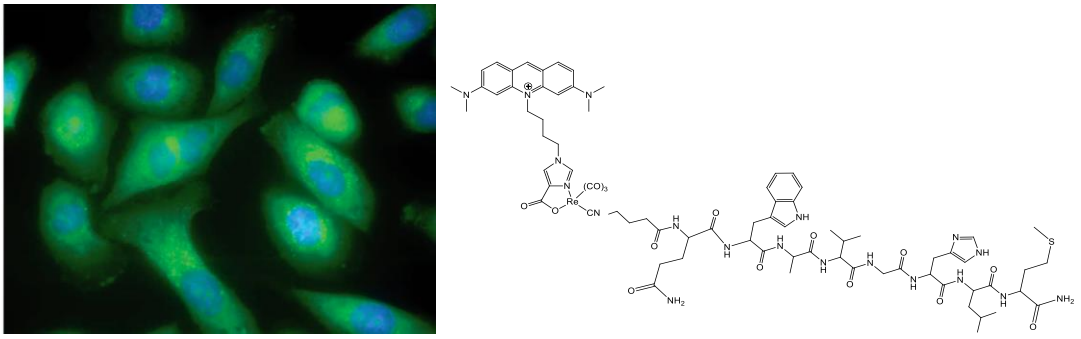

a) **b)**

Figure 7.1. A rhenium tricarbonyl complex conjugated to a bombesin analogue and an intercalator, (right), visualised in fixed PC-3 cells by fluorescence microscopy (left), where green represents the complex and blue the DAPI nuclear stain. [157]

Furthermore bombesin analogues target numerous tumours notably prostate, breast, gastrointestinal and lung cancer, making it an attractive peptide as a component of a molecular imaging agent. Bombesin is a 14-amino acid peptide isolated from amphibian skin, is an analogue of the gastrin-releasing peptide found in mammalians and possesses strong affinity for a G protein-coupled receptor known

as GRPR.

The first *in vivo* investigation of bombesin analoges was carried out by Van de Wiele *et al.* showing targeting of breast and prostate cancer patients in 2000. More recently tricarbonyl rhenium and technetium complexes with acridine derivatives showed nuclear uptake *via* fluorescence and activity based studies respectively.[44] Alberto *et al.* developed rhenium and technetium complexes comprising of a DNA interchelator for nuclear targeting, a biologically active molecule (here a bombesin analogue) and a linker, cleavable upon cell entry displaying uptake in both the nucleus and the cytoplasm *(Figure 7.1).* [157, 158]

In addition to bombesin-targeted copper thiosemicarbazonato complexes mentioned in the Introduction, copper and gallium bombesin-conjugates have been synthesised paving the way for further investigations with this peptide. For example, a bombesin analogue conjugated to NO2A radiolabelled with ^{64}Cu allowed visualisation of PC-3 xenografts, with preliminary *in vitro* studies recently carried out on a new cyclam bombesin derivative.[53, 159] A DOTA-PEG$_4$-BN(7-14) bombesin analogue was labelled with $^{67/68}$Ga and ^{177}Lu, showing good tumour uptake in PC-3 xenografted nude mice, where $^{67/68}$Ga can act as a diagnostic radionuclide and ^{177}Lu as a therapeutic.[99]

Conjugation of a bombesin analogue to the acenaphthenequinone bis(thiosemicarbazonato) complex could result in the development of dual-modal fluorescent and PET or SPECT imaging probes with potential for simultaneous therapy due to their cytotoxicity. Furthermore, cell studies under normoxic conditions have shown that all compounds have toxicity towards non-cancerous as well as cancerous cells *(Chapter 6).* Therefore, it would be beneficial to add a targeting group such as bombesin onto the compounds for added cancer selectivity. For complexes that are found not to be hypoxia selective, this would provide a means of targeting cancer and thus the aim of this chapter was to synthesise an acenaphtenequinone bis(thiosemicarbazonato) complex conjugated to bombesin. The first objective was to synthesise a stable and intrinsically fluorescent precursor, which *via* a linker could be attached to the peptide, followed by its spectroscopy and in vitro characterisation. Finally the goal of this Chapter was to investigate the

possibility to couple the complex to the peptide and analyse it by the same means as the precursor.

7.2 Attempted ligand synthesis

A free ligand mono(thiosemicarbazonato) ligand was attempted by my mixing 1 equivalent of thiocarbohydrazide with an equivalent of acenaphthenequinone in 150 mL of ethanol *(Figure 7.2)*. Upon reflux 4 drops of glacial acetic acid were added and after 3 hours the suspension was filtered whilst hot yielding a yellow solid, which was analysed by mass spectrometry and NMR spectroscopy.

Following this, the reaction was repeated with an excess of thiocarbohydrazide, in 30 mL of ethanol and with 4 drops of acetic acid as before. After three hours the reaction was filtered, producing a similarly coloured powder. Furthermore, from the filtrate crystals suitable for X-ray diffraction formed overnight *(Figure 7.3)*.

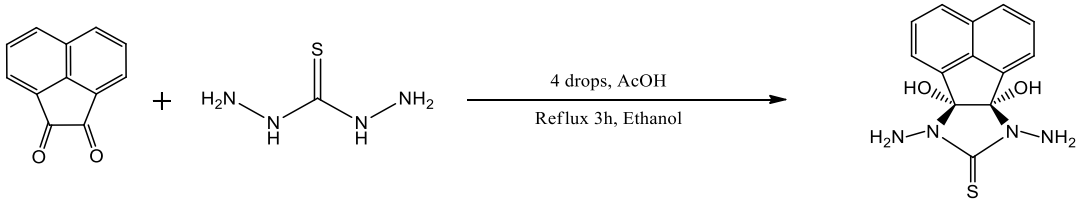

Figure 7.2. Synthesis attempt to make a free ligand suitable for peptide conjugation

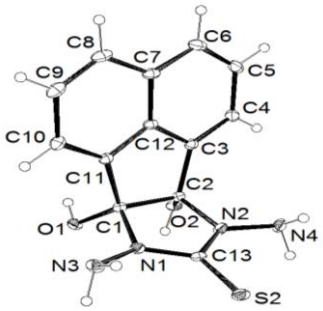

Figure 7.3. ORTEP representation of the free ligand produced by the reaction described above.

The NMR spectra were identical for the solid and the crystals from this reaction as well as the solid from the reaction using one equivalent of thiocarbohydrazide, indicating that the same product had been formed. The crystal structure (below) as well as a mass spectrum of 289.074 confirmed that the desired product of a

thiosemicarbazonato free ligand analogous to those of previous chapters as well as suitable for addition of a targeting group had not been formed and that another route should be pursued (the calculated value was 289.075).

7.3 Initial attempts *via* protecting group chemistries

7.3.1 Synthesis of the mono-substituted t-Boc protected amine thiosemicarbazide

A zinc precursor complex with t-Boc protected amines which could be de-protected under acidic conditions to a mono-substituted t-Boc protected amine thiosemicarbazide was therefore desirable. Prior to the synthesis of the complex DFT calculations were carried out, which confirmed the theoretical thermodynamic stability of the complex *(Figure 7.4)*.

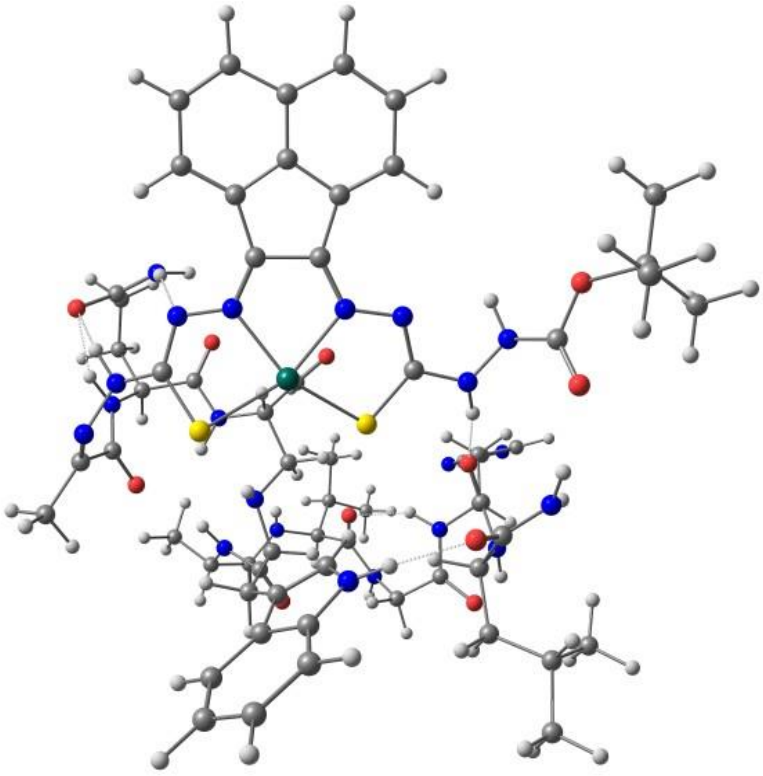

Figure 7.4. DFT optimisation of the symmetric isomer of a zinc bis(thiosemicarbazonato complex with a 7 amino acid bombesin analogue as one substituent and a t-Boc protected amine as the other in the gas phase by B3LYP 6-31G(d,p). Where grey = carbon, white = hydrogen, blue = nitrogen, red = oxygen, dark green = zinc.

Firstly 500 mg of thiocarbohydrazide was stirred in 5 mL DMSO for 20 minutes, followed by dropwise addition of an equivalent of Boc anhydride (1030 mg). After stirring at room temperature for 2 hours the reaction was quenched by adding 5 mL of water dropwise. The solution was frozen using dry ice and acetone, which lead to the precipitation of a white solid. Mass spectrometry and NMR spectroscopy showed that the resultant product was a mixture of a mono-substituted and a bis-substituted thiocarbohydrazide. TLC plates showed that both compounds formed long tails for a broad range of concentrations tested and therefore would not be readily isolated by a separation column. Purifications and extractions based upon solubility were also found to be unsuccessful and since the zinc complex synthesis described in Chapter 3 requires vast excess of thiosemicarbazide separation by semi-preparative HPLC was not a practical alternative.

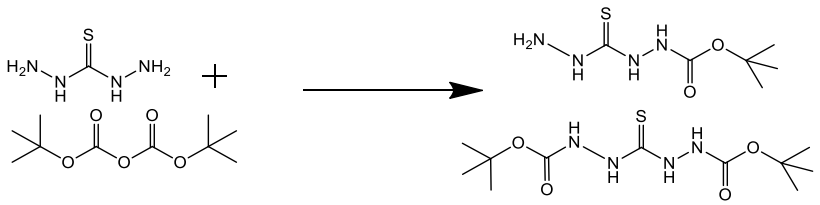

Figure 7.5. Synthesis of mono-substituted and bis-substituted thiocarbohydrazide

The reaction conditions were therefore modified. Firstly using more dilute conditions resulted in very little precipitation; secondly using four equivalents of thiocarbohydrazide yielded a mixture of thiocarbohydrazide as well as the other two aforementioned products. This was confirmed by mass spectrometry m/z values of 129.02 for thiocarbohydrazide, 229.07 for mono-substituted thiocarbohydrazide and 329.13 for bis-substituted thiocarbohydrazide.

7.3.2 Attempt to synthesise a Zinc(II) complex incorporated a t-Boc protected thiosemicarbazide

Using the assumption that the bis-substituted t-Boc protected thiocarbohydrazide would not react with diketone acenaphthenequinone and would possess significantly different solubility to the resultant zinc complex a synthesis was attempted using a mixture that did not include thiocarbohydrazide. An initial trial using a 50 mg mass of acenaphthenequinone was undertaken under analogous conditions as were used for the synthesis of the zinc bis(thiosemicarbazonato) complexes in 2 mL of glacial acetic acid. This method was not successful, producing a black solid, which was likely a polymer.

Next, these conditions were modified to be carried out in 50 mL of 1,4-dioxane with 1 mL of acetic acid, over molecular sieves *(Figure 7.6)*. After 30 hours the reaction was filtered whilst hot, which gave a white solid corresponding to crushed sieves. The filtrate was allowed to cool to room temperature resulting in the precipitation of an orange solid, in which mass spectrometry confirmed the presence of the desired compound, whilst NMR spectroscopy showed that the product was impure. The temperature of the filtrate was reduced, which resulted in further precipitation, with the orange solid produced giving similar results as described above. Therefore, the filtrate was rotary evaporated and washed with 50 mL of diethyl ether providing the desired product that by NMR spectroscopy showed significantly better purity, which was confirmed by LC-MS, and gave 34% yield and was successful on only one occasion.

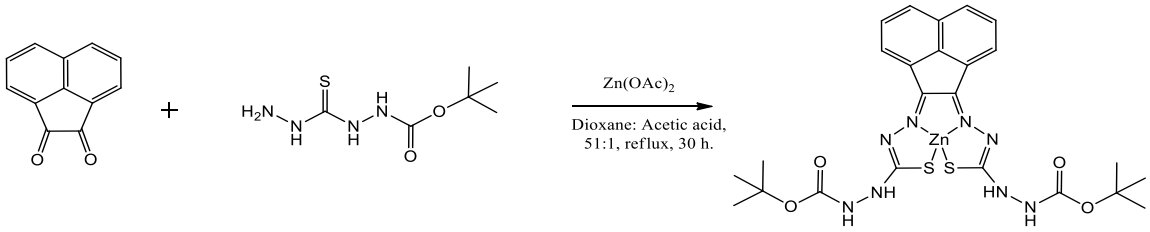

Figure 7.6. Synthesis of acenaphthenequinone t-Boc protected amine zinc bis(thiosemicarbazone (**1e**)

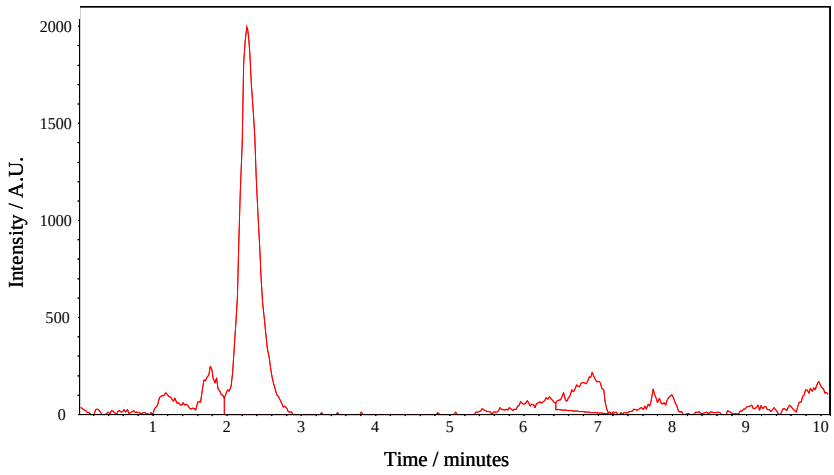

Figure 7.7. Chromatogram of **1e** from HLPC, showing a single major peak at 2.4 minutes

The compound, characterised by LC-MS, which gave peaks for $[M-H]^-$ and $[2M-H]^-$ m/z at 619.09 and 1243.18 respectively with a single LC trace at 2.4 minutes and was investigated by ^{1}H NMR spectroscopy *(Figure 7.7)*.

7.3.2.1 NMR spectroscopy study of t-Boc protected bis(thiosemicarbazonato) complex, ***1e***

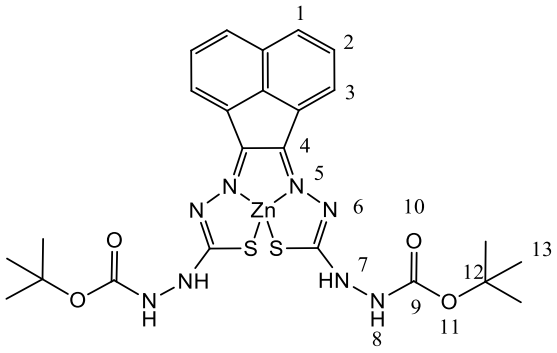

Figure 7.8. Numbering of atoms of **1e**.

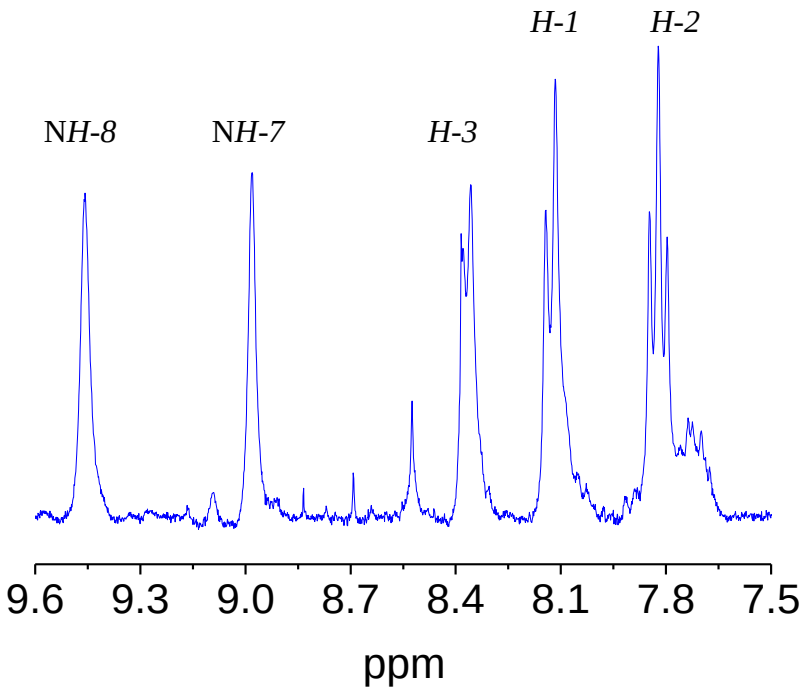

Figure 7.9. Selected resonances from the ^{1}H NMR spectroscopy of **1e** in the region of δ 7.5-9.6 ppm.

Due to exchange with deuterated solvent N*H* protons appear as broad singlets. The spectra show two sets of doublets and one triplet as would be expected from an aromatic backbone *(Figures 7.8 and 7.9)*. This is indicative of a predominantly symmetric structure, however small peaks such as at 8.46 signify that there may be a small proportion of asymmetric isomers present, which would be consistent with previous studies by the group [31]. A singlet would be expected of the *tert*-butyl groups and since this is not a clean signal and a greater integral than would be expected is observed, it may also indicate some asymmetric isomer presence.

7.3.3 Spectroscopic investigations in solution

An initial 200-800 nm 2D scan in DMSO at 100 μM was used in order to assess intrinsic fluorescence of **1e**, the excitation wavelength of maximum emission and the range of excitation and emission *(Figure 7.10*). The compound has a broad excitation and emission of 260-660 nm and 480-755 nm respectively, with the excitation wavelength resulting in maximum emission at 510 nm at 572.5 nm. It may be possible that interchange with the dimeric form of the compound may reduce fluorescence

emission. Compound **1e** has been shown to be weakly fluorescent and therefore has potential for fluorescence imaging.

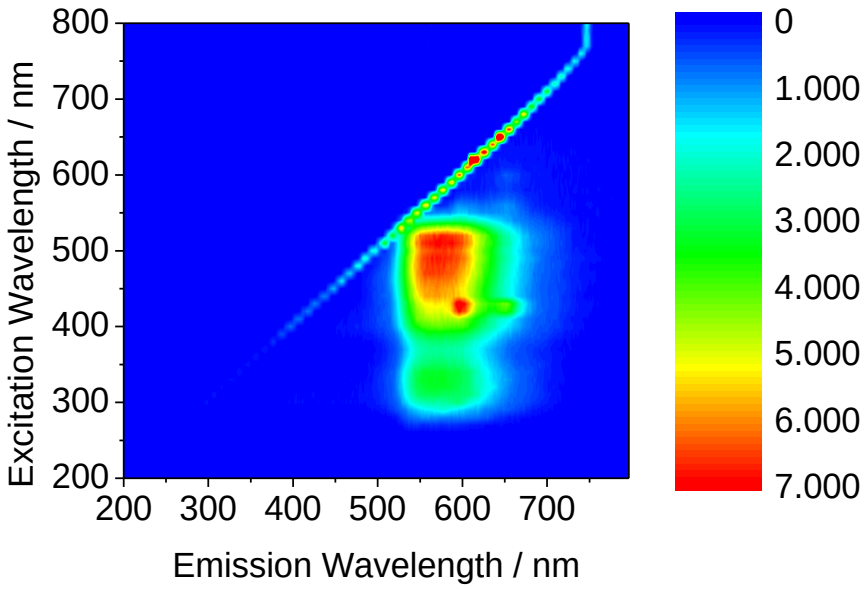

Figure 7.10. 2D fluorescence scan of the **1e** in DMSO at 100 μM.

Quantum yield is the proportion of absorbed and emitted photons and has been estimated in DMSO at 100 μM as 0.007 by:

$$\Phi_S = \Phi_R \cdot \left(\frac{D_S}{D_R}\right) \cdot \left(\frac{A_R}{A_S}\right) \cdot \left(\frac{I_R}{I_S}\right) \cdot \left(\frac{\eta_S}{\eta_R}\right)^2$$

Where Φ = quantum yield, D = integrated area under emission band, S = sample, A = absorbance of solution at excitation wavelength, R = reference, η = refractive index of solvent, I = maximum intensity of excitation band $[Ru(bipy)_3][PF_6]_2$ in water was used as a reference, with a quantum yield of 0.042. The quantum yield result confirms that the compound is weakly fluorescent in comparison with previously synthesised compounds.[47]

7.3.5 Synthesis of t-Boc protected amine copper(II) bis(thiosemicarbazonato) complex

The analogous copper complex (**2e**) was synthesised by stirring with 2 equivalents of copper acetate with **1e** in methanol for 72 h, following isolation of a black solid by rotary evaporation in 40% yield.

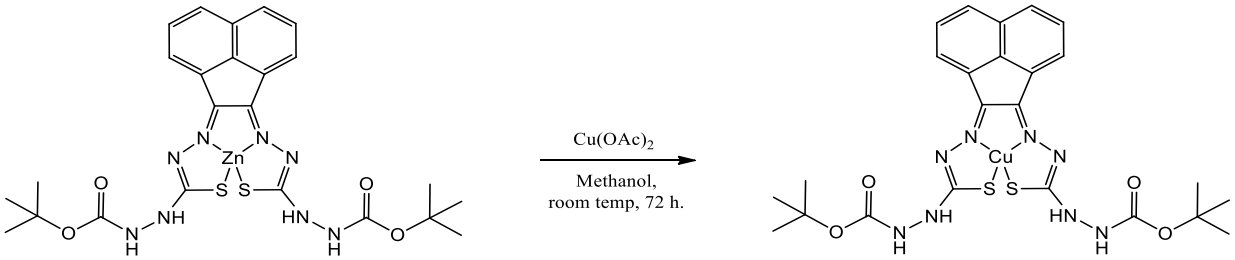

Figure 7.11. Synthesis of acenaphthenequinone t-Boc protected amine copper bis(thiosemicarbazone (**2e**)

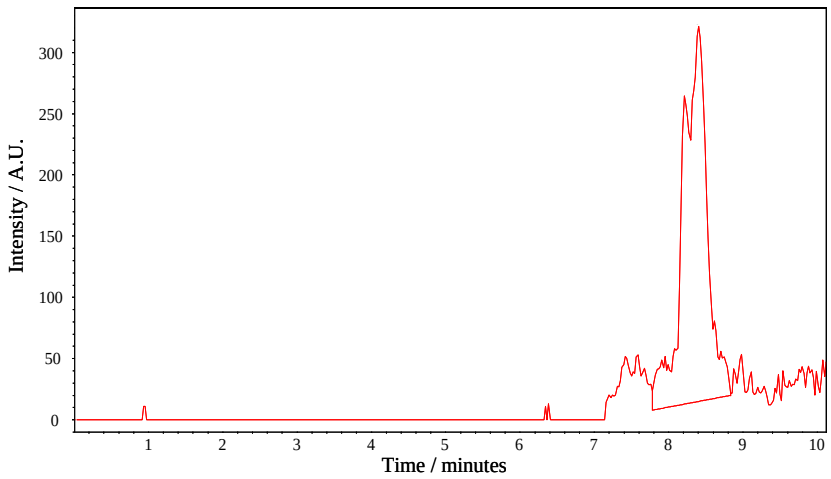

Figure 7.12. HPLC trace of compound **2e**.

7.3.6 Radiolabelling experiments

7.3.6.1 Radiolabelling with Copper-64

The complex, **1e** was radiolabelled with ^{64}Cu, using $^{64}Cu(OAc)_2$ as the starting material. After 2 h stirring at room temperature the desired ^{64}Cu complex had not been cleanly made; however after 24 h the radio-trace appeared quite clean *(Figure 7.13)*, indicating that the complex can be radiolabelled cleanly despite it not being a rapid process. It is possible that some of these peaks represent the mono-deprotected, di-deprotected, a dimeric form of the compound and asymmetric isomers.

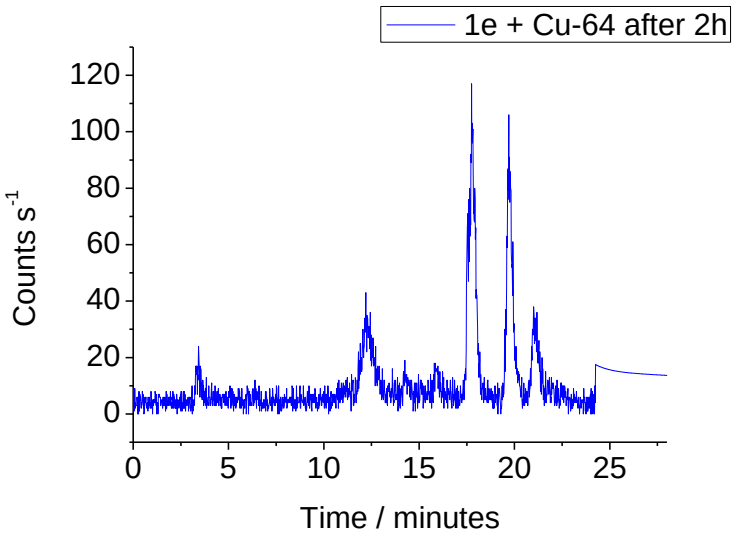

(a)

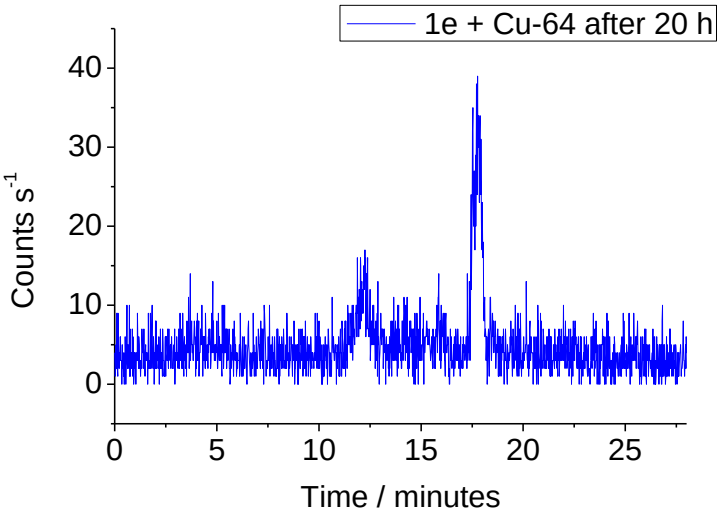

(b)

Figure 7.13. Transmetallation of **1e** to **2e** with Cu-64 (a) after ca. 2 hours and (b) after ca. 24 hours

7.3.6.2 Radiolabelling with Indium-111

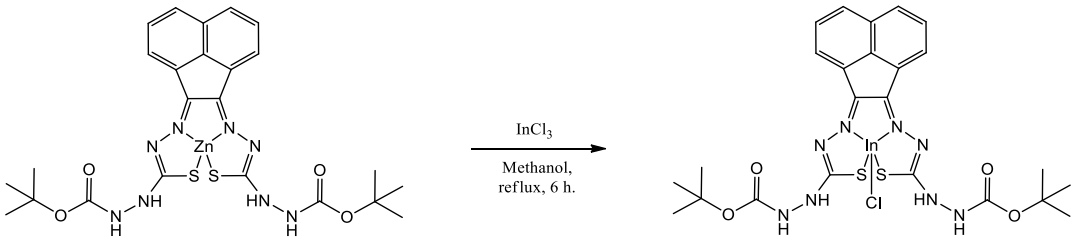

Figure 7.14. Synthesis of acenaphthenequinone t-Boc protected amine indium(III)chloride bis(thiosemicarbazone) (**4e**)

1e was further radiolabelled with indium-111 yielding two major peaks, one indicative of $^{111}InCl_3$ at 3.8 minutes and the other at 7.6 minutes could be due to the indium(III) tert-butyl carbamate (**4e**) substituted bis(thiosemicarbazonato) complex *(Figure 7.15)*. There was sufficient **1e** for radiolabelling, however there was not enough to make **4e** to enable spectroscopic characterisation. Peak-splitting observed in the Radio channel could be explained by formation of a mixture of symmetrical and unsymmetrical isomers, or could be explained by de-protection of the *tert*-butyl groups resulting in the formation of two species of similar size and polarity. NMR spectroscopy studies of **4e** once it is synthesised in sufficient quantities would determine the proportion of the respective isomers. Unfortunately the reproducibility of the mono-substituted t-Boc protected thiocarbohydrazide synthesis was poor and other synthetic routes were investigated.

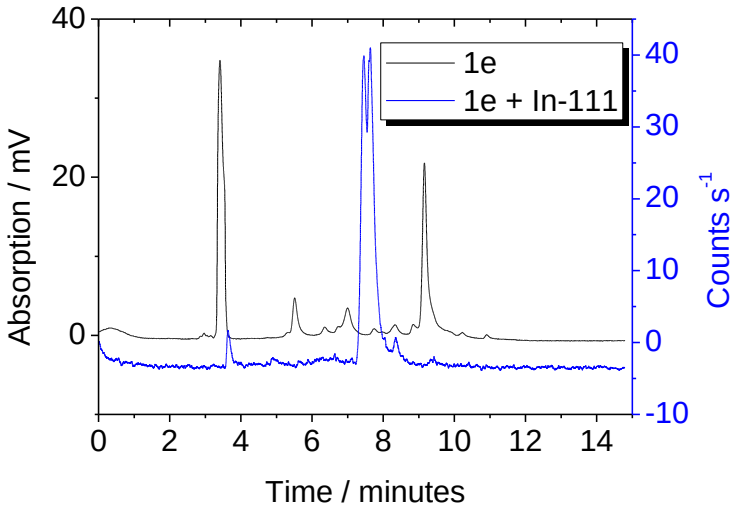

Figure 7.15. 1e complex radiolabelled with In-111

7.4 Synthesis of an asymmetric zinc complex precursor

As an alternative synthetic means of developing a peptide-targeted bis(thiosemicarbazonato) complex, an equivalent of mono-substituted thiosemicarbazone, i.e. **ia**-**id**, was added to three equivalents of zinc acetate. To this a vast excess of thiocarbohydrazide was added, with the mixture refluxed in acetic acid for 30 h. The suspension was filtered whilst hot and washed with 100 mL of diethyl ether giving a yellow solid for **1aN** and **1bN**, a dark red solid for **1cN** and a brown solid for **1dN**. Successful synthesis was confirmed by ES-MS, with m/z values of 420.00, 434.02, 482.02 and 446.02 for **1aN**, **1bN**, **1cN** and **1dN** respectively and by ^{1}H-NMR spectroscopy *(Figures 7.17-7.19).*

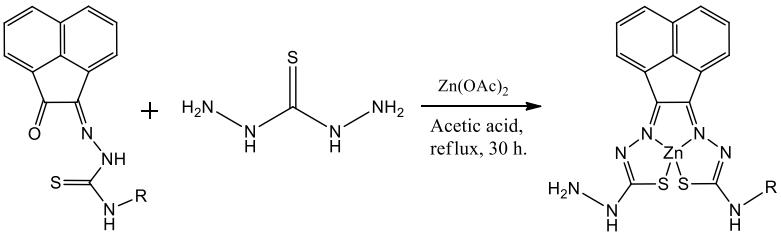

Figure 7.16. Reaction scheme for amine-functionalised zinc bis(thiosemicarbazonato) complexes.

Interestingly, the ^{1}H NMR spectroscopy or **1cN** clearly shows the presence of one isomer, with *H-1* present as one doublet representing 2 protons, which would be otherwise non-equivalent for the asymmetric isomer. The *H-2* and *H-2'* resonances were non-equivalent, but overlapping, indicating that the amine group does have a small effect on the symmetry of the complex. The exchange observed in previous chapters would in fact cause two isomers to be formed as below, which would display up to six resonances for *H-2* and *H-2'*. Contrary to **1cN**, **1bN** appears to exist as more than one isomer.

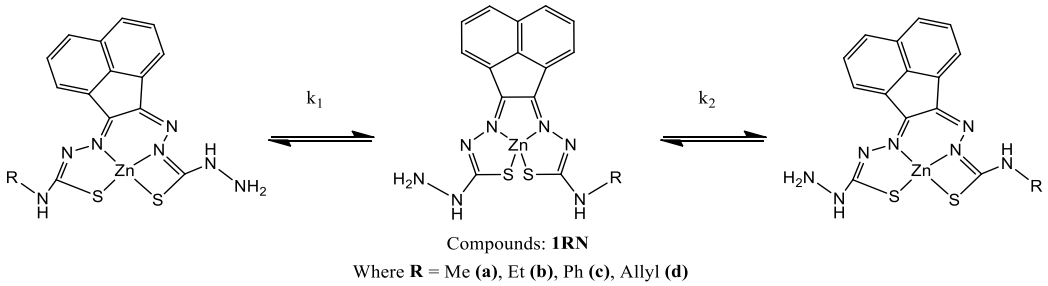

Figure 7.17. Proposed isomeric exchange for amine-functionalised zinc complexes

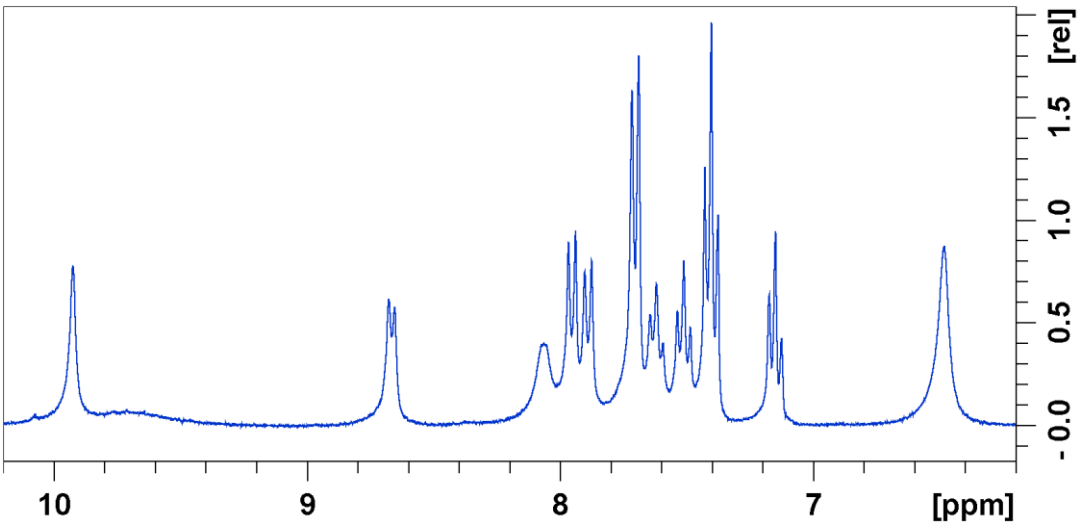

Figure 7.18. ^{1}H-NMR spectroscopy of **1cN** in d_6-DMSO, 300 MHz.

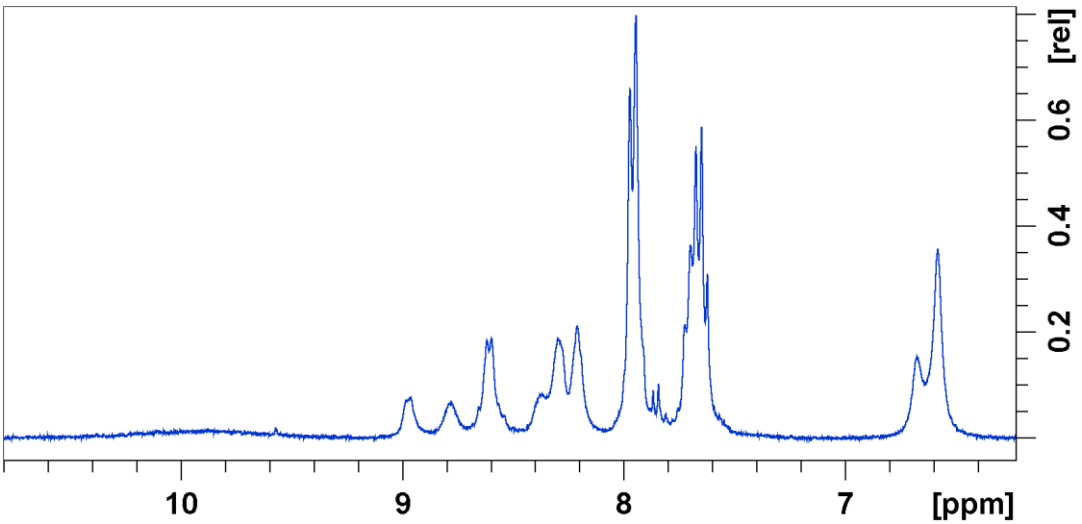

Figure 7.19. ^{1}H-NMR spectroscopy of **1bN** in d_6-DMSO, 300 MHz.

Furthermore in order to synthesise a gallium complex the asymmetric ethyl and amine-substituted 50 mg of zinc **1bN** was heated into 2.5 mL of DMSO, to which an excess of gallium chloride was added and 30 mL of MeOH. This was refluxed under an

atmosphere of nitrogen for 6 hours and was filtered after cooling to room temperature. The solution was removed *in vacuo* and the resultant material washed with 10 mL of ethyl acetate, followed by two times 10 mL of diethyl ether. This yielded an orange solid of 45 mg, which was confirmed as **3bN** by m/z of 438.01 by mass spectrometry and ^{1}H NMR, which displayed the presence of one isomer only *(Figure 7.20)*.

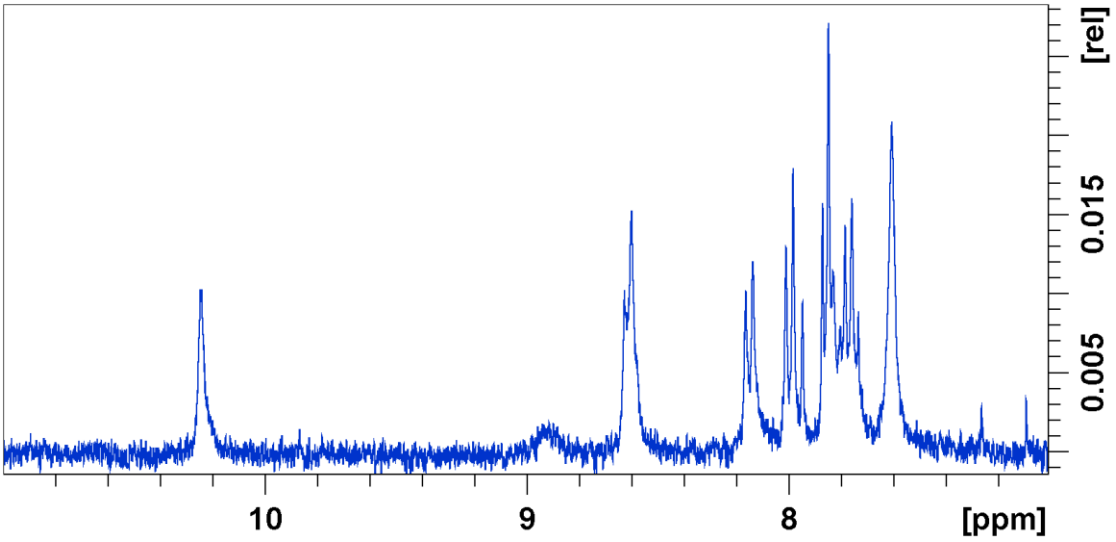

Figure 7.20. ^{1}H-NMR spectroscopy of **3bN** in d_6-DMSO, 300 MHz.

7.4.1 Fluorescence spectroscopy

Fluorescence spectra were obtained in DMSO for initial scans between 200-800 nm, in order to obtain information about intrinsic fluorescence and $\lambda_{em\text{-}max}$ using solutions of 100 μM. Ranges of absorption and emission, which are important with regards to cytotoxicity assays and fluorescence imaging, were also assessed using the 2D contours as a guideline *(Figures 7.21-7.22 and Table 7.1)*. Relevant cytotoxicity assays use absorbance readings at 570 nm, therefore there should be minimal or no excitation at this wavelength, which was true for each complex. Fluorescence emission corresponding to the amine-substituted zinc and gallium complexes was notably weaker than previously characterised symmetric zinc complexes and gallium complexes. Interestingly the λ_{max} of emission was blue shifted, yet with λ_{max} of excitation being brought to 470 nm. Furthermore, the excitation and emission maxima of gallium complex **3bN** (340 nm, 526 nm) were significantly lower than that of **3b** (500 nm, 556 nm), indicating a large Stoke's shift for this complex. The excitation range of **3bN** was

lower than **3b**; however the range of emission was broader. The amine group therefore has a considerable influence on the spectroscopic properties of these complexes.

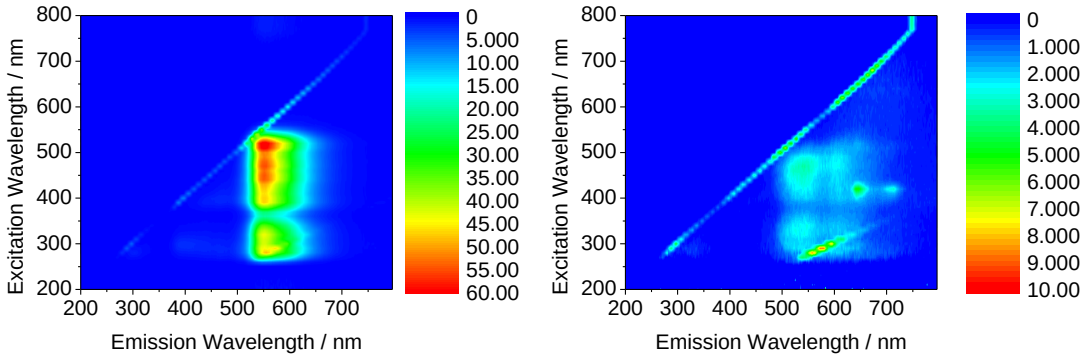

a) **b)**

Figure 7.21. 2D fluorescence scan in DMSO at 100 μM a) of **1d**, b) of **1dN**

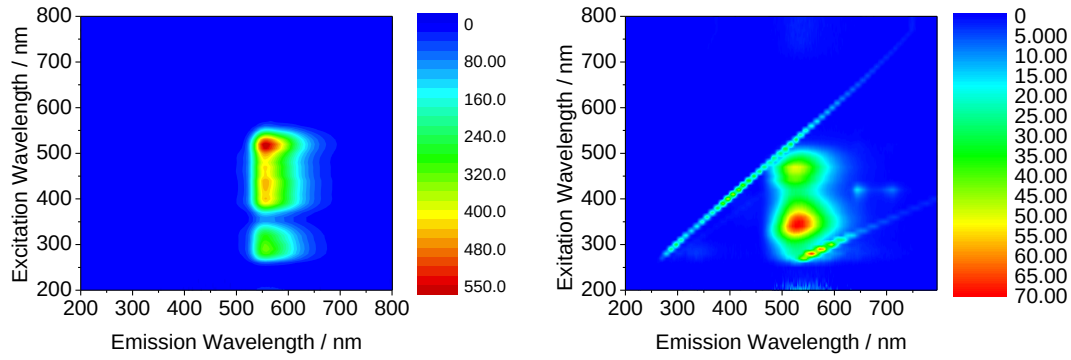

a) **b)**

Figure 7.22. Fluorescence mapping: 2D fluorescence scan in DMSO at 100 μM a) of **3b**, b) of **3bN**

Table 7.1. Fluorescence spectroscopy of zinc and gallium bis(thiosemicarbazonato) complexes

Compound	$\lambda_{ex\text{-}max}$ / nm	Excitation range / nm	$\lambda_{em\text{-}max}$ / nm	Emission range / nm
1c	440	250-590	581.5	535-723.5
1d	520	250-570	551	490-695
1cN	470	250-650	553	496-734
1dN	470	260-570	539	480-738
3b	500	250-570	556	500-685
3bN	340	250-530	526	459.5-684.5

7.4.2 *In vitro* cellular imaging

7.4.2.1 Laser scanning confocal microscopy and fluorescence lifetime imaging study

Cells were cultured using standard protocols, analogous with earlier investigations on fluorescent thiosemicarbazones and following the same method as described in previous chapters. As was observed above, fluorescence was weak, however emission significantly greater than autofluorescence was measured within the cell when incubated in cancer cells at 100 μM. In agreement with the study on symmetric bis(thiosemicarbazonato) complexes of this family of compounds, uptake appeared to be well dispersed within the cytoplasm of the cell. The uptake of the zinc bis(thiosemicarbazonato) complexes (**1bN**, **1cN** and **1dN**) with an amine functionality displayed comparable uptake to each other when comparing the different substituent complexes *(Figure 7.23)*.

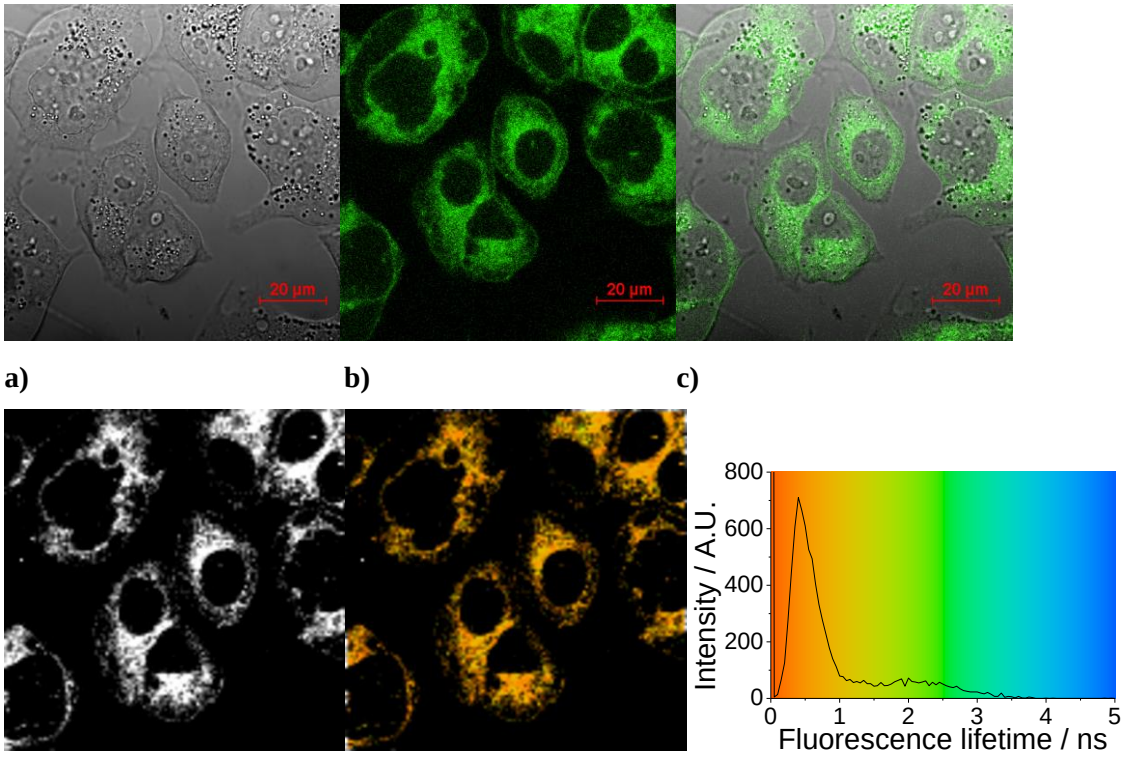

Figure 7.23. Two-photon fluorescence imaging of complex **1bN**, 100 μM, 1% DMSO, λ_{ex} = 910 nm, incubated in MCF-7 cells for 20 minutes. a) DIC micrograph. b) Micrograph of green channel with excitation at 488 nm. c) Overlay of a) and b). e) Fluorescence intensity profile. f) Fluorescence lifetime map (τ_m). g) The corresponding lifetime distribution plot in ns.

The TCSPC in DMSO at 10 mM of these zinc complexes were similar each with a major component of ca. 0.05 ns, with a minor component at ca. 0.2 ns. The minor component observed in solution closely resembled the major component acquired in cancer cells at both wavelengths for all cell lines that these compounds were tested in indicating stability and a conformational change in presence of cells. Furthermore, the asymmetric gallium complex, **3bN**, with slightly stronger fluorescence was observable in HeLa and PC-3 cells at 50 μM, displayed similar uptake as was displayed by the analogous zinc complex *(Figure 7.24)*. The fluorescence lifetime (TCSPC) of **3bN** in DMSO, 10 mM possessed two components, which when excited by 810 nm and 910 nm gave comparable results of ca. 0.65 ns and 2.4 ns, each of almost equal weighting.

The same components for complex **3bN** were observed in HeLa and PC-3 cells, with the shorter component of 0.465 ns, 0.266 ns FWHM and 0.442 ns, 0.274 respectively accounting for 86 % of the fluorescence lifetime indicating a difference in molecular conformation in the cellular environment. In the same way, these data and the agreement in solution and in cells provide strong evidence that this complex remains intact *in vitro*. Interestingly this shows a large difference in fluorescence lifetime when changing the metal, which was much more significant when comparing the lifetimes of the symmetric bis(thiosemicarbazonato) complexes.

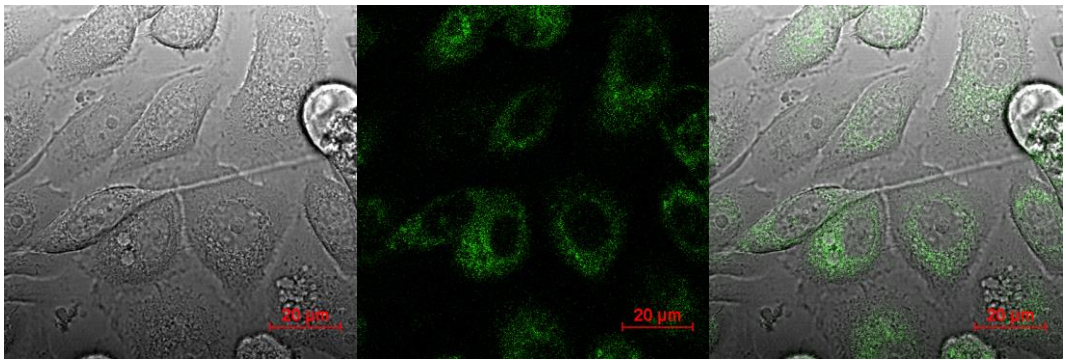

a) **b)** **c)**

Figure 7.24. Single-photon confocal microscopy images of **3bN** in PC-3 cells, 50 μM, 0.5% DMSO, 20 minutes, at 37°C (a) DIC image, (b) excitation at 488 nm, emission >505 nm, (c) is an overlay of (a) and (b) Scalebar: 20 μm.

7.4.3 *In vitro* cytotoxicity investigations

After demonstrating that these novel complexes enter cells it was possible to estimate their cytotoxicity, using the same method as described in Chapter 6 to obtain MI_{50} values. These were determined in HeLa cells as 8 μM ± 2μM for **1aN**, 38 μM ± 8 μM for **1bN**, 0.68 μM ± 0.08 μM for **1cN** and 16 μM ± 1 μM for **1dN**. It is interesting and surprising that symmetric zinc complexes **1b** and **1c** possessed comparable cytotoxicity, yet the modification of functionality to include an amine group resulted in a decrease in cytotoxicity for **1bN** and an increase in cytotoxicity for **1cN**. Furthermore **3bN** did not cause 100% cell death indicating its low cytotoxicity. The MI_{50} value was therefore determined to be of greater than 47 μM ± 6 μM, which is significantly less toxic than **3b** (1.6 μM ± 0.2 μM), since **3b** and **3bN** possess similar solubility. This indicates a notable difference in cellular activity followed by this molecular alteration, but also greater suitability as a diagnostic, which requires low cytotoxicity.

7.4.4 Derivatisation of a targeting peptide model

These complexes possessing an amine group were designed to allow a targeting group such as a peptide to be added and due to the suitability observed it was appropriate to continue and attempt to couple these complexes. A seven amino acid peptide, bombesin analogue was synthesised by Jennifer Williams and Fatima Merzoug *via* solid state synthesis and purified using semi-preparative HPLC by the author. Prior to peptide coupling it was necessary to derivatise the peptide with a linker, for which purpose pyruvic acid was utilised. An equivalent of pyruvic acid was added to coupling agents EDC (1-ethyl-3-(3'-dimethylaminopropyl) carbodiimide) and HOBt (hydroxybenzotriazole) on ice in DMF. After 45 minutes 5 mg, (1 equivalent) of bombesin was added followed by dropwise addition of DIPEA (*N*,*N'*-diisopropylethylamine) until pH 8 was reached. This was allowed to react for 2 hours and was subsequently extracted from DMF and purified using a solid phase extraction cartridge, with the resultant product confirmed by mass spectrometry and HPLC.

7.4.5 Peptide coupling to a zinc(II) complex

Following this 5 mg of derivatised bombesin analogue (4.55 μmols) was added to 2.0 mg (4.55 μmols) of zinc complex, compound **1bN** or compound **1dN** in 400 μL of DMSO, for the purpose of synthesising compound **1bB** (ethyl derivative) or **1dB** (allyl derivative) *(Figure 7.25)*. To this mixture 10 mL of HPLC grade methanol was added followed by 1 drop of concentrated HCl (32%), resulting in an instant colour change from dark orange to yellow. After stirring at 30°C for ca. 16 hours, the solution became pale orange and was freeze-dried *in vacuo*. Reaction mixtures of complexes **1bB** and **1dB** were then purified using semi-preparative HPLC as below, λ_{abs} = 400 nm *(Figures 7.32-7.33, Figures B.4-5)*. Preliminary imaging in three cancer cell lines has been carried out, demonstrating characteristics significantly different from other bis(thiosemicarbazonato) complexes previously observed. Attempts have been made to ionise the new complex for analysis by mass spectrometry, but have so far been unsuccessful.

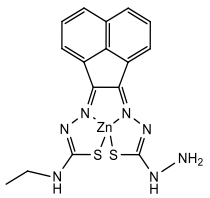

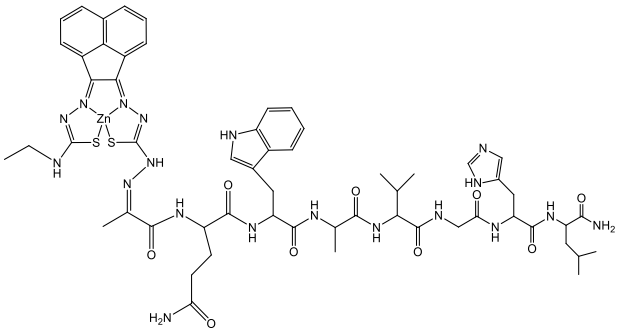

Compound **1bN** Compound **1bB**

Figure 7.25. Molecular diagrams of zinc bis(thiosemicarbazonato) complexes (left) the amine functionalised precursor (right) the bombesin analogue conjugated complex.

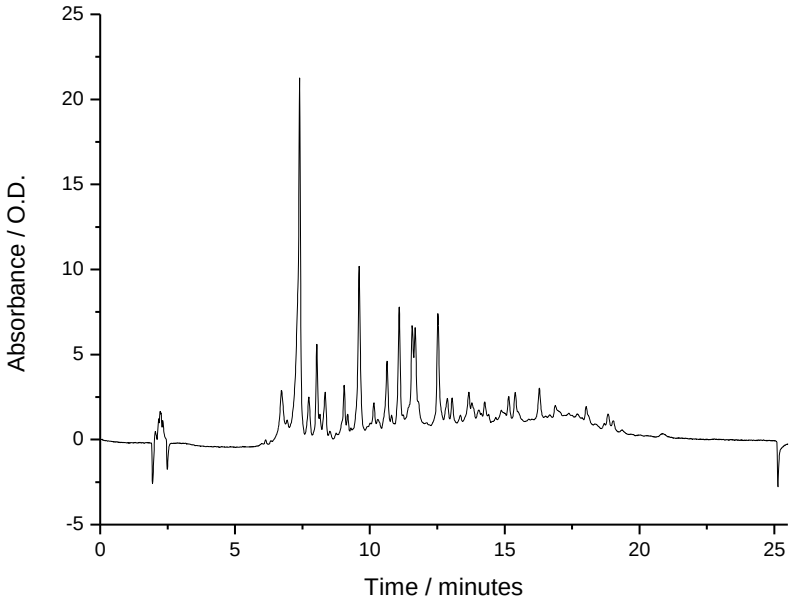

Figure 7.26. HPLC of compound **1bB** reaction mixture (λ_{abs} = 400 nm), reference peaks to note under the same conditions – compound **1bN** R_t = 9.2 minutes and derivatised bombesin analogue R_t = 4.8 minutes (HPLC method E).

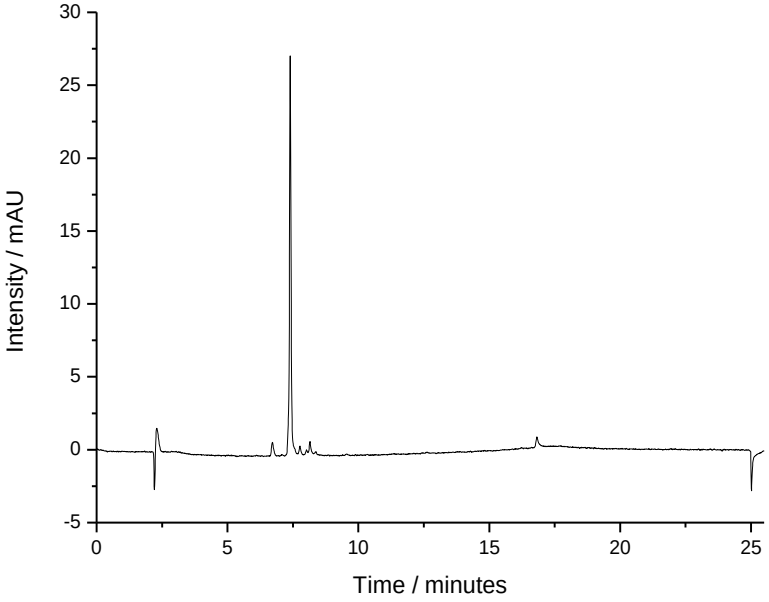

Figure 7.27. HPLC of purified compound **1bB** (λ_{abs} = 400 nm), HPLC method E.

Due to limited access to facilities, initial *in vitro* experiments were carried out on a reaction mixture of compound **1bB**. This was analysed using HPLC and showed a single major peak that did not correspond to starting materials and was rotary evaporated and freeze-dried overnight *(Figure 7.28 and 7.29)*.

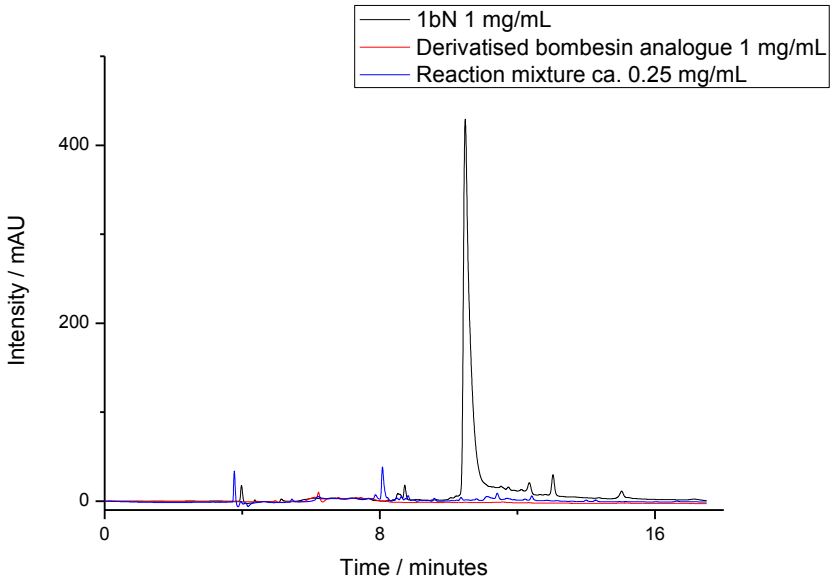

Figure 7.28. HPLC traces of the derivatised bombesin (red), the zinc complex **1bN** starting material (black) and the reaction mixture (blue) with the derivatised bombesin analogue (red), at 400 nm, HPLC method B.

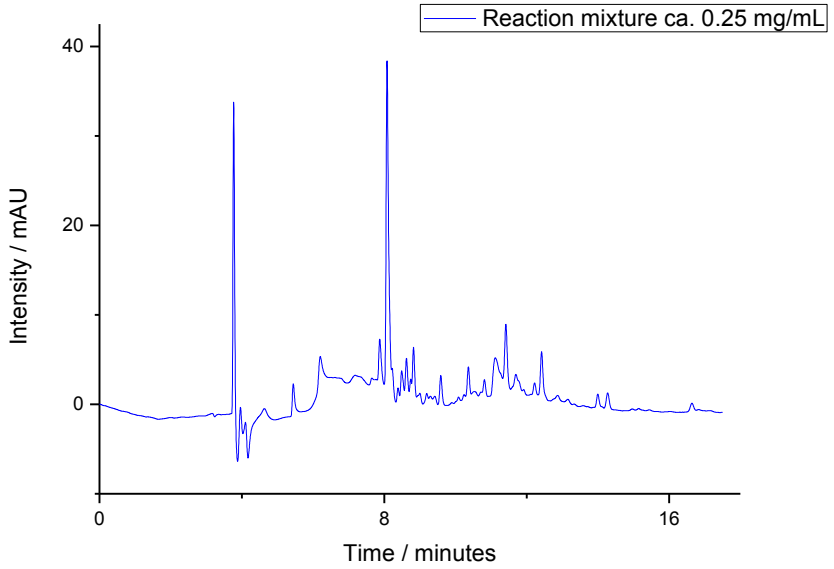

Figure 7.29. HPLC trace of the reaction mixture at 400 nm, HPLC method B.

7.4.6 Initial solution study, cell uptake study, laser scanning confocal microscopy and two-photon fluorescence lifetime study

7.4.6.1 Solution and HeLa cell study

The fluorescence lifetime of the reaction mixture of complex **1bB** in solution (10 mM in DMSO) was found to contain 3 components, the first at 0.030 ns (77.2%), the second at 0.670 ns (21.3%) and the third at 2.307 ns (1.5%), χ^2 = 1.28. Complex **1bN** in solution (10 mM in DMSO) was found to contain 2 components, the first at 0.045 ns (92.7%) and the second at 0.236 ns (7.3%), which displayed precipitation (χ^2 = 3.28). The bombesin-conjugated complex reaction mixture, displayed uptake in all three cell lines tested HeLa (cervical cancer), PC-3 (prostate cancer) and MCF-7 (breast cancer) cells. Interestingly the characteristics and uptake demonstrated by the complex was very cell line dependent, which is unprecedented for this family of complexes. In HeLa, the conjugated complex **1bB** was modelled to two component fluorescence lifetimes with χ^2 = 1.20, τ_1 = 0.689 ns, 0.406 ns FWHM, 80%; τ_2 = 3.333 ns, 1.450 FWHM, 20%, which is similar to the lifetimes to the minor components observed in solution and indicates stability as well as interaction with cells or cellular media *(Figure 7.30)*.

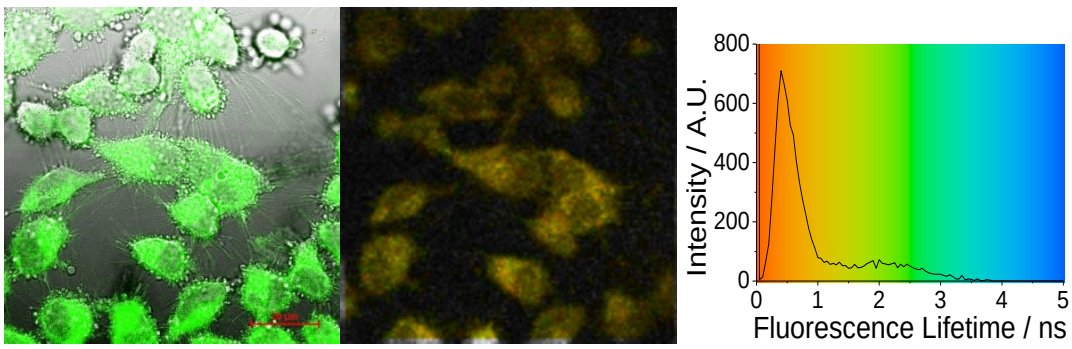

a) **b)** **c)**

Figure 7.30. (a – c) Microscopy of complex **1bB**, 100 μM, 1% DMSO**,** incubated in HeLa cells for 20 minutes where a) single-photon confocal overlay of DIC channel and with excitation at 488 nm Scalebar = 20 μm, b) and c) two-photon fluorescence imaging where b) the fluorescence lifetime map of τ_m and c) is the corresponding lifetime distribution plot in ns of τ_m.

7.4.5.2 PC-3, prostate cancer cell line

The data obtained in PC-3 cells was particularly interesting in that the complex appeared to greatly damage the plasma membrane, almost instantly after addition of the complex, which was monitored by plasma membrane colocalisation with Alexa Fluor dye *(Figure 7.32)*. This is an effect that had not previously been observed for this family of compounds. Further work could be to carry out lactate dehydrogenase (LDH) assays to test for cell membrane damage. The fluorescence lifetime was modelled to 2 components, which were χ^2 = 1.25, τ_1 = 0.660 ns, 0.329 ns, 80% and τ_2 = 3.515 ns, 2.570 ns, 20%, again displaying highly comparable data to the minor components in solution as was observed in solution indicating that the complex is most likely stable and interacts with cells and/or cellular media *(Figure 7.31)*.

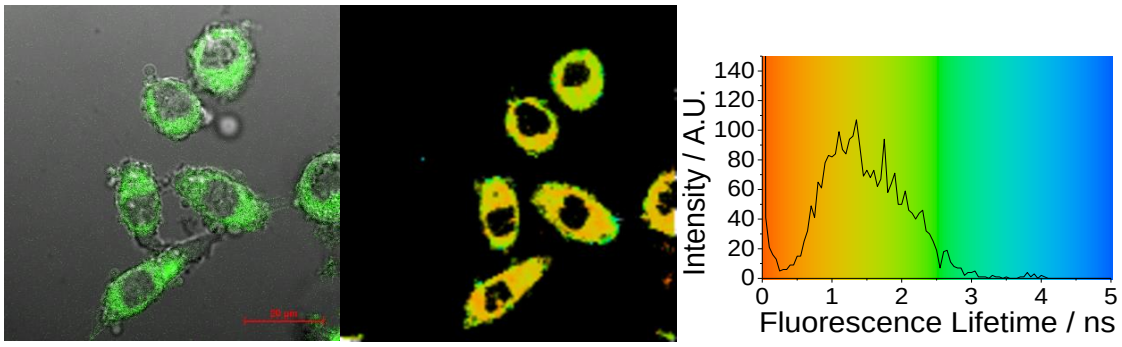

a) **b)** **c)**

Figure 7.31. (a – c) Microscopy of complex **1bB**, 100 μM, 1% DMSO**,** incubated in PC-3 cells for 20 minutes where a) single-photon confocal overlay of DIC channel and with excitation at 488 nm Scalebar = 20 μm, b) and c) two-photon fluorescence imaging where b) the fluorescence lifetime map of τ_m and c) is the corresponding lifetime distribution plot in ns of τ_m.

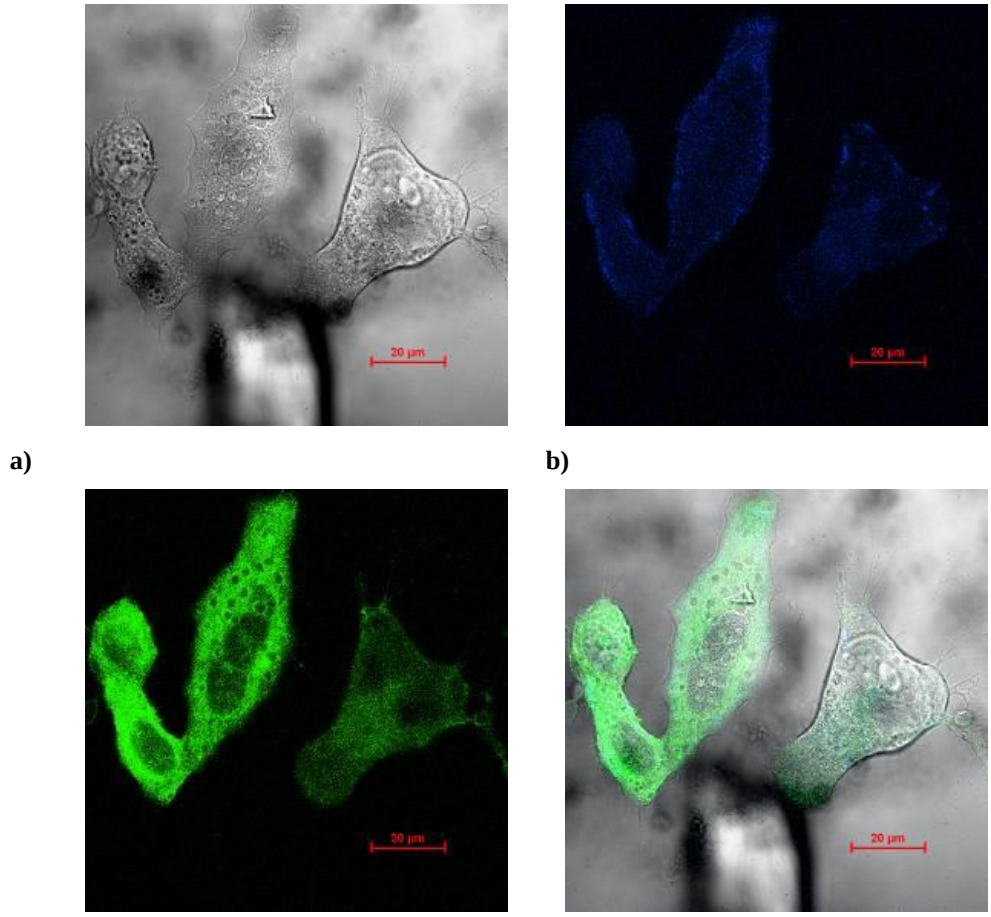

Figure 7.32. PC-3 cells stained with Alexa fluor plasma membrane dye after addition of complex **1bB**, final concentration within 5 minutes of addition at 100 μM, 1% DMSO, final concentration a) represents the DIC channel, (b) corresponds to excitation at 405 nm, (c) excitation at 488 nm and (d) are an overlay of the three channels were acquired addition. (Precipitation was observable since no cell washing occurred to enable the image to be taken as soon as the compound was added.) Scalebar: 20 μm.

7.4.6.3 MCF-7, breast cancer cell line

Complex **1bB** reaction mixture primarily entered the plasma membrane of MCF-7, but slowly entered the cytoplasm, where it possessed a lower fluorescence lifetime indicated by the orange colour as opposed to the green observed in the membrane itself *(Figure 7.32)*, displaying a very large contrast when compared to the uptake of complex **1bN** in the same cell line under identical conditions *(Figure 7.23)*. As was observed in HeLa and PC-3 cells the fluorescence lifetime possessed two components (χ^2 = 1.21, τ_1 = 1.299 ns, 0.523 ns FWHM 75%, τ_2 = 5.170 ns, 2.007 ns FWHM, 25%) whereby the lifetimes were longer in comparison to those acquired in solution, which is attributable to the larger lifetime observed in the cell membrane of MCF-7 cells. Plasma membrane

uptake was confirmed by plasma membrane colocalisation with Alexa Fluor dye *(Appendix Figures G.58-59).*

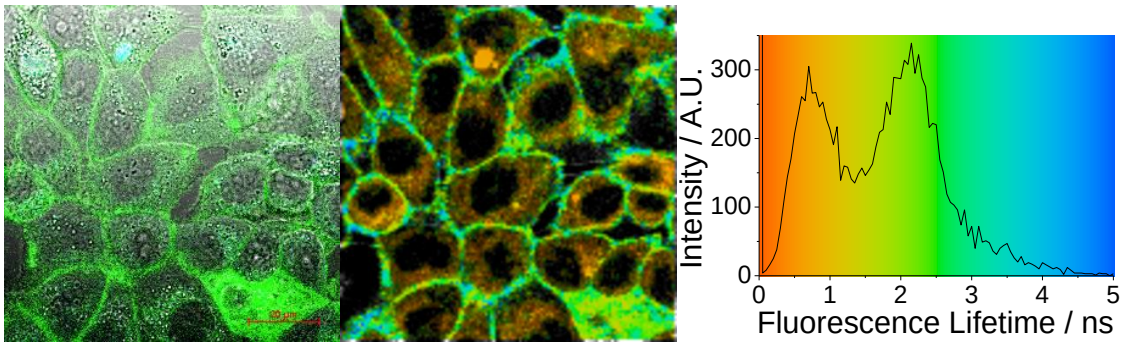

a) **b)** **c)**

Figure 7.33. (a – c) Microscopy of complex **1bB**, 100 μM, 1% DMSO**,** incubated in MCF-7 cells for 20 minutes where a) single-photon confocal overlay of DIC channel and with excitation at 488 nm. Scalebar = 20 μm, b) and c) two-photon fluorescence imaging where b) the fluorescence lifetime map of τ_m and c) is the corresponding lifetime distribution plot in ns of τ_m.

7.4.7 *In vitro* experiments performed on the purified complexes

Following purification, the complexes **1bB** and **1dB** were added to cells *(Figure 7.34 and Appendix Figures G.61-64).* Complex **1dB** did not display good FLIM data in cells, which could be attributed to optimal emission with λ_{ex} = 543 nm *(Appendix Figure G.62).* Compound **1bB** demonstrated presence of 3 components in the fluorescence lifetime, when excited by 810 nm and by 910 nm, whereby at 810 nm τ_1 was 0.050 ns (83.6%), τ_2 was 0.728 ns (11.0%) and τ_3 was 3.508 ns (5.3%), χ^2 = 2.72. At 910 nm the first component was 0.050 ns (corresponding to 74.0%), with a second component of 0.855 ns (22.9%) and third component of 7.232 ns (3.1%), χ^2 = 1.06.

These values are different from those acquired from the reaction mixture, in that τ_1 is slightly lower and τ_2 is greater, which could be indicative of removal of impurities. The allyl-substituted complex possessed similar data to the ethyl functionalised-complex with slightly higher fluorescence lifetimes observed when exciting at 910 nm (χ^2 = 1.21), for example τ_2 at 810 nm was 0.832 ns (8.3%) and was 0.830 ns (13.1%) at 910 nm and τ_3 was 4.422 ns (2.5%) at 810 nm and 9.302 ns (2.2%) at 910 nm. The major components where comparable at 0.048 ns (89.2%) and 0.049 ns (79.3%) respectively.

When incubated in cells complex **1bB** possessed similar behaviour as before in that most of the uptake was observed in the cell membrane and the cytoplasm, giving comparable results as were seen before purification in HeLa and PC-3 cells *(Figure 7.34)*. In MCF-7 distribution of the compound within the cell appeared similar to the other cell lines, therefore not giving an identical result as before, nevertheless minor components of the solution data closely match the fluorescence lifetimes observed in cells for the major component of 0.690 ns, 0.615 ns FWHM. Likewise in HeLa and PC-3 cell data were similar to the second component measured in solution whereby in HeLa at 810 nm the data were modelled to one component, which was 0.872 ns ± 0.490 ns FWHM, with the two components present when incubated in PC-3 at 810 nm were 0.889 ns ± 0.418 ns FWHM (first component) and 3.682 ns, 1.596 ns FWHM (second component). This is indicative of the likely stability of the complex and its interaction with cells/cellular media. Attempts were made to ionise the compound by MALDI-TOF mass spectrometry, which were unsuccessful. These experiments however, present interesting results and advance this research towards targeted small molecules for personalised medicine.

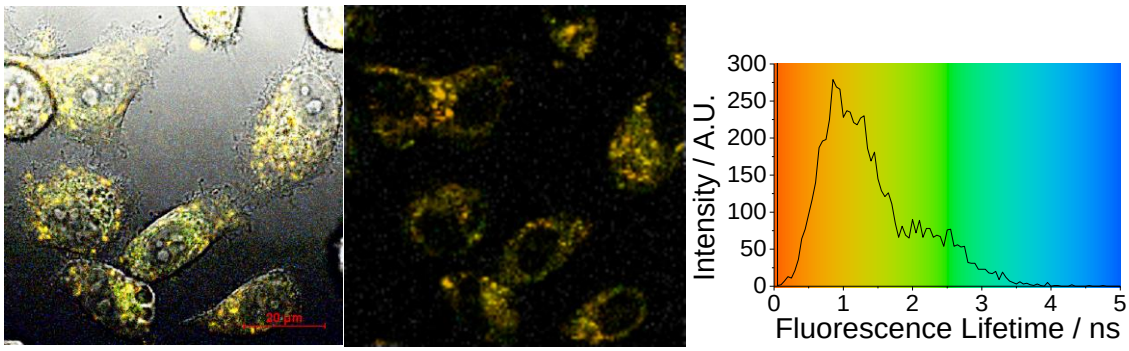

a) **b)** **c)**

Figure 7.34. Compound **1bB**, 1% 100 µM in PC-3 a) FLIM colour map where χ^2 = 1.27, lifetime is 0.889 ns ± 0.418 ns FWHM, range of FLIM image is 0 to 5 ns, where λ_{ex} = 810 nm and b) is an overlay of DIC image and λ_{ex} = 488 nm, scalebar = 20 µm. τ_1 = 0.804 ns, 0.720 ns FWHM 79%, τ_2 = 3.682 ns, 1.596 ns FWHM, 19%.

7.5 Summary to Chapter 7

A number of approaches for the development of a targeted intrinsically fluorescent bis(thiosemicarbazonato) complex were attempted. Amine-functionalised zinc complexes and a gallium complex were synthesised and characterised displaying suitable properties as molecular imaging probes, showing uptake and stability within cells. A seven amino-acid analogue of bombesin was derivatised with pyruvic acid and a coupling reaction with zinc complexes was attempted. HPLC data were promising, however it could not confirm the presence of the desired peptide-conjugated complex.

Chapter 8. Conclusions and further work

The synthesis and characterisation of a number of intrinsically fluorescent acenaphthenequinone zinc(II), copper(II), gallium(III) and indium(III) bis(thiosemicarbazone) complexes was carried out. ^{64}Cu, ^{68}Ga and ^{111}In were successfully used for clean and rapid radiolabelling by transmetallation from the zinc precursors. Biomimetic stability tests were performed using UV-Visible and fluorescence spectroscopy, which found the complexes to possess suitable properties for *in vitro* kinetic stability assays, cytotoxicity assays and cell uptake experiments.

The kinetic stability of the complexes was assayed with water, DMSO and PBS as well as Glutathione (GSH), L-cysteine, L-histidine, L-methionine, citric acid, ethylenediaminetetraacetic acid (EDTA) and biomimetic Eagle's modified essential media (EMEM) (both with and without foetal calf serum). These tests indicated excellent kinetic stability for the zinc and indium complexes, and appropriate stability for the gallium complexes for cellular experiments. Moreover, the complexes were tested with biologically relevant pH buffers and media, which indicated that the gallium complexes possessed sufficient stability between pH 2.5 and 7.35 within the timeframe of a cellular assay. The zinc and indium complexes, furthermore demonstrated kinetic stability within the range of pH 4.4 to 12.7 for up to 24 hours.

Subsequent fluorescence lifetime imaging experiments confirmed the stability of the bis(thiosemicarbazonato) complexes in solution and in biological cells. To the best of the author's knowledge this was the first report in the literature of the use of this technique to assess the stability of a transition metal complex in biological cells.

As a consequence, a range of novel bis(thiosemicarbazonato) complexes, as well as previously synthesised compounds, were studied *in vitro*, all showing cell uptake and varying degrees of cytotoxicity. Colocalisation stains were used to evaluate the uptake in numerous organelles, including the nucleus, cell membrane, lysosome, mitochondria and endoplasmic reticulum. The gallium and indium complexes displayed nuclear uptake, while many of the complexes were seen to enter the lysosome and mitochondria.

Furthermore the phenyl-substituted derivatives localised mainly in the endoplasmic reticulum.

These findings provide some insight into possible mechanisms of action. Further studies would be required to confirm these hypotheses using biological assays. Interestingly, photoactivity was observed for some of the compounds. The ethyl-functionalised acenaphthenequinone gallium(III) bis(thiosemicarbazonato) complex, in particular, displayed a significant change of uptake to form a punctuated appearance upon irradiation at 488 nm wavelength. Exclusively under these conditions cells were also observed to undergo blebbing, indicating cell death. This seems to indicate that these compounds could have potential for photodynamic therapy. A preliminary study was carried out to determine structural changes after irradiation using LEDs. NMR spectroscopy showed the presence of a new species, which, however, was not in sufficient proportions to allow assignment. Future work should investigate the structural changes initiated by light using high-powered lasers, in addition to by MI_{50} cytotoxicity experiments carried out under light irradiation.

The cytotoxicity of these complexes was evaluated with cells incubated in the dark using MTT and LDH assays. Results showed that a lower concentration was required to cause cell death in the cancerous cell line, HeLa, compared to the healthy cell line, FEK-4. Since some degree of toxicity was observed in non-cancerous cells, new zinc precursors and a gallium precursor featuring an amine group were synthesised to enable more selective targeting of cancer cells. Attempts to attach a targeting peptide *via* standard coupling reactions with a bombesin analogue were carried out. The product of which was purified by HPLC, with attempts to obtain a mass spectrum unsuccessful. Future work should explore different methods for coupling the precursor complexes to peptides and ionisation of the desired product. The crude and purified zinc complex reacted with a bombesin analogue were investigated for cell uptake. Each entered cells and possessed a comparable major fluorescence lifetime component with minor component solution data, which was different from the analogous amine-derivatised zinc complex. This therefore represents an advance towards attaching targeting these compounds to biologically active molecules for personalised medicine.

In vivo experiments in nude mice were carried out to assess the uptake of radiolabelled ^{64}Cu and ^{68}Ga and biodistribution of ^{64}Cu with a normoxic PC-3 Xenografted tumour (by collaborators in the Jason Lewis Group, MSKCC, NYC). These experiments showed very little uptake in the normoxic tumour combined with low non-target organ uptake compared to Cu[ATSM]. This may be seen as a promising result for an intended hypoxic selective probe. Furthermore, *in vitro* studies (carried out by collaborator Dr Israt S. Alam, Imperial College London) showed hypoxia selectivity in the case of gallium and indium complexes **3d**, **4c** and **4d**. Future work should therefore include an investigation of hypoxic selectivity in nude mice to enable comparisons with the normoxic study. Moreover, the mechanism of hypoxic selectivity should be tested by cyclic voltammetry.

Finally, if some of the compounds synthesised during the course of this PhD are found to possess hypoxia selectivity *in vivo*, the major goal of developing and testing an intrinsically fluorescent, kinetically stable, hypoxic selective – and potentially therapeutic – molecular agent will have been achieved.

Chapter 9. Experimental

9.1 General Information

Mass spectrometry data was acquired on a Bruker Daltonics ESI-TOF and NMR spectra on a Bruker 300 Ultrashield^{TM} (^{1}H: 300 MHz, ^{13}C: 75.5 MHz). Mass spectrometry was carried out in HPLC-grade methanol or distilled water, in some cases with 1% DMSO. NMR spectroscopy solvents, acenaphthenequinone, Zinc acetate, copper acetate, gallium trichloride and indium trichloride were obtained commercially and used as received. Gallium trichloride and indium trichloride were weighed out in an MBraun glovebox at O_2, H_2O > 0.3 ppm.

Continuous wave electron paramagnetic resonance (cwEPR) spectra at the X-band (9.450 GHz) were measured at 1mM in DMF at 60 K with a Bruker EMX spectrometer by Dr M. W. Jones, University of Oxford.

Elemental analyses were carried out by Mr Alan Carver, University of Bath, in parallel with A. Rosie Chhatwal (for compounds **iia**-**iid** and **2a**-**2d**.)

Crystal structure determination by X-ray diffraction

Single crystal X-ray diffraction data were obtained by Dr Gabriele Kociok-Köhn, Dr Sofia I. Pascu or Dr Simon K. Brayshaw for compounds **iib$_{s\text{-}s}$**, **iid**, **L$_B$**, **1c**, **2c**, **3a**, **3b**, **3c**, **4a**, **4b**, **4c** and **4d**. Crystals were selected using the oil drop technique, in perfluoropolyether oil and mounted at 150(2) K with an Oxford Cryostream N_2 open-flow cooling device. Intensity data for **2c**, **3a**, **3c**, **4a** – **4d** were collected on an Nonius Kappa CCD single crystal diffractometer using graphite monochromated Mo-Kα radiation (λ = 0.71073 Å). Data were processed using the Nonius Software.[160] For **L$_B$**, **1c** and **3b** data were collected on an Oxford Diffraction Gemini single crystal diffractometer at 150 K. Data were processed using the Oxford Diffraction software package (CrysAlisPro Version 1.171.33.55). Data for **iib$_{S\text{-}S}$** and **iid** were collected at Diamond using Synchrotron radiation (λ = 0.68890 Å) on a CrystalLogic Kappa (3

circle), Rigaku Saturn724 at 100K. Data were processed using the Rikagu software package (CrystalClear-SM Expert 2.0 r5).

For most structures a symmetry-related (multi-scan) absorption correction had been applied. Crystal parameters and details on data collection, solution and refinement for the complexes are provided in Tables A.1, A.2 and A.3.

The structures were solved by direct methods using the programmes SIR97[161] or SHELXS-97[162] followed by full-matrix least squares refinement on F^2 using SHELXL-97[162] implemented in the WINGX-1.80 suite of programmes throughout. Additional programmes used for analysing data and graphically handling them included: SHELXle,[163] PLATON,[164] and ORTEP 3 for windows. Hydrogen atoms were placed onto calculated positions and isotropically refined using a riding model.

HPLC characterisation was carried out by one of the following methods

HPLC method A was carried out using a Symmetry® C-18 column (4.6 x 260 mm) with UV/visible detection measured at λ_{obs} = 200 nm, 300 nm, 400 nm, 450 nm, 500 nm, 600 nm, 700 nm and 800 nm. The gradient elution was 1.1 mL/minute, with 0.1% TFA MilliQ water as solvent A and 0.1% TFA MeCN as solvent B. Start 95 % A reverse gradient until 5% A at 7.5 minutes, isocratic until 15 minutes, reverse gradient until 17.5 minutes 95% A, then hold to 18 minutes.

HPLC method B was carried out using a Symmetry® C-18 column (4.6 x 260 mm) with UV/visible detection measured at eight wavelengths from λ_{obs} = 200 nm, 220 nm, 280 nm, 300 nm, 400 nm, 450 nm, 500 nm, 600 nm, 700 nm and 800 nm. The gradient elution was 0.8 mL/minute, with 0.1% TFA MilliQ water as solvent A and 0.1% TFA MeCN as solvent B. Start 95 % A reverse gradient until 5% A at 7.5 minutes, isocratic until 15 minutes, reverse gradient until 17.5 minutes 95% A, then hold to 18 minutes.

HPLC method C was carried out using a Acclaim® 120 C-18 column (4.6 x 150 mm) with UV/visible detection measured at up to four λ_{obs} = 214 nm, 220 nm, 254 nm, 280 nm, 300 nm and 400 nm. The gradient elution was 1.0 mL/minute, with 0.1% TFA MilliQ water as solvent A and 0.1% TFA MeCN as solvent B. Start 95 % A reverse

gradient until 5% A at 7.5 minutes, isocratic until 15 minutes, reverse gradient from 15.1 minutes 95% A, then hold to 18 minutes.

HPLC method D was carried out using a Waters C-18 column (4.6 x 250 mm) with UV/visible detection measured at up to four λ_{obs} = 254 nm. The gradient elution was 1.0 mL/minute, with 0.1% TFA MilliQ water as solvent A and 0.1% TFA MeCN as solvent B. Start 95 % A reverse gradient until 5% A at 12 minutes, isocratic until 15 minutes, reverse gradient from 15.1 minutes 95% A, then hold until 21 minutes.

HPLC method E was carried out using a Acclaim® 120 C-18 column (4.6 x 150 mm) with UV/visible detection measured at up to four λ_{obs} = 214 nm, 220 nm, 254 nm, 280 nm, 300 nm and 400 nm. The gradient elution was 1.0 mL/minute, with 0.1% TFA MilliQ water as solvent A and 0.1% TFA MeCN as solvent B. Start 95 % A reverse gradient until 5% A at 10 minutes, isocratic until 15 minutes, reverse gradient from 15.1 minutes 95% A, then hold to 18 minutes.

HPLC method F was carried out using a Waters C-18 column (4.6 x 250 mm) with UV/visible detection measured at λ_{obs} = 254 nm. The gradient elution was 1.0 mL/minute, with 0.1% TFA MilliQ water as solvent A and 0.1% TFA MeCN as solvent B. Start 95 % A, reverse gradient until 5% A at 10 minutes, isocratic until 12 minutes, reverse gradient until 95% A at 14 minutes, then hold to 15 minutes at 95% A.

HPLC method G was carried out using a Waters C-18 column (4.6 x 250 mm) with UV/visible detection measured at up to four λ_{obs} = 214 nm, 220 nm, 254 nm, 280 nm, 300 nm and 400 nm. The gradient elution was 1.0 mL/minute, with 0.1% TFA MilliQ water as solvent A and 0.1% TFA MeCN as solvent B. Start 95 % A reverse gradient until 5% A at 15 minutes, isocratic until 22.5 minutes, reverse gradient from 22.6 minutes 95% A, then hold to 25.5 minutes.

HPLC method H was carried out using an Eclipse C-18 column (2 x 50 mm) with UV/visible detection measured at up to four λ_{obs} = 214 nm, 220 nm, 254 nm, 280 nm, 300 nm and 400 nm. The gradient elution was 1.0 mL/minute, with 0.1% TFA MilliQ

water as solvent A and 0.1% TFA MeOH as solvent B. Start 95 % A reverse gradient until 5% A at 8 minutes, hold until 10 minutes.

HPLC method I was carried out using a Phenomenex Ultracarb C-18 column (4.6 x 150 mm) with UV/visible detection measured at up to four λ_{obs} = 254 nm. The gradient elution was 1.0 mL/minute, with 0.1% TFA MilliQ water as solvent A and 0.1% TFA MeOH as solvent B. Start 95 % A reverse gradient until 5% A at 12 minutes, hold until 15 minutes.

Semi-Preparative HPLC was carried out using a Phenomenex® Gemini C-18 column (10 x 250 mm) with UV/visible detection measured at up to four λ_{obs} = 214 nm, 220 nm, 254 nm, 280 nm, 300 nm and 400 nm. The gradient elution was 1.0 mL/minute, with 0.1% TFA MilliQ water as solvent A and 0.1% TFA MeCN as solvent B. Start 95 % A reverse gradient until 5% A at 15 minutes, isocratic until 22.5 minutes, reverse gradient from 22.6 minutes 95% A, then hold to 25.5 minutes.

General Radiochemistry Procedures

Copper and indium experiments were carried out at either University of Oxford or University of Cambridge under the supervision of Prof Jonathan R. Dilworth or Dr Franklin I. Aigbirhio respectively. The zinc complex was prepared as either 1 mg/mL or 2 mg/mL in DMSO. For copper $^{64}Cu^{2+}$ was extracted from the nickel target and purified from $^{64}Ni^{2+}$ using an ion exchange column. An aqueous $^{64}CuCl_2$ solution was acquired in 0.1 mol.dm^{-3} HCl, which was diluted with 0.2 mL $^{64}CuCl_2$ in 0.1 mol.dm^{-3} $Na(CH_3CO_2)$. 200 µL of < 10 MBq $^{64}Cu(CH_3CO_2)_2$ was added to 100 µL of 1 mg/mL zinc complex in DMSO and 400 µL water in a 2 mL reaction vial. After stirring at room temperature 25 µL of this solution was entered into the HPLC, which was combined with both a UV tracer detecting at 254 nm and NI scintillation crystal detection with approximately a 10s delay. For indium 50 µL of the zinc complex in DMSO at a concentration of 1 mg/mL was added to 150 µL of MeOH and 2.5 µL $^{111}InCl_3$, < 10 MBq per experiment. The solutions were stirred at 60 ^{o}C and entered into the HPLC after ca. 1h. Gallium experiments were carried out by Mr Frazer Twyman, Hammersmith Hospital, Imperial College London, whereby 10 mL of 0.1M HCl was

used to elute ca. 6mCi of $^{68}Ga^{3+}$ from the generator and was subsequently trapped on a 30 mg/mL Strata X-C cartridge. This was eluted with 700 μL of 0.02M HCL / 98% acetone and dried for 15 minutes under a stream of nitrogen at 110^{o}C. Next, 25 μL of 2 mg/mL zinc complex in DMSO and 2 mL of HPLC-grade ethanol. The solution was heated for 30 minutes at 90 ^{o}C. HPLC methods F, G, H and I were used in all cases.

Log *P* calculations

^{64}CuEt/ ^{111}In (ca. 0.5 MBq) in 0.5 mL de-ionized water was added to 0.5 mL of octanol in an Eppendorf tube. The tube was vigorously vortexed for 5 min and centrifuged at 5000×g for 5 min. Aliquots (50 μL) of both aqueous and octanol layers were collected in triplicate and the associated activity counted using a gamma counter (Triathler, Hidex). *Log P* values were then calculated and compared with that of Cu[ATSM] standard, using the formula:

$\log P = \log(\text{counts(octanol)})/\text{counts}(H_2O))$

Animal Xenograft Models

All experiments were carried out following an Institutional Animal Care and Use Committee-approved protocol, Memorial Sloan-Kettering Cancer Center, New York by Dr Brian Zeglis. Athymic mice aging six to eight weeks were obtained from Taconic Farms Incorporated (Hudson, NY). The animals were given ca. 1 week prior to treatment to acclimatise in ventilated cages and were provided with food and water *ad libitum*. Xenografts were induced on the right shoulder by subcutaneous injection of 100 μL of 3 x 10^6 PC-3 cells.

Small-animal PET imaging

Small-animal PET imaging was performed at MSKCC, New York, on a micro-PET R4 rodent scanner (Concorde Microsystems) by Dr Brian Zeglis. Mice were injected with complex radiolabelled with Cu-64 or Ga-68 of 10-15 MBq and anesthetised by inhalation of 2% isoflurane (Baxter Healthcare, Deerfield, IL)/oxygen gas mixture. The animal was positioned on the scanner bed with anesthesia maintained by a 1% isoflurane/gas mixture. Measurements for each mouse were recorded using static scans

at time points between 30 minutes and 24 hours. Each scan occurred for between 10 and 45 minutes and contained at least 20 million coincident events. The energy window used was 350-700 keV, with a coincidence timing window of 6 ns. Data were arranged into 2D histograms by Fourier rebinning, and transverse images were reconstructed by filtered back-projection into a 128 x 128 x 63 (0.72 x 0.72 x 1.3 mm^3) matrix. Images were normalised to correct for non-uniformity of response of the PET, dead-time count losses, positron branching ratio, and physical decay to the time of injection but no attenuation, scatter, or partial-volume averaging correction was applied. The counting rates of the reconstructed images were converted to activity concentrations (percentage of injected dose [%ID] per gram of tissue) using a calibration factor based on the image of a mouse-sized water-equivalent phantom containing either Cu-64 or Ga-68. ASIPro VM^{TM} software (Concorde Microsystems) was used to analyse the data.

Biodistribution study

Biodistribution experiments were carried out at MSKCC, New York, by Dr Brian Zeglis, with mice bearing PC-3 tumour grafts as described above and randomised prior to the study. Prior to intravenous tail injection with Cu-64 radiolabelled **2b** and **2c** (0.5 – 1.0 MBq) the mice were gently warmed with a heat lamp for 5 minutes. Mice were euthanised by CO_2 gas asphyxiation at 1h, 2h, 6h, 12h and 24h, after which organs (including the tumour) were removed, rinsed with water, dried in air, weighed and counted using a Cu-64 calibrated gamma counter. Count data were converted to activity concentrations (percentage of injected dose [%ID] per gram of tissue).”

UV-visible spectra were obtained using a Perkin-Elmer Spectrometer, Lamda 650 in DMSO and processed using UV Winlab 3 software. The orientation of the 1.00 cm quartz cuvette was the same for each experiment for consistency.

Fluorescence spectra were measured in a 1.00 cm quartz cuvette using a Perkin-Elmer LS55 luminescence spectrophotometer. A scan from 200-800nm with increments of 10nm was initially carried out to discover excitation wavelength of maximum emission ($\lambda_{ex\text{-}max}$) and wavelength of maximum emission ($\lambda_{em\text{-}max}$). Quantum yields were estimated by reference to $[Ru(bipy)_3](PF_6)_2$ in water (Φ_R = 0.042 in water at 420 nm) using the equation:

$$\Phi_S = \Phi_R \cdot (D_S/D_R) \cdot (A_R/A_S) \cdot (I_R/I_S) \cdot (\eta_S/\eta_R)^2$$

Φ is the quantum yield, D is the integrated area of the emission band, A is the absorption of the solution at the excitation wavelength, I is the maximum intensity of the excitation band and η is the refractive index of the solvent. S is the sample and R is the reference $[Ru(bipy)_3](PF6)_2$.

Fluorescence pH and biomimetic media studies

Buffers from pH 1.1 to pH 10 were made using a Fisher brand Hydrus 600 pH meter in order to investigate the stability of compounds by fluorescence spectroscopy. The following buffer systems were used, following the procedure described in "Buffers: A guide for the preparation and use of buffers in biological systems"; Chandra Mohan, 1997.[165]

pH Buffer systems

1.1KCl/HCl

2.0 KCl/HCl

3.0 Citric acid/Sodium citrate dehydrate OR Glycine / HCl

5.0 Citric acid/Sodium citrate dehydrate OR Acetic Acid / Sodium acetate

7.0 Citric acid/Dibasic Sodium phosphate OR Sodium phosphate Monobasic / Sodium phosphate Dibasic

9.0 Glycine/Sodium Hydroxide

10.0 Sodium Carbonate Anhydrous/Sodium Hydrogen Carbonate

A 4 mL solution of twice the final concentration was added to 4 mL of the buffer system or biomimetic media and then scanned for fluorescence between 200-800nm with an excitation wavelength of λ_{max}. If precipitation was observed samples were filtered using a Millex^{TM} 0.22 μm filter prior to scanning. Eagle's Minimum Essential Medium containing 0.5% penicillin/streptomycin and 1% glutamine was used to assess the stability of the compounds in biomimetic media and also in relevance to the cell studies. Two equivalents of biologically relevant agents glutathione (GSH), L-cysteine, L-histidine, L-methionine or citric acid or chelator ethylenediaminetetraacetic acid (EDTA) were used.

Cell culturing and cell plate preparation.

Cells were cultured at 37 ˚C in a humidified atmosphere in air and diluted once confluence had been reached. Culture occurred in Eagle's Minimum Essential Medium (EMEM) for HeLa (cervical cancer cells) and FEK-4 (epithelial fibroblast cells), Dulbecco's Modified Eagle's Medium (DMEM) for MCF-7, RPMI 1640 for PC3 (prostate cancer cells) and Weymouth's medium for EMT6 (murine breast carcinoma). The media contained foetal calf serum (FCS) (10% for HeLa, PC-3, EMT6 and MCF-7 and 15% for FEK-4), 0.5% penicillin/streptomycin (10,000 IU mL^{-1}/10,000 mg mL^{-1}) and 200 mM L-Glutamine (5 mL). All steps were performed in absence of phenol red. Surplus supernatant containing dead cell matter and excess protein was aspirated. The live adherent cells were then washed with 2 x 10 mL aliquots of phosphate buffer saline (PBS) solution to remove any remaining media containing FCS, which inactivates trypsin. Cells were resuspended in solution by incubation in 3 mL of trypsin–PBS solution (0.25% trypsin) for 5 min at 37 ˚C. After trypsinisation, 5 mL of medium containing 10% serum was added to inactivate the trypsin and the solution was centrifuged for 5 min (1000 rpm, 25 ºC) to remove any remaining dead cell matter. The supernatant liquid was aspirated and 5 mL of cell medium (10% or 15% FCS) was added to the cell matter left behind. Cells were counted using a haemocytometer and then seeded as appropriate.

MTT assays. Cells cultured as above were plated (5 x 10^4 cells mL^{-1}) and left for 48 h to adhere fully. All steps were carried out in the absence of phenol red. (a) For MI_{50} estimations by MTT assays, cells were incubated with each compound tested for 48 h at 37 ˚C. Concentrations used were 1 nM, 100 nM, 1 µM, 10 µM, 50 µM, 100 µM and 250 µM(1% DMSO, 99% Eagle's Modified Essential Medium containing FCS at standard concentration of the cell line). Subsequently, cells were washed three times with PBS and 100 mL of MTT was added (0.5 mg mL^{-1}, 10% PBS: SFM) followed by a 2 h incubation. Following aspiration, 100 mL of DMSO was added and 96 well plates were read at an ELISA plate reader, Molecular Devices Versa Max (BN02877). Data were obtained from five consistent results and MI_{50} was calculated using Origin 8 as half the height of the fitted curve for each compound and for each individual experiment. Due to background absorbance, 100% cell death would not correspond to zero absorbance, therefore the height of the curve was calculated as the highest absorbance of the fit plot

minus the minimum absorbance of the curve, at which point death of all cells has been achieved. Where 100% cell death had not been attained, in the case of compounds **iib** and **3bN**, the MI_{50} was calculated using the same method in that the minimum absorbance of the fitted curve was subtracted. This value therefore indicates the minimum MI_{50} for this compound and is stated in the text/figure legend. The mean MI_{50} was calculated from the average of the five MI_{50} values obtained from five consistent experiments. The error reported was the standard error of the mean and shown as ± S.E.M.

(b) Time lapse studies by MTT assays were carried out in HeLa, MCF-7 and FEK-4 cells by an analogous method to that described at (a) above, but under serum free EMEM conditions aiming to link directly cytotoxicity tests to fluorescence imaging experiments. Concentrations used were 10 μM and 50 μM in 1% DMSO, 99% Eagle's Modified Essential Medium. Conclusions were reached following observations of cells' viability within 1 h incubation (37 °C) interval.

LDH assay

The medium containing serum was aspirated and the compounds were added in serum free medium (SFM). After drug treatment, the supernatant was removed and added to a separate 96 well plate. To the remaining cells 100 μL SFM containing SDS was added. A preliminary study showed that the optimum percentage of SDS for FEK-4 and MCF-7 cells was 0.015% and for HeLa cells 0.1 %. These were mixed by pipette and 20 μL of LDH reaction kit, Roche Scientific ® (1:40 catalyst:dye) was added to each well. After 20 min the 96 well plates were read by Molecular Devices Versa Max (BN02877) at 570 nm. % LDH leakage was calculated by supernatant OD divided by (supernatant OD + cell OD).

Fluorescence microscopy. At Bath fluorescence microscopy experiments were carried out on a Nikon eclipse TE2000 epi-fluorescence or a Zeiss LSM510META microscope, whereas at the Rutherford Appleton Laboratory a modified Nikon TE2000-U microscope was used. For all fluorescence microscopy experiments, cells were cultured as above and plated in glass-bottomed dishes as 1.5 x 10^5 cells per dish (*ca.* 60% coverage) and incubated for 12 h for HeLa, EMT-6 and FEK-4, 48 h for MCF-7 and 72 h for PC-3 cells. All steps were carried out in the absence of phenol red. This timing

was found to be minimum necessary for the two different cell lines to adhere to the glass bottomed Petri dishes used for imaging. Prior to compound addition, cells were washed 3 times with PBS, before adding serum free medium (2 mL). Subsequently, a small volume of medium was removed (10 mL) and compound in DMSO was added to obtain a final volume of 1 mL and the desired concentration. The final concentration of compounds on the cell plate was 50 mM in medium, containing 0.5% DMSO or 1% DMSO, depending on the compound solubility. After 20 min or 1 h incubation with the compound cells were washed 3 times with PBS and fresh serum free medium was added (1 mL) and images were recorded immediately.

Co-localisation studies. Cells were cultured using standard protocols, as described above, in RPMI-1640 (PC-3). Prior to addition of any commercial co-localisation dye, cells were washed 5 times with PBS. Protocols adapted from *Invitrogen* were used throughout.

(*a*) *Hoechst* A stock solution of 100 mg mL^{-1} Hoechst 33342 (*Invitrogen*) was prepared in sterile MilliQ water. To 10 μL of the stock solution, a volume of 990 μL was added giving a final concentration of 1 mg mL^{-1}. After cells were incubated with this solution for 30 min a further 5 washings with PBS were carried out, before the addition of 1 mL of SFM. Subsequently, a small volume of serum free medium (SFM) was removed (e.g. 10 μL) and compound in DMSO was added in equal volume to what was removed, to obtain a final volume of 1 mL and the desired concentration (50 mM in cell medium containing 0.5% DMSO). After 20 min or 1 h incubation with the compound cells were washed 3 times with PBS and fresh serum free medium was added (1 mL) and images were recorded immediately.

(*b*) *Mitotracker* A stock solution of 20 μM Mitotracker® Red FM (*Invitrogen*) was prepared in DMSO. To 10 μL of stock solution, 990 μL was added giving a final concentration of 200 nM. After cells were incubated with this solution for 30 min a further 5 washings with PBS were carried out, before the addition of 1 mL of SFM. Subsequently, a small volume of SFM was removed (e.g. 10 μL) and compound in DMSO was added in equal volume to what was removed, to obtain a final volume of 2mL and the desired concentration (50 mM in cell medium containing 0.5% DMSO).

After 20 min or 1 h incubation with the compound cells were washed 3 times with PBS and fresh serum free medium was added (1 mL) and images were recorded immediately.

(*c*) *Lysotracker* A stock solution of 20 μM Lysotracker® Red DND-99 (*Invitrogen*) was prepared in DMSO. To 10 μL of stock solution, 990 μL was added giving a final concentration of 200 nM. After cells were incubated with this solution for 60 min a further 3 washings with PBS were carried out, before the addition of 1 mL of SFM. Subsequently, a small volume of SFM was removed (e.g. 10 μL) and compound in DMSO was added in equal volume to that which was removed to obtain a final volume of 1 mL and the desired concentration (50 mM in cell medium containing 0.5% DMSO). After 20 min or 1 h incubation with the compound cells were washed 3 times with PBS and fresh serum free medium was added (1 mL) and images were recorded immediately.

(d) ER tracker

A stock solution of 100 μM ER-tracker® Red (*Invitrogen*) was prepared in DMSO. To 10 μL of stock solution, 990 μL was added giving a final concentration of 100 μM. After cells were incubated with this solution for 20 min a further 3 washings with HBSS were carried out, before the addition of 1 mL of SFM. Subsequently, a small volume of SFM was removed (e.g. 10 μL) and compound in DMSO was added in equal volume to that which was removed to obtain a final volume of 1 mL and the desired concentration (e.g. 50 mM in cell medium containing 0.5% DMSO). After 20 min or 1 h incubation with the compound cells were washed 3 times with PBS and fresh serum free medium was added (1 mL) and images were recorded immediately.

(e) Nile Red

A stock solution of 10 μg/mL Nile Red (*Invitrogen*) was prepared in DMSO. To 10 μL of stock solution, 990 μL was added giving a final concentration of 100 ng/mL. After cells were incubated with this solution for 10 min a further 3 washings with HBSS were carried out, before the addition of 1 mL of SFM. Subsequently, a small volume of SFM was removed (e.g. 10 μL) and compound in DMSO was added in equal volume to that which was removed to obtain a final volume of 1 mL and the desired concentration (e.g. 50 mM in cell medium containing 0.5% DMSO). After 20 min or 1 h incubation with

the compound cells were washed 3 times with PBS and fresh serum free medium was added (1 mL) and images were recorded immediately.

(f) Alexa Fluor

A stock solution of 50 μg/mL Alexa fluor® 350 conjugate (*Invitrogen*) was prepared in HBSS (Hank's Buffered Salt Solution). To 10 μL of stock solution, 990 μL was added giving a final concentration of 100 μM. After cells were incubated with this solution for 10 min a further 3 washings with HBSS were carried out, before the addition of 1 mL of SFM. Subsequently, a small volume of SFM was removed (e.g. 10 μL) and compound in DMSO was added in equal volume to that which was removed to obtain a final volume of 1 mL and the desired concentration (e.g. 50 mM in cell medium containing 0.5% DMSO). After 20 min or 1 h incubation with the compound cells were washed 3 times with PBS and fresh serum free medium was added (1 mL) and images were recorded immediately.

Fixed cell imaging

Cells were plated in a Petri dish containing a glass cover slip. Before fluorescence imaging, the serum containing medium was replaced with SFM. After the drug treatment cells were fixed by inverting the coverslip placing it onto 50 μL of paraformaldehyde-PBS (4% paraformaldehyde). After 15 min, the coverslip was mounted to a slide using Vectashield®, hard set mounting medium with DAPI (Vector Laboratories, Inc.)

Two-photon excitation experiments were performed at the Rutherford Appleton Laboratory following the methodology described in Botchway *et al.* 2008[137] and in our recent publication (Pascu *et al.* 2011[138]) with assistance of Dr S Botchway, Dr P Burgos, Mr A. Mckenzie and Mr A. Henman. An optical parametric oscillator was pumped by a mode locked Mira titanium sapphire laser (Coherent Lasers Ltd), generating 180 fs pulses at 75 MHz and emitting light at a wavelength of 580-630nm nm. The laser was pumped by a solid state continuous wave 532 nm laser (Verdi V18, Coherent Laser Ltd), with the oscillator fundamental output of 915 ± 2 nm or 810 ± 2 nm. The laser beam was focused to a diffraction limited spot through a water immersion ultraviolet

corrected objective (Nikon VC x60, NA1.2) and specimens illuminated at the microscope stage of a modified Nikon TE2000-U with UV transmitting optics.

The focused laser spot was raster scanned using an XY galvanometer (GSI Lumonics). Fluorescence emission was collected without de-scanning, bypassing the scanning system and passed through a coloured glass (BG39) filter. The scan was operated in normal mode and line, frame and pixel clock signals were generated and synchronised with an external fast microchannel plate photomultiplier tube used as the detector (R3809-U, Hamamatsu, Japan). These were linked *via* a Time-Correlated Single Photon Counting (TCSPC)PCmodule SPC830. Lifetime calculations were obtained using SPCImage analysis software (Becker and Hickl, Germany) or Edinburgh Instruments F900 TCSPC analysis software. Preliminary single-photon FLIM investigations were conducted using the Becker and HicklDCS120 system with a 40 ps 473 nm diode laser.

Fluorescence imaging of the nucleus and chromosomes

Due to the observed nuclear uptake a preliminary investigation was carried out at the Rutherford Appleton Laboratory with Dr Yusuf Mohammed and Ms Ana Estandarte to assess whether the complexes bind to chromosomes. Non-cancerous lung cell line CCD37-LU was cultured in DMEM containing 10% foetal bovine serum (FBS) and 1% L-Glutamine at 37°C in a 5% CO_2 incubator. Chromosomes were isolated *via* a Colcemid (Gibco BRL) treatment before cells were trypsinised and subsequently resuspended in pre-warmed KCl hypotonic solution (0.075M) at 37°C for 12 minutes. This was followed by fixing in a 3:1 methanol/acetic acid solution, which was added onto a glass microscope slide, to which 100 µL of Compound **4d** (100 µM) was aliquoted and was washed with DMSO after 15 minutes. Finally images were acquired using a Zeiss Axio Imager 2 microscope, which showed uptake of the complex in both the nucleus and in chromosomes.

***In vitro* hypoxia testing study**

Cells were cultured as described above with the final concentration on the cell plate 50 µM, containing 4% DMSO for 20 minutes with the hypoxia investigation carried out by Dr Israt S. Alam, Imperial College London. Normoxic conditions were 20.7% O_2 and 5% CO_2 at 37 °C, with hypoxic samples pre-incubated for 20 minutes at 1% O_2, 5% CO_2 at

37 °C before complex addition. Cells were washed 3 times with PBS, which was replaced with 2mL of serum free media, with images recorded immediately.

Flow cytometry studies

Cells were seeded as 3 x10^5 cells per well in a 6 well plate and incubated for ca. 12 h. The cells were subsequently washed twice with PBS, with the media replaced with serum free medium and compound of 50 μM 4%, DMSO final concentration. This was incubated for 20 minutes at 20.7% O_2 and 5% CO_2 at 37°C for the normoxic sample. Hypoxic conditions were obtained by pre-incubating the cells for 20 minutes at 1% O_2 and 5% CO_2 at 37°C, followed by incubation of a further 20 minutes under the same conditions with the compound. Following this cells were washed three times with PBS, trypsinised and centrifuged at 600g for three minutes. The precipitate was washed with PBS, resuspended in 1 mL of serum free medium, kept on ice and analysed in an LSRII cytometer (BD Biosciences, Rockville, MD USA), with 10 000 cells counted per event. Each experiment was carried out at least three times, with data analysis performed using FlowJo software (TreeStar, USA).

Radioactive cell uptake investigation

Cells were seeded as 3 x10^5 cells per well in a 6 well plate and incubated for ca. 12 h. The cell medium was aspirated and replaced with serum free medium containing the Ga-68 radiolabelled complex (following the radiochemical procedure above). This was incubated at 20.7% O_2 and 5% CO_2 at 37°C for the normoxic sample. Hypoxic conditions were obtained by pre-incubating the cells for 20 minutes at 1% O_2 and 5% CO_2 at 37°C, followed by incubation under the same conditions with the compound for the time course of the study. Cell plates were put on ice, washed 3 times with ice-cold PBS and lysed using 0.2 mL RIPA buffer for 10 minutes (Thermo Fisher Scientific Inc., Rockford, IL, USA). PBS (0.5 mL) was added to each well and cell lysates were transferred to counting tubes, with measurements of decay-corrected radioactivity performed using a gamma counter (Cobra II Auto-Gamma counter, Packard Biosciences Co, Pangbourne, UK). Aliquots were snap-frozen and subsequently protein determination was carried out using a BCA 96-well plate assay (Thermo Fisher Scientific Inc., Rockford, IL, USA). Decay corrected counts were corrected to protein concentration, with data presented as percent of total radioactivity per mg of protein,

Statistical analysis

Data were expressed as mean ± standard error of the mean (SEM), unless stated in the text. Student's *t* test (Prism v5.0 software for windows, GraphPad Software, San Diego, CA, USA) was used to assess the significance of comparison between two data sets. If $P \leq 0.05$ the differences between groups were regarded as significant.

9.2 Syntheses

Mono(substituted) 4-methyl-3-thiosemicarbazone acenaphthenequinone (ia)

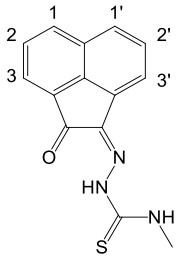

For Compound **ia**, acenaphthenequinone (0.50 g, 2.74 mmol) and 4-methyl-3-thiosemicarbazide (0.29 g, 2.80 mmol) were added in absolute ethanol (15 mL) and refluxed for 2 hours. 10 drops of conc. HCl were added upon reflux. The solid was isolated by filtration whilst hot, resuspended in hot methanol (10 mL) and stirred for 15 minutes before filtering and washing with further methanol. The resultant yellow solid (0.60 g, 2.25 mmol, 82%), compound **ia**, was dried *in vacuo*.

^{1}H NMR (300 MHz, d_6–DMSO, 25 °C): δ 12.65 (s, 1H, N-N*H*), 9.38 (m, 1H, N*H*Me), 8.38 (d, 1H, *H-3*, *J* = 8.3 Hz), 8.14 (d, 1H, *H-3'*, *J* = 8.3 Hz), 8.10 (d, 1H, *H-1*, *J* = 7.1 Hz), 7.98 (d, 1H, *H-1'*, *J* = 6.9 Hz), 7.88 (overlapping t, 2H, *H-2*), 7.85 (overlapping t, 2H, *H-2'*), 3.13 (d, 3H, (C*H*$_3$)). **^{13}C NMR** (75.5 MHz, d_6–DMSO, 25°C): δ 188.6, 178.0, 139.1, 137.2, 132.9, 130.5, 130.1, 130.0, 129.0, 128.7, 127.2, 122.6, 118.3, 31.5. **Mass spectrum** ESI-MS calcd for $C_{14}H_{12}N_3OS^+$ $[M + Na]^+$ 292.0515, found m/z = 292.0494.

Mono(substituted) 4-ethyl-3-thiosemicarbazone acenaphthenequinone (ib)

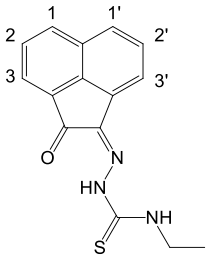

For Compound **ib**, acenaphthenequinone (0.50 g, 2.74 mmol) and 4-ethyl-3-thiosemicarbazide (0.36 g, 3.00 mmol) were added in absolute ethanol (15 mL) and refluxed for 2 hours. 10 drops of conc. HCl were added upon reflux. The solid was isolated by filtration whilst hot, resuspended in hot methanol (10mL) and stirred for 15 minutes before filtering and washing with further methanol. The resultant yellow solid (0.66 g, 2.33 mmol, 85%), compound **ib**, was dried *in vacuo*.

^{1}H NMR (300 MHz, d_6–DMSO, 25°C): δ 12.60 (s, 1H, N-N*H*), 9.42 (t, 1H,N*H*Et, *J* = 5.9 Hz), 8.38 (d, 1H, *H-3*, *J* = 8.2 Hz), 8.14 (d, 1H, *H-3'*, *J* = 8.3 Hz), 8.10 (d, 1H, *H-1*, *J* = 7.0 Hz), 8.01 (d, 1H, *H-1'*, *J* = 6.9 Hz*)*, 7.88 (t+t,2H, *H-2* and *H-2'*), 3.68 (m, 2H, (C*H*$_2$)CH$_3$), 1.23 (t, 3H, CH$_2$C*H*$_3$, *J* = 7.2 Hz). **^{13}C NMR** (75.5 MHz, d_6 –DMSO, 25 °C): δ 188.5, 176.9, 139.1, 137.2, 132.8, 130.5, 130.1, 129.9, 128.9, 128.6, 127.1, 122.5, 118.3, 39.1, 14.1. **Mass spectrum** ESI-MS calcd for $C_{15}H_{14}N_3OS^+$ $[M + Na]^+$ 306.0677, found 306.0667.

Mono(substituted) 4-phenyl-3-thiosemicarbazone acenaphthenequinone (ic)

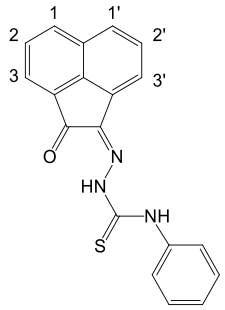

For Compound **ic**, acenaphthenequinone (0.5136 g, 2.81 mmol) was added to 1.1 equivalents of 4-phenyl-3-thiosemicarbazide (0.5116 g, 3.05 mmol) were added in absolute ethanol (15mL) and refluxed for 2 hours. 10 drops of conc. HCl were added upon reflux. The solid was isolated by filtration whilst hot, resuspended in hot methanol (10mL) and stirred for 15 minutes before filtering and washing with further methanol. The resultant light orange solid (0.800 g, 2.41 mmol, 85%), compound **ic**, was dried *in vacuo*.

^{1}H-NMR (300 MHz, d_6-DMSO, 25°C): δ 12.79 (s, 1H, N-N*H*), 10.93 (s, 1H, N*H*Ph), 8.36 (d, 1H, *H-3*, *J* = 8.1 Hz), 8.13 (d, 1H, *H-3'*, *J* = 8.3 Hz), 8.10 (d, 1H, *H-1*, *J* = 6.9 Hz), 8.08 (d, 1H, *H-1'*, *J* = 7.0 Hz), 7.86 (overlapping t, 1H, *H-2*), 7.82 (overlapping t, 1H, *H-2'*), 7.65 (obscured d, 2H, o-*H*), 7.45 (t, 2H, m-*H*, *J* = 7.6 Hz, 8.3 Hz), 7.29 (m, 1H, o-*H*). **^{13}C-NMR** (75.5 MHz, d_6-DMSO, 25^{o}C): δ 188.6, 176.6, 139.4, 138.5, 137.7, 132.8, 130.4, 129.99, 129.93, 128.9, 128.6, 128.4, 127.2, 125.8, 122.5, 120.9, 118.8. **Mass spectrum** ESI-MS calcd for $C_{19}H_{14}N_3OS^+$ $[M+H]^+$ 332.0858, found 332.0861. **Elem. Anal.**: Found: C; 68.10 %, H; 3.96 %, N; 13.10 %, Calc.: C; 68.86 %, H; 3.95 %, N; 12.68 %.

Mono(substituted) 4-allyl-3-thiosemicarbazone acenaphthenequinone (id)

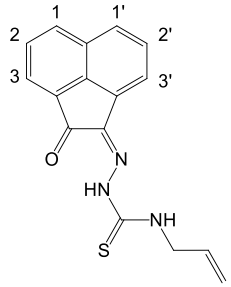

For Compound **id**, acenaphthenequinone (0.500 g, 2.745 mmol) and 4-allyl-3-thiosemicarbazide (0.393 g, 3.293 mmol) were added in absolute ethanol (15mL) and refluxed for 2 hours. 10 drops of conc. HCl were added upon reflux. The solid was isolated by filtration whilst hot, resuspended in hot methanol (10mL) and stirred for 15 minutes before filtering and washing with further methanol. The resultant yellow solid (0.595 g, 1.723 mmol, 63%), compound **id**, was dried *in vacuo*.

^{1}H NMR (d_6-DMSO, 25 °C): δ 12.61 (s, 1H, N-N*H'*), 9.57 (t, 1H, N*H*Allyl, *J* = 6.0 Hz), 8.34 (d, 1H, *H-3*, *J* = 8.2 Hz), 8.11 (d, 1H, *H-3'*, *J* = 8.3 Hz), 8.06 (d, 1H, *H-1'*, *J* = 7.0 Hz), 7.96 (d, 1H, *H-1*, *J* = 6.9 Hz), 7.85 (overlapping t, 1H, *H-2* or *H-2'*), 7.81 (overlapping t, 1H, *H-2* or *H-2'*), 5.95 (m, 1H, -CH_2CHCH_2), 5.27 + 5.21 (q, 1H, H_{trans}, *J* = 17.3 Hz), 5.19 + 5.15 (q, 1H, H_{cis}, *J* = 10.3 Hz), 4.30 (ddt, 2H, -CH_2CHCH_2). **^{13}C NMR** (d_6-DMSO, 25 ◦C): δ 188.5, 177.5, 139.1, 137.3, 134.0, 132.8, 130.4, 130.0, 129.9, 128.9, 128.6, 127.1, 122.5, 118.4, 116.3, 46.5. **Mass spectrum** ESI-MS calcd for $C_{16}H_{13}N_3NaOS^+$ 318.0677 $[M+Na]^+$, found 318.0665. **Elem. Anal.**: Found: C; 65.09 %, H; 4.43 %, N; 14.21 %, Calc.: C; 65.06 %, H; 4.44 %, N; 14.23 %.

Bis(substituted) 4-methyl-3-thiosemicarbazone acenaphthenequinone (iia)

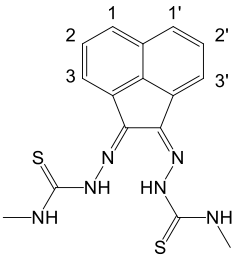

Acenaphthenequinone (0.25g, 0.137 mmol) and methyl thiosemicarbazide (0.43 g, 0.411 mmol) were suspended in 40mL ethanol and refluxed for 4 hours. 10 drops of conc. HCl were added upon reflux. The solid was isolated by filtration whilst hot, resuspended in hot methanol (10 mL) and stirred for 15 minutes before filtering and

washing with further methanol. The resultant yellow solid (266.6 mg, 54 %), compound **iia**, was dried *in vacuo*.

^{1}H NMR- (300 MHz, d_6-DMSO, 25ºC) δ 12.60 (s, 1H, N-N*H'*), 11.29 (s, 1H, N-N*H*), 9.15 (m, 1H, N*H'*CH_3), 8.86 (m, 1H, N*H*CH_3), 8.20 (d 1H, *H-1*, *J* = 7.3 Hz), 8.13 (d, 1H, *H-3'*, *J* = 8.3 Hz), 8.07 (d, 1H, *H-1'*, *J* = 7.0 Hz), 8.03 (d, 1H, *H-3*, *J* = 8.3 Hz), 7.79 (m, 2H, *H-2* and *H-2'*), 3.11 (m, 6H, overlapping CH_3 groups).**^{13}C NMR**- (75.5 MHz, d_6-DMSO, 25ºC) δ 178.42, 138, 136.45, 133.23, 130.25, 129.20, 128.20, 128.18, 127.03, 125.02, 31.79, 31.6. **Mass spectrum** ESI-MS calcd for $C_{16}H_{15}N_6S_2^-$ $[M-H]^-$ 355.0800, found 355.0804 **Elem. Anal.**: Found C; 53.7 %, H, 4.51 %, N; 23.4 %, Calc.: C; 53.91 %, H; 4.52 %, N; 23.58 %.

Bis(substituted) 4-ethyl-3-thiosemicarbazone acenaphthenequinone (iib)

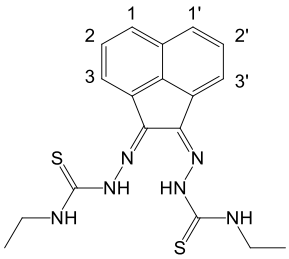

Acenenaphthenequinone (0.25 g, 0.137 mmol) and 4-ethyl-3thiosemicarbazide (0.48 g, 0.411 mmol) were suspended in 40 mL ethanol and refluxed. 10 drops of conc. HCl were added upon reflux. The solid was isolated by filtration whilst hot, resuspended in hot methanol (10 mL) and stirred for 15 minutes before filtering and washing with further methanol. The resultant yellow solid (446.7mg, 85%), compound i**ib**, was dried *in vacuo*.

^{1}H NMR- (300 MHz, d_6-DMSO, 25ºC) 12.55 (s, 1H, N-N*H'*), 11.21 (s, 1H, N-N*H*), 9.19 (t, 1H, N*H'*Et, *J* = 6.0 Hz), 8.80 (t, 1H, N*H*Et, *J* = 5.5 Hz), 8.19 (d, 1H, *H-1*, *J* = 7.2 Hz), 8.13 (d, 1H, *H-3'*, *J* = 8.3 Hz), 8.09 (d, 1H, *H-1'*, *J* = 7.0 Hz), 8.03 (d, 1H, *H-3*, *J* = 8.3 Hz), 7.79 (overlapping t, 2H, *H-2* and *H-2'*), 3.66 (m, 4H, C*H*$_2$$CH_3$), 1.24 (m, 6H, CH_2C*H*$_3$). **^{13}C NMR**- (75.5 MHz, d_6-DMSO, 25ºC) δ 178.77, 176.92, 139.25, 139.16, 136.66, 133.06, 130.04, 128.69, 128.58, 128.12, 128.35, 126.17, 124.64, 119.60, 31.05 **Mass spectrum** ESI-MS calcd for $C_{18}H_{19}N_6S_2$ $[M-H]^-$ 383.1113, found 383.1155. **Elem. Anal.**: Found C; 56.1 %, H, 5.23 %, N; 21.8 %. Calc.: C; 56.22 %, H; 5.24 %, N; 21.86 %.

Bis(substituted) 4-phenyl-3-thiosemicarbazone acenaphthenequinone (iic)

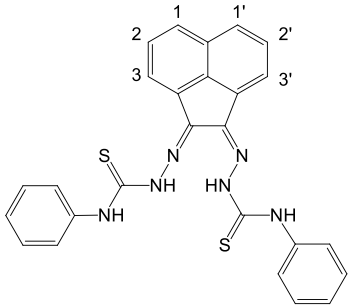

Acenaphthenequinone (0.25g, 0.137mmol) and 4-phenyl-3thiosemicarbazide (0.68g, 0.411mmol) were suspended in 40mL ethanol and refluxed 4hours. 10 drops of conc. HCl were added upon reflux. The solid was isolated by filtration whilst hot, resuspended in hot methanol (10 mL) and stirred for 15 minutes before filtering and washing with further methanol. The resultant yellow solid (549 mg, 83%), compound **iic**, was dried *in vacuo*.

^{1}H NMR: (300 MHz, d_6-DMSO, 25ºC), δ 12.95 (s, 1H,N-N(*H'*)), 11.54 (s, 1H, N-N*H*), 10.74 (s, 1H, N*H*Ph or N-N*H'*), 10.67 (s, 1H, N*H*Ph or N-N*H'*), 8.30 (overlapping d, 2H, *H-1* and *H-1'*, *J* = 7.6 Hz and 7.4 Hz), 8.18 (d, 1H, *H-3* or *H-3'*, *J* = 8.4 Hz), 8.07 (d, 1H, *H-3* or *H-3'*, *J* = 8.3 Hz), 7.84 (m, 4H, *H-2* and *H-2'*, o-*H'*), 7.68 (d, 2H, o-*H'*, *J* = 8.1 Hz), 7.43 (m, 4H, m-*H* and m-*H'*), 7.25 (overlapping t, 2H, p-*H* and p-*H'*). **^{13}C NMR**: (75.5 MHz, d_6-DMSO, 25ºC) δ 178.41, 176.55, 138.89, 138.81, 132.70, 130.0, 129.14, 128.34, 127.76, 127.00, 125.76, 124.30. **Mass spectrum** ESI-MS calcd for $C_{26}H_{19}N_6S_2^-$ $[M-H]^-$ 479.1118, found 479.1194. **Elem. Anal.**: Found C; 64.75 %, H, 4.19 %, N; 7.55 %. Calc.: C; 64.98 %, H, 4.19 %, N; 17.49 %.

Bis(substituted) 4-allyl-3-thiosemicarbazone acenaphthenequinone (iid)

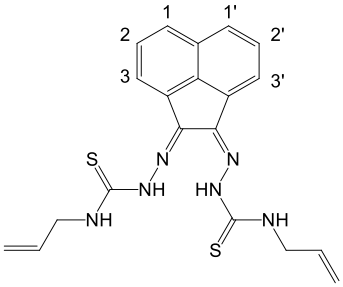

Acenaphthenequinone (0.25g, 0.137mmol) and 4- allyl 3-thiosemicarbazide (0.54 g, 0.411 mmol) were suspended in 40mL ethanol and were refluxed. 10 drops of conc. HCl were added upon reflux. The solid was isolated by filtration whilst hot, resuspended in hot methanol (10 mL) and stirred for 15 minutes before filtering and washing with further methanol. The resultant yellow solid (415 mg, 74%), compound **iid**, was dried *in vacuo*.

^{1}H NMR: (300 MHz, d_6-DMSO, 25ºC) δ 12.63 (s,1H, N-N*H'*), 11.27 (s,1H, N-N*H*), 9.32 (t, 1H, N*H*Allyl, *J* = 6.0 Hz), 9.02 (t, 1H, N*H'*Allyl, *J* = 5.7 Hz), 8.21 (d, 1H, *H-1* or *H-1'*, *J* = 7.2 Hz), 8.11 (overlapping d, 2H, *H-3* and *H-3'*), 8.01 (d, 1H, *H-1* or *H-1'*, *J* = 7.1 Hz), 7.80 (overlapping t, 1H, *H-2* or *H-2'*), 7.78 (overlapping t, 1H, *H-2* or *H-2'*), 5.95 (m, 2H, CH_2CHCH_2) 5.35 + 529 (ddt, 2H, H_{trans}, *J* = 17.4 Hz), 5.25 + 5.18 (ddt, 2H, H_{trans}, *J* = 17.4 Hz), 5.17 + 5.14 (m, 2H, H_{cis}, *J* = 10.6 Hz), 4.31 (m, 4H, CH_2CHCH_2), . **^{13}C NMR**: (75.5 MHz, d_6-DMSO, 25ºC) δ 182.52, 178.14, 138.23, 136.45, 134.86, 134.40, 133.21, 130.32, 129.28, 128.88, 128.55, 128.18, 127.09, 124.93, 116.83, 116.28, 47.07, 46.52. **Mass spectrum** ESI-MS calcd for $C_{20}H_{19}N_6S_2^-$ $[M-H]^-$ 407.1113, found 407.1106. **Elem. Anal.**: Found C; 58.9 %, H; 4.94 %, N; 20.5 %. $C_{20}H_{20}N_6S_2$. Calc.: C; 58.80 %, H, 4.93 %, N; 20.57 %.

Zinc(II) bis(4-methyl-3-thiosemicarbazone) acenaphthenequinone (1a)

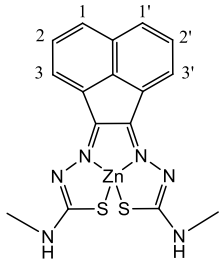

Zinc complex **1a** was prepared by suspending 1 equivalent of acenaphthenequinone (502 mg, 2.76 mmols) and 3 equivalents of zinc acetate (1.82 g, 8.29 mmols) in acetic acid at 60 ^{o}C. Vast excess 4-methyl-3-thiosemicarbazide (2.95 g, 28.04 mmols) was

added, the temperature increased to 120 ^{o}C and refluxed for 30h. Isolation was achieved by hot filtration, followed by washing with 100 mL diethyl ether, yielding an orange powder of 601 mg, 1.43 mmols, 52%. Comparison of ^{1}H NMR spectra of these products with literature data, as well as mass spectroscopy, confirmed the desired structures.

^{1}H NMR (d_6-DMSO, 25 ^{o}C): δ 8.19 (d, 2H, *H-1*, *J* = 6.8 Hz), 7.99 (d, 2H, *H-3*, *J* = 8.3 Hz), 7.85 (m, 2H, N-*H*), 7.76 (apparent t, 2H, *H-2*, *J* = 7.9 and 7.4 Hz), 3.04 (d, 6H, C*H*$_3$, *J* = 3.9Hz), 1.91 (3H, C*H*$_3$, acetic acid) **^{13}C NMR** (300 MHz, d_6–DMSO, 25°C): δ 179.2, 140.0, 138.1, 130.6, 128.6, 128.2, 126.9, 123.1, 29.4. **Mass spectrum** ESI-MS calcd for $C_{16}H_{15}N_6S_2Zn^+$ $[M + H]^+$ 419.0086, found 419.0101. **HPLC** (Method H): R_t = 2.0 mins.

Zinc(II) bis(4-ethyl-3-thiosemicarbazone) acenaphthenequinone (1b)

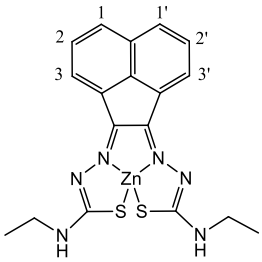

Zinc complex **1b** was prepared by suspending 1 equivalent of acenaphthenequinone (498 mg, 2.73 mmols) and 3 equivalents of zinc acetate (1.763 g, 8.03 mmols) in acetic acid at 60 ^{o}C. Vast excess of 4-ethyl-3-thiosemicarbazide (3.229 g, 27.09 mmols) was added, the temperature increased to 120 ^{o}C and was refluxed for 30h. Isolation was achieved by hot filtration, followed by washing with 100 mL diethyl ether, yielding an orange powder of 603 mg, 1.35 mmols, 49%. Comparison of ^{1}H NMR spectra of these products with literature data, as well as mass spectroscopy, confirmed the desired structures.

^{1}H NMR (d_6-DMSO, 25 ^{o}C): δ 8.17 (d, 2H, *H-1*, *J* = 7.0 Hz), 7.98 (d, 2H, *H-3*, *J* = 8.1 Hz), 7.91 (m, 2H, N*H*Et), 7.75 (t, 2H, *H-2*, *J* = 7.7 Hz), 3.57 (q, 4H, C*H*$_2$CH$_3$, *J* = 3.4 Hz and 3.6 Hz), 1.23 (t, 6H, CH$_2$C*H*$_3$, *J* = 7.2 Hz).**^{13}C NMR** (300 MHz, d_6–DMSO, 25°C): δ 178.8, 140.0, 138.3, 130.9, 129.0, 128.6, 127.2, 123.1, 37.5, 14.8. **Mass spectrum** ESI-MS calcd for $C_{18}H_{19}N_6S_2Zn^+$ $[M + H]^+$ 447.0399, found 447.0396.

Zinc(II) bis(4-phenyl-3-thiosemicarbazone) acenaphthenequinone (1c)

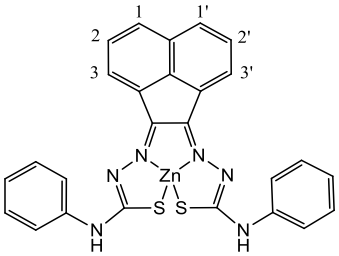

Zinc complex **1c** was prepared by suspending 1 equivalent of acenaphthenequinone (0.504 g, 2.77 mmols) and 3 equivalents of zinc acetate (1.81 g, 8.25 mmols) in acetic acid at 60 ^{o}C. 4-phenyl-3-thiosemicarbazide was added, the temperature increased to 120 ^{o}C and was refluxed for 30h. Isolation was achieved by hot filtration, followed by washing with 100 mL diethyl ether, yielding a red powder of 1.020 g, 1.88 mmols, 68%. Comparison of ^{1}H NMR spectra of these products with literature data, as well as mass spectroscopy, confirmed the desired structures.

^{1}H NMR (d_6-DMSO, 25 ^{o}C): δ 10.03 (s, 2H N*H*Ph), 8.25 (d, 2H, *H-1*, *J* = 7.0 Hz), 8.10 (d, 2H, *H-3*, *J* = 8.2 Hz), 7.93 (d, 4H, o-*H*, *J* = 7.7 Hz), 7.85 (t, 2H, *H-2*, *J* = 7.1 Hz), 7.42 (t, 4H, m-*H* and m-*H'*, *J* = 7.9 Hz), 7.08 (t, 2H, p-*H* and p-*H'*, *J* = 7.3Hz). **^{13}C NMR** (300 MHz, d_6–DMSO, 25 ˚C): δ 177.2, 142.3, 140.5, 138.6, 130.7, 128.6, 128.3, 128.0, 127.5, 123.5, 122.7, 120.9. **Mass spectrum** ESI-MS calcd for $C_{26}H_{19}ZnN_6S_2^+$ [M + H]$^+$ 543.0399, found 543.0348.

Zinc(II) bis(4-allyl-3-thiosemicarbazone) acenaphthenequinone (1d)

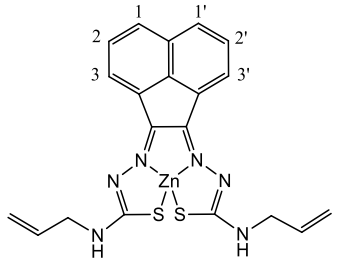

Zinc complex **1d** was prepared by suspending 1 equivalent of acenaphthenequinone (0.502 mg, 2.76 mmols) and 3 equivalents of zinc acetate (1.815 g, 8.27 mmols) in acetic acid at 60 ^{o}C. Vast excess of 4-allyl -3-thiosemicarbazide was added the temperature increased to 120 ^{o}C and refluxed for 30h. Isolation was achieved by hot filtration, followed by washing with 100 mL diethyl ether, yielding an orange powder of 62%. Comparison of ^{1}H NMR spectra of these products with literature data, as well as mass spectroscopy, confirmed the desired structures.

^{1}H NMR (d_6-DMSO, 25 ^{o}C): δ 8.18 (d, 2H, *H-1*, *J = 6.8 Hz*), 7.95 (t, 2H, N*H*), 7.89 (d, 2H, *H-3*, *J* = 8.1 Hz), 7.68 (apparent t, 2H, *H-2*, *J* = 8.1 Hz and 7.2 Hz), 6.00 (m, 2H, -CH_2CHCH_2), 5.27 (dd, 2H, H_{trans}), 5.15 (dd, 2H, H_{cis}), 4.18, (bm, 4H, -CH_2CHCH_2). **^{13}C NMR** (300 MHz, d_6-DMSO, 25 °C): δ 175.3, 155.4, 146.3, 135.3, 130.5, 129.9, 128.4, 126.9, 122.9, 117.1, 47.9. **Mass spectrum** ESI-MS calcd for $C_{20}H_{19}N_6S_2Zn^+$ [M + H]$^+$ 471.0396, found 471.0404.

Zinc(II) bis(t-Boc-protected amine thiosemicarbazone) acenaphthenequinone (1e)

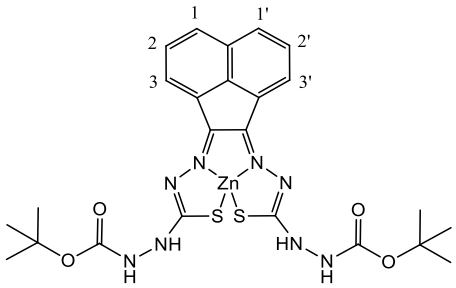

Acenaphthenequinone (50 mg, 0.274 mmols) and zinc acetate (183 mg, 0.833 mmols) in 2:98 acetic acid:dioxane were added in the presence of activated molecular sieves was heated to 60°C. A mixture of Monoboc thiosemicarbazide (*tert*-butyl-2-hydrazinecarbonothioyl)hydrazinecarboxylate) and the di-substituted-boc, was added in excess to a suspension and the temperature raised to 110 °C. This was refluxed for 30 h and by filtrated whilst hot. The filtrate was dried *in vacuo*, washed with 50 mL diethyl ether and dried once more *in vacuo*. The product was obtained as an orange solid (58 mg, 0.093 mmols, 34%). Elemental analysis indicated that this complex could not be isolated in high purity.

^{1}H NMR (d_6-DMSO, 25 ^{o}C): δ 9.39 (s, 2H, N*H*), 8.92 (s, 2H, N*H*), 8.30 (d, 2H, *H-1*, *J* = 7.1 Hz), 8.06 (d, 2H, *H-3*, *J* = 8.2 Hz), 7.76 (t, 2H, *H-2*, *J* = 7.6 Hz), 3.50 (d, 1H, dioxane), 1.91 (s, 1H, acetic acid), 1.48 (s, 18H, *t-Boc*). **Mass spectrum** ESI-MS calcd for $C_{24}H_{27}N_8O_4S_2Zn^-$ [M-H]$^-$ 619.0913, found 619.0893. **Elem. Anal.**: Found C; 35.3 %, H; 4.42 %, N; 18.05 %. Calc. C; 46.34 %; H; 4.54 %; N; 18.01 %. **HPLC** (Method H): R_t = 2.4 mins.

Copper(II) bis(4-methyl-3-thiosemicarbazone) acenaphthenequinone (2a)

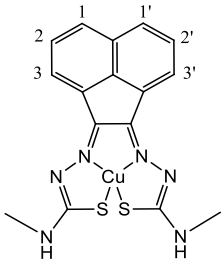

Synthesised from the proligand: 1 equivalent compound **iia** (0.1g, 0.028 mmol) and 3 equivalents copper acetate (0.152g, 0.0842mmol) were stirred at rt in 50 mL methanol for 24 hours. This was filtered and washed with water and diethyl ether yielding a brown solid 82.9 mg, 70.5%. Synthesis *via* zinc complex: **1a** (50 mg, 0.119 mmols) was added to two equivalents of copper acetate (49.2 mg, 0.247 mmols) in methanol and stirred at room temperature for 24h, filtered and washed with diethyl ether. This yielded 36 mg (0.086 mmols, 72%) of brown solid. **Mass spectrum** ESI-MS calcd for $C_{16}H_{15}CuN_6S_2^+$ $[M + H]^+$, 418.0090, found 418.0092. **Elem. Anal.**: Found: C; 45.6 %, H; 3.85 %, N; 18.8 %. Calc.: C; 45.97 %, H; 3.38 %, N; 20.11 %. **HPLC** (Method A): R_t = 11.3 mins, (Method H): R_t = 8.1 mins.

Copper(II) bis(4-ethyl-3-thiosemicarbazone) acenaphthenequinone (2b)

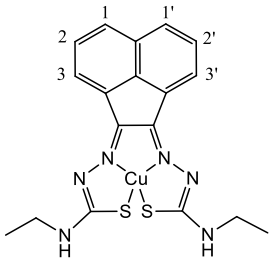

Synthesis from proligand: 1 equivalent bis ethyl thiosemicarbazone ligand (0.15g, 0.390 mmol) and 3 equivalents copper acetate (0.254g, 1.10 mmol) were stirred at rt in 50 mL methanol for 24 hours. This was filtered and washed with water and diethyl ether giving a brown solid, yielding 67.8 mg, 0.152 mmols, 39%. Synthesis from the zinc complex: **1b** (50 mg, 0.112 m mols) was added to two equivalents of copper acetate (44.5 mg, 0.223 mmol) in methanol. This was stirred at rt in 50 mL methanol for 24 hours. It was filtered and washed with water and diethyl ether yielding a brown solid of 26.6 mg, 0.060 mmols, 53%. **Mass spectrum** ESI-MS calcd for $C_{18}H_{19}CuN_6S_2^+$ $[M + H]^+$ 446.0403, found 446.0400. **Elem. Anal.**: Found: C; 47.9 %, H; 4.05 %, N; 17.60 %. Calc.: C; 47.73 %, H; 4.64%, N; 17.58%. **HPLC** (Method H): R_t = 9.3 mins.

Copper(II) bis(4-phenyl-3-thiosemicarbazone) acenaphthenequinone (2c)

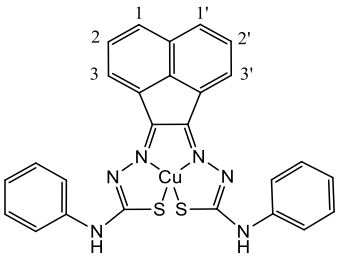

Synthesis from zinc bis phenyl thiosemicarbazone: The zinc complex **1c**, (101 mg, 0.186 mmols) added to two equivalents of copper acetate (77 mg, 0.386 mmols) in methanol and stirred at room temperature for 24h. The product (67 mg, 0.124 mmols, 66%) was isolated by filtration and washing with water and diethyl ether.

Mass spectrum ESI-MS calcd for $C_{26}H_{17}CuN_6S_2^-$ $[M-H]^-$ 540.0258, found 540.0237. **Elem. Anal.**: Found: C; 55.8 %, H, 3.50 %; N; 14.60 %. Calc. (+MeOH): C; 56.48 %, H, 3.86 %, N; 14.64 %. **HPLC** (Method D): R_t = 14.9 mins.

Copper(II) bis(4-allyl-3-thiosemicarbazone) acenaphthenequinone (2d)

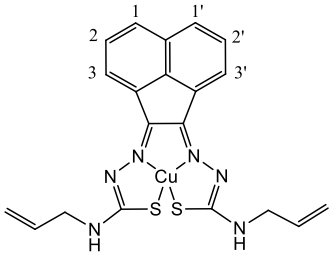

Synthesis from the ligand: 1 equivalent bis allyl thiosemicarbazone (0.2g, 0.049 mmol) and 3 equivalents copper acetate (0.32g, 0.147 mmol) were stirred at rt in 50 mL methanol for 24 hours. This was filtered and washed with water and diethyl ether yielding a brown solid of 95mg, 41%. Synthesis from zinc complex: **1d**, (52 mg, 0.110 mmols) added to two equivalents of copper acetate (44 mg, 0.223 mmols) in methanol and stirred at room temperature for 24h. The product (33 mg, 0.070 mmols, 64%) was isolated by filtration and washing with water and diethyl ether. **Mass spectrum** ESI-MS calcd for $C_{20}H_{17}N_6S_2Cu^-$ $[M-H]^-$ 468.0258, found 468.0260. **Elemental Analysis**: Found: C; 49.85 %, H, 3.82 %, N; 17.0 %. Calc.: C; 51.10 %, H,3.86 %, N; 17.88 %. **HPLC** (Method H): R_t = 9.4 mins.

Copper(II) bis(t-Boc-protected amine thiosemicarbazone) acenaphthenequinone (2e)

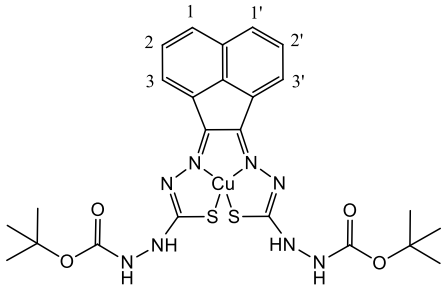

The zinc complex **1e**, (20 mg, 0.032 mmols) was added to two equivalents of copper acetate in methanol and stirred at room temperature for 24h. The product was isolated by rotary evaporation yielding 8 mg of very dark brown solid (0.013 mmols, 40%).
Mass spectrum ESI-MS calcd for $C_{24}H_{27}CuN_8O_4S_2^-$ $[M-H]^-$ 618.0898, found 618.0761.
HPLC (Method H): R_t = 8.5 mins.

Gallium(III) chloride bis(4-methyl-3-thiosemicarbazone) acenaphthenequinone (3a)

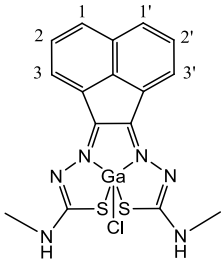

A suspension of zinc bis(4-methyl-3-thiosemicarbazide) acenaphthenequinone (0.101 g, 0. 242 mmol) in MeOH (50 mL) was added to $GaCl_3$ (0.193 g, 1.11 mmol). The resulting suspension was heated at reflux for 6 h. The red solid that precipitated on cooling to room temperature was then isolated by filtration, washed with Et_2O and dried under vacuum (0.0395 g, 0.086 mmol, 36%). The (*E*,*E*) and (*E*,*Z*) isomers were found to be present in the integral ratio of 57:43 (favouring the (*E*,*E*) isomer) in d_6-DMSO by ^{1}H NMR analysis.
(*E*,*E*) isomer (57% relative abundance) **^{1}H NMR** (d_6-DMSO, 25 °C): δ 8.81 (broad s, 2H, N*H*), 8.29 (d, 2H, *H-1*, *J* = 6.8 Hz), 8.19 (d, 2H, *H-3*, *J* = 8.3 Hz), 7.88 (t, 2H, *H-2*, *J* = 4.5 Hz), 3.11 (d, 6H, CH_3). (*E*,*Z*) isomer (43% relative abundance) **^{1}H NMR** (d_6-DMSO, 25 °C): δ 9.53 (apparent d, 1H, N*H*, *J* = 4.1 Hz), 8.90 (apparent d, 1H, N(*H'*), *J* = 4.5 Hz), 8.58 (d, 1H, *H-1* or *H-1*, *J* = 7.0Hz ‘), 8.16 (obscured d, 1H, *H-1* or *H-1'*), 8.07 (d, 1H, *H-3* or *H-3', J* = 8.2Hz), 7.94 (d, 1H, *H-3* or *H-3', J* = 6.9 Hz), 7.84 (t, 1H,

H-2 or *H-2'*, *J* = 7.7Hz), 7.80 (t, 1H, *H-2* or *H-2'*, *J* = 7.6Hz), 3.16 (d, 3H, *CH*$_3$ or *CH*$_3$*'*, *J* = 4.4 Hz*)*, 3.12 (obscured d, 3H, *CH*$_3$ or *CH*$_3$*'*). **^{13}C NMR** (*d*$_6$-DMSO, 25 °C): δ 178.7, 174.7, 170.7, 147.5, 142.4, 138.9, 138.8, 136.0, 132.3, 130.4, 129.7, 129.4, 129.1, 129.04, 128.95, 128.90, 128.6, 127.4, 126.2, 124.6, 118.4, 33.2, 30.2 29.4, 27.1. **Mass spectrum** ESI-MS calcd for $C_{16}H_{13}ClGaN_6S_2^-$ $[M-H]^-$ 456.9587, found 458.9605. **Elemental analysis**: Calc.: C; 41.81 %, H; 3.07 %, N; 18.28 %, Found: C; 41.8 %, H; 3.04 %, N; 18.0 %.

Gallium(III) chloride bis(4-ethyl-3-thiosemicarbazone) acenaphthenequinone (3b)

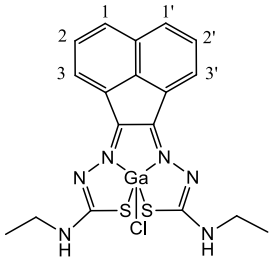

A suspension of zinc bis(4-ethyl-3-thiosemicarbazide) acenaphthenequinone (0.216 g, 0.482 mmol) in MeOH (50 mL) was added to $GaCl_3$ (0.420 g, 1.478 mmol). The resulting suspension was heated at reflux for 6 h. The red solid that precipitated on cooling to room temperature was then isolated by filtration, washed with Et_2O and dried under vacuum (0.146 g, 0.299 mmols, 62%).

The (*E*,*E*) and (*E*,*Z*) isomers were found to be present in the integral ratio of approximately 1:1 in *d*$_6$-DMSO by ^{1}H NMR analysis. (*E*,*Z*) isomer (51%). **^{1}H NMR** (*d*$_6$-DMSO, 25 ^{o}C): δ 9.58 (t, 1H, N*H*), 8.87 (t, 1H, N*H'*), 8.50 (d, 1H, *H-1*, *J* = 7.0 Hz), 8.11 (d, 1H, *H-3'*, *J* = 8.3 Hz), 8.03 (d, 1H, *H-3*, *J* = 8.1 Hz), 7.93 (d, 1H, *H-1'*, *J* = 6.9 Hz), 7.83 (apparent t, 1H, *H-2*), 7.76 (apparent t, 1H, *H-2'*), 3.61 + 3.56 (m, 4H, C*H*$_2$), 1.26 + 1.25 (two t, 6H, C*H*$_3$, *J* = 7.2 Hz). (*E*,*E*) isomer (49%): δ 8.79 (broad t, 2H, N*H*), 8.16 (d, 2H, *H-1*, *J* = 7.0 Hz), 8.09 (d, 2H, *H-3*, *J* = 8.3 Hz), 7.75 (apparent t, 2H, *H-2*), 3.59 (m, 4H, C*H*$_2$), 1.25 (t, 6H, C*H*$_3$, *J* = 7.2 Hz). **^{13}C NMR** (*d*$_6$-DMSO, 25 °C): δ 177.56, 173.20, 169.93, 138.72, 138.50, 135.84, 132.28, 130.25, 129.65, 129.31, 128.92, 128.47, 127.00, 126.83, 126.06, 124.23, 118.39, 114.13, 41.87, 38.34, 37.57, 14.60, 14.07, 13.67. **Mass spectrum** ESI-MS calcd for $C_{18}H_{17}ClGaN_6S_2$ $[M-H]^-$ 484.9900, found 484.9907.

Gallium(III) chloride bis(4-phenyl-3-thiosemicarbazone) acenaphthenequinone (3c)

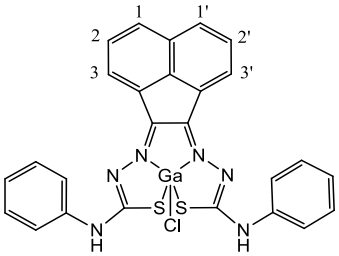

A suspension of zinc bis(4-phenyl-3-thiosemicarbazide) acenaphthenequinone (0.100 g, 0.184 mmol) in MeOH (50 mL) was added to $GaCl_3$ (0.1567 g, 0.551 mmol). The resulting suspension was heated at reflux for 6 h. The red solid that precipitated on cooling to room temperature was then isolated by filtration, washed with Et_2O and dried under vacuum (72.4 mg, 0.124 mmols, 67%). The (*E*,*E*) and (*E*,*Z*) isomers were found to be present in the integral ratio of approximately 1:1 in d_6-DMSO by ^{1}H NMR analysis. (*E*,*Z*):(*E*,*E*) 27:73%. NMR data of the (*E*,*Z*) isomer was not assigned due to major overlapping with (*E*,*E*) peaks and poorly defined signals.

(*E*,*E*) isomer (73%). **^{1}H NMR** (d_6-DMSO, 25 °C): δ 10.81 (s, 2H, N*H*), 8.28 (two overlapping d, 4H, *H-3 + H-1*), 7.97 (apparent t, 2H, *H-2*), 7.87 (d, 4H, o-*H*, *J = 8.0 Hz*), 7.50 (apparent t, 4H, m-*H*), 7.20 (t, 2H, p-*H*, *J = 7.3 Hz*). **^{13}C NMR** (75.5 MHz, *d*6-DMSO, 25 °C): weak due to poor solubility

Mass spectrum ESI-MS calcd for $[C_{26}H_{17}ClGaN_6S_2]^-$ $[M-H]^-$ 580.9900, found 580.9915.

Gallium(III) chloride bis(4-allyl-3-thiosemicarbazone) acenaphthenequinone (3d)

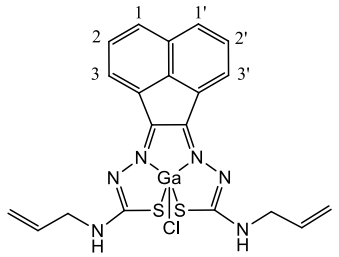

A suspension of zinc bis(4-allyl-3-thiosemicarbazide) acenaphthenequinone (0.050 g, 0.106 mmol) in MeOH (50 mL) was added to $GaCl_3$ (0.284 g, 1.635 mmol). The resulting suspension was heated at reflux for 6 h. After allowing cooling a red solid was then isolated by filtration, washed with Et_2O and dried under vacuum (0.029 g, 0.057 mmol, 54%). (*E*,*Z*) isomer (62% relative abundance) **^{1}H NMR** (300 MHz, d_6-DMSO, 25 °C): δ 9.78 (m, 1H, N*H*), 9.08 (m, 1H, N*H´*), 8.52 (d, 1H, *H-1*, *J* = 7.2 Hz), 8.12 (overlapping d, 1H, *H-1*), 8.05 (d, 1H, *H-3*, *J* = 8.3 Hz), 7.94 (d, 1H, *H-1*, *J* = 7.0 Hz),

7.79 (overlapping t, 1H, *H-2* or *H-2*), 7.77 (overlapping t, 1H, *H-2* or *H-2*), 5.87–6.09 (m, 2H, CH2C*H*CH2, 5.30 (two overlapping dd, 2H, H_{trans}), 5.17 (two overlapping dd, 2H H_{cis}), 4.23 (m, 2H, CH_2CHCH$_2$), 4.17 (m, 2H, CH_2CHCH$_2$). (*E*,*E*) isomer (38% relative abundance) **^{1}H NMR** (300 MHz, d_6-DMSO, 25 ◦C): δ 9.02 N*H*, 8.21 (d, *H-3*, *J* = 7.2 Hz), 8.15 *H-1*, 7.84 *H-2*, 5.87-6.09 (m, CH$_2$C*H*CH$_2$), 5.28 (dd, H_{trans}), 5.21 (dd, H_{cis}.), 4.23 (m, 2H, CH_2CHCH$_2$). **^{13}C NMR** (d_6-DMSO, 25 ◦C): δ 178.5, 170.3, 147.6, 142.6, 138.8, 135.9, 134.2, 133.7, 133.3, 132.2, 129.7, 129.6, 129.5, 128.9, 128.7, 128.5, 127.1, 127.0, 125.9, 124.4, 118.5, 117.3, 116.6, 116.5, 48.9, 45.7, 45.0. **Mass spectrum** ESI-MS calcd for $C_{20}H_{17}ClGaN_6S_2^-$ [M - H]$^-$ 508.9900, found 508.9911. **Elem. Anal.**: Found C; 45.7%, H; 3.45 %, N; 15.6 %. Calc. (for 3·MeOH): C; 46.39 %, H; 4.08 %, N; 15.46 %,

Indium(III) chloride bis(4-methyl-3-thiosemicarbazone) acenaphthenequinone (4a)

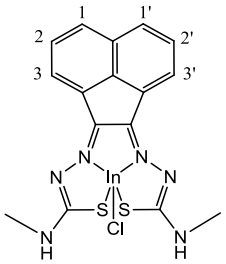

A suspension of zinc bis(4-methyl-3-thiosemicarbazide) acenaphthenequinone (0.155 g, 0. 370 mmol) in MeOH (50 mL) was added to $InCl_3$ (0.365 g, 1.652 mmol). The resulting suspension was heated at reflux for 6 h. The red solid that precipitated on cooling to room temperature was then isolated by filtration, washed with Et2O and dried under vacuum (0.116 g, 0.230 mmol, 62%).

^{1}H NMR (d_6-DMSO, 25 °C): δ 8.42 (d, 2H, *H-1*, *J* = 6.6 Hz), 8.09 (d, 2H, *H-3*, *J* = 8.1 Hz), 7.98 (m, 2H, N*H*), 7.75 (apparent t, 2H, *H-2*, *J* = 7.4 Hz and 7.9 Hz), 3.11 (d, 6H, CH_3, *J* = 4.7 Hz). **^{13}C NMR** (d_6-DMSO, 25 °C): δ 176.2, 139.9, 137.2, 130.3, 128.7, 128.6, 127.3, 124.2, 29.2. **Mass spectrum** ESI-MS calcd for $C_{16}H_{13}ClInN_6S_2^-$ [M - H]$^-$ 502.9370, found 502.9375. **Elem. Anal.**: Calc.: C; 38.07 %, H; 2.80 %, N; 16.65 %, Found C; 37.65 %, H; 2.77 %, N; 16.2 %.

Indium(III) chloride bis(4-ethyl-3-thiosemicarbazone) acenaphthenequinone (4b)

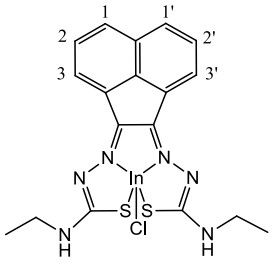

A suspension of zinc bis(4-ethyl-3-thiosemicarbazide) acenaphthenequinone (0.155 g, 0. 370 mmol) in MeOH (50 mL) was added to $InCl_3$ (0.365 g, 1.652 mmol). The resulting suspension was heated at reflux for 6 h. The red solid that precipitated on cooling to room temperature was then isolated by filtration, washed with Et2O and dried under vacuum (0.116 g, 0.230 mmol, 62%).

^{1}H NMR (d_8-THF, 25 ^{o}C): δ 8.29 (d, 2H, *H-1*, *J = 6.9 Hz*), 7.92 (d, 2H, *H-3*, *J = 8.3 Hz*), 7.68 (m, 4H, *NH + H-2)*, 3.72 (m, 4H, CH_2), 1.34 (t, 6H, CH_3, *J = 7.3 Hz*).

^{13}C NMR (d_8-THF, 25 ^{o}C): δ 175.3, 142.4, 139.7, 131.8, 129.3, 129.2, 128.9, 125.5, 39.1, 14.7. **Mass spectrum** ESI-MS calcd for $C_{18}H_{17}ClInN_6S_2^-$ $[M-H]^-$ 530.9683, found 530.9679. **Elem. Anal.**: Found: C; 38.80 %, H; 3.42 %, N; 14.60 %. Calc. (for 1·MeOH): C; 40.40 %, H; 3.93 %, N; 14.88 %.

Indium(III) chloride bis(4-phenyl-3-thiosemicarbazone) acenaphthenequinone (4c)

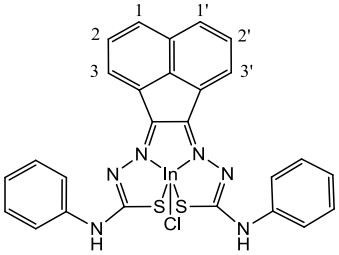

A suspension of zinc bis(4-phenyl-3-thiosemicarbazide) acenaphthenequinone (0.100 g, 0. 1838 mmol) in MeOH (50 mL) was added to $InCl_3$ (0.365 g, 1.652 mmol). The resulting suspension was heated at reflux for 6 h. **4c** was isolated from the filtrate, which was dried under vacuum and subsequently washed with water and diethyl ether (49.9 mg, 0.079 mmol, 43%).

^{1}H NMR (*d_8*-THF, 25 ^{o}C): δ 9.60 (s,2H,*NH*Ph), 8.40 (d, 2H, *H-3*, *J* = 7.0 Hz), 8.04 (d, 2H, *H-1*, *J* = 8.2 Hz), 7.85 (d, 4H, *o-H*, *J = 7.6 Hz*), 7.73 (apparent t, 2H, *H-2*,), 7.42 (t, 4H, *m-H*, *J = 7.9 Hz*), 7.13 (t, 2H, *p-H*, *J = 7.4 Hz*). **^{13}C NMR** (*d_8*-THF, 25 ^{o}C): δ 174.2, 144.5, 141.0, 136.9, 132.0, 129.8, 129.6, 129.5, 128.7, 125.4, 124.7, 123.0. **Mass**

spectrum ESI-MS calcd for $C_{26}H_{17}ClInN_6S_2^-$ [M-H]$^-$ 626.9683, found 626.9716. **Elem. Anal.**:. Found C; 45.90 %, H; 3.27 %, N; 12.10 %. Calc. (for 2·H_2O): C; 46.97 %, H; 3.34 %, N; 12.64 %

Indium(III) chloride bis(4-allyl-3-thiosemicarbazone) acenaphthenequinone (4d)

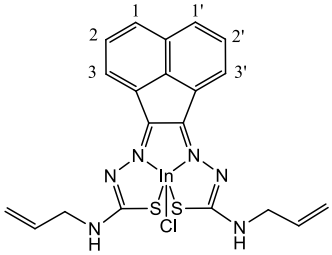

A suspension of zinc bis(4-allyl-3-thiosemicarbazide) acenaphthenequinone (0.100 g, 0. 212 mmol) in MeOH (50 mL) was added to $InCl_3$ (0.209 g, 0.946 mmol). The resulting suspension was heated at reflux for 6 h. The red solid that precipitated on cooling to room temperature was then isolated by filtration, washed with Et2O and dried under vacuum (0.031 g, 0.056 mmol, 27%). **^{1}H NMR** (300 MHz, d_6-DMSO, 25 °C): δ 8.35 (br s, 2H, *H-1*), 8.18 (s, 2H, N*H*), 8.04 (d, 2H, *H-3*, *J* = 8.2 Hz), 7.79 (t, 2H, *H-2*, *J* = 7.6 Hz), 6.01 (m, 2H, CH_2CHCH_2), 5.29 (dd, 2H, H_{trans}, *J* = 17.1 Hz), 5.14 (dd, 2H, H_{cis}, *J* = 10.3 Hz), 4.19 (s, 4H, CH_2CHCH_2). **^{13}C NMR** (75.5 MHz, d_6-DMSO, 25 °C): δ 176.0, 140.1, 137.2, 135.3, 130.3, 128.7, 127.4, 124.0, 115.9, 44.7. **Mass spectrum** ESI-MS calcd for $C_{20}H_{17}ClInN_6S_2^-$ [M+H]$^-$ 554.9683, found 554.9683 **Elem. Anal.**:. Found C; 42.40 %, H; 3.24 %, N; 14.8 %. Calc. (for 1·MeOH): C; 42.83 %, H; 3.77 %, N; 14.27 %

Bis-acenaphthenequinone bridged thiosemicarbazonato proligand (L_B)

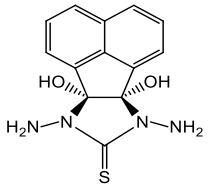

Excess of thiocarbohydrazide (1.43 g, 13.47 mmol) with an equivalent of acenaphthenequinone (0.5 g, 2.74 mmols) in 30 mL of ethanol *(Figure 7.2)*. Upon reflux four drops of glacial acetic acid were added and after 3 hours the suspension was filtered whilst hot yielding a yellow solid (247.9 mg, 0.86 mmols). Crystals precipitated (372.9 mg, 1.29 mmols) from the filtrate and possessed identical spectral properties as the solid.

^{1}H NMR (300 MHz, d_6-DMSO, 25 °C): δ 7.88 (overlapping d, 2H, *H-3*, *J* = 8.1 Hz), 7.73 (overlapping d, 2H, *H-1*, *J* = 6.9 Hz), 7.63 (overlapping t, 2H, *H-2*), 6.98 (s, 2H, O*H*), 4.61 (s, 4H, NH_2). **^{13}C NMR** (75.5 MHz, d_6-DMSO, 25 °C): δ 180.2, 139.2, 134.7, 130.4, 128.1, 125.2, 121.1, 95.5. **Mass spectrum** ESI-MS calcd for $C_{13}H_{13}N_4O_2S^+$ 289.0754, found 289.0741.

Zinc(II) 4-methyl-3-thiosemicarbazone-thiocarbohydrazide acenaphthenequinone (1aN)

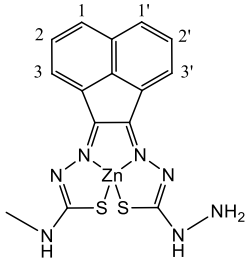

Zinc complex **1aN** was prepared by suspending 1 equivalent of compound **ia** (0.1044g, 0.38 mmol) and 3 equivalents of zinc acetate (0.2486, 1.13 mmol) in 10 mL of acetic acid at 60 ^{o}C. 3 equivalents of thiocarbohydrazide (0.1196g, 1.12 mmol) was added, the temperature increased to 120 ^{o}C and refluxed for 30h. Isolation was achieved by hot filtration, followed by washing with 5 mL of THF and 100 mL diethyl ether, yielding yellow powder of 0.1215 g, 0.28 mmol, 74%.

^{1}H NMR (300 MHz, d_6-DMSO, 25 ^{o}C): All peaks: δ 9.96 (very broad, 1.3H, NH, (*E*,*E*)), 8.95 (broad, 0.3H, N*H*, (*E*,*Z*)), 8.77 (broad, 0.3H, N*H*, (*E*,*Z*)), 8.15-8.75 (m, 2H, Ar-*H-1/3*) 7.80-8.05 (m, 2H, Ar-*H-1/3*), 6.71 (broad, 0.46H, NH_2, (*E*,*Z*)), 6.60 (broad, 1.04H, NH_2, (*E*,*E*)), 3.01-3.14 (m, 3H, CH_3). **^{13}C NMR** (75.5 MHz, d_6-DMSO, 25 °C)**:** δ 178.08, 175.59, 145.85, 135.09, 130.59, 129.51, 128.42, 127.81, 127.36, 127.11, 126.39, 120.17, 30.32, 22.64. **Mass spectrum** ESI-MS calcd for $C_{15}H_{14}N_7S_2Zn^+$ $[M+H]^+$ 420.0043, found 420.0066; $C_{15}H_{12}N_7S_2Zn^-$ $[M-H]^-$ 417.9887, found 417.9911. **HPLC** (Method B): R_t = 9.8 mins.

Zinc(II) 4-ethyl-3-thiosemicarbazone-thiocarbohydrazide acenaphthenequinone (1bN)

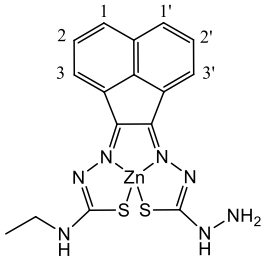

A suspension of compound **ib** (250.6 mg, 0.885 mmols) was added to three equivalents of zinc acetate (587.3 mg, 2.68 mmols) was heated to 60°C in 10 mL of acetic acid. Three equivalents of thiocarbohydrazide (285.6 mg, 2.69 mmols) were added and the temperature increased to 120°C. This was refluxed for 28 h and then filtered whilst hot, washed with 5 mL of THF, 100 mL of diethyl ether, and dried under vacuum, yielding a yellow powder of 221.6 mg, 0.510 mmols, 58 %.

^{1}H NMR: (300 MHz, d_6-DMSO, 25 °C) All peaks: δ 9.87 (1H, very broad peak, N*H* [*E*,*E*,]), 8.98 (0.39 H, N*H*, (*E*,*Z*)), 8.75 (0.36 H, N*H'*, (*E*,*Z*)), 8.15-8.63 (m, 2H, Ar-*H-1/3*), 7.68 (overlapping t, 2H, *H-2* and *H-2'*), 6.64 (0.7H, NH_2'), 6.54 (1H, NH_2), 3.60 (t, 2H, CH_2), 1.28 (t, 3H, CH_3). **^{13}C NMR** (75.5 MHz, d_6-DMSO, 25 °C): δ 177.48, 175.67, 135.01, 130.67, 129.52, 128.35, 127.35, 125.76, 120.12, 37.96, 22.76, 14.18. **Mass spectrum** ESI-MS calcd for $C_{16}H_{16}N_7S_2Zn^+$ $[M + H]^+$ 434.0200, found 434.0211. **HPLC** (Method B): R_t = 10.5 mins, (Method E): R_t = 9.2 mins.

Zinc(II) 4-phenyl-3-thiosemicarbazone-thiocarbohydrazide acenaphthenequinone (1cN)

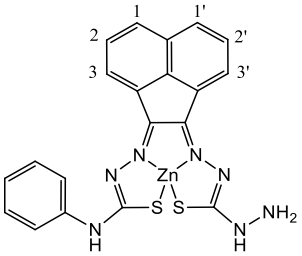

A suspension of compound **ic** (0.1025 g, 0.31 mmol) was added to three equivalents of zinc acetate (0.2048 g, 0.93 mmols) using was heated to 60°C in 10 mL of acetic acid. Three equivalents of (0.0998g, 0.94 mmol) thiocarbohydrazide were added and the temperature increased to 120°C. This was refluxed for 28 h and then filtered whilst hot,

washed with 5 mL of THF, 100 mL of diethyl ether, and dried under vacuum, yielding a dark red powder of 0.0982 g, 0.20 mmol, 65%.

^{1}H-NMR (300 MHz, d_6-DMSO, 25 °C): δ 9.92 2H (s, N*H* and N*H'* overlapping), 8.67 (broad d, 1H, *H-3* or *H-3'*), 8.07 (broad, 1H, *H-3* or *H-3'*), 7.95 1H (d, H1 or H1*'*, J = 8.29 Hz) and 7.89 1H (d, *H-1* or *H-1'*), 7.71 (d, 2H,*o-H*), 7.62 (d, 1H, *H-2* or *H-2'*), 7.51 (t, 1H, *H-2* or *H-2'*), 7.40 (t, 2H, *m-H*), 7.16 (t, 1H, *p-H*), 6.55 (s, 2H, NH_2). **^{13}C NMR** (75.5 MHz, d_6-DMSO, 25 °C): δ 140.15, 135.02, 130.30, 128.54, 128.01, 125.74, 123.65, 122.70, 22.49. **Mass spectrum** ESI-MS calcd for $C_{20}H_{16}N_7S_2Zn^+$ $[M+H]^+$ 482.0200, found 482.0200.

Zinc(II) 4-allyl-3-thiosemicarbazone-thiocarbohydrazide acenaphthenequinone (1dN)

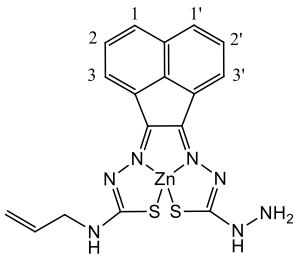

A suspension of compound **id** (0.1034g, 0.35 mmol)was added to three equivalents of zinc acetate (0.2228g, 1.01 mmol) using was heated to 60°C in 10 mL of acetic acid. Three equivalents of thiocarbohydrazide (0.1091, 1.02 mmol) were added and the temperature increased to 120°C. This was refluxed for 28 h and then filtered whilst hot, washed with 5 mL of THF, 100 mL of diethyl ether, and dried under vacuum, yielding a light brown powder of 0.0787g, 0.17 mmol, 48%.

(*E*,*E*) isomer, 67 % **^{1}H NMR** (300 MHz, d_6-DMSO, 25 ^{o}C): δ 9.82 (s, 1H, N*H*), 8.99 (s, 1H, N*H'*), 8.60 (d, 1H, *H-1*), 8.38 (broad, 1H, *H-1'*), 7.98 (d+d, 2H, *H-3*, *J* = 7.9 Hz), 7.68 (d+d, 2H, *H-2*), 6.59 (d, 2H, NH_2), 6.01 (m, 1H, CH_2CHCH_2), 5.28 (dd, 1H, H_{trans}), 5.14 (dd, 1H, H_{cis}), 4.18 (bm, 2H, CH_2CHCH_2). (*E*,*Z*) isomer contained many overlapping peaks and was not assignable. **^{13}C NMR** (75.5 MHz, d_6-DMSO, 25 °C): (Weak data due to poor solubility) δ 129.54, 115.75, 128.27, 127.26, 125.92, 115.75, 45.38, 22.61. **Mass spectrum** ESI-MS calcd for $C_{17}H_{16}N_7S_2Zn^+$ $[M+H]^+$ 446.0200, found 446.0192. **HPLC** (Method B): R_t = 10.9 mins, (Method E): R_t = 9.3 mins.

Gallium(III) 4-ethyl-3-thiosemicarbazone-thiocarbohydrazide acenaphthenequinone (3bN)

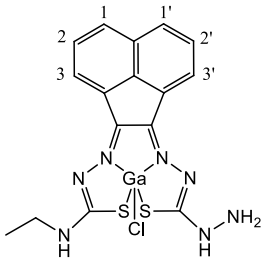

50 mg, 0.115 mmols of zinc **1bN** was solubilised in 2.5 mL of DMSO, to which an excess of gallium chloride was added and 30 mL of MeOH. This was refluxed under an atmosphere of nitrogen for 6 hours and was filtered after cooling to room temperature. The solution was removed *in vacuo* and the resultant material washed with 10 mL of ethyl acetate, followed by two times 10 mL of diethyl ether. This yielded an orange solid of 45 mg, 0.095 mmols, 82.6% (*E*,*E*) isomer. **^{1}H NMR** (300 MHz, d_6-DMSO, 25 ^{o}C): δ 10.25 (s, 1H, N*H*), 8.60 (t, 1H, N*H*, *J* = 6.41 Hz), 8.15 (d, 1H, *H-3*, *J* = 8.3 Hz), 7.98 (m, 1H, *H-3*', *J* = 8.2 Hz), 7.85 (m, 2H, *H-1*/*1'*) 7.75 (m, 2H, *H-2*/*2'*), 7.61 (s, 2H, NH_2), 4.12 (broad, 2H, CH_2), 1.30 (t, 3H, CH_3, *J* = 7.3 Hz). **^{13}C NMR** (75.5 MHz, d_6-DMSO, 25 °C): δ 129.81, 129.38, 128.27, 126.96, 125.78, 117.81, 37.96, 13.88. **Mass spectrum** ESI-MS calcd for $C_{20}H_{16}N_7S_2GaCl^-$ 471.9696, found 471.9729. **HPLC** (Method D): R_t = 7.8 mins.

Bombesin analogue

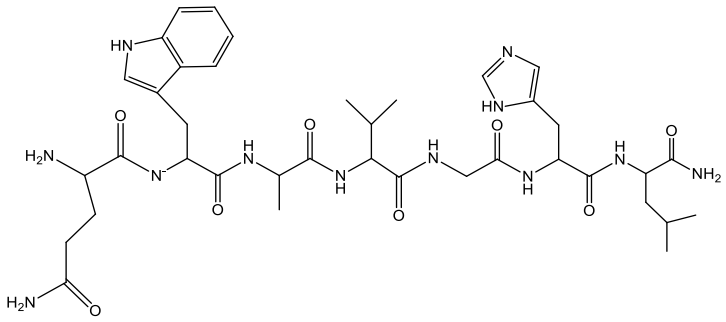

Fmoc-protected rink amide resin (1g, 0.5 mmols) was swelled in a peptide vessel for 20 min with DCM. This was subsequently deprotected using a solution of 20% piperidine in DMF, with deprotection confirmed by Kaiser-test. For the first step, three equivalents of the amino-acid (Fmoc-Leu-OH, 530 mg, 1.5 mmols) of HOBt (203 mg, 1.5 mmols) and of base *N,N′*-Diisopropylcarbodiimide (235 μL, 1.5 mmols) in DMF was added to the resin. This was to react for 90 minutes, followed by deprotection using 20% piperidine in DMF as confirmed by the Kaiser-test. Subsequent steps used three equivalents of amino acids, 1.9 equivalents of HOBt (360 mg) and 6 equivalents of *N,N′*-Diisopropylcarbodiimide and were followed by deprotection as described above. The amino acids were Fmoc-His(Trt)-OH (619.7 mg), Fmoc-Gly-OH (446 mg), Fmoc-Val-OH (509.1 mg),Fmoc-Ala-OH (467 mg), Fmoc-Trp(Boc)-OH (790 mg), Fmoc-Gln(Trt)-OH (916.05 mg), respectively. Finally the peptide was t-boc deprotected by stirring for three hours with a cocktail of 95% TFA, 2.5% TIS and 2.5% H_2O, with resin beads filtered and the solution collected. This was freeze-dried *in vacuo* and purified using semi-preparative HPLC yielding 60 mg of peptide.

Mass spectrum ESI-MS calcd for $C_{38}H_{57}N_{12}O_8^+$ 807.4417, found 807.4403. **HPLC** (Method E): R_t = 5.4 mins.

Derivatised bombesin analogue

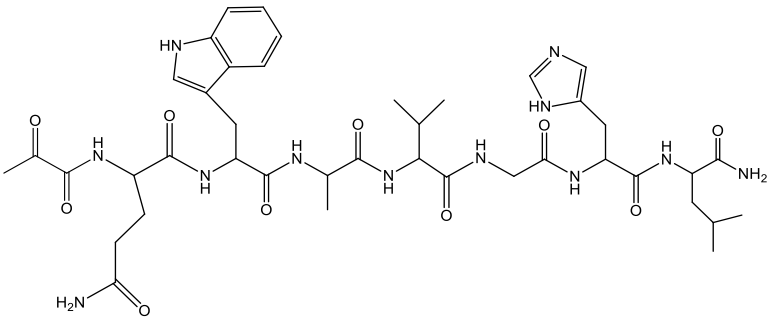

An equivalent of pyruvic acid (0.4 mg, 4.55 μmols) was added to coupling agents EDC (1-ethyl-3-(3'-dimethylaminopropyl) carbodiimide) (0.9 mg, 5.80 μmols) and HOBt (hydroxybenzotriazole) (0.86 mg, 6.37 μmols) on ice in DMF, which was achieved using 10x stock solutions in DMF. After 45 minutes 5 mg, (1 equivalent, 4.55 μmols) of bombesin was added followed by dropwise addition of DIPEA (*N*,*N'*-diisopropylethylamine) until pH 8 was reached. This was allowed to react for 2 hours and was subsequently extracted from DMF and purified using a solid phase extraction cartridge. **Mass spectrum** ESI-MS calcd for $C_{41}H_{57}N_{12}O_{10}^-$ 877.4321, found 877.4377. **HPLC** (Method E): R_t = 4.8 mins.

Ethyl-bombesin derivatised zinc complex, 1bB

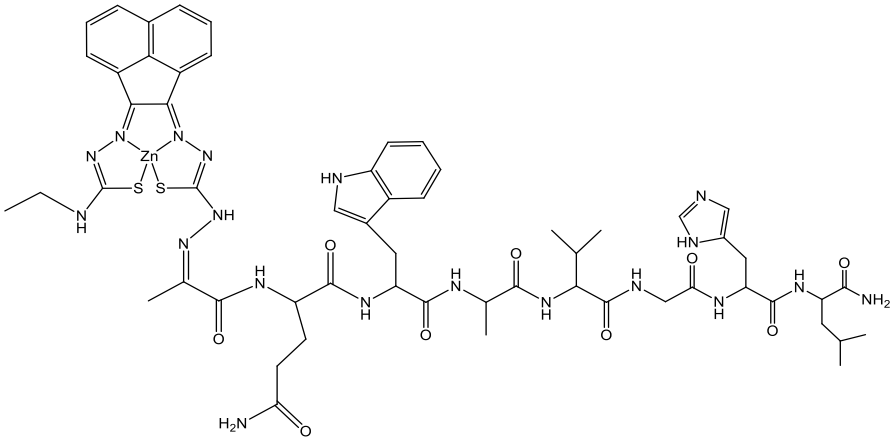

Following this 5 mg of derivatised bombesin analogue (4.55 μmols) was added to 2.0 mg (4.55 μmols) of zinc complex, compound **1bN** in 400 μL of DMSO, for the purpose of synthesising compound **1bB**. To this mixture 10 mL of HPLC grade methanol was added followed by 1 drop of concentrated HCl (32%), resulting in an instant colour change from dark orange to yellow. After stirring at 30°C for ca. 16 hours, the solution became pale orange and was freeze-dried *in vacuo*.

Allyl-bombesin derivatised zinc complex, 1dB

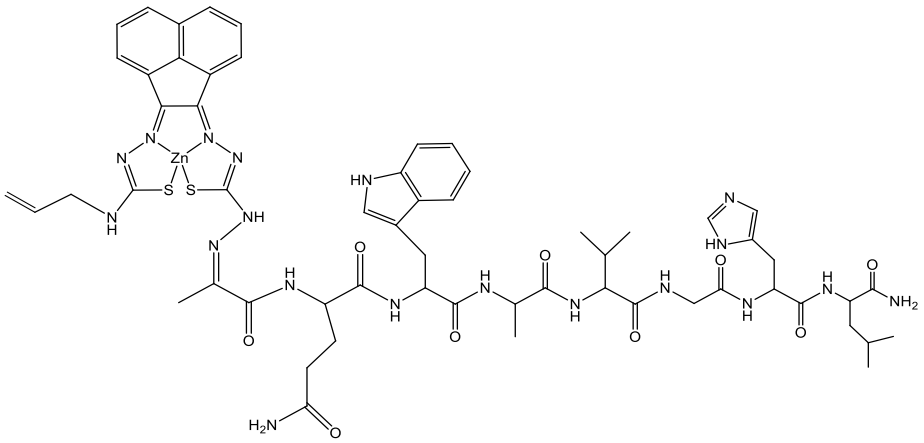

Following this 5 mg of derivatised bombesin analogue (4.55 μmols) was added to 2.0 mg (4.55 μmols) of zinc complex, compound **1dN** in 400 μL of DMSO, for the purpose of synthesising compound **1dB**. To this mixture 10 mL of HPLC grade methanol was added followed by 1 drop of concentrated HCl (32%), resulting in an instant colour change from dark orange to yellow. After stirring at 30°C for ca. 16 hours, the solution became pale orange and was freeze-dried *in vacuo*.

10. References

1. Office for National Statistics, 2010.
2. P. D. Sasieni, J. Shelton, N. Ormiston-Smith, C. S. Thomson and P. B. Silcocks, *British Journal of Cancer*, 2011, **105**, 460-465.
3. J. M. Brown and W. R. William, *Nat. Rev. Cancer*, 2004, **4**, 437-447.
4. P. Burgman, J. A. O'Donoghue, J. S. Lewis, M. J. Welch, J. L. Humm and C. C. Ling, *Nucl. Med. Biol.*, 2005, **32**, 623-630.
5. J. M. Brown, *Mol. Med. Today*, 2000, **6,** 157-162.
6. K. A. Krohn, J. M. Link and R. P. Mason, *Journal of Nuclear Medicine*, 2008, **49**, 129S-148S.
7. A. L. Harris, *Nat. Rev. Cancer*, 2002, **2**, 38-47.
8. J. Zhou, T. Schmid, S. Schnitzer and B. Bruene, *Cancer Letters*, 2006, **237**, 10-21.
9. T. F. Massoud and S. S. Gambhir, *Genes Dev.*, 2003, **17**, 545-580.
10. M. Rudin and R. Weissleder, *Nat. Rev. Drug Discovery*, 2003, **2**, 123-131.
11. P. Millet, C. Graf, A. Buck, B. Walder, G. Westera, W. Broggini, M. Arigoni, D. Slosman, C. Bouras and V. Ibanez, *Journal of Cerebral Blood Flow and Metabolism*, 2000, **20**, 1587-1603.
12. *http://www.molecularimagingcenter.org/index.cfm?PageID=8594&RPID=7165*, MICoE newsletter, 2007-1.
13. A. Elliott, *Nucl. Instrum. Methods Phys. Res., Sect. A*, 2005, **546**, 1-13.
14. M. Hamoudeh, M. A. Kamleh, R. Diab and H. Fessi, *Adv. Drug Delivery Rev.*, 2008, **60**, 1329-1346.
15. S. Bhattacharyya and M. Dixit, *Dalton Trans.*, 2011, **40**, 6112-6128.
16. B. J. Pichler, H. F. Wehrl and M. S. Judenhofer, *Journal of Nuclear Medicine*, 2008, **49**, 5S-23S.
17. J. R. Dilworth and S. J. Parrott, *Chem. Soc. Rev.*, 1998, **27**, 43-55.
18. K. E. Linder, Y. W. Chan, J. E. Cyr, M. F. Malley, D. P. Nowotnik and A. D. Nunn, *J. Med. Chem.*, 1994, **37**, 9-17.
19. J. Giglio, S. Fernandez, H.-J. Pietzsch, S. Dematteis, M. Moreno, J. P. Pacheco, H. Cerecetto and A. Rey, *Nucl. Med. Biol.*, 2012, **39**, 679-686.
20. M. Bartholomae, J. Valliant, K. P. Maresca, J. Babich and J. Zubieta, *Chem. Commun.*, 2009, **5**, 493-512.
21. K. K. W. Lo, M. W. Louie and K. Y. Zhang, *Coord. Chem. Rev.*, 2010, **254**, 2603-2622.
22. K. K. W. Lo, S. P. Y. Li and K. Y. Zhang, *New J. Chem.*, 2011, **35**, 265-287.
23. A. J. Amoroso, M. P. Coogan, J. E. Dunne, V. Fernandez-Moreira, J. B. Hess, A. J. Hayes, D. Lloyd, C. Millet, S. J. A. Pope and C. Williams, *Chem. Commun.*, 2007, 3066-3068.
24. A. J. Amoroso, R. J. Arthur, M. P. Coogan, J. B. Court, V. Fernandez-Moreira, A. J. Hayes, D. Lloyd, C. Millet and S. J. A. Pope, *New J. Chem.*, 2008, **32**, 1097-1102.
25. V. Fernandez-Moreira, F. L. Thorp-Greenwood, A. J. Amoroso, J. Cable, J. B. Court, V. Gray, A. J. Hayes, R. L. Jenkins, B. M. Kariuki, D. Lloyd, C. O. Millet, C. F. Williams and M. P. Coogan, *Org. Biomol. Chem.*, 2010, **8**, 3888-3901.

26. F. L. Thorp-Greenwood, V. Fernandez-Moreira, C. O. Millet, C. F. Williams, J. Cable, J. B. Court, A. J. Hayes, D. Lloyd and M. P. Coogan, *Chem. Commun.*, 2011, **47**, 3096-3098.
27. E. Ferri, D. Donghi, M. Panigati, G. Prencipe, L. D'Alfonso, I. Zanoni, C. Baldoli, S. Maiorana, G. D'Alfonso and E. Licandro, *Chem. Commun.*, 2010, **46**, 6255-6257.
28. M. W. Louie, H. W. Liu, M. H. C. Lam, T. C. Lau and K. K. W. Lo, *Organometallics*, 2009, **28**, 4297-4307.
29. M. Sagnou, S. Tzanopoulou, C. P. Raptopoulou, V. Psycharis, H. Braband, R. Alberto, I. C. Pirmettis, M. Papadopoulos and M. Pelecanou, *Eur. J. Inorg. Chem.*, 2012, 4279-4286.
30. L. Raszeja, A. Maghnouj, S. Hahn and N. Metzler-Nolte, *Chembiochem*, 2011, **12**, 371-376.
31. N. Viola-Villegas, A. E. Rabideau, J. Cesnavicious, J. Zubieta and R. P. Doyle, *Chemmedchem*, 2008, **3**, 1387-1394.
32. M. W. Louie, H. W. Liu, M. H. C. Lam, Y. W. Lam and K. K. W. Lo, *Chem.--Eur. J.*, 2011, **17**, 8304-8308.
33. K. K. W. Lo, M. W. Louie, K. S. Sze and J. S. Y. Lau, *Inorg. Chem.*, 2008, **47**, 602-611.
34. M. W. Louie, M. H. C. Lam and K. K. W. Lo, *Eur. J. Inorg. Chem.*, 2009, 4265-4273.
35. N. E. Bruckmann, S. Kogel, A. Hamacher, M. U. Kassack and P. C. Kunz, *Eur. J. Inorg. Chem.*, 2010, 5063-5068.
36. S. Tzanopoulou, I. C. Pirmettis, G. Patsis, M. Paravatou-Petsotas, E. Livaniou, M. Papadopoulos and M. Pelecanou, *J. Med. Chem.*, 2006, **49**, 5408-5410.
37. S. Tzanopoulou, M. Sagnou, M. Paravatou-Petsotas, E. Gourni, G. Loudos, S. Xanthopoulos, D. Lafkas, H. Kiaris, A. Varvarigou, I. C. Pirmettis, M. Papadopoulos and M. Pelecanou, *J. Med. Chem.*, 2010, **53**, 4633-4641.
38. T. L. Mindt, C. Mueller, M. Melis, M. de Jong and R. Schibli, *Bioconjugate Chem.*, 2008, **19**, 1689-1695.
39. T. L. Mindt, C. Mueller, F. Stuker, J.-F. Salazar, A. Hohn, T. Mueggler, M. Rudin and R. Schibli, *Bioconjugate Chem.*, 2009, **20**, 1940-1949.
40. T. M. Piscaer, C. Mueller, T. L. Mindt, E. Lubberts, J. A. N. Verhaar, E. P. Krenning, R. Schibli, M. De Jong and H. Weinans, *Arthritis and Rheumatism*, 2011, **63**, 1898-1907.
41. T. L. Mindt, C. Schweinsberg, L. Brans, A. Hagenbach, U. Abram, D. Tourwe, E. Garcia-Garayoa and R. Schibli, *Chemmedchem*, 2009, **4**, 529-539.
42. T. L. Mindt, H. Struthers, B. Spingler, L. Brans, D. Tourwe, E. Garcia-Garayoa and R. Schibli, *Chemmedchem*, 2010, **5**, 2026-2038.
43. R. F. Vitor, I. Correia, M. Videira, F. Marques, A. Paulo, J. C. Pessoa, G. Viola, G. G. Martins and I. Santos, *Chembiochem*, 2008, **9**, 131-142.
44. T. Esteves, C. Xavier, S. Gama, F. Mendes, P. D. Raposinho, F. Marques, A. Paulo, J. C. Pessoa, J. Rino, G. Viola and I. Santos, *Org. Biomol. Chem.*, 2010, **8**, 4104-4116.
45. S. Clede, F. Lambert, C. Sandt, Z. Gueroui, M. Refregiers, M.-A. Plamont, P. Dumas, A. Vessieres and C. Policar, *Chem. Commun.*, 2012, **48**, 7729-7731.
46. T. Koullourou, L. S. Natrajan, H. Bhavsar, S. J. A. Pope, J. H. Feng, J. Narvainen, R. Shaw, E. Scales, R. Kauppinen, A. M. Kenwright and S. Faulkner, *J. Am. Chem. Soc.*, 2008, **130**, 2178-2179.

47. A. Boulay, M. Artigau, Y. Coulais, C. Picard, B. Mestre-Voegtle and E. Benoist, *Dalton Trans.*, 2011, **40**, 6206-6209.
48. P. J. Blower, J. S. Lewis and J. Zweit, *Nucl. Med. Biol.*, 1996, **23**, 957-980.
49. R. E. Mewis and S. J. Archibald, *Coord. Chem. Rev.*, 2010, **254**, 1686-1712.
50. J. D. Silversides, R. Smith and S. J. Archibald, *Dalton Trans.*, 2011, **40**, 6289-6297.
51. D. J. Liu, D. Overbey, L. D. Watkinson, C. J. Smith, S. Daibes-Figueroa, T. J. Hoffman, L. R. Forte, W. A. Volkert and M. F. Giblin, *Bioconjugate Chem.*, 2010, **21**, 1171-1176.
52. H. C. Cai, Z. B. Li, C. W. Huang, A. H. Shahinian, H. Wang, R. Park and P. S. Conti, *Bioconjugate Chem.*, 2010, **21**, 1417-1424.
53. S. R. Lane, P. Nanda, T. L. Rold, G. L. Sieckman, S. D. Figueroa, T. J. Hoffman, S. S. Jurisson and C. J. Smith, *Nucl. Med. Biol.*, 2010, **37**, 751-761.
54. M. Fani, L. Del Pozzo, K. Abiraj, R. Mansi, M. L. Tamma, R. Cescato, B. Waser, W. A. Weber, J. C. Reubi and H. R. Maecke, *Journal of Nuclear Medicine*, 2011, **52**, 1110-1118.
55. H.-Y. Lee, Z. Li, K. Chen, A. R. Hsu, C. Xu, J. Xie, S. Sun and X. Chen, *Journal of Nuclear Medicine*, 2008, **49**, 1371-1379.
56. Y. Zhang, H. Hong, J. W. Engle, Y. N. Yang, C. P. Theuer, T. E. Barnhart and W. B. Cai, *Mol. Pharmaceutics*, 2012, **9**, 645-653.
57. S. H. Li, B. Goins, L. J. Zhang and A. D. Bao, *Bioconjugate Chem.*, 2012, **23**, 1322-1332.
58. D. L. Chen and F. Dehdashti, *Proceedings of the American Thoracic Society*, 2005, **2**, 541-544.
59. K. A. Wood, W. L. Wong and M. I. Saunders, *Nucl. Med. Biol.*, 2008, **35**, 393-400.
60. J. R. Dilworth and R. Hueting, *Inorg. Chim. Acta*, 2012, **389**, 3-15.
61. Y. Yoshii, T. Furukawa, Y. Kiyono, R. Watanabe, T. Mori, H. Yoshii, T. Asai, H. Okazawa, M. J. Welch and Y. Fujibayashi, *Nucl. Med. Biol.*, 2011, **38**, 151-157.
62. A. R. Cowley, J. J. Davis, J. R. Dilworth, P. S. Donnelly, R. Dobson, A. Nightingale, J. M. Peach, B. Shore, D. Kerr and L. Seymour, *Chem. Commun.*, 2005, 845-847.
63. D. Dayal, D. Palanimuthu, S. V. Shinde, K. Somasundaram and A. G. Samuelson, *J. Biol. Inorg. Chem.*, 2011, **16**, 621-632.
64. J. P. Holland, V. Fisher, J. A. Hickin and J. M. Peach, *Eur. J. Inorg. Chem.*, 2010, 48-58.
65. J. P. Holland, P. J. Barnard, S. R. Bayly, H. M. Betts, G. C. Churchill, J. R. Dilworth, R. Edge, J. C. Green and R. Hueting, *Eur. J. Inorg. Chem.*, 2008, 1985-1993.
66. Y. Altun and F. Koseoglu, *J. Solution Chem.*, 2005, **34**, 213-231.
67. S. R. Bayly, R. C. King, D. J. Honess, P. J. Barnard, H. M. Betts, J. P. Holland, R. Hueting, P. D. Bonnitcha, J. R. Dilworth, F. I. Aigbirhio and M. Christlieb, *Journal of Nuclear Medicine*, 2008, **49**, 1862-1868.
68. P. D. Bonnitcha, S. R. Bayly, M. B. M. Theobald, H. M. Betts, J. S. Lewis and J. R. Dilworth, *J. Inorg. Biochem.*, 2010, **104**, 126-135.
69. J. Chan, A. L. Thompson, M. W. Jones and J. M. Peach, *Inorg. Chim. Acta*, 2010, **363**, 1140-1149.

70. P. Heffeter, C. Pirker, C. R. Kowol, G. Herrman, R. Dornetshuber, W. Miklos, U. Jungwirth, G. Koellensperger, B. K. Keppler and W. Berger, *Biochem. Pharmacol.*, 2012, **83**, 1623-1633.
71. A. Castineiras, M. Gil, E. Bermejo and D. X. West, *Polyhedron*, 2001, **20**, 449-454.
72. P. J. Jansson, P. C. Sharpe, P. V. Bernhardt and D. R. Richardson, *J. Med. Chem.*, 2010, **53**, 5759-5769.
73. H. Beraldo, *Quim. Nova*, 2004, **27**, 461-471.
74. W. X. Hu, W. Zhou, C. N. Xia and X. Wen, *Bioorg. Med. Chem. Lett.*, 2006, **16**, 2213-2218.
75. A. I. Matesanz, C. Pastor and P. Souza, *Inorg. Chem. Commun.*, 2007, **10**, 97-100.
76. A. G. Quiroga and C. N. Ranninger, *Coord. Chem. Rev.*, 2004, **248**, 119-133.
77. S. L. Zheng and X. M. Chen, *Aust. J. Chem.*, 2004, **57**, 703-712.
78. Y. Hai, J. J. Chen, P. Zhao, H. B. Lv, Y. Yu, P. Y. Xu and J. L. Zhang, *Chem. Commun.*, 2011, **47**, 2435-2437.
79. C. S. He, X. H. Qian, Y. F. Xu, C. M. Yang, L. Y. Yin and W. P. Zhu, *Dalton Trans.*, 2011, **40**, 1034-1037.
80. A. Ojida, T. Sakamoto, M. Inoue, S. Fujishima, G. Lippens and I. Hamachi, *J. Am. Chem. Soc.*, 2009, **131**, 6543-6548.
81. C. R. Kowol, R. Trondl, V. B. Arion, M. A. Jakupec, I. Lichtscheidl and B. K. Keppler, *Dalton Trans.*, 2010, **39**, 704-706.
82. S. P. Wu, I. Lee, P. P. Ghoroghchian, P. R. Frail, G. Zheng, J. D. Glickson and M. J. Therien, *Bioconjugate Chem.*, 2005, **16**, 542-550.
83. B. A. Smith, S. Z. Xiao, W. Wolter, J. Wheeler, M. A. Suckow and B. D. Smith, *Apoptosis*, 2011, **16**, 722-731.
84. B. A. Smith, S. T. Gammon, S. Xiao, W. Wang, S. Chapman, R. McDermott, M. A. Suckow, J. R. Johnson, D. Piwnica-Worms, G. W. Gokel, B. D. Smith and W. M. Leevy, *Mol. Pharmaceutics*, 2011, **8**, 583-590.
85. W. M. Leevy, S. T. Gammon, J. R. Johnson, A. J. Lampkins, H. Jiang, M. Marquez, D. Piwnica-Worms, M. A. Suckow and B. D. Smith, *Bioconjugate Chem.*, 2008, **19**, 686-692.
86. K. M. DiVittorio, W. M. Leevy, E. J. O'Neil, J. R. Johnson, S. Vakulenko, J. D. Morris, K. D. Rosek, N. Serazin, S. Hilkert, S. Hurley, M. Marquez and B. D. Smith, *Chembiochem*, 2008, **9**, 286-293.
87. X. R. Liu, D. F. Cheng, B. D. Gray, Y. Z. Wang, A. Akalin, M. Rusckowski, K. Y. Pak and D. J. Hnatowich, *Nucl. Med. Biol.*, 2012, **39**, 709-714.
88. Y. Kurishita, T. Kohira, A. Ojida and I. Hamachi, *J. Am. Chem. Soc.*, 2010, **132**, 13290-13299.
89. A. Ojida, K. Honda, D. Shinmi, S. Kiyonaka, Y. Mori and I. Hamachi, *J. Am. Chem. Soc.*, 2006, **128**, 10452-10459.
90. A. J. Moro, J. Schmidt, T. Doussineau, A. Lapresta-Fernandez, J. Wegener and G. J. Mohr, *Chem. Commun.*, 2011, **47**, 6066-6068.
91. A. Jayasree, S. Sasidharan, M. Koyakutty, S. Nair and D. Menon, *Carbohydr. Polym.*, 2011, **85**, 37-43.
92. T. K. Nayak and M. W. Brechbiel, *Bioconjugate Chem.*, 2009, **20**, 825-841.
93. S. Chaves, A. C. Mendonca, S. M. Marques, M. I. Prata, A. C. Santos, A. F. Martins, C. Geraldes and M. A. Santos, *J. Inorg. Biochem.*, 2011, **105**, 31-38.

94. S. Nomura, N. Funabashi, M. Tsubura, M. Uehara, Y. Shiina, M. Daimon, K. Tateno, T. Nagai and I. Komuro, *International Journal of Cardiology*, 2011, **150**, E81-E84.
95. S. Yamazaki, M. Okano, N. Toita, N. Hatano, I. Kobayashi, N. Kawamura and K. Kobayashi, *Pediatrics International*, 2009, **51**, 587-590.
96. A. Vijayananthan, A. Arumugam, G. Kumar and D. Harichandra, *Biomedical imaging and intervention journal*, 2008, **4**, e23.
97. E. Even-Sapir and O. Israel, *European Journal of Nuclear Medicine and Molecular Imaging*, 2003, **30**, S65-S81.
98. H. X. Guo, J. Q. Yang, N. Shenoy and Y. B. Miao, *Bioconjugate Chem.*, 2009, **20**, 2356-2363.
99. H. W. Zhang, J. Schuhmacher, B. Waser, D. Wild, M. Eisenhut, J. C. Reubi and H. R. Maecke, *European Journal of Nuclear Medicine and Molecular Imaging*, 2007, **34**, 1198-1208.
100. J. Van Riet, D. Rattat, A. Verbruggen, L. Mortelmans and F. M. Mottaghy, *Clinical Nuclear Medicine*, 2009, **34**, 27-28.
101. D. W. Hwang, H. Y. Ko, S.-K. Kim, D. Kim, D. S. Lee and S. Kim, *Chem.--Eur. J.*, 2009, **15**, 9387-9393.
102. S. J. DeNardo, R. W. Liu, H. Albrecht, A. Natarajan, J. L. Sutcliffe, C. Anderson, L. Peng, R. Ferdani, S. R. Cherry and K. S. Lam, *Journal of Nuclear Medicine*, 2009, **50**, 625-634.
103. D. Wild, E. Christ, M. E. Caplin, T. R. Kurzawinski, F. Forrer, M. Brandle, J. Seufert, W. A. Weber, J. Bomanji, A. Perren, P. J. Ell and J. C. Reubi, *Journal of Nuclear Medicine*, 2011, **52**, 1073-1078.
104. A. Iagaru, S. S. Gambhir and M. L. Goris, *Journal of Nuclear Medicine*, 2008, **49**, 1809-1812.
105. M. Yoshimoto, K. Ogawa, K. Washiyama, N. Shikan, H. Mori, R. Amano and K. Kawai, *Int. J. Cancer*, 2008, **123**, 709-715.
106. C. Li, W. Wang, Q. P. Wu, K. Shi, J. Houston, E. Sevick-Muraca, L. Dong, D. Chow, C. Charnsangavej and J. G. Gelovani, *Nucl. Med. Biol.*, 2006, **33**, 349-358.
107. F. Alshoukr, A. Prignon, L. Brans, A. Jallane, S. Mendes, J. N. Talbot, D. Tourwe, J. Barbet and A. Gruaz-Guyon, *Bioconjugate Chem.*, 2011, **22**, 1374-1385.
108. W. Wang, S. Ke, S. Kwon, S. Yallampalli, A. G. Cameron, K. E. Adams, M. E. Mawad and E. M. Sevick-Muraca, *Bioconjugate Chem.*, 2007, **18**, 397-402.
109. K. Saatchi, P. Soema, N. Gelder, R. Misri, K. McPhee, J. H. E. Baker, S. A. Reinsberg, D. E. Brooks and U. O. Hafeli, *Bioconjugate Chem.*, 2012, **23**, 372-381.
110. H. Xu, P. K. Eck, K. E. Baidoo, P. L. Choyke and M. W. Brechbiel, *Bioorg. Med. Chem.*, 2009, **17**, 5176-5181.
111. T. Barrett, Y. Koyama, Y. Hama, G. Ravizzini, I. S. Shin, B. S. Jang, C. H. Paik, Y. Urano, P. L. Choyke and H. Kobayashi, *Clinical Cancer Research*, 2007, **13**, 6639-6648.
112. M. Ogawa, C. A. S. Regino, J. Seidel, M. V. Green, W. Z. Xi, M. Williams, N. Kosaka, P. L. Choyke and H. Kobayashi, *Bioconjugate Chem.*, 2009, **20**, 2177-2184.
113. C. Yoshida, A. B. Tsuji, H. Sudo, A. Sugyo, C. Sogawa, M. Inubushi, T. Uehara, T. Fukumura, M. Koizumi, Y. Arano and T. Saga, *Nucl. Med. Biol.*, 2011, **38**, 331-337.

114. S. Hoppmann, Z. Miao, S. L. Liu, H. G. Liu, G. Ren, A. D. Bao and Z. Cheng, *Bioconjugate Chem.*, 2011, **22**, 413-421.
115. L. Li, F. Turatti, D. Crow, J. R. Bading, A. L. Anderson, E. Poku, P. J. Yazaki, L. E. Williams, D. Tamvakis, P. Sanders, D. Leong, A. Raubitschek, P. J. Hudsony, D. Colcher and J. E. Shively, *Journal of Nuclear Medicine*, 2010, **51**, 1139-1146.
116. K. M. Clark, J. Bendix, A. F. Heyduk and J. W. Ziller, *Inorg. Chem.*, 2012, **51**, 7457-7459.
117. I. L. Fedushkin, M. V. Moskalev, A. N. Lukoyanov, A. N. Tishkina, E. V. Baranov and G. A. Abakumov, *Chem.--Eur. J.*, 2012, **18**, 11264–11276.
118. W. Zhu, M. Dai, Y. Xu and X. Qian, *Bioorg. Med. Chem.*, 2008, **16**, 3255-3260.
119. J. P. Holland, P. J. Barnard, D. Collison, J. R. Dilworth, R. Edge, J. C. Green, J. M. Heslop, E. J. L. McInnes, C. G. Salzmann and A. L. Thompson, *Eur. J. Inorg. Chem.*, 2008, 3549-3560.
120. J. A. Moore, K. Vasudevan, N. J. Hill, G. Reeske and A. H. Cowley, *Chem. Commun.*, 2006, 2913-2915.
121. E. Hollo-Sitkei, G. Szalontai, I. Lois, A. Gomory, F. Pollreisz, L. Parkanyi, H. Jude and G. Besenyei, *Chem.--Eur. J.*, 2009, **15**, 10620-10633.
122. L. Alsop, A. R. Cowley, J. R. Dilworth, P. S. Donnelly, J. M. Peach and J. T. Rider, *Inorg. Chim. Acta*, 2005, **358**, 2770-2780.
123. S. I. Pascu, P. A. Waghorn, B. W. C. Kennedy, R. L. Arrowsmith, S. R. Bayly, J. R. Dilworth, M. Christlieb, R. M. Tyrrell, J. Zhong, R. M. Kowalczyk, D. Collison, P. K. Aley, G. C. Churchill and F. I. Aigbirhio, *Chemistry-an Asian Journal*, 2010, **5**, 506-519.
124. R. Pedrido, M. J. Romero, M. R. Bermejo, A. M. Gonzalez-Noya, I. Garcia-Lema and G. Zaragoza, *Chem.--Eur. J.*, 2008, **14**, 500-512.
125. E. Lopez-Torres, M. A. Mendiola and U. J. Pastor, *Inorg. Chem.*, 2006, **45**, 3103-3112.
126. D. Witt, *Synthesis-Stuttgart*, 2008, **16**, 2491-2509.
127. S. I. Pascu, P. A. Waghorn, T. D. Conry, H. M. Betts, J. R. Dilworth, G. C. Churchill, T. Pokrovska, M. Christlieb, F. I. Aigbirhio and J. E. Warren, *Dalton Trans.*, 2007, 4988-4997.
128. S. I. Pascu, P. A. Waghorn, T. D. Conry, B. Lin, H. M. Betts, J. R. Dilworth, R. B. Sim, G. C. Churchill, F. I. Aigbirhio and J. E. Warren, *Dalton Trans.*, 2008, 2107-2110.
129. J. R. Lakowicz, *Principles of fluorescence spectroscopy*, Springer, 4th edn., 2006.
130. P. G. Bush, D. L. Wokosin and A. C. Hall, *Frontiers in Bioscience*, 2007, **12**, 2646-2657.
131. B. G. Wang, K. Koenig and K. J. Halbhuber, *Journal of Microscopy-Oxford*, 2010, **238**, 1-20.
132. J. J. Hunter, J. I. W. Morgan, W. H. Merigan, D. H. Sliney, J. R. Sparrow and D. R. Williams, *Progress in Retinal and Eye Research*, 2012, **31**, 28-42.
133. W. Becker, *Journal of Microscopy*, 2012, **247**, 119-136.
134. N. I. Cade, G. Fruhwirth, S. J. Archibald, T. Ng and D. Richards, *Biophys. J.*, 2010, **98**, 2752-2757.
135. S. Despa, P. Steels and M. Ameloot, *Anal. Biochem.*, 2000, **280**, 227-241.
136. J. R. Lakowicz and H. Szmacinski, *Journal of Fluorescence*, 1996, **6**, 83-95.
137. S. W. Botchway, A. W. Parker, R. H. Bisby and A. G. Crisostomo, *Microscopy Research and Technique*, 2008, **71**, 267-273.

138. R. L. Arrowsmith, P. A. Waghorn, M. W. Jones, A. Bauman, S. K. Brayshaw, Z. Hu, G. Kociok-Koehn, T. L. Mindt, R. M. Tyrrell, S. W. Botchway, J. R. Dilworth and S. I. Pascu, *Dalton Trans.*, 2011, **40**, 6238-6252.
139. B. Rajwa, T. Bernas, H. Acker, J. Dobrucki and J. P. Robinson, *Microscopy Research and Technique*, 2007, **70**, 869-879.
140. S. H. Huang, A. A. Heikal and W. W. Webb, *Biophys. J.*, 2002, **82**, 2811-2825.
141. A. A. Wilson, L. Jin, A. Garcia, J. N. DaSilva and S. Houle, *Appl. Radiat. Isot.*, 2001, **54**, 203-208.
142. P. D. Bonnitcha, A. L. Vavere, J. S. Lewis and J. R. Dilworth, *J. Med. Chem.*, 2008, **51**, 2985-2991.
143. A. R. Cowley, J. R. Dilworth, P. S. Donnelly, E. Labisbal and A. Sousa, *J. Am. Chem. Soc.*, 2002, **124**, 5270-5271.
144. L. E. Santos-Figueroa, M. E. Moragues, M. M. M. Raposo, R. M. F. Batista, S. P. G. Costa, R. C. M. Ferreira, F. Sancenon, R. Martinez-Manez, J. Vicente Ros-Lis and J. Soto, *Org. Biomol. Chem.*, 2012, **10**, 7418-7428.
145. P. J. Barnard, S. R. Bayly, J. P. Holland, J. R. Dilworth and P. A. Waghorn, *Quarterly Journal of Nuclear Medicine and Molecular Imaging*, 2008, **52**, 235-244.
146. J. J. Steffan, J. L. Snider, O. Skalli, T. Welbourne and J. A. Cardelli, *Traffic*, 2009, **10**, 737-753.
147. S. Y. Sharp, P. M. Rogers and L. R. Kelland, *Clinical Cancer Research*, 1995, **1**, 981-989.
148. J. P. Holland, J. A. Hickin, E. Grenville-Mathers, T. Nguyen and J. M. Peach, *J. Chem. Res.-S*, 2008, 702-703.
149. A. L. Vavere and J. S. Lewis, *Dalton Trans.*, 2007, 4893-4902.
150. T. J. Wadas, E. H. Wong, G. R. Weisman and C. J. Anderson, *Chemical Reviews*, 2010, **110**, 2858-2902.
151. M. Hada, H. L. Wu and F. A. Cucinotta, *Mutation Research-Fundamental and Molecular Mechanisms of Mutagenesis*, 2011, **711**, 187-192.
152. J. S. Y. Lau, P. K. Lee, K. H. K. Tsang, C. H. C. Ng, Y. W. Lam, S. H. Cheng and K. K. W. Lo, *Inorg. Chem.*, 2009, **48**, 708-718.
153. I. H. Hall, C. B. Lackey, T. D. Kistler, J. S. Ives, H. Beraldo, L. J. Ackerman and D. X. West, *Arch. Pharm.*, 2000, **333**, 217-225.
154. D. D'Amours, S. Desnoyers, I. D'Silva and G. G. Poirier, *Biochem. J.*, 1999, **342**, 249-268.
155. A. Al-Nahhas and S. Fanti, *European Journal of Nuclear Medicine and Molecular Imaging*, 2012, **39**, 1-3.
156. M. Fani and H. R. Maecke, *European Journal of Nuclear Medicine and Molecular Imaging*, 2012, **39**, 11-30.
157. K. Zelenka, L. Borsig and R. Alberto, *Org. Biomol. Chem.*, 2011, **9**, 1071-1078.
158. K. Zelenka, L. Borsig and R. Alberto, *Bioconjugate Chem.*, 2011, **22**, 958-967.
159. C. C. Liolios, C. Zikos, E. Fragogeorgi, D. Benaki, M. Pelecanou, I. Pirmettis, N. Ioannidis, Y. Sanakis, C. P. Raptopoulou, V. Psycharis, A. Terzis, F. Boschetti, M. S. Papadopoulos, G. Sivolapenko and A. D. Varvarigou, *Eur. J. Inorg. Chem.*, 2012, 2877-2888.
160. Z. Otwinowski and W. Minor, *Macromolecular Crystallography, Pt A*, 1997, **276**, 307-326.
161. A. Altomare, M. C. Burla, M. Camalli, G. L. Cascarano, C. Giacovazzo, A. Guagliardi, A. G. G. Moliterni, G. Polidori and R. Spagna, *J. Appl. Crystallogr.*, 1999, **32**, 115-119.

162. G. M. Sheldrick, *Acta Crystallogr., Sect. A*, 2008, **64**, 112-122.
163. C. B. Huebschle, G. M. Sheldrick and B. Dittrich, *J. Appl. Crystallogr.*, 2011, **44**, 1281-1284.
164. P. Vandersluis and A. L. Spek, *Acta Crystallogr., Sect. A*, 1990, **46**, 194-201.
165. C. Mohan, *Buffers: A guide for the preparation and use of buffers in biological systems*, 1997.

Appendix A. X-ray crystallography data

Table A.1. X-ray crystallography data of **iib$_{S-S}$**, **iid**, **L$_B$** and **1c**.

	Sulfur-bridged dimer, **iib$_{S-S}$**	**iid**	**L$_B$**	**1c**
Empirical formula	$C_{36}H_{38}N_{12}S_4$	$C_{20}H_{20}N_6S_2$	$C_{13}H_{12}N_4O_2S$	$C_{32}H_{36}N_6O_3S_5Zn$
Formula weight / g mol^{-1}	767.02	408.54	288.33	778.34
Crystal system	Orthorhombic	Triclinic	Triclinic	Monoclinic
Space group	P 2_1 2_1 2_1	P $\bar{1}$	P $\bar{1}$	P 2_1/n
a (Å)	8.535(2)	7.859(7)	10.1253(4)	17.6908(13)
b (Å)	19.120(5)	11.040(9)	10.5869(4)	7.7955(6)
c (Å)	22.172(6)	12.049(9)	12.7786(5)	25.4735(18)
α (deg)	90	90.546(6)	110.818(4)	90
β (deg)	90	95.3880(10)	90.107(3)	96.074(7)
γ (deg)	90	110.304(13)	95.659(4)	90
V (Å^3)	3618.2(16)	975.1(14)	1273.14(9)	3493.3(4)
Z	4	2	4	4
μ (mm^{-1})	0.310	0.292	0.262	1.045
ρ (g cm^{-3})	1.408	1.391	1.504	1.480
θ range (°)	2.06 to 24.99	2.58 to 24.35	2.85 to 32.53	2.94 to 28.23
Measured/independent reflections/ R_{int}	28222 / 6895 / 0.2717	6825 / 3176 / 0.0509	17266 / 8480 / 0.0162	22724 / 7566 / 0.0297
R_1,[a] wR_2 [$I > 2\sigma(I)$][b]	0.0993, 0.2568	0.0574, 0.1398	0.0331, 0.0869	0.0283, 0.0579
R_1,[a] wR_2 (all data)[b]	0.1038, 0.2669	0.0802, 0.1510	0.0463, 0.0901	0.0463, 0.0598

iib$_{S-S}$ Potential Hydrogen atoms on N5 and N8. However, attaching these to the parent atoms changed the R value from 9.93 to a higher 9.97 %. Initially all N-H hydrogen atoms were refined freely but a couple of them had too low temperature factors. For N_5H_5 and N_8H_8 however the temperature factor shot up to unrealistic numbers.

L$_B$. The asymmetric unit contains two independent molecules of the proligand. All N-H and O-H hydrogen atoms have been located in the difference Fourier map and refined freely.

1c. The asymmetric unit contains two independent molecules of the DMSO and one DMSO adduct

Table A.2.X-ray crystallography data of **2c**, **3a**, **3b** and **3c**.

	2c	**3a**	**3b**	**3c**
Empirical formula	$C_{34}H_{34}CuN_6O_2S_2$	$C_{44}H_{52}Cl_2Ga_2N_{12}O_3S_4$	$C_{18}H_{18}ClGaN_6S_2$	$C_{34}H_{34}ClGaN_6O_2S_2$
Formula weight / g mol^{-1}	686.33	1135.56	487.69	727.96
Crystal system	Monoclinic	Triclinic	Triclinic	Triclinic
Space group	P 2_1/c	P $\bar{1}$	P $\bar{1}$	P $\bar{1}$
a (Å)	9.1524(3)	10.4126(2)	9.5451(17)	10.2706(4)
b (Å)	30.0870(13)	13.4257(3)	10.1534(13)	16.1315(5)
c (Å)	11.5913(6)	19.4955(5)	11.2953(19)	21.9814(8)
α (deg)	90	109.6470(10)	77.537(13)	69.885(2)
β (deg)	105.227(2)	101.2810(10)	68.181(16)	78.060(2)
γ (deg)	90	96.9310(10)	81.795(13)	75.348(3)
V ($Å^3$)	3079.8(2)	2465.32(10)	989.9(3)	3279.6(2)
Z	4	2	2	4
μ (mm^{-1})	0.888	1.424	5.260	1.090
ρ (g cm^{-3})	1.480	1.530	1.636	1.474
θ range (°)	3.25 to 25.14	4.12 to 27.61	4.2780 to 44.5780	3.58 to 25.04
Measured/independent reflections/ R_{int}	41071 / 5418 / 0.2864	41691 / 11236 / 0.0713	3077 / 1550 / 0.0349	37704 / 11493 / 0.1358
R_1,[a] wR_2 [$I > 2\sigma(I)$][b]	0.0737, 0.1024	0.0480, 0.1076	0.0631, 0.0690	0.0564, 0.1055
R_1,[a] wR_2 (all data)[b]	0.1963, 0.1300	0.0739, 0.1205	0.0937, 0.0729	0.1211, 0.1278

2c. The asymmetric unit contains two independent molecules of THF

3a. The asymmetric unit contains two isomers of the gallium complex, **3a** and one independent molecule of DMSO.

3c. The asymmetric unit contains two independent molecules of the gallium complex, **3c** and four independent molecules of THF.

Table A.3. X-ray crystallography data of **4a**, **4b**, **4c** and **4d**.

	4a	**4b**	**4c**	**4d**
Empirical formula	$C_{16}H_{14}ClInN_6S_2$	$C_{18}H_{18}ClInN_6S_2$	$C_{30}H_{26}ClInN_6OS_2$	$C_{20}H_{18}ClInN_6S_2$
Formula weight / g mol^{-1}	504.72	532.77	700.96	556.8
Crystal system	Orthorhombic	Triclinic	Triclinic	Monoclinic
Space group	P n c a	P $\bar{1}$	P $\bar{1}$	C 2/c
a (Å)	13.7789(6)	7.8549(6)	10.3834(4)	32.4924(5)
b (Å)	28.9035(17)	11.7751(7)	12.3013(5)	7.61040(10)
c (Å)	17.8248(11)	12.0197(10)	12.3563(6)	23.5627(4)
α (deg)	90	114.501(4)	96.575(2)	90
β (deg)	90	93.823(4)	103.147(3)	116.7250(10)
γ (deg)	90	94.215(5)	106.324(3)	90
V (Å^3)	7098.9(7)	1003.09(13)	1447.80(11)	5204.16(14)
Z	16	2	2	8
μ (mm^{-1})	1.732	1.537	1.089	1.199
ρ (g cm^{-3})	1.889	1.764	1.608	1.570
θ range (°)	2.96 to 25.04	5.77 to 25.12	3.08 to 25.09	3.55 to 27.48
Measured/independent reflections/ R_{int}	41697 / 5990 / 0.1610	11618 / 3510 / 0.0616	18028 / 5099 / 0.1119	34588 / 5944 / 0.0734
R_1,[a] wR_2 [$I > 2\sigma(I)$][b]	0.1062, 0.1747	0.0408, 0.0870	0.0497, 0.1132	0.0348,0.0762
R_1,[a] wR_2 (all data)[b]	0.1868, 0.1982	0.0611, 0.0968	0.0755, 0.1271	0.0551,0.0846

4a. The asymmetric unit contains two independent molecules of the indium complex, **4a**. This was a very small, weak diffracting crystal. Hence the high R-(int) and high R factor.

4 non H atoms had to be refined isotropically.

4b. Hydrogen atoms attached to N have been located in the difference Fourier map and freely refine with idealised bond lengths.

4c. The asymmetric unit contains one molecule of THF.

4d. The asymmetrical unit consists of one In compound, **4d**, one half molecule of THF which lies on a twofold axis and half a molecule of 1,4-Dioxane. The half molecule of 1,4-Dioxane is disordered over two sites with 25% occupancy. The O of the Dioxane are refined anisotropically and the C atoms of this solvent are refine

isotropically. There is hydrogen bonding between N-H and the THF and Cl...H-N of the neighbouring molecule.

Appendix CIF Contents

All CIFs are stored on the accompanying DVD

1. Crystallographic Information File for **iib$_{S\text{-}S}$,** sulphur-bridged ethyl-substituted bis(thiosemicarbazonato) proligand dimer.
2. Crystallographic Information File for **iid**, allyl-substituted bis(thiosemicarbazone) proligand
3. Crystallographic Information File for **L$_B$**, bridged thiosemicarbazone proligand
4. Crystallographic Information File for **1c**, zinc phenyl-substituted bis(thiosemicarbazonato) complex
5. Crystallographic Information File for **2c,** copper phenyl-substituted bis(thiosemicarbazonato) complex
6. Crystallographic Information File for **3a**, gallium methyl-substituted bis(thiosemicarbazonato) complex
7. Crystallographic Information File for **3b**, gallium ethyl-substituted bis(thiosemicarbazonato) complex
8. Crystallographic Information File for **3c**, gallium phenyl-substituted bis(thiosemicarbazonato) complex
9. Crystallographic Information File for **4a**, indium methyl-substituted bis(thiosemicarbazonato) complex
10. Crystallographic Information File for **4b**, indium ethyl-substituted bis(thiosemicarbazonato) complex
11. Crystallographic Information File for **4c**, indium phenyl-substituted bis(thiosemicarbazonato) complex
12. Crystallographic Information File for **4d**, indium allyl-substituted bis(thiosemicarbazonato) complex

Appendix B. HPLC traces

HPLC traces for compounds without elemental analysis and/or X-ray crystal structures, and where solubility in DMSO was very poor, HPLC data is shown to represent complex purity.

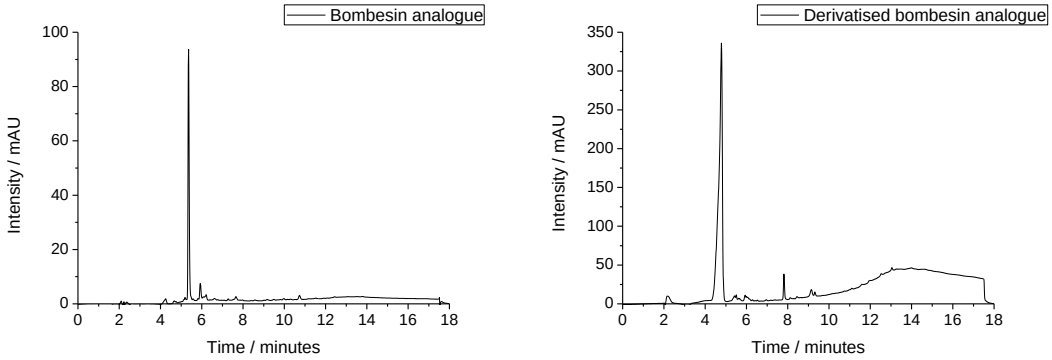

Figure B.1. HPLC traces of: bombesin analogue (left), of derivatised bombesin analogue (right), method E, λ_{obs} = 280 nm.

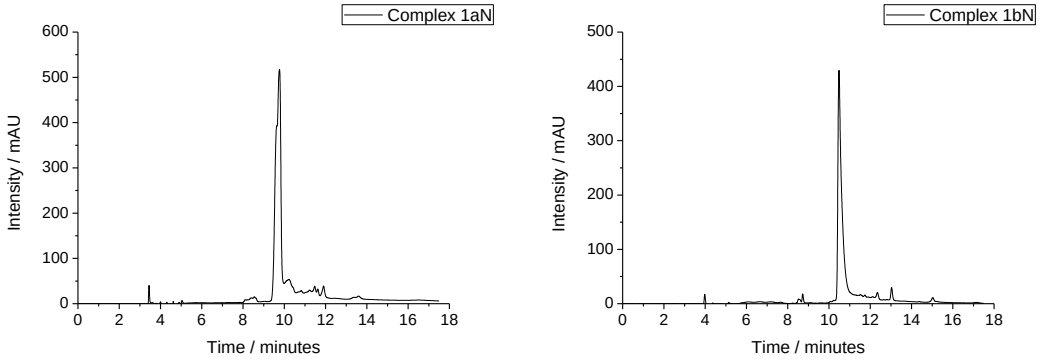

Figure B.2. HPLC traces of: complex **1aN** (left), of complex **1bN** bombesin analogue (right), method B, λ_{obs} = 400 nm.

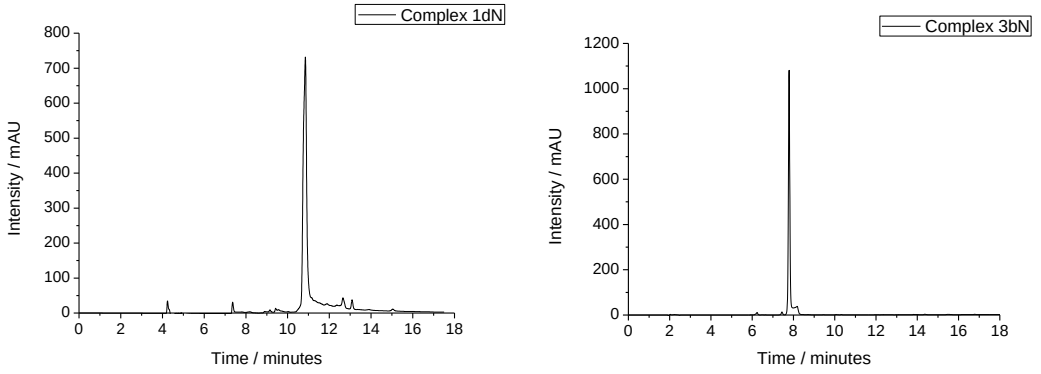

Figure B.3. HPLC traces of: complex **1dN** (left), method B, λ_{obs} = 400 nm, complex **3bN** (right), method D, λ_{obs} = 400 nm.

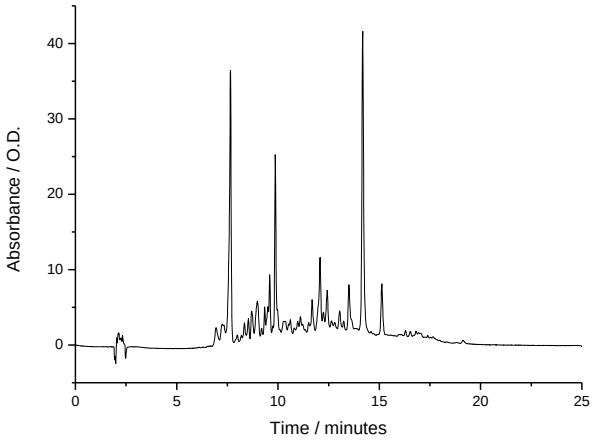

Figure B.4. HPLC of compound **1dB** reaction mixture, λ_{obs} = 400 nm, reference peaks to note under the same conditions – compound **3** R_t = 9.3 minutes and derivatised BBN R_t = 4.8 minutes (HPLC method E).

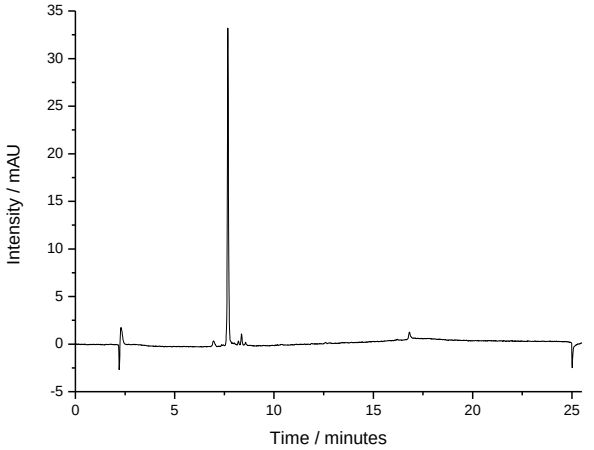

Figure B.5. HPLC of purified compound from **1dB** reaction mixture, λ_{obs} = 400 nm (HPLC method E).

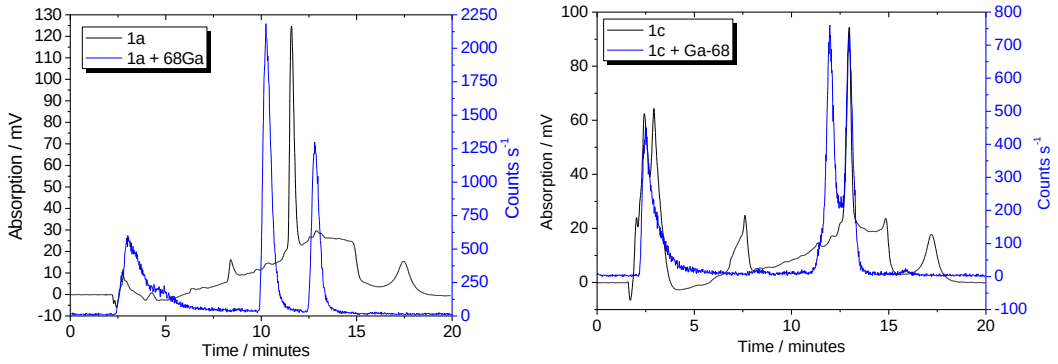

a) **b)**

Figure B.6. Overlay of UV-HPLC trace (black) of aromatic zinc bis(thiosemicarbazonato) precursor a) **1a** (R = methyl) and b) **1c** (R = phenyl) with the radio-HPLC trace (blue) of aromatic ^{68}GaCl bis(thiosemicarbazonato) complex.

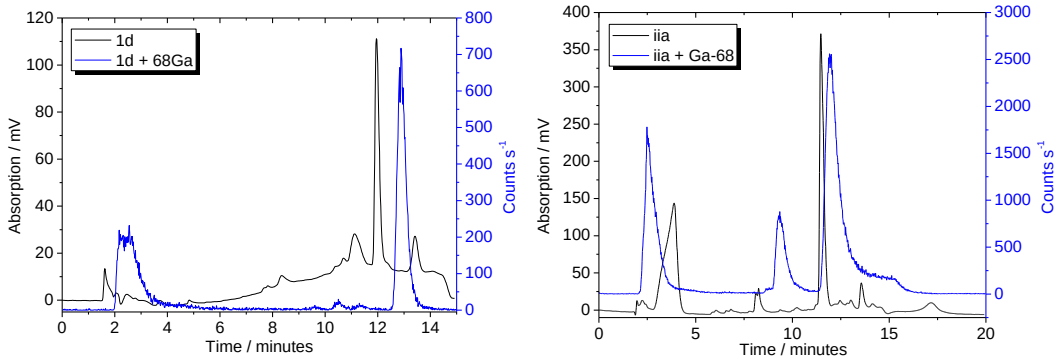

a) **b)**

Figure B.7. Overlay of UV-HPLC trace (black) of aromatic zinc bis(thiosemicarbazonato) precursor a) **1d** (R = allyl) and aromatic free ligand bis(thiosemicarbazonato) precursor b) **iia** (R = methyl) with the radio-HPLC trace (blue) of aromatic ^{68}GaCl bis(thiosemicarbazonato) complex.

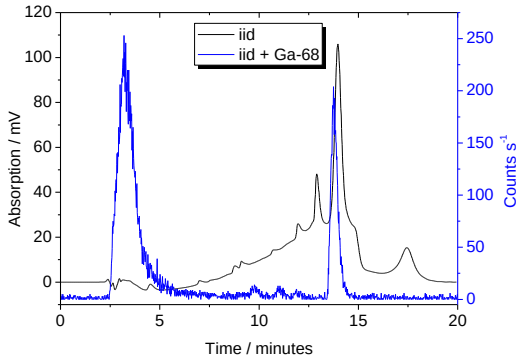

Figure B.8. Overlay of UV-HPLC trace (black) of aromatic free ligand bis(thiosemicarbazonato) precursor **iid** (R = methyl) with the radio-HPLC trace (blue) of aromatic ^{68}GaCl bis(thiosemicarbazonato) complex.

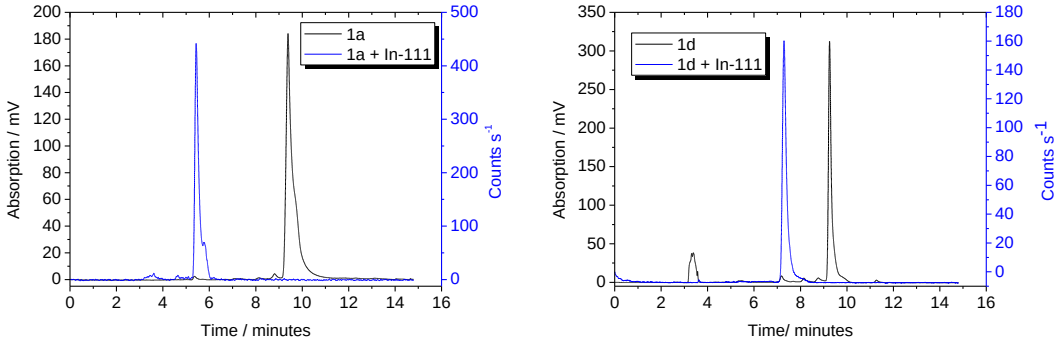

Figure B.9. Overlay of UV-HPLC trace (black) of aromatic zinc bis(thiosemicarbazonato) precursor with the radio-HPLC trace (blue) of aromatic ^{111}InCl bis(thiosemicarbazonato) complex with **a) 1a** and **b) 1d**.

Appendix C. Fluorescence spectroscopy

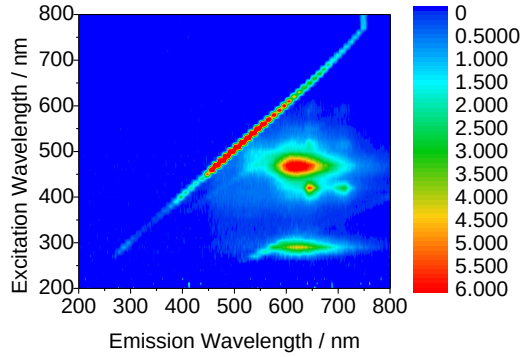

Figure C.1. 2D representation of the fluorescence of compound **iia**.

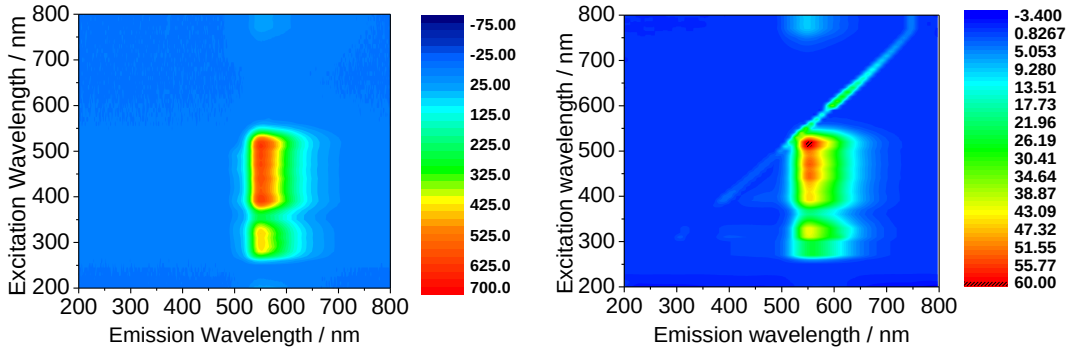

a) **b)**

Figure C.2. 100 µM in DMSO where left represents a 2D plot of complexes a) **3a** and b) **3d**[2]

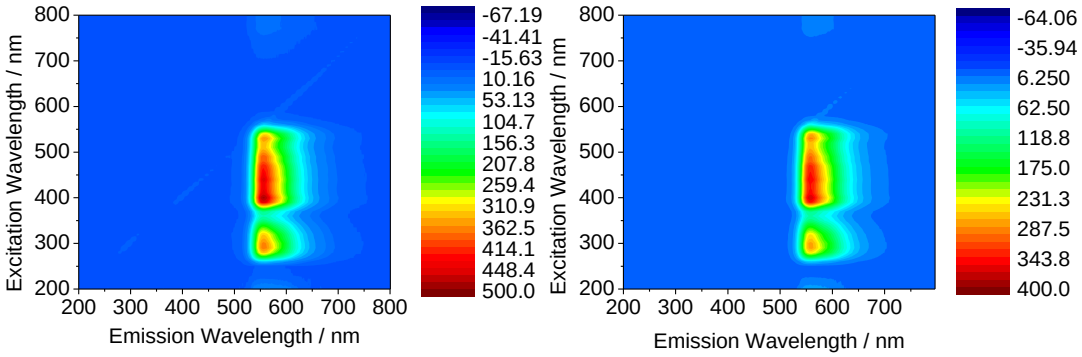

Figure C.3. 100 µM in DMSO where left represents a 2D plot of complexes a) **4c** and b) **4d**

[2] Spectrum **3d** was acquired with Brett Kennedy

Appendix D. Stability Assays using UV-visible and Fluorescence Spectroscopy

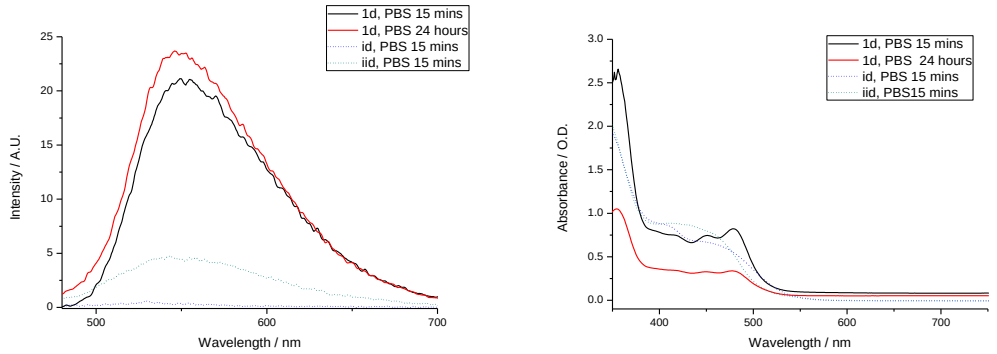

Figure D.1. PBS challenges (50% DMSO, 50% PBS) for compound **1d** at 100 µM, by fluorescence spectroscopy (left) UV/Vis (right) monitored at time intervals up to 24h at room temperature.

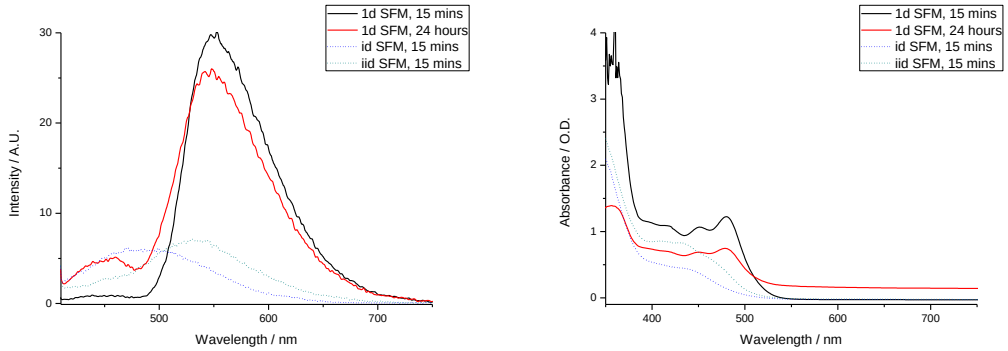

Figure D.2. EMEM SFM challenges (50% DMSO, 50% SFM) for compound **1d** at 100 µM, by fluorescence spectroscopy (left) UV/Vis (right) monitored at time intervals up to 24h at room temperature.

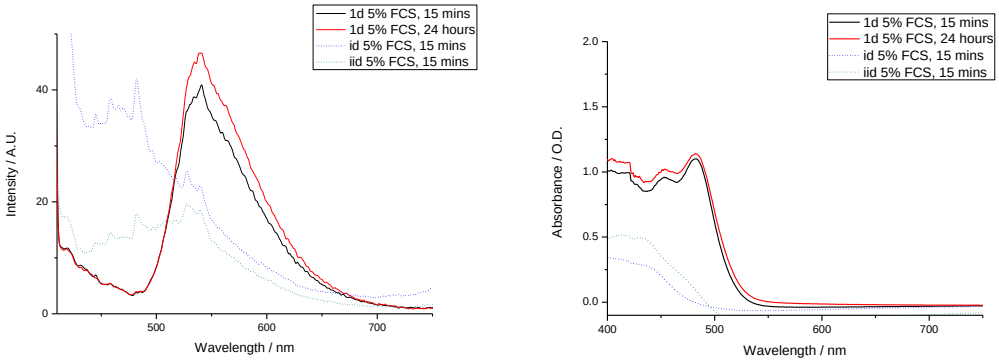

Figure D.3. FCS assay (50% DMSO, 45% EMEM, 5% FCS) for compound **1d** at 100 µM, by fluorescence spectroscopy (left) UV/Vis (right) monitored at time intervals up to 24h at room temperature.

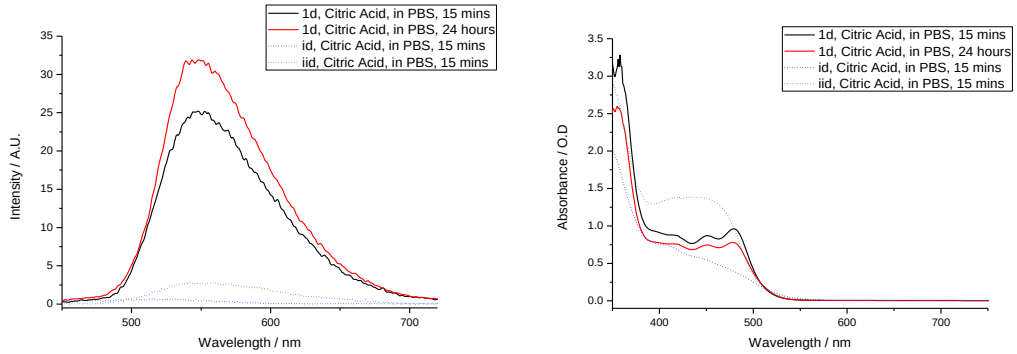

Figure D.4. Citric acid challenges (50% DMSO, 50% water, 2 eq of citric acid) for compound **1d** at 100 µM, by fluorescence spectroscopy (left) UV/Vis (right) monitored at time intervals up to 24h at room temperature.

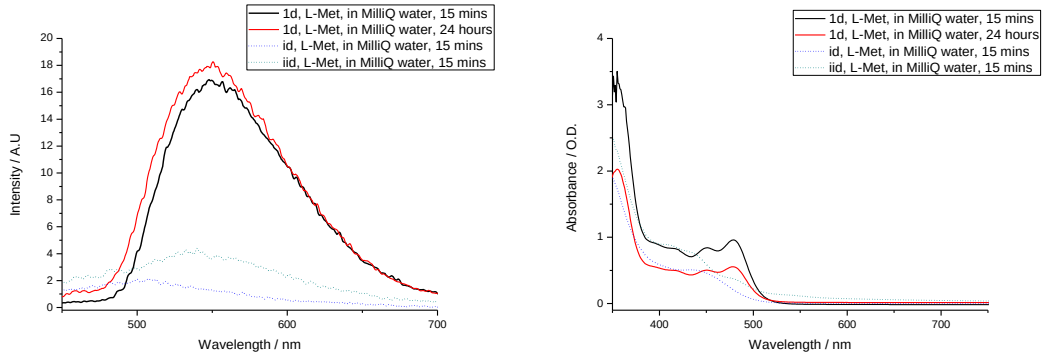

Figure D.5. L-methionine challenges (50% DMSO, 50% water, 2 eq of L-methionine) for compound **1d** at 100 µM, by fluorescence spectroscopy (left) UV/Vis (right) monitored at time intervals up to 24h at room temperature.

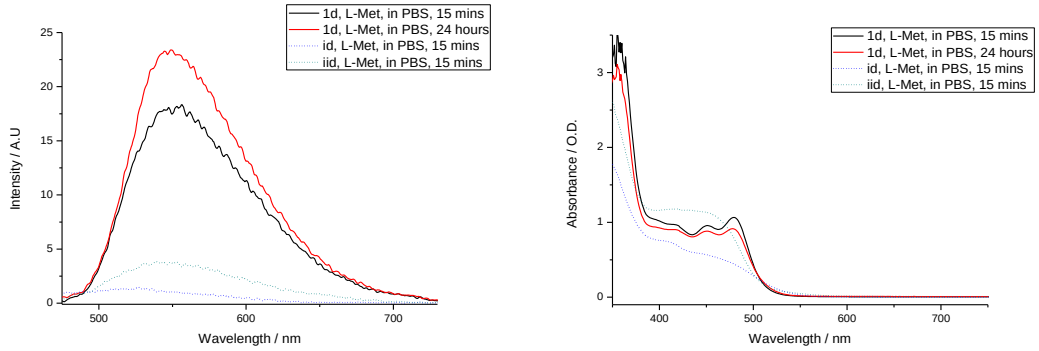

Figure D.6. L-methionine challenges (50% DMSO, 50% PBS, 2 eq of L-methionine) for compound **1d** at 100 µM, by fluorescence spectroscopy (left) UV/Vis (right) monitored at time intervals up to 24h at room temperature.

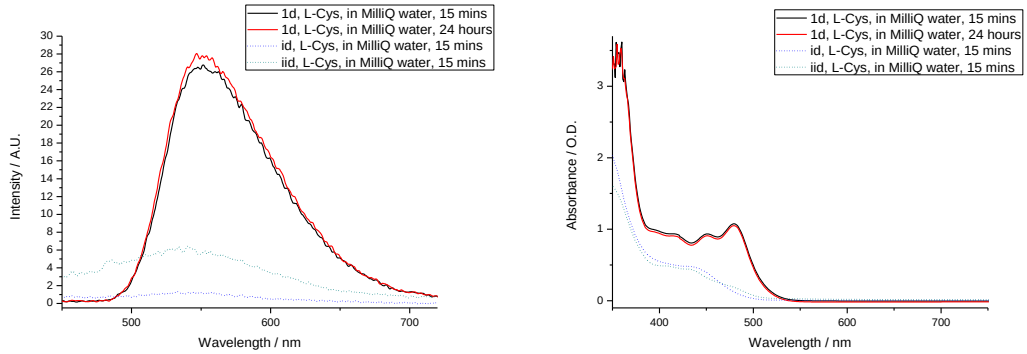

Figure D.7. L-cysteine challenges (50% DMSO, 50% water, 2 eq of L-cysteine) for compound **1d** at 100 µM, by fluorescence spectroscopy (left) UV/Vis (right) monitored at time intervals up to 24h at room temperature.

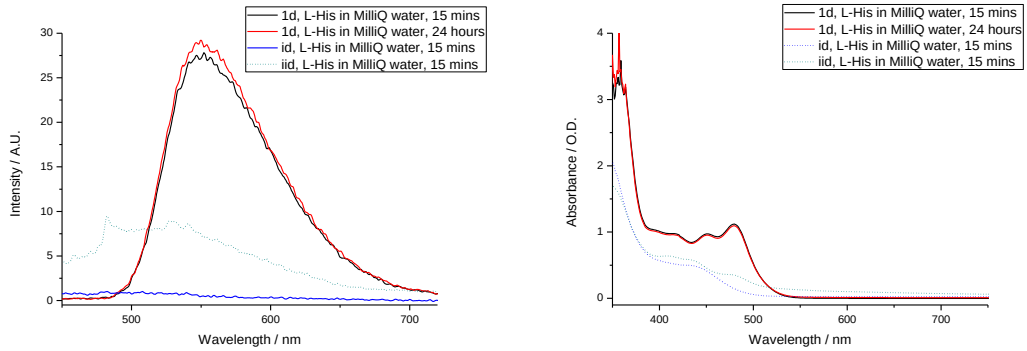

Figure D.8. L-histidine challenges (50% DMSO, 50% water, 2 eq of L- histidine) for compound **1d** at 100 µM, by fluorescence spectroscopy (left) UV/Vis (right) monitored at time intervals up to 24h at room temperature.

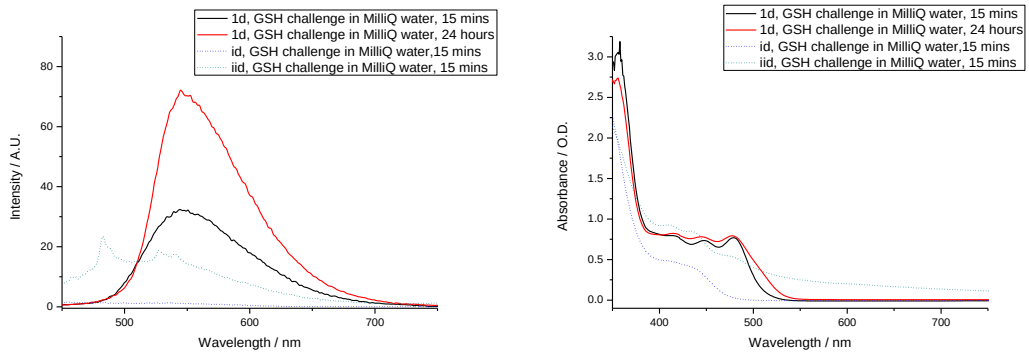

Figure D.9. Glutathione challenges (50% DMSO, 50% water, 2 eq of Glutathione) for compound **1d** at 100 µM, by fluorescence spectroscopy (left) UV/Vis (right) monitored at time intervals up to 24h at room temperature.

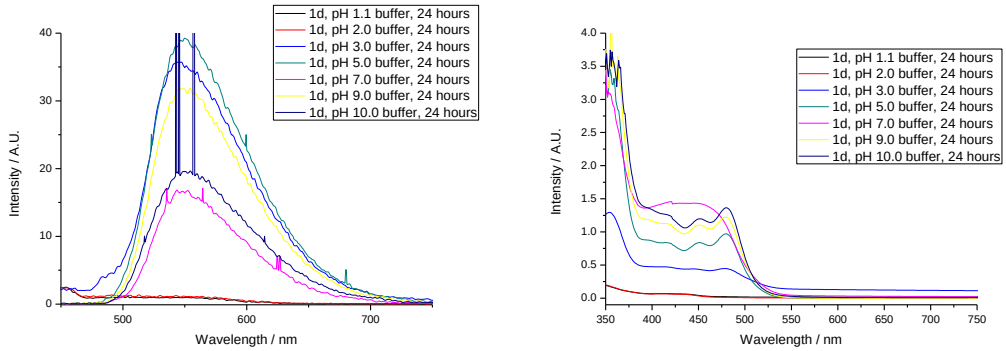

Figure D.10. All Buffer challenges (50% DMSO, 50% water) for compound **1d** at 100 µM by fluorescence spectroscopy (left) and UV/Vis (right) monitored at 24 hours at room temperature.

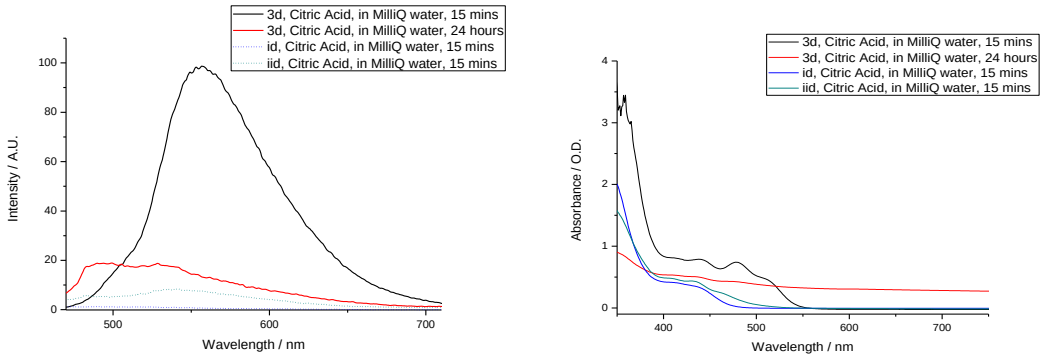

Figure D.11. Citric acid challenges (50% DMSO, 50% water, 2 eq of citric acid) for compound **3d** at 100 µM, by fluorescence spectroscopy (left) UV/Vis (right) monitored at time intervals up to 24h at room temperature.

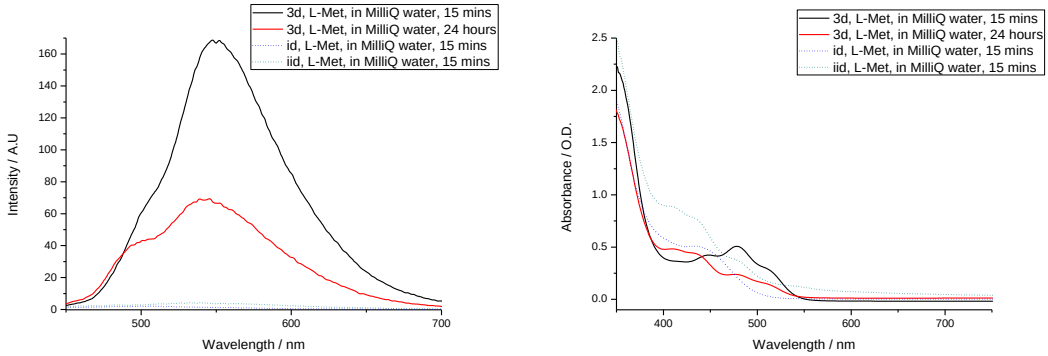

Figure D.12. L-methionine challenges (50% DMSO, 50% water, 2 eq of L-methionine) for compound **3d** at 100 µM, by fluorescence spectroscopy (left) UV/Vis (right) monitored at time intervals up to 24h at room temperature.

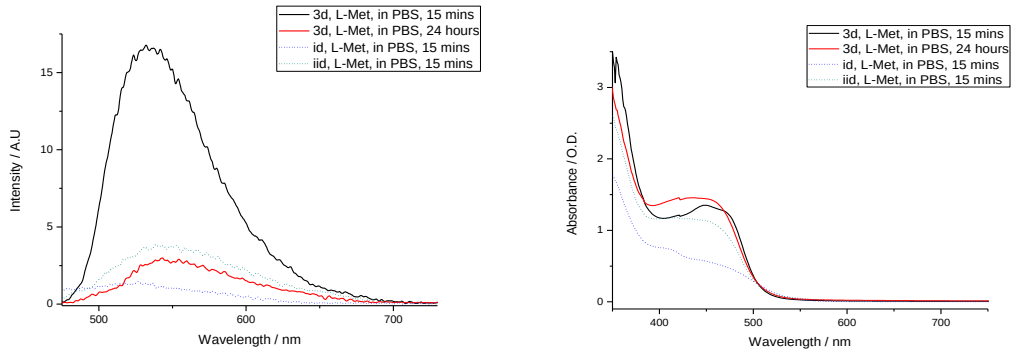

Figure D.13. L-methionine challenges (50% DMSO, 50% PBS, 2 eq of L-methionine) for compound **3d** at 100 µM, by fluorescence spectroscopy (left) UV/Vis (right) monitored at time intervals up to 24h at room temperature.

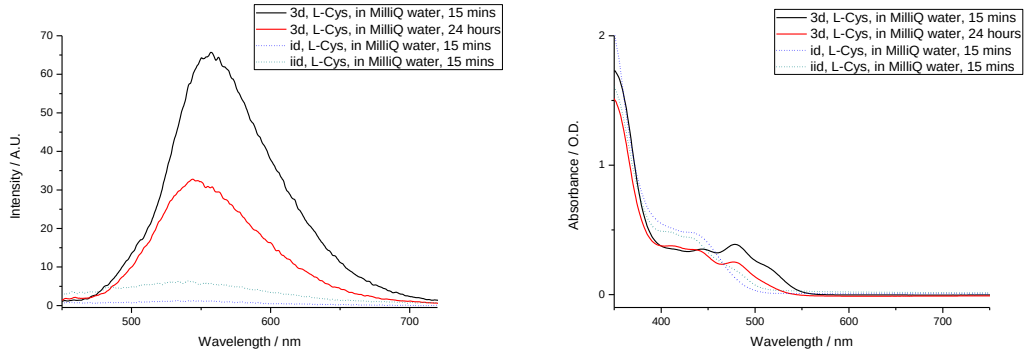

Figure D.14. L-cysteine challenges (50% DMSO, 50% water, 2 eq of L-cysteine) for compound **3d** at 100 µM, by fluorescence spectroscopy (left) UV/Vis (right) monitored at time intervals up to 24h at room temperature.

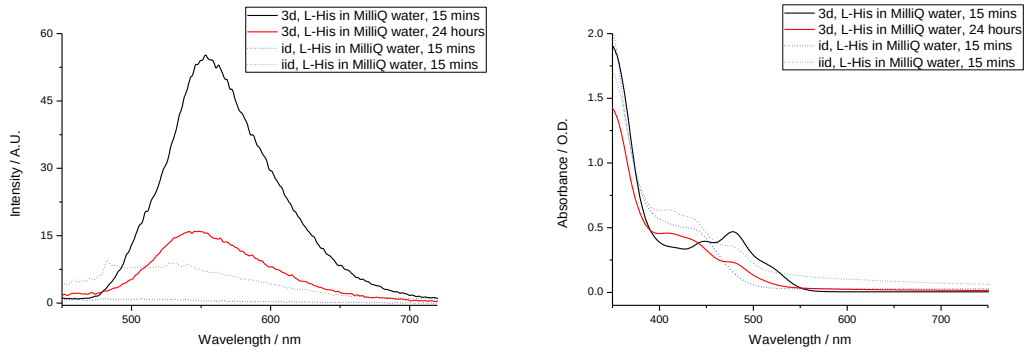

Figure D.15. L-histidine challenges (50% DMSO, 50% water, 2 eq of L- histidine) for compound **3d** at 100 µM, by fluorescence spectroscopy (left) UV/Vis (right) monitored at time intervals up to 24h at room temperature.

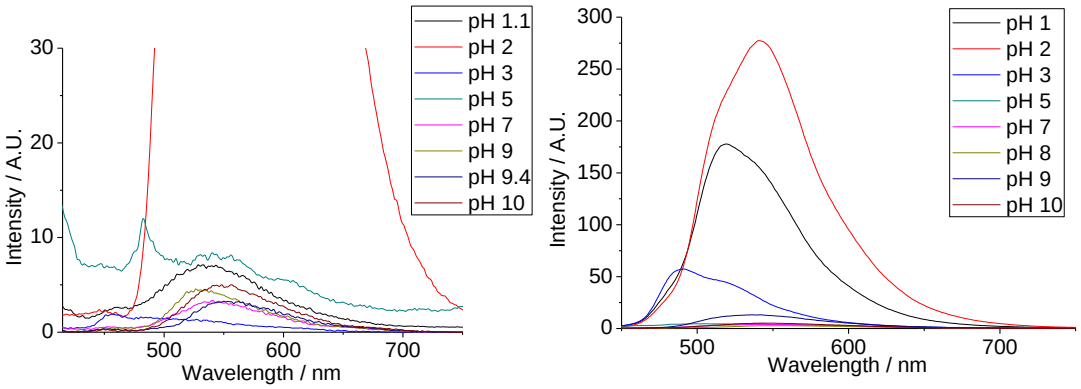

Figure D.16. Fluorescence spectroscopy buffer assay (a) **3a** pH study Arbitrary Units pH 2 >> pH 5 > pH 1.1 > pH 10 ≥ pH 9 > pH7 ≥ pH 9.4 > pH3. 0-40 and fluorescence intensity of complex with buffer. **3d** pH study where pH 2 > pH1.1 > pH 3 ≥ pH 9 > pH 10 > pH 5 ≥ pH 7 ≥ pH 8. ***3d** pH study was carried out with Brett Kennedy.

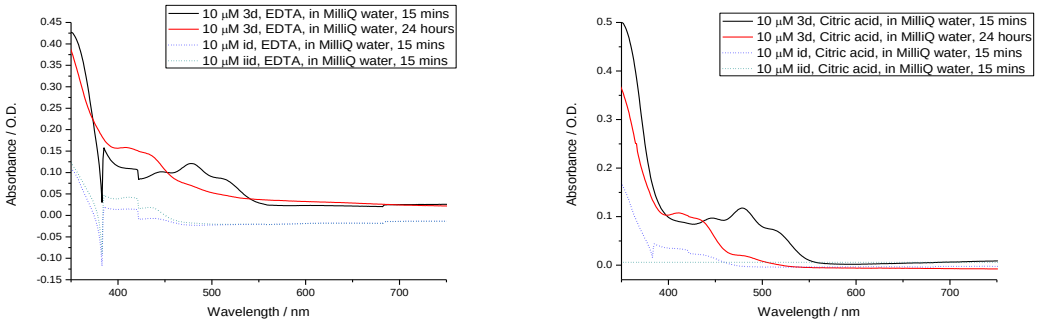

a) **b)**

Figure D.17. (a) Citric acid challenges (50% DMSO, 50% water, 2 eq of citric acid) **(b)** EDTA challenges (50% DMSO, 50% water, 2 eq of EDTA) for compound **3d** at 10 μM by UV/Vis monitored at time intervals up to 24h at room temperature.

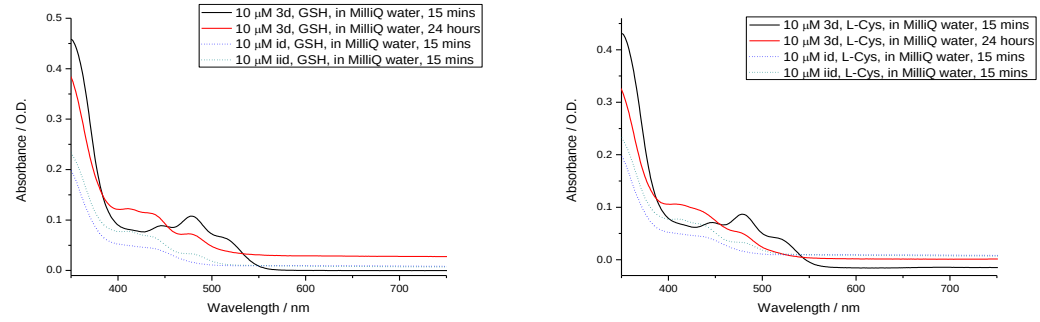

a) **b)**

Figure D.18. (a) Glutathione challenges (50% DMSO, 50% water, 2 eq of Glutathione) **(b)** L-cysteine challenges (50% DMSO, 50% water, 2 eq of L-cysteine) for compound **3d** at 10 μM by UV/Vis monitored at time intervals up to 24h at room temperature.

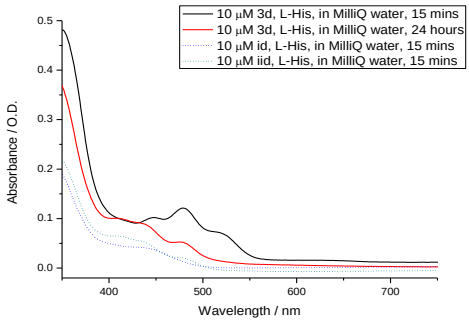

Figure D.19. L-Histidine challenges (50% DMSO, 50% water, 2 eq of L-Histidine) for compound **3d** at 10 μM by UV/Vis monitored at time intervals up to 24h at room temperature.

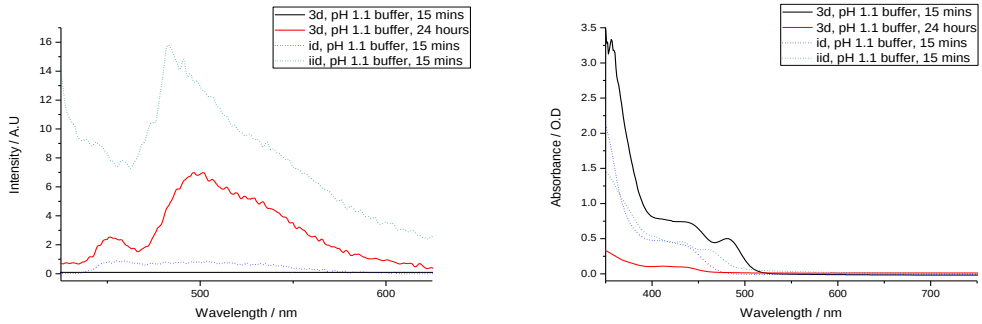

Figure D.20. Buffer challenges (50% DMSO, 50% water, pH 1.1 buffer, blank measured pH 1.6) for compound **3d** at 100 μM by fluorescence spectroscopy (left) and UV/Vis (right) monitored at time intervals up to 24h at room temperature.

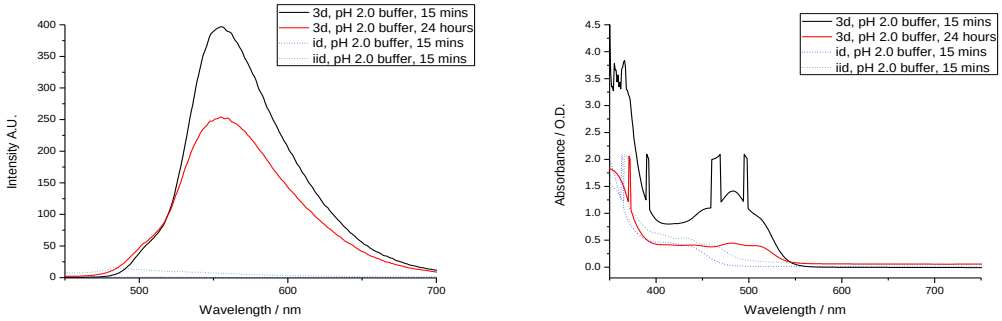

Figure D.21. Buffer challenges (50% DMSO, 50% water, pH 2.0 buffer, blank measured pH 2.5) for compound **3d** at 100 μM by fluorescence spectroscopy (left) and UV/Vis (right) monitored at time intervals up to 24h at room temperature.

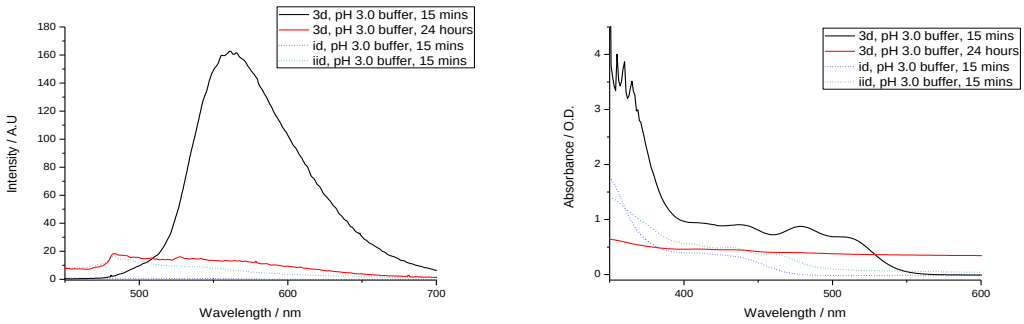

Figure D.22. Buffer challenges (50% DMSO, 50% water, pH 3.0 buffer, blank measured pH 4.4) for compound **3d** at 100 µM by fluorescence spectroscopy (left) and UV/Vis (right) monitored at time intervals up to 24h at room temperature.

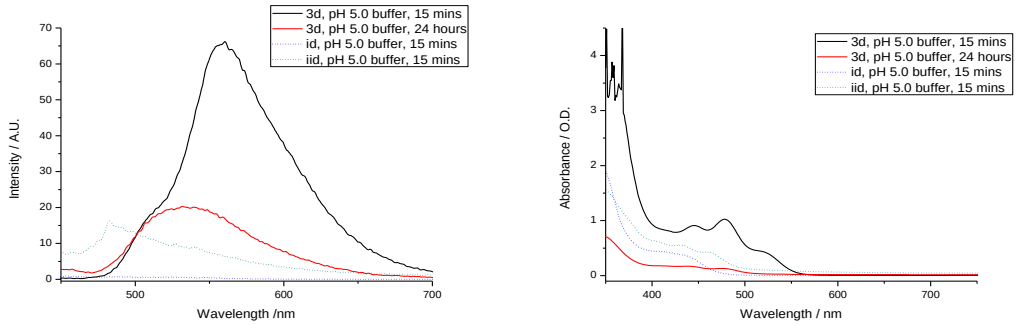

Figure D.23. Buffer challenges (50% DMSO, 50% water, pH 5.0 buffer, blank measured pH 6.9) for compound **3d** at 100 µM by fluorescence spectroscopy (left) and UV/Vis (right) monitored at time intervals up to 24h at room temperature.

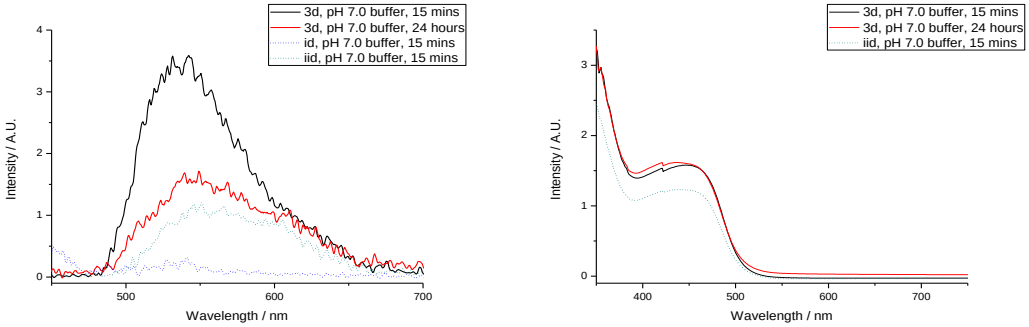

Figure D.24. Buffer challenges (50% DMSO, 50% water, pH 7.0 buffer, blank measured pH 9.4) for compound **3d** at 100 µM by fluorescence spectroscopy (left) and UV/Vis (right) monitored at time intervals up to 24h at room temperature.

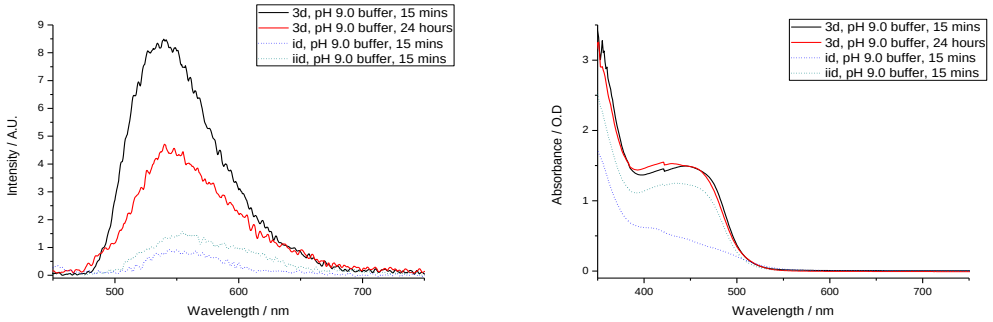

Figure D.25. Buffer challenges (50% DMSO, 50% water, pH 9.0 buffer, blank measured pH 9.35) for compound **3d** at 100 µM by fluorescence spectroscopy (left) and UV/Vis (right) monitored at time intervals up to 24h at room temperature.

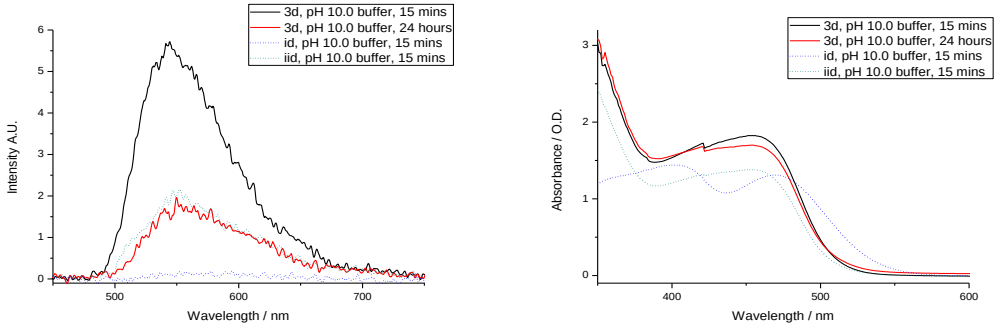

Figure D.26. Buffer challenges (50% DMSO, 50% water, pH 10.0 buffer, blank measured pH 12.7) for compound **3d** at 100 µM by fluorescence spectroscopy (left) and UV/Vis (right) monitored at time intervals up to 24h at room temperature.

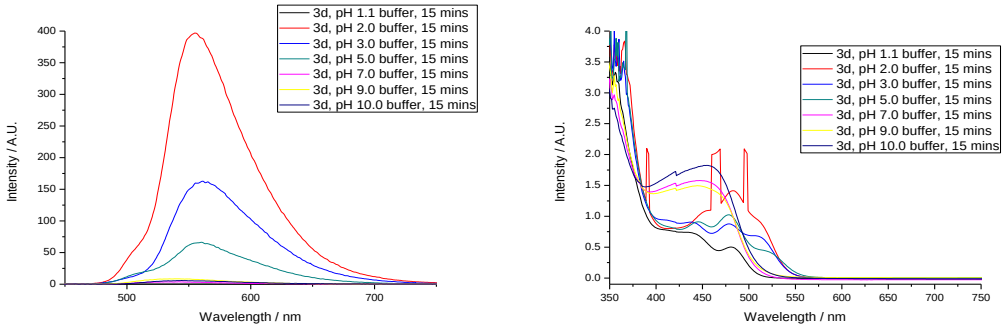

Figure D.27. All buffer challenges (50% DMSO, 50% water) for compound **3d** at 100 µM by fluorescence spectroscopy (left) and UV/Vis (right) monitored at 15 minutes at room temperature.

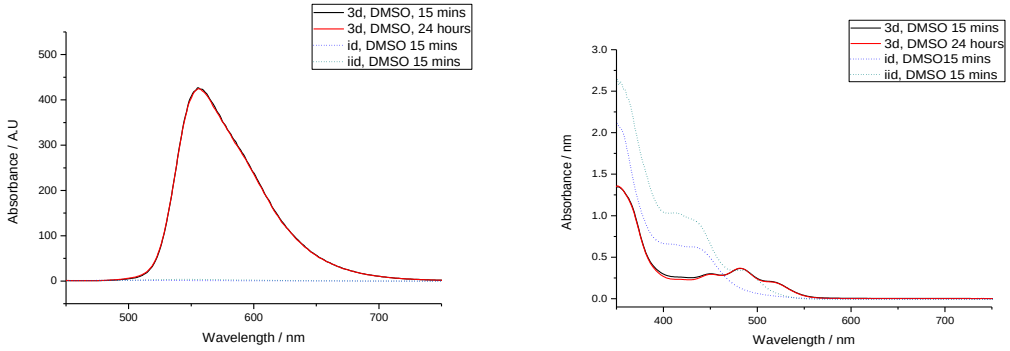

Figure D.28. DMSO challenges for compound **3d** at 100 µM, by fluorescence spectroscopy (left) UV/Vis (right) monitored at time intervals up to 24h at room temperature.

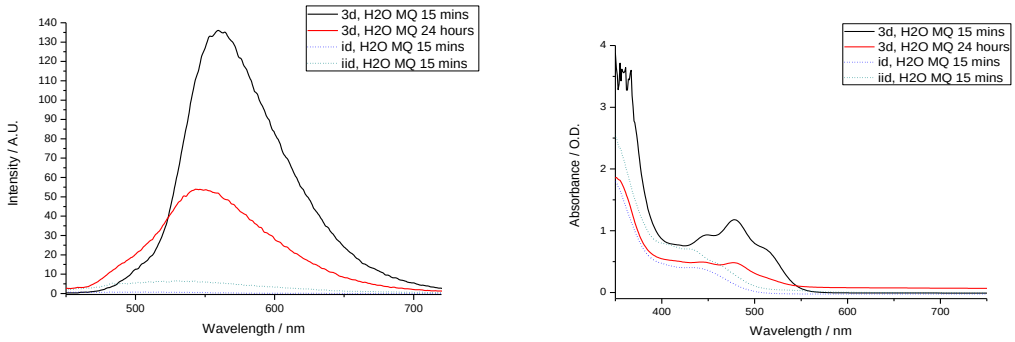

Figure D.29. Water challenges (50% DMSO, 50% water) for compound **3d** at 100 µM, by fluorescence spectroscopy (left) UV/Vis (right) monitored at time intervals up to 24h at room temperature.

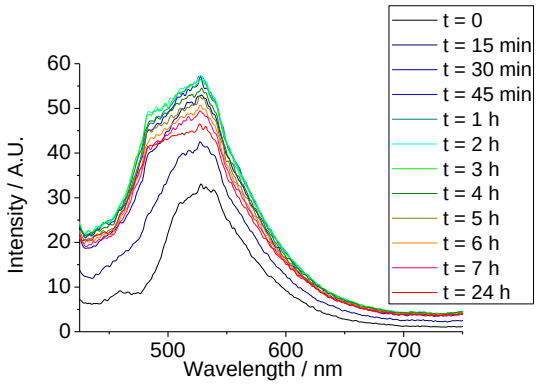

Figure D.30. 3b FCS assay

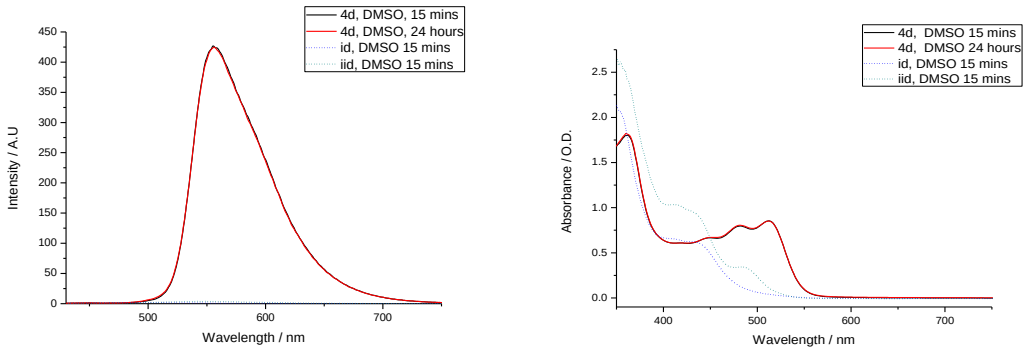

Figure D.31. DMSO challenges for compound **4d** at 100 µM, by fluorescence spectroscopy (left) UV/Vis (right) monitored at time intervals up to 24h at room temperature.

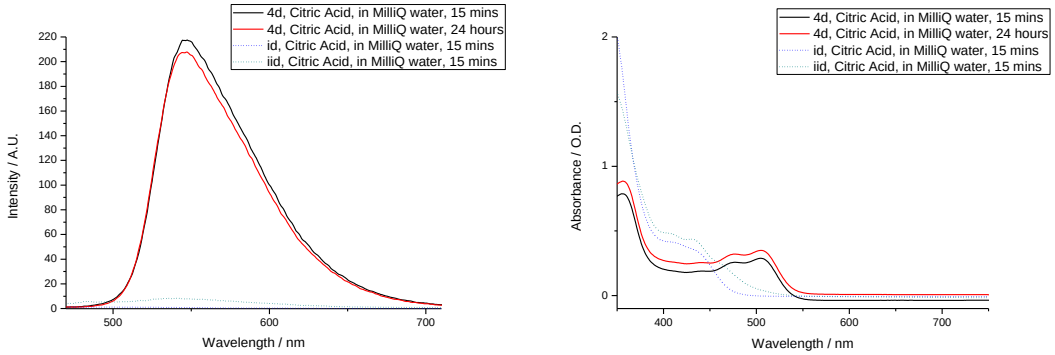

Figure D.32. Citric acid challenges (50% DMSO, 50% water, 2 eq of citric acid) for compound **4d** at 100 µM, by fluorescence spectroscopy (left) UV/Vis (right) monitored at time intervals up to 24h at room temperature.

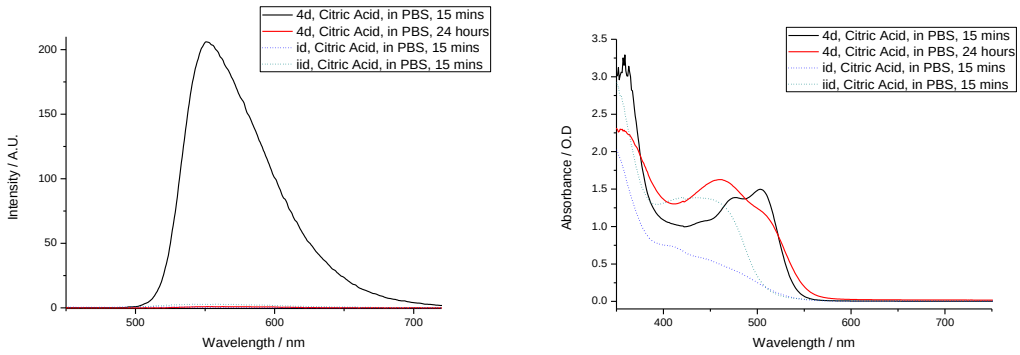

Figure D.33. Citric acid challenges (50% DMSO, 50% PBS, 2 eq of citric acid) for compound **4d** at 100 µM, by fluorescence spectroscopy (left) UV/Vis (right) monitored at time intervals up to 24h at room temperature.

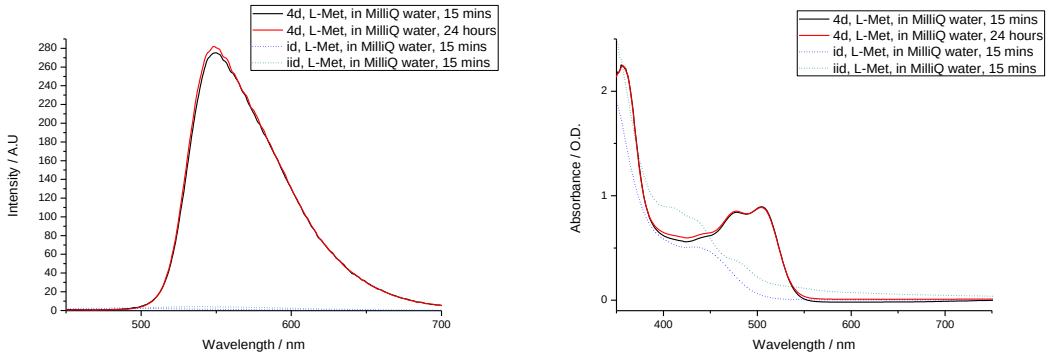

Figure D.34. L-methionine challenges (50% DMSO, 50% water, 2 eq of L-methionine) for compound **4d** at 100 µM, by fluorescence spectroscopy (left) UV/Vis (right) monitored at time intervals up to 24h at room temperature.

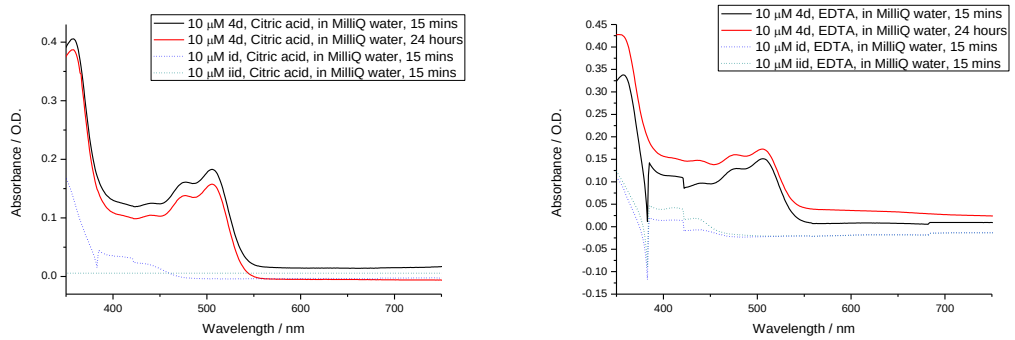

a) **b)**

Figure D.35. (a) Citric acid challenges (50% DMSO, 50% water, 2 eq of citric acid) **(b)** EDTA challenges (50% DMSO, 50% water, 2 eq of EDTA) for compound **4d** at 10 µM by UV/Vis monitored at time intervals up to 24h at room temperature.

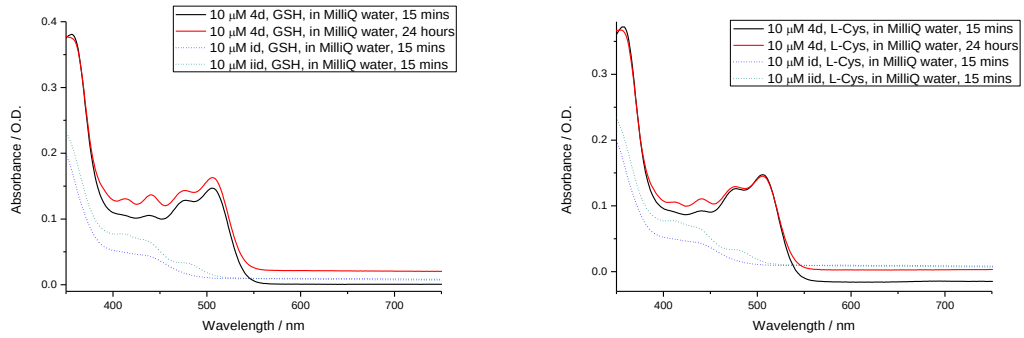

a) **b)**

Figure D.36. (a) Glutathione challenges (50% DMSO, 50% water, 2 eq of Glutathione) **(b)** L-cysteine challenges (50% DMSO, 50% water, 2 eq of L-cysteine) for compound **3d** at 10 µM by UV/Vis monitored at time intervals up to 24h at room temperature.

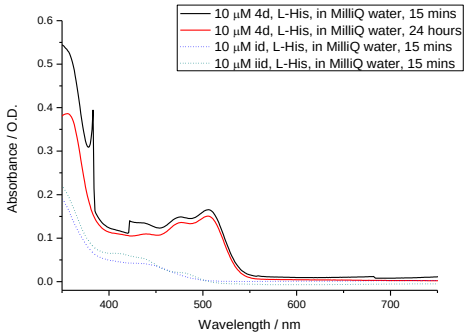

Figure D.37. L-Histidine challenges (50% DMSO, 50% water, 2 eq of L-Histidine) for compound **4d** at 10 μM by UV/Vis monitored at time intervals up to 24h at room temperature.

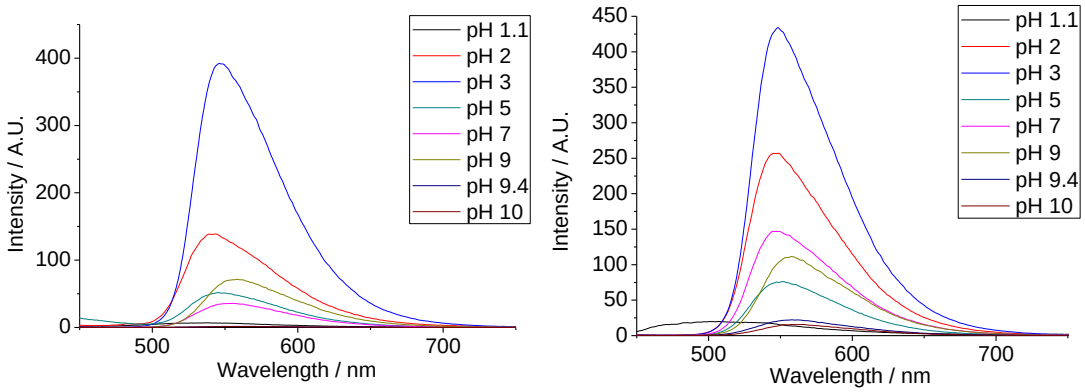

a) **b)**

Figure D.38. Fluorescence spectroscopy buffer assay **a) 4a** pH study where and fluorescence intensity of complex with buffer. pH 3 > pH 2 > pH 9 > pH 7 > pH 5 ≥ pH 9.4 ≈ pH 10 ≈ pH 1.1, b) **4b** pH study where and fluorescence intensity of complex with buffer. pH 3 > pH 2 > pH 7 > pH 9 > pH 5 > pH 1.1 ≥ pH 9.4 ≥ pH 10.

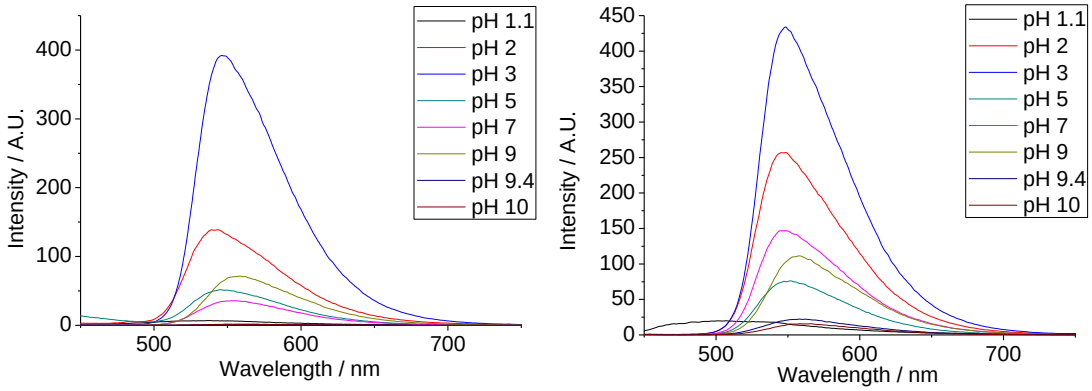

a) **b)**

Figure D.39. Fluorescence spectroscopy buffer assay **a) 4a** pH study where and fluorescence intensity of complex with buffer. pH 3 > pH 2 > pH 9 > pH 7 > pH 5 ≥ pH 9.4 ≈ pH 10 ≈ pH 1.1, b) **4b** pH study

where and fluorescence intensity of complex with buffer. pH 3 > pH 2 > pH 7 > pH 9 > pH 5 > pH 1.1 ≥ pH 9.4 ≥ pH 10.

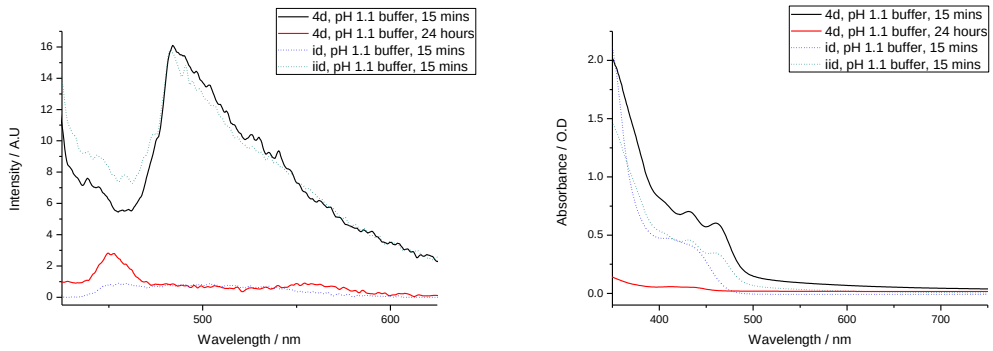

Figure D.40. Buffer challenges (50% DMSO, 50% water, pH 1.1 buffer, blank measured pH 1.6) for compound **4d** at 100 µM by fluorescence spectroscopy (left) and UV/Vis (right) monitored at time intervals up to 24h at room temperature.

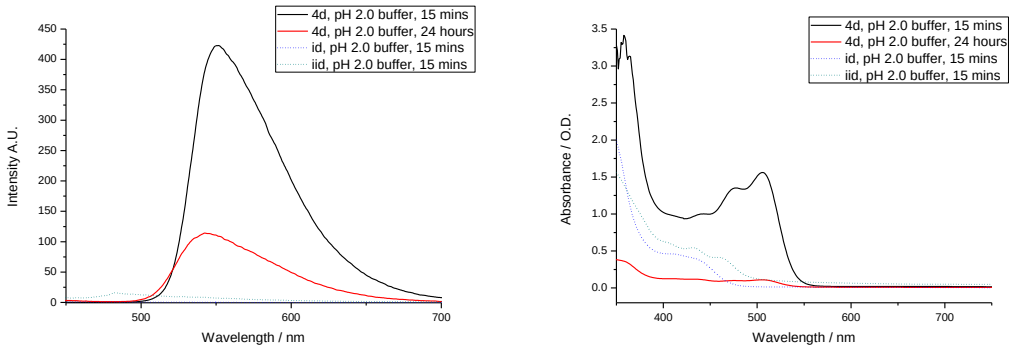

Figure D.41. Buffer challenges (50% DMSO, 50% water, pH 2.0 buffer, blank measured pH 2.5) for compound **4d** at 100 µM by fluorescence spectroscopy (left) and UV/Vis (right) monitored at time intervals up to 24h at room temperature.

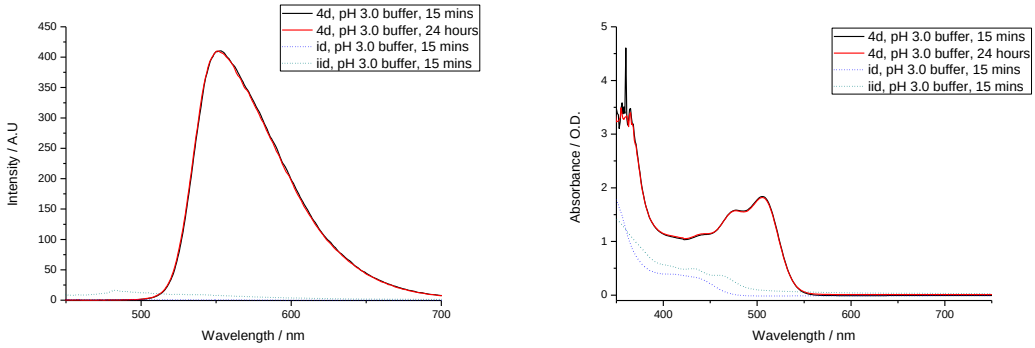

Figure D.42. Buffer challenges (50% DMSO, 50% water, pH 3.0 buffer, blank measured pH 4.4) for compound **4d** at 100 µM by fluorescence spectroscopy (left) and UV/Vis (right) monitored at time intervals up to 24h at room temperature.

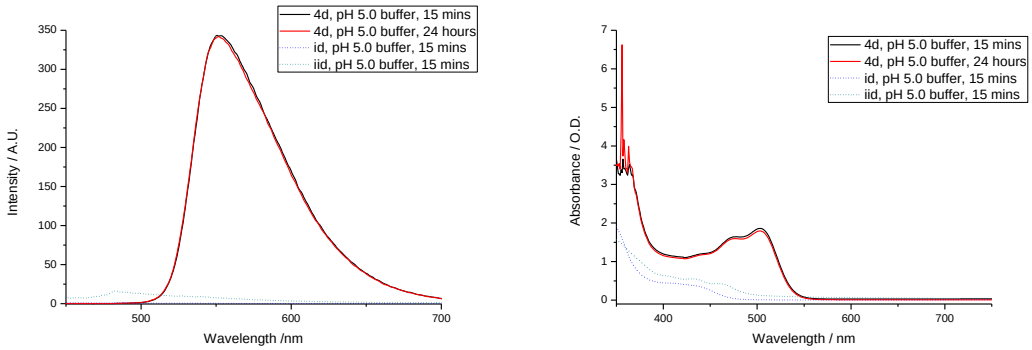

Figure D.43. Buffer challenges (50% DMSO, 50% water, pH 5.0 buffer, blank measured pH 6.9) for compound **4d** at 100 µM by fluorescence spectroscopy (left) and UV/Vis (right) monitored at time intervals up to 24h at room temperature.

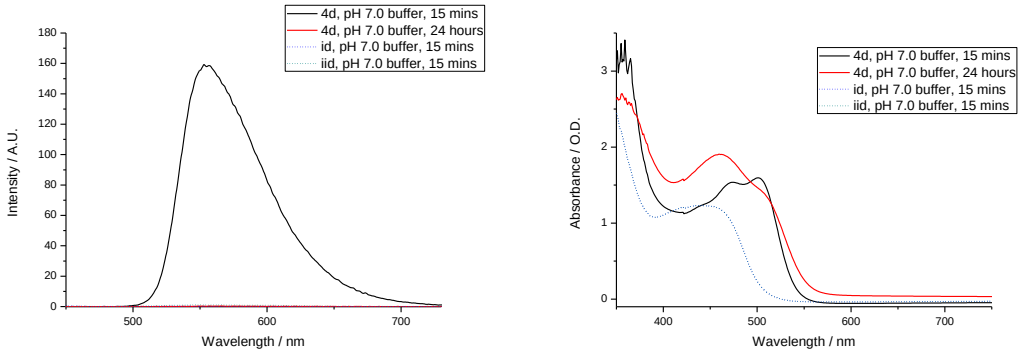

Figure D.44. Buffer challenges (50% DMSO, 50% water, pH 7.0 buffer, blank measured pH 9.4) for compound **4d** at 100 µM by fluorescence spectroscopy (left) and UV/Vis (right) monitored at time intervals up to 24h at room temperature.

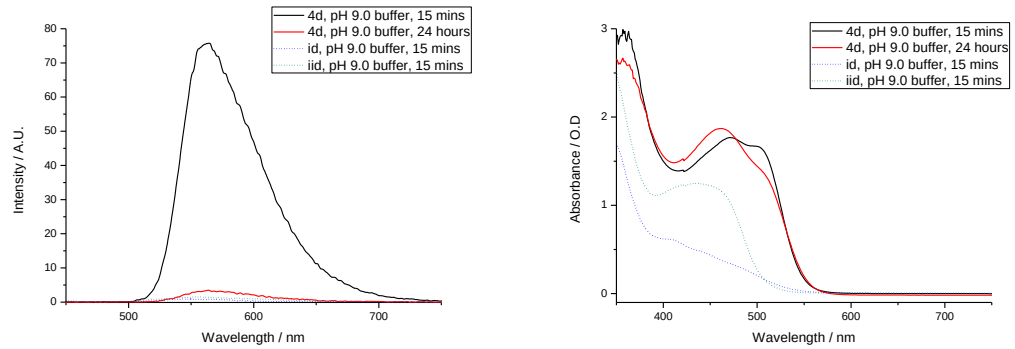

Figure D.45. Buffer challenges (50% DMSO, 50% water, pH 9.0 buffer, blank measured pH 9.35) for compound **4d** at 100 µM by fluorescence spectroscopy (left) and UV/Vis (right) monitored at time intervals up to 24h at room temperature.

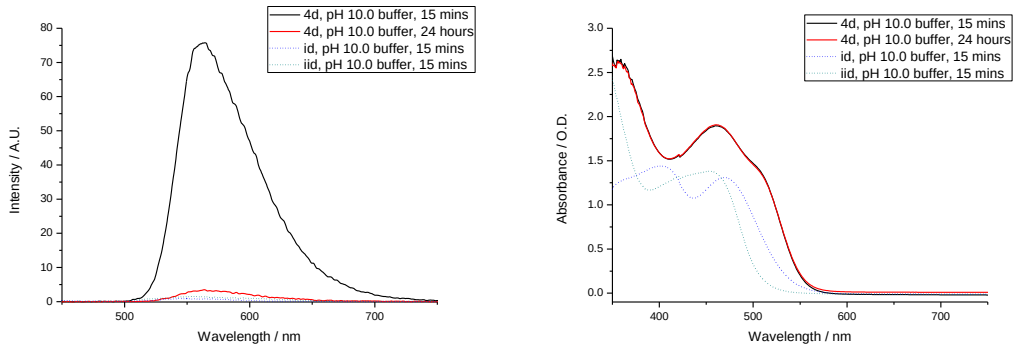

Figure D.46. Buffer challenges (50% DMSO, 50% water, pH 10.0 buffer, blank measured pH 12.7) for compound **4d** at 100 µM by fluorescence spectroscopy (left) and UV/Vis (right) monitored at time intervals up to 24h at room temperature.

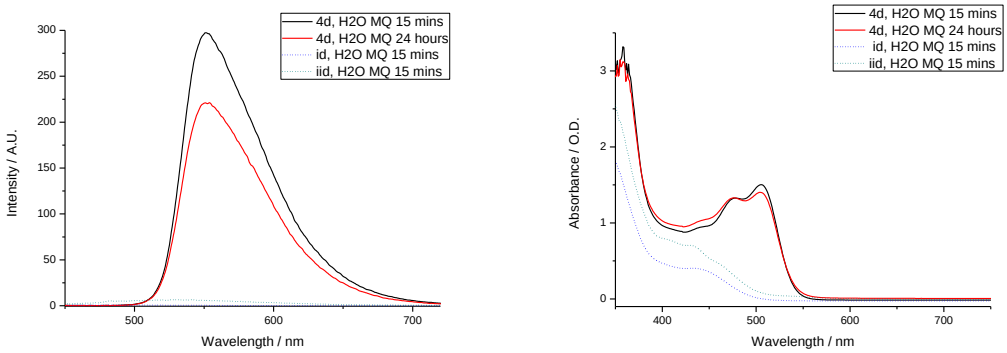

Figure D.47. Water challenges (50% DMSO, 50% water) for compound **4d** at 100 µM, by fluorescence spectroscopy (left) UV/Vis (right) monitored at time intervals up to 24h at room temperature.

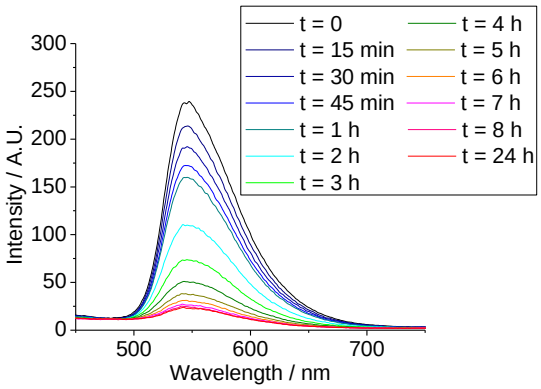

Figure D.48. 4b FCS assay

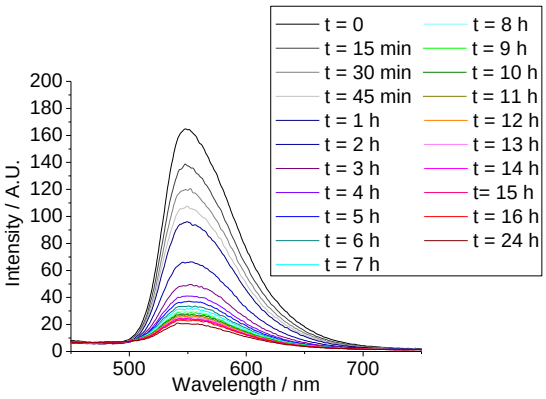

Figure D.49. 4d FCS assay

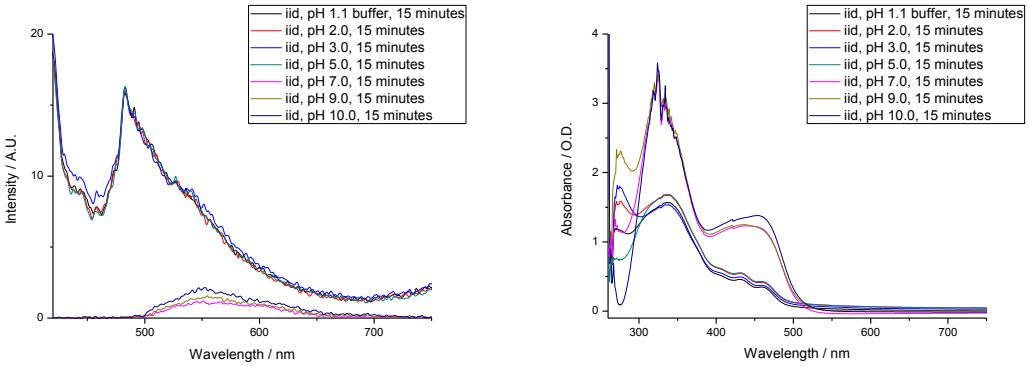

Figure D.50. All Buffer challenges (50% DMSO, 50% water) for compound **iid** at 100 µM by fluorescence spectroscopy (left) and UV/Vis (right) monitored at 15 minutes at room temperature.

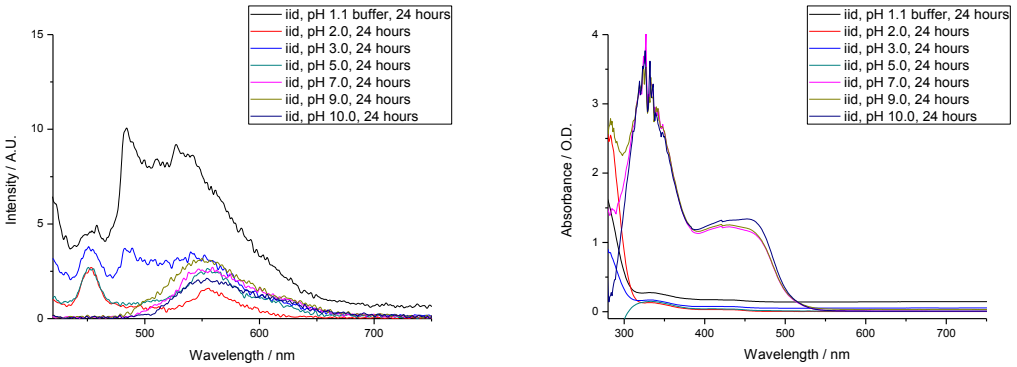

Figure D.51. All Buffer challenges (50% DMSO, 50% water) for compound **iid** at 100 µM by fluorescence spectroscopy (left) and UV/Vis (right) monitored at 24 hours at room temperature.

Appendix E. Two-photon Time Correlated Single Photon Counting data of DMSO solutions at 10 mM

Table E.1. Two-photon Time Correlated Single Photon Counting data of solutions in DMSO of free ligands, nd = not done.

	ia	**ib**	**ic**	**id**
10 mM	χ^2 = 1.15	χ^2 = 1.30	nd	χ^2 = 1.13
λ_{ex} = 810 nm	0.568 ns 67.6%	0.468 ns 68.4%		4.1288 ns 64.6%
	3.6706 ns 32.4%	3.2237 ns 31.6%		0.583 ns 35.4%
10 mM	χ^2 = 1.38	nd	χ^2 = 1.31	χ^2 = 1.34
λ_{ex} = 910 nm	0.388 ns 63.9%		0.413 ns 75.1%	0.339 ns 87.2%
	4.236 ns 36.1%		5.1734 ns 24.9%	3.848 ns 12.8%

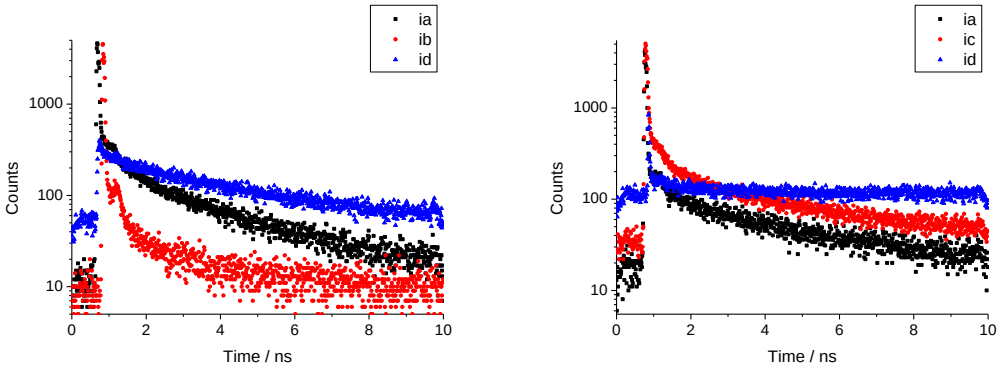

Figure E.1. TCSPC decay curves for mono(substituted) proligands 810 nm (left) 910 nm (right)

Table E.2. Two-photon Time Correlated Single Photon Counting data of solutions in DMSO of free ligands.

	iia	**iib**	**iic**	**iid**
10 mM	χ^2 = 1.88	χ^2 1.63	χ^2 = 1.71	χ^2 = 1.36
λ_{ex} = 810 nm	0.226 ns 95.7%	0.183 ns 98%	0.158 ns 98.7%	0.243 ns 97.8%
	2.576 ns 4.3%	3.969 ns 2%	2.380 ns 1.3%	4.621 ns 2.2%
10 mM	χ^2 = 1.21	χ^2 = 1.14	χ^2 = 1.52	χ^2 = 1.25
λ_{ex} = 910 nm	0.231 ns 89.2 %	0.235 ns 90 %	0.169 ns 99.2%	0.258 ns 94.1%
	2.117 ns 10.8 %	3.102 ns 10 %	4.119 ns 0.8%	6.488 ns 5.9%

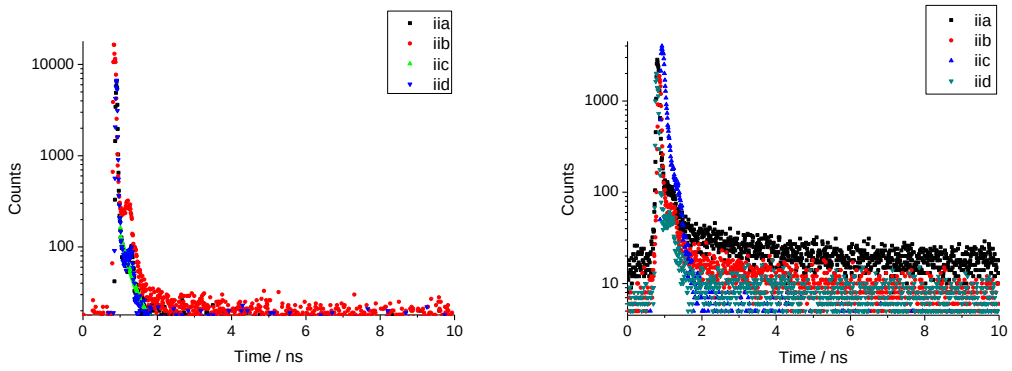

Figure E.2. TCSPC decay curves for bis(substituted) proligands 810 nm (left) 910 nm (right)

Table E.3. Two-photon Time Correlated Single Photon Counting data of solutions in DMSO of zinc bis(thiosemicarbazonato)complexes.

	1b λ_{ex} = 810 nm	**1b** λ_{ex} = 910 nm	**1d** λ_{ex} = 910 nm
10 mM	χ^2 = 1.52	χ^2 = 1.25	χ^2 = 1.56
	0.261 ns 98.2%	0.275 ns 100%	0.266 ns 99.7%
	0.597 ns 1.8%		1.201 ns 0.3%

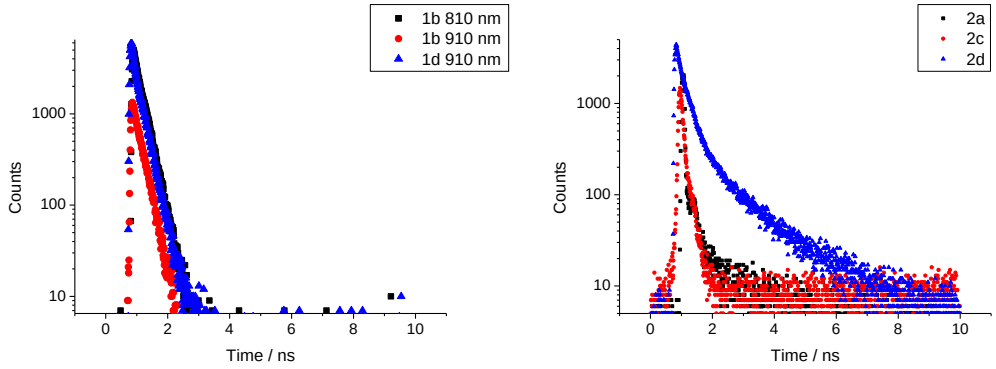

Table E.4. Two-photon Time Correlated Single Photon Counting data of solutions in DMSO of copper bis(thiosemicarbazonato)complexes λ_{ex} = 910 nm.

	2a	**2c**	**2d**
10 mM	χ^2 = 1.70	χ^2 = 1.13	χ^2 = 1.24
λ_{ex} = 910 nm	0.213 ns 90.5%	0.294 ns 91.05%	0.287 ns 91.4%
	1.826 ns 9.5%	1.469 ns 9.76%	1.545 ns 8.6%

Table E.5. Two-photon Time Correlated Single Photon Counting data of solutions in DMSO of gallium bis(thiosemicarbazonato) complexes, nd = not done.

	3a	**3b**	**3c**	**3d**
10 mM	χ^2 = 1.08	χ^2 = 1.15	χ^2 = 1.67	nd
λ_{ex} = 810 nm	0.295 ns 58.3%	0.250 ns 63.7%	0.170 ns 97.4%	
	0.744 ns 41.7%	0.873 ns 36.3%	0.603 ns 2.6%	
10 mM	χ^2 = 1.22	χ^2 = 1.25	χ^2 = 1.32	χ^2 = 1.44
λ_{ex} = 910 nm	0.436 ns 57.8 %	0.362 ns 52.4%	0.123 ns 85.9%	0.306 ns 69.1%
	0.976 ns 42.2 %	0.889 ns 47.6%	4.099 ns 4.1%	0.871 ns 30.9%

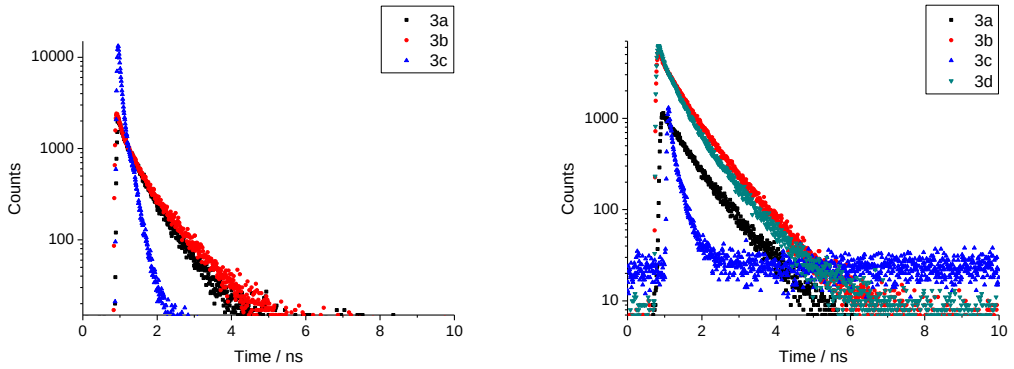

Figure E.3. TCSPC decay curves for gallium bis(thiosemicarbazonato) complexes 810 nm (left) 910 nm (right)

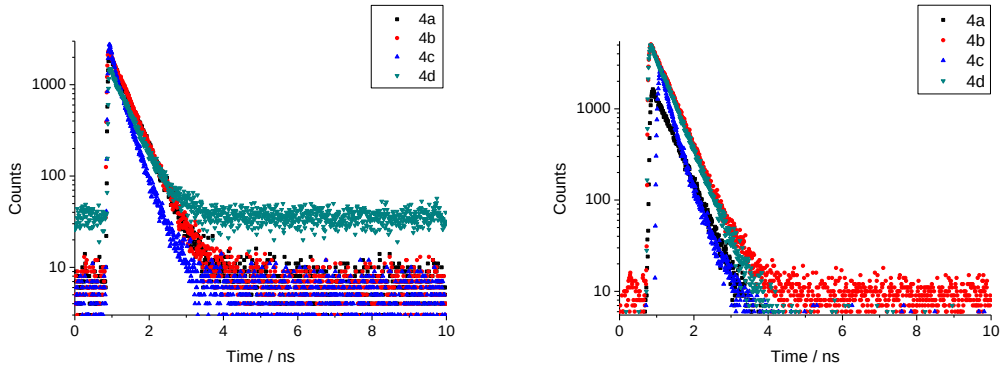

Figure E.4. TCSPC decay curves for indium bis(thiosemicarbazonato) complexes 810 nm (left) 910 nm (right)

Table E.6. Two-photon Time Correlated Single Photon Counting data of 10 mM solutions in DMSO of amine-functionalised bis(thiosemicarbazonato) complexes, with high χ^2 indicating precipitation for zinc complexes.

	1aN	**1bN**	**1cN**	**1dN**	**3bN**
λ_{ex} = 810 nm	χ^2 = 1.83	χ^2 = 1.40	χ^2 = 1.46	χ^2 = 1.84	χ^2 = 1.33
	0.203 ns,	0.208 ns,	0.230 ns,	0.218 ns,	0.640 ns,
	98.7%	99.1%	95.1%	97.8%	50.5%
	1.479 ns. 1.3%	1.502 ns, 0.9%	1.173 ns, 4.9%	1.499 ns, 2.2%	2.373 ns,
					49.5%
λ_{ex} = 910 nm	χ^2 = 1.45	χ^2 = 1.68	χ^2 = 1.42	χ^2 = 1.26	χ^2 = 1.13
	0.226 ns,	0.195 ns,	0.210 ns,	0.244 ns,	0.653 ns,
	95.9%	97.5%	95.2%	96.3%	49.7%
	1.310 ns, 4.1%	0.721 ns, 2.5%	0.828 ns, 4.8%	1.448 ns, 3.7%	2.405 ns,
					50.3%

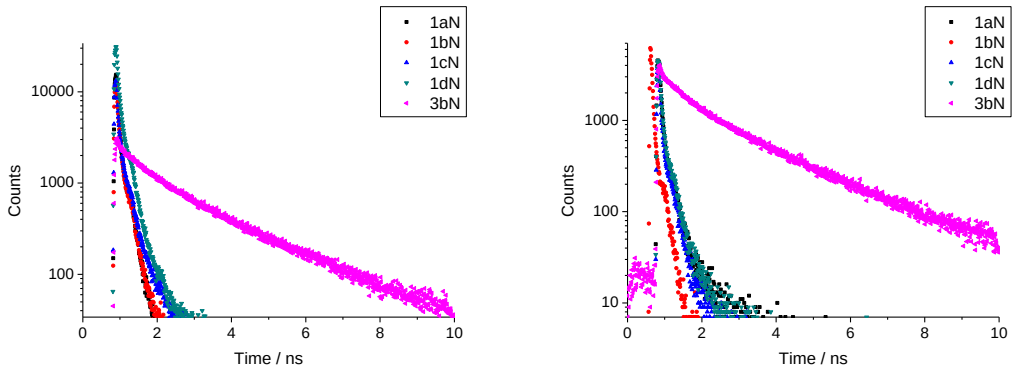

Figure E.5. TCSPC decay curves for amine-functionalised zinc and gallium bis(thiosemicarbazonato) complexes 810 nm (left) 910 nm (right)

Appendix F. Two-photon Fluorescence lifetime imaging data of in cancer cells

Table F.1. Two-photon fluorescence lifetime imaging data in HeLa and PC-3 cells of free ligands at 100 μM concentration.

Compound	**ia**	**ia**	**ic**
Cell line	HeLa	PC-3	HeLa
χ^2	1.43	1.22	1.16
λ /nm	910	910	910
τ_1 / ns	0.176	0.199	0.12
FWHM / ns	0.052	0.19	0.225
τ_1 %	51	80	91
τ_2 / ns	2.924	2.583	6.129
FWHM / ns	1.507	1.114	1.048
τ_2 %	49	20	8

Table F.2. Two-photon fluorescence lifetime imaging data in HeLa and PC-3 cells of ligand precursors, λ_{ex} = 810 nm, at 100 μM concentration.

Compound	**iia**	**iib**	**iic**	**iic**	**iid**
Cell line	HeLa	HeLa	HeLa	PC-3	HeLa
χ^2	1.50	1.26	1.15	1.13	1.23
τ_1 %	86	81	100	86	80
τ_1 / ns	0.903	0.868	1.803	0.233	0.725
FWHM / ns	0.415	0.642	0.617	0.204	0.358
τ_2 %	14	19		14	20
τ_2 / ns	3.549	3.218		2.087	3.128
FWHM / ns	1.479	2.695		1.543	1.712

Table F.3. Two-photon fluorescence lifetime imaging data in HeLa and PC-3 cells of ligand precursors, λ_{ex} = 910 nm, at 100 μM concentration.

Compound	**iia**	**iib**	**iic**	**iid**	**iia**	**iib**	**iic**	**iid**
Cell line	HeLa	HeLa	HeLa	HeLa	PC-3	PC-3	PC-3	PC-3
χ^2	1.54	1.05	1.38	1.33	1.48	1.21	1.47	1.21
τ_1 %	100	100	100	92	100	80	100	90
τ_1 / ns	3.062	2.522	0.344	0.307	2.469	0.081	0.531	0.164
FWHM / ns	0.42	0.303	0.9	0.575	1.293	0.202	0.506	0.544
τ_2 %				8		20		10
τ_2 / ns				0.436		0.434		0.418
FWHM / ns				0.653		0.209		0.455

Table F.4. Two-photon fluorescence lifetime imaging data in cancer cells of copper bis(thiosemicarbazonato) complexes, at 50 μM concentration.

Compound	**1b**	**1b**	**1c**	**1d**
Cell line	MCF-7	HeLa	HeLa	HeLa
χ^2	1.67	1.77	1.15	1.30
λ /nm	810	910	910	910
τ_1 %	93.4	94.8	100	100
τ_1 / ns	0.152	0.217	0.284	0.266
FWHM / ns	0.093	0.098	0.087	0.146
τ_2 %	6.6	5.2		
τ_2 / ns	0.433	0.505		
FWHM / ns	0.625	0.821		

Table F.5. Two-photon fluorescence lifetime imaging data in HeLa cells of copper bis(thiosemicarbazonato) complexes, at 50 μM concentration.

Compound	**2c**	**2d**
χ^2	1.19	1.27
τ_1 %	100	100
τ_1 / ns	0.343	0.297
FWHM / ns	0.095	0.13

Table F.6. Two-photon fluorescence lifetime imaging data in HeLa, λ_{ex} = 810 nm, at 50 μM concentration.

Compound	**3b**	**3c**
χ^2	1.58	1.18
τ_1 %	89	84
τ_1 / ns	0.309	0.308
FWHM / ns	0.095	0.196
τ_2 %	11	16
τ_2 / ns	2.026	2.523
FWHM / ns	0.865	1.562

Table F.7. Two-photon fluorescence lifetime imaging data, λ_{ex} = 910 nm in HeLa, PC-3 and MCF-7 cells of gallium bis(thiosemicarbazonato) complexes, at 50 μM concentration, where * and ** refer to before and after irradiation at 488 nm for 9 minutes.

Compound	**3a**	**3b**	**3c**	**3d**	**3b***	**3b****	**3c***	**3c****	**3b***	**3b****	**3c***	**3c****
Cell line	HeLa				PC-3				MCF-7			
χ^2	1.19	1.19	1.17	1.47	1.27	1.18	1.16	1.01	1.21	1.27	1.12	1.37
τ_1 %	96	100	100	94	92	91	100	100	100	100	80	80
τ_1 / ns	0.166	0.348	0.32	0.125	0.291	0.364	0.674	0.281	0.65	2.001	1.155	1.113
FWHM / ns	0.124	0.161	0.142	0.078	0.116	0.187	0.772	0.035	0.449	1.118	0.029	0.148
τ_2 %	4			6	8	9					20	20
τ_2 / ns	0.588			0.361	0.475	0.475					0.567	0.575
FWHM / ns	0.406			0.229	0.094	0.163					0.228	0.086

Table F.8. Two-photon fluorescence lifetime imaging data in HeLa and PC-3 cells of indium bis(thiosemicarbazonato) complexes, at 50 μM concentration λ_{ex} = 910 nm.

Compound	**4a**	**4b**	**4c**	**4d**	**4a**	**4b**	**4c**	**4d**
Cell line	HeLa				PC-3			
χ^2	1.63	1.51	1.86	1.57	1.37	1.67	1.67	1.39
τ_1 %	100	100	100	100	100	100	100	83
τ_1 / ns	0.35	0.384	0.244	0.343	0.298	0.323	0.653	0.27
FWHM / ns	0.118	0.088	0.072	0.175	0.031	0.045	0.947	0.069
τ_2 %								17
τ_2 / ns								0.593
FWHM / ns								0.347

Table F.9. Two-photon fluorescence lifetime imaging data in HeLa and PC-3 cells of amine-functionalised bis(thiosemicarbazonato) complexes, λ_{ex} = 810 nm.

Compound	**1bN**	**1dN**	**3bN**	**3bN**	**3bN**
Conc. / μM	100	100	100	50	100
χ^2	1.31	1.43	1.43	1.31	1.18
Cell line	HeLa	PC-3	HeLa	PC-3	PC-3
τ_1 %	90	91	86	100	86
τ_1 / ns	0.283	0.230	0.465	0.629	0.442
FWHM / ns	0.256	0.103	0.266	0.322	0.274
τ_2 %	10	9	14		14
τ_2 / ns	1.738	1.315	2.462		1.948
FWHM / ns	1.8401	1.197	1.599		1.06

Table F.10. Two-photon fluorescence lifetime imaging data in HeLa and PC-3 cells of amine-functionalised bis(thiosemicarbazonato) complexes, λ_{ex} = 910 nm.

Compound	**1bN**	**1cN**	**1cN**	**1dN**
Conc. / μM	100	100	100	100
χ^2	1.33	1.17	1.60	1.55
Cell line	MCF-7	MCF-7	HeLa	PC-3
τ_1 %	100	100	80	100
τ_1 / ns	0.354	0.498	0.176	0.522
FWHM / ns	0.218	0.165	0.177	0.331
τ_2 %			20	
τ_2 / ns			0.468	
FWHM / ns			0.329	

Appendix G. Fluorescence microscopy in biological cells

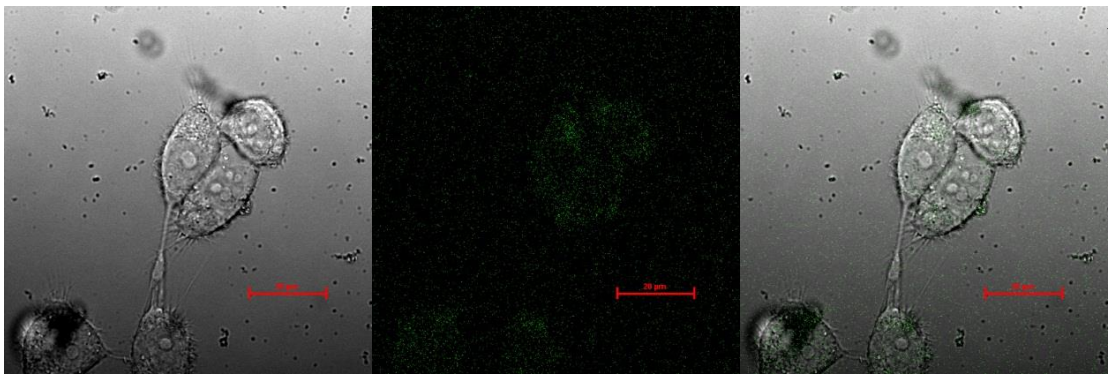

a) **b)** **c)**

Figure G.1. Single-photon confocal fluorescence microscopy of **ia** at 100 μM, 1% DMSO 30 mins, HeLa. a) DIC micrograph. b) Micrograph with excitation at 488 nm. c) Overlay image of a) and b).

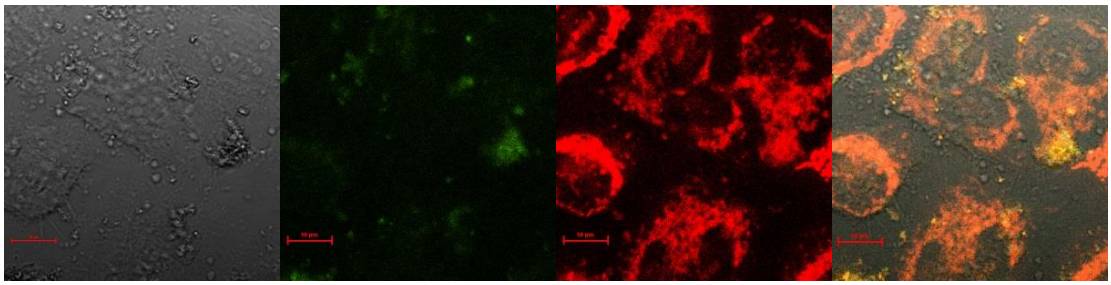

a) **b)** **c)** **d)**

Figure G.2. Single-photon confocal fluorescence microscopy of **ia** at 50 μM, 0.5% DMSO, 20 mins, HeLa, incubated with mitotracker. a) DIC micrograph. b) Micrograph with excitation at 488 nm. c) Micrograph with excitation at 543 nm. d) Overlay image of a), b) and c).

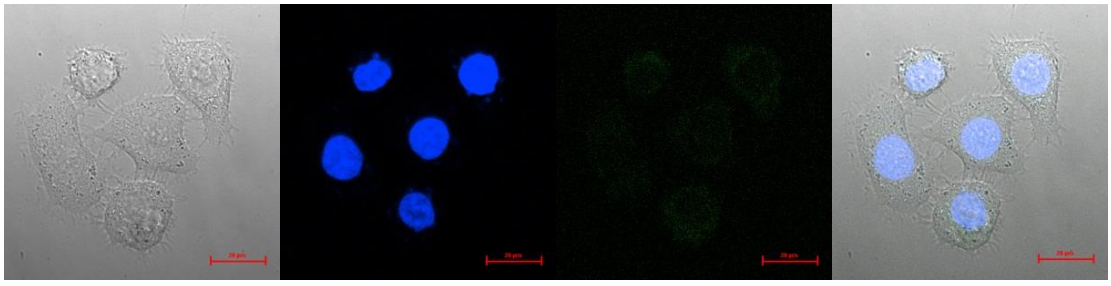

a) **b)** **c)** **d)**

Figure G.3. Single-photon confocal fluorescence microscopy of **ia** at 100 μM, 1% DMSO, 20 mins, PC-3, incubated with mitotracker . a) DIC micrograph. b) Micrograph with excitation at 405 nm, c) Micrograph with excitation at 488 nm. d) Overlay image of a), b) and c).

a) **b)** **c)**

Figure G.4. Single-photon confocal fluorescence microscopy of **iid** at 50 µM, 0.5% DMSO, 20 minutes, washed then 100 µM, 1% DMSO, incubated for 20 minutes, then washed in FEK-4. a) DIC micrograph. b) Micrograph with excitation at 488 nm. c) Overlay image of a) and b). Scalebar: 20 µm

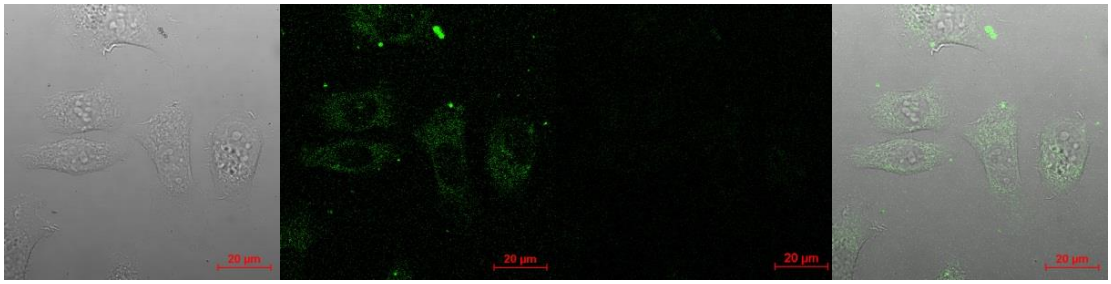

a) **b)** **c)** **d)**

Figure G.5. Single-photon confocal fluorescence microscopy of **iib** at 100 µM, 1% DMSO, 20 minutes, in PC-3. a) DIC micrograph. b) Micrograph with excitation at 488 nm. c) Micrograph with excitation at 543 nm, d) Overlay image of a), b) and c). Scalebar: 20 µm

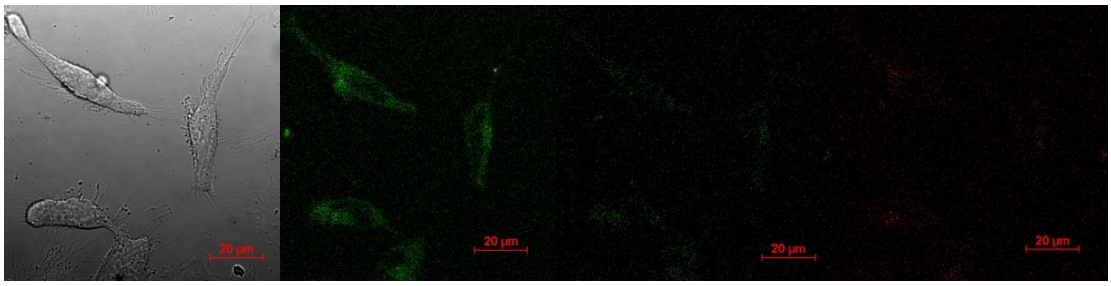

a) **b)** **c)** **d)**

Figure G.6. Single-photon confocal fluorescence microscopy of **iib** at 100 µM, 1% DMSO, 20 minutes, in HeLa. a) DIC micrograph. b) Micrograph with excitation at 405 nm (green channel). c) Micrograph with excitation at 488 nm (green channel). d) Micrograph with excitation at 488 nm. (green channel). Scalebar: 20 µm.

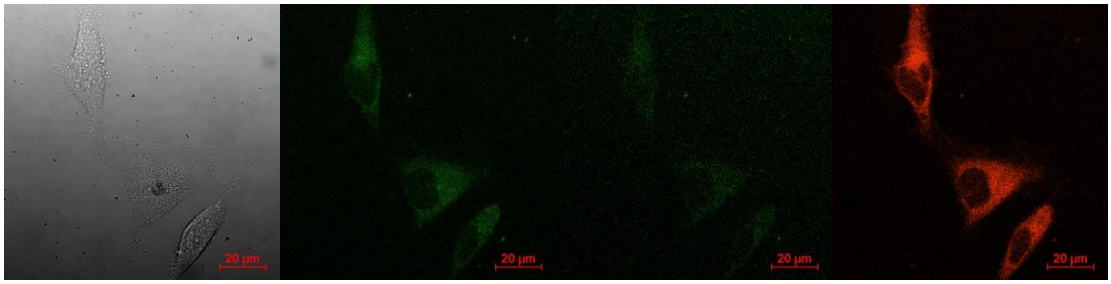

a) **b)** **c)** **d)**

Figure G.7. Single-photon confocal fluorescence microscopy of **iid** at 100 μM, 1% DMSO, 20 minutes, in HeLa. a) DIC micrograph. b) Micrograph with excitation at 405 nm (green channel). c) Micrograph with excitation at 488 nm (green channel). d) Micrograph with excitation at 488 nm. (green channel). Scalebar: 20 μm.

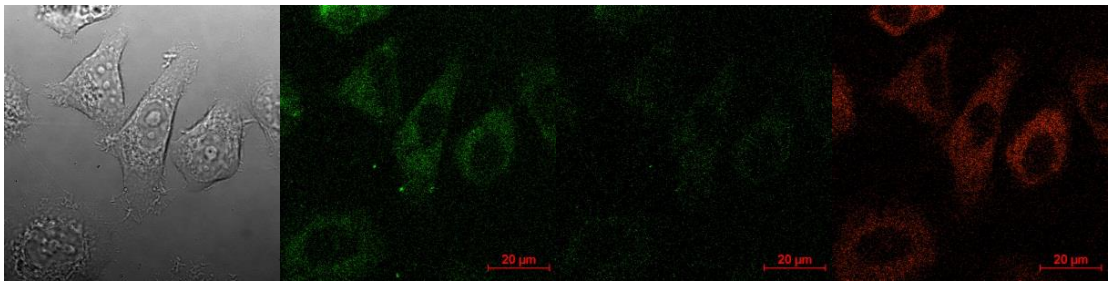

a) **b)** **c)** **d)**

Figure G.8. Single-photon confocal fluorescence microscopy of **iid** at 100 μM, 1% DMSO, 20 minutes, in PC-3. a) DIC micrograph. b) Micrograph with excitation at 405 nm (green channel). c) Micrograph with excitation at 488 nm (green channel). d) Micrograph with excitation at 488 nm. (green channel). Scalebar: 20 μm.

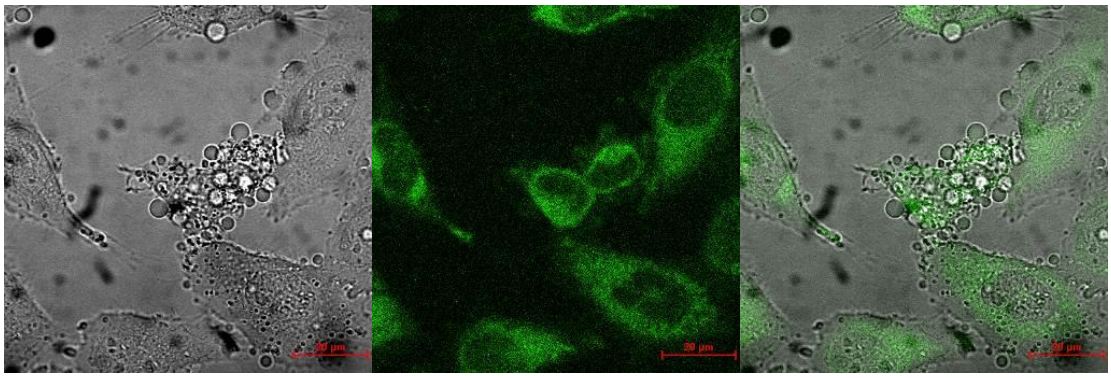

a) **b)** **c)**

Figure G.9. Confocal microscopy of HeLa cells incubated with **1d** at 50 μM, 0.5% DMSO, for 20 minutes, at 37 ˚C. c) Overlay of a) DIC image and of b) micrograph with excitation at 488 nm.

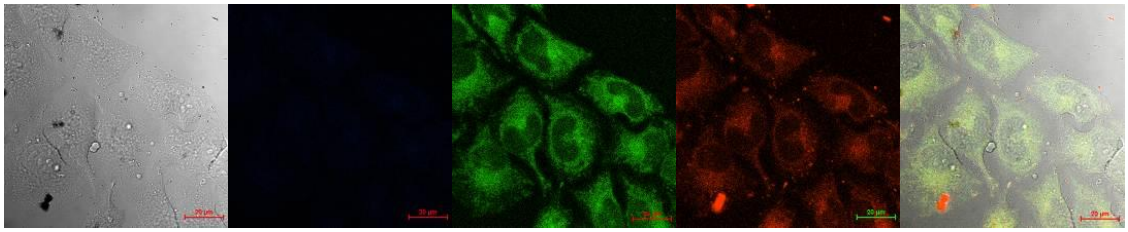

a) **b)** **c)** **d)** **e)**

Figure G.10. Confocal microscopy of HeLa cells incubated with **1b** at 100 μM, 1% DMSO, for 20 minutes, at 37. Where **(e)** Overlay of **(a)** the DIC image **b)** micrograph with excitation of 405 nm, **(c)** the micrograph with excitation of 488 nm and **(d)** the micrograph with excitation of 543 nm.

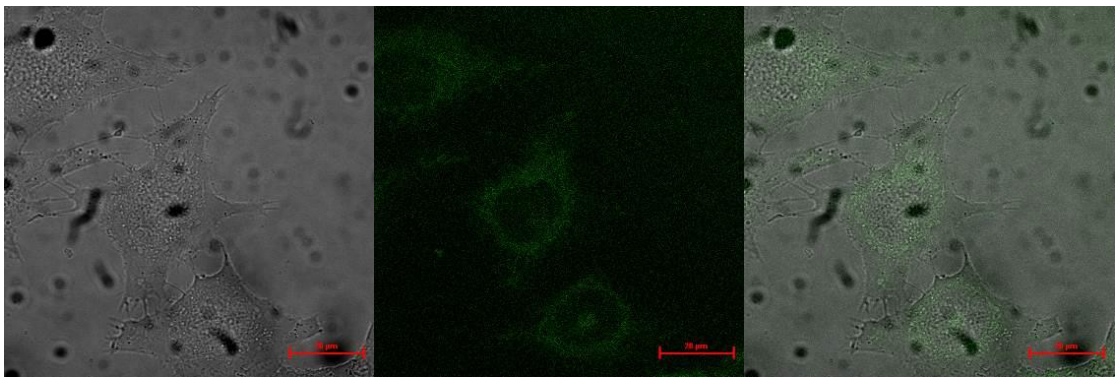

a) **b)** **c)**

Figure G.11. Confocal microscopy of HeLa cells incubated with **2d** at 50 μM, 0.5% DMSO, for 60 minutes, at 37 ˚C. c) Overlay of a) DIC image and of **b)** micrograph with excitation at 488 nm.

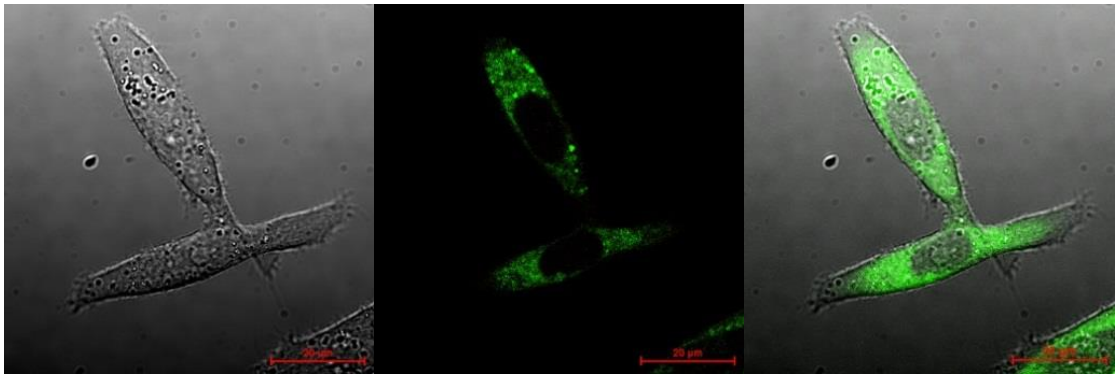

a) **b)** **c)**

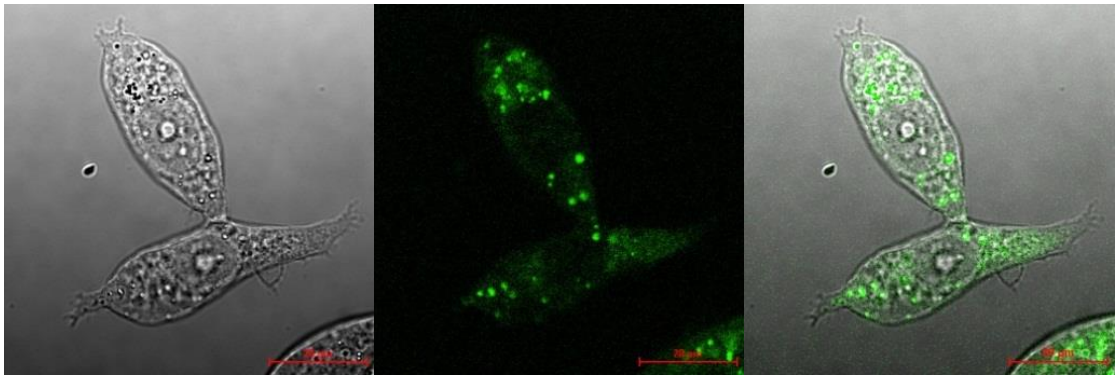

d) **e)** **f)**

Figure G.12. Complex **3b** at 50 µM, 0.5% DMSO, irradiation experiment at 488 nm in PC-3 cells: (a – c) before irradiation and (d – f) after irradiation for ca. 10 minutes, DIC image (a, d), micrograph of cells after excitation at 488 nm (b, e, compound, green channel), micrograph of cells after excitation at 543 nm (d, i, compound, red channel). (c) Overlay of (a) and (b) images, whereas (f) Overlay of images (d) and (e). Scalebar: 20 µm.

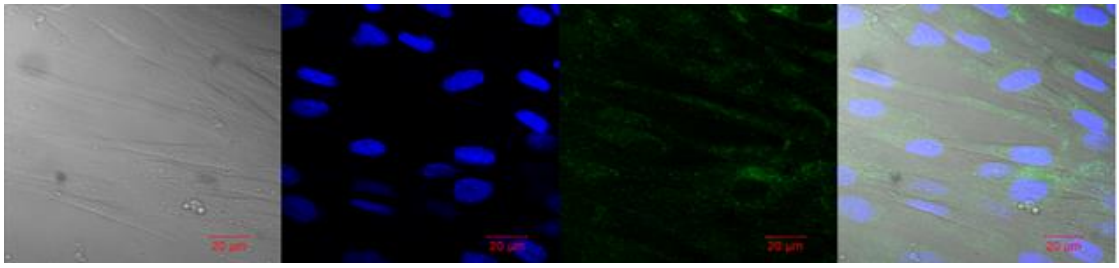

a) **b)** **c)** **d)**

Figure G.13. Complex **3d** at 50 µM, 0.5% DMSO, 20 minutes irradiation experiment at 488 nm in FEK-4 cells: a) DIC image. b) Micrograph of cells after excitation at 405 nm. c) Micrograph of cells after excitation at 488 nm (compound, green channel). (d) Overlay of (a), (b) and (c). Scalebar: 20 µm.

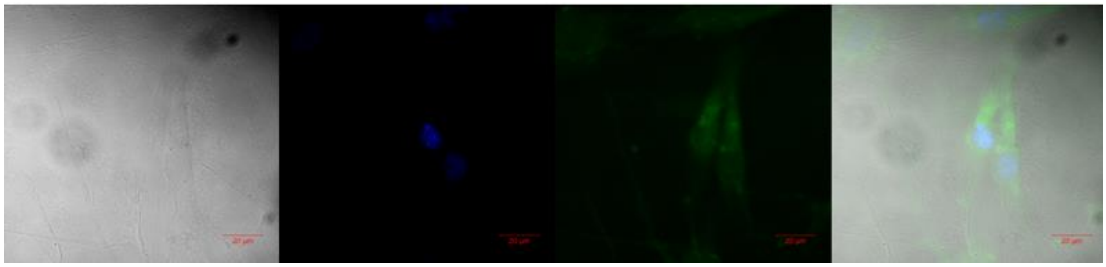

a) **b)** **c)** **d)**

Figure G.14. Complex **3d** irradiation experiment at 488 nm in FEK-4 cells, 100 µM, 1 % DMSO, ca. 3 hours. (a, f) DIC image. (b, g) Micrograph of cells after excitation at 405 nm. (c, h) Micrograph of cells after excitation at 488 nm (compound, green channel). (d) Overlay of (a), (b) and (c) images, scalebar: 20 µm.

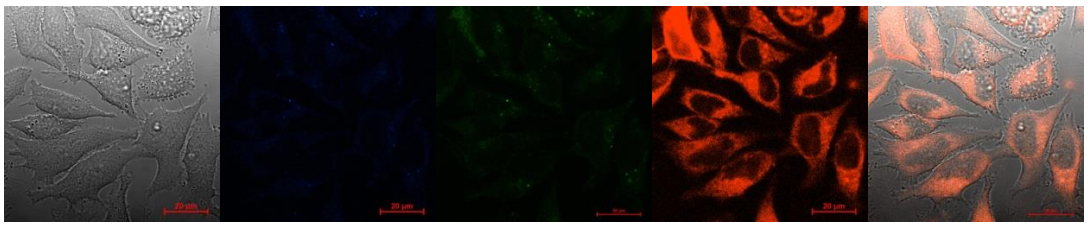

a) **b)** **c)** **d)** **e)**

Figure G.15. Complex **3c** irradiation experiment at 488 nm in HeLa cells: (a – e) with no added stain DIC image (a), micrograph of cells after excitation at 405 nm (b), micrograph of cells after excitation at 488 nm (c, compound, green channel), micrograph of cells after excitation at 543 nm (d, compound, red channel). Image (d) Overlay of (a), (b) and (c) images. Scalebar: 20 µm.

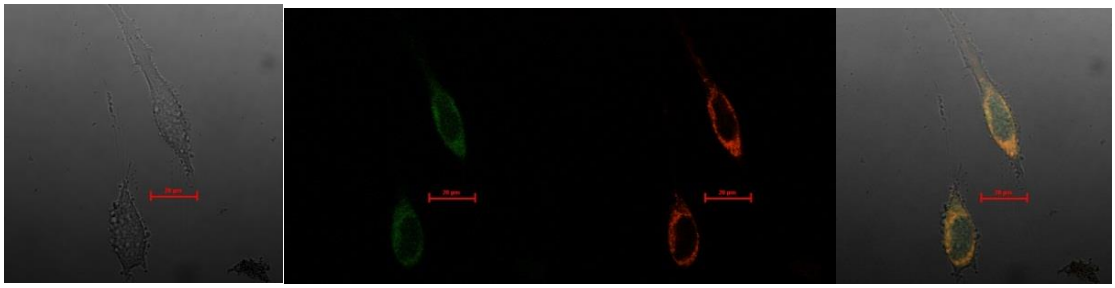

a) **b)** **c)** **d)**

Figure G.16. Complex **3a** and Mitotracker in HeLa cells: DIC image (a), micrograph of cells after excitation at 488 nm (b, compound, green channel), micrograph of cells after excitation at 543 nm (c, red channel). Image (d) Overlay of (a), (b) and (c) images suggesting mitochondria localisation of 3. Scalebar: 20 µm

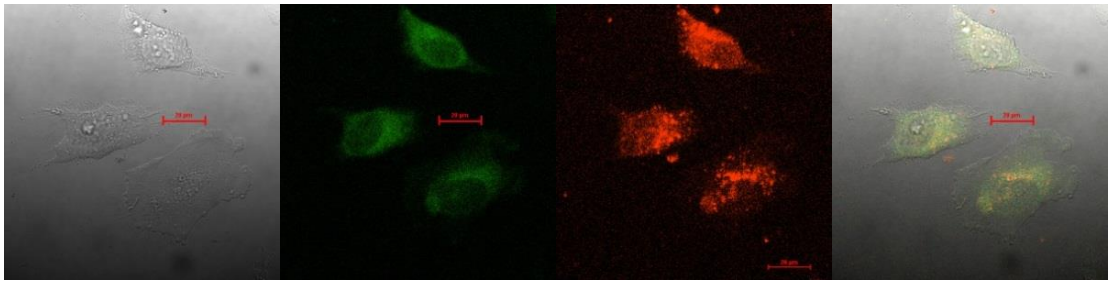

a) **b)** **c)** **d)**

Figure G.17. Complex **3a** and Lysotracker in HeLa cells: DIC image (a), micrograph of cells after excitation at 488 nm (b, compound, green channel), micrograph of cells after excitation at 543 nm (c, compound, red channel). Image (d) Overlay of (a), (b) and (c) images suggesting some lysosome localisation. Scalebar: 20 μm

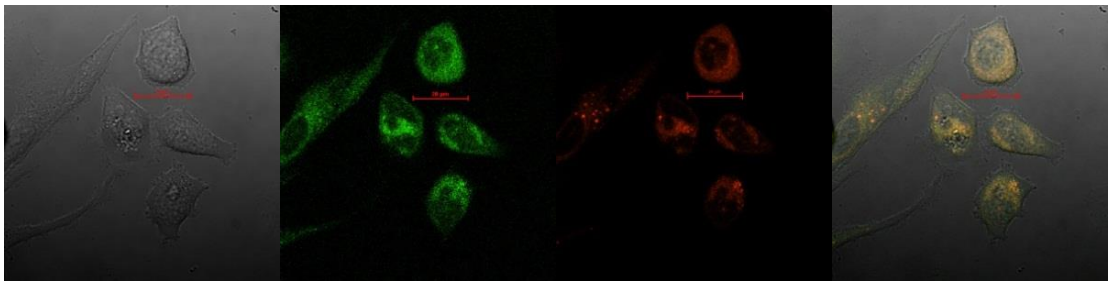

a) **b)** **c)** **d)**

Figure G.18. Complex **3a** and Lysotracker in PC-3 cells: DIC image (a), micrograph of cells after excitation at 488 nm (b, compound, green channel), micrograph of cells after excitation at 543 nm (c, compound, red channel). Image (d) Overlay of (a), (b) and (c) images suggesting lysosome localisation. Scalebar: 20 μm

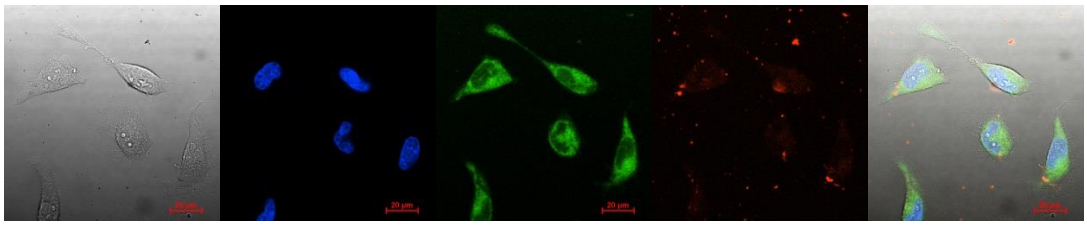

a) **b)** **c)** **d)** **e)**

Figure G.19. Complex **3b** and Hoechst (nuclear stain) in HeLa cells at 37°C: DIC image (a), micrograph of cells after excitation at 405 nm (b, Hoechst, blue channel), micrograph of cells after excitation at 488 nm (c, compound, green channel), micrograph of cells after excitation at 543 nm (d, compound, red channel). Image (e) Overlay of (a), (b), (c) and (d) images suggesting some lysosome localisation. Scalebar: 20 μm.

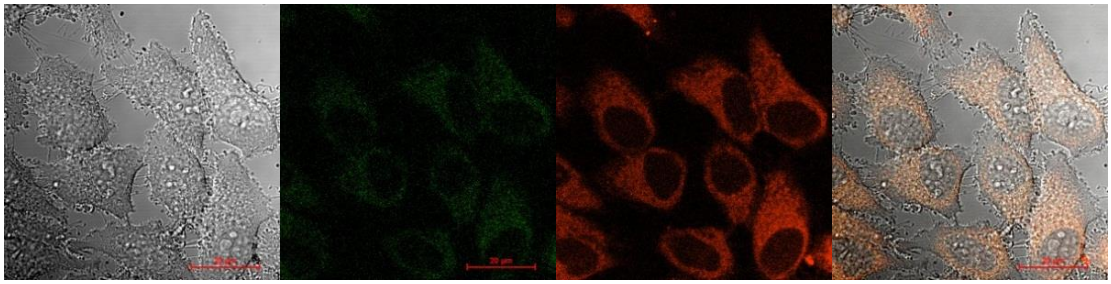

a) **b)** **c)** **d)**

Figure G.20. Single-photon confocal microscopy images of **3b** in HeLa cells incubated at 4 ^{o}C, (a) DIC image, (b) excitation at 405 nm, emission 420-480 nm (c) excitation at 488 nm, emission >505 nm, (d) Overlay of (a), (b) and (c). Scalebar: 20 μm.

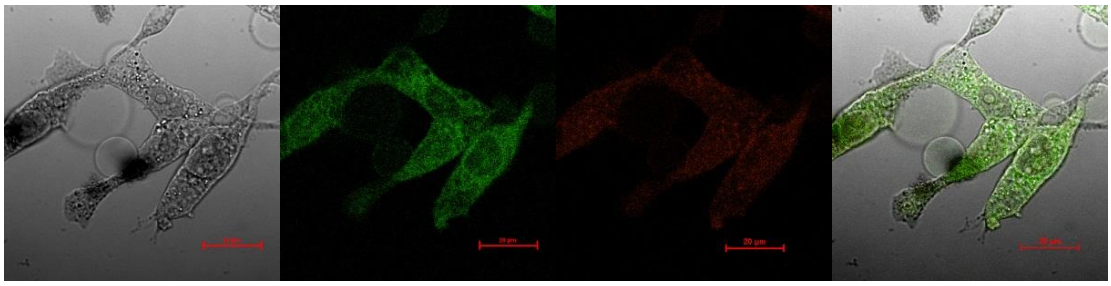

a) **b)** **c)** **d)**

Figure G.21. Single-photon confocal microscopy images of **4a** in PC-3 cells,30 minute incubation (a) DIC image, (b) excitation at 488 nm, emission >505 nm, (c) Overlay of (a) and (b). Scalebar: 20 μm

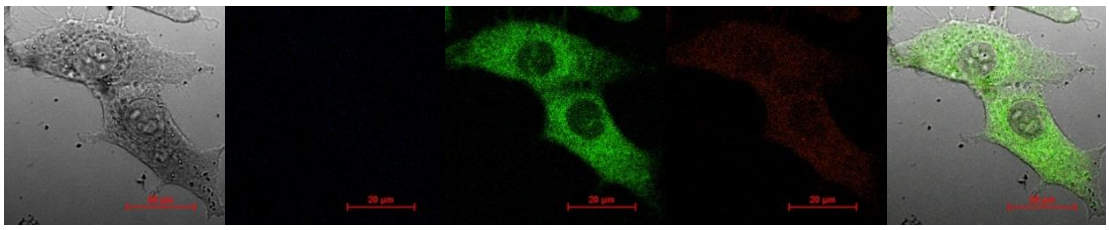

a) **b)** **c)** **d)** **e)**

Figure G.22. Single-photon confocal microscopy images of **4b** in PC-3 cells, 20 minute incubation, 50 μM 0.5% DMSO (a) DIC image, (b) excitation at 405 nm, emission 420-480 nm (c) excitation at 488 nm, emission >505 nm, (d) micrograph of cells after excitation at 543 nm and (e) Overlay of (a), (b), (c) and (d) Scalebar: 20 μm

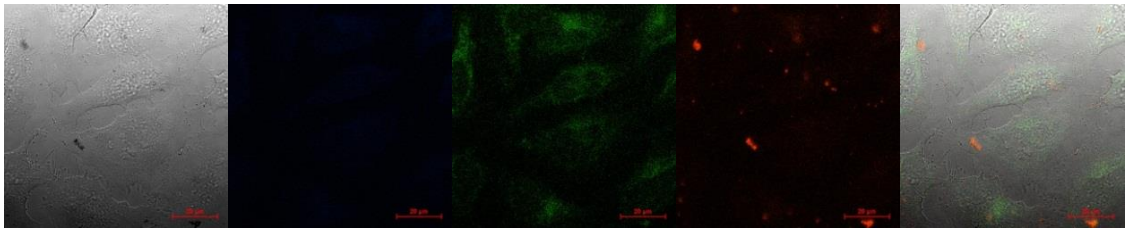

a) **b)** **c)** **d)** **e)**

Figure G.23. Single-photon confocal microscopy images of **4c** in HeLa cells, 20 minute incubation, 50 µM 0.5% DMSO at 37°C (a) DIC image, (b) excitation at 405 nm, emission 420-480 nm (c) excitation at 488 nm, emission >505 nm, (d) micrograph of cells after excitation at 543 nm and (e) Overlay of (a), (b), (c) and (d) Scalebar: 20 µm

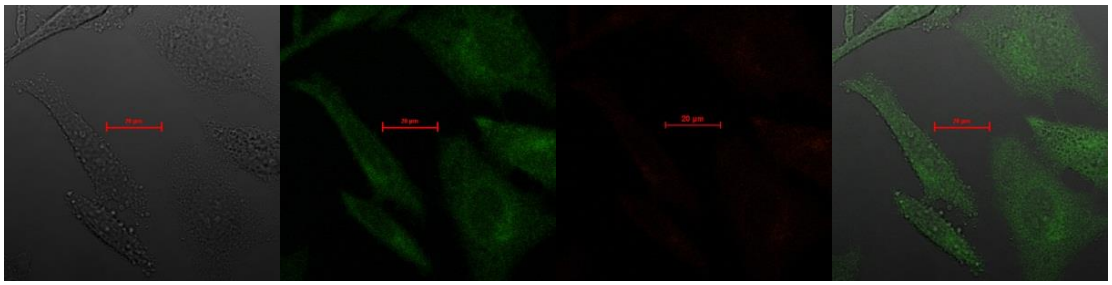

a) **b)** **c)** **d)**

Figure G.24. Single-photon confocal microscopy images of **4a** in HeLa cells (a) DIC image, (b) excitation at 488 nm, emission >505 nm, (c) micrograph of cells after excitation at 543 nm and (d) Overlay of (a), (b) and (c). Scalebar: 20 µm

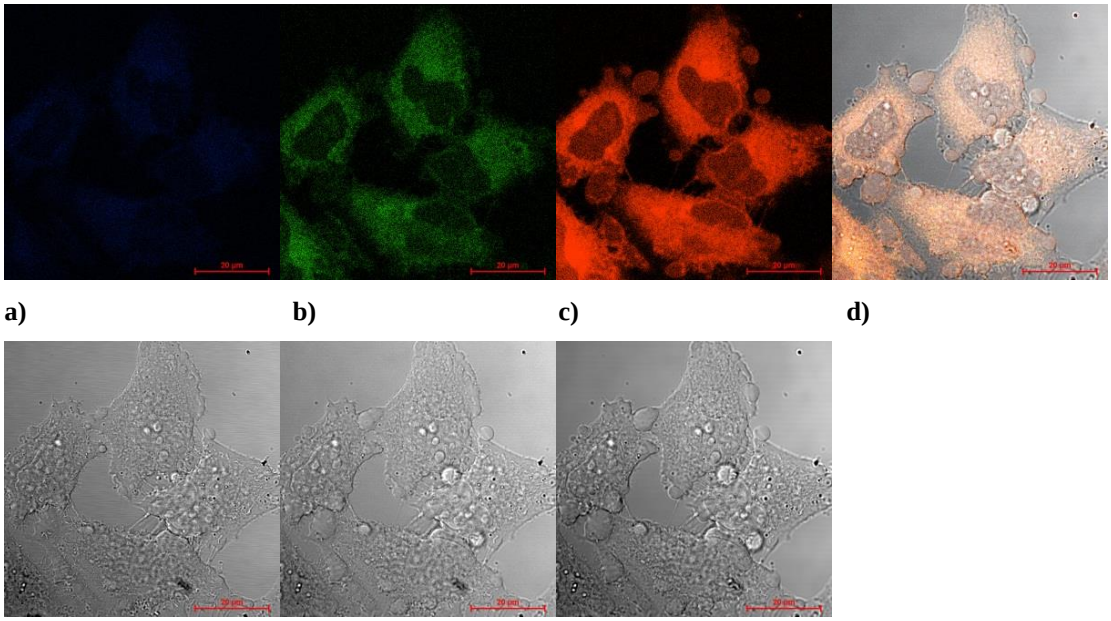

a) **b)** **c)** **d)**

e) **f)** **g)**

Figure G.25. Single-photon confocal microscopy images of **4b** in HeLa cells, 20 minute incubation, 50 µM 0.5% DMSO at 4°C (a) excitation at 405 nm, emission 420-480 nm, (b) excitation at 488 nm, emission >505 nm, (c) micrograph of cells after excitation at 543 nm and (d) Overlay of (a), (b), (c) and (g), (e) is the DIC image from excitation at 405 nm, (f) is the DIC image from excitation at 488 nm, (g) is the DIC image from excitation at 543 nm. Scalebar: 20 µm.

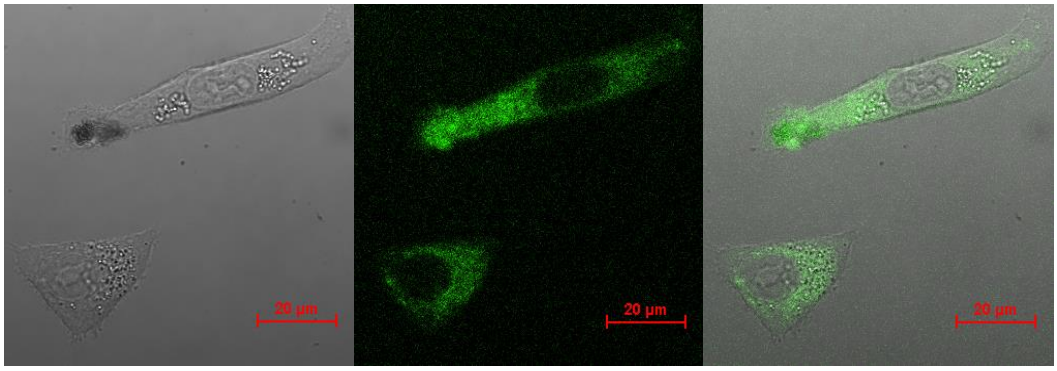

a) **b)** **c)**

Figure G.26. Single-photon confocal microscopy images of **4c** in PC-3 cells, before irradiation at 488 nm 20 minute incubation, 50 µM 0.5% DMSO at 37°C (a) DIC image, (b) excitation at 405 nm, emission 420-480 nm (c) excitation at 488 nm, emission >505 nm, (d) micrograph of cells after excitation at 543 nm and (e) Overlay of (a), (b), (c) and (d) Scalebar: 20 µm

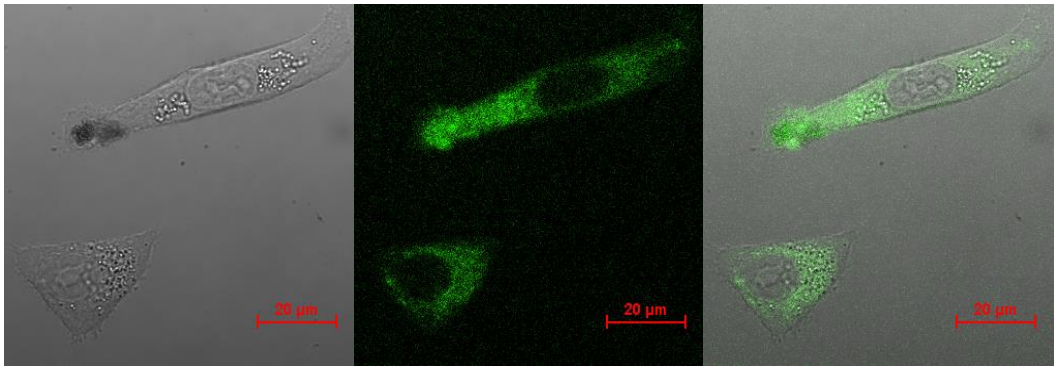

a) **b)** **c)**

Figure G.27. Single-photon confocal microscopy images of **4c** in PC-3 cells, after irradiation at 488 nm 20 minute incubation, 50 µM 0.5% DMSO at 37°C (a) DIC image, (b) excitation at 405 nm, emission 420-480 nm (c) excitation at 488 nm, emission >505 nm, (d) micrograph of cells after excitation at 543 nm and (e) Overlay of (a), (b), (c) and (d) Scalebar: 20 µm.

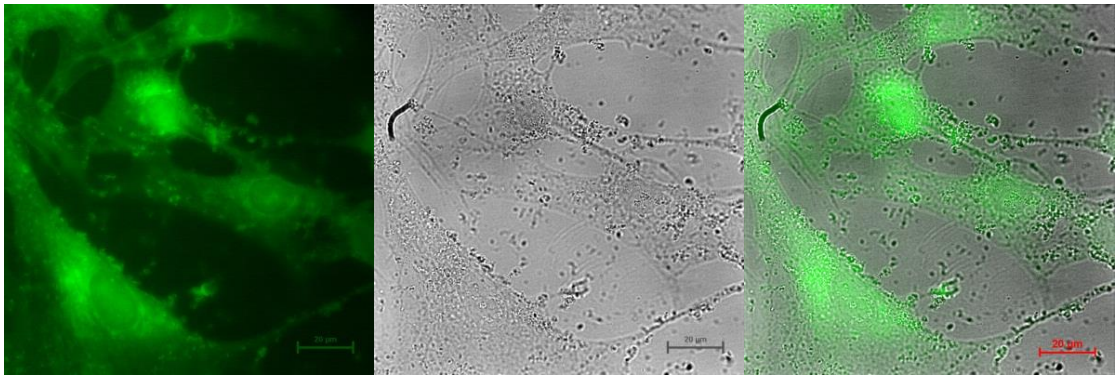

a) **b)** **c)**

Figure G.28. Single-photon Epi-fluorescence microscopy images of **4d** in HeLa cells, 3 hour incubation, 100 µM, 1% DMSO at 37°C (a) DIC image, (b) excitation at 488 nm, emission >505 nm, (c) Overlay of (a) and (b). Scalebar: 20 µm.

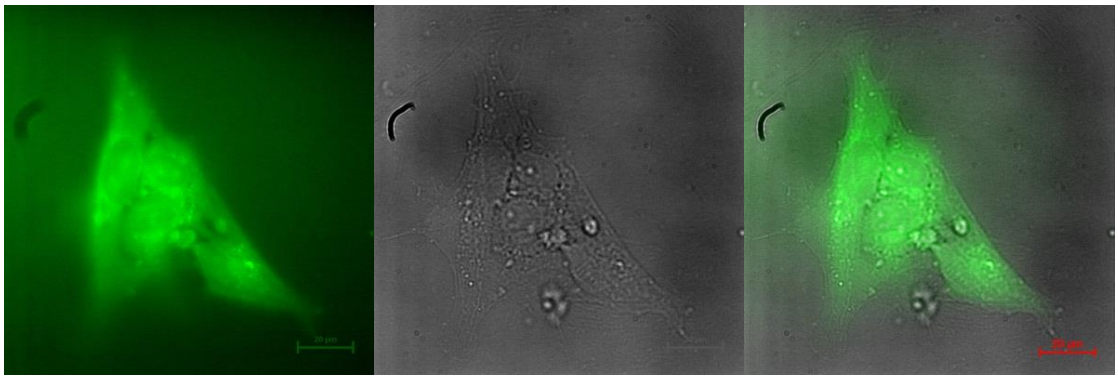

a) **b)** **c)**

Figure G.29. Single-photon Epi-fluorescence microscopy images of **4d** in HeLa cells, 3 hour incubation, 100 µM, 1% DMSO at 4°C (a) DIC image, (b) excitation at 488 nm, emission >505 nm, (c) Overlay of (a) and (b). Scalebar: 20 µm.

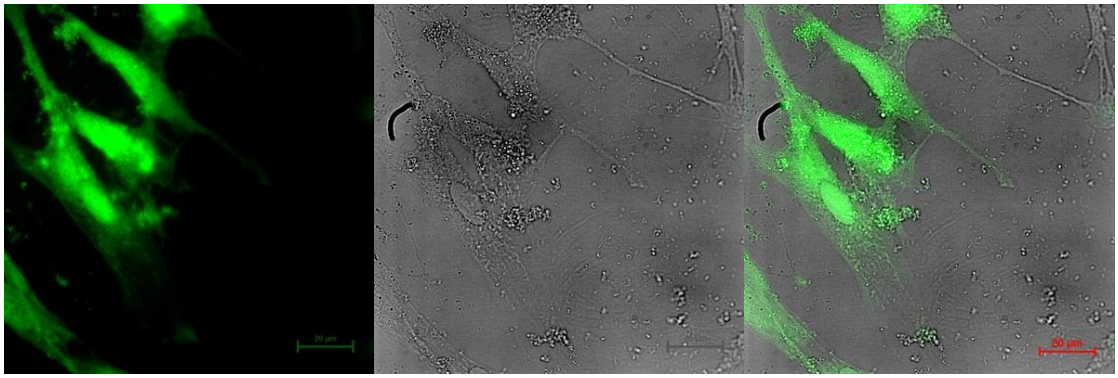

a) **b)** **c)**

Figure G.30. Single-photon confocal microscopy images of **4b** in FEK-4 cells, 3 hour incubation, 100 µM, 1% DMSO at 37°C (a) DIC image, (b) excitation at 488 nm, emission >505 nm, (c) Overlay of (a) and (b). Scalebar: 20 µm.

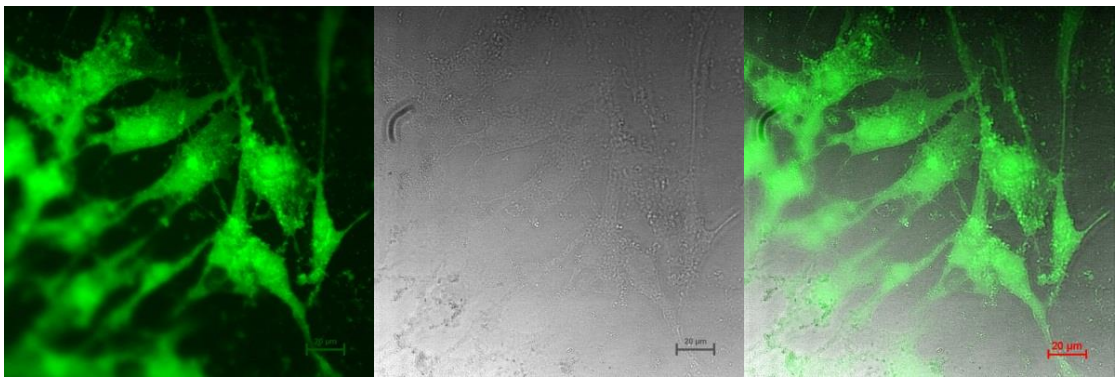

a) **b)** **c)**

Figure G.31. Single-photon confocal microscopy images of **4b** in FEK-4 cells, 3 hour incubation, 100 µM, 1% DMSO at 4°C (a) DIC image, (b) excitation at 488 nm, emission >505 nm, (c) Overlay of (a) and (b). Scalebar: 20 µm.

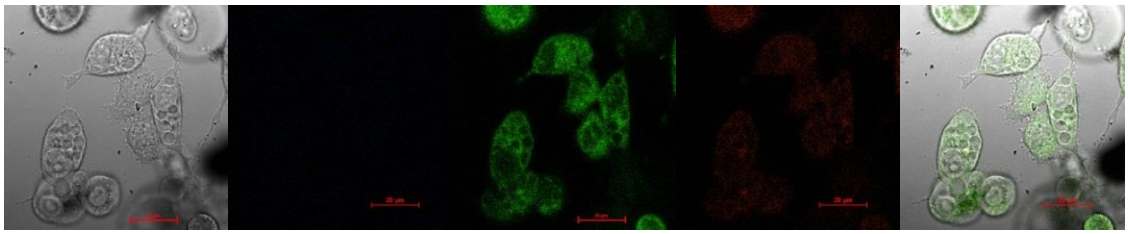

a) **b)** **c)** **d)** **e)**

Figure G.32. Single-photon confocal microscopy images of **4d** in PC-3 cells, 30 minute incubation, 50 µM 0.5% DMSO at 37°C (a) DIC image, (b) excitation at 488 nm, emission >505 nm, (c) Overlay of (a) and (b). Scalebar: 20 µm

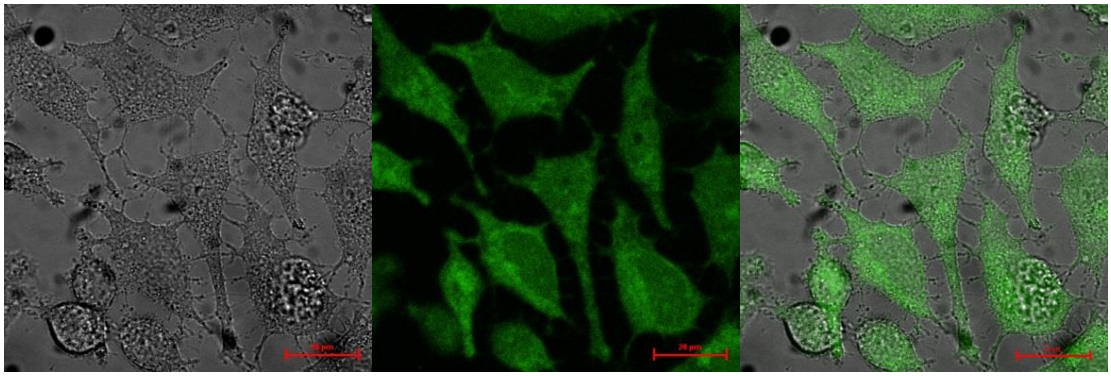

a) **b)** **c)**

Figure G.33. Single-photon confocal microscopy images of **4d** in HeLa cells, 60 minute incubation, 50 µM 0.5% DMSO at 37°C (a) DIC image, (b) excitation at 488 nm, emission >505 nm, (c) Overlay of (a) and (b). Scalebar: 20 µm

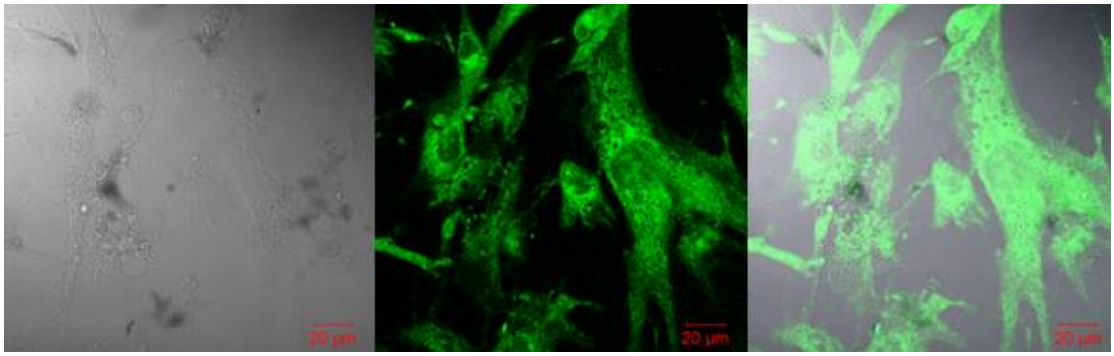

a) **b)** **c)**

Figure G.34. Single-photon confocal microscopy images of **4d** in, FEK-4 cells 100 µM, 1% DMSO 60 minute incubation, at 37°C (a) DIC image, (b) excitation at 488 nm, emission >505 nm, (c) Overlay of (a) and (b). Scalebar: 20 µm

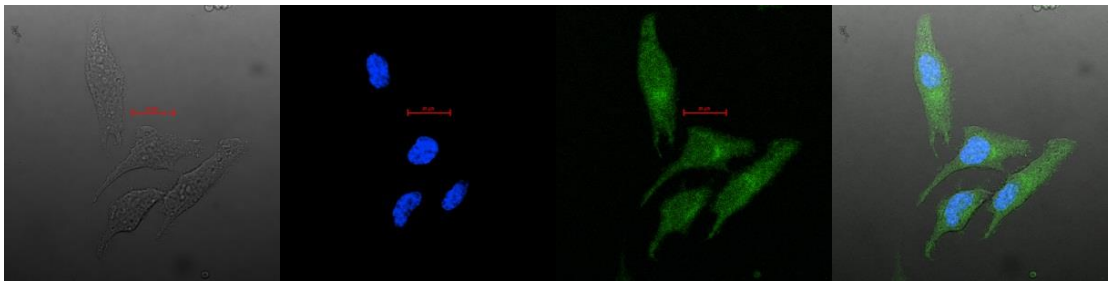

a) **b)** **c)** **d)**

Figure G.35. Single-photon confocal microscopy images of **4a** and Hoechst stain in HeLa cells after 20 minutes, (a) DIC image, (b) excitation at 405 nm, emission 420-480 nm (c) micrograph of cells after excitation at 543 nm and (d) Overlay of (a), (b) and (c). Scalebar: 20 µm

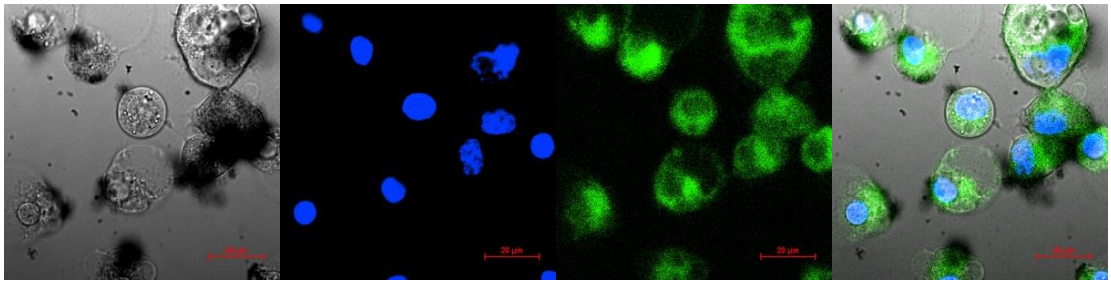

a) **b)** **c)** **d)**

Figure G.36. Single-photon confocal microscopy images of **4c** and Hoechst 6 hour in PC-3 cells, 20 minute incubation, 50 µM 0.5% DMSO at 37°C (a) DIC image, (b) excitation at 488 nm, emission >505 nm, (c) micrograph of cells after excitation at 543 nm, (d) Overlay of (a), (b) and (c). Scalebar: 20 µm.

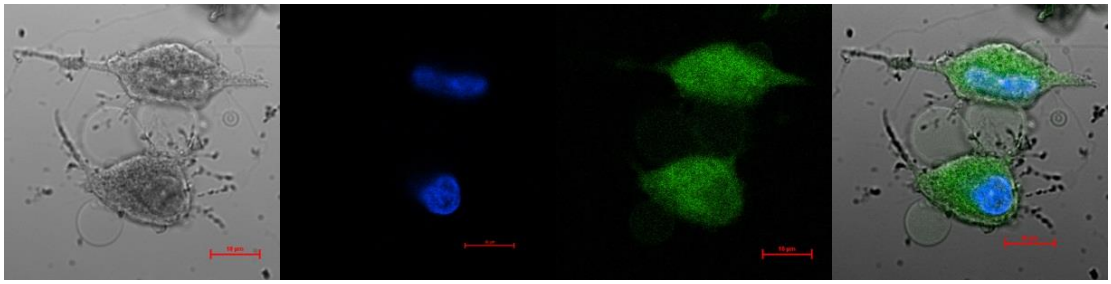

a) **b)** **c)** **d)**

Figure G.37. Single-photon confocal microscopy images of **4a** and Hoechst stain in HeLa cells, 60 minute incubation (a) DIC image, (b) excitation at 405 nm, emission 420-480 nm (c) excitation at 488 nm, emission >505 nm, (d) Overlay of (a), (b) and (c). Scalebar: 20 µm

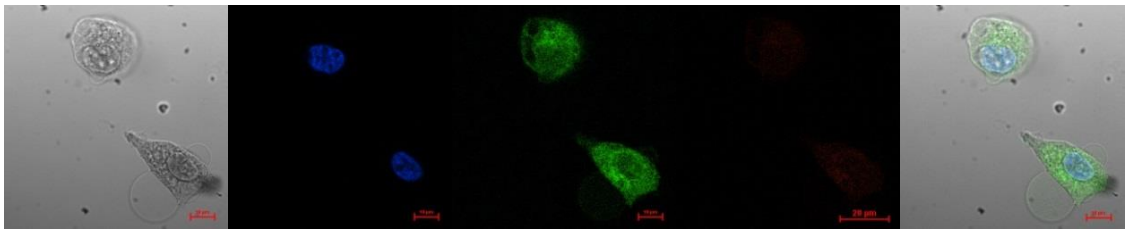

a) **b)** **c)** **d)** **e)**

Figure G.38. Single-photon confocal microscopy images of **4a** and Hoechst stain in PC-3 cells, 60 minute incubation (a) DIC image, (b) excitation at 405 nm, emission 420-480 nm (c) excitation at 488 nm, emission >505 nm, (d) Overlay of (a), (b) and (c). Scalebar: 20 µm

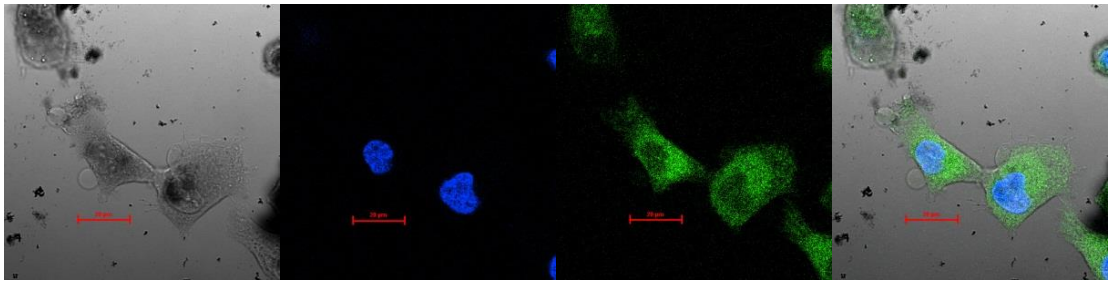

a) **b)** **c)** **d)**

Figure G.39. Single-photon confocal microscopy images of **4d** and Hoechst stain in PC-3 cells, 20 minute incubation, 50 µM 0.5% DMSO at 37°C (a) DIC image, (b) excitation at 405 nm, emission 420-480 nm (c) excitation at 488 nm, emission >505 nm, (d) Overlay of (a), (b) and (c). Scalebar: 20 µm

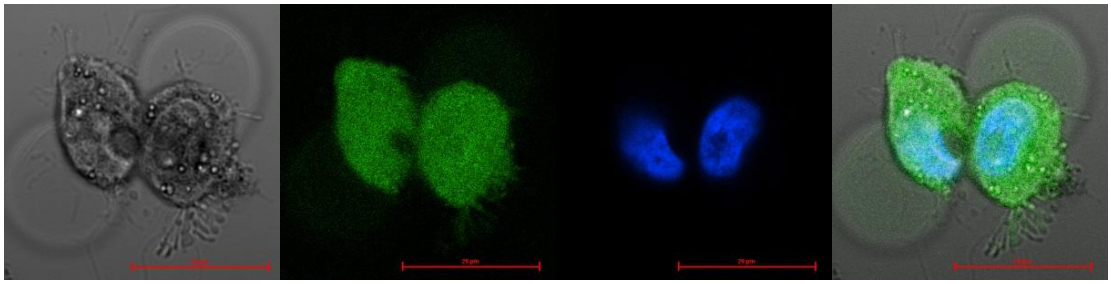

a) **b)** **c)** **d)**

Figure G.40. Single-photon confocal microscopy images of **4d** and Hoechst stain in PC-3 cells, 60 minute incubation, 50 µM 0.5% DMSO at 37°C (a) DIC image, (b) excitation at 405 nm, emission 420-480 nm (c) excitation at 488 nm, emission >505 nm, (d) Overlay of (a), (b) and (c). Scalebar: 20 µm

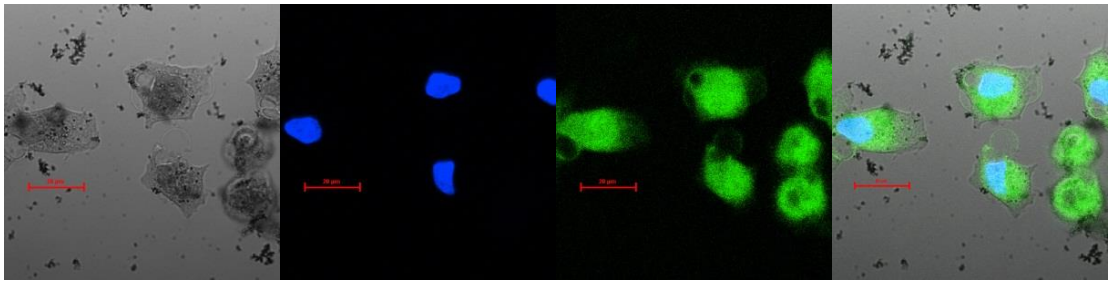

a) **b)** **c)** **d)**

Figure G.41. Single-photon confocal microscopy images of **4a** and Hoechst stain in PC-3 cells, 6 hour incubation, 50 µM 0.5% DMSO at 37°C (a) DIC image, (b) excitation at 405 nm, emission 420-480 nm (c) excitation at 488 nm, emission >505 nm, (d) Overlay of (a), (b) and (c). Scalebar: 20 µm

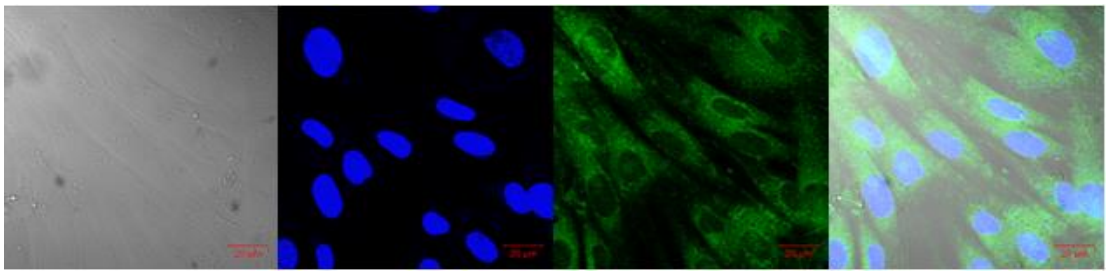

a) **b)** **c)** **d)**

Figure G.42. Single-photon confocal microscopy images of **4d** and Hoechst stain in FEK-4 cells, 50 µM, 0.5% DMSO, 30 minutes at 37°C (a) DIC image, (b) excitation at 405 nm, emission 420-480 nm (c) excitation at 488 nm, emission >505 nm, (d) Overlay of (a), (b) and (c). Scalebar: 20 µm

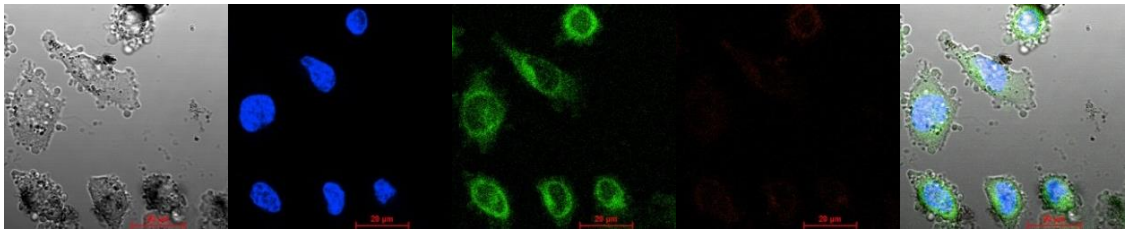

a) **b)** **c)** **d)** **e)**

Figure G.43. Single-photon confocal microscopy images of **4b** in HeLa cells stained with Hoechst, 20 minute incubation, 50 µM 0.5% DMSO (a) DIC image, (b) excitation at 405 nm, emission 420-480 nm (c) excitation at 488 nm, emission >505 nm, (d) micrograph of cells after excitation at 543 nm and (e) Overlay of (a), (b), (c) and (d) Scalebar: 20 µm.

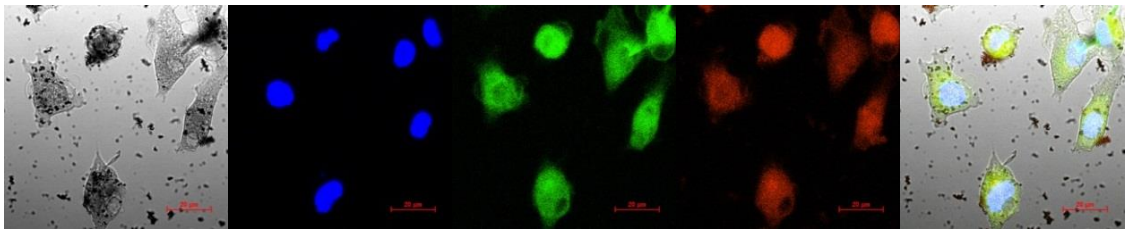

a) **b)** **c)** **d)** **e)**

Figure G.44. Single-photon confocal microscopy images of **4b** in PC-3 cells, 6 hour incubation, 50 µM 0.5% DMSO (a) DIC image, (b) excitation at 405 nm, emission 420-480 nm (c) excitation at 488 nm, emission >505 nm, (d) micrograph of cells after excitation at 543 nm and (e) Overlay of (a), (b), (c) and (d) Scalebar: 20 µm

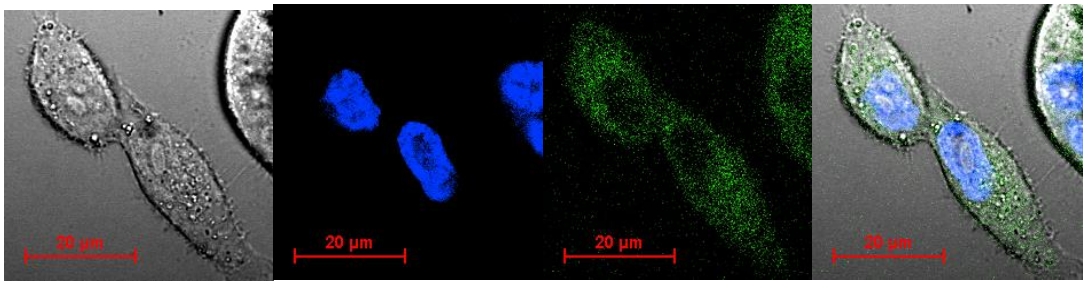

a) **b)** **c)** **d)**

Figure G.45. Single-photon confocal microscopy images of **4c** and Hoechst 1 hour in PC-3 cells, 20 minute incubation, 50 µM 0.5% DMSO at 37°C (a) DIC image, (b) excitation at 488 nm, emission >505 nm, (c) micrograph of cells after excitation at 543 nm, (d) Overlay of (a), (b) and (c). Scalebar: 20 µm.

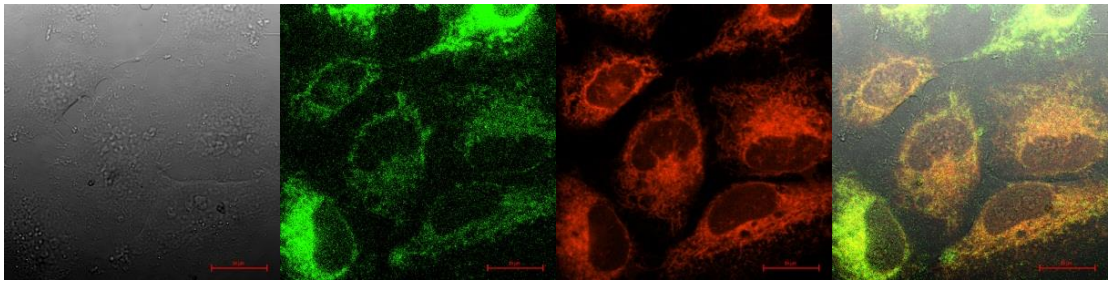

a) **b)** **c)** **d)**

Figure G.46. Single-photon confocal microscopy images of **4c** in HeLa cells stained with ER tracker, 20 minute incubation, 50 µM 0.5% DMSO at 37°C (a) DIC image, (b) excitation at 405 nm, emission 420-480 nm (c) excitation at 488 nm, emission >505 nm, (d) micrograph of cells after excitation at 543 nm and (e) Overlay of (a), (b), (c) and (d) Scalebar: 20 µm.

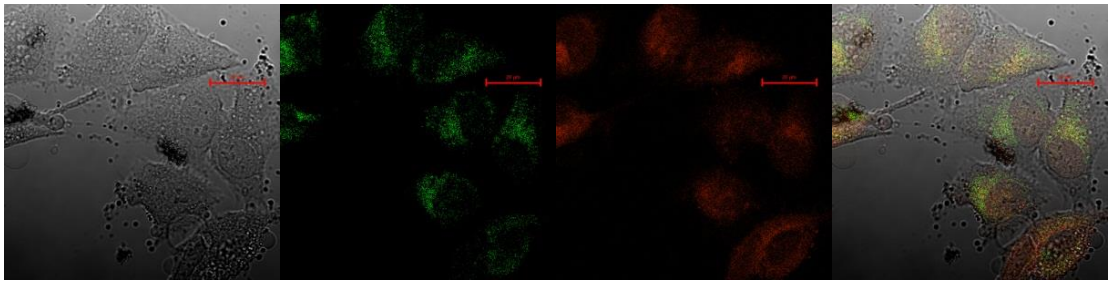

a) **b)** **c)** **d)**

Figure G.47. Single-photon confocal microscopy images of **4a** and Mitotracker Red in HeLa cells, 20 minute incubation (a) DIC image, (b) excitation at 488 nm, emission >505 nm, (c) micrograph of cells after excitation at 543 nm, (d) Overlay of (a), (b) and (c). Scalebar: 20 µm

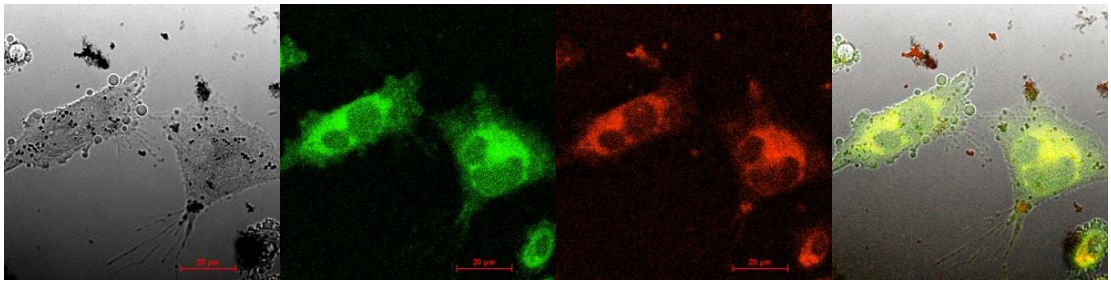

a) **b)** **c)** **d)**

Figure G.48. Single-photon confocal microscopy images of **4c** and Mitotracker in PC-3 cells, 20 minute incubation, 50 µM 0.5% DMSO at 37°C (a) DIC image, (b) excitation at 488 nm, emission >505 nm, (c) micrograph of cells after excitation at 543 nm, (d) Overlay of (a), (b) and (c). Scalebar: 20 µm

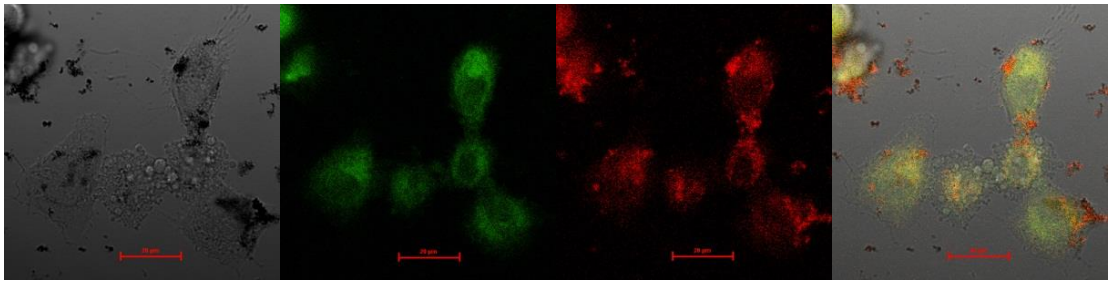

a) **b)** **c)** **d)**

Figure G.49. Single-photon confocal microscopy images of **4d** and Mitotracker Red in HeLa cells, 20 minute incubation, 50 µM 0.5% DMSO at 37°C (a) DIC image, (b) excitation at 488 nm, emission >505 nm, (c) micrograph of cells after excitation at 543 nm, (d) Overlay of (a), (b) and (c). Scalebar: 20 µm

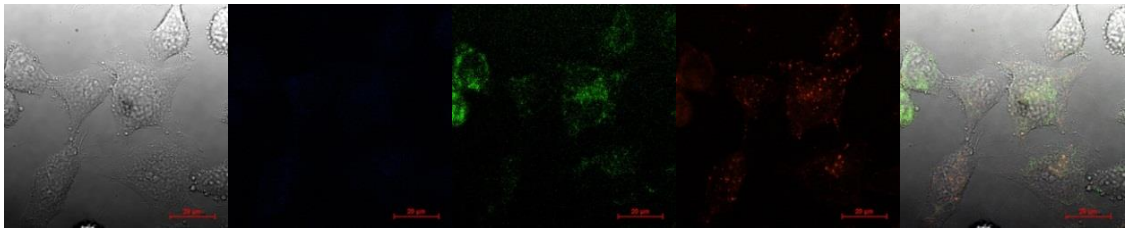

a) **b)** **c)** **d)** **e)**

Figure G.50. Single-photon confocal microscopy images of **4c** after a 20 minute incubation in HeLa cells, incubated with Lysotracker Red, 50 µM 0.5% DMSO at 37°C (a) DIC image, (b) excitation at 405 nm, emission 420-480 nm (c) excitation at 488 nm, emission >505 nm, (d) micrograph of cells after excitation at 543 nm and (e) Overlay of (a), (b), (c) and (d) Scalebar: 20 µm.

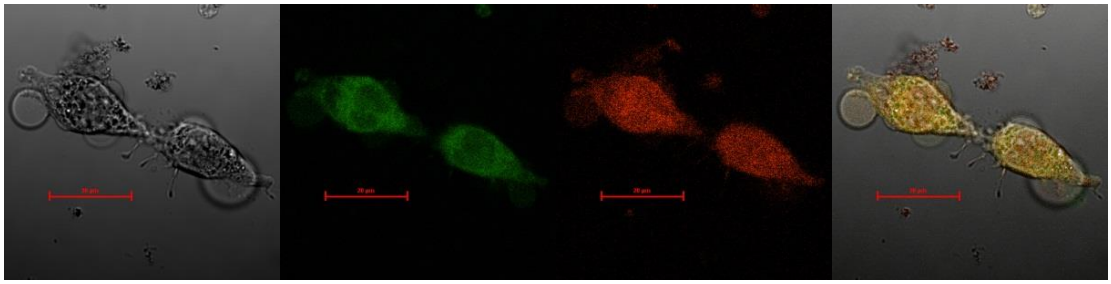

a) **b)** **c)** **d)**

Figure G.51. Single-photon confocal microscopy images of **4d** and Lysotracker Red in HeLa cells, 20 minute incubation, 50 µM 0.5% DMSO at 37°C (a) DIC image, (b) excitation at 488 nm, emission >505 nm, (c) micrograph of cells after excitation at 543 nm, (d) Overlay of (a), (b) and (c). Scalebar: 20 µm

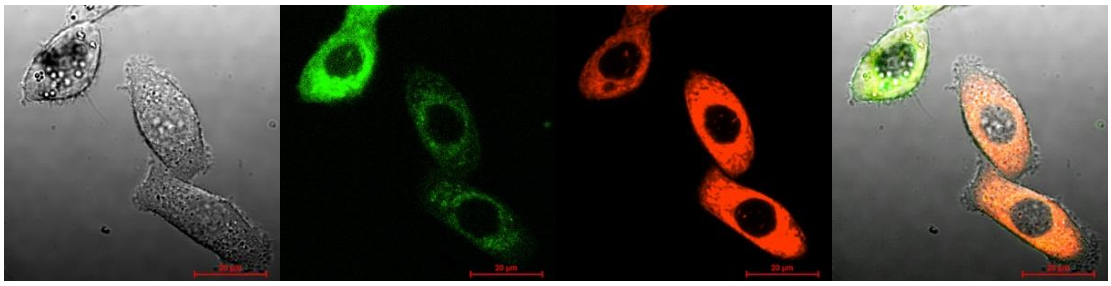

a) **b)** **c)** **d)**

Figure G.52. Single-photon confocal microscopy images of **4c** and ER tracker in PC-3 cells, 20 minute incubation, 50 µM 0.5% DMSO at 37°C (a) DIC image, (b) excitation at 488 nm, emission >505 nm, (c) micrograph of cells after excitation at 543 nm, (d) Overlay of (a), (b) and (c). Scalebar: 20 µm

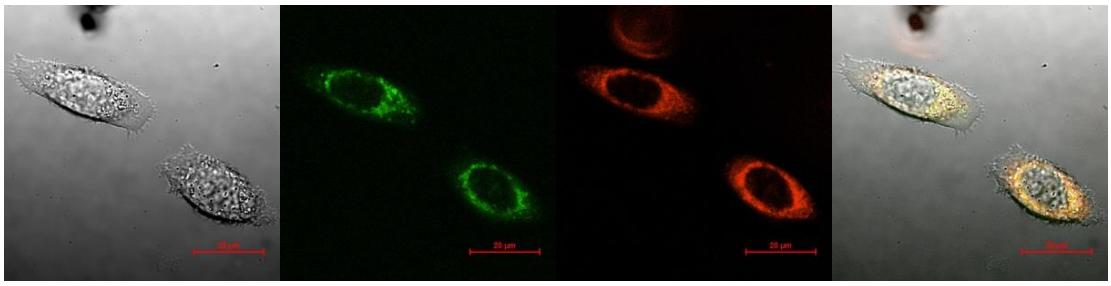

a) **b)** **c)** **d)**

Figure G.53. Single-photon confocal microscopy images of **4c** and Mitotracker in PC-3 cells, 20 minute incubation, 50 µM 0.5% DMSO at 37°C (a) DIC image, (b) excitation at 488 nm, emission >505 nm, (c) micrograph of cells after excitation at 543 nm, (d) Overlay of (a), (b) and (c). Scalebar: 20 µm

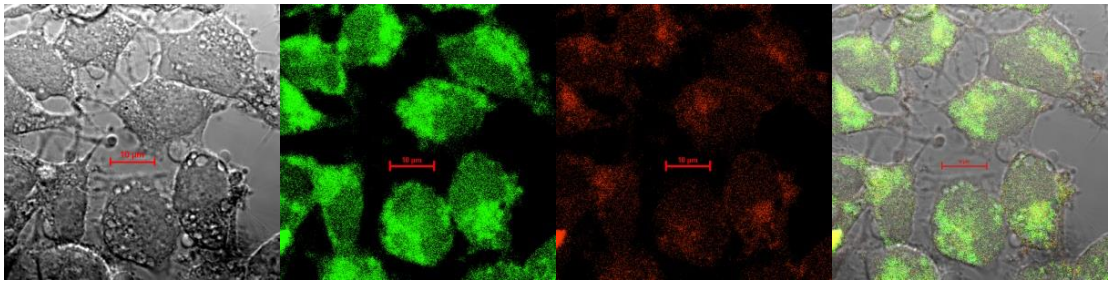

a) **b)** **c)** **d)**

Figure G.54. Single-photon confocal microscopy images of **4a** and Lysotracker Red in HeLa cells, 20 minute incubation (a) DIC image, (b) excitation at 488 nm, emission >505 nm, (c) micrograph of cells after excitation at 543 nm, (d) Overlay of (a), (b) and (c). Scalebar: 20 μm

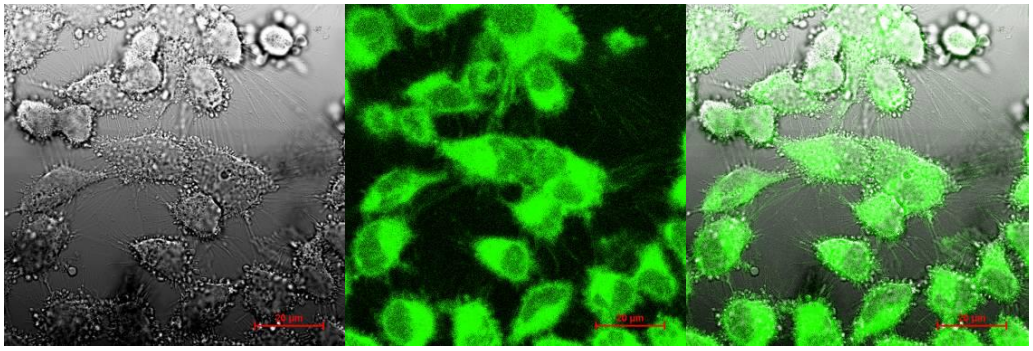

a) **b)** **c)**

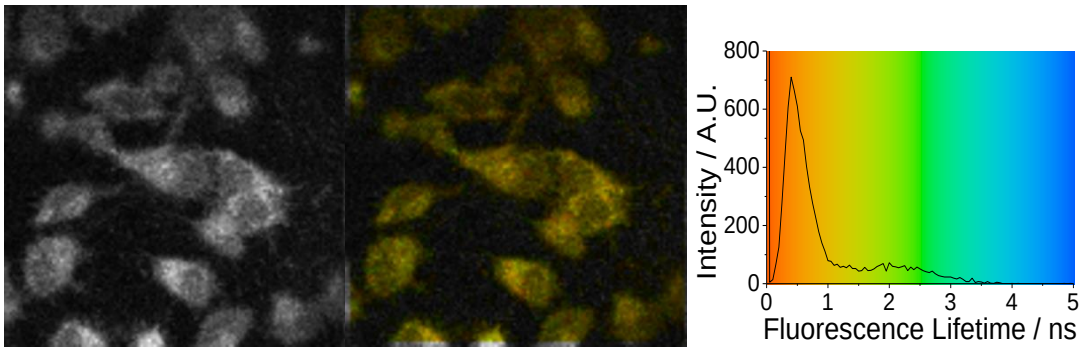

e) **f)** **g)**

Figure G.55. (a – c) Single-photon confocal microscopy of complex **1bB** reaction mixture, 100 μM, 1% DMSO**,** incubated in HeLa cells for 20 minutes where **a)** DIC channel, **b)** excitation at 488 nm and **c)** overlay image of **(a)** and **(b)**. Scalebar = 20 μm. Two-photon fluorescence imaging of complex **2**, 100 μM, 1% DMSO, λ_{ex} = 910 nm, incubated in HeLa cells for 20 minutes where **e)** is the fluorescence intensity profile, **f)** is the fluorescence lifetime map of tm and **g)** is the corresponding lifetime distribution plot in ns of tm.

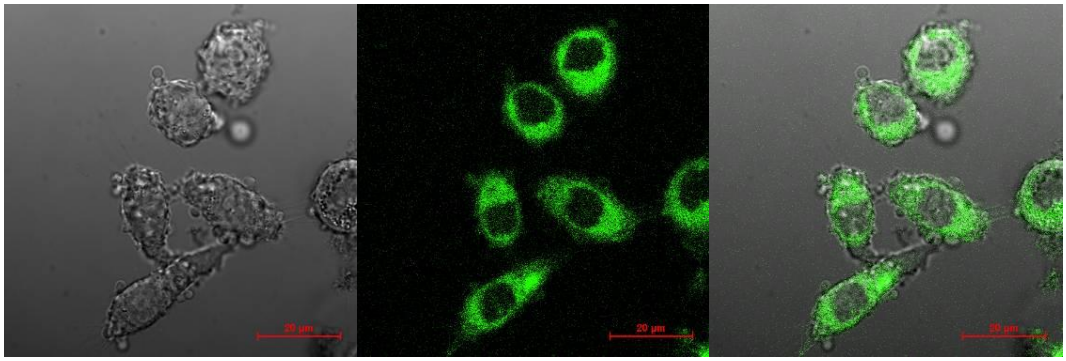

a) **b)** **c)**

Figure G.56. Single-photon confocal microscopy of complex **1bB** reaction mixture, 100 μM, 1% DMSO**,** incubated in PC-3 cells for 20 minutes where a) DIC channel, b) excitation at 488 nm and c) overlay image of (a) and (b). Scalebar = 20 μm

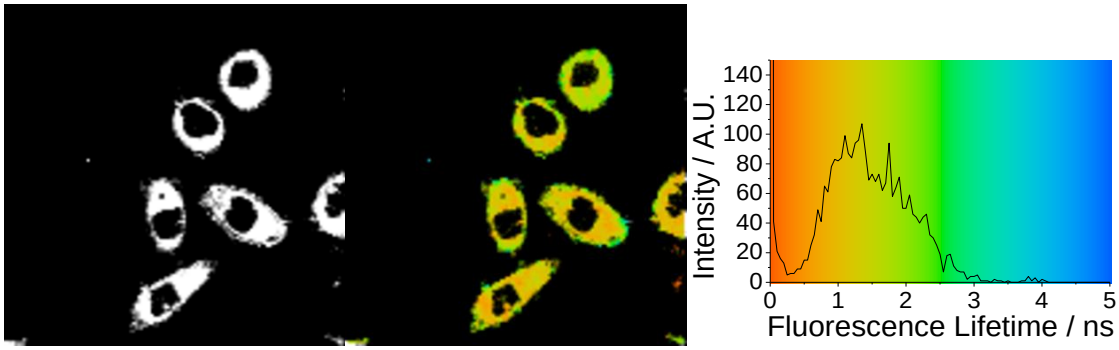

a) **b)** **c)**

Figure G.57. Two-photon fluorescence imaging of complex **1bB** reaction mixture, 100 μM, 1% DMSO**,** λ_{ex} = 910 nm, incubated in PC-3 cells for 20 minutes where a) is the fluorescence intensity profile, b) is the fluorescence lifetime map and c) is the corresponding lifetime distribution plot in ps.

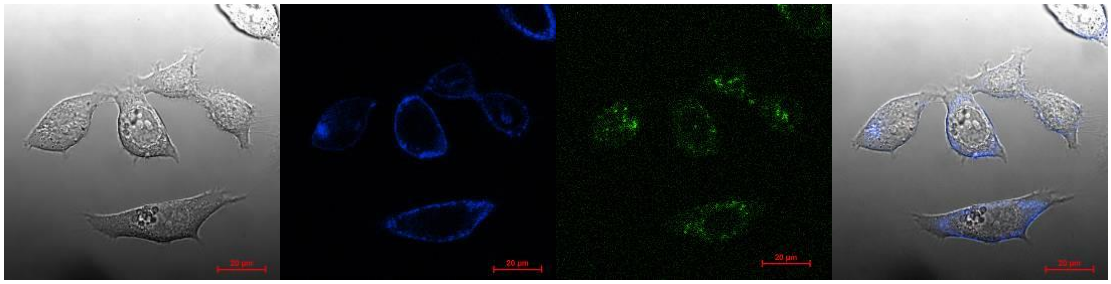

a) **b)** **c)** **d)**

Figure G.58. PC-3 cells stained with Alexa fluor plasma membrane dye, before (above) and after (below) addition of complex **1bB** reaction mixture, final concentration after addition was 100 μM, 1% DMSO. a) and e) represent the DIC channel, (b) and (f) correspond to excitation at 405 nm, (c) and (g) excitation at 488 nm and (d) and (h) are an overlay of the three channels.

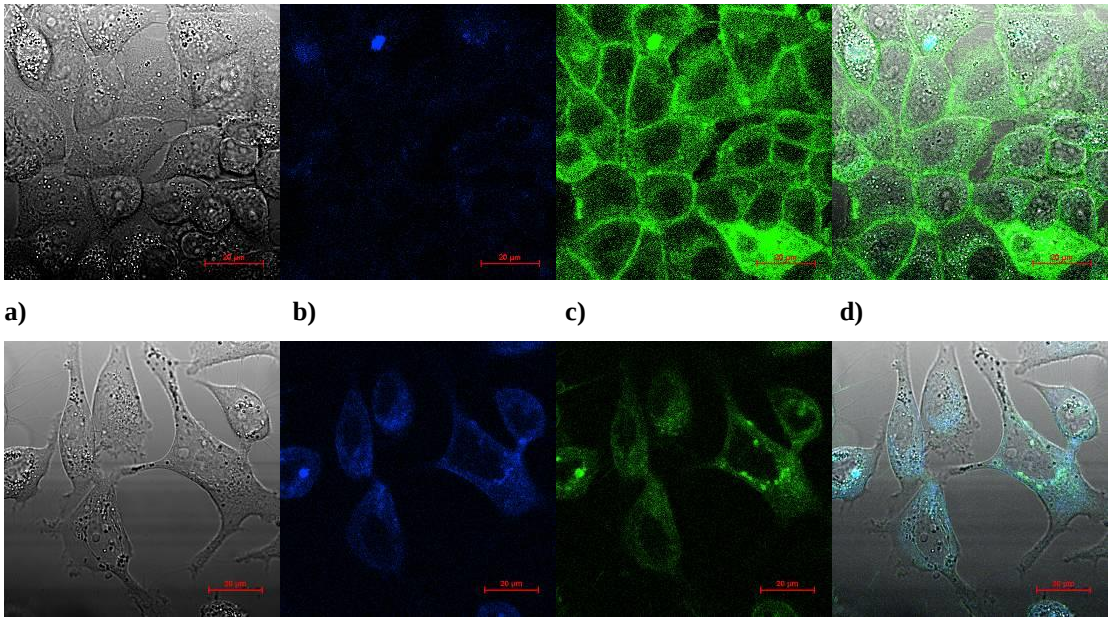

a) **b)** **c)** **d)**

e) **f)** **g)** **h)**

Figure G.59. MCF-7 cells incubated with complex **1bB** reaction mixture for 20 minutes at 100 μM, 1% DMSO before (above) and after (below) addition of Alexa Fluor plasma membrane stain. a) and e) represent the DIC channel, (b) and (f) correspond to excitation at 405 nm, (c) and (g) excitation at 488 nm and (d) and (h) are an overlay of the three channels. (e) – (h) were acquired within 5 minutes of addition and (b) shows background emission before addition of the Alexa Fluor plasma membrane stain. (Precipitation was observable since no cell washing occurred to enable the image to be taken as soon as the compound was added.) Scalebar: 20 μm.

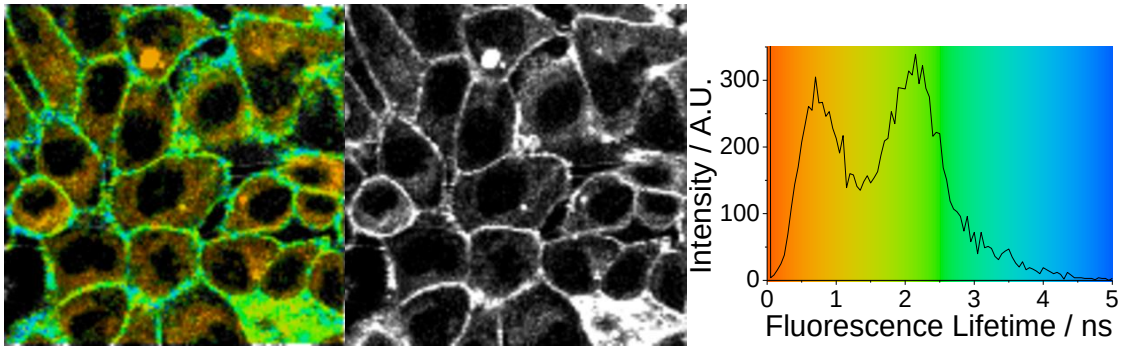

a) **b)** **c)**

Figure G.60. Two-photon fluorescence imaging of complex **1bB** reaction mixture, 100 μM, 1% DMSO**,** λ_{ex} = 910 nm, incubated in MCF-7 cells for 20 minutes where a) is the fluorescence intensity profile, b) is the fluorescence lifetime map and c) is the corresponding lifetime distribution plot in ns.

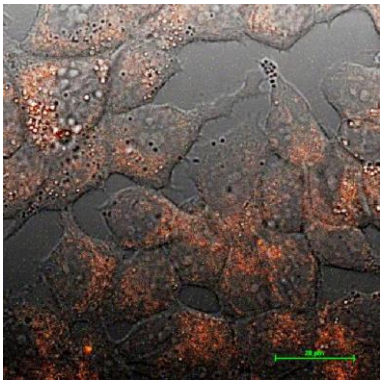

Figure G.61. Purified compound **1bB**, 5% 500 µM in MCF-7 Overlay of DIC image and λ_{ex} = 543 nm, scalebar = 20 µm.

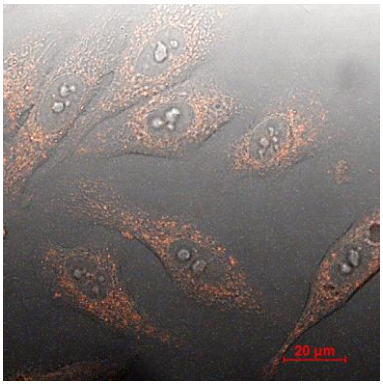

Figure G.62. Overlay image of purified compound **1dB** in PC-3 cells, 5% DMSO 500 µM, DIC and λ_{ex} = 543 nm channels, scalebar = 20 µm.

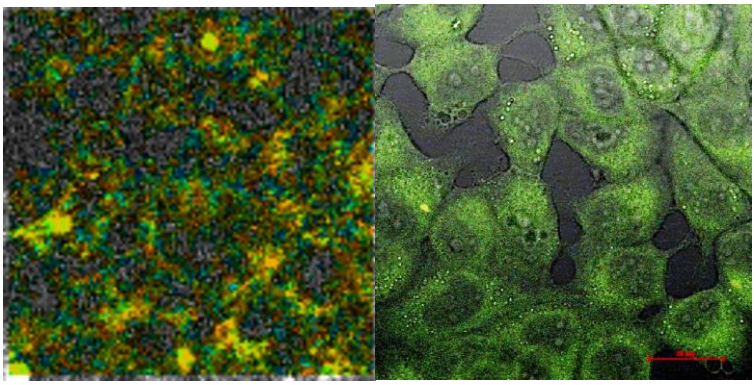

a) **b)**

Figure G.63. Purified compound **1bB**, 1% 100 µM in MCF-7 a) FLIM colour map where lifetime τ_1 = 690 ns, 0.615 FWHM, τ_2 = 0.984 ns, 0.944 ns FWHM, range of FLIM image is 0 to 5 ns, χ^2 = 1.08 where λ_{ex} = 810 nm and b) Overlay of DIC image and λ_{ex} = 488 nm, scalebar = 20 µm.

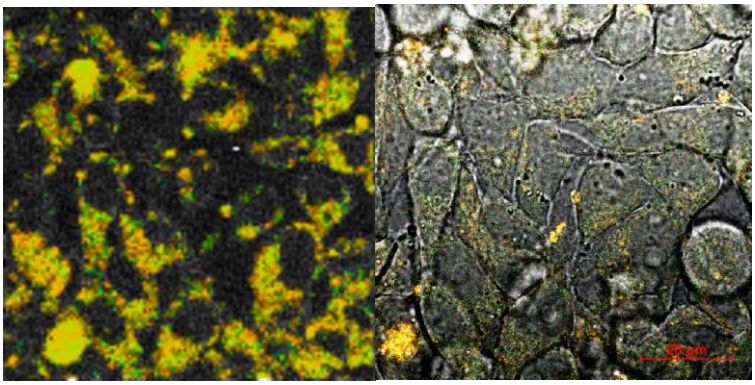

a) **b)**

Figure G.64. Purified compound **1bB**, 1% 100 µM in HeLa a) FLIM colour map where lifetime is 0.872 ns ± 0.490 ns FWHM, range of FLIM image is 0 to 5 ns, χ^2 = 1.15 where λ_{ex} = 810 nm and b) Overlay of DIC image and λ_{ex} = 488 nm, scalebar = 20 µm. 1 component

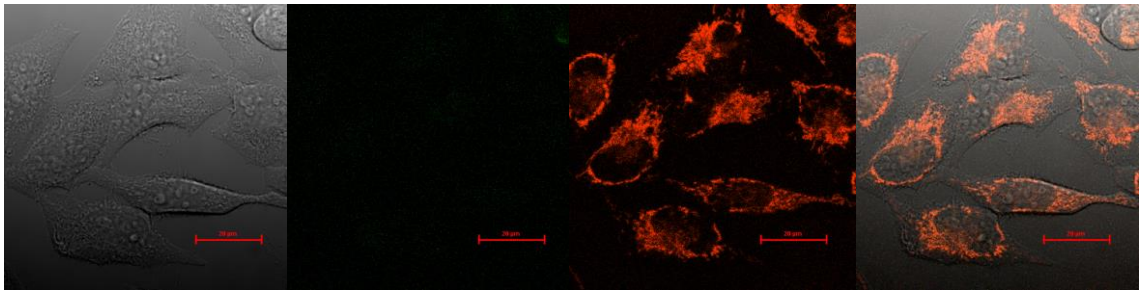

a) **b)** **c)** **d)**

Figure G.65. (a-d) Control experiments in HeLa incubation time 30 min: (a) DIC image, b) ex 488 nm, emission 516-530 nm, c) Mitotracker stain: ex 543 nm, em 605-675 nm, d) overlay (a-c).

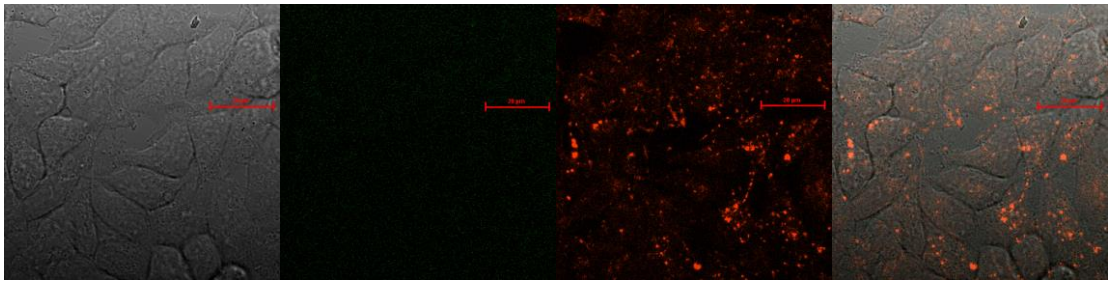

a) **b)** **c)** **d)**

Figure G.66. (a-d) Control experiments in HeLa incubation time 60 min: (a) DIC image, b) ex 488 nm, emission 516-530 nm, c) Lysotracker stain: ex 543 nm, em 605-675 nm, d) overlay (a-c).

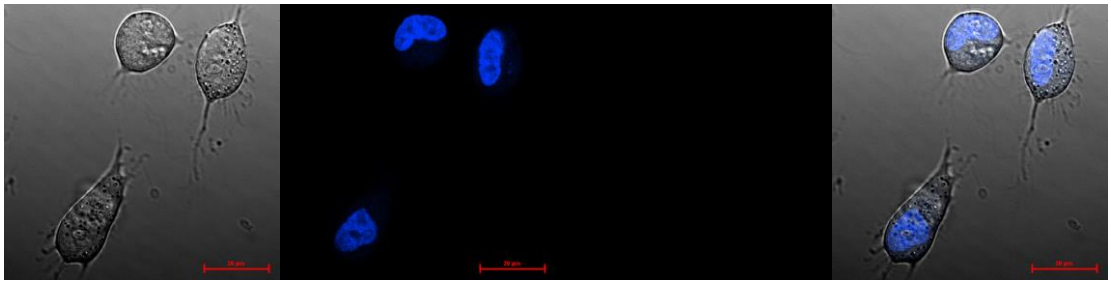

a) **b)** **c)** **d)**

Figure G.67. Single-photon confocal microscopy images of Hoechst in HeLa, (a) DIC image, (b) excitation at 405 nm emission at 451 (c) excitation at 488 nm, emission 516 nm, (c) an overlay of the previous three images.

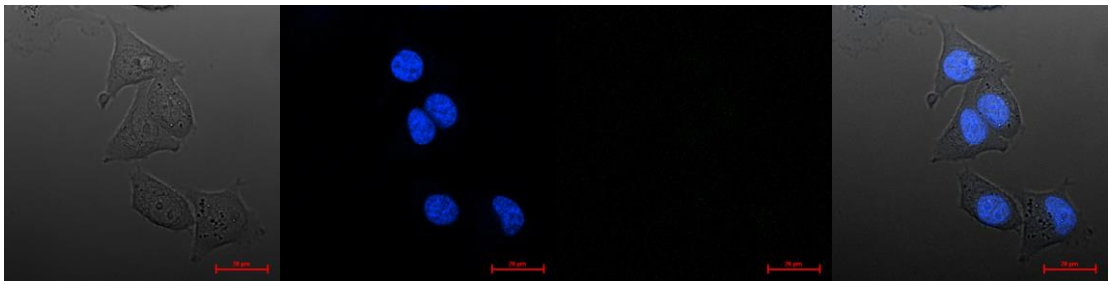

a) **b)** **c)** **d)**

Figure G.68. Single-photon confocal microscopy images of Hoechst in PC-3, (a) DIC image, (b) excitation at 405 nm emission at 451 (c) excitation at 488 nm, emission 516 nm, (c) an overlay of the previous three images.

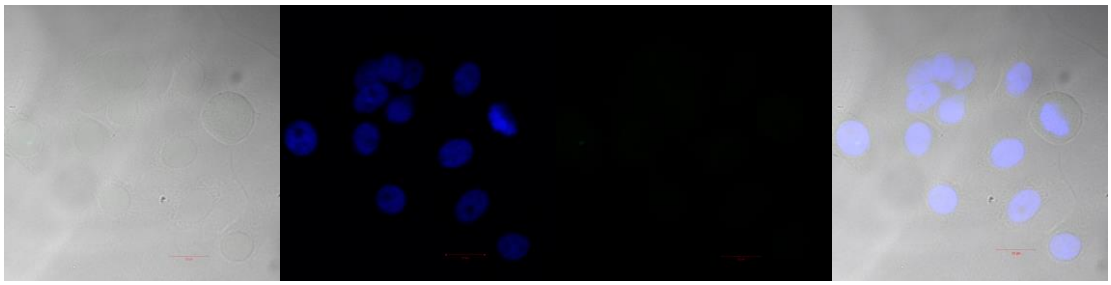

a) **b)** **c)** **d)**

Figure G.69. Single-photon confocal microscopy images of DAPI in HeLa (fixed cells), (a) DIC image, (b) excitation at 405 nm, emission 420-480 nm (c) excitation at 488 nm, emission >505 nm, (d) overlay of (a)+(b)+(c)

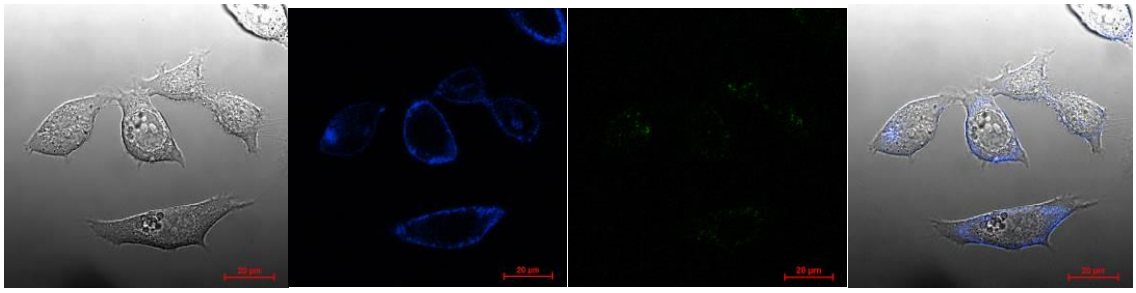

a) **b)** **c)** **d)**

Figure G.70. Single-photon confocal microscopy images of PC-3 cells stained with Alexa fluor plasma membrane dye, a) represent the DIC channel, (b) correspond to excitation at 405 nm, (c) excitation at 488 nm and (d) are an overlay of the three channels.

Appendix H. MTT MI_{50} cytotoxicity investigation

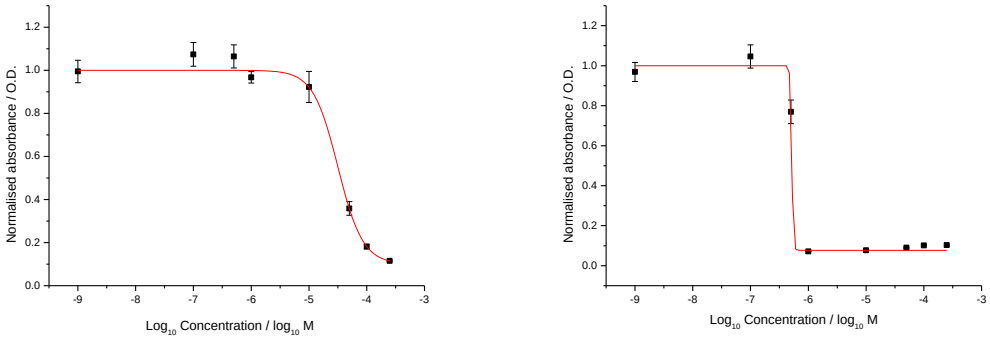

a) **b)**

Figure H.1. Scatter graph representing MI_{50} in HeLa cells a) of Cis-Platin b) of Cu[ATSM]

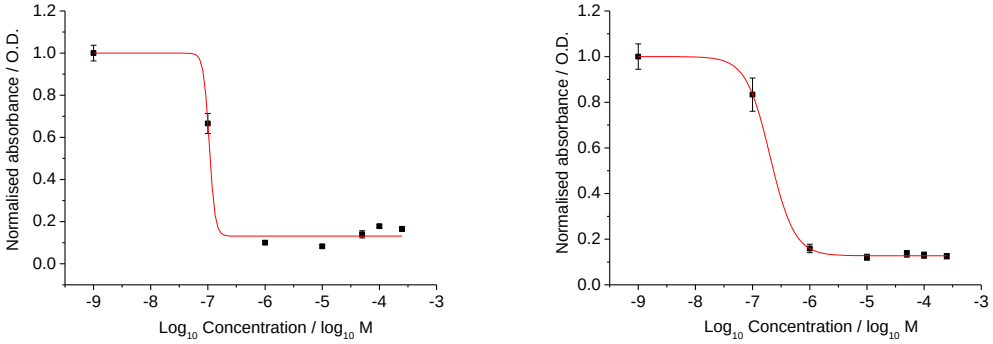

a) **b)**

Figure H.2. Scatter graph representing MI50 in HeLa cells a) of **ia** b) of **id**

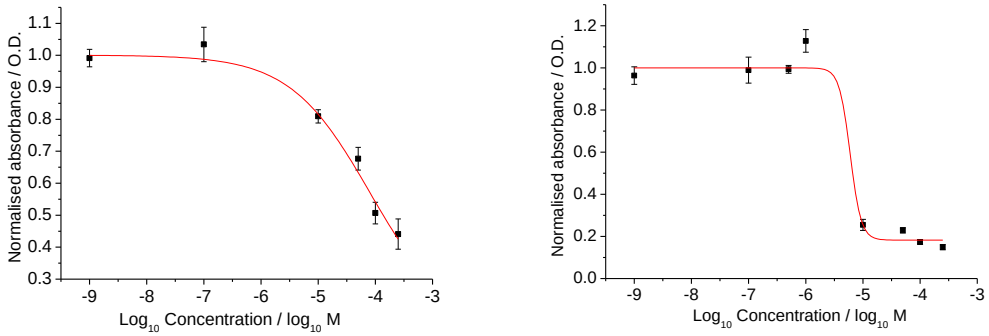

a) **b)**

Figure H.3. Scatter graph representing MI_{50} in HeLa cells a) of **iib** b) of **iic**

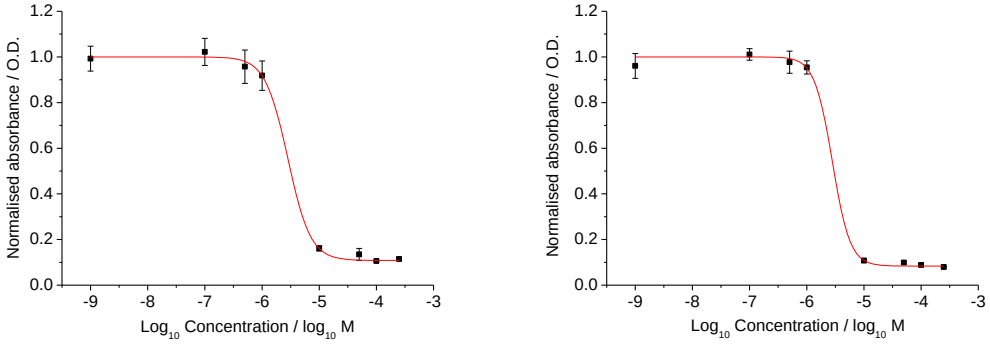

a) **b)**

Figure H.4. Scatter graph representing MI_{50} in HeLa cells a) of **1b** b) of **1c**

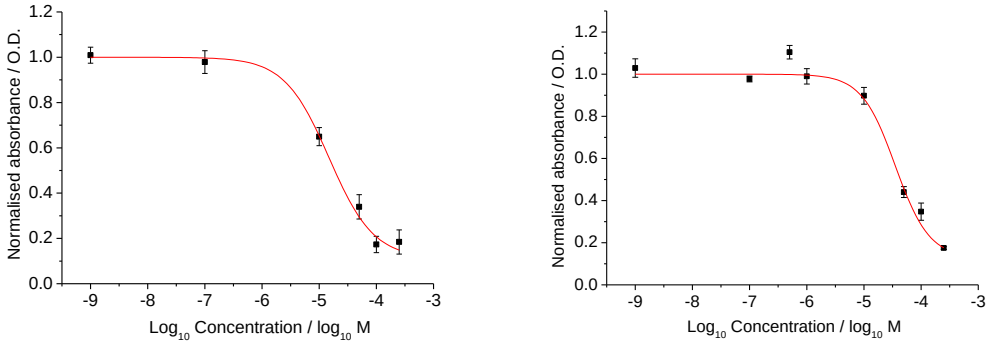

a) **b)**

Figure H.5. Scatter graph representing MI_{50} in HeLa cells a) of **2b** b) of **2c**

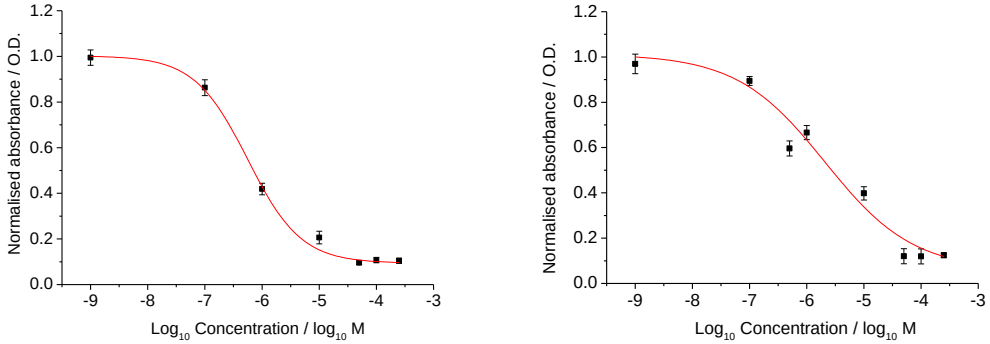

a) **b)**

Figure H.6. Scatter graph representing MI_{50} in HeLa cells a) of **3a** b) of **3b**

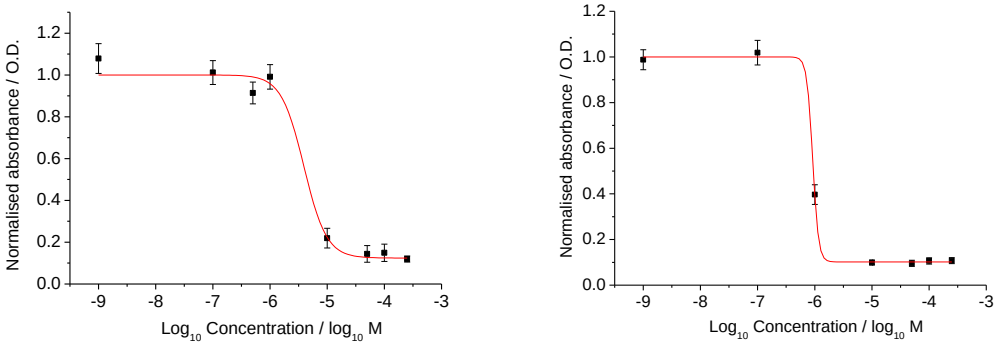

a) **b)**

Figure H.7. Scatter graph representing MI_{50} in HeLa cells a) of **3c** b) of **3d**

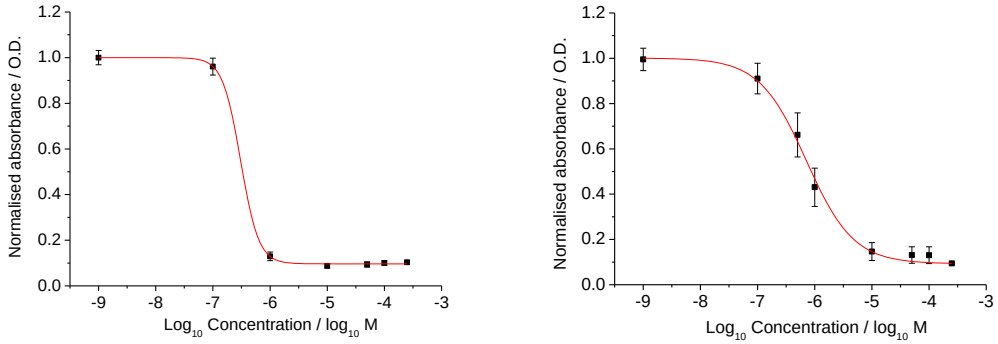

a) **b)**

Figure H.8. Scatter graph representing MI_{50} in HeLa cells a) of **4a** b) of **4b**

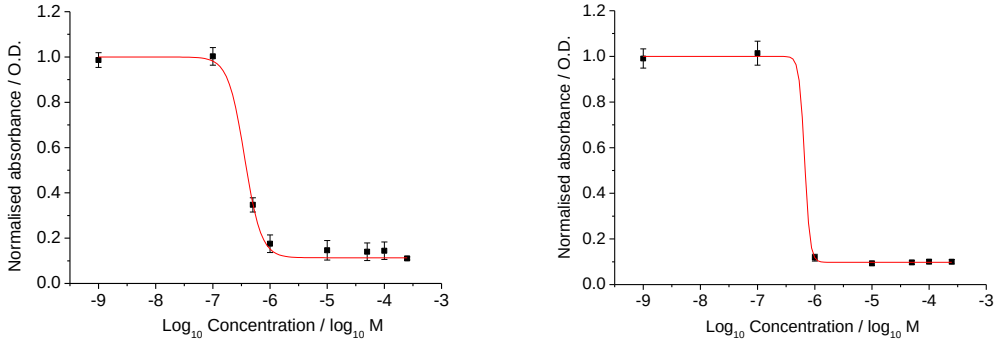

a) **b)**

Figure H.9. Scatter graph representing MI_{50} in HeLa cells a) of **4c** b) of **4d**

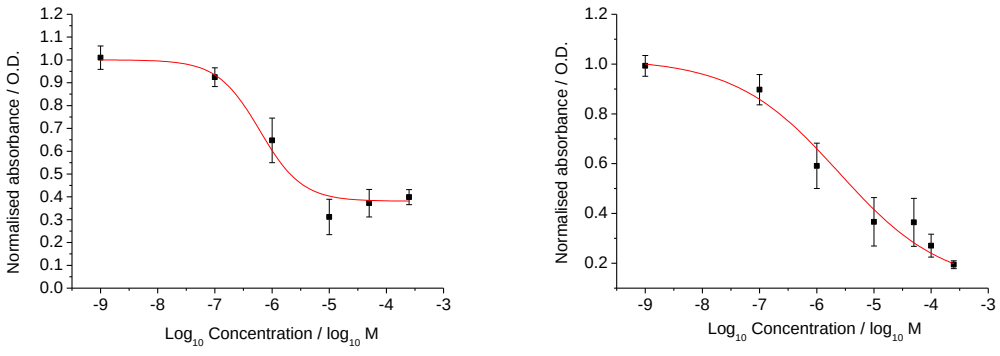

a) **b)**

Figure H.10. Scatter graph representing MI_{50} in FEK-4 cells a) of **ia** b) of **id**

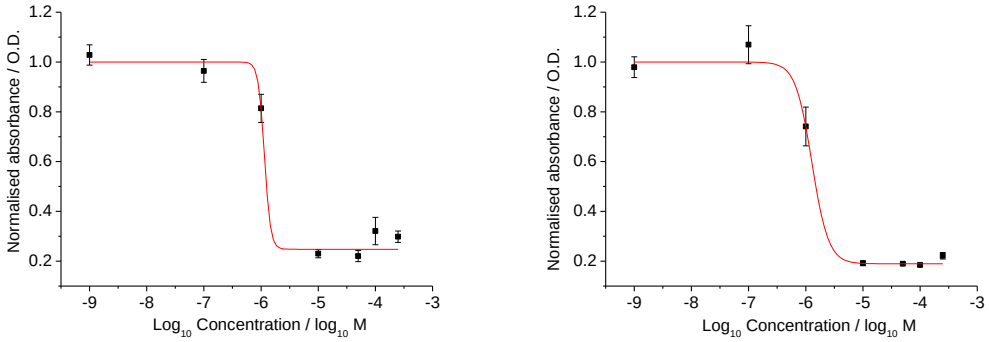

a) **b)**

Figure H.11. Scatter graph representing MI_{50} in FEK-4 cells a) of **3a** b) of **3d**

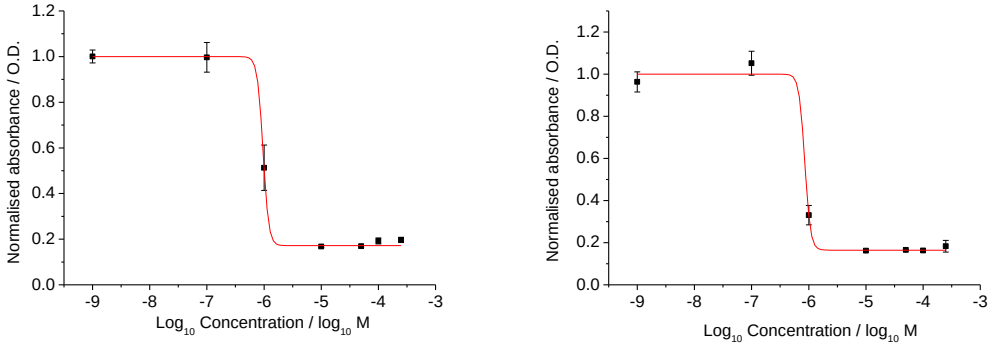

a) **b)**

Figure H.12. Scatter graph representing MI_{50} in FEK-4 cells a) of **4a** b) of **4d**

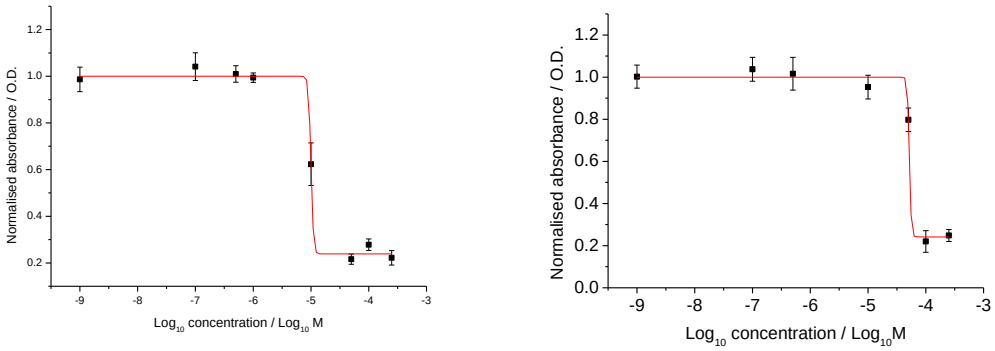

a) **b)**

Figure H.13. Scatter graph representing MI_{50} in HeLa cells a) of **1aN** b) of **1bN**

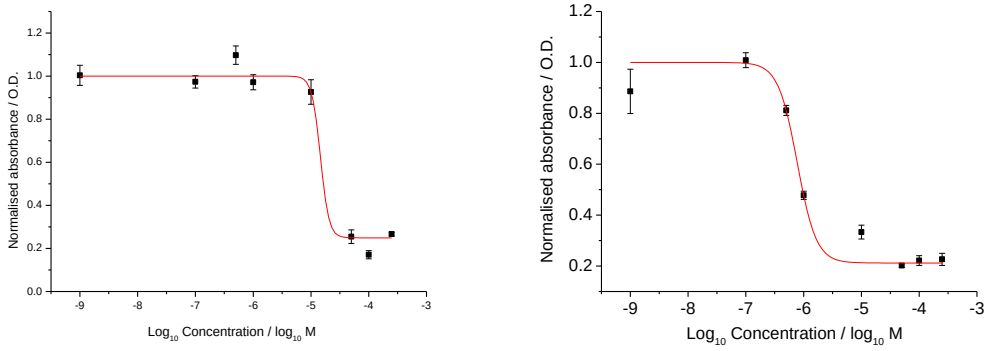

a) **b)**

Figure H.14 Scatter graph representing MI_{50} in HeLa cells a) of **1cN** b) of **1dN**

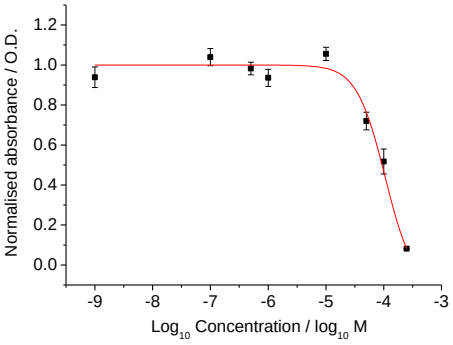

Figure H.15. Scatter graph representing MI_{50} in HeLa cells of **3bN**

Appendix I. Miscellaneous

Table I.1. Table representing the VT-NMR data of **3a**.

T	**3a'**	**3a**	K	ln(K)	1/T
299.9	1	1	1	0	0.003334
258.8	1	1.26	1.26	0.231112	0.003864
245.3	1	1.445	1.445	0.368109	0.004077
232.1	1	1.5	1.5	0.405465	0.004308

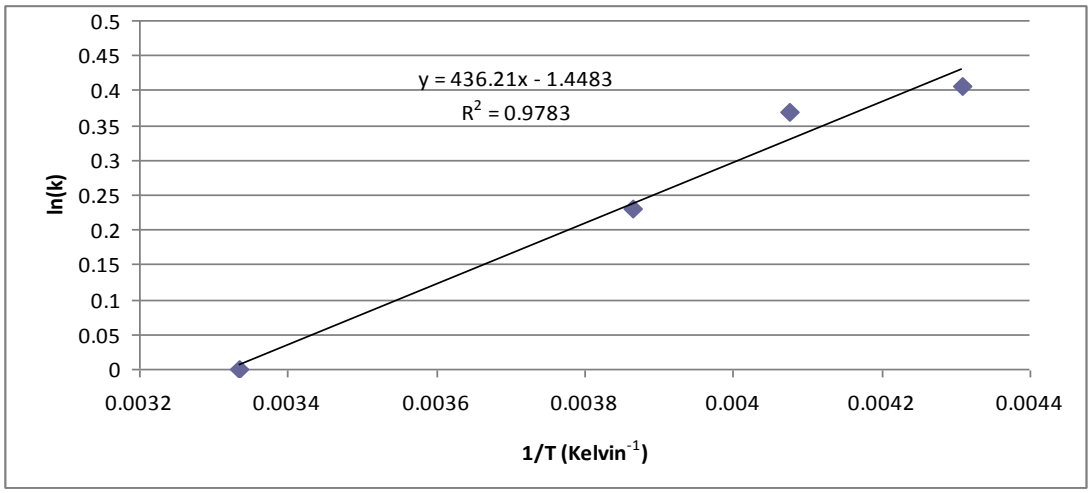

Figure I.1. Van't Hoff analysis of **3a** VT-NMR data.

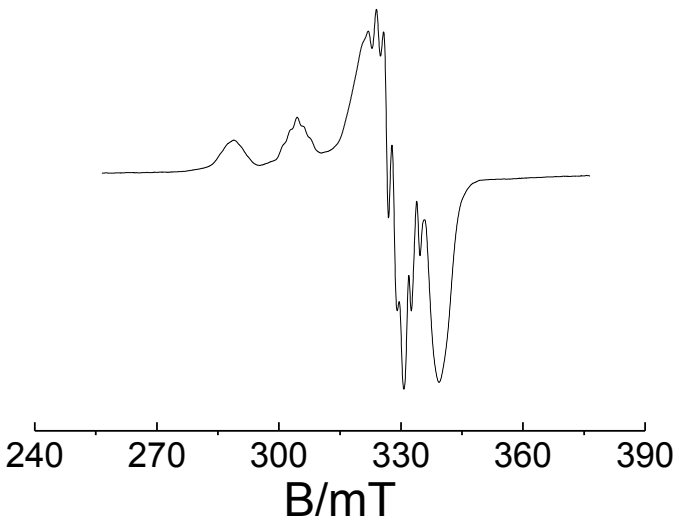

Figure I.2. Continuous wave electron paramagnetic resonance (cwEPR) spectrum at the X-band (9.450 GHz) of **2c**.

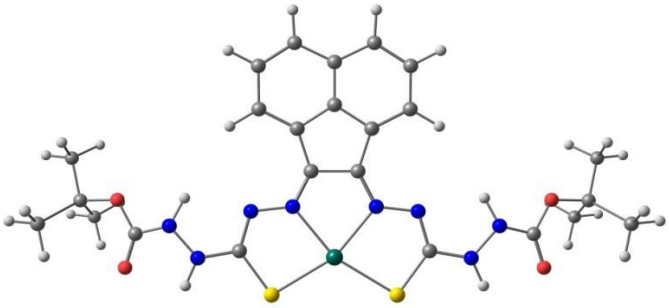

Figure I.3. DFT optimisation of a symmetric zinc t-boc protected amine bis(thiosemicarbazonato complex in the gas phase by B3LYP 6-31G(d,p). Where grey = carbon, white = hydrogen, blue = nitrogen, red = oxygen, green = zinc.

TD-DFT was calculated for the first 24 excited states using uB3LYP 6-31++ (d,p) methodology, of which excited state 13 had the most significant oscillator strength, f:

Excited State 1: 2.419-B 1.3461 eV 921.04 nm f=0.0001 <S**2>=1.212

139A ->140A	-0.31840
120B ->139B	-0.10709
122B ->139B	-0.17645
134B ->139B	0.11989
137B ->139B	0.36601
138B ->139B	0.80277
138B ->140B	0.22422

This state for optimization and/or second-order correction.

" Total Energy, E(TD-HF/TD-KS) = -3766.95660896"

Copying the excited state density for this state as the 1-particle RhoCI density.

Excited State 2: 3.190-B 1.4050 eV 882.46 nm f=0.0000 <S**2>=2.294

139A ->140A	-0.61794
137B ->139B	-0.21181
138B ->139B	-0.30491
138B ->140B	0.64846

Excited State 3: 2.011-B 2.0065 eV 617.91 nm f=0.0044 <S**2>=0.761

139A ->140A	-0.13068
120B ->139B	-0.12925
122B ->139B	-0.18300
126B ->139B	0.16620
134B ->139B	0.13649
137B ->139B	0.78692
137B ->140B	-0.10186
138B ->139B	-0.49426

Excited State 4: 2.985-A 2.0290 eV 611.07 nm f=0.0000 <S**2>=1.977

134A ->141A	0.16587
135A ->140A	0.12227
136A ->140A	0.13565
138A ->140A	0.65825
139A ->141A	-0.42794
134B ->141B	-0.16414
135B ->140B	-0.12621
136B ->140B	-0.16641
138B ->141B	0.45109

Excited State 5: 2.780-A 2.0489 eV 605.13 nm f=0.0001 <S**2>=1.683

134A ->141A	-0.14678
135A ->140A	-0.11089
136A ->140A	-0.19074
138A ->140A	0.73136
139A ->141A	0.38127
134B ->141B	0.14886
135B ->140B	0.10097
136B ->140B	0.11897
138B ->141B	-0.38966

Excited State 6: 2.008-B 2.1182 eV 585.32 nm f=0.1578 <S**2>=0.758

137A	->140A	0.13205
139A	->140A	0.63940
129B	->139B	-0.24638
137B	->139B	0.15213
137B	->140B	0.14280
138B	->140B	0.67095

Excited State 7: 2.014-A 2.1446 eV 578.12 nm f=0.0000 <S**2>=0.764

121B	->139B	0.38639
127B	->139B	0.29992
135B	->139B	-0.54211
136B	->139B	0.64503

Excited State 8: 2.005-B 2.3985 eV 516.93 nm f=0.0155 <S**2>=0.755

114B	->139B	-0.29409
124B	->139B	0.63691
128B	->139B	0.59834
129B	->139B	-0.30489

Excited State 9: 3.455-B 2.5144 eV 493.09 nm f=0.0004 <S**2>=2.734

137A	->140A	-0.66339
137B	->140B	0.70183

Excited State 10: 3.387-A 2.5192 eV 492.15 nm f=0.0001 <S**2>=2.619

134A	->141A	-0.16621
135A	->140A	0.11370
136A	->140A	0.60944
137A	->141A	0.11349
139A	->141A	0.18211
134B	->141B	0.16799
135B	->139B	-0.20003
136B	->139B	-0.24892
136B	->140B	-0.55172
137B	->141B	-0.10917
138B	->141B	-0.19821

Excited State 11: 2.134-A 2.6056 eV 475.84 nm f=0.0008 <S**2>=0.889

136A	->140A	0.21057
121B	->139B	-0.14225
135B	->139B	0.62814
135B	->140B	-0.10025
136B	->139B	0.66814
136B	->140B	-0.22286

Excited State 12: 2.012-B 2.6118 eV 474.71 nm f=0.0732 <S**2>=0.762

137A	->140A	0.13214
139A	->140A	0.14621
111B	->139B	0.17725
114B	->139B	0.41816
117B	->139B	-0.25326
118B	->139B	-0.30034
124B	->139B	0.50314
129B	->139B	0.52414
138B	->140B	0.13315

Excited State 13: 2.009-B 2.7221 eV 455.48 nm f=0.3843 <S**2>=0.759

137A	->140A	-0.69617
139A	->140A	0.17516
137B	->140B	-0.65166
138B	->140B	0.15402

Excited State 14: 2.024-A 2.8421 eV 436.24 nm f=0.1143 <S**2>=0.774

136A	->140A	0.29657
139A	->141A	0.62764
136B	->140B	0.34796
138B	->141B	0.60354

Excited State 15: 2.319-A 2.8883 eV 429.27 nm f=0.0189 <S**2>=1.094

135A	->140A	0.16389
121B	->139B	-0.55446
123B	->139B	-0.15587
127B	->139B	-0.32730
130B	->139B	0.11040
131B	->139B	-0.20337
133B	->139B	-0.16735
135B	->139B	-0.45639
135B	->140B	-0.28937
136B	->139B	0.22114
136B	->140B	0.18909
138B	->141B	-0.14996

Excited State 16: 2.130-A 2.9296 eV 423.21 nm f=0.0812 <S**2>=0.884

136A	->140A	0.47187
139A	->141A	-0.27165
121B	->139B	0.21841
127B	->139B	0.11444
130B	->139B	-0.12501
131B	->139B	0.16854
133B	->139B	0.15351
135B	->139B	0.12231
135B	->140B	-0.31493
136B	->140B	0.59438
138B	->141B	-0.29517

Excited State 17: 3.171-A 2.9353 eV 422.39 nm f=0.0106 <S**2>=2.264

134A	->141A	-0.15688
135A	->140A	0.63724
136A	->140A	-0.37834
139A	->141A	0.12868
121B	->139B	0.20344
127B	->139B	0.11085
134B	->141B	0.13880
135B	->139B	0.11120
135B	->140B	-0.50643

Excited State 18: 3.353-B 2.9412 eV 421.54 nm f=0.0000 <S**2>=2.561

134A	->140A	0.67766
134B	->139B	-0.38705
134B	->140B	-0.57894

Excited State 19: 2.020-A 2.9685 eV 417.67 nm f=0.0243 <S**2>=0.770

135A	->140A	0.16639
121B	->139B	-0.25131
127B	->139B	-0.16191
130B	->139B	-0.47586
131B	->139B	0.51837
133B	->139B	0.54790
135B	->139B	-0.12508
135B	->140B	0.11858

Excited State 20: 2.248-B 3.0099 eV 411.92 nm f=0.0000 <S**2>=1.014

129A	->140A	0.17886
134A	->140A	0.12314
138A	->141A	0.89200
134B	->139B	0.32223
134B	->140B	-0.10067

Excited State 21: 2.171-B 3.0340 eV 408.65 nm f=0.0003 <S**2>=0.928

134A	->140A	0.28532
138A	->141A	-0.35699
120B	->139B	-0.13108
122B	->139B	-0.13091
134B	->139B	0.79131
134B	->140B	-0.20281
137B	->139B	-0.25079

Excited State 22: 2.015-B 3.1599 eV 392.36 nm f=0.0012 <S**2>=0.765

120B	->139B	0.45938
122B	->139B	0.73800
122B	->140B	-0.11023
126B	->139B	-0.16282
134B	->139B	0.26844
137B	->139B	0.28482

Excited State 23:	3.461-A	3.2001 eV	387.44 nm	f=0.0014 <S**2>=2.744
	126A ->141A	-0.10820		
	134A ->141A	0.52780		
	135A ->140A	0.14162		
	136A ->140A	0.10122		
	137A ->141A	-0.20697		
	139A ->141A	0.32499		
	139A ->143A	-0.10461		
	126B ->141B	0.10960		
	134B ->141B	-0.52630		
	137B ->141B	0.16666		
	138B ->141B	-0.31435		
	138B ->143B	0.10626		

Excited State 24:	2.017-B	3.2349 eV	383.27 nm	f=0.1058 <S**2>=0.768
	134A ->140A	0.62921		
	134B ->140B	0.75113		

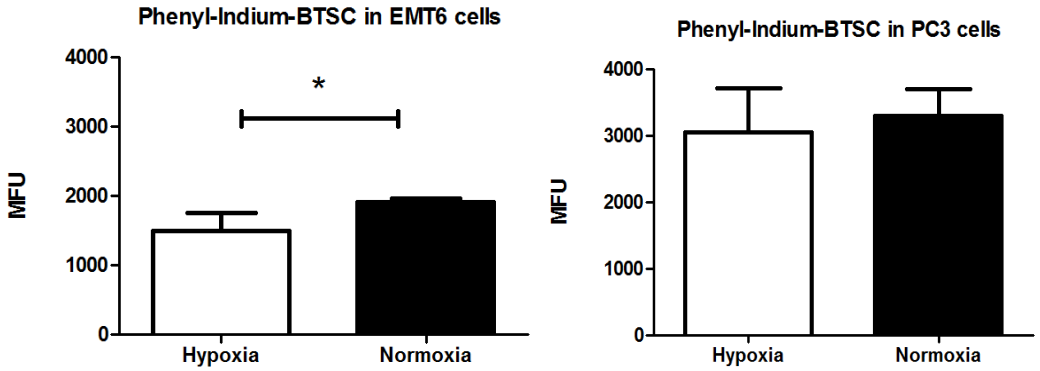

Figure I.4. Flow cytometry studies under normoxia and hypoxia of **4c (a)** in EMT6 and **(b)** in PC-3 cells.

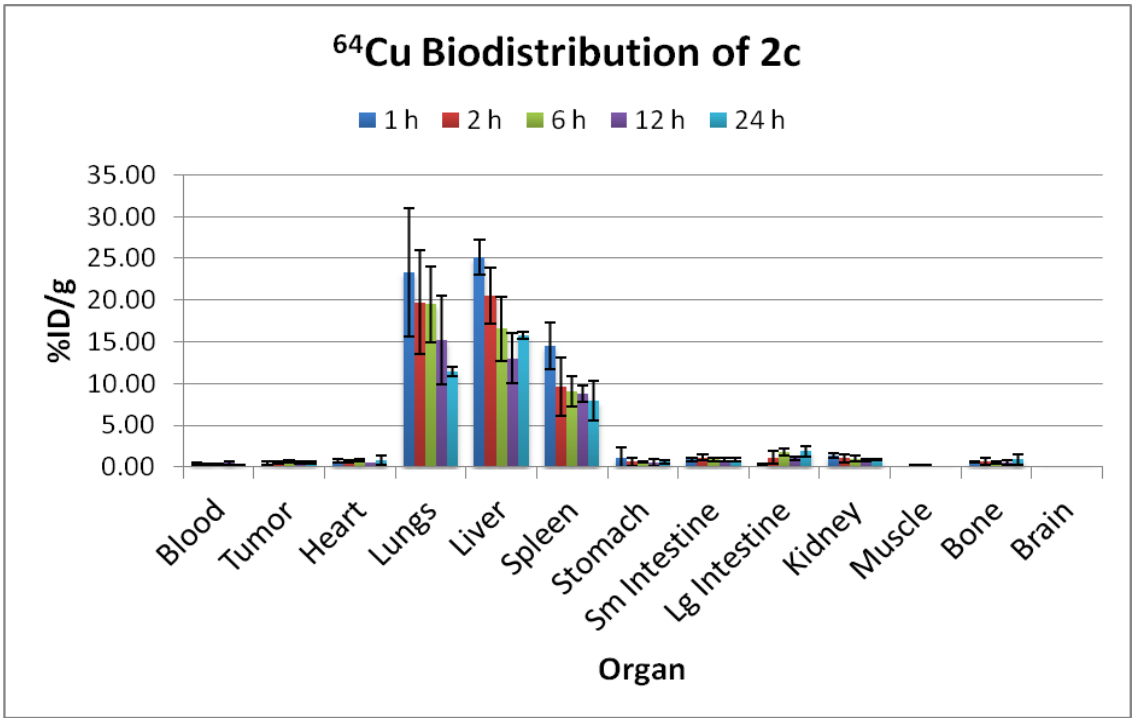

Figure I.5. Biodistribution study in nude mice, of **2c**.

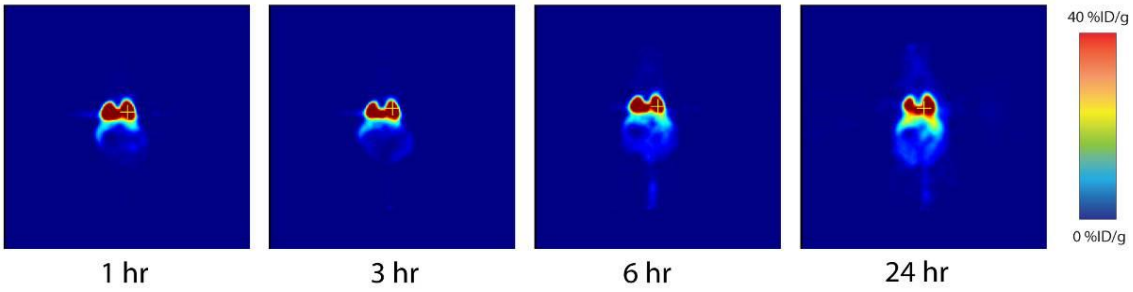

a) **b)** **c)** **d)**

Figure I.6. MicroPET images of in nude mice, **2c**, where (a), (b), (c) and (d) are at timepoints 1h, 3h, 6h, and 24 h respectively.